

N75-71754

**NASA**

CONFERENCE ON AIRCRAFT AERODYNAMICS

National Aeronautics and Space Administration

May 1966

REPRODUCED BY  
NATIONAL TECHNICAL  
INFORMATION SERVICE  
U.S. DEPARTMENT OF COMMERCE  
SPRINGFIELD, VA. 22161

55

## PREFACE

The papers presented at this conference contain information on recent research efforts of the National Aeronautics and Space Administration in the field of aircraft aerodynamics. The presentations were made according to subject matter, as follows: (1) Experimental Techniques, (2) Stability and Control, (3) Propulsion Aerodynamics, (4) Subsonic and Transonic Aerodynamics, (5) Supersonic Aerodynamics, and (6) Summary Reports (on V/STOL and hypersonic cruise aerodynamics).

Contributors include NASA staff members from the Ames, Flight, Langley, and Lewis Research Centers, as well as representatives of North American Aviation, Inc., Lockheed-California Co., and The Boeing Company.

## CONTENTS

PREFACE . . . . .	iii
-------------------	-----

### EXPERIMENTAL TECHNIQUES

1. DRAG MEASUREMENTS FROM DIFFERENT WIND TUNNELS . . . . . Ralph P. Bielat, Arvo A. Luoma, and James C. Daugherty	1
2. USE OF GRIT-TYPE BOUNDARY-LAYER-TRANSITION TRIPS ON WIND-TUNNEL MODELS . . . . . Albert L. Braslow, Raymond M. Hicks, and Roy V. Harris, Jr.	19
3. WIND-TUNNEL--FLIGHT CORRELATION OF SHOCK-INDUCED SEPARATED FLOW . Donald L. Loving	37
4. SOME RECENT DEVELOPMENTS OF DYNAMIC TECHNIQUES FOR WIND TUNNELS . Harleth G. Wiley, Robert A. Kilgore, and Jean Gilman, Jr.	45

### STABILITY AND CONTROL

5. SOME CONFIGURATION EFFECTS ON STATIC STABILITY OF AIRPLANES AT HIGH ANGLES OF ATTACK AND LOW SPEEDS . . . . . Edward J. Ray, Vernard E. Lockwood, and William P. Henderson	61
6. AERODYNAMIC-CENTER CONSIDERATIONS OF WINGS AND WING-BODY COMBINATIONS . . . . . John E. Lamar and William J. Alford, Jr.	75
7. RECENT AERODYNAMIC STUDIES APPLICABLE TO HIGH PERFORMANCE MANEUVERING AIRCRAFT . . . . . Robert T. Taylor	89
8. A SUMMARY OF NASA DATA RELATIVE TO EXTERNAL-STORE SEPARATION CHARACTERISTICS . . . . . Linwood W. McKinney and Edward C. Polhamus	105
9. STUDY OF LOW-SPEED FLYING QUALITIES OF VERY LARGE AIRPLANES BY MEANS OF AN IN-FLIGHT SIMULATOR . . . . . Robert O. Schade and Richard F. Vomaske	123

Preceding page blank

## PROPULSION AERODYNAMICS

ASSESSMENT OF THE EFFECTS OF INLET SPILLAGE, BYPASS, AND BLEED AIR ON THE PERFORMANCE OF SUPERSONIC CRUISE AIRPLANES . . . . .	139
Lowell E. Hasel, Robert L. Weirich, and Vincent R. Mascitti	
11. PERFORMANCE SUMMARY OF A TWO-DIMENSIONAL AND AN AXISYMMETRIC SUPERSONIC-INLET SYSTEM . . . . .	157
Norman E. Sorensen, Warren E. Anderson, Norman D. Wong, and Donald B. Smeltzer	
2. AN EVALUATION OF TRANSONIC SPILLAGE DRAG BASED ON TEST RESULTS FROM LARGE-SCALE INLET MODELS . . . . .	171
Warren E. Anderson, Martine W. Petersen, and Norman E. Sorensen	
13. INITIAL FLIGHT EXPERIENCE WITH THE XB-70 AIR-INDUCTION SYSTEM . . . . .	185
Ronald H. Smith and William G. Schweikhard	
4. A STUDY OF THE PROBLEMS OF CONTROL OF A SUPERSONIC INLET . . . . .	195
John J. Gawienowski and John L. Benson	
5. SUMMARY OF RESEARCH ON JET-EXIT INSTALLATIONS . . . . .	209
Blake W. Corson, Jr., and James W. Schmeer	
6. JET-EXIT AND AIRFRAME INTERFERENCE STUDIES ON TWIN-ENGINE-FUSELAGE AIRCRAFT INSTALLATIONS . . . . .	229
Jack F. Runckel	
17. STATIC-TEST RESULTS FROM EXHAUST NOZZLES WITH NOVEL FEATURES FOR SUPERSONIC-AIRCRAFT APPLICATIONS . . . . .	245
Fred W. Steffen and Donald L. Bresnahan	
8. WIND-TUNNEL STUDIES OF NACELLE INTERFERENCE DRAG AT HIGH SUBSONIC SPEEDS INCLUDING THE EFFECT OF POWERED JETS . . . . .	259
James C. Patterson, Jr.	

## SUBSONIC AND TRANSONIC AERODYNAMICS

9. GROUND EFFECTS RELATED TO LANDING OF AIRPLANES WITH LOW-ASPECT-RATIO WINGS . . . . .	271
William B. Kemp, Jr., Vernard E. Lockwood, and W. Pelham Phillips	
20. FLIGHT STUDIES OF GROUND EFFECTS ON AIRPLANES WITH LOW-ASPECT-RATIO WINGS . . . . .	285
L. Stewart Rolls, C. Thomas Snyder, and William G. Schweikhard	

21. EXPERIMENTAL AND THEORETICAL STUDIES OF WING-LEADING-EDGE VORTEX FLOW . . . . .	297
Mark W. Kelly, Victor R. Corsiglia, and David G. Koenig	
22. SOME RECENT STUDIES OF HIGH-LIFT FLAPS ON COMPOSITE WING PLANFORMS . . . . .	313
Alexander D. Hammond	
23. STUDIES OF VARIOUS FACTORS AFFECTING DRAG DUE TO LIFT AT SUBSONIC SPEEDS . . . . .	327
William P. Henderson	
4. SUMMARY OF EXTERNAL-STORE DRAG . . . . .	341
Barrett L. Shrout and Thomas C. Kelly	
25. STATUS OF RESEARCH ON A SUPERCRITICAL WING . . . . .	367
Richard T. Whitcomb and James A. Blackwell, Jr.	

## SUPERSONIC AERODYNAMICS

26. CURRENT METHODS FOR PREDICTION AND MINIMIZATION OF LIFT-INDUCED DRAG AT SUPERSONIC SPEEDS . . . . .	383
Harry W. Carlson and F. Edward McLean	
7. A NUMERICAL TECHNIQUE FOR ANALYSIS OF WAVE DRAG AT LIFTING CONDITIONS . . . . .	399
Roy V. Harris, Jr.	
28. AN INTEGRATED APPROACH TO THE ANALYSIS AND DESIGN OF WINGS AND WING-BODY COMBINATIONS IN SUPERSONIC FLOW . . . . .	409
Ralph L. Carmichael and Frank A. Woodward	
9. SONIC-BOOM CHARACTERISTICS OF PROPOSED SUPERSONIC AND HYPERSONIC AIRPLANES . . . . .	421
F. Edward McLean, Harry W. Carlson, and Lynn W. Hunton	
30. CONSIDERATIONS REGARDING THE EVALUATION AND REDUCTION OF SUPERSONIC SKIN FRICTION . . . . .	437
John B. Peterson, Jr., and William J. Monta	
11. THE PROBLEM OF ROUGHNESS DRAG AT SUPERSONIC SPEEDS . . . . .	455
K. R. Czarnecki	
32. EFFECTS OF PLANFORM VARIATIONS ON THE AERODYNAMIC CHARACTERISTICS OF LOW-ASPECT-RATIO WINGS WITH CRANKED LEADING EDGES . . . . .	469
Edward J. Hopkins, Raymond M. Hicks, and Ralph L. Carmichael	

33. RECENT RESULTS ON THE AERODYNAMICS OF WINGED MISSILES . . . . . 485  
M. Leroy Spearman and William A. Corlett

SUMMARY REPORTS

34. SOME HIGHLIGHTS OF RECENT V/STOL AERODYNAMICS RESEARCH . . . . . 497  
John P. Campbell

35. A REVIEW OF HYPERSONIC CRUISE VEHICLES . . . . . 523  
David E. Fetterman, Charles H. McLellan, L. Robert Jackson,  
Beverly Z. Henry, Jr., and John R. Henry

UNCLASSIFIED

## 1. DRAG MEASUREMENTS FROM DIFFERENT WIND TUNNELS

By Ralph P. Bielat, Arvo A. Luoma,  
NASA Langley Research Center

and James C. Daugherty  
NASA Ames Research Center

## SUMMARY

This paper examines the question: How good a correlation can be obtained from drag measurements made in different wind-tunnel facilities? The correlations considered pertain only to drag data which were obtained on the same models from investigations in various wind tunnels where special efforts were made to duplicate the exact test conditions.

Drag data obtained for the same model in different wind tunnels at subsonic, transonic, and supersonic speeds agreed within 3 percent, provided the tests were made in accordance with the rules and techniques developed for wind-tunnel tests at these speeds. In the application of these rules and techniques, proper consideration must be given to model support systems, transition strips, tunnel wall effects, test limitations, and so forth. Large-scale models, which permit high values of model Reynolds numbers, can be tested at subsonic speeds in relatively small transonic tunnels, and a high level of confidence can be placed in the results of such tests. Good correlation exists between model data obtained in the wind tunnel and by the rocket technique where the tunnel constraints are not present.

## INTRODUCTION

An accurate assessment of the drag characteristics is essential in the design of a new airplane. To a large extent, this assessment is based upon the results of extensive wind-tunnel investigations of scaled models of the airplane. Because the conception of the airplane is relatively fluid during the early design stages, the wind-tunnel models of the airplane will usually differ in numerous details, and often in scale, from each other and will invariably differ from the "final" conception of the airplane. The correlation of the drag data of such models, consequently, can become a difficult problem, particularly when the tests are made in different tunnels. Unsatisfactory correlation in drag measurements often can be reconciled when proper consideration is given to differences in models, test conditions, test techniques, test limitations, data acquisition, data accuracy, data corrections, and so forth.

~~CONFIDENTIAL~~

UNCLASSIFIED

This paper examines the question: How good a correlation can be obtained from drag measurements made in different wind-tunnel facilities? The correlations considered pertain only to drag data which were obtained on the same models from investigations in various wind tunnels where special efforts were made to duplicate the exact test conditions. First, some of the testing techniques required to obtain reliable aerodynamic data at transonic speeds are discussed, and then comparisons of the experimental drag measurements from different transonic wind tunnels are shown. Second, some of the problems associated with testing large models at subsonic speeds in a transonic wind tunnel are considered, and then some experimental results from two transonic tunnels are compared. Third, data obtained in the wind tunnel are compared with data obtained by the rocket technique on an identical model. Last, tests conducted at supersonic speeds are discussed and then comparative data from different tunnels are presented. No attempt is made in this paper to correlate wind-tunnel results with full-scale flight results or to extend wind-tunnel results to full-scale Reynolds numbers.

#### SYMBOLS

$c$	chord of airfoil section, in.
$C_D$	drag coefficient
$\Delta C_D$	rise in drag coefficient above minimum value
$\frac{\Delta C_D}{(\Delta C_L)^2}$	drag-rise factor
$C_{D,b}$	base drag coefficient
$C_{D,min}$	minimum value of drag coefficient
$C_L$	lift coefficient
$\Delta C_L$	change in lift coefficient from value corresponding to minimum drag coefficient
$l_s$	axial distance required for model nose shock to traverse the supersonic flow to test-section boundary and reflect back to test-section center line, in.
$M$	Mach number
$R$	Reynolds number

t maximum thickness of airfoil section, in.  
x axial distance from model base to mean location of tunnel normal shock, in.  
 $\alpha$  angle of attack, deg  
 $\Lambda$  sweep angle of wing, deg

## DISCUSSION

### Testing Techniques at Transonic Speeds

Model size in relation to tunnel size is one of the critical problems to be considered when testing at transonic and supersonic speeds; the significance of this relationship is illustrated in figure 1. In order to assure interference-free data, the model must be sufficiently short to avoid impingement of boundary-reflected disturbances from the tunnel walls on the model, or even close to the base of the model, as indicated by the schematic drawing in the figure. In figure 1 the approximate shock-reflection distance  $l_s$  in inches is plotted against free-stream Mach number for airplane-type configurations for three NASA tunnels differing in size. The shock-reflection distances for the Langley 8-foot transonic pressure tunnel were experimentally determined for a wing-body model of high fineness ratio. A discussion of the Langley 8-foot transonic pressure tunnel results, including the applicability of the results to other models differing in size or shape, is given in reference 1. The approximate shock-reflection distances shown in the figure for the other two tunnels are estimates based on the Langley 8-foot transonic pressure tunnel results and the relative sizes of the tunnels.

The primary purpose of this figure is to illustrate the fact, which is well known to transonic and supersonic wind-tunnel engineers, that when the same model is tested in a larger wind tunnel interference-free data can be obtained at lower supersonic Mach numbers. As an example, an investigation was made in the Langley 8-foot transonic pressure tunnel on a 43-inch-long model, and it was found that a supersonic Mach number of 1.2 was required before interference-free supersonic data were obtained. Figure 1 indicates that tests of the same model in the larger wind tunnels would give interference-free data at a Mach number of approximately 1.1 in the Ames 11-foot transonic tunnel and approximately 1.07 in the Langley 16-foot transonic tunnel.

Each combination of test model and wind tunnel, however, offers a somewhat different problem with regard to the effects of boundary-reflected disturbances. Therefore, if a precise determination of the shock-reflection distances and the minimum supersonic Mach number for interference-free testing is needed for a specific model in a given wind tunnel, then actual experimental interference studies are necessary at the supersonic Mach numbers.

Figure 2 illustrates the effects of boundary-reflected disturbances on drag when the same 43-inch-long model is tested in two different-size wind tunnels at Mach numbers less than the minimums shown in figure 1. Drag coefficient is plotted as a function of Mach number in figure 2. It should be pointed out that the zero for the drag scale has been suppressed in this figure and also in several of the figures to follow. Note that the effect of boundary-reflected disturbances on drag (affected test points shown by the solid symbols) extends over a substantially larger Mach number range in the smaller wind tunnel than in the larger wind tunnel. The solid symbols in the figure show data in a Mach number range in which data normally would not be obtained in either tunnel in tests of models of this size.

Figure 3 illustrates the problems associated with testing the model in the vicinity of the tunnel normal shock. (See ref. 2.) Shown plotted in this specific example is the drag coefficient as a function of the distance of the model base from the tunnel normal-shock position, where  $x = 0$  represents the model base in the normal shock as indicated by the dashed model lines. These data are for a free-stream Mach number of 1.2. Although the data were obtained in a solid-throat tunnel, the general results are applicable to any transonic or supersonic tunnel. It is quite obvious that the positive pressures associated with the tunnel normal shock can produce very significant drag reductions as the base of the model approaches the shock location, and tests of the model generally should not be made under conditions where the data can be affected by the proximity of the tunnel normal shock.

Most models are supported by stings in the wind tunnel. Such stings must be carefully designed if valid drag information is to be obtained, especially in transonic testing. A general recommendation for transonic testing is a sting which has a small ratio of sting diameter to model-base diameter, which has a constant-diameter section approximately 5 model-base diameters long, and which has a sting flare angle (total) no greater than approximately  $6^\circ$ . Some insight into the nature and magnitude of sting interference can be found in references 3 to 7.

Some specific examples of the effects of support interference at transonic speeds other than the interference caused by the usual sting supports will now be discussed. Figure 4 illustrates the effect of support-strut interference on the drag coefficient of a missile configuration at  $0^\circ$  angle of attack. (See ref. 8.) The strut was used to stiffen the sting in a lateral plane, especially at angle of attack. The strut had a chord of 3 inches and a thickness ratio of 21 percent, and was located 4 base diameters downstream of the model. The upper curves represent the total drag coefficient and the lower curves represent the forebody drag coefficient. The drag coefficients for this figure are based on body cross-sectional area. These data show that the presence of the strut caused reductions in the total drag coefficient, especially near  $M = 1.0$ . However, these reductions in the drag coefficient are due only to increases in the base pressure caused by the presence of the strut, since the forebody drag coefficients are unaffected by the presence of the strut.

Figure 5 illustrates the effect of support interference on drag for an airplane configuration which has both base and boattailing areas subject to the

influence of the pressure field of the support. The upper sketch shows an auxiliary support system which was used to obtain combined pitch and sideslip angles of the model. The middle sketch schematically illustrates a mockup of the above auxiliary support system. This mockup consisted of a dummy support, as shown. Tests were made with the dummy support on and off (as indicated by the middle and bottom sketches) in order to determine the interference of the auxiliary support. Minimum drag coefficient is plotted as a function of Mach number; in this case, the drag has not been corrected for base drag. Note the drag reductions for Mach numbers less than 1.2, and particularly the large reductions at speeds near sonic, caused by the positive pressure field with the dummy support on. Figure 6 shows the same comparison as in figure 5 except that in this case the minimum drag values have been corrected for base drag. Again note the effect of the dummy support on the drag. The drag reduction is less than that shown in figure 5, but it is still substantial near a Mach number of 1.0 because of the model boattailing.

#### Models and Test Conditions for Comparisons

Some of the drag measurements from different wind-tunnel facilities are compared next. In each of the comparisons, the same physical model was tested in two or more wind tunnels, and usually the same sting and the same internal balance were used. In each comparison the model was tested in the different wind tunnels at the same test conditions, except in one or two cases where the Reynolds numbers were somewhat different. Transition was fixed according to the methods described in reference 9 in order to insure a turbulent boundary layer on the models. A discussion of the use of grit-type boundary-layer transition strips on wind-tunnel models is given by Braslow, Hicks, and Harris in paper no. 2.

#### Comparisons at Transonic Speeds

The first of the comparisons shows the variation of the minimum drag coefficient with Mach number for a variable-sweep configuration (fig. 7). Sweep angles of  $26^\circ$  and  $72.5^\circ$  are shown. Air flowed through the ducts, and the drag has been corrected for the internal drag as well as for the base drag so that the drag coefficient is the minimum net external drag. The tests were conducted in three NASA facilities: the Ames 11-foot transonic tunnel and the Langley 8-foot and 16-foot transonic tunnels. The data shown are for a constant Reynolds number of  $2.5 \times 10^6$  per foot. The data from the Langley 16-foot transonic tunnel were obtained at somewhat different Reynolds numbers, however, and these data have been corrected for the difference in skin friction between the test Reynolds number and the constant Reynolds number value of  $2.5 \times 10^6$  per foot. Attention is again called to the fact that the origin for the drag scale is not shown in the figure. Note the correlation which has been obtained in the three facilities throughout the Mach number range shown. For example, the spread in the faired curves amounts at most to about 5 counts of drag (where one count of drag is equivalent to a drag coefficient of 0.0001), or 2 to 3 percent, in the subsonic Mach number range and about 2 or 3 counts of drag, or 1 percent, at supersonic speeds.

Figure 8 shows the variation with Mach number of the minimum drag coefficient and figure 9 shows the drag-due-to-lift factor (for lift coefficients up to about 0.3) for two wing sweep angles for a V/STOL configuration. The wind-tunnel tests were made in the NASA Langley 8-foot transonic pressure tunnel (ref. 10) and in the National Aero- and Astronautical Research Institute (NLR) 6.55- by 5.25-foot subsonic-transonic pressure wind tunnel, Amsterdam, Netherlands. As with the previous model (fig. 7), air flowed through the ducts and the drag has been corrected for the internal drag and base drag. The Reynolds numbers in the two facilities were approximately the same. Again, note the correlation which exists in both the minimum drag coefficient and drag-due-to-lift factor in both facilities. At most, the difference in the drag data amounts to about 7 counts of drag, or 3 percent.

The data presented in figures 10 and 11 are for a delta-wing configuration. Figure 10 shows the minimum drag coefficient and figure 11 shows the drag-due-to-lift factor (for lift coefficients up to about 0.3) plotted against Mach number. The wind-tunnel tests were made in the NASA Langley 8-foot transonic pressure tunnel and in the Cornell Aeronautical Laboratory 8-foot transonic wind tunnel for a constant Reynolds number of  $2.5 \times 10^6$  per foot. The maximum spread between the faired drag curves amounts to 4 counts of drag, or 3 percent.

#### Large Models at Subsonic Speeds

In wind-tunnel tests, a large model is desirable since the model Reynolds numbers will be higher. At transonic and supersonic speeds the model size is usually limited by the problem of boundary-reflected disturbances existing at Mach numbers greater than 1. This constraint on model size does not exist, of course, when the tests are to be made only at subsonic speeds. Since the wind tunnel with slotted or porous walls has greatly reduced or eliminated the solid-blockage interference, a substantially larger model can be used for subsonic tests in a transonic (slotted) wind tunnel than can be used for subsonic tests in a comparable closed-throat tunnel. However, the problem of the downwash due to the tunnel-boundary interference on the lift of a large model is still to be considered. This type of interference is a function of the cross-sectional shape of the tunnel; the type, distribution, and amount of tunnel wall ventilation; the ratio of wing span to tunnel width; the ratio of wing area to tunnel cross-sectional area; and the lift coefficient. A recent theoretical analysis of tunnel-boundary interference (ref. 11) includes calculations of the spanwise variation of the interference and the effect of sweepback. Theory indicates that for a large model in the Langley 8-foot transonic pressure tunnel, the interference of the tunnel walls on the average induced flow is small, with the spanwise variation from wing root to wing tip being approximately twice the average value.

Figures 12 and 13 show comparative drag data at high subsonic Mach numbers on the same 5-foot-span model of a large subsonic transport. The model was investigated in the Langley 8-foot transonic pressure tunnel and in the considerably larger Langley 16-foot transonic tunnel. The Reynolds number was the same in both tests. The drag and lift data shown are the mean results obtained from tests of the model upright and inverted. The data from both tunnels have been corrected for the internal drag of the four engines, for base drag, for

buoyancy, and for the average downwash due to the tunnel-boundary interference on lift. This interference at a lift coefficient of 0.5, for example, was estimated to be an average downflow to the model of only  $0.05^\circ$  in the Langley 8-foot transonic pressure tunnel and  $0.01^\circ$  in the Langley 16-foot transonic tunnel. The effect of the interference correction on drag coefficient at a lift coefficient of 0.5 was to reduce the drag coefficient by 0.0005 in the 8-foot tunnel tests and by 0.0001 in the 16-foot tunnel tests.

Figure 12 presents the drag polar at a Mach number of 0.775, which corresponds to the approximate cruise Mach number. The Reynolds number was  $3.5 \times 10^6$  per foot. Again note that the drag scale does not start at zero. The agreement is seen to be satisfactory, the scatter in the data being no greater than about 4 counts of drag, or 1 percent, near the cruise lift. Figure 13 shows the variation of drag with Mach number at a constant lift coefficient of 0.48. The maximum spread between the curves is about 10 counts of drag, or 3 percent.

#### Comparison of Drag Results From Wind-Tunnel and Rocket-Technique Tests

The next logical question to be asked is: How well does the drag of a model measured in the wind tunnel correlate with the drag of the same model measured in free flight where the wind-tunnel constraints, such as boundary-reflected disturbances, are not present? Figure 14 shows a comparison of the drag coefficients of a four-engine delta-wing configuration from measurements in free flight by the rocket technique and in the Langley 16-foot transonic tunnel. The rocket and wind-tunnel models were identical as regards scale, surface smoothness, and so forth, and the Reynolds numbers for the two sets of data were about  $4.0 \times 10^6$  per foot. In both cases, air flowed through the nacelles, and the drag data have been corrected for internal drag and base drag. Note the correlation which has been obtained between the rocket and wind-tunnel drag measurements. These investigations were made approximately 10 years ago. Although the rocket data extend to higher supersonic values than indicated, the Mach number capability of the tunnel at that time was limited to a maximum of about 1.12. The wind-tunnel data for Mach numbers of 1.05 and 1.12 shown by the solid symbols were affected by wind-tunnel boundary-reflected disturbances. These affected test points are included in the figure to illustrate further the problems of boundary-reflected disturbances which were discussed earlier.

#### Comparisons at Supersonic Speeds

The next correlation is for tests conducted at supersonic speeds. The requirements regarding the techniques for testing at supersonic speeds are not nearly as stringent as those for transonic testing. For example, the requirements for the sting-support system can be relaxed; and the chief consideration is to determine the model scale so that the model lies well within the Mach rhombus throughout the supersonic speed range. Experience has shown that it

is somewhat more difficult to achieve a turbulent boundary layer on models at supersonic speeds because of the thicker and more stable boundary layer present on the models. In the correlations which follow, however, transition was fixed on the models by using proper grit-type boundary-layer transition strips in a manner which assured turbulent conditions over the model surfaces.

Figure 15 shows the lift-drag polar for a delta-wing configuration at a Mach number of 3.0. This model is the same one that was used to obtain the transonic data presented in figures 10 and 11. Figure 16 shows the lift-drag polar for an arrow-wing configuration, also at a Mach number of 3.0; this configuration was investigated without nacelles and vertical tails. The tests of both configurations were made in the Langley Unitary Plan wind tunnel and in the Ames 8- by 7-foot supersonic wind tunnel at a constant Reynolds number of  $3.0 \times 10^6$  per foot. Good correlation obviously has been achieved. The maximum scatter of the test points from the faired line amounts to 2 counts of drag, or less than 2 percent.

#### CONCLUDING REMARKS

Numerous comparisons have shown that drag data obtained for the same model in different wind tunnels at subsonic, transonic, and supersonic speeds agreed within 3 percent, provided the tests were made in accordance with the rules and techniques developed for wind-tunnel tests at these speeds. In the application of these rules and techniques, proper consideration must be given to model support systems, transition strips, tunnel wall effects, test limitations, and so forth. It has been further demonstrated that large-scale models, which permit high values of model Reynolds numbers, can be tested at subsonic speeds in relatively small transonic tunnels, and a high level of confidence can be placed in the results of such tests. It has also been shown that good correlation exists between model data obtained in the wind tunnel and by the rocket technique where the tunnel constraints are not present.

## REFERENCES

1. Wright, Ray H.; Ritchie, Virgil S.; and Pearson, Albin O.: Characteristics of the Langley 8-Foot Transonic Tunnel With Slotted Test Section. NACA Rept. 1389, 1958. (Supersedes NACA RM L51H10 by Wright and Ritchie and RM L51K14 by Ritchie and Pearson.)
2. Ritchie, Virgil S.: Effects of Certain Flow Nonuniformities on Lift, Drag, and Pitching Moment for a Transonic-Airplane Model Investigated at a Mach Number of 1.2 in a Nozzle of Circular Cross Section. NACA RM L9E20a, 1949.
3. Hart, Roger G.: Effects of Stabilizing Fins and a Rear-Support Sting on the Base Pressures of a Body of Revolution in Free Flight at Mach Numbers From 0.7 to 1.3. NACA RM L52E06, 1952.
4. Love, Eugene S.: A Summary of Information on Support Interference at Transonic and Supersonic Speeds. NACA RM L53K12, 1954.
5. Tunnell, Phillips J.: An Investigation of Sting-Support Interference on Base Pressure and Forebody Chord Force at Mach Numbers From 0.60 to 1.30. NACA RM A54K16a, 1955.
6. Lee, George; and Summers, James L.: Effects of Sting-Support Interference on the Drag of an Ogive-Cylinder Body With and Without a Boattail at 0.6 to 1.4 Mach Number. NACA RM A57I09, 1957.
7. Cahn, Maurice S.: An Experimental Investigation of Sting-Support Effects on Drag and a Comparison With Jet Effects at Transonic Speeds. NACA Rept. 1353, 1958. (Supersedes NACA RM L56F18a.)
8. Mugler, John P., Jr.: Transonic Wind-Tunnel Investigation of the Static Longitudinal Aerodynamic Characteristics of Five Nose Cones Designed for Supersonic Impact. NASA TM X-432, 1961.
9. Braslow, Albert L.; and Knox, Eugene C.: Simplified Method for Determination of Critical Height of Distributed Roughness Particles for Boundary-Layer Transition at Mach Numbers From 0 to 5. NACA TN 4363, 1958.
10. Luoma, Arvo A.: Longitudinal Aerodynamic Characteristics at Transonic Speeds of a V/STOL Airplane Configuration With a Fixed Delta Wing Having Auxiliary Variable-Sweep Outboard Panels. NASA TM X-661, 1961.
11. Wright, Ray H.; and Barger, Raymond L.: Wind-Tunnel Lift Interference on Sweptback Wings in Rectangular Test Sections With Slotted Top and Bottom Walls. NASA Rept. R-241, 1966.

### SHOCK-REFLECTION DISTANCE

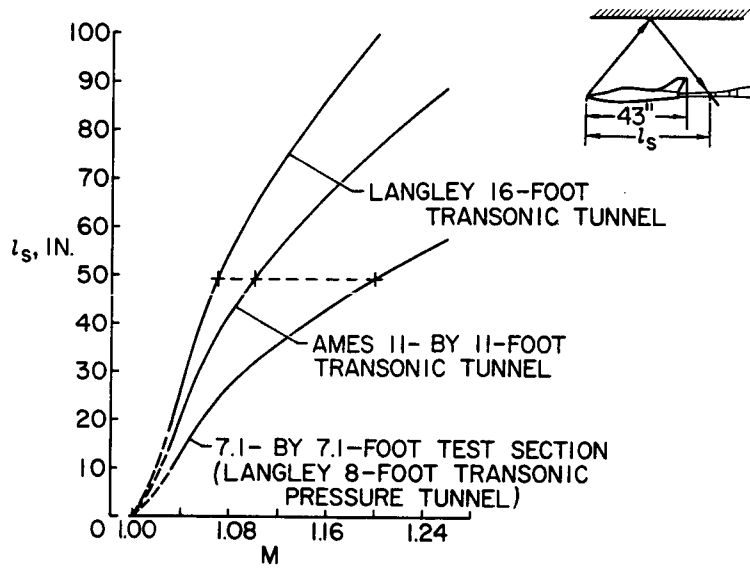


Figure 1

### BOUNDARY-REFLECTED DISTURBANCES

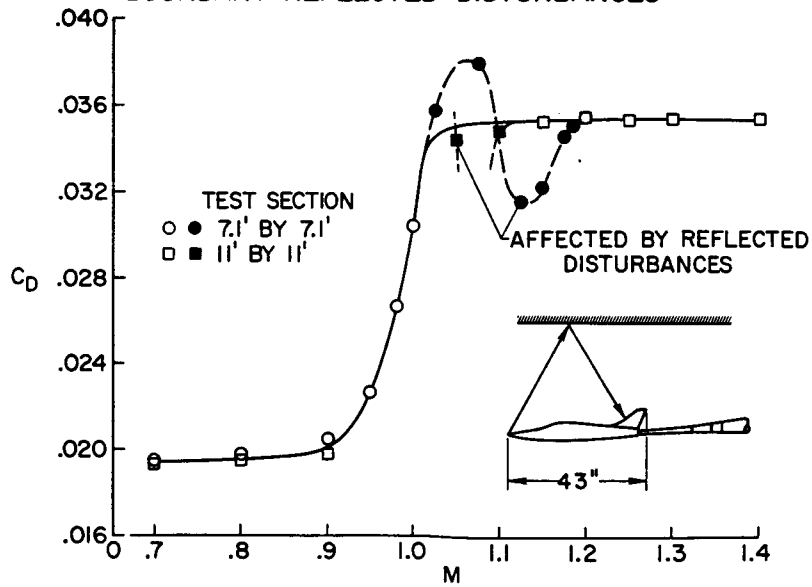


Figure 2

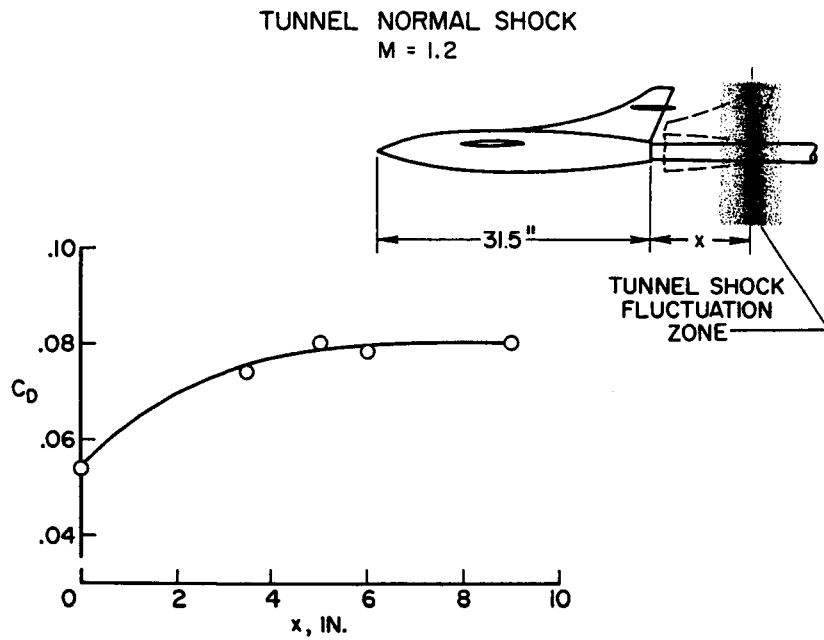


Figure 3

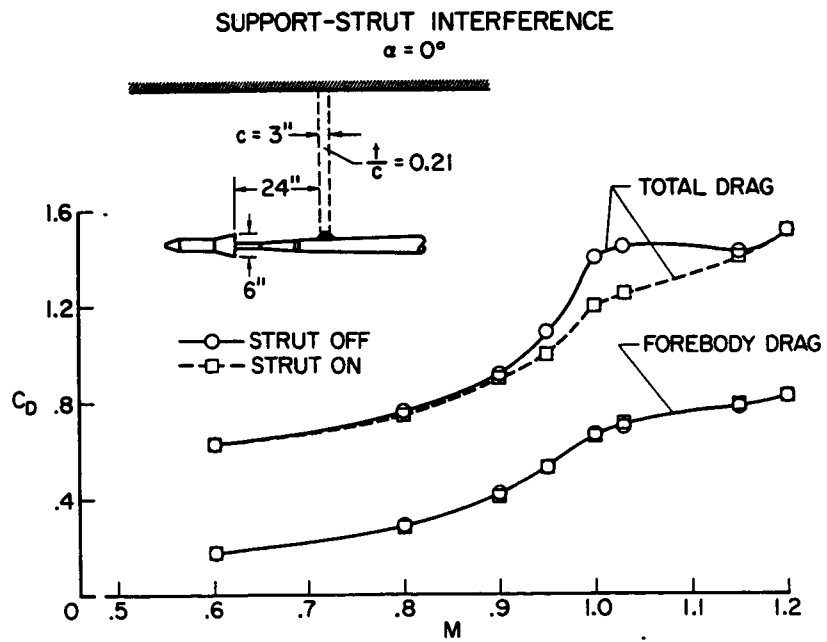


Figure 4

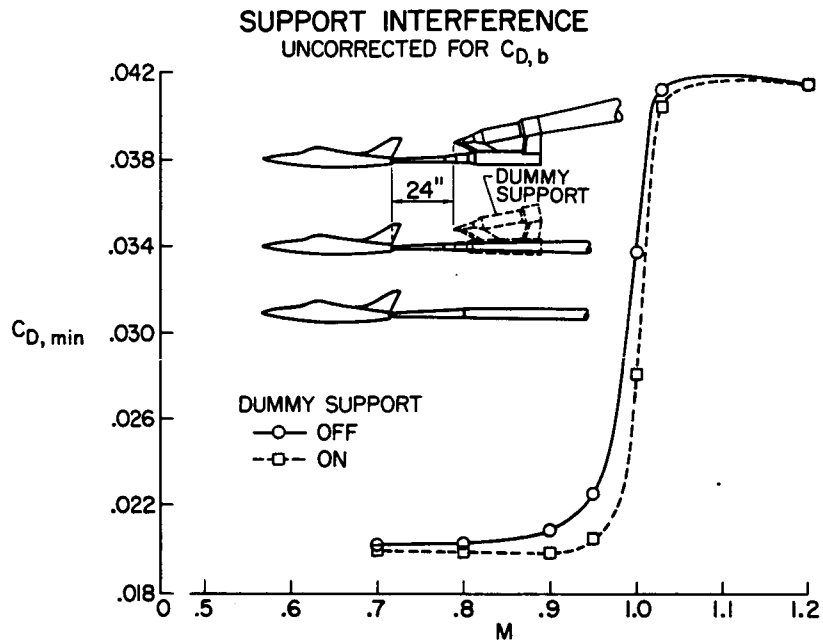


Figure 5

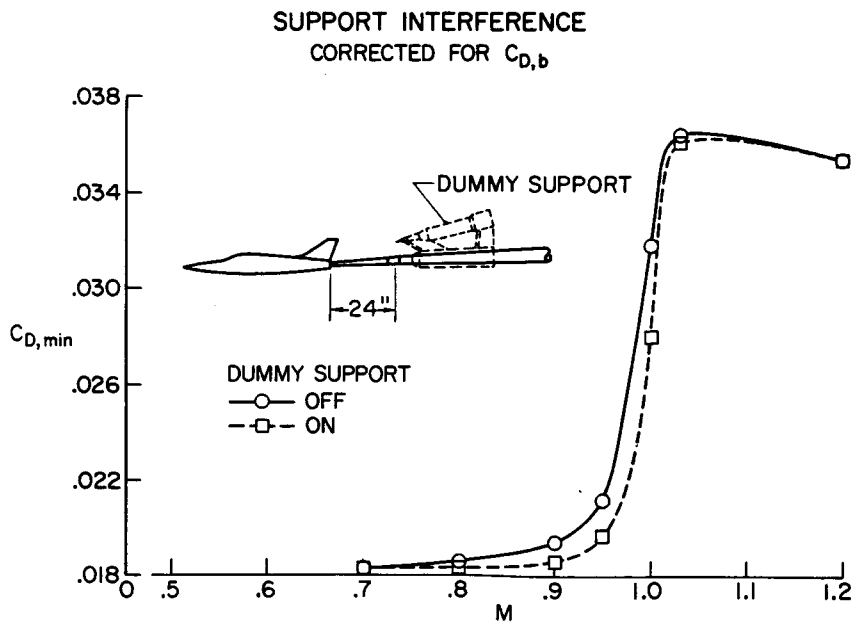


Figure 6

TRANSONIC MINIMUM DRAG  
 VARIABLE SWEEP; R/FT =  $2.5 \times 10^6$

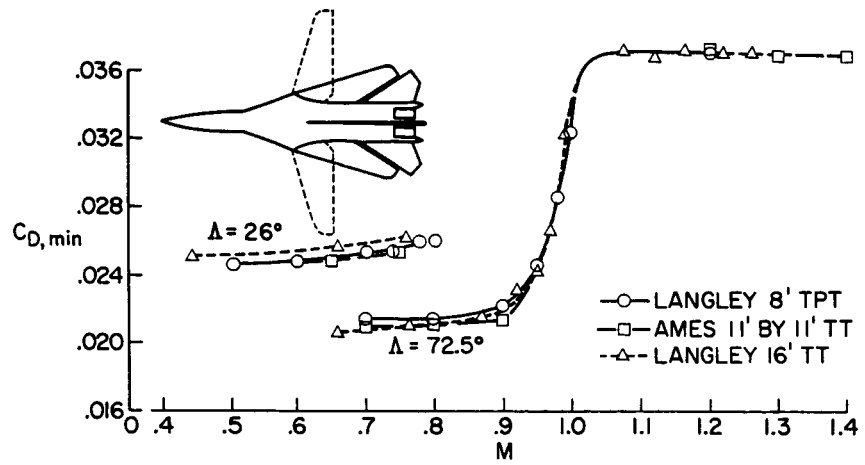


Figure 7

TRANSONIC MINIMUM DRAG  
 V/STOL

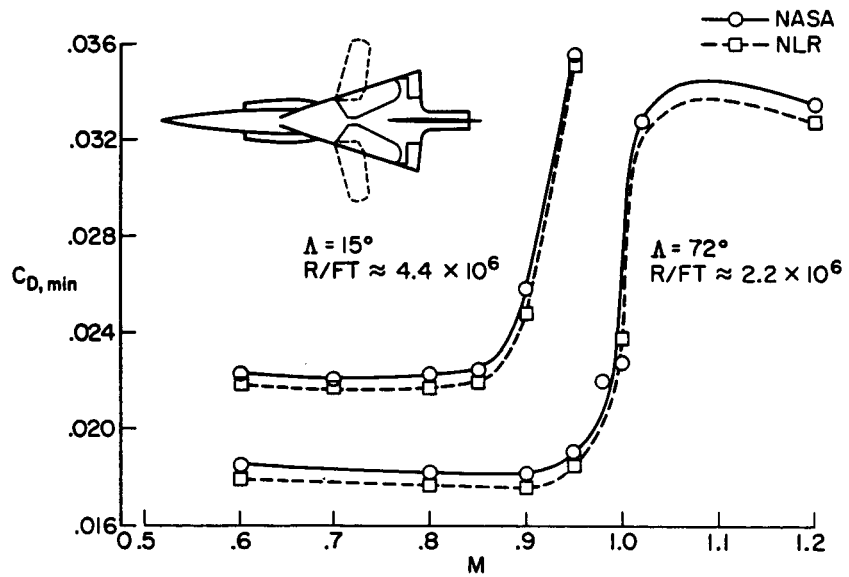


Figure 8

DRAG-DUE-TO-LIFT FACTOR  
 $V/STOL$

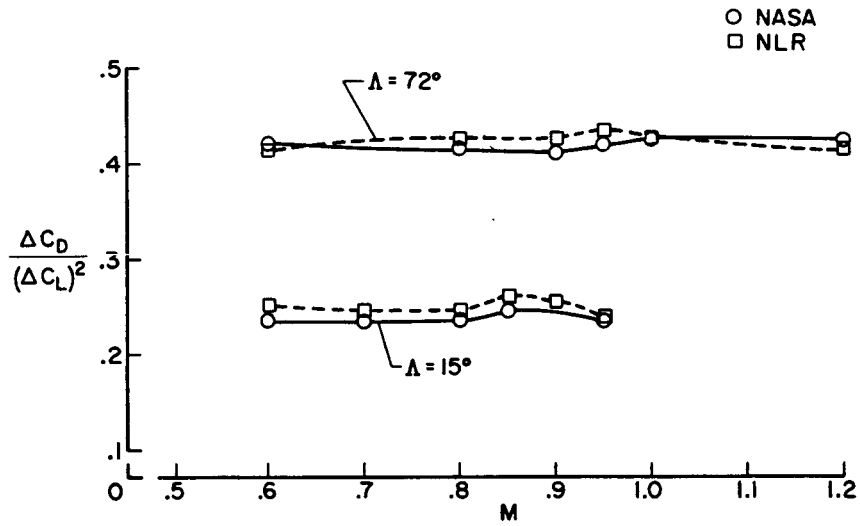


Figure 9

TRANSONIC MINIMUM DRAG  
 DELTA WING ;  $R/FT = 2.5 \times 10^6$

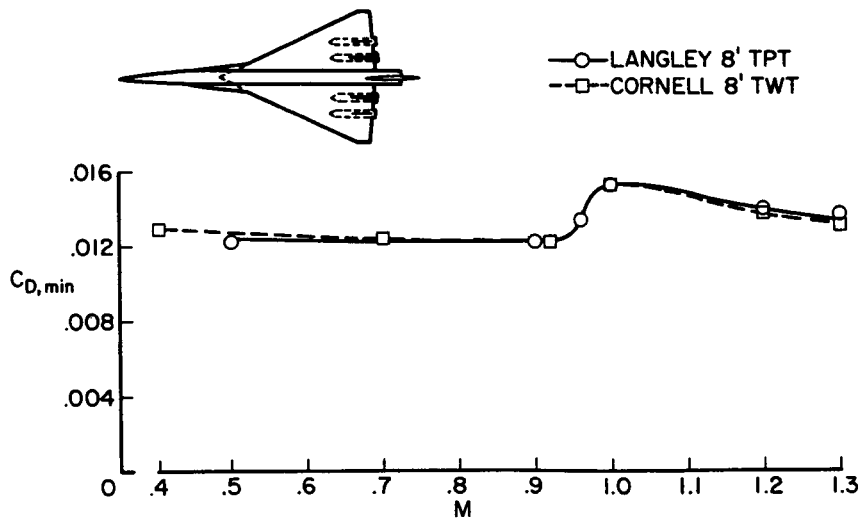


Figure 10

DRAG-DUE-TO-LIFT FACTOR  
 DELTA WING ; R/FT =  $2.5 \times 10^6$

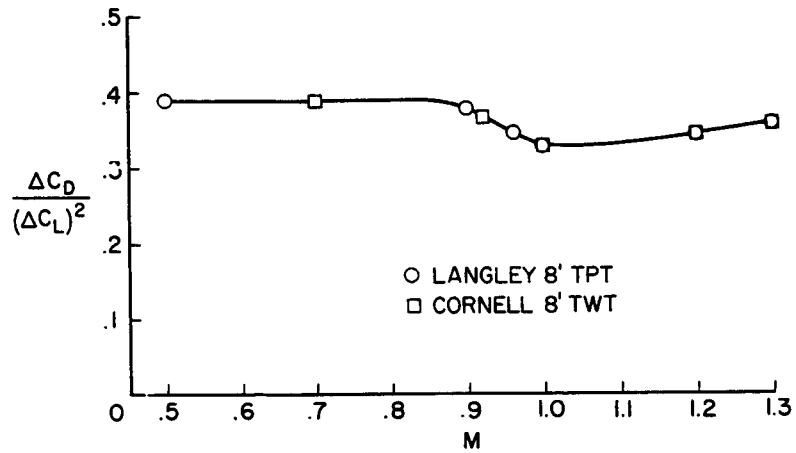


Figure 11

SUBSONIC DRAG POLAR  
 LARGE SUBSONIC TRANSPORT; M=0.775; R/FT=3.5 X 10<sup>6</sup>

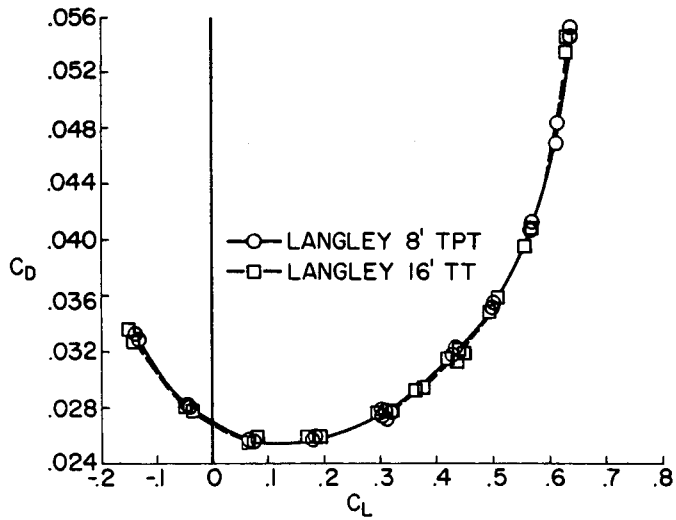


Figure 12

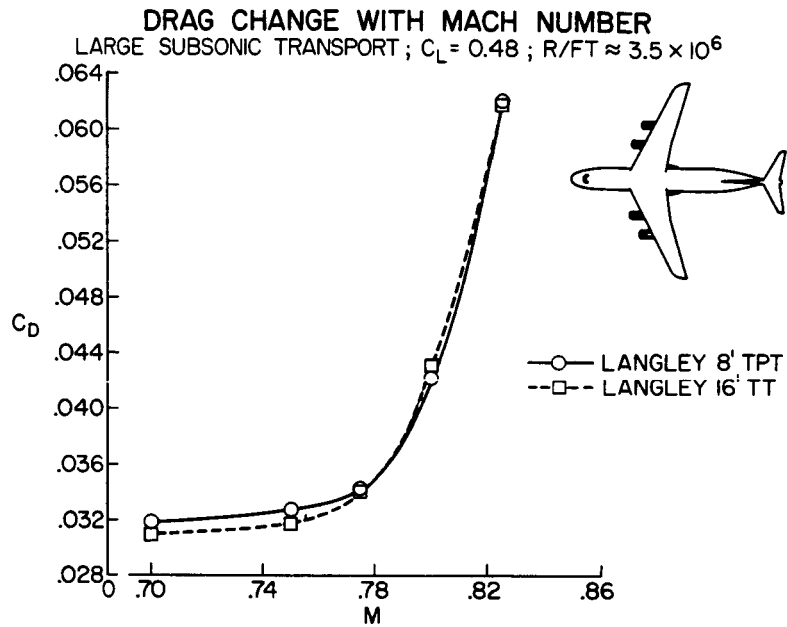


Figure 13

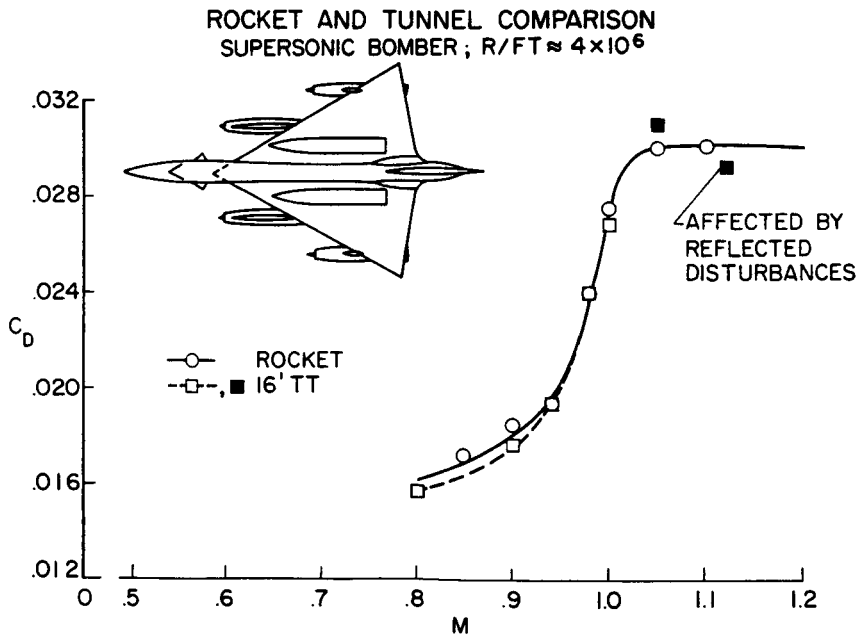


Figure 14

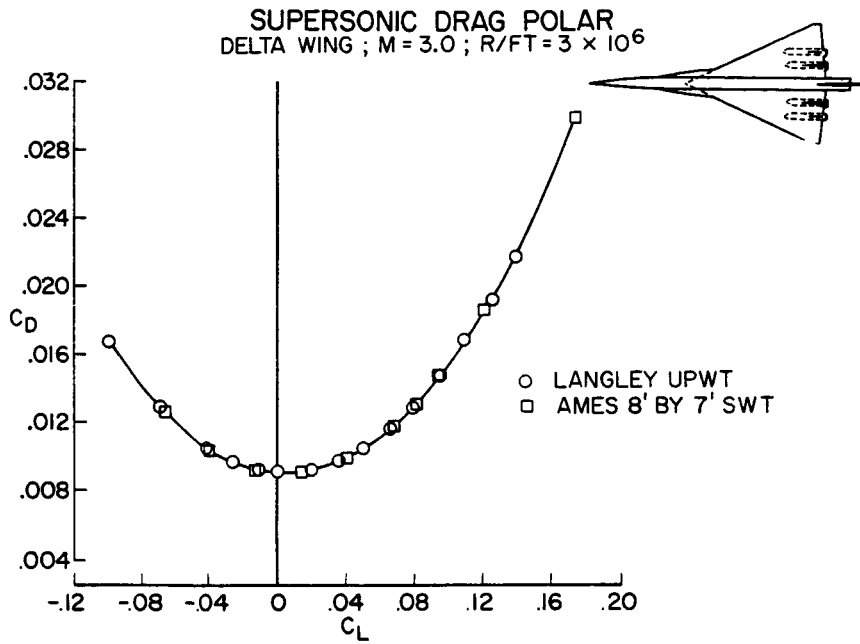


Figure 15

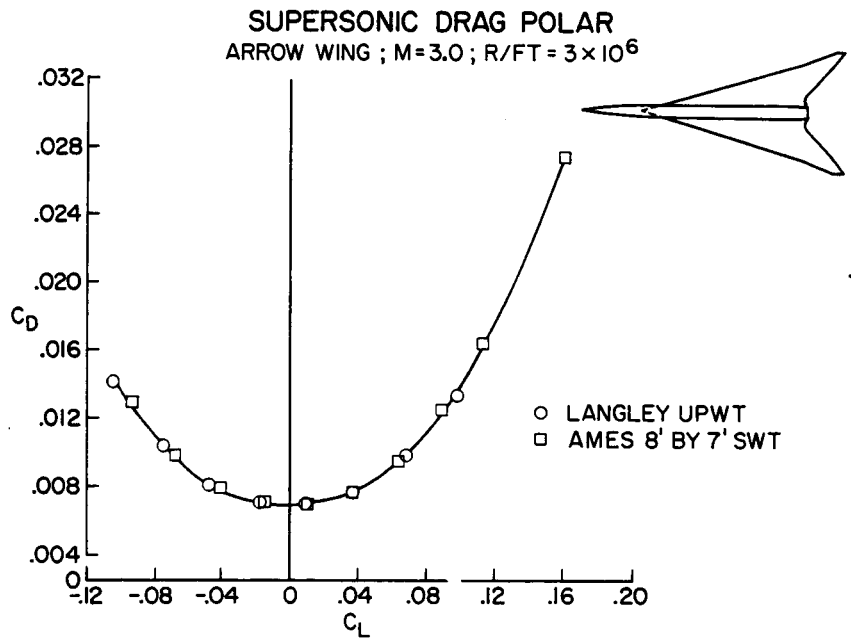


Figure 16

## 2. USE OF GRIT-TYPE BOUNDARY-LAYER-TRANSITION TRIPS

[U]

### ON WIND-TUNNEL MODELS

By Albert L. Braslow  
NASA Langley Research Center

Raymond M. Hicks  
NASA Ames Research Center

and Roy V. Harris, Jr.  
NASA Langley Research Center

### SUMMARY

X66 20043

Some general guidelines that are applicable to grit-type boundary-layer-transition trips located near the leading edges of model components are presented. Conditions that permit transition to be fixed at the roughness at subsonic and supersonic speeds without a resultant grit drag are reviewed. In certain cases in which grit drag is unavoidable, two methods - the choice of which depends upon the characteristics of the wind tunnel used - for correcting for such drag are discussed. At hypersonic speeds, the problem of fixing boundary-layer transition without distorting the turbulent-boundary-layer velocity profile has not been solved.

### INTRODUCTION

Accurate determination of the low-lift drag characteristics of full-scale aircraft from small-scale wind-tunnel tests usually requires that boundary-layer transition from laminar to turbulent flow be artificially fixed near the leading edges of the various model components. An extrapolation to the full-scale Reynolds number can then be made for aircraft protuberances and surface irregularities that are not simulated on the model. The use of three-dimensional or grit-type roughness as a boundary-layer-transition trip has met with the most success and is the subject of this paper. The appendix presents some recent information on the use of triangular particles cut from adhesive tape as a trip.

### SYMBOLS

$C_D$  drag coefficient  
 $C_{D,min}$  minimum drag coefficient

Preceding page blank

$C_{D,o}$	zero-lift drag coefficient
$C_L$	lift coefficient
$k$	roughness height
$M$	free-stream Mach number
$R/ft$	unit Reynolds number (Reynolds number per foot based on free-stream velocity and kinematic viscosity), $V_\infty/\nu_\infty$
$R_k$	roughness Reynolds number based on roughness height and velocity and kinematic viscosity at top of roughness, $u_k k/\nu_k$
$R_{k,cr}$	value of $R_k$ for initiation of artificial transition
$R_x$	Reynolds number based on free-stream conditions and distance of roughness from leading edge, $V_\infty x/\nu_\infty$
$R_{x,min}$	minimum value of $R_x$ below which an increase in roughness height is required to initiate artificial transition
$u$	local streamwise component of velocity inside boundary layer
$u_k$	local streamwise component of velocity inside boundary layer at top of roughness particle
$V_\infty$	free-stream velocity
$x$	distance of roughness from leading edge
$\delta$	total thickness of boundary layer
$\nu_k$	coefficient of kinematic viscosity at top of roughness particle
$\nu_\infty$	free-stream kinematic viscosity

#### DISCUSSION

No single trip configuration is effective or, in fact, desirable, regardless of tunnel test conditions or model configuration. A single set of specifications for a trip design, therefore, cannot be designated. However, some general guidelines that are applicable to all grit-type trips are

- (1) The roughness bands should be narrow. Wide bands are unnecessary, and they create drag if carried to extremes.

(2) The roughness should be sparsely distributed. It is undesirable to pack the roughness densely because a densely packed band will act as a two-dimensional trip. Two-dimensional trips are unsatisfactory because reasonable heights do not fix transition at the trip location.

(3) Care should be taken not to build up layers of adhesive which can form spanwise ridges at the edge of the trip. These ridges also tend to make the trip act as a two-dimensional step.

With these general guidelines in mind, a choice of particle size and location must be made. The proper choice is not an obvious one. Several factors are involved that require careful consideration. The primary factor involved in the artificial fixing of transition is Mach number, and subsonic speeds will be considered first. Before proceeding with the discussion, however, the boundary-layer parameters to be used are defined with the aid of figure 1. Shown, to an exaggerated scale, is the total boundary-layer thickness as the boundary layer grows along a surface. A roughness particle is shown located a distance  $x$  from the surface leading edge. The height of the particle is designated as  $k$ . Also shown is a sketch of the boundary-layer velocity profile at the roughness location. A roughness Reynolds number is formed based on the roughness height  $k$  and the local flow conditions at the top of the roughness - that is, the velocity at the top of the roughness  $u_k$  and the kinematic viscosity at the top of the roughness  $\nu_k$ . For roughness Reynolds numbers less than a certain value, the roughness has no effect on the location of the natural transition. When the roughness Reynolds number reaches a critical value, designated by the subscript  $cr$ , transition moves forward of its natural location. At subsonic speeds, transition moves very close to the roughness when the critical value is attained. Many experimental investigations have determined that the value of the critical Reynolds number is approximately 600 at subsonic speeds (for a ratio of particle height to width of 1). (See ref. 1 or 2.) With this value of roughness Reynolds number as a criterion, the minimum roughness height required to initiate artificial transition can be calculated for the given test conditions and for a selected distance of the roughness from the leading edge. A Reynolds number based on this distance  $x$  and the free-stream flow conditions has been designated as  $R_x$ .

#### Subsonic Considerations

Figures 2 and 3 present examples of subsonic drag data plotted against roughness height. In figure 2 are results for a rather large range of roughness height on a variable-sweep fighter configuration; whereas, in figure 3 are results for a more limited range of roughness height on fighter and transport configurations. The values of roughness height  $k$  for a roughness Reynolds number of 600 are indicated by the vertical tick for each test. For all the configurations presented, an increase in roughness height by a factor of 2 over that indicated by  $R_k = 600$  can be tolerated with very little or no drag increase. The drag coefficients measured in this range of roughness height varied within only  $\pm 1\frac{1}{2}$  counts, that is,  $\pm 0.00015$ . Therefore, choice of a

roughness grit somewhat larger than that indicated for  $R_k = 600$  will enable drag measurements to be made at subsonic speeds without the need for any corrections due to roughness drag. Use of a nominal grit size one size larger than that determined for  $R_k = 600$  is recommended to insure a margin of conservatism for transition. This recommendation would appear to be a good one because the average height of roughness in three-dimensional grit has been found to be somewhat smaller than the nominal height. The results of careful measurements of the particles in representative carborundum-grit trips are presented in figures 4 and 5.

The shape of the curve of drag coefficient plotted against roughness height (fig. 2) is a function of particle frontal area and average dynamic pressure over the particles. For each particle that is somewhat higher than the boundary-layer thickness, indicated in figure 2 by the arrow, the drag is about proportional to only the particle frontal area, because the average dynamic pressure over the particle height is approximately constant. As the particle height is changed for each particle immersed in the boundary layer, however, the average dynamic pressure over the particle height changes with a change in height. The drag varies in this region, therefore, with the change in average dynamic pressure as well as with the frontal area. The exact shape of the drag-coefficient curve for carborundum-type grit, then, can be different for different trips because of the variation of particle sizes present in the grit and because of a variation in boundary-layer thickness across the span when the grit location from the leading edge is not constant.

The important point to be reiterated is that for all the examples of subsonic data shown, the drag variation with roughness height approaches a plateau region for nominal grit sizes smaller than the boundary-layer thickness but larger than the value determined for  $R_k = 600$ . This desirable plateau region occurs only when another important criterion is satisfied. This criterion will be indicated in the following discussion.

Figure 6, which repeats the curve from figure 2 for the variable-sweep configuration that was obtained at a tunnel unit Reynolds number of  $5.9 \times 10^6$ , shows the effect of decreasing unit Reynolds number. When the unit Reynolds number was reduced from  $5.9 \times 10^6$  to  $3.0 \times 10^6$ , transition was still fixed at the roughness height equivalent to a roughness Reynolds number of 600, and a plateau region was once again obtained. When the unit Reynolds number was further reduced to  $1 \times 10^6$ , it appears that a value of  $R_x$  of 600 was not sufficient to fix transition at the roughness. The increase in height required to fix transition prevented the attainment of a plateau region - that is, there was always a large variation of drag coefficient with roughness height. It appears possible to correlate the conditions at which a value of  $R_k$  greater than 600 is required to fix transition at the roughness on the basis of  $R_x$ , the previously mentioned length Reynolds number based on the distance from the leading edge to the roughness location. Values of  $R_x$  based on the distance to the trip at the mean-aerodynamic-chord location are presented in figure 6 for the three unit Reynolds numbers. The effect of  $R_x$  on the critical

roughness Reynolds number  $R_{k,cr}$  is shown by figure 7. The shaded band represents dozens of data points. The value of  $R_{k,cr}$  is constant at about 600, except at the low values of the length Reynolds number  $R_x$ . At the low values of  $R_x$  - resulting from either a decrease in tunnel unit Reynolds number or a decrease in distance - the critical roughness Reynolds number increases; therefore, the roughness height required to induce transition increases. These larger heights will cause roughness drag large enough to eliminate the plateau region, as previously indicated for the low Reynolds number curve in figure 6. For subsonic tests, it is usually possible to locate the roughness at a length Reynolds number of at least  $0.1 \times 10^6$ , while maintaining a location far enough forward to have essentially full-chord turbulent flow. It can be seen that  $0.1 \times 10^6$  is about the value at which  $R_{k,cr}$  departs from the constant value of 600. The previous data showing the plateau region for the fighter and transport configurations (figs. 2 and 3) were obtained for values of  $R_x$  greater than  $0.1 \times 10^6$ .

#### Supersonic Considerations

At supersonic Mach number, selection of grit height and location becomes more complicated. Firstly, as indicated in figure 8, an increase in Mach number increases the value of  $R_{x,min}$ , which is defined as the value of  $R_x$  below which  $R_{k,cr}$  increases. (See fig. 7.) For combinations of roughness location and tunnel unit Reynolds number resulting in values of  $R_x$  smaller than these minimum values, it becomes increasingly difficult to induce transition. Secondly, for values of  $R_x$  greater than  $R_{x,min}$ , the value of roughness Reynolds number at which transition starts to move forward of its natural position  $R_{k,cr}$  also increases with increasing Mach number greater than about 3.6. This, too, results in an increase in required roughness height at the higher Mach numbers. Thirdly, as Mach number increases, the roughness Reynolds number must be increased to a value greater than the critical value in order to move transition forward to the vicinity of the roughness, as indicated by the upper curve in the right-hand plot of figure 8. The increase in  $R_k$  to a value greater than the critical value is not required at the lower Mach numbers where  $R_{k,cr}$  is sufficient to induce transition in the vicinity of the roughness. Parts of these curves are shown dashed because very few data are available to establish the values quantitatively. The limited data that are available up to Mach 6, however, do indicate the trends plotted.

It is apparent from figure 8 that at hypersonic speeds, fixing transition on wind-tunnel models becomes increasingly difficult. In fact, roughness height several times larger than the boundary-layer thickness was required to fix transition at a trip at a Mach number of 6. Severe, undesirable distortions of the boundary-layer velocity profile accompany such large roughness. Discussion of the significance of the transition-fixing difficulty with regard to hypersonic wind-tunnel testing is included in paper no. 35 by David E. Fetterman et al.

Further discussion herein of supersonic data will be restricted to Mach numbers up to 3 - the range of interest for the supersonic transport. It has already been indicated that at Mach numbers up to 3, a roughness height equivalent to a value of  $R_k$  of about 600 will fix transition very near the roughness so long as the value of  $R_x$  at the roughness is greater than the minimum value indicated in figure 8. It is not always possible or practical, however, to locate roughness far enough rearward dimensionally or to operate at a unit Reynolds number high enough to obtain a value of  $R_x$  at least that large. In other words, in some supersonic wind tunnels, the maximum tunnel unit Reynolds number or the model scale is not large enough to produce these minimum values of  $R_x$  for roughness located as near the leading edge as desired. In tunnels with larger unit Reynolds number capabilities, it may not be feasible to run all tests at the maximum unit Reynolds number condition because of considerations such as angle-of-attack restrictions due to balance limitations at the higher dynamic pressures. For supersonic tests, therefore, a need usually exists for the use of roughness configurations that cause grit drag. A correction for this grit drag must, of course, be determined. Two methods are being used, the choice of which depends upon the characteristics of the wind tunnel used.

Figure 9 illustrates a technique that can be used for determining the grit drag in wind tunnels having a variable Reynolds number capability. The technique is limited, however, to those wind tunnels with a sufficiently high unit Reynolds number and free-stream turbulence level to produce essentially all-turbulent flow on the model surfaces at the highest unit Reynolds number without artificial trips. The data shown in the figure were taken at a Mach number of 2.75 with a delta-wing-body model. Shown on the left-hand side of the figure is a log-scale plot of the zero-lift drag coefficient as a function of the free-stream unit Reynolds number. The circular symbols represent free transition and the square symbols represent measurements with transition trips located near the model leading edges. The roughness particles were sized to produce transition at the trip at the test Reynolds number per foot of  $3 \times 10^6$ , which is the highest unit Reynolds number at which complete lift-drag polars could be taken without exceeding the model balance limits. A comparison with turbulent theory and observation of sublimation material placed on the model surfaces during the tests indicate that the model without trips had essentially all-turbulent flow at unit Reynolds number of about  $6 \times 10^6$  and greater. By extrapolating along the theoretical turbulent curve for a smooth flat plate back to the test Reynolds number per foot of  $3 \times 10^6$ , the grit drag is obtained as the difference between the extrapolated smooth value and the drag measured with the grit. The increment in drag coefficient due to the grit was 0.0005 in this test. On the right-hand side of figure 9, the square symbols represent the measured variation of drag coefficient with lift coefficient for the model with fixed transition at the Reynolds number per foot of  $3 \times 10^6$ . The solid line is the corrected polar which has been adjusted for the grit-drag increment.

Figure 10 illustrates a technique that can be used for grit-drag determination in wind tunnels which do not have a variable Reynolds number capability

or which cannot achieve a sufficiently high Reynolds number to produce all-turbulent flow on the model surfaces without artificial trips. The data shown in this figure were taken with the same delta-wing model as in the previous figure, at the same Mach number of 2.75, and at a unit Reynolds number of  $3 \times 10^6$ . On the left-hand side of the figure is a plot of the variation of the drag coefficient with lift coefficient for the model with artificial trips of different roughness heights. Each of the particle sizes shown was sufficiently large to produce transition at the trip. In order to determine the all-turbulent drag of the model without trips, the data are cross-plotted in the right-hand plot of the figure as a function of the particle size squared at various values of lift coefficient. The parameter  $k^2$  is used rather than  $k$  because, for these roughness heights which are all greater than the boundary-layer thickness, the drag is about proportional to a characteristic area as discussed previously. The arrow indicates the roughness height equal to the boundary-layer thickness at zero lift. The all-turbulent drag of the smooth model is obtained by extrapolating linearly to zero roughness height. The corrected all-turbulent drag polar for the model is shown as the solid line in the left-hand plot of the figure.

Figure 11 shows a comparison of the corrected drag polar for the model as determined by the two techniques. The circular symbols represent the corrected drag polar as determined by the variable Reynolds number technique and the square symbols represent the corrected drag polar as determined by the variable roughness height technique. As can be seen in the figure, the agreement in this case is excellent.

Determination of the correct slope of  $C_D$  plotted against  $k^2$  in the variable roughness size method, however, is not as simple as the curves of figure 10 may indicate. This fact is explained by figure 12 in which the zero-lift drag-coefficient curve is repeated as the solid line but additional points of larger and smaller roughness heights are included. If the two larger particles are considered in the fairing, as indicated by the dashed line, the lower resultant slope of  $C_{D,0}$  plotted against  $k^2$  results in a significant change in the grit-drag correction. These larger particles are over three times as high as the boundary-layer thickness, and other experiments have indicated that particles of such magnitude can either decrease or increase the local skin friction behind the roughness because of distortions in the boundary-layer velocity profiles. Roughness too much larger than the boundary-layer thickness, therefore, should be avoided, but it is not clear at present how large a roughness can be tolerated. Additional work is underway to define better the height limitations. For the smallest roughness height investigated and for natural transition, visual-observation techniques of the boundary-layer condition can be used to determine the amount of laminar flow present. With calculations of the drag decrement associated with the laminar flow, additional points may be provided to help determine the slope of the curve. It is clear that in applying the variable roughness size method for evaluating the roughness drag, extreme care is required in determining the boundary-layer conditions through the range of roughness height so that an educated judgment can be used in fairing the slope of  $C_D$  plotted against  $k^2$ .

## General Considerations

The discussion of the use of transition trips on wind-tunnel models has been restricted in this paper to the problem of determining full-scale low-lift drag characteristics. So long as the flow over the surfaces of wind-tunnel models remains attached, the other force and moment coefficients measured at small scale will, for all practical purposes, be equal to the full-scale characteristics. If, however, regions of flow separation exist at test conditions, the characteristics may be affected by the differences between the test and full-scale Reynolds numbers. Some aspects of the flow-separation problem are discussed in paper no. 3 by Donald L. Loving and in paper no. 23 by William P. Henderson.

A final point to be made concerns the previously mentioned variation of particle height present in a trip composed of distributed grit. Although this is not a serious problem, further sieving of the grit before application would certainly be helpful. Also, the use of other types of three-dimensional roughness rather than grit in an attempt to provide uniform and more easily controllable trips has been under investigation for some time. Although all pertinent problems have not yet been completely resolved, recent results for one of these types appear encouraging and some of the information on this roughness is included in the appendix.

## CONCLUDING REMARKS

It is possible to fix boundary-layer transition far forward on wind-tunnel models at subsonic speeds with grit-type transition trips having little or no grit drag. This is possible also at supersonic speeds, but only if a sufficiently high test Reynolds number is attainable. Testing expediency or tunnel characteristics, however, usually dictate the use of trips, at supersonic speeds, that produce grit drag. Two methods of correcting for this grit drag, depending upon the tunnel characteristics, are currently being used. At hypersonic speeds, the problem of fixing boundary-layer transition near the leading edges of the model components without distorting the turbulent-boundary-layer velocity profile has not been solved.

## APPENDIX

### TRIANGULAR PARTICLES OF ADHESIVE TAPE FOR BOUNDARY-LAYER TRANSITION

Two practical difficulties encountered in the use of carborundum roughness particles are the lack of uniformity of the particle pattern (caused by large variations in size and shape of the individual particles) and the length of time required for application. These problems are accentuated when it is necessary to repeat the application of the roughness bands several times as is done in one of the currently used techniques for assessing the particle-drag penalty.

A type of three-dimensional roughness which offers promise of eliminating these difficulties consists of triangular particles cut from adhesive tape. The size and shape of these particles can be accurately controlled and no additional bonding agent is required to affix the particles to the model surface, with a resultant savings in time for application. Triangular particles of this type have been tested at the University of Maryland in a water tunnel (refs. 3 and 4) and at the Ames Research Center in air. In both studies, the triangular roughness particle was shown to be more effective in promoting artificial transition than spherical roughness particles of the same height.

Results obtained from tests at supersonic speeds at Ames are shown in figure 13. The ratio of minimum spherical trip Reynolds number to minimum triangular trip Reynolds number for transition near the roughness is plotted against Mach number for station Reynolds numbers from  $0.025 \times 10^6$  to  $0.6 \times 10^6$  and for particles with height greater than the boundary-layer thickness. These results show that for the conditions of figure 13, the particle height required to fix transition near the roughness is less for triangular trips than for spherical trips. At the top of figure 13 is a sketch showing the dimensions and orientation with respect to the free stream of the triangular trips used in the Ames tests. Triangles with apex angles ranging from  $45^\circ$  to  $135^\circ$  were found to produce only small variations in the transition-promoting effectiveness in the studies of reference 4. However, it has been found in both the Ames and the University of Maryland studies that a reduction in effectiveness will be realized if the apex of the triangle does not point into the flow.

Although the use of triangular roughness appears encouraging, further investigation is required in the following problem areas:

- (1) The amount of distortion of the boundary layer caused by the triangular trips as compared with the spherical trips
- (2) The drag penalty of the triangular trips compared with the spherical trips
- (3) The effect of wing leading-edge sweep on the transition-promoting effectiveness of the triangular trips

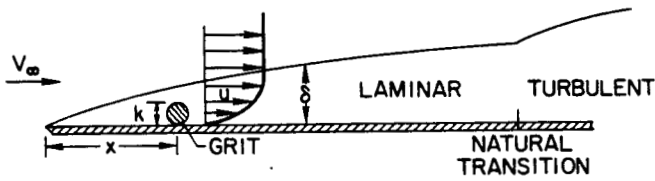
APPENDIX - Concluded

- (4) The effect of pressure gradient on the transition-promoting effectiveness of the triangular trips
- (5) The effectiveness of triangular trips with heights less than the boundary-layer thickness

#### REFERENCES

1. Braslow, Albert L.: Review of the Effect of Distributed Surface Roughness on Boundary-Layer Transition. AGARD Rept. 254, Apr. 1960.
2. Von Doenhoff, Albert E.; and Braslow, Albert L.: The Effect of Distributed Surface Roughness on Laminar Flow. Boundary Layer and Flow Control, Vol. 2, G. V. Lachmann, ed., Pergamon Press, 1961, pp. 657-681.
3. Hama, Francis R.: An Efficient Tripping Device. J. Aeron. Sci. (Readers' Forum), vol. 24, no. 3, Mar. 1957, pp. 236-237.
4. Hegarty, John C.; and Hama, Francis R.: Further Investigations on the Triangular-Patch Stimulator. Tech. Note BN-107 (AFOSR TN-57-616, ASTIA AD 136 605), Inst. Fluid Dyn. Appl. Math., Univ. of Maryland, June 1957.

DEFINITION OF BOUNDARY-LAYER PARAMETERS



$R_k = \frac{u_k k}{\nu_k}$  ROUGHNESS REYNOLDS NUMBER

$R_{k, cr}$  VALUE OF  $R_k$  FOR FORWARD MOVEMENT OF TRANSITION

$R_x = \frac{V_\infty x}{\nu_\infty}$  REYNOLDS NUMBER BASED ON DISTANCE OF ROUGHNESS FROM LEADING EDGE

Figure 1

SUBSONIC VARIATION OF  $C_{D,min}$  WITH ROUGHNESS HEIGHT  
 VARIABLE-SWEEP FIGHTER,  $M=0.7$

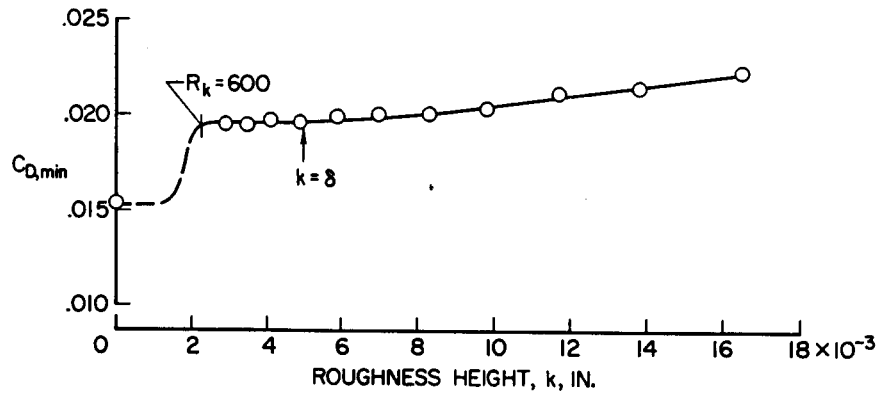


Figure 2

SUBSONIC VARIATION OF  $C_{D,min}$  WITH ROUGHNESS HEIGHT  
 OTHER CONFIGURATIONS;  $M \approx 0.7$

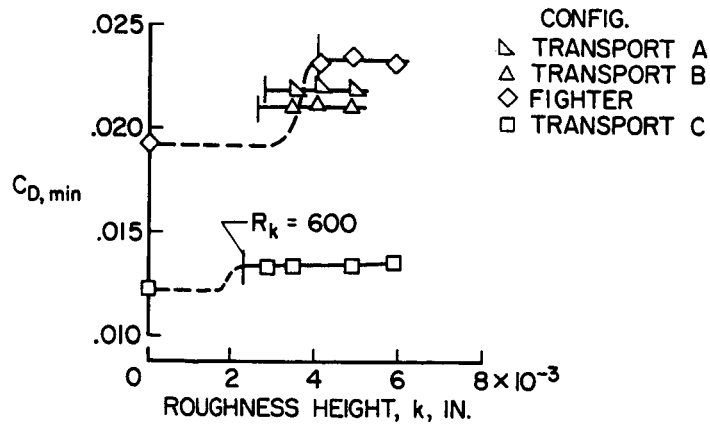


Figure 3

DISTRIBUTION OF MEASURED HEIGHTS OF PARTICLES IN  
A TYPICAL CARBORUNDUM TRANSITION TRIP  
GRIT NO. 30 TO NO. 80

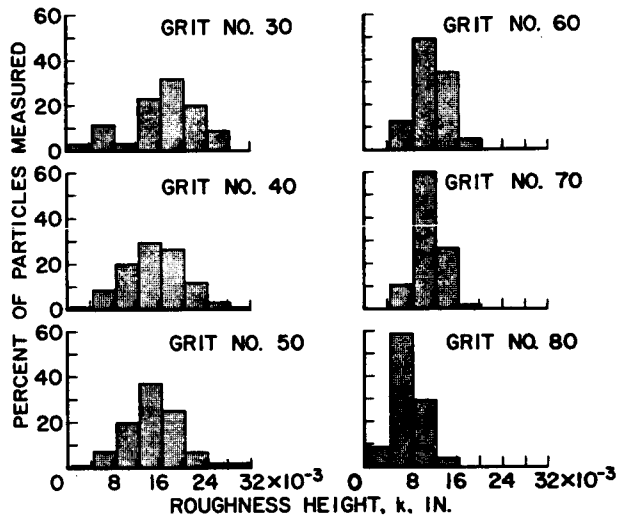


Figure 4

DISTRIBUTION OF MEASURED HEIGHTS OF PARTICLES IN  
A TYPICAL CARBORUNDUM TRANSITION TRIP  
GRIT NO. 90 TO NO. 240

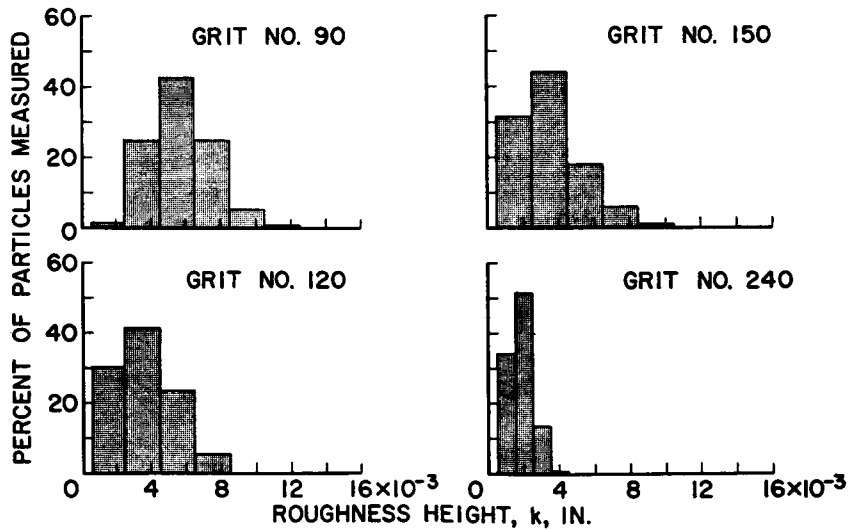


Figure 5

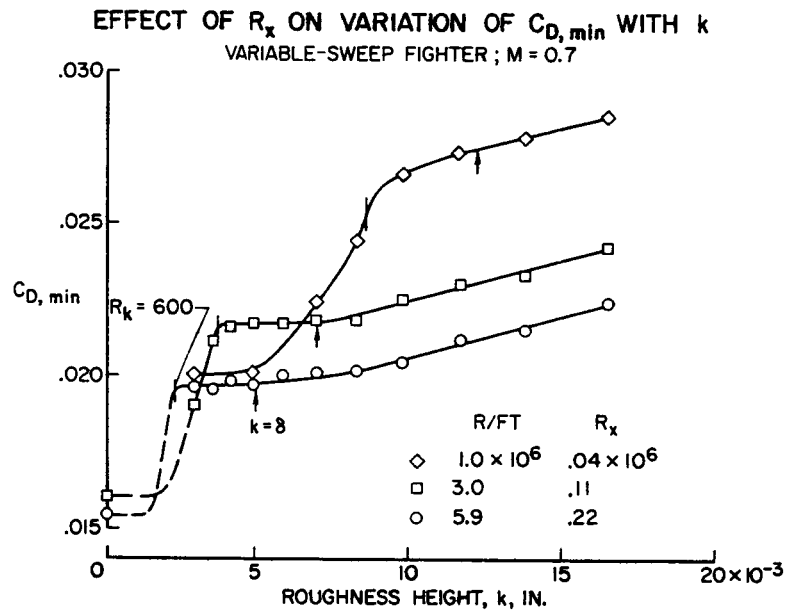


Figure 6

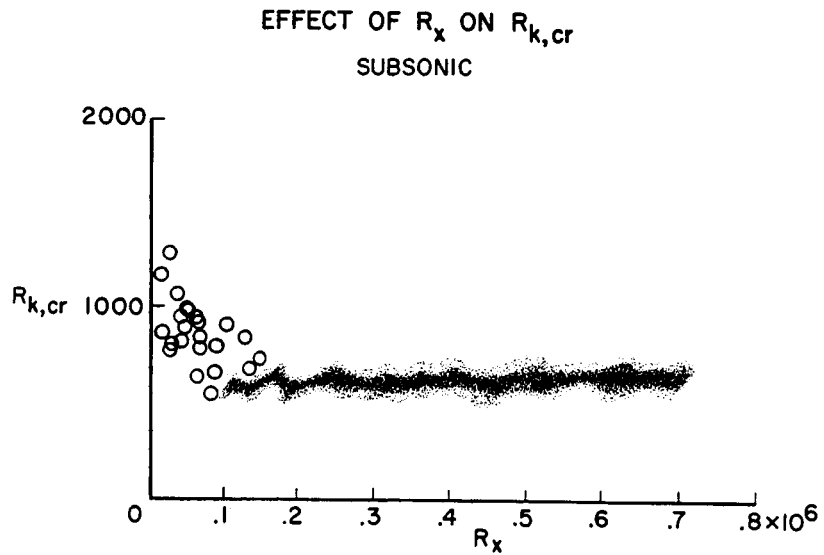


Figure 7

EFFECT OF M ON BOUNDARY-LAYER TRANSITION CRITERIA

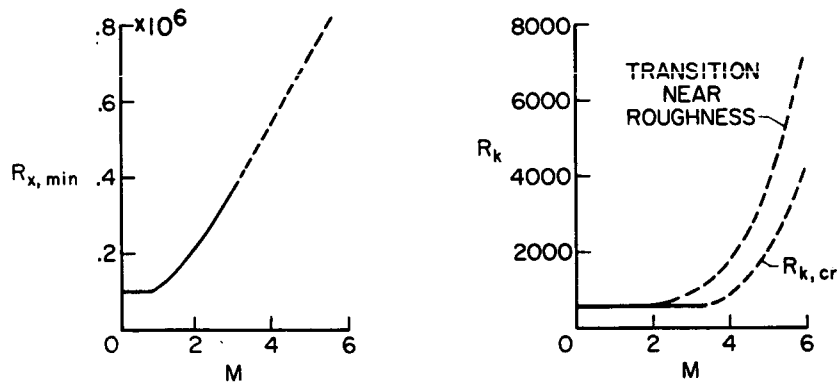


Figure 8

GRIT-DRAG DETERMINATION BY  
VARIABLE REYNOLDS NUMBER METHOD

$M = 2.75$

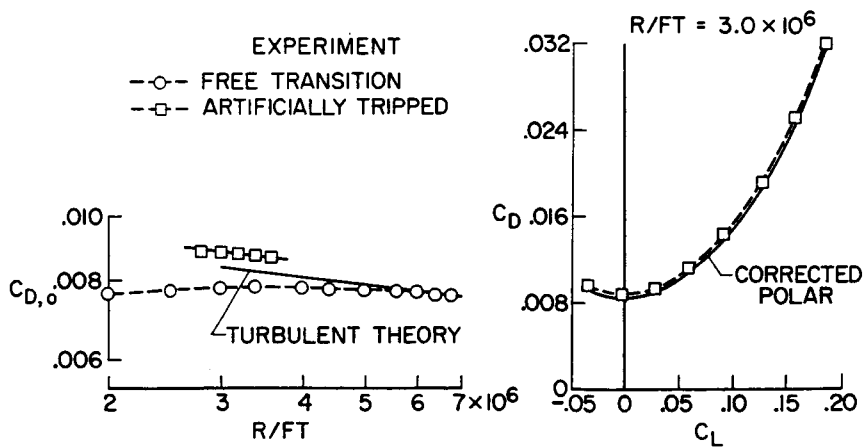


Figure 9

GRIT-DRAG DETERMINATION BY VARIABLE  
ROUGHNESS SIZE METHOD

$M=2.75$  ;  $R/FT = 3.0 \times 10^6$

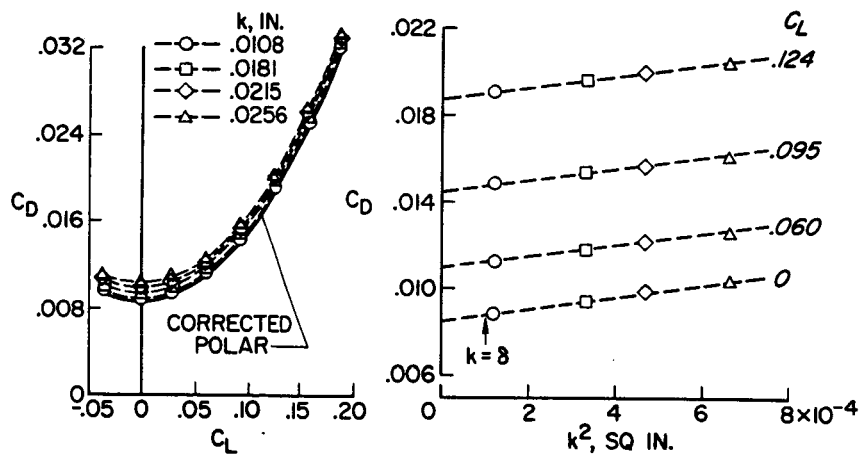


Figure 10

COMPARISON OF CORRECTED POLARS

$M=2.75$  ;  $R/FT = 3.0 \times 10^6$

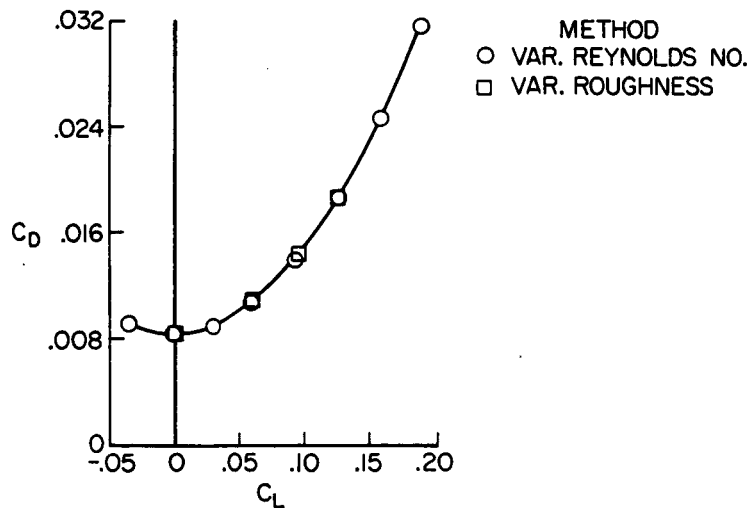


Figure 11

SUPERSONIC VARIATION OF  $C_{D,o}$  WITH  $k^2$   
 $M = 2.75$  ;  $R/FT = 3.0 \times 10^6$

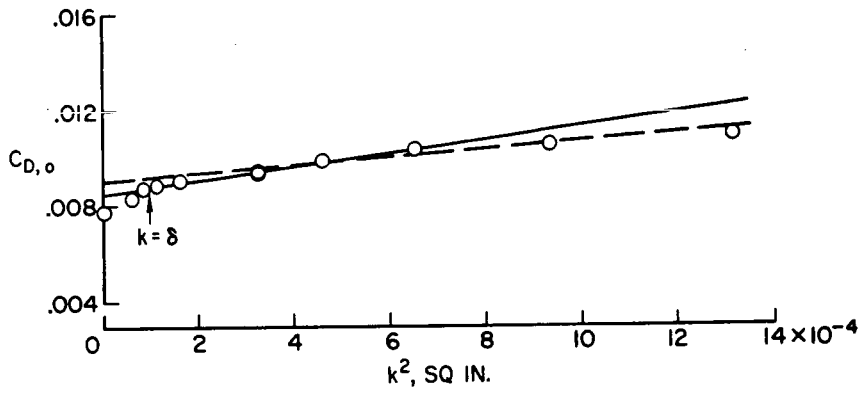


Figure 12

RATIO OF MINIMUM SPHERICAL TRIP REYNOLDS  
 NUMBER TO MINIMUM TRIANGULAR TRIP REYNOLDS  
 NUMBER FOR TRANSITION NEAR ROUGHNESS

$\frac{k}{\delta} > 1$ ;  $R_x = 0.025 \times 10^6$  TO  $0.6 \times 10^6$

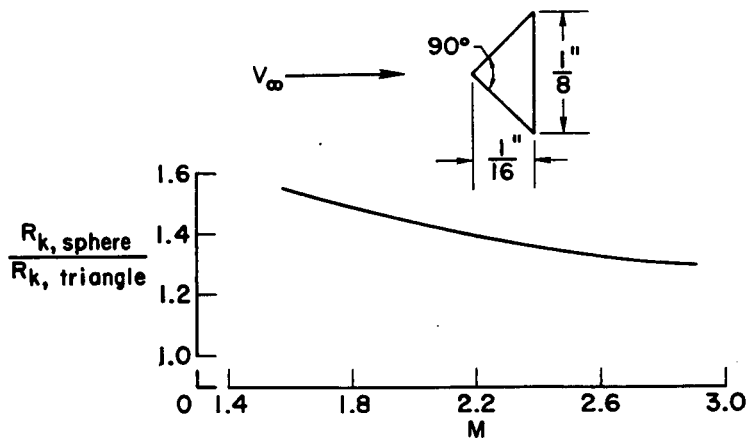


Figure 13

### 3. WIND-TUNNEL—FLIGHT CORRELATION OF

#### SHOCK-INDUCED SEPARATED FLOW

By Donald L. Loving  
NASA Langley Research Center

#### SUMMARY

A preliminary study is made of the discrepancies between wind-tunnel predictions and actual flight results for conditions of supercritical separated flow. The limited results obtained for two combinations of Mach number and lift, both involving supercritical-flow separation, suggest that the problem is related to Reynolds number and that an improvement in the correlation might be obtained by fixing the transition on a model so as to produce a relative boundary-layer thickness at the trailing edge comparable to that calculated to exist in flight. The need for continued research is indicated.

#### INTRODUCTION

The purpose of this discussion is to caution experimenters concerning the use of wind-tunnel results in predicting flight loads and moments when supercritical separated flow is present. Whenever separated flow has been observed on wind-tunnel models, the extrapolation of these results to flight conditions has always been subject to question. The discrepancies between aerodynamic results from flight and wind-tunnel investigations disclosed herein should not come as a surprise. They are merely additional evidence of the problem associated with separated flows.

Two combinations of Mach number and lift, both involving supercritical flow separation, are examined. One is for Mach numbers above cruise at lifting conditions near cruise, and the other is for Mach numbers near cruise at lifting conditions higher than cruise.

An example of the difficulty that might be encountered was observed during recent flight tests of a cargo-transport airplane. At supercritical Mach numbers the wing pressures and pitching moments of the airplane were considerably different from those predicted in wind-tunnel tests. No general procedure has been developed for resolving such discrepancies. Investigations are being conducted, however, to provide a better understanding of the factors involved, and the results herein are presented to report on the progress of these efforts.

## SYMBOLS

$C_D$	drag coefficient, $\text{Drag}/q_\infty S$
$C_L$	lift coefficient, $\text{Lift}/q_\infty S$
$C_m$	pitching-moment coefficient, $\text{Pitching moment}/q_\infty S \bar{c}$
$C_p$	local pressure coefficient, $(p_l - p_\infty)/q_\infty$
$b$	span of wing, meters
$c$	chord of wing, meters
$\bar{c}$	mean aerodynamic chord of wing, meters
$M$	free-stream Mach number
$p_l$	local static pressure, newtons/meter <sup>2</sup>
$p_\infty$	free-stream static pressure, newtons/meter <sup>2</sup>
$q_\infty$	free-stream dynamic pressure, newtons/meter <sup>2</sup>
$S$	total area of wing, meters <sup>2</sup>
$x$	longitudinal distance, measured from wing leading edge, meters
$\alpha_f$	angle of attack of fuselage, degrees

## DISCUSSION

An indication of the differences between wind-tunnel and flight data is shown by the pressure distributions in figures 1 and 2. In figure 1 is shown a comparison of the chordwise pressure distributions on the upper surface of a cargo-transport wing at a Mach number of 0.75, for a fuselage angle of attack of  $-0.6^\circ$ , where the lift coefficients for the complete configurations are slightly less than 0.3 and the wing pressures are all subcritical. Transition was fixed near the leading edge of the wind-tunnel model by the method discussed in paper number 2 by Braslow, Hicks, and Harris. The data are for the approximate 40-percent-semispan station. The chordwise trend of the pressures shows good agreement in shape between the wind-tunnel and flight results, although a small increase in the negative pressure-coefficient level is noted for the flight results.

In figure 2 is shown the same type of comparison at a higher-than-cruise Mach number of 0.85 for an angle of attack of approximately  $0^\circ$ . The lift coefficients associated with these wind-tunnel and flight conditions are 0.24 and

0.34, respectively. The flow over the wing for these conditions is supercritical. For example, a local supercritical Mach number of about 1.32 is associated with the flight peak pressure. As may be seen, the pressure distributions obtained in the wind tunnel and in flight are markedly dissimilar in shape. The adverse pressure gradients in this plot indicate that the location of the flight shock and attendant separation is rearward of that in the wind tunnel by about 20 percent chord. Associated with this shift in shock, of course, is a rearward shift of the center of pressure and therefore more negative pitching moments relative to values predicted from the wind-tunnel tests.

Because of the possible impact of this discrepancy on the satisfactory prediction of loads, stability, and performance of aircraft of this type, an investigation has been undertaken to resolve this difficulty.

A wind-tunnel investigation of several twist distributions indicated that differences in wing flexibility did not greatly contribute to the differences between wind-tunnel and flight results. It then was assumed that the problem might be associated with Reynolds number or scaling effects. Consideration of various factors suggested that the difficulty might be caused by differences in the boundary-layer conditions that affect shock-induced flow separation. At a given free-stream Mach number, the parameter that has the largest effect on shock-boundary-layer interaction is the boundary-layer thickness. For the particular problem of supercritical-flow separation the "relative thickness" was presumed to be a major factor. Relative thickness is defined as the ratio of the absolute thickness at any station to chord length. A study of these effects was thus considered a reasonable approach.

Figure 3 illustrates, in an exaggerated manner, the relative thickness effect. Since the relative thickness of the turbulent boundary layer varies inversely with a power (1/5) of the Reynolds number, the relative thickness at any given percent chord station would be greater on a small-scale wind-tunnel model with transition fixed near the leading edge than on a similar full-scale wing with natural transition in flight. When the local flow becomes sonic for both of these configurations, the displacement of the separated flow would tend to push the shock and accompanying separation farther forward on the wind-tunnel model.

It appeared, therefore, that the solution to the problem might be to develop a method that would provide a turbulent boundary layer near the trailing edge of the wind-tunnel model with the same relative thickness as would be encountered in actual flight.

With this objective as a goal, a transition strip was moved progressively rearward on a model during tests conducted in the Langley 8-foot transonic pressure tunnel. Theoretically, as the strip is moved downstream the extent of laminar flow ahead of the strip will increase, and the distance over which the turbulent layer can build up will be reduced. As a result, at any given position downstream of the strip, the turbulent layer will become thinner and tend to approach the relative thickness of the boundary layer in flight. It then was reasoned that when supercritical-flow conditions were reached on the two configurations, the shock position on the model would tend to approach the same

position as on the airplane. The thinnest turbulent layer would be attained, of course, with the strip removed.

Figure 4 shows the effect on the chordwise supercritical-pressure distribution of moving the transition strip on the model. The test conditions and the wing are the same as those used to obtain the previously presented pressure data (fig. 2). However, for these results, the model was tested with the tail off, and the fuselage was somewhat different. The changes should not have any effect on the basic phenomena under discussion. As the strip was moved from 7.5 percent chord to 50 percent chord, the shock position moved rearward. Visual observations of the flow pattern, obtained by the fluorescent-oil film method (ref. 1), indicated that a number of isolated roughness particles present on the surface of the wing produced wedges of turbulent flow in the predominantly laminar flow ahead of the strip, and the average location of transition for the strip at 50 percent chord was actually near 40 percent chord. When the strip was removed, visual observations of the flow patterns for this natural-transition condition indicated that the average location of transition was near 50 percent chord, which means that, along with turbulent wedges in the laminar boundary layer over the forward portion of the wing, some laminar flow extended behind the 50 percent chord. The shock moved farther rearward to the downstream position shown in this figure. When the flight data points from figure 2 are compared with these natural transition model results, the shock positions appear to be, for all practical purposes, the same. For this particular natural transition location, calculations were made and indicated that the relative thickness of the boundary layer at the trailing edge of the model was the same as that of the full-scale airplane in flight.

These recent results appear to give evidence that the relative boundary-layer thickness at the trailing edge may be a primary parameter in determining the shock location and resultant pressure distribution. Additional experimentation is necessary, of course, to validate this tentative conclusion. The results thus far obtained, however, do indicate that the discrepancies between wind-tunnel and flight data are a relative boundary-layer thickness effect; that is, a scale effect.

The changes in aerodynamic forces that occurred as the transition strip was moved are presented in figure 5 for a near-cruise angle of attack of  $2^\circ$  and a Mach number of 0.85. Plotted in this figure as solid lines are the variations of lift, drag, and pitching-moment coefficients as a function of the transition-strip location. The short-dash lines indicate the level of the forces and moment with the transition strip removed. The difference between the lift and drag for the usual forward position of a transition strip and the values obtained with natural transition is indicative of an increase in lift-drag ratio of about 20 percent. Of even more importance for the same test conditions, the variation of pitching moment is representative of a rearward shift in the center of pressure of 11 percent.

The results of this wind-tunnel investigation on a high-aspect-ratio subsonic wing at above-cruise Mach numbers, near cruise lift, provide evidence that the discrepancy between wind-tunnel and flight pressure and force data apparently results from a relative boundary-layer-thickness effect on supercritical-flow separation. It would be expected that the same phenomena also would exist near

the cruise Mach number, but at higher-than-cruise lift, since shock-induced separation also occurs for these conditions. In figure 6 are plotted the wind-tunnel pitching-moment coefficients as a function of lift for the same model just discussed with two extreme boundary-layer test conditions at a Mach number of 0.75. For the configuration with transition fixed near the leading edge ( $x/c = 0.075$ ) a reduction in stability occurs at lift coefficients slightly above cruise. When the strip is removed, not only are the pitching-moment coefficients more negative, but the trend toward instability is delayed to a higher lift coefficient. An examination of the wind-tunnel pressure data (which are not presented) indicated that this difference is associated with the same separation phenomena just described for the subsonic wing operating beyond its cruise Mach number; with the transition strip removed, shock-induced separation occurred farther rearward along the chord. As was indicated in the previous discussion, it is probable that the natural-transition configuration more nearly simulates flight conditions than the fixed-transition configuration. Available flight data do not go up to the point of divergence, so they have not been included in the figure.

#### CONCLUDING REMARKS

Because, at supercritical speeds, pressure distributions obtained from model and full-scale flight tests may be different, a study has been made for the purpose of improving this correlation.

On the basis of this study, a reasonable assumption appears to be that the problem is one of a Reynolds number effect on shock-induced boundary-layer separation. This effect appears associated with differences between the relative thickness of the boundary layer on models and full-scale airplanes.

At the present time no conclusive means are established for exactly simulating the supercritical-flow phenomena on models as they exist in flight. On the basis of present knowledge, however, it does appear that full-scale characteristics may be obtained, at least, on subsonic wings by locating transition on a model so as to produce the same relative boundary-layer thickness at the trailing edge as has been calculated to exist in flight.

Until this or other methods can be more definitely established, it is suggested as an interim recommendation that wind-tunnel studies be made with transition occurring at various locations. In this manner, at least, the sensitivity of shock-induced separation to modification of the boundary-layer conditions can be determined.

#### REFERENCE

1. Loving, Donald L.; and Katzoff, S.: The Fluorescent-Oil Film Method and Other Techniques for Boundary-Layer Flow Visualization. NASA MEMO 3-17-59L, 1959.

**SUBCRITICAL PRESSURE DISTRIBUTION**  
 $M=0.75; \alpha_f = -0.6^\circ$

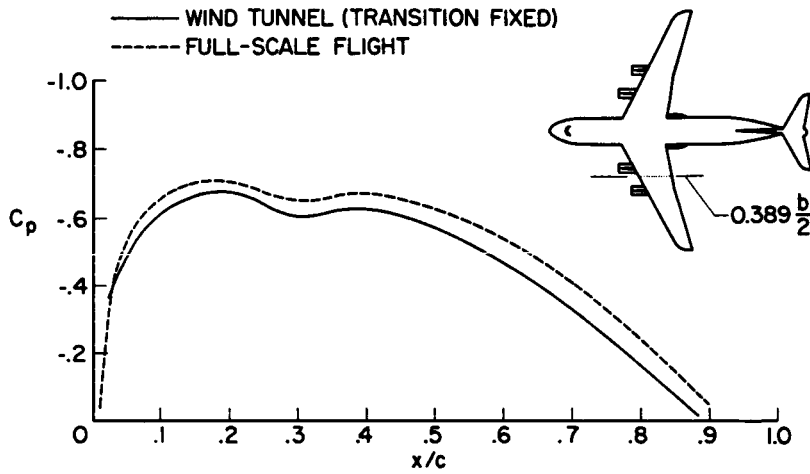


Figure 1

**SUPERCritical PRESSURE DISTRIBUTION**  
 $M=0.85; \alpha_f \approx 0^\circ$

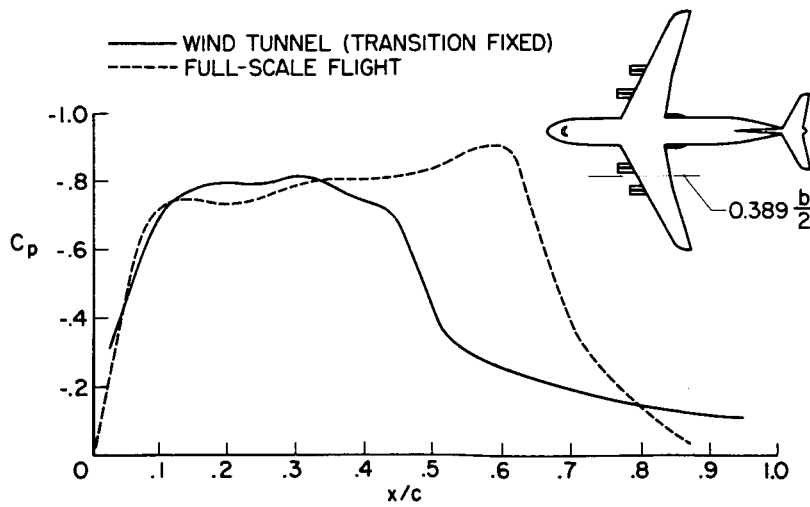


Figure 2

EFFECT OF BOUNDARY LAYER ON SHOCK-INDUCED SEPARATION

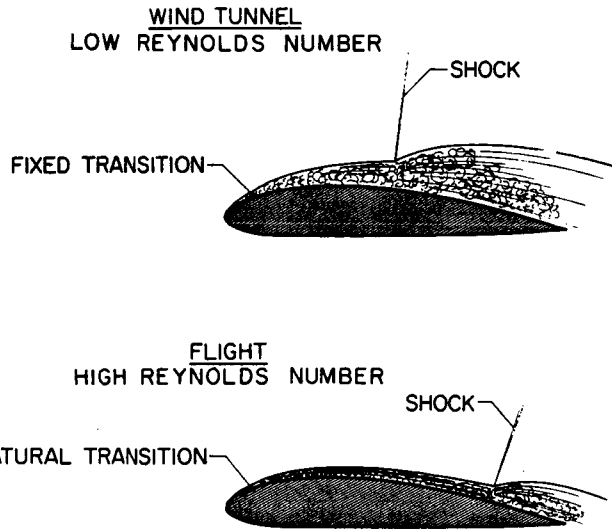


Figure 3

EFFECT OF TRANSITION LOCATION ON PRESSURE DISTRIBUTION  
 $M=0.85; \alpha_f = 0^\circ$

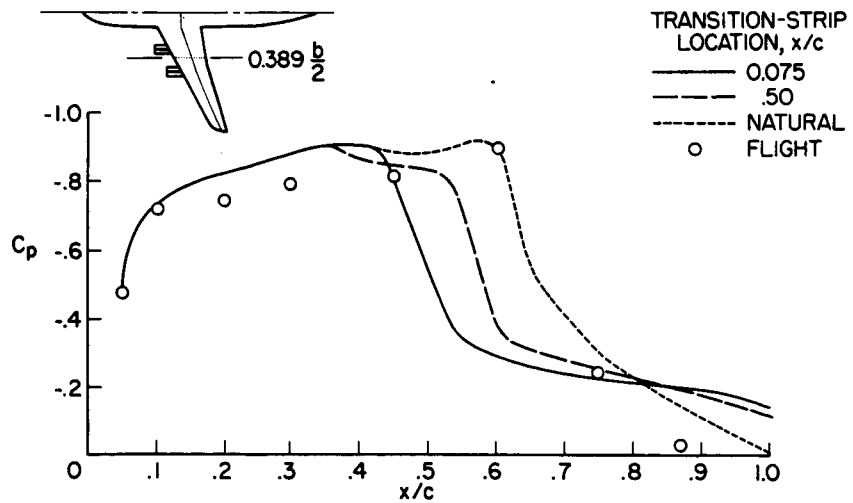


Figure 4

### EFFECT OF TRANSITION LOCATION ON FORCES

$M=0.85; \alpha_f=2^\circ$

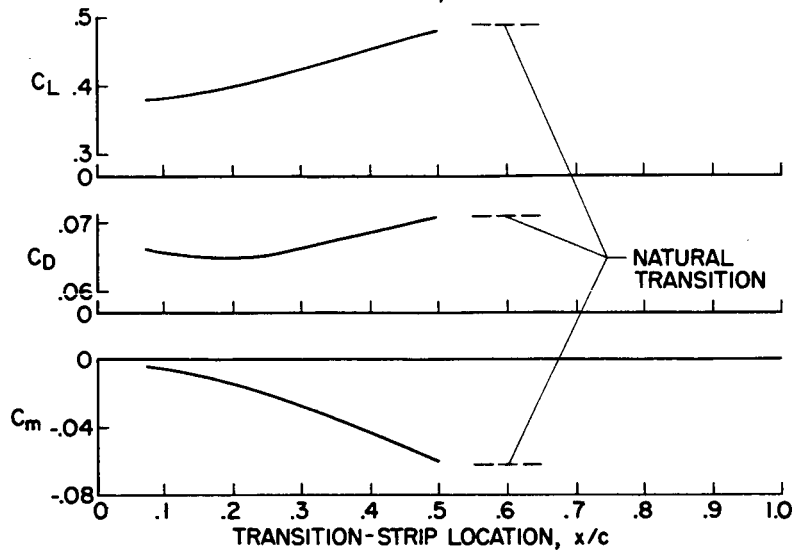


Figure 5

### EFFECT OF TRANSITION ON PITCH WIND TUNNEL; $M=0.75$

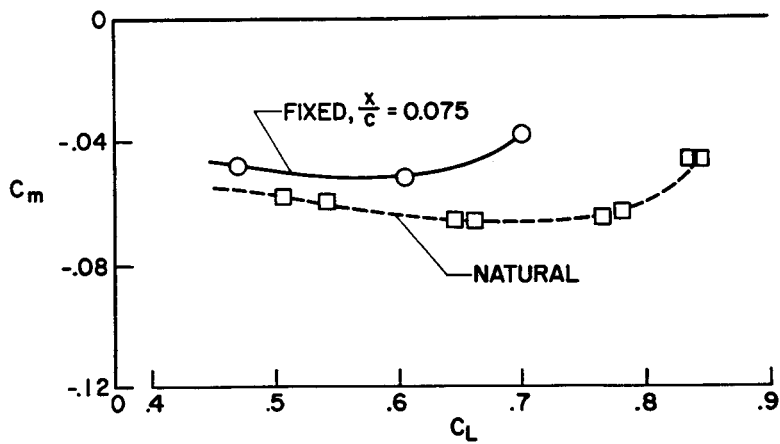


Figure 6

#### 4. SOME RECENT DEVELOPMENTS OF DYNAMIC TECHNIQUES FOR WIND TUNNELS

By Harleth G. Wiley, Robert A. Kilgore,  
and Jean Gilman, Jr.  
NASA Langley Research Center

#### SUMMARY

Some recent developments in improved dynamic techniques for wind-tunnel research are discussed. A new method for experimental gust research permits measurement of the response of a dynamically scaled model to a gust field generated in a wind tunnel by an oscillating airstream. Preliminary investigations indicate that the technique should be useful for determination of aerodynamic-structural transfer functions and dynamic-stability derivatives. Two types of magnetic model suspension and balance systems for wind tunnels that have been developed in the United States and in Europe are described. The National Aeronautics and Space Administration is sponsoring in-house and contract studies to define the engineering problems of developing these magnetic suspension systems into operational wind-tunnel research facilities. Equipment has been developed for determining the significant and unpredictable damping derivatives of current aircraft configurations at high angles of attack and in regions of gross aerodynamic instabilities. Experimental research with these techniques provides the basis for developing methods for more accurately predicting damping levels and trends, especially at flight angles of attack.

#### INTRODUCTION

Many of the dynamic problems of current and proposed aircraft configurations arise from the inability of researchers to predict, by reliable theory, the mechanics of the aerodynamic phenomena involved. The dynamic aerodynamic characteristics of configurations with swept wings, complex engine packages, and slender bodies are difficult to predict theoretically at realistic angles of attack. In addition, the aeroelastic study is becoming increasingly complex because of more flexible structures and more stringent mission requirements. Aerodynamic and structural responses, of course, can be obtained by full-scale flight tests, and some dynamic characteristics can be measured with pilotless free-flight model tests. However, one of the best approaches to the fundamental understanding and ultimate solution of these dynamic problems continues to be from experiments in the controlled environment of the wind tunnel. Therefore, efforts have continued within NASA to develop and improve wind-tunnel techniques for studying these dynamic problems.

The purpose of this paper is to review recent developments for three separate dynamic techniques for wind tunnels. The three areas to be discussed are: (1) An oscillating airstream technique for determining gust response, (2) recent

developments in magnetic model suspension and balance systems, and (3) techniques for measuring dynamic-stability derivatives at angles of attack.

### SYMBOLS

$C_{l_p}$	damping-in-roll parameter
$C_{m_q} + C_{m_{\dot{\alpha}}}$	oscillatory damping-in-pitch parameter
$C_{n_r} - C_{n_{\dot{\beta}}} \cos \alpha$	oscillatory damping-in-yaw parameter
$C_{l_p} + C_{l_{\dot{\beta}}} \sin \alpha$	oscillatory damping-in-roll parameter
$k$	reduced-frequency parameter
$M$	Mach number
$V$	stream velocity
$\alpha$	angle of attack
$\theta_v$	vane amplitude

### DISCUSSION

#### Oscillating Airstream Technique

A system for measuring the response of an aeroelastically scaled model to an oscillating vertical gust field, generated by oscillating vanes, has been developed. A plan view of the major components of the system is presented in figure 1. A set of biplane vanes is located on each wall in the entrance nozzle of the Langley transonic dynamics tunnel. The three-dimensional vanes have a span of 3.5 feet and a panel aspect ratio of 1.2. The biplane vanes on each tunnel wall are hydraulically driven and are synchronized to oscillate sinusoidally in pitch. The vertical velocity component of the flow field generated by the oscillating vanes causes an oscillation of the airstream, which simulates a time-varying vertical gust field of controlled frequency in the test section. A complete description of the principle and details of the technique is contained in references 1 and 2.

The vanes are located well upstream in the subsonic portion of the entrance nozzle so that local shock waves cannot be generated on the vanes. Thus, tests can be made at transonic speeds in the test section without shock interference from the vanes. In addition, the test area lies between the vane wakes so that

the spanwise gust distribution in the test area is essentially uniform (within about 10 percent) and allows tests of models with spans up to about 6 feet.

The oscillator system was designed for operation at vane amplitudes  $\theta_v$  from  $3^\circ$  to  $12^\circ$  at frequencies up to 20 cycles per second. Currently, however, operation is power limited by the power absorbed by the aerodynamic damping of the vanes, which is a function of vane amplitude and dynamic pressure. Figure 2 presents the typical variation of gust amplitudes obtained at the center line of the test area for various gust frequencies. These particular calibrations were made for Freon as the test medium and for Mach numbers of 0.8, 1.0, and 1.1. The vane amplitude  $\theta_v$  was  $9^\circ$ . Although the characteristic decrease in gust amplitude with increasing frequency is appreciable, as shown in figure 2, the gust amplitude at the higher frequencies appears to be adequate for test purposes.

For the initial development tests, a simple dynamically scaled model was mounted in the test area on a two-cable support system with sufficient freedom to allow the model to be flown by remote control. Thus, both the rigid-body response and the structural response of the model to the oscillating airstream simulates free-flight response to vertical gusts. A trailing umbilical cable carries control signals to the model and data measurements of the model flight characteristics. (Snubber cables, which are slack in flight, are used as safety restraints as explained in reference 2.)

As an illustration of the usefulness of the technique, some preliminary measurements, at a Mach number of 1.0, of the acceleration response at the center of gravity of the dynamically scaled airplane model are presented in figure 3. (The reduced-frequency parameter  $k$  covers only the short-period, rigid-body frequency range for the purposes of this discussion. Actually, the attainable reduced frequency for these test conditions is about three times that shown.) The experimental normal-acceleration functions are shown as symbols and the calculated normal acceleration is shown as the solid line. At a reduced frequency of about 0.006 a model plunging mode is apparent. This secondary plunging mode is introduced by the characteristics of the cable-support system which modify the otherwise free-flight response of the model. Modifications to the cable support system probably can reduce the model response in the plunging mode obtained in these preliminary tests. The second peak is the longitudinal response of the model in the short-period, rigid-body mode. The calculated and experimental values of the normal-acceleration function are in reasonably good agreement. The discrepancies may well be due to the rigid-body stability derivatives that were used for these preliminary calculations or to possible undefined effects of the cable support system. Further details of these preliminary tests and calibrations are presented in reference 2.

The initial development tests show that a satisfactory experimental technique for subjecting a dynamically scaled model to a controlled gust field has been developed. A method for mounting the model to simulate the free-flight modes is available. Although several improvements are needed, the technique, when fully developed, should be especially valuable for experimental research in two dynamic problem areas. First, it should permit better determination and evaluation of transfer functions at transonic speeds. These functions can be

derived from experimental measurement of the amplitude and phase of model response to gust inputs through ranges of gust frequencies. The functions relate the instantaneous loads and structural response of aerodynamic configurations to gusts and turbulence caused by atmospheric phenomena or by man-made explosions. These frequency-response functions are especially critical for the design of aircraft for low-altitude high-speed missions and for large flexible aircraft and boosters with low natural frequencies and low load factors. In addition, the technique should be adaptable to the determination of dynamic-stability derivatives for both rigid and flexible aerodynamic configurations.

### Magnetic Suspension and Balance Systems

Magnetic suspension and balance systems for wind tunnels have been developed both in the United States and in Europe. This discussion is a résumé of recent progress in the area and of the contribution of NASA in sponsoring research contracts and grants to study the problems of developing two types of magnetic suspension systems into operational wind-tunnel research facilities. The two systems differ fundamentally in the type and degree of restraint imposed on the model by the magnetic fields.

The first system provides firm magnetic control in all major model degrees of freedom. This type of magnetic suspension system was first developed in France. (See ref. 3.) A similar system has been developed at the Massachusetts Institute of Technology (MIT) under sponsorship of the U.S. Air Force (ref. 4). The fundamentals of these systems are shown in figure 4. The magnetic fields of direct-current lift coils act on a cylindrical iron core embedded within a nonmagnetic model. Light and photocell systems sense vertical movement of the model and control the current to the two lift coils to maintain the desired model vertical position. The angle of attack can be changed by raising or lowering the two horizontal light and photocell systems relative to each other. Similar lateral coils and position-sensing systems are mounted in a horizontal plane to control the side forces. A large air-core drag coil surrounds the tunnel upstream of the model to hold the model against the drag forces.

The elimination of the aerodynamic interference of mechanical support structures is the obvious primary advantage of this system. Thus, measurements of heat-transfer rates, aerodynamic pressures, and forces and moments are unaffected by flow distortions; and studies of true wakes and base effects can be made. In addition, the systems should be adaptable to forced-response dynamic-stability testing. However, these devices as they now exist are subject to several operational problems. The asymmetrically arranged support coils cause complicated magnetic-field and model-position interactions. The optical position-sensing schemes work well only for symmetrical models or for models with straight-line elements. Finally, for use in large wind tunnels, the physical size and power requirements of the coils are large, especially if the coils are operated at normal temperature.

The Langley Research Center is now sponsoring a research contract with MIT to study some of these problems as they apply to a magnetic suspension and balance system for a 15-inch-diameter, Mach 10, hypersonic wind tunnel. These

studies have resulted in an advanced concept of symmetrical coil arrangements to minimize magnetic-field interactions. More versatile position-sensing devices are being investigated. In addition, the studies show that for the 15-inch-diameter hypersonic wind tunnel, coil sizes and power requirements are large but appear feasible, even with normal-temperature coil construction.

The second magnetic suspension concept is a system that is uniquely adapted to simulated free flight in that it allows model response in certain degrees of freedom. A pilot facility was built at the Langley Research Center to verify the concept and to permit component development (ref. 5). The device, in its simplest form, utilizes a single, large, direct-current coil encircling the wind-tunnel test section, as illustrated in figure 5. The magnetic field generated by the single coil is axially symmetrical and diverges from the center line. A sphere of magnetic material is suspended in the field. When the sphere is fixed in the axial position by the typical position-sensing and current-control system, the divergent field stabilizes the sphere toward the center line. This 4.75-inch-inside-diameter pilot facility suspended an iron sphere successfully in 1964. Results from subsequent tests showed that a combined 12-pound load applied to a 3-inch-diameter sphere could be supported with a total power expenditure of less than 5000 watts.

It is conceived that a special magnetic material with negligible eddy-current losses will allow the sphere to rotate freely about any of its axes. The magnetic sphere could then be mounted at the center of gravity of an aerodynamic model of nonmagnetic material. This concept could be used in a wind tunnel to allow dynamic simulation of an aerodynamic body in free flight, with virtually complete rotational response about all major axes.

An advanced concept of the magnetic suspension system just described, but with three-dimensional magnetic model control, was developed by the University of Virginia for the study of wakes and sphere drag (ref. 6). More recent developments were presented in a paper by Dr. H. M. Parker of the University of Virginia at a symposium at Wright Patterson Air Force Base, April 1966. The Langley Research Center has recently sponsored a grant to the University of Virginia for a study of the engineering aspects of scaling up this three-dimensional magnetic system to a more useful size. In this study the feasibility of using supercooled or superconducting coils for magnet construction is being explored. These techniques offer the possibility of large reductions in coil size and power requirements.

Thus, two basic types of magnetic model suspension systems for wind tunnels have been developed and are being successfully operated. The advantages of these new systems are obvious. Both in-house and contract efforts are presently under way at the Langley Research Center to define the problems of developing both magnetic suspension systems into operational wind-tunnel research facilities.

#### Techniques for Measuring Dynamic-Stability Derivatives

The third experimental technique to be discussed involves the measurement of rigid-body dynamic-stability derivatives. Much dynamic research is

accomplished at the Langley Research Center with the well-known free-flight-model techniques in the full-scale tunnel at low speeds. Equipment and techniques also are available at the Ames and Langley Research Centers of NASA for the measurement of damping derivatives at moderate to high Mach numbers. The present discussion is confined, however, to the rigidly forced dynamic-stability mechanisms developed at Langley especially for investigating configurations at appreciable angles of attack. These devices permit experimental determination of the theoretically unpredictable damping derivatives at angles of attack where separated flow may be present and in regions of gross aerodynamic instabilities. A résumé of the capabilities of the existing Langley dynamic-stability equipment, and the characteristics of several new devices which should be in operation within the year, is presented in table I.

TABLE I.- EXPERIMENTAL DYNAMIC-STABILITY CAPABILITIES

Mode	Damping derivatives	Mach number	Angle of attack, deg	Amplitude, deg	Frequency, cps
Steady roll	$C_{l_p}$	0.2 to 1.0	$\pm 35$	-----	3 to 10 (rps)
Oscillatory pitch or Oscillatory yaw	$C_{m_q} + C_{m_{\dot{\alpha}}}$	0.13	$\pm 180$	0 to 30	0 to 2
		0.2 to 1.2	-5 to 64	$\frac{1}{2}, 1, 2$	3 to 30
Oscillatory yaw	$C_{n_r} - C_{n_{\dot{\beta}}} \cos \alpha$	1.5 to 4.6	-3 to 25	$\frac{1}{2}, 1, 2$	3 to 30
		10.0	-18 to 24	1.2	*5 to 60
Oscillatory roll	$C_{l_p} + C_{l_{\dot{\beta}}} \sin \alpha$	0.13	$\pm 180$	0 to 30	0 to 2
		0.2 to 1.2	-2 to 22	2.5	*3 to 30

\*Equipment under construction.

As shown, the steady-state rolling derivatives can be obtained at Mach numbers from 0.2 to 1.0 for angles of attack from  $-35^\circ$  to  $35^\circ$ . The oscillatory pitching, yawing, and rolling derivatives can be determined over a wide range of Mach numbers and angles of attack. The dynamic-stability equipment described in table I can be operated through the full Reynolds number ranges of the wind tunnels in which they are used. Although not shown in the table, these dynamic-stability devices also can obtain the aerodynamic stiffness derivatives and the pertinent lateral cross derivatives, where applicable.

These experimental techniques are used extensively for investigations of the rigid-body dynamic-stability characteristics of current aircraft and spacecraft configurations. A chart of some of the research accomplished, and that presently underway, is presented in figure 6. The horizontal bars indicate the Mach number ranges for which research has been accomplished for a broad range of configuration types. (The results of some of these investigations are presented in references 7 to 27.) The programs have involved studies of the effects on the pitching, yawing, and rolling derivatives of configuration-component breakdowns, angle of attack, Mach number, Reynolds number, and oscillation frequency and amplitude. The research has provided a better understanding of some of the aerodynamic phenomena involved and should provide the basis for development of better methods of prediction, especially at angles of attack where flow separation occurs.

These wind-tunnel investigations have uncovered some interesting and significant damping trends for several current aircraft configurations. The variation of pitch damping with angle of attack at a Mach number of 0.40 for two airplane models with moderately swept subsonic-wing configurations is presented in figure 7. (Positive aerodynamic damping is indicated by the arrow.) The characteristics of a typical, swept-wing, subsonic transport with four wing-mounted jet engines are shown by the solid curve (from ref. 8). The dashed line indicates the pitch-damping characteristics of a variable-sweep fighter model with the wings swept  $20^\circ$ . (For the latter tests the highly-swept inboard leading edge, or glove, was removed. This change resulted in a relatively thick, subsonic type of wing, with the leading edge straight in to the fuselage.) The pitch damping for both configurations is about constant at the lower angles of attack, but becomes negative near the stall region. The negative pitch damping near the stall for these subsonic, swept-wing configurations may well expedite entry into the stall and/or intensify a pitch-up tendency. Incorporation of the highly swept inboard glove on the variable-sweep fighter model considerably increased the level of pitch damping near the stall as shown in figure 7.

From the data of figure 7 it is also apparent that the levels of pitch damping determined at an angle of attack of  $0^\circ$  cannot reasonably be extrapolated to the higher angles of attack. In addition, it is obvious that rigidly forced dynamic-stability mechanisms are required for investigations of unstable flight regions such as those shown here.

The Langley rigidly forced dynamic-stability equipment is especially useful for investigations of high-angle-of-attack phenomena such as the deep stall of T-tail airplane configurations. The pitch-damping characteristics of a T-tail transport model with aft-fuselage-mounted jet engines are presented in figure 8. (The typical decrease in damping near the stall previously discussed is also a characteristic of this T-tail configuration.) In the deep-stall region, near an angle of attack of  $40^\circ$ , sharply decreased damping is also evident.

Although this unexpected, and theoretically unpredicted, decrease in pitch damping is not understood at present, research on T-tail configurations is continuing. The characteristic itself may be quite significant. Simulator studies at Langley, of the characteristics of T-tail airplanes, show that decreased or

negative pitch damping is beneficial in preventing "lock-in" at a deep-stall attitude (ref. 28). Thus, the seemingly adverse decreased damping characteristic may well prove to be helpful. The ability to define, experimentally, unpredictable damping phenomena such as those just discussed again illustrates the value of these techniques for investigations of dynamic-stability derivatives at pertinent angles of attack.

#### CONCLUDING REMARKS

Several experimental dynamic techniques for wind-tunnel research have been reviewed. One such technique is a new method for experimental gust research. This method permits measurement of the response of a dynamically scaled model to a gust field generated in a wind tunnel by an oscillating airstream. In addition, studies are being undertaken both at the Langley Research Center and under NASA contract to define the engineering problems associated with the development of two types of magnetic-suspension systems into operational wind-tunnel research facilities. Techniques have also been developed for determining the significant and unpredictable damping derivatives of current aircraft configurations at high angles of attack and in regions of gross aerodynamic instabilities. Experimental research with these techniques provides the bases for developing methods for more accurately predicting damping levels, especially at flight angles of attack.

## REFERENCES

1. Reid, Charles F., Jr.; and Wrestler, Clifton G., Jr.: An Investigation of a Device to Oscillate a Wind-Tunnel Airstream. NASA TN D-739, 1961.
2. Gilman, Jean, Jr.; and Bennett, Robert M.: A Wind-Tunnel Technique for Measuring Frequency-Response Functions for Gust Load Analyses. AIAA Paper No. 65-787, 1965.
3. Tournier, M.; and Laurenceau, P.: Suspension magnétique d'une maquette en soufflerie. La Rech. Aeron., no. 59, July-Aug. 1957, pp. 21-26.
4. Tilton, Edward Lee, III; Parkin, William J.; Covert, Eugene E.; Coffin, James B.; and Chrisinger, John E.: The Design and Initial Operation of a Magnetic Model Suspension and Force Measurement System. ARL-63-16, U.S. Air Force, Aug. 1962.
5. Hamlet, Irvin L., and Kilgore, Robert A.: Some Aspects of an Air-Core Single-Coil Magnetic-Suspension System. NASA Paper presented at the ARL Symposium on Magnetic Suspension and Balance Systems. (Wright-Patterson Air Force Base, Ohio), Apr. 13-14, 1966.
6. Parker, H. M.; and Kuhlthau, A. R.: A Magnetic Wind Tunnel Balance. U.S. Air Force AFOSR-64-0567, U.S. Air Force, Feb. 1964.
7. Wright, Bruce R.; and Brower, Margaret L.: Aerodynamic Damping and Oscillatory Stability in Pitch for a Model of a Typical Subsonic Jet-Transport Airplane. NASA TN D-3159, 1966.
8. Delaney, Bobby R.; and Thompson, Wilson E.: Dynamic Stability Characteristics in Pitch and in Yaw for a Model of a Variable-Sweep Supersonic Transport Configuration at Mach Numbers of 2.40, 2.98, and 3.60. NASA TM X-761, 1963.
9. Wright, Bruce R.; and Averett, Benjamin T.: Transonic Aerodynamic Damping and Oscillatory Stability in Yaw and Pitch for a Model of a Variable-Sweep Supersonic Transport Airplane. NASA TM X-1207, 1966.
10. Hillje, Ernest R.; and Wiley, Harleth G.: Transonic Dynamic Stability Characteristics in Pitch and in Yaw for a Model of a Variable-Sweep Airplane Configuration Capable of Low-Level Supersonic Attack. NASA TM X-618, 1962.
11. Hassell, James L., Jr.: Low-Speed Flight Characteristics of a Variable-Wing-Sweep Fighter Model. NASA TM X-1036, 1965.
12. Hayes, William C., Jr.; and Thompson, Wilson E.: Wind-Tunnel Measurements at Subsonic and Transonic Speeds of the Rolling Stability Derivatives of a Variable-Sweep Airplane Configuration - Outer Wing Panels Swept  $108^{\circ}$ . NASA TM X-465, 1961.

13. Hayes, William C., Jr.; Kemp, William B., Jr.; and Thompson, Wilson E.: Wind-Tunnel Measurements and Estimated Values of the Rolling Stability Derivatives of a Variable-Sweep Airplane Configuration at Subsonic and Transonic Speeds. NASA TM X-600, 1961.
14. Boisseau, Peter C.: Investigation of the Low-Speed Stability and Control Characteristics of a 1/7-Scale Model of the North American X-15 Airplane. NACA RM L57D09, 1957.
15. Hassell, James L., Jr.; and Hewes, Donald E.: Investigation of the Subsonic Stability and Control Characteristics of a 1/7-Scale Model of the North American X-15 Airplane With and Without Fuselage Forebody Strakes. NASA TM X-210, 1960.
16. Johnson, Joseph L., Jr.: Wind-Tunnel Investigation of Low-Subsonic Flight Characteristics of a Model of a Canard Airplane Designed for Supersonic Cruise Flight. NASA TM X-299, 1960.
17. Kilgore, Robert A.; and Hillje, Ernest R.: Some Transonic Dynamic Longitudinal and Directional Stability Parameters of a Canard Airplane Model Designed for Supersonic Flight. NASA TM X-533, 1961.
18. Bielat, Ralph P.; and Wiley, Harleth G.: Dynamic Longitudinal and Directional Stability Derivatives for a 45° Sweptback-Wing Airplane Model at Transonic Speeds. NASA TM X-39, 1959.
19. Hassell, James L., Jr.: Investigation of the Low-Subsonic Stability and Control Characteristics of a 1/3-Scale Free-Flying Model of a Lifting-Body Reentry Configuration. NASA TM X-297, 1960.
20. Johnson, Joseph L., Jr.: Wind-Tunnel Investigation at Low Subsonic Speeds of the Static and Oscillatory Stability Characteristics of Models of Several Space Capsule Configurations. NASA TM X-285, 1960.
21. Igoe, William B.; and Hillje, Ernest R.: Transonic Dynamic Stability Characteristics of Several Models of Project Mercury Capsule Configurations. NASA TM X-554, 1961.
22. Wright, Bruce R.; and Kilgore, Robert A.: Aerodynamic Damping and Oscillatory Stability in Pitch and Yaw of Gemini Configurations at Mach Numbers From 0.50 to 4.63. NASA TN D-3334, 1966.
23. Boisseau, Peter C.: Low-Speed Static and Oscillatory Stability Characteristics of a Model of the Apollo Launch-Escape Vehicle and Command Module. NASA TM X-894, 1963.
24. Kilgore, Robert A.; and Averett, Benjamin T.: Wind-Tunnel Measurements of Some Dynamic Stability Characteristics of 0.055-Scale Models of Proposed Apollo Command Module and Launch-Escape Configurations at Mach Numbers From 2.40 to 4.65. NASA TM X-769, 1963.

25. Averett, Benjamin T.; and Kilgore, Robert A.: Dynamic-Stability Characteristics of Models of Proposed Apollo Configurations at Mach Numbers From 0.30 to 1.20. NASA TM X-912, 1964.
26. Averett, Benjamin T.; and Wright, Bruce R.: Some Dynamic-Stability Characteristics of Models of Proposed Apollo Configurations at Mach Numbers From 1.60 to 2.75. NASA TM X-971, 1964.
27. Averett, Benjamin T.: Dynamic-Stability Characteristics in Pitch of Models of Proposed Apollo Configurations at Mach Numbers From 0.30 to 4.63. NASA TM X-1127, 1965.
28. Lina, Lindsey J.; and Moul, Martin T.: A Simulator Study of T-Tail Aircraft in Deep Stall Conditions. AIAA Paper No. 65-781, 1965.

PLAN VIEW OF OSCILLATING AIRSTREAM SYSTEM

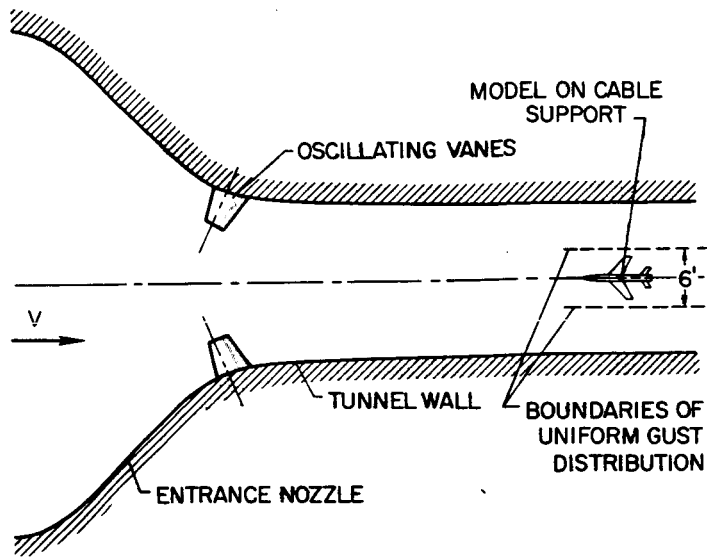


Figure 1

VARIATION OF GUST AMPLITUDE WITH FREQUENCY  
 FREON;  $M=0.8$  TO  $1.1$ ;  $\theta_v=9^\circ$

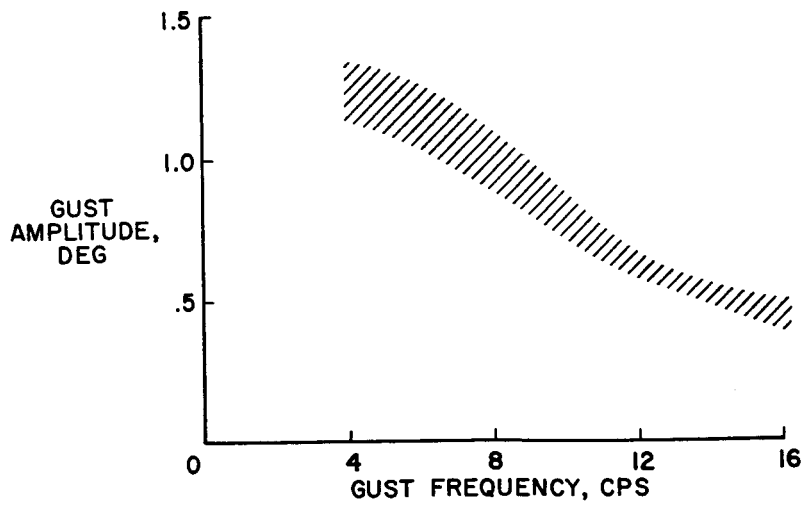


Figure 2

ACCELERATION RESPONSE AT CENTER OF GRAVITY  
M=1.0

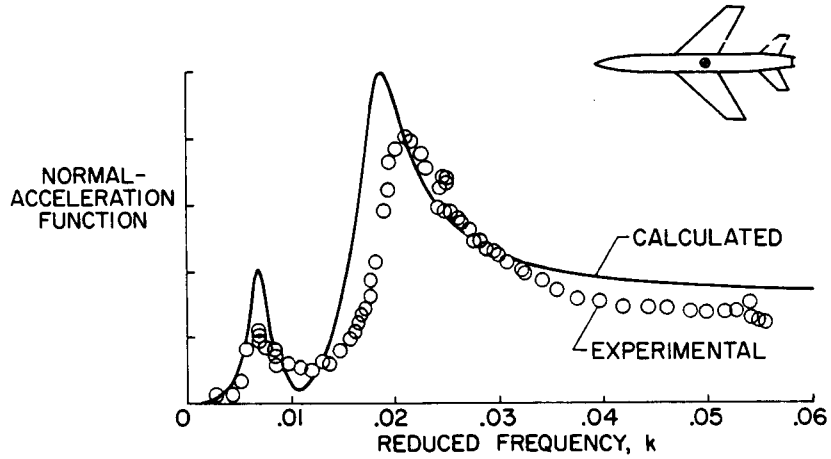


Figure 3

MULTIPLE-CONTROL MAGNETIC SUSPENSION SYSTEM

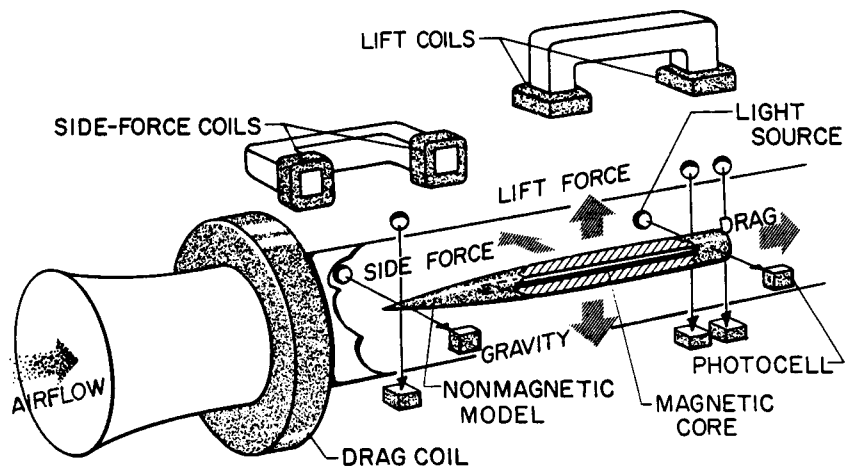


Figure 4

### FREE-RESPONSE MAGNETIC SUSPENSION SYSTEM

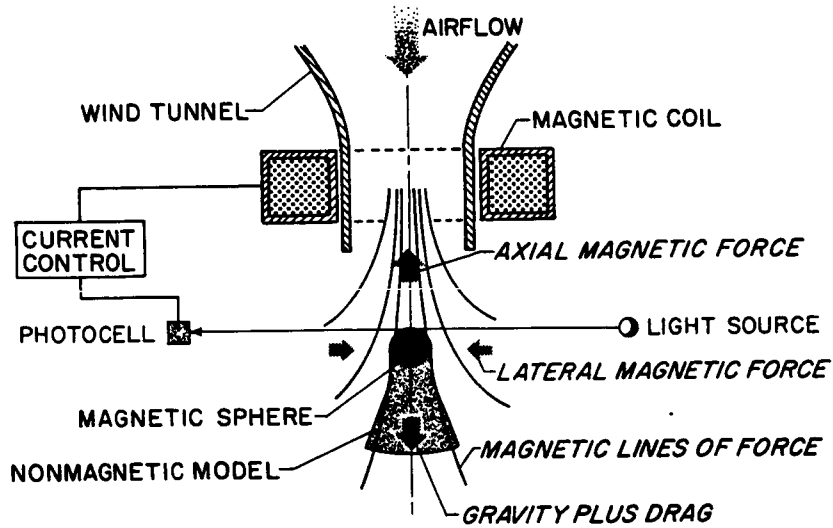


Figure 5

### RECENT DYNAMIC-STABILITY PROGRAMS AT LANGLEY

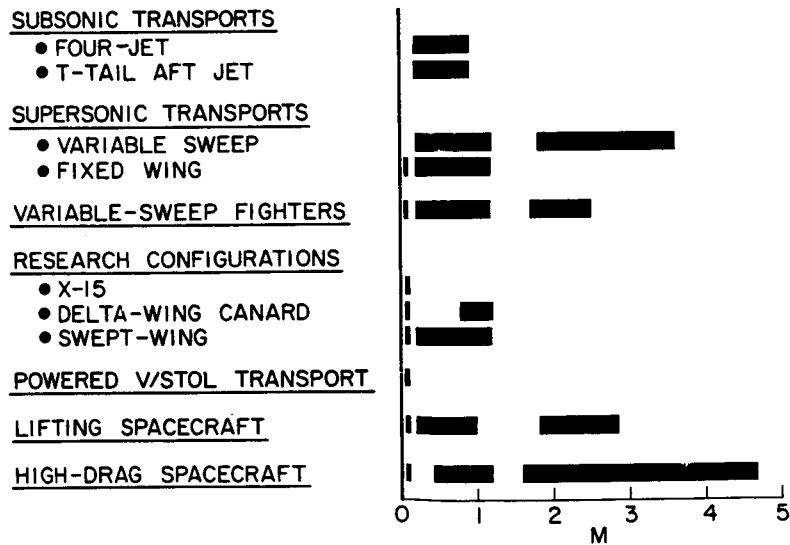


Figure 6

PITCH DAMPING FOR SUBSONIC-WING CONFIGURATIONS  
M=0.40

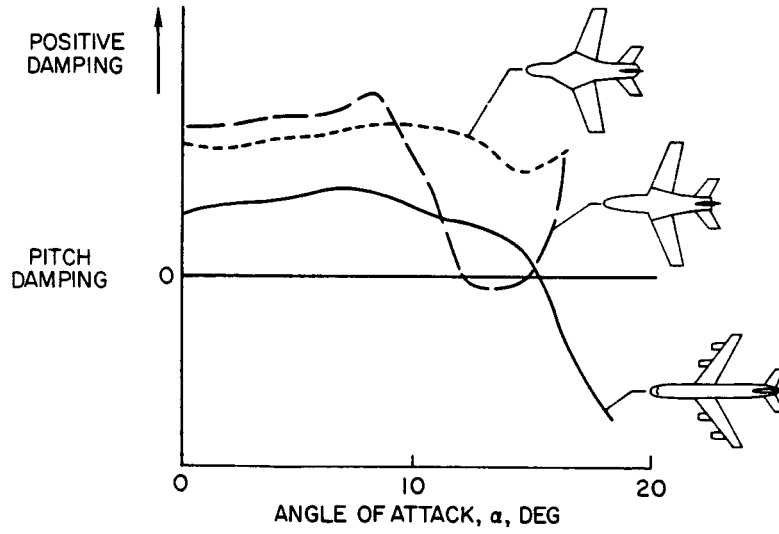


Figure 7

PITCH DAMPING OF T-TAIL CONFIGURATION  
M=0.40

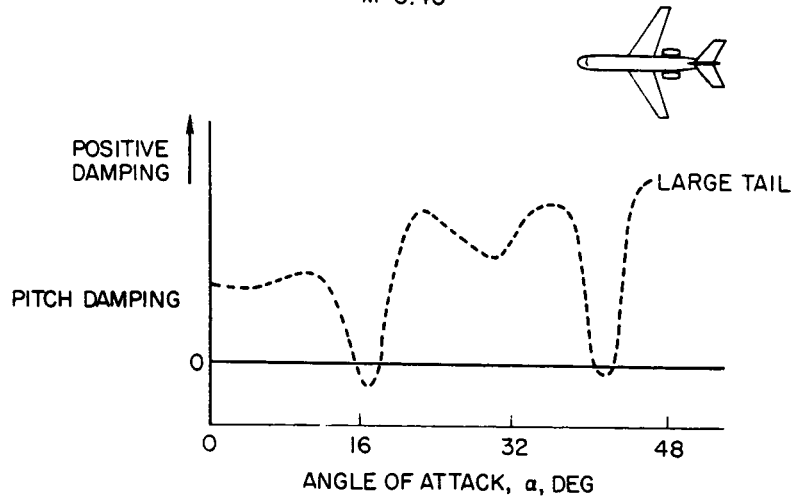


Figure 8

## 5. SOME CONFIGURATION EFFECTS ON STATIC STABILITY OF AIRPLANES

### AT HIGH ANGLES OF ATTACK AND LOW SPEEDS

By Edward J. Ray, Vernard E. Lockwood,  
and William P. Henderson  
NASA Langley Research Center

#### SUMMARY

A review has been made to examine some of the problems and possible solutions regarding stability at high angles of attack and low speeds. Pitch-up of fixed-wing configurations has been alleviated by the employment of wing leading edge and canard devices. Pitch-up for variable-sweep-wing configurations can be alleviated by a low horizontal tail, free-floating the forewing, reduction of the forewing sweep, or deflection of the forewing. The deep-stall characteristics of T-tail airplanes can be improved by increasing the ratio of tail span to nacelle span and by careful selection of nacelle position. Indications are that directional stability at high angles of attack can be improved by proper selection of fuselage cross-section shape. Directional stability for certain configurations can be improved by placing the vertical tail surfaces near the wing tips.

#### INTRODUCTION

The design requirements necessary for good performance at high speeds often result in undesirable low-speed stability characteristics at moderate and high angles of attack. Although many contemporary airplanes incorporate elaborate stability augmentation devices, it is still desirable to strive for good unaugmented stability characteristics.

The purpose of this paper is to review some of the problems and possible solutions regarding high angle-of-attack stability at subsonic Mach numbers. The scope of this presentation includes a discussion of the pitch-up problems of fixed-wing and variable-sweep-wing configurations, the deep-stall characteristics of T-tail airplanes, and the effects of fuselage cross-section shape and vertical tail position on directional stability.

#### SYMBOLS

b                    reference wing span  
 $b_n$                 nacelle span

$b_t$	horizontal tail span
$\bar{c}$	wing mean geometric chord
$C_m$	pitching-moment coefficient, $\frac{\text{Pitching moment}}{qS\bar{c}}$
$C_{m,t}$	pitching-moment coefficient provided by horizontal tail
$C_{m,.40\bar{c}}$	pitching-moment coefficient at 40 percent wing mean geometric chord
$C_n$	yawing-moment coefficient, $\frac{\text{Yawing moment}}{qSb}$
$C_{n\beta}$	directional stability parameter, $\frac{\partial C_n}{\partial \beta}$
$C_p$	pressure coefficient, $\frac{P_{\text{local}} - P_{\text{free stream}}}{q_{\text{free stream}}}$
$\Delta C_p$	difference in pressure coefficient between upper and lower surface of wing
$C_Y$	side-force coefficient, $\frac{\text{Side force}}{qS}$
$h_t$	vertical distance from nacelle plane of symmetry to mean chord plane of horizontal tail
$i_t$	horizontal tail incidence (positive trailing edge down), degrees
$l_n$	longitudinal distance from aft end of nacelle to quarter-chord of mean geometric chord of horizontal tail
$M$	Mach number
$p$	pressure
$q$	dynamic pressure
$S$	reference wing area
$S_c$	exposed canard area
$V$	free-stream air velocity

$V_C$	cross-wind velocity
$\alpha$	angle of attack, degrees
$\beta$	sideslip angle, degrees
$\Lambda$	leading-edge sweep of forewing or outer wing panel, degrees
$\delta_f$	deflection of wing leading-edge flaps (positive leading edge up), degrees

#### FIXED-WING CONFIGURATIONS

The longitudinal stability problems which arise at low speeds for one particular high performance supersonic transport concept are illustrated in figure 1. The basic configuration, shown at the top of the figure, incorporated a warped wing with sharp leading edges and cranked wing tips. The extreme instability for the basic arrangement results from the sharp leading edges of the wing and the combined planform effects of the cranked wing tips and trailing-edge cutout.

An extensive wind-tunnel investigation was conducted in the Langley high-speed 7- by 10-foot tunnel to determine whether the longitudinal stability characteristics of this configuration could be improved. The sketch at the lower right of figure 1 indicates the modifications which were made to the configuration. An inboard portion of the wing leading edge was deflected downward and a comparatively smaller outboard segment was deflected upward. In addition, the radius of the inboard half of the wing leading edge was increased. The leading-edge modifications did not affect the maximum lift-drag ratio at low speeds. These modifications resulted in a favorable redistribution of lift over the wing and a consequent improvement in the stability characteristics. An increment in maximum lift-drag ratio of about 0.60 over that obtained for the basic configuration can be expected when the outboard flap is undeflected. However, a slight destabilizing tendency in the pitching-moment variation with lift coefficient is noted. The increased leading-edge radius of the modified configuration could be incorporated without diminishing the supersonic performance capabilities of the configuration (ref. 1). Longitudinal stability problems, however, might be encountered at other flight conditions when the wing leading edge is undeflected.

Variable-geometry canard devices have been envisioned as a method which might be utilized to reduce pitch nonlinearities and increase the trimmed lift coefficient at landing and take-off attitudes. The pitching-moment characteristics for the basic configuration have been repeated in figure 2. Pitching-moment results are also shown for the basic configuration with two variable-sweep-canard arrangements which form part of the main wing when in the retracted position. These pitch data have been adjusted to the same level of stability at low angles of attack. This adjustment required a 4-percent forward shift in center of gravity for the small canard arrangement and an 8-percent shift for the large canard arrangement. For this configuration, a forward shift in center of gravity would result in a trim drag penalty at the cruise Mach number. These

data indicate that longitudinal stability at the higher angles of attack can be improved considerably by sweeping a relatively small portion of the wing forward and deflecting a portion of the forewing. Additional improvements in the pitch characteristics of the canard configurations might be expected by incorporating the additional wing leading-edge modifications shown in figure 1. From a comparison of figures 1 and 2 at landing and take-off attitudes, the nose-up moments of the canard configurations are substantially higher than those indicated for the modified configuration shown in figure 1. The positive moments would allow a trailing-edge-down control deflection and a consequent improvement in the trimmed lift. In addition, flap deflections on the canard surface would provide additional nose-up moments for trimming which would enable an increase in the deflection of the high-lift devices. The unfavorable forward shift in aerodynamic center resulting from sweeping the canard forward might be diminished by utilizing an extended trailing-edge-flap arrangement. Extending the flaps would reduce the trailing-edge cutout and have a favorable effect on the linearity of the pitch curve.

#### VARIABLE-SWEEP-WING CONFIGURATIONS

One of the problems which has faced the designer of supersonic airplanes is the incompatibility between the wing geometry requirements for high-speed and low-speed flight. For variable-sweep-wing airplanes, the large highly swept area ahead of the movable wing is essential to minimize aerodynamic-center travel with wing sweep. This area generally results in a loss in longitudinal stability in the intermediate to high range of angle of attack for the low-sweep conditions. In order to better understand this aerodynamic behavior, pressure distributions for an outboard-pivot-variable-sweep-wing—fuselage combination have been determined and compared with static pitching-moment results. The results of this study are shown in figure 3. The variations of pressure coefficients over the wing, at two different angles of attack, have been superimposed on tuft sketches. From this figure at an angle of attack of about  $6^\circ$ , in the linear range of pitch data, the pressure distributions indicate typical potential angle-of-attack loading with no tip separation. At an angle of attack of about  $16^\circ$ , after the loss in stability occurs, the tuft sketch at the right of the figure illustrates the strong leading-edge vortex system on the highly swept inboard portion of the wing. The influence of this vortex system is reflected in the pressure distributions shown at the right. The center of pressure on the inboard section moved aft slightly; however, the loading ahead of the moment center was substantially increased. As the vortex system moves spanwise across the wing, high angularities are induced on the outboard panel at low speeds. The induced angularities on the movable wing panel result in separation on the outer panel, as indicated by the flattening of the chordwise pressure distributions. Although the center of pressure on the outer sections moves aft slightly with increasing angle of attack, the magnitude of the lift at the wing tip remains essentially the same. The instability noted in the pitch curve, therefore, results from the combined effects of outer panel stall and the nonlinear lift on the inboard wing panel.

Several methods which have been shown to be successful in alleviating this pitch-up problem are illustrated in figure 4. Pitching-moment results are shown

for several arrangements of a variable-sweep-wing supersonic configuration which incorporates a relatively low horizontal tail. The longitudinal stability characteristics of the basic configuration are considerably better than the pitch characteristics indicated for the variable-sweep arrangement discussed previously because of the low horizontal tail and the improved stall characteristics of the outer wing panels. These data indicate the additional improvements in pitch characteristics which might be obtained by varying the geometry of the forewing. On the left of figure 4, pitch data are shown for the outboard-pivot-variable-sweep-wing configuration, with several different forewing sweeps. These results illustrate that if a reduction in forewing sweep can be tolerated, from a performance standpoint, a stabilizing tendency can be obtained. If the cruise Mach number of the airplane dictates the employment of a highly swept forewing, the unfavorable effects of the forewing might be reduced at subsonic speeds by deflecting a portion of the fixed wing. The effect of deflecting the forewing is illustrated at the right of figure 4. The sketch indicates the portion of forewing which was deflected. The pitching-moment results indicate that deflecting the forewing  $40^\circ$  would tend to increase stability in the high angle-of-attack region. References 2 and 3 indicate the effects of forewing sweep and deflection on similar variable-sweep-wing supersonic transport concepts.

The adverse effects of the highly swept fixed-wing area can be diminished further by the utilization of a free-floating apex or by the incorporation of a double pivot arrangement. Figure 5 indicates the profound improvements in longitudinal stability characteristics which can be obtained by these methods. These effects are discussed in detail in references 4 and 5.

#### DEEP-STALL CHARACTERISTICS OF T-TAIL AIRPLANES

There has been a great deal of research on T-tail airplanes during the past several years. The purpose of the present discussion is to review the longitudinal stability problems associated with T-tail transport airplanes and to indicate the profound effect of several configuration variables. Figure 6 shows the longitudinal stability characteristics for a typical T-tail configuration with aft-mounted engines over a large angle-of-attack range. The curve for the tail-off configuration indicates a stable break after the wing stalls and a trend towards nose-down moments. Recent research has indicated that substantial improvements in the longitudinal stability characteristics of T-tail airplanes can be obtained by the employment of auxiliary horizontal tails and by careful tailoring of the wing and fuselage designs. (See refs. 6 and 7.) When the T-tail is added to this arrangement, an extreme loss in longitudinal stability is encountered which is followed by a stable trim point at an angle of attack of about  $40^\circ$ . Adequate control must be provided in the so-called "deep-stall" region or the airplane would remain locked in at these extremely high angles of attack. For this configuration, a horizontal tail setting of  $5^\circ$  provided a nose-down moment, which would enable the airplane to rotate towards the unstalled condition.

The extreme loss in longitudinal stability indicated for this configuration is associated with the loss in horizontal tail contribution when the T-tail

passes through the airplane wake system. The sketch at the lower right of figure 6 illustrates the behavior of the T-tail airplane in the deep-stall region. The vector  $V$  shown in the sketch represents the relative air velocity. At these extremely high angles of attack the wing wake, reinforced by more profound nacelle-pylon wake, envelopes the horizontal tail and renders it nearly ineffective. In the deep-stall region the airplane might actually plunge downward along the flight path indicated by the dashed line even though the airplane attitude is relatively level. T-tail research has indicated that, for this particular configuration, the loss in horizontal tail contribution can be correlated closely with the relationship between the nacelle and horizontal tail positions.

The configuration sketch at the top of figure 7 indicates the pertinent dimensions of the T-tail model in terms of wing mean geometric chord  $\bar{c}$  and wing span  $b$ . In addition, the configuration variables which are used in this correlation are defined in the configuration sketch. At the bottom of the figure, the loss in tail contribution, shown as the ordinate of the plot, is the ratio of the reduction in tail contribution to the maximum pitching-moment coefficient provided by the horizontal tail. The loss in tail contributions has been plotted against the ratio of nacelle distance ahead of the tail to horizontal tail height above the nacelle. The data points were obtained by varying the tail height (open symbols) and the nacelle distance (half-closed symbols) and by combined variations of the nacelle and horizontal tail arrangements (square symbols). The lines represent results for various ratios of tail span to nacelle span. The data for a ratio of tail span to nacelle span equal to 1.37 indicate that, for variations of either tail height or nacelle distance, the loss in tail contribution can be correlated with the ratio of the nacelle distance to horizontal tail height. The other data indicate that, as the ratio of tail span to nacelle span is increased, the loss in horizontal tail contribution is reduced. These results represent data for a particular configuration; however, the trends indicated should generally apply to other T-tail airplanes with aft-mounted engines.

#### EFFECT OF FUSELAGE CROSS-SECTION SHAPE

#### AND VERTICAL TAIL POSITION ON DIRECTIONAL STABILITY

Many present-day airplanes employ noncircular fuselage cross-section shapes. An interesting effect of fuselage cross-section shape on directional stability at the higher angles of attack was noted from results obtained in the Langley high-speed 7- by 10-foot tunnel. (See fig. 8.) A sketch of the complete configuration is shown at the top of the figure. The configuration employing the circular forebody exhibits a reduction in directional stability with increasing angle of attack. This effect is associated with the loss of vertical tail effectiveness caused by the adverse sidewash from the wing and forebody (ref. 8). With the noncircular forebody, there is a large increase in directional stability in the intermediate range of angle of attack and considerably higher directional stability up to the maximum angle of attack. In order to obtain a better understanding of this effect, the two forebodies were tested alone. The directional stability parameters of the two different forebodies are shown at the right of figure 8. These parameters were obtained by assuming the

center-of-gravity location and reference geometry of the complete configuration. At lower angles of attack, both forebodies indicated a destabilizing effect but, at the higher angles of attack, the directional stability parameter of the non-circular forebody became positive. These results indicate that the favorable effects noted for the configuration with the noncircular forebody were largely dependent upon the direct contribution of the forebody. In the higher angle-of-attack region, a force opposed to the normal cross-flow component is developed on the noncircular forebody as a result of the asymmetric flow characteristics on the body. (See refs. 9 and 10.) The additional differences between the directional stability of the two complete configurations are associated with the wing-body interference and the forebody effect on the sidewash characteristics. Since these effects are associated with nonpotential flow, the noncircular body was tested to higher Reynolds numbers to determine whether the favorable effects would diminish. At a Reynolds number comparable to about one-half the full-scale condition for a landing supersonic transport configuration, the favorable side force was increased considerably for the modified circular forebody. It should be noted, however, that nose bluntness has a pronounced effect on the side-force variation with angle of attack. Removing the pointed nose and rounding the fore part of the remaining body resulted in a negative side force which was practically invariant with angle of attack.

Another approach to improving the directional stability at high angles of attack would, of course, be to select a vertical tail position which avoids the adverse sidewash effects. One such approach is the addition of ventral fins, which has been widely accepted. Another method which is quite compatible with the aerodynamic design of a supersonic cruise concept is the use of twin tails. In figure 9, the directional stability parameter  $C_{n\beta}$  is presented for the

cranked wing tip configuration with outboard vertical tails and with the vertical tail located on the after portion of the fuselage. The tail volume of the two vertical tail arrangements was nearly equal. These data show that the directional stability of the configuration having the vertical tail on the fuselage center line diminished with increasing angle of attack. The loss in directional stability for this configuration results from the unfavorable sidewash angularities generated on the vertical tail by the wing-fuselage vortex system. The outboard vertical tails, located in a favorable sidewash field, became more effective at the higher angles of attack. In addition, the outboard vertical tails were found to have a favorable effect on the longitudinal stability characteristics of the configuration.

#### CONCLUDING REMARKS

A review has been made to ascertain some of the problems and possible solutions regarding high angle-of-attack stability of modern aircraft at subsonic Mach numbers. Several design changes and their favorable effect on subsonic stability at high angles of attack are as follows:

1. The pitch-up of highly swept fixed-wing configurations has been alleviated by the employment of wing leading-edge and canard devices.

2. Pitch-up for variable-sweep-wing configurations can be alleviated by a low horizontal tail, reduction of the forewing sweep, a free-floating forewing, a folding forewing, or deflection of the forewing.

3. The deep-stall characteristics of T-tail airplanes can be improved by increasing the ratio of tail span to nacelle span and by careful selection of nacelle position.

4. Indications are that directional stability at high angles of attack can be improved by proper selection of fuselage cross-section shape.

5. Directional stability for certain configurations can be improved by placing the vertical tail surfaces near the wing tips.

## REFERENCES

1. Morris, Odell A.; and Fournier, Roger H.: Aerodynamic Characteristics at Mach Numbers 2.30, 2.60, and 2.96 of a Supersonic Transport Model Having a Fixed, Warped Wing. NASA TM X-1115, 1965.
2. Lockwood, Vernard E.; and Thompson, Wilson E.: Low-Speed Characteristics of a Variable-Sweep Supersonic Transport Model With a Blended Engine Fuselage and Engine-Mounted Tails. NASA TM X-1038, 1964.
3. Lockwood, Vernard E.: High-Lift Characteristics of a Variable-Sweep Supersonic Transport Model With a Blended Engine-Fuselage and Engine-Mounted Horizontal Tails. NASA TM X-1199, 1966.
4. Polhamus, Edward C.; Alford, William J., Jr.; and Foster, Gerald V.: Subsonic and Supersonic Aerodynamic Characteristics of an Airplane Configuration Utilizing Double-Pivot Variable-Sweep Wings. NASA TM X-743, 1962.
5. Polhamus, Edward C.; and Hammond, Alexander D.: Subsonic Aerodynamic Characteristics of an Airplane Configuration Utilizing a Variable-Sweep Wing Having a Free-Floating Apex. NASA TM X-1126, 1965.
6. Ray, Edward J.; and Taylor, Robert T.: Effect of Configuration Variables on the Subsonic Longitudinal Stability Characteristics of a High-Tail Transport Configuration. NASA TM X-1165, 1965.
7. Taylor, Robert T.; and Ray, Edward J.: Deep-Stall Aerodynamic Characteristics of T-Tail Aircraft. Conference on Aircraft Operating Problems, NASA SP-83, 1965, pp. 113-121.
8. Stone, Ralph W., Jr.; and Polhamus, Edward C.: Some Effects of Shed Vortices on the Flow Fields Around Stabilizing Tail Surfaces. AGARD Rept. 108, 1957.
9. Polhamus, Edward C.; Geller, Edward W.; and Grunwald, Kalman J.: Pressure and Force Characteristics of Noncircular Cylinders as Affected by Reynolds Number With a Method Included for Determining the Potential Flow About Arbitrary Shapes. NASA TR R-46, 1959.
10. Polhamus, Edward C.: Effect of Flow Incidence and Reynolds Number on Low-Speed Aerodynamic Characteristics of Several Noncircular Cylinders With Applications to Directional Stability and Spinning. NASA TR R-29, 1959. (Supersedes NACA TN 4176.)

EFFECT OF WING MODIFICATIONS  
M = 0.14

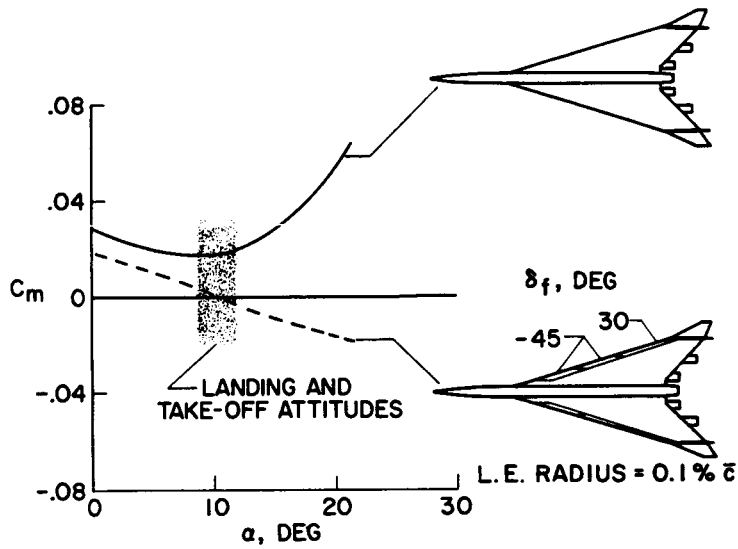


Figure 1

EFFECT OF FORWARD AUXILIARY SURFACE  
M = 0.14

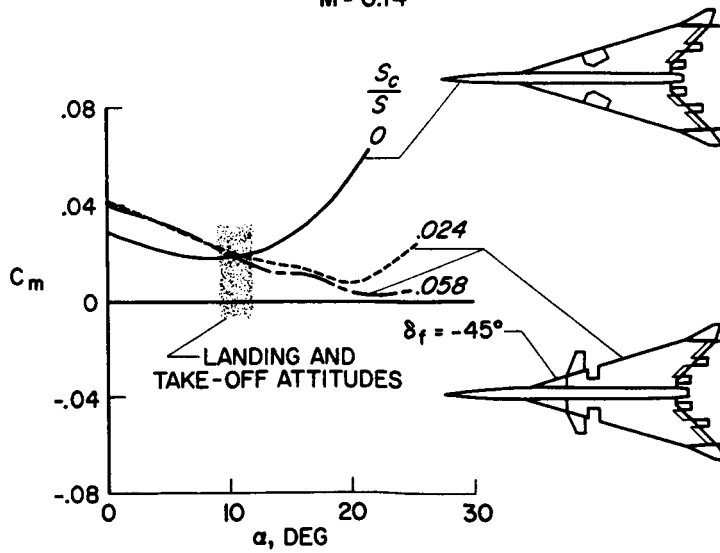


Figure 2

CORRELATION OF LOAD DISTRIBUTION WITH PITCHING MOMENT  
 $M=0.23$

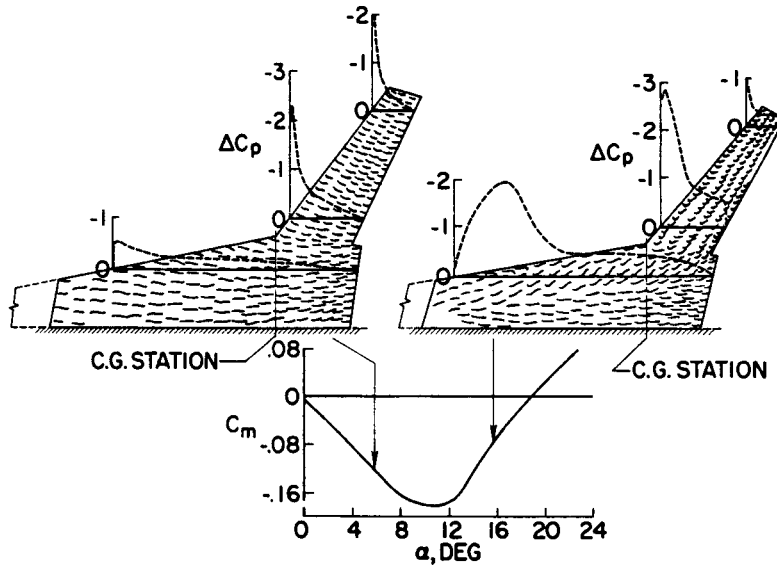


Figure 3

EFFECT OF FOREWING GEOMETRY  
 $M=0.10$

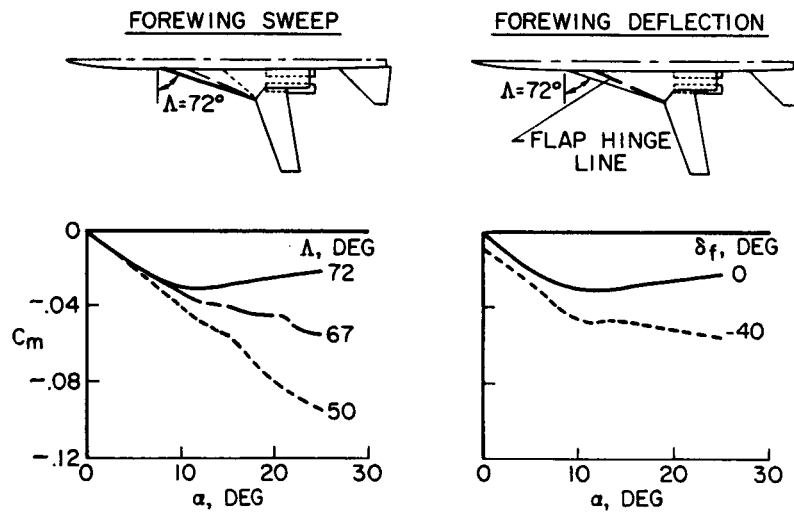


Figure 4

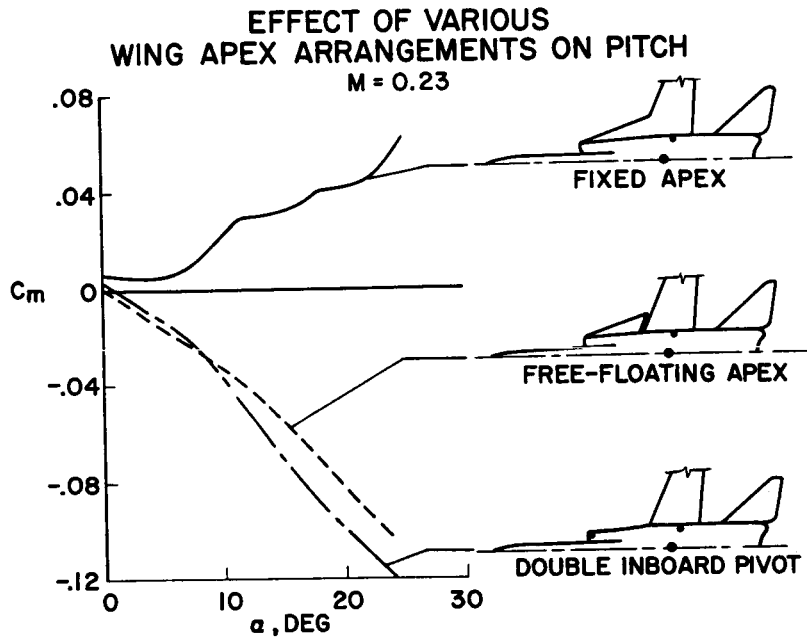


Figure 5

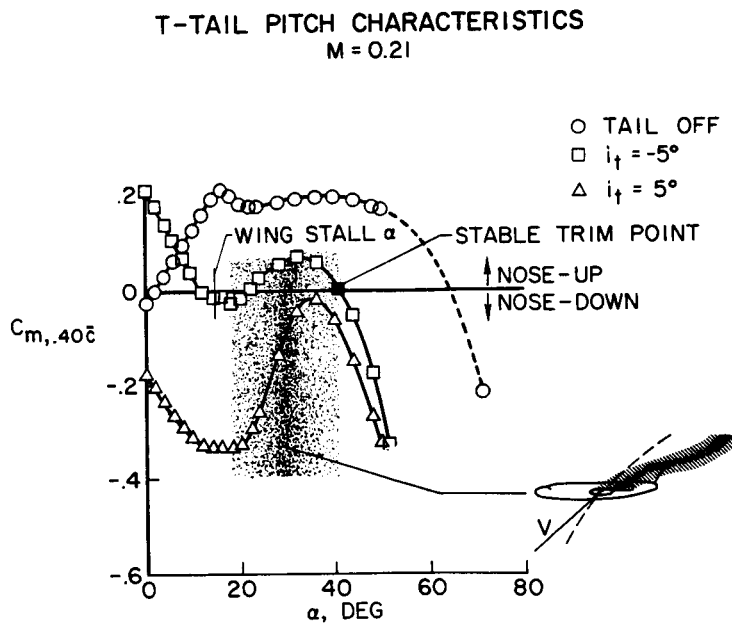


Figure 6

CORRELATION OF NACELLE LENGTH AND TAIL HEIGHT  
 $M = 0.21$

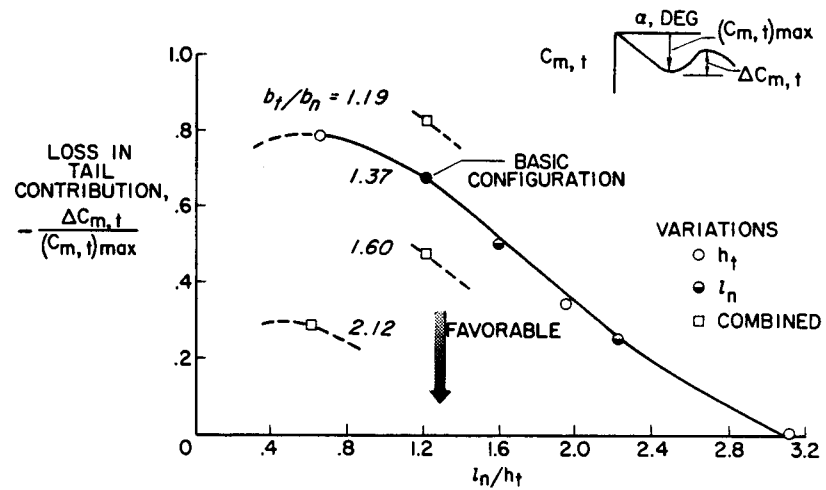
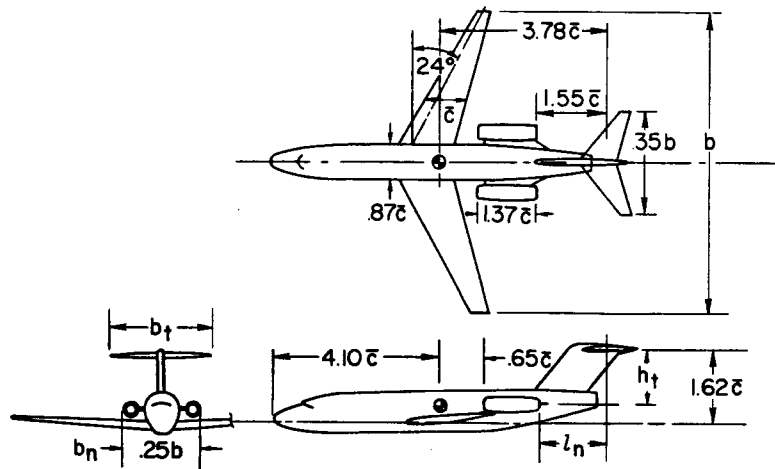


Figure 7

### EFFECT OF FUSELAGE CROSS SECTION

M = 0.20

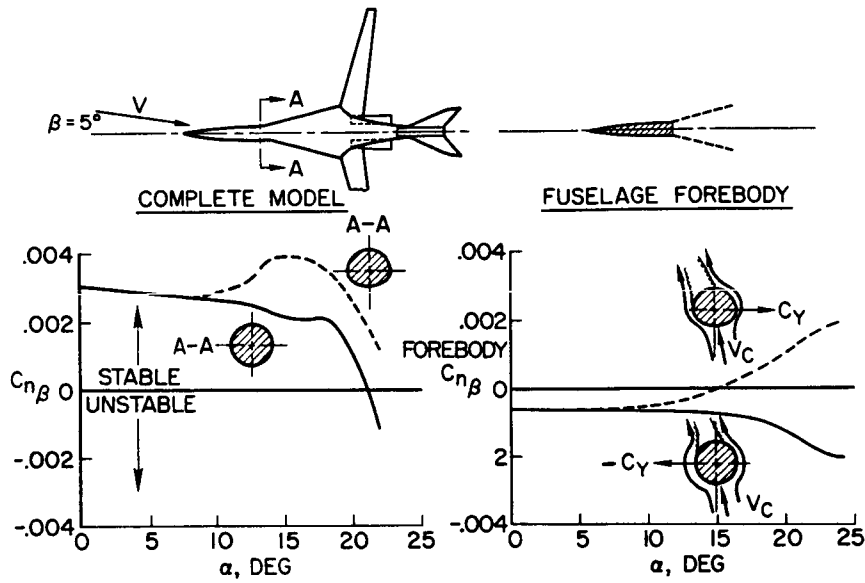


Figure 8

### EFFECT OF VERTICAL-TAIL POSITION

M = 0.14

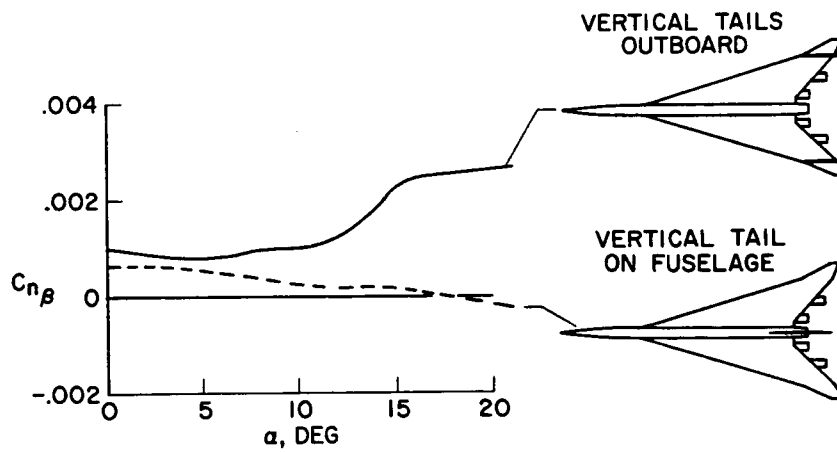


Figure 9

## 6. AERODYNAMIC-CENTER CONSIDERATIONS OF WINGS AND WING-BODY COMBINATIONS

By John E. Lamar and William J. Alford, Jr.  
NASA Langley Research Center

### SUMMARY

Aerodynamic-center variations with Mach number are considered for wings of different planform. The normalizing parameter used is the square root of the wing area, which provides a more meaningful basis for comparing the aerodynamic-center shifts than does the mean geometric chord. The theoretical methods used are shown to be adequate for predicting typical aerodynamic-center shifts, and ways of minimizing the shifts for both fixed and variable-sweep wings are presented.

### INTRODUCTION

In the design of supersonic aircraft, a detailed knowledge of the aerodynamic-center position is important in order to minimize trim drag, maximize load-factor capability, and provide acceptable handling qualities. One of the principal contributions to the aerodynamic-center movement is the well-known change in load distribution with Mach number in going from subsonic to supersonic speeds. In addition, large aerodynamic-center variations are quite often associated with variable-geometry features such as variable wing sweep.

The purpose of this paper is to review the choice of normalizing parameters and the effects of Mach number on the aerodynamic-center movement of rigid wing-body combinations at low lift. For fixed wings the effects of both conventional and composite planforms on the aerodynamic-center shift are presented, and for variable-sweep wings the characteristic movements of aerodynamic-center position with pivot location and with variable-geometry apex are discussed.

Since systematic experimental investigations of the effects of planform on the aerodynamic-center movement with Mach number are still limited, the approach followed herein is to establish the validity of the computational processes by illustrative comparison with experiment and then to rely on theory to show the systematic variations. The two theories used in this paper are for the wing alone in unseparated flow. One is a modified Multhopp subsonic lifting-surface theory developed by the senior author (unpublished), and the other is a supersonic lifting-surface theory (ref. 1). For wings experiencing separated flow these theories are not adequate for predicting the aerodynamic-center movement.

## SYMBOLS

A	aspect ratio
a	distance from apex of high-sweep wing to apex of low-sweep wing (see fig. 10)
b	span
$C_L$	lift coefficient
$C_p$	pressure coefficient, $\frac{P_{\text{local}} - P_{\text{free stream}}}{q}$
$\Delta C_p$	incremental pressure coefficient, $C_{p,\text{upper}} - C_{p,\text{lower}}$
$\bar{c}$	mean geometric chord
$c_r$	root chord of basic planform
$c_t$	tip chord of basic planform
d	longitudinal distance from root trailing edge to tip trailing edge
K	constant
l	longitudinal distance from apex to tip trailing edge
M	Mach number
p	static pressure
q	free-stream dynamic pressure
S	wing area
x	chordwise distance from apex of high-sweep wing to plane-of-symmetry intercept with trailing edge of free-floating apex
$\bar{x}_M$	chordwise distance from a reference point to aerodynamic center at any Mach number
$\bar{x}_{M=0}, \bar{x}_{M=0.2}, \bar{x}_{M=0.25}$ $\bar{x}_{M=2}, \bar{x}_{M=3}$	} chordwise distance from a reference point to aerodynamic center at specific Mach number indicated by subscript
$\Delta \bar{x}$	

$y_b$	spanwise distance from plane of symmetry to leading-edge break
$y_p$	spanwise distance from plane of symmetry to pivot
$\alpha$	angle of attack
$\Lambda$	leading-edge sweep of wing
$\Lambda_o$	leading-edge sweep of outer panel
$\Lambda_t$	leading-edge sweep of cranked wing tip
$\lambda$	taper ratio

#### REQUIREMENT OF A NORMALIZING PARAMETER

A knowledge of the actual dimensional movement of the aerodynamic center is required in order to determine the out-of-trim moments which must be balanced by the control surface. Thus, in the selection of a normalizing parameter the need for a reference length which, for a given wing area, is independent of planform is considered to be of primary importance. The reference length selected is the square root of the wing area  $\sqrt{S}$ , which, of course, is independent of planform and therefore provides fractional aerodynamic-center movements that are proportional to the actual dimensional shifts.

The customary use of the mean geometric chord  $\bar{c}$ , although adequate for normalizing the aerodynamic-center shift for a given planform, is not convenient when comparing planforms, since the magnitude of  $\bar{c}$  is dependent upon planform. The relationship between  $\bar{c}$  and  $\sqrt{S}$  is given both algebraically and graphically in figure 1 for wings which fit within the geometry limitations shown and may be of help in transferring aerodynamic-center shifts from one normalizing parameter to another.

#### DISCUSSION

##### Comparison of Theory and Experiment

Some typical experimentally determined aerodynamic-center shifts with Mach number (ref. 2), which are useful in evaluating the theories and the previously mentioned normalizing parameters, are presented in figures 2 and 3.

The experimental shifts, together with theoretical predictions, are shown in figure 2 for a series of delta wings with aspect ratios ranging from 2 to 4. In this figure  $\Delta\bar{x}$  is the distance between the aerodynamic-center location at a Mach number of 0.25 and the aerodynamic-center location at any Mach number. The mean geometric chord  $\bar{c}$  and the square root of the wing area  $\sqrt{S}$  are

used as normalizing parameters, and both  $\Delta\bar{x}/c$  and  $\Delta\bar{x}/\sqrt{S}$  are plotted as functions of Mach number. When the aerodynamic-center shift is based on the respective  $\bar{c}$ , the delta wing with the lowest aspect ratio has the smallest incremental change in aerodynamic-center location at the supersonic Mach numbers. However, when the aerodynamic-center shift is based on the respective  $\sqrt{S}$ , all three wings exhibit essentially the same fractional change in aerodynamic-center location throughout the Mach number range. The theories predict reasonably well the aerodynamic-center shifts for these delta-wing-bodies.

Figure 3 presents three wing-body combinations and illustrates the effect of wing sweep and taper ratio on the aerodynamic-center shift with Mach number. The wings are of aspect ratio 3 and have planforms ranging from a trapezoidal shape to a delta shape. Of the three wing-body combinations shown, the delta-wing-body configuration is seen to exhibit the smallest change in aerodynamic-center location for Mach numbers greater than 1 when  $\bar{c}$  is used as the normalizing parameter. However, when  $\sqrt{S}$  is used as the normalizing parameter, the aerodynamic-center shift for the sweptback-wing-body configuration is almost as small. Again the agreement between theory and experiment is reasonable.

When the trapezoidal, sweptback, and delta planforms are sized for take-off and landing conditions at  $\alpha = 12^\circ$ , the lift developed on each planform is taken into account, as shown in figure 4. The delta wing no longer exhibits the smallest aerodynamic-center shift since its value of lift-curve slope is the lowest.

### Fixed-Wing Studies

In figures discussed subsequently, the aerodynamic-center shifts have been computed by the theoretical methods. For wings which have fixed planforms, the reference length is the  $\sqrt{S}$  of each planform.

The results of one such aerodynamic-center study for a series of conventional fixed wings with planform variation in sweep and in taper and notch ratios are presented in figure 5. For a delta wing,  $d/l = 0$  and for an arrow wing,  $d/l > 0$ . For illustrative purposes both the effect of changing the leading-edge sweep and the notch ratio when the taper ratio is zero and the effect of changing the taper and notch ratios when the leading-edge sweep angle is  $60^\circ$  are presented.

When the taper ratio is zero, a decrease in  $\Delta\bar{x}/\sqrt{S}$  of about 0.05 occurs as the notch ratio is increased from 0 to 0.5 for leading-edge sweep angles of  $45^\circ$  and  $60^\circ$ . For a sweep angle of  $70^\circ$ ,  $\Delta\bar{x}/\sqrt{S}$  at first decreases approximately 0.01 and then increases about 0.01 above its value at  $d/l = 0$ . At any particular notch ratio, the wing with the lowest sweep shows the smallest aerodynamic-center shift.

When the wing leading-edge sweep angle is  $60^\circ$ , decreases in  $\Delta\bar{x}/\sqrt{S}$  of 0.05, 0.09, and 0.12 occur over the range of notch ratios considered for taper ratios of 0, 0.25, and 0.50, respectively. At any particular notch ratio, the

wing with the lowest taper ratio exhibits the smallest aerodynamic-center shift. When the supersonic Mach number is other than 3, different trends in the aerodynamic-center movement may occur with increasing notch ratio.

One method of minimizing the aerodynamic-center shift of an arrow wing is to reduce the sweep of the wing tip by shearing it forward. Some calculated results illustrating this technique are presented in figure 6. The basic arrow wing has a sweep of  $74^\circ$ , and  $\Delta\bar{x}/\sqrt{S}$  is reduced to about half its original value by shearing the tip forward from  $74^\circ$  to  $55^\circ$ . The reason for this reduction is that wings with cranked tips carry more of the loading inboard where the sweep is higher and where the value of lift-curve slope is less influenced by Mach number. Thus, the inner panel tends to pull the aerodynamic center forward with increasing supersonic Mach number.

One method of reducing the aerodynamic-center shift of a delta wing is the addition of a forewing inboard. In figure 7 the effect of such an addition is presented as a function of the leading-edge-break location and apex extension. A reduction in the aerodynamic-center shift is obtained for each apex location as  $\frac{y_b}{b/2}$  is increased from 0 to 0.5. At any particular value of leading-edge-break ratio within the range examined, the wing with the most forward apex or the longest root chord has the smallest aerodynamic-center shift, because the inboard sweeps are higher and therefore the inner panel has a lower aspect ratio which gives it an essentially invariant value of lift-curve slope with Mach number. However, the outer panel has a higher aspect ratio and lower sweep, and the value of lift-curve slope decreases with increasing supersonic Mach number. Thus, the inner panel carries proportionally more of the loading. The aerodynamic center is forced forward with increasing values of leading-edge-break ratio because of the area added inboard. Experimental substantiation of this low level of aerodynamic-center shift, with a model that had a wing which covered most of the body, was provided by Hopkins, Hicks, and Carmichael in paper no. 32 of this conference. (See also ref. 3.)

In addition, wing-body combinations exhibit smaller aerodynamic-center shifts than does the wing alone because the body acts as a forewing with a very low value of leading-edge-break ratio.

#### Variable-Sweep-Wing Studies

For wings with variable sweep, a problem in aerodynamic-center variation, in addition to that caused by the Mach number effect, results from changes in the wing sweep. The shift resulting from wing-sweep changes must be minimized in order to make variable-sweep wings competitive, from aerodynamic-center considerations, with fixed wings. To illustrate this problem, the theoretical loading distributions of a variable-sweep wing with an outboard pivot (ref. 4) at a Mach number of 0.23 and at low lift is presented in figure 8. At the top of this figure the variable-sweep wing is shown in its low-sweep and high-sweep positions, and superimposed on the low-sweep planform are its theoretical and experimental chordwise pressure loadings which are seen to be in good agreement. At the bottom of the figure the theoretical longitudinal loading distributions

for both sweeps have been computed at  $C_L = 0.12$  and projected onto the plane of symmetry. As the outer panel is swept back, the inner panel carries more of the loading and thus tends to balance out the additional moments created by the reduced outer-panel loadings acting through longer moment arms. In this example, because of the outboard location of the pivot, the aerodynamic center, as given by the chordwise location of the lift vector, actually shifts slightly forward.

A study was undertaken to determine the effect that the pivot location has on the aerodynamic-center shift, and the results are presented in figure 9. In this figure and in figure 10, the reference planform area is taken for the wing in its high-sweep position.

Each pivot lies on the loci of points from which the outer panel can be swept from its high-sweep position to a low-sweep position. The relative chordwise location of the pivot determines the chordwise position of the outer panel at low sweep without changing the sweep angle or the semispan.

The results of the theoretical study show that the total aerodynamic-center shift  $\Delta\bar{x}/\sqrt{S}$  (see fig. 9) can be reduced from 0.2 to 0.1 by moving the pivot outboard. The dashed line is used as a reference to indicate that portion of the total shift caused by the change in Mach number from 0.2 to 2 at  $\Lambda_0 = 70^\circ$ . The remaining shift is attributed to the change in sweep from  $15^\circ$  to  $70^\circ$  at  $M = 0.2$ . The movement of the pivot outboard changes only the part of the shift dependent on sweep. By proper positioning of the pivot, this part of the shift can be eliminated. When the sweep effect causes the aerodynamic center to move ahead of its low-speed high-sweep position, the Mach number effect is reduced.

These results are supported by experimental data for a similar wing-body combination. Figure 9 shows that a reduction in the total aerodynamic-center shift of 0.07 occurs as the spanwise location of the pivot is moved from one extreme to the other. The characteristics of this combination and how the pivot location affects maneuverability considerations are discussed by Taylor in paper no. 7 of this conference.

In paper no. 5, Ray, Lockwood, and Henderson note that if a high inboard sweep is required for supersonic flight, then at subsonic speeds and low outer-panel sweep, devices such as the double inboard pivot (ref. 5) and the free-floating apex (ref. 6) can be used to eliminate the resulting pitch-up. These devices also provide a means of controlling the aerodynamic-center movement, as illustrated in figure 10, where they are shown to have the following two features in common: (1) When the outer panel is in its low-sweep position, the forewing or apex is either pivoted inside the fuselage or allowed to free-float carrying no load; and (2) when the outer panel is swept back, the apex is affixed to the front of the outer panel and forms a continuous leading edge.

Lifting-surface calculations have been made to illustrate the effect of the amount of the apex which is folded or free-floated. Varying amounts of the apex have been removed to represent the aerodynamic effect of both concepts. With the removal, subsonically, of an increasingly large amount of the apex

(correlated with the chordwise distance  $x$ ), the total aerodynamic-center shift decreases from about 0.18 to 0. Again the dashed line represents that portion of the shift due to changing the Mach number from 0 to 3 when  $\Lambda_0 = 71.5^\circ$ . The effect of changing the sweep  $\Lambda_0$  from  $71.5^\circ$  to  $25^\circ$  at  $M = 0$  makes up the remainder of the shift.

When  $x/a = 0$ , the change in wing sweep has essentially no effect; consequently, almost all the aerodynamic-center shift is due to the change in Mach number. However, when  $x/a = 1.0$ , the sweep effect is large enough to cancel all the Mach number effect.

It should be noted that the aerodynamic-center shift may also be minimized by changing the supersonic Mach number or by changing the center-of-gravity location at the different sweeps and Mach numbers.

## CONCLUSIONS

A general conclusion of this study is that, when comparing aerodynamic-center movements of wings of different planform, a normalizing parameter independent of planform, such as the square root of the wing area, is more appropriate than the customarily used mean geometric chord, which is dependent on planform. The following specific conclusions were reached:

1. The theoretical methods have been demonstrated to be adequate for predicting the aerodynamic-center shift with Mach number for a variety of wing planforms, but are not suitable for determining the absolute aerodynamic-center location at any Mach number since body and interference effects are not included.
2. For fixed wings, the aerodynamic-center shift can be controlled by proper selection of sweep and of taper and notch ratios and by inboard and outboard area proportioning with different degrees of sweep.
3. For variable-sweep wings the aerodynamic-center shift can be controlled by pivot location and by apex devices, such as the double inboard pivot and the free-floating apex.

## REFERENCES

1. Middleton, Wilbur D.; and Carlson, Harry W.: A Numerical Method for Calculating the Flat-Plate Pressure Distributions on Supersonic Wings of Arbitrary Planform. NASA TN D-2570, 1965.
2. Hall, Charles F.: Lift, Drag, and Pitching Moment of Low-Aspect-Ratio Wings at Subsonic and Supersonic Speeds. NACA RM A53A30, 1953.
3. Tumilowicz, Robert A.: Characteristics of a Family of Double-Delta Wings Designed to Reduce Aerodynamic Center Shift With Mach Number. M.S. Thesis, Polytech. Inst. Brooklyn, 1965.
4. Baals, Donald D.; and Polhamus, Edward C.: Variable Sweep Aircraft. Astronaut. Aerospace Eng., vol. 1, no. 5, June 1963, pp. 12-19.
5. Polhamus, Edward C.; Alford, William J., Jr.; and Foster, Gerald V.: Subsonic and Supersonic Aerodynamic Characteristics of an Airplane Configuration Utilizing Double-Pivot Variable-Sweep Wings. NASA TM X-743, 1962.
6. Polhamus, Edward C.; and Hammond, Alexander D.: Subsonic Aerodynamic Characteristics of an Airplane Configuration Utilizing a Variable-Sweep Wing Having a Free-Floating Apex. NASA TM X-1126, 1965.

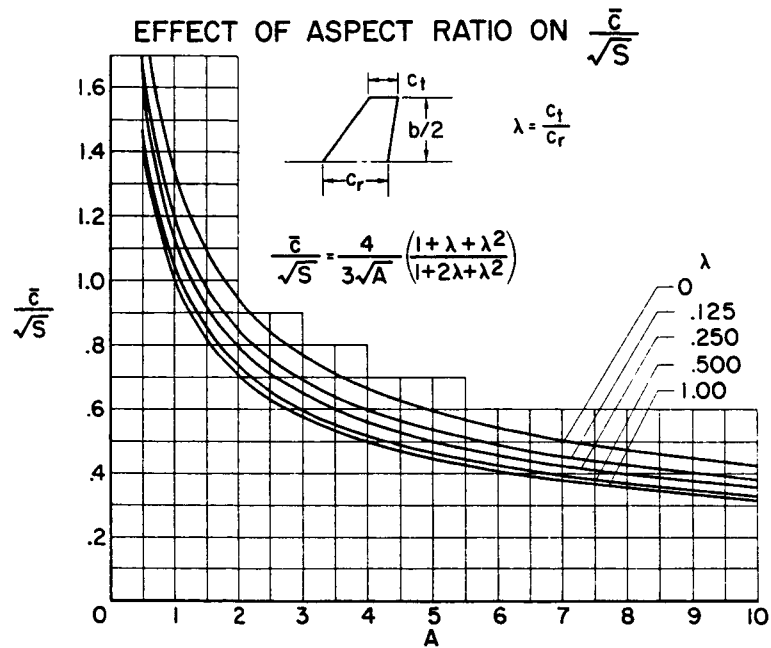


Figure 1

### EFFECT OF ASPECT RATIO AND SWEEP

$\Delta \bar{x} = \bar{x}_M - \bar{x}_{M=0.25}; \lambda = 0$

EXP	WING-ALONE THEORY	A	Λ, DEG	
○	—	2	63.5	
□	- - -	3	53	
◇	- · -	4	45	

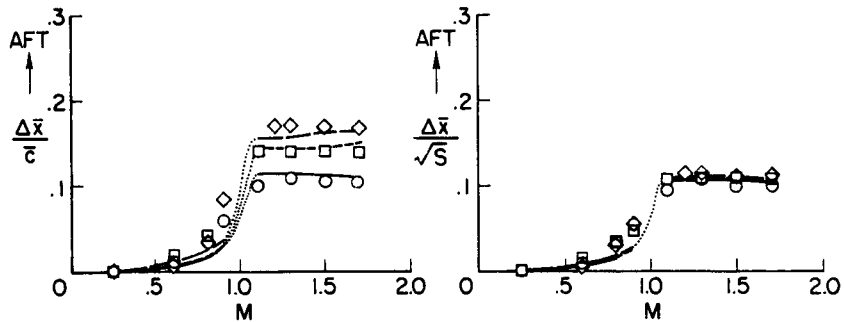


Figure 2

### EFFECT OF SWEEP AND TAPER

$$\Delta \bar{x} = \bar{x}_M - \bar{x}_{M=0.25}; A=3$$

EXP	WING-ALONE THEORY	$\Lambda$ , DEG	$\lambda$	
○	—	20	.39	
□	- - -	45	.40	
◇	- - -	53	0	

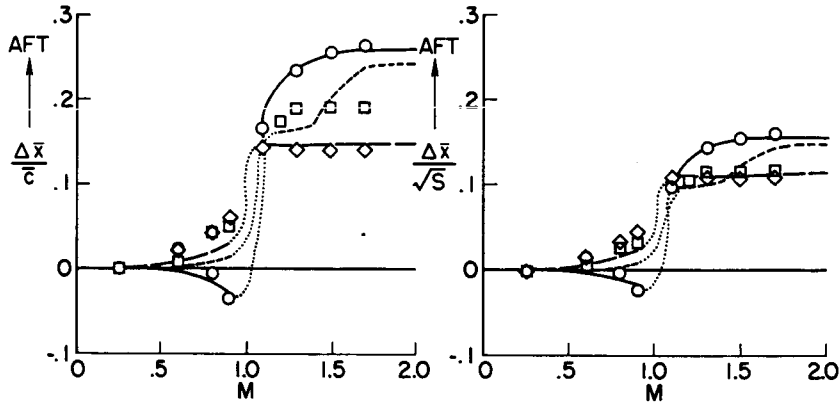


Figure 3

### EFFECT OF WING SIZING FOR LOW-SPEED CONDITIONS

$$\Delta \bar{x} = \bar{x}_M - \bar{x}_{M=0.25}; A=3$$

EXP	WING-ALONE THEORY	$\Lambda$ , DEG	$\lambda$	
○	—	20	.39	
□	- - -	45	.40	
◇	- - -	53	0	

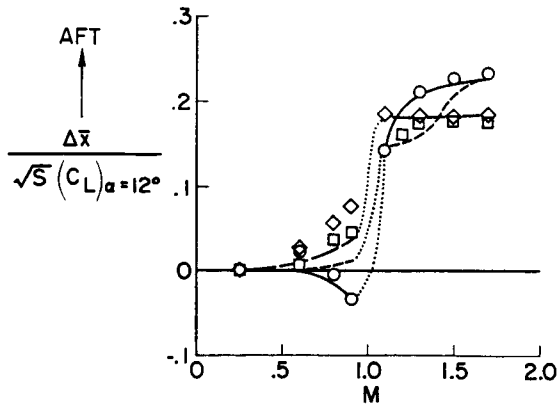


Figure 4

CONVENTIONAL-PLANFORM VARIATION

$$\Delta \bar{x} = \bar{x}_M = 3 - \bar{x}_M = 0$$

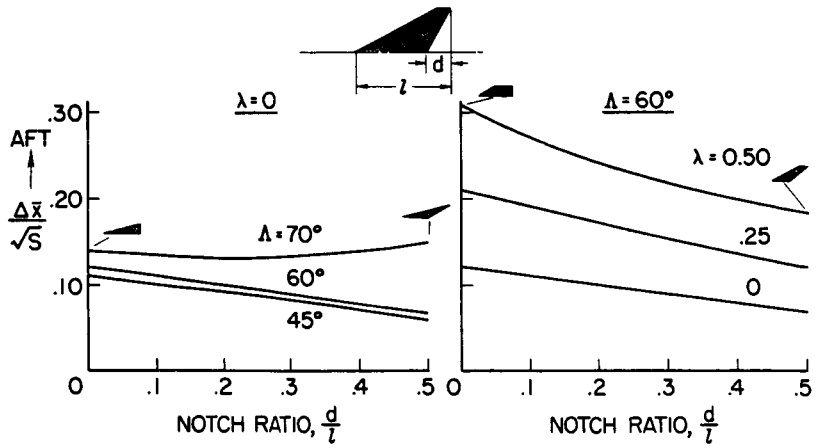


Figure 5

COMPOSITE PLANFORMS

EFFECT OF CRANKED-TIP SWEEP;  $\Delta \bar{x} = \bar{x}_M = 3 - \bar{x}_M = 0$ ;  $\frac{y_b}{b/2} = 0.73$

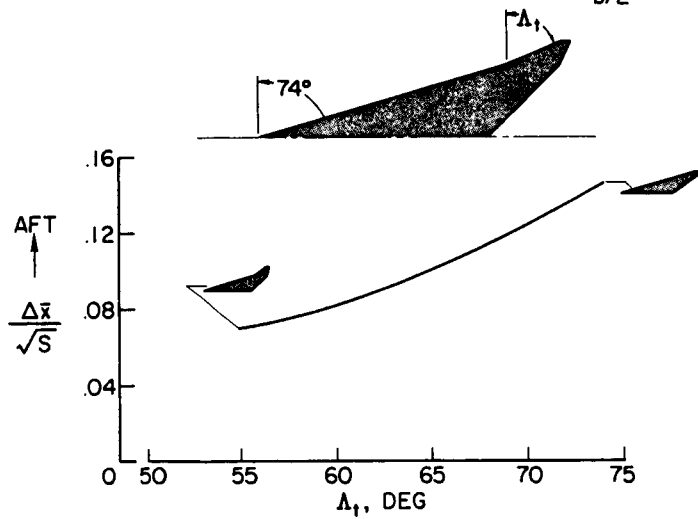


Figure 6

COMPOSITE PLANFORMS  
EFFECT OF LEADING-EDGE BREAK LOCATION;  $\Delta\bar{x} = \bar{x}_M = 3 - \bar{x}_M = 0$

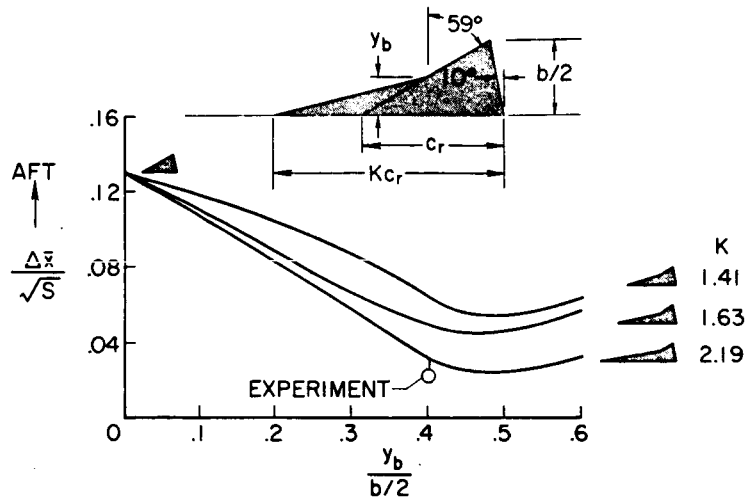


Figure 7

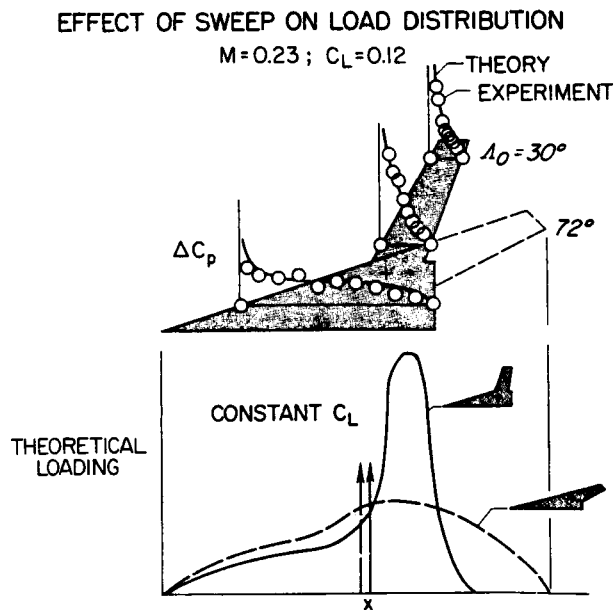


Figure 8

### EFFECT OF SPANWISE LOCATION OF PIVOT

$$\Delta \bar{x} = (\bar{x}_{M=2})_{\Lambda_0=70^\circ} - (\bar{x}_{M=0.2})_{\Lambda_0=15^\circ}$$

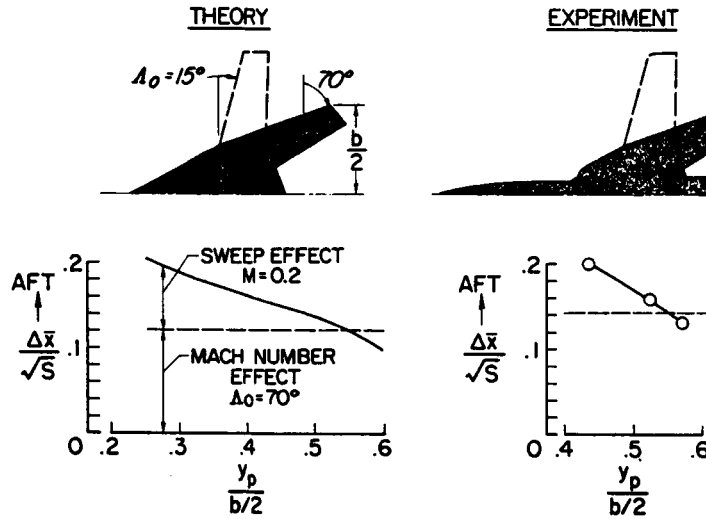


Figure 9

### EFFECT OF VARIABLE-GEOMETRY APEX

$$\Delta \bar{x} = (\bar{x}_{M=3})_{\Lambda_0=71.5^\circ} - (\bar{x}_{M=0})_{\Lambda_0=25^\circ}$$

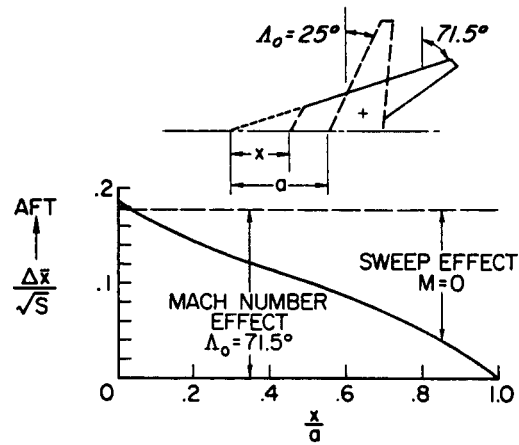


Figure 10

7. RECENT AERODYNAMIC STUDIES APPLICABLE TO  
HIGH PERFORMANCE MANEUVERING AIRCRAFT

By Robert T. Taylor  
NASA Langley Research Center

SUMMARY

Recent emphasis on air-to-air combat has led the NASA to intensify the research of methods for improving the maneuvering normal load factor while retaining a high degree of performance for other combat missions.

The results of recent wing buffeting tests at high subsonic speeds have shown that the use of trailing-edge flaps delays buffeting onset by delaying separation. The static margin at supersonic speeds can be reduced and the normal load factor increased with the use of either retractable canards or variable sweep aft horizontal tails. Positioning the horizontal tail low on the fuselage was shown to be superior on two counts: (1) At supersonic speeds the lower tail experiences an increase in control effectiveness with increasing lift, and (2) the complete configuration aerodynamic center shift with Mach number is smaller with the low tail.

INTRODUCTION

The trend to design one aircraft to accomplish a variety of missions leads to compromises which limit the maneuverability of the aircraft. As an example of the conflicting requirements, the high wing loading dictated by gust alleviation in the low level supersonic interdiction mission tends to produce limits on the maneuvering normal load factor at moderate dynamic pressures. Recent emphasis on maneuverability in air-to-air combat has led NASA to intensify research into the methods by which improvements in load factor may be realized while retaining a high level of performance for other missions.

Figure 1 will serve to illustrate the subjects chosen for discussion in this paper. The typical load factors are shown as a function of Mach number at a wing loading of 100 pounds per square foot at 36 000 and 60 000 feet. The structural limit of fighter aircraft is shown at a load factor of 7.33. Normally, below the structural line, the load factor is restrained by aerodynamic considerations; note that the maximum lift coefficient  $C_{L,max}$  limits the load factor at low speed. At Mach numbers between 0.60 and 1.0, buffeting limits the load factor rather than  $C_{L,max}$ . At supersonic speeds aerodynamic longitudinal control power usually curtails the load factor as shown by the position of the control boundary below the  $C_{L,max}$  curve. The effect of increasing altitude is shown by comparison of the supersonic load factors at altitudes of 36 000 and 60 000 feet. The obvious result is a

decreased load factor at all Mach numbers due to the reduced dynamic pressure. For a typical engine size it would be possible to maintain speed at the load factors indicated along the dashed line. At load factors higher than this line, the aircraft will decelerate, but it is still useful to study ways to increase load factor in the direction of  $C_{L,max}$  or the structural limit especially at the higher altitudes in order to improve maneuverability.

The maneuverability considerations given in this paper are as follows: Results of some recent buffet tests, made in an attempt to raise the buffet limit at subsonic speeds, are presented. The effect of static margin changes at supersonic speeds, investigated in an attempt to raise the control limit, is discussed in terms of instantaneous load factor. Also, some methods of increasing longitudinal control power at supersonic speeds are presented.

#### COEFFICIENTS AND SYMBOLS

b	wing span
$C_L$	lift coefficient
$C_{L,max}$	maximum lift coefficient
$C_m$	pitching-moment coefficient
$\bar{c}$	mean aerodynamic chord
F	net thrust
h	altitude
$i_t$	tail incidence
M	Mach number
$\dot{m}_1$	primary flow rate
$\dot{m}_2$	secondary flow rate
n	load factor, $\frac{\text{Lift}}{\text{Weight}}$
S	reference area
$S_{basic}$	basic reference area
$S_t$	exposed tail area
W	weight

$y_f$	lateral extent of trailing-edge flap
$y_p$	lateral distance to wing pivot
$z_t$	tail height
$\delta_f$	flap deflection
$\delta_j$	jet deflection
$\Lambda_t$	tail leading-edge sweep angle
$\Lambda_w$	wing leading-edge sweep angle
$\lambda$	taper ratio
$\sigma$	root-mean-square bending moment

Subscripts:

max	maximum
T	take-off conditions

## RESULTS AND DISCUSSION

### Buffeting at High Subsonic Speeds

Aerodynamic buffeting at high subsonic speeds has been defined as a structural response to separated flow caused by shock—boundary-layer interaction. The aircraft designer has control of a number of parameters such as wing airfoil section, sweepback, aspect ratio, and, at the higher subsonic speeds, variations in the vehicle area diagram (ref. 1), all of which have an influence on buffeting. The compromises in a given design, however, usually are made in a direction to improve performance rather than buffeting.

The wind tunnel is a powerful experimental tool for assessing wing buffeting onset. This fact has been shown by comparison of a number of model and full-scale airplane tests. (See refs. 2, 3, and 4.) Tests of a general research nature have been undertaken recently at Langley Research Center and are intended to explore means of raising the lift at which buffeting first occurs. Figure 2 illustrates some of these results. The root-mean-square value of the oscillating bending strain  $\sigma$  is plotted as a function of  $C_L$  for three wing sweeps of the model shown. An NACA 2408 wing section, parallel to free stream, was used on the outer panel in the  $25^\circ$  sweep position. The values of  $\sigma$  were obtained by monitoring the output of a strain gage mounted in the root section of the wing as indicated in the sketch. These data were acquired at a Mach number of 0.86. The rapid increase in  $\sigma$  at about

$C_L = 0.50$  is taken as the onset of buffeting. For the flight conditions listed in the figure, a wing loading of 100 pounds per square foot and an altitude of 36 000 feet, the maximum load factor before buffeting onset is only 1.25. Changing wing sweep angle from  $25^\circ$  through  $45^\circ$  is seen to have only a minor effect on the initial buffeting. However, past onset at  $C_L = 0.80$ , the effect of increasing sweep angle is a marked reduction in buffeting intensity.

Whereas the sweep effect shown is beneficial, the objective of the program is to delay the buffeting onset to a higher lift. One possible method of alleviating buffeting onset is through the use of trailing-edge flaps, which allow the high loads to develop at low angles of attack. The physical effect on the wing is a smoothing of the chordwise loading and the delay of separation. Some buffeting measurements are shown for a configuration with trailing-edge flaps in figure 3.

The root-mean-square bending moment  $\sigma$  is shown in figure 3 as a function of  $C_L$  for a wing sweep of  $35^\circ$  at a Mach number of 0.86. The flaps-retracted (dashed) curve is repeated for reference. Other curves represent data for flaps extended  $1/3$  of the local chord from about  $1/4$  to  $3/4$  of the wing semispan. A comparison of the flaps-retracted curve with that for the flaps extended at zero deflection reveals that the additional wing area simply reduces the buffeting intensity, having a negligible effect on buffet onset. As the flap is deflected, however, the onset point moves to a value of  $C_L$  of about 0.67. With the assumptions of the previous figure, the maximum load factor before buffet onset is approximately 1.7.

The flap span and flap chord were selected arbitrarily for these tests. It was assumed that some span at the tip of the wing would be required for an aileron roll control, and therefore the flap span was limited. It is of interest to assess the effect of flap span. Figure 4 shows similar results obtained with a plain flap on which the span was varied. The root-mean-square fluctuating moment is plotted as a function of the lift coefficient at a Mach number of 0.86. The flap deflection for the solid and broken curves is  $\delta_f = 10^\circ$ . The dashed curve is repeated once more for reference. The broken curve represents data for a flap extended from about  $1/4$  to  $3/4$  of the wing semispan. The solid curve shows data taken when the flap is deflected  $10^\circ$  from  $1/4$  of the wing semispan to the wing tip. These data indicate that the improvement in lift at which buffeting occurs is not sensitive to the span of the plain flap tested.

These data do not represent any attempt to optimize the flap configuration or flap deflections but are presented to indicate some early results of a program recently undertaken by the NASA to improve buffeting.

### Supersonic Considerations

As mentioned earlier the supersonic maneuverability is usually limited by the control power available. In order to move the control boundary toward the structural limit or the lift limit, two different approaches may be considered. First, reducing the supersonic longitudinal stability level will increase the

amount of instantaneous load factor for a given control and, second, the control power itself could be improved, thus increasing the load factor.

### Longitudinal Stability

Various wing geometry effects are shown in figure 5. The first effect to be noted in this figure is the effect of planform noted in paper no. 6 by Lamar and Alford where it was indicated that the clipped arrow wing had less aerodynamic center shift than did the delta wing. On the left is a comparison of an arrow and two delta wings, all clipped to a taper ratio of 0.125. All wings had a leading-edge sweep angle of  $60^\circ$ . Similar planforms were shown in paper no. 6. The effect of this reduced aerodynamic center shift on the trimmed normal load factor plotted against altitude is shown for  $M = 3.0$ . The assumed conditions are  $W/S = 100$  pounds per square foot for the basic wing and a constant tail load available for trim at the maximum load factor. A comparison of the load factors at a 70 000-foot altitude indicates that the arrow wing (dashed curve) gives 4.0g, whereas the delta (dot-dash curve) at the same wing area has 2.3g. This difference in load factor is due to the difference in aerodynamic center shift between these two planforms.

The second effect depends on the size of the wing. An examination of the lift-curve slopes of the two wing shapes at subsonic speeds showed the arrow wing to have the lower landing speed at a given angle of attack. Increasing the size of the delta by a factor of 1.3 to give comparable landing performance and locating the wing to give the same subsonic static margin appeared logical. The results of these changes in the wing are indicated by the solid curve which shows an even lower trimmed load factor at Mach 3.0 ( $n = 2.0$ ). This result, even though surprising at first, is easily understood when the assumption of a constant tail load is recalled. The larger wing has a larger load shift measured in feet at the higher Mach numbers; the constant tail power then cannot balance as high a value of wing lift and if the airplane weight is constant the trimmed load factor decreases. Increasing the wing size decreases the supersonic maximum trimmed load factor when the aerodynamic control power is limited. If, on the other hand, the configuration is limited in lift and not limited in control, increasing the wing size increases the available load factor; therefore, wing loading, for the conditions considered, is not a unique parameter for the determination of maximum load factor at supersonic speeds.

Figure 6 illustrates the effect of pivot location for the variable sweep wing. The wing pivot location is given in terms of the semispan of the high sweep wing. Paper no. 6 discussed the aerodynamic center shift with sweep and its sensitivity to the location of the wing pivot. The reduction in static margin afforded by the pivot change accounts for the increase in load factor shown in the figure. At 60 000 feet, the pivot at 42 percent of the semispan gives a load factor of 1.5 whereas the pivot at 56 percent of the semispan gives about 2.2.

Although the Mach effect on the wing is the primary cause of the increase in stability in going from subsonic to supersonic speeds, application of variable geometry to other components of the aircraft could be utilized to offset the effect of the undesirable supersonic loading. Two possible methods which have been studied are shown in figure 7.

The retractable canard concept illustrated on the left of figure 7 (refs. 5, 6, and 7) had a highly swept wing and a low aft horizontal tail for control. With the canard retracted, the subsonic conditions fix the center of gravity. At a supersonic speed of about  $M = 2.0$  with  $W/S = 100$  pounds per square foot, the available load factor is about 2.6 at an altitude of 60 000 feet. As the canard is extended at supersonic speeds, the reduction in static margin allows trim to a load factor of 4.6 with the same control deflection. If the canard can be unfolded with some positive incidence, the gain in load factor can be even higher.

Another concept for the reduction of the supersonic static margin is the variable sweep horizontal tail, illustrated on the right of figure 7. This concept assumes that, to reduce the wave drag, the tail must be swept back during supersonic flight (ref. 8). At subsonic speed, however, the tail may be unswept to furnish a greater span and increased effectiveness, thereby allowing a more aft center of gravity. The lower supersonic static margin due to this more aft center of gravity improves the load factor to about 6.5 with the variable sweep tail as contrasted with about 2.2 for the forward center of gravity associated with the fixed tail. The effectiveness of the concept is sensitive to the tail arm however, as it is possible for the tail arm to decrease faster than effectiveness increases on short coupled configurations.

#### Longitudinal Control

The replacement of the elevator control with the all-movable horizontal tail was probably the first step toward improved supersonic longitudinal control effectiveness; all-movable tails have been widely accepted for many years. The advantages of tail length, size, and efficient planform with regard to control effectiveness are obvious, but quite often compromises must be made because of considerations such as aircraft length or weight. One approach which may be open to the designer, however, is to locate the horizontal tail in the most advantageous flow field. At subsonic speeds the importance of the vertical location of the horizontal tail is well documented and the desirability of a low tail position for stability is generally accepted. In order to determine the effect of the vertical location of the horizontal tail on supersonic maneuverability, a systematic investigation was recently undertaken by the NASA. The configuration studied is shown in figure 8.

Two sizes of the horizontal tail were tested. The sizes and locations were selected to keep the horizontal-tail volume coefficient a constant. Each tail then was tested in two vertical locations, in the chord plane of the wing and  $0.06\bar{c}$  below the wing. Control effectiveness as well as the stability contribution of each tail was measured. The effect of vertical position for the small tail is shown in figure 9.

Presented in figure 9, for a Mach number of 2.16, is pitching-moment coefficient as a function of lift coefficient for the chord-plane tail (shown dashed) and for the low tail (shown solid). Note that both tails show the same stability level and essentially the same level of control effectiveness at zero lift. As lift increases the chord-plane tail loses effectiveness and the low

tail gains effectiveness with the result that the low tail trims at a lift coefficient which is 40 percent higher than that associated with the chord-plane tail, both having  $-20^\circ$  incidence.

Essentially the same result was found when the large closely coupled tails were tested as shown in figure 10. The pitching-moment coefficient is plotted as a function of lift coefficient at a Mach number of 2.16 for the chord-plane tail (dashed) and the low tail (solid). Compared as before with the same moment reference (or center of gravity), the low tail shows about a 50-percent increase in trimmed  $C_L$  with  $-20^\circ$  of incidence.

Further tests on this model showed that the low tail has, as might be expected, a higher stability contribution at subsonic speeds due to its position below the high downwash field of the wing and, therefore, less stability increase with Mach number. If the results are compared on the basis of both the low tail and the chord-plane tail having the same static margin at  $M = 0.90$ , the low tail result is even more dramatic. These data, adjusted, are shown as the dotted curve (extrapolated to trim as the supersonic tests were not carried to sufficiently high lift). These effects for the large closely coupled tail are shown in figure 11 in which load factors as a function of altitude are compared. At 60 000 feet the chord-plane tail gives a load factor of 2.6. At the same center of gravity the low tail gives 3.8. At a static margin equal to that of the configuration with the chord-plane tail at  $M = 0.90$ , the value (extrapolated) for the low tail is 5.8.

Another method, which appears to offer a great deal of promise for enhancing load factor at supersonic speeds, involved deflecting the thrust of the jet engine. A possible method of deflecting the thrust is illustrated in figure 12. On the right of the figure a duct is shown schematically. Hot gas is taken from the convergent section and bypassed around the throat and re-injected in the divergent section where it separates the main flow in a controlled manner proportional to the injected flow. The effect of deflection of the gross thrust at  $M = 2.16$  on load factor is a function of altitude. The solid curve shows the available load factor with  $-25^\circ$  incidence of the horizontal tail (data from ref. 9). The dashed curve shows the calculated load factor as the exhaust of the engine is deflected  $-5^\circ$  in combination with deflection of the horizontal tail. The engine is assumed to be sized to give a thrust-weight ratio of 0.80 at take-off conditions. Once again at 60 000 feet the load factor has improved from about 2.2 to about 5.6 as a result of deflection of the thrust.

Data obtained on a similar nozzle configuration indicate that to deflect the jet  $-5^\circ$ , about 6 percent of the primary nozzle flow is required for re-injection.

#### CONCLUDING REMARKS

In conclusion, some results of recent wing buffeting tests have shown that the moderate increases in wing sweep for variable sweep wings provide a significant reduction in the buffeting intensity at high subsonic speed. The use of

trailing-edge flaps delays buffeting onset by redistributing the chord load and delaying separation.

A number of methods were shown whereby the static margin at supersonic speeds can be reduced with a consequent improvement in the normal load factor. These methods included retractable canards and variable sweep aft horizontal tails.

Positioning the horizontal tail low on the fuselage as opposed to positioning on the chord plane of the wing was shown to be superior on two counts: (1) the lower tail experiences an increase in control effectiveness with lift whereas the effectiveness of the chord-plane tail decreases as lift increases, and (2) the aerodynamic center shift with Mach number appears to be much smaller when the tail is mounted low on the fuselage. An alternate system for aerodynamic control is discussed, which involves deflection of the main flow of the jet engines; approximately 6 percent of the main nozzle flow is required to deflect the jet  $-5^\circ$ .

## REFERENCES

1. Davis, Don D., Jr.; and Wornom, Dewey E.: Buffet Tests of an Attack-Airplane Model With Emphasis on Analysis of Data From Wind-Tunnel Tests. NACA RM L57H13, 1958.
2. Huston, Wilbur B.; Rainey, A. Gerald; and Baker, Thomas F.: A Study of the Correlation Between Flight and Wind-Tunnel Buffeting Loads. NACA RM L55E16b, 1955.
3. Huston, Wilbur B.: A Study of the Correlation Between Flight and Wind-Tunnel Buffet Loads. AGARD Rept. 111, Apr.-May 1957.
4. Mabey, D. G.: Comparison of Seven Wing Buffet Boundaries Measured in Wind Tunnels and in Flight. Tech. Rept. No. 64013, Brit. R.A.E., Sept. 1964.
5. Spencer, Bernard, Jr.: Stability and Control Characteristics at Low Subsonic Speeds of an Airplane Configuration Having Two Types of Variable-Sweep Wings. NASA TM X-303, 1960.
6. Foster, Gerald V.; and Morris, Odell A.: Stability and Control Characteristics at a Mach Number of 1.97 of an Airplane Configuration Having Two Types of Variable-Sweep Wings. NASA TM X-323, 1960.
7. Spearman, M. Leroy; and Foster, Gerald V.: A Summary of Research on Variable-Sweep Fighter Airplanes. NASA TM X-1185, 1965.
8. Phillips, W. Pelham; and Taylor, Robert T.: Longitudinal Aerodynamic Characteristics at Mach Numbers From 0.28 to 2.50 of a Multipurpose Tactical Airplane Configuration Having Variable-Sweep Wings and Externally Mounted Engines. NASA TM X-840, 1963.
9. Shaw, David S.: Supersonic Investigation of the Static Stability, Performance, and Control of a Variable-Sweep Tactical Fighter Model - Phase 1. NASA TM X-1045, 1965.

ILLUSTRATIVE LOAD FACTOR DIAGRAMS  
 W/S = 100 LB/SQ FT

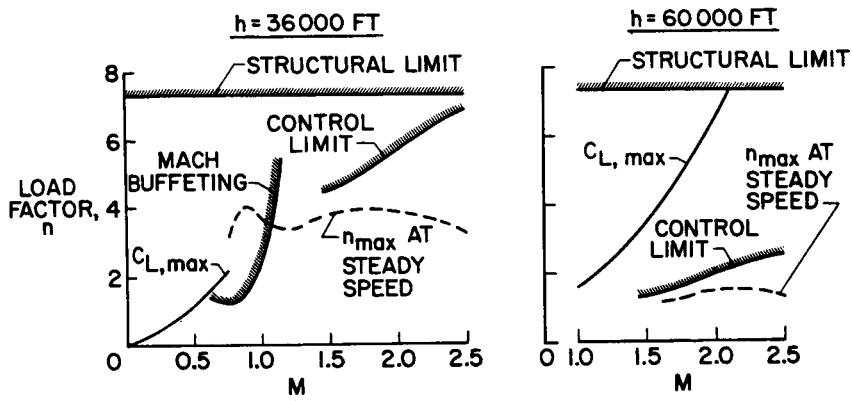


Figure 1

EFFECT OF WING SWEEP ON BUFFETING MOMENT  
 $M = 0.86$

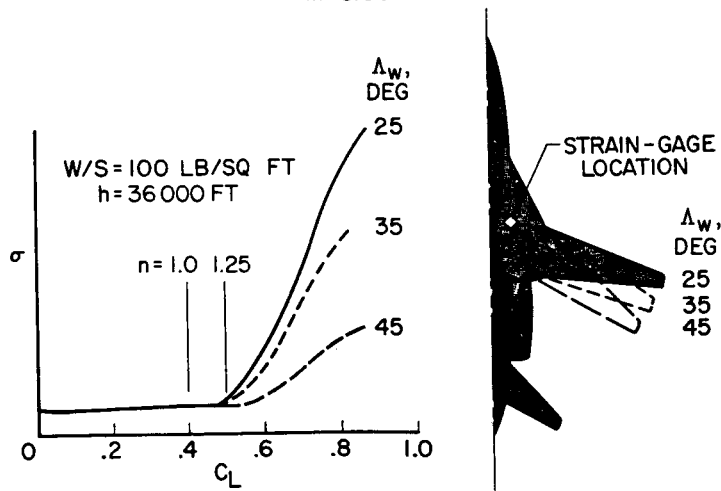


Figure 2

EFFECT OF FLAP DEFLECTION ON BUFFETING MOMENT

$M=0.86$ ;  $\Delta_w=35^\circ$

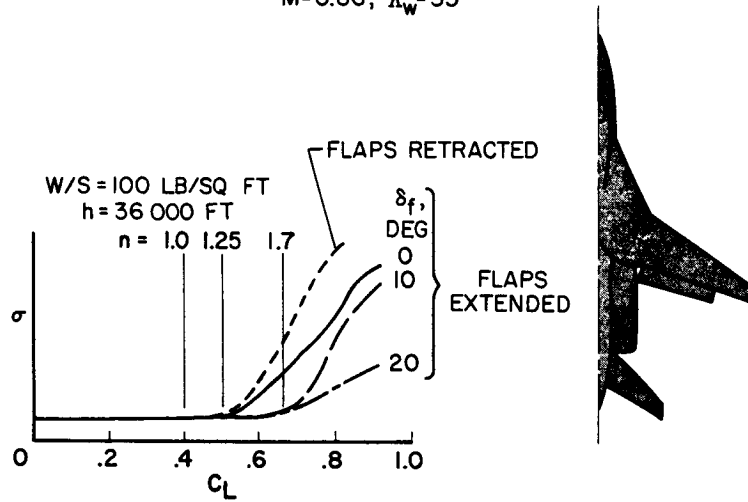


Figure 3

EFFECT OF FLAP SPAN ON BUFFETING MOMENT

$M=0.86$ ; PLAIN FLAPS;  $\Delta_w=35^\circ$

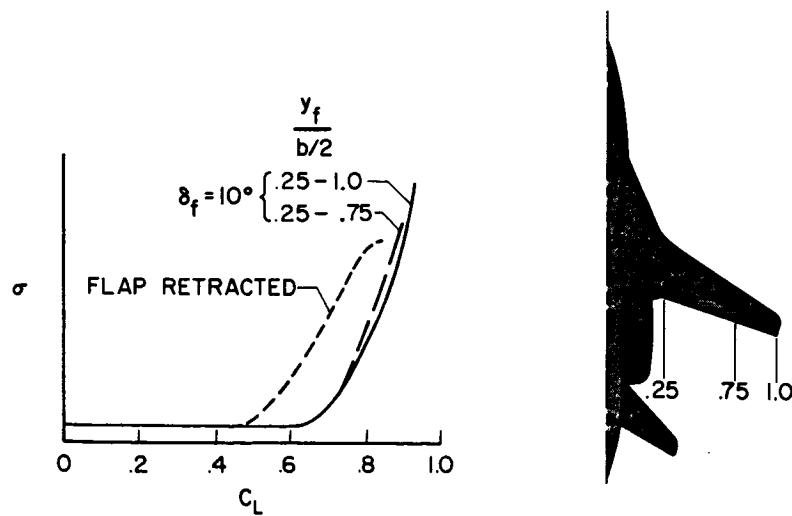


Figure 4

**EFFECT OF WING GEOMETRY**  
 CONSTANT TAIL LOAD,  $W/S_{basic} = 100 \text{ LB/SQ FT}$

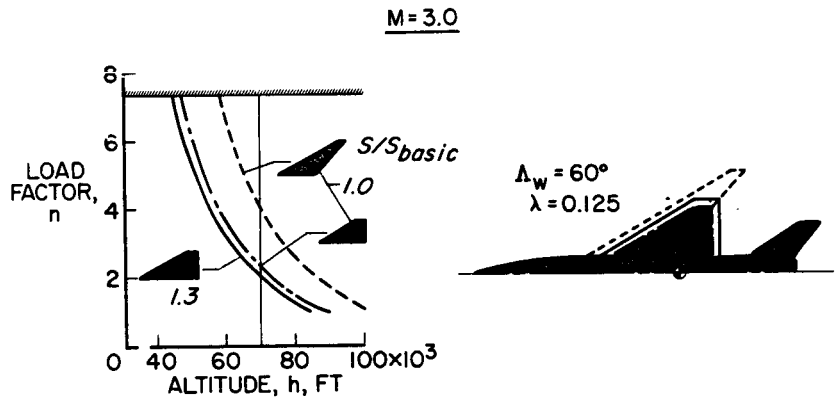


Figure 5

**EFFECT OF PIVOT LOCATION**  
 $W/S = 100 \text{ LB/SQ FT}$

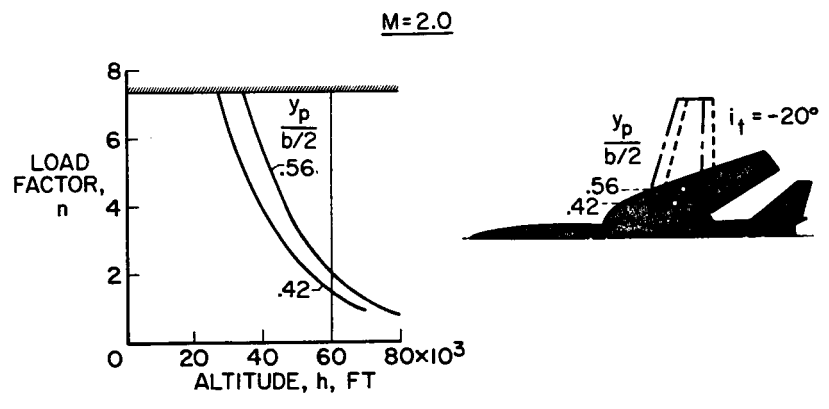


Figure 6

### EFFECT OF VARIABLE-GEOMETRY SURFACES

$M=2.0$ ;  $W/S=100$  LB/SQ FT;  $i_1=-20^\circ$

CANARD EXTENDED  
AT  $M>1$

TAIL UNSWEPT  
AT  $M<1$

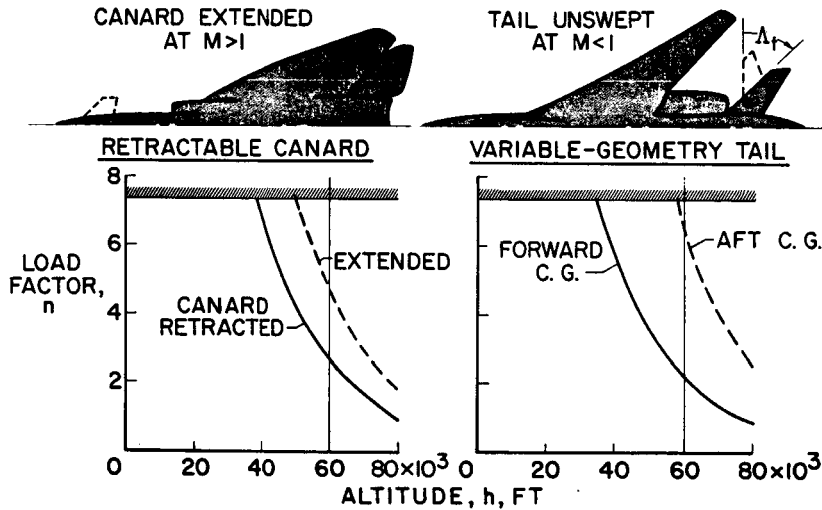


Figure 7

### SCOPE OF HORIZONTAL-TAIL-LOCATION STUDY

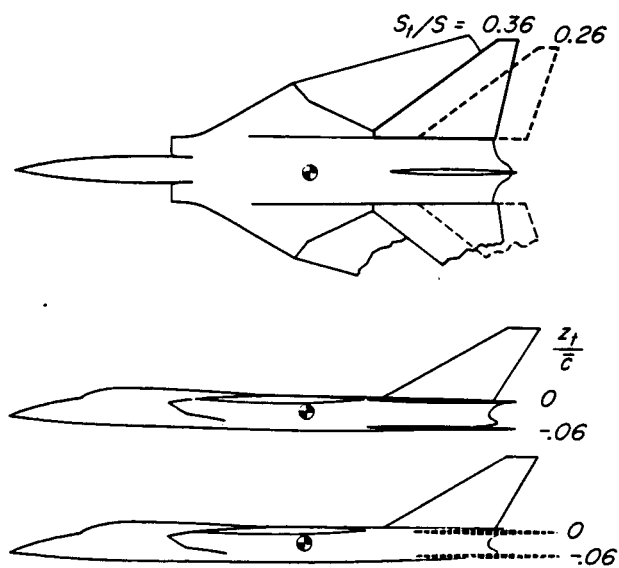


Figure 8

EFFECT OF HORIZONTAL-TAIL LOCATION  
 $M = 2.16; S_t/S = 0.26$

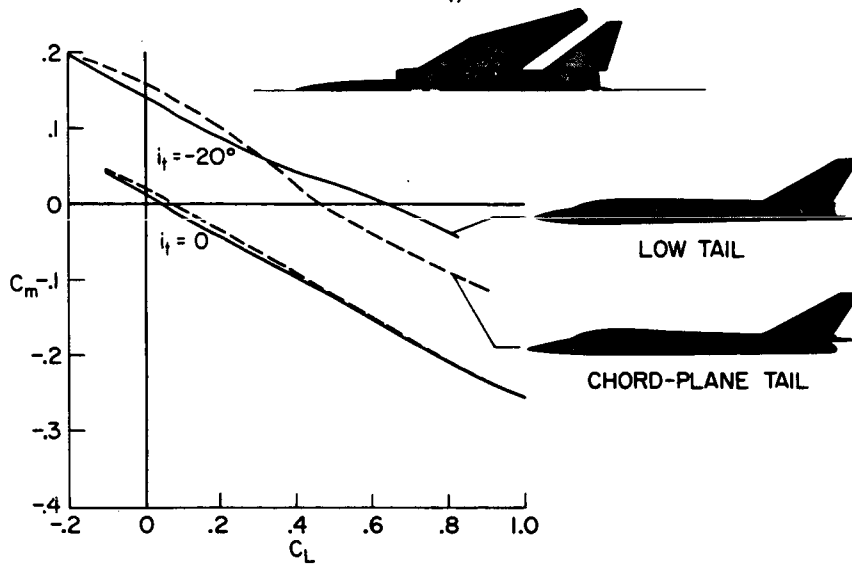


Figure 9

EFFECT OF HORIZONTAL-TAIL LOCATION  
 $M = 2.16; S_t/S = 0.36$

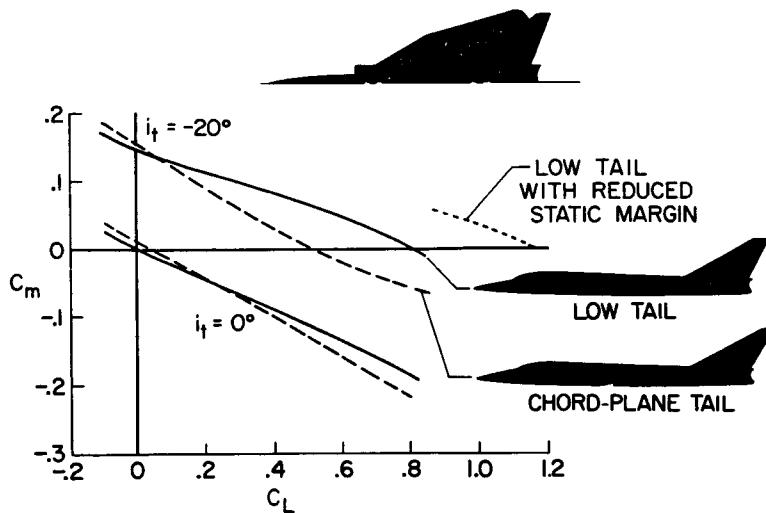


Figure 10

VARIATION OF LOAD FACTOR WITH ALTITUDE  
 $M=2.16$ ;  $W/S = 100$  LB/SQ FT;  $S_t/S = 0.36$

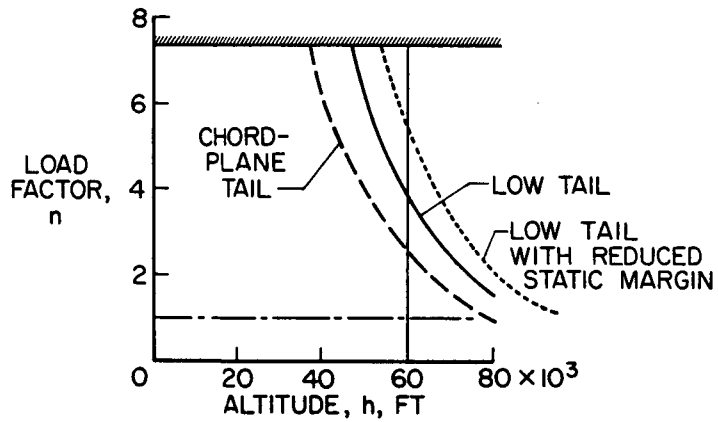


Figure 11

CALCULATED EFFECT OF THRUST DEFLECTION  
 $M=2.16$ ;  $(F/W)_T = 0.80$ ;  $W/S = 100$  LB/SQ FT

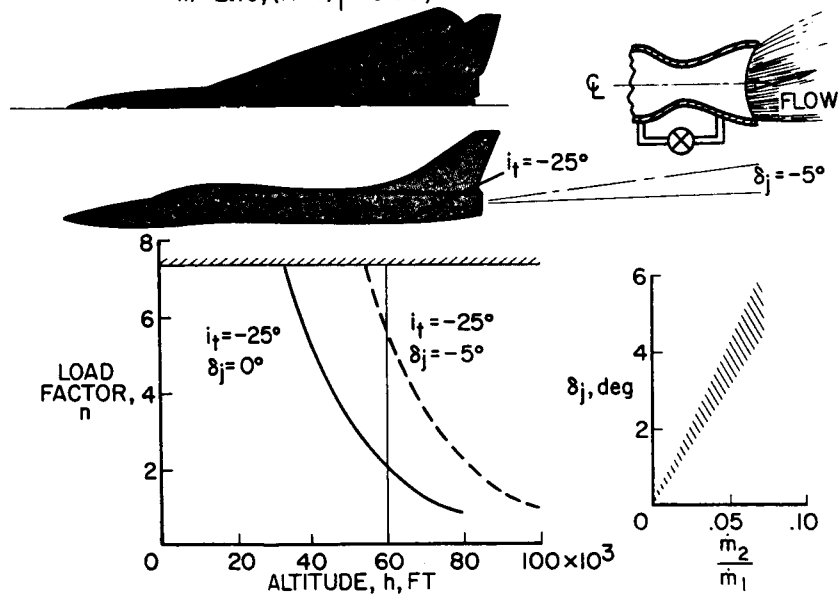


Figure 12

## 8. A SUMMARY OF NASA DATA RELATIVE TO EXTERNAL-STORE

### SEPARATION CHARACTERISTICS

By Linwood W. McKinney and Edward C. Polhamus  
NASA Langley Research Center

#### SUMMARY

The available NACA and NASA data relating to the carriage and separation characteristics of external stores are summarized, and some typical aerodynamic characteristics of stores in the carriage position are presented. Some of the subsonic interference origins and methods of combining experimental flow fields with theory to predict store forces and moments are illustrated by a comparison of calculated and measured store normal force and pitching moment. The effects of various combinations of speed, dive angle, airplane load factor, and store density on the separation characteristics are illustrated by using calculated store trajectories. This paper includes a bibliography of NACA and NASA reports relative to the release of stores from airplanes.

#### INTRODUCTION

Operational experience by the military services during the past year has focused attention on problems associated with the release of various types of external stores. While a considerable amount of research relative to the carriage and release of external stores was done by the NACA in the past, research on stores during the last 10 years has been concentrated primarily in the area of the release characteristics of internally carried stores and the effect of external stores on aircraft stability and performance, with some related work on the separation characteristics of lifting reentry research vehicles from a carrier airplane. However, in view of the current interest in the carriage and release characteristics of external stores, it was believed that a summary of the available NACA and NASA data would be useful to those engaged in developing and evaluating analytical methods of studying these problems.

The purpose of this paper is to describe the configurations which have been studied and the range of variables covered, to present some typical aerodynamic characteristics of stores in the carriage position, and to illustrate the effect of these characteristics on the separation characteristics of a store under various delivery conditions. A bibliography of NACA and NASA reports related to the release of stores from airplanes is also included.

## SYMBOLS

A	wing aspect ratio
$a_y$	lateral acceleration, feet/second <sup>2</sup>
$a_z$	vertical acceleration, feet/second <sup>2</sup>
b	wing span, feet
c	local wing chord, feet
$\bar{c}$	wing mean aerodynamic chord, feet
$C_m$	store pitching-moment coefficient referred to 0.462l, $\frac{\text{Store pitching moment}}{qS_S l}$
$C_N$	store normal-force coefficient, $\frac{\text{Store normal force}}{qS_S}$
$C_n$	store yawing-moment coefficient referred to 0.462l, $\frac{\text{Store yawing moment}}{qS_S l}$
$C_p$	pressure coefficient
$C_y$	store side-force coefficient, $\frac{\text{Store side force}}{qS_S}$
EAS	equivalent airspeed, knots
$i_S$	store incidence angle relative to wing reference line, degrees
l	store length, feet
M	Mach number
$\Delta n$	airplane incremental load factor, referred to steady equilibrium flight conditions
q	dynamic pressure, pounds/foot <sup>2</sup>
S	airplane wing area, feet <sup>2</sup>
$S_S$	store reference area, maximum frontal area of body, feet <sup>2</sup>
t/c	wing thickness ratio
W	airplane weight, pounds

$W_s$	store weight, pounds
$W/S$	airplane wing loading, pounds/foot <sup>2</sup>
$\alpha_w$	angle of attack of airplane wing, degrees
$\gamma$	dive (flight-path) angle, degrees
$\lambda$	taper ratio
$\Lambda_c/4$	wing sweep of quarter-chord line, degrees

#### CONFIGURATIONS STUDIED

The major portion of the wind-tunnel studies for wing-pylon-store configurations which are applicable to the current problem area utilized one of the two test methods shown in figure 1. The top sketch illustrates the method in which the aerodynamic forces and moments of the store in the carriage position are measured by means of a strain-gage balance mounted within the store and attached to the wing pylon. Data obtained by this method can be used to determine the store carriage loads and the initial separation characteristics of the store. The lower sketch illustrates the method in which the store is supported by a sting through an internal strain-gage balance. In addition to providing carriage loads, the sting-support method allows the store to be tested at various positions and attitudes relative to the airplane and thereby provides store aerodynamic data which can be used to compute both the release and the trajectory characteristics of the store.

Comparisons between computed trajectories using aerodynamic data obtained by this technique and trajectory measurements made in flight and with free-fall techniques are given in references 1 and 2, respectively, and indicate a satisfactory agreement.

The use of free-fall and forced-ejection methods by NASA has been directed primarily toward ejection from bomb bays rather than the release of external stores, and will not be discussed here. However, a bibliography of this work is included. It should also be pointed out that problems associated with scaling (refs. 3 to 6) and simulation of release conditions, such as dive angle, tend to limit the usefulness of the free-fall and forced-ejection methods. The configurations studied by the techniques shown in figure 1 are described in figures 2 and 3. The configurations studied by the pylon-support method are shown in figure 2, and the configurations studied by the sting-support method are shown in figure 3. A bottom view of the airplane is shown and the various stores tested are shown in the carriage position. The alternate location of the store is shown by the dotted outline. The table under the sketches lists some of the pertinent geometric characteristics of the wings, the Mach number ranges of the test, the facility used, the reference containing the data of the more important variables studied, and the type of data obtained.

Wing planforms cover the sweep range from  $0^\circ$  to  $47^\circ$  and include a  $60^\circ$  delta wing. Aspect ratios from 4 to 7.7 were covered. The Mach numbers ranged from approximately 0 to 2.01. Both finned and unfinned stores have been investigated. In general, the configurations studied are representative of rather large stores primarily because the balances required for the smaller stores were not available. Five-component force data are available for configurations 1 to 5; pressure distributions on the stores were measured for configurations 6 to 8; for configuration 8, complete wing pressure distributions were measured without the store and with the store in two vertical locations. Five-component force data have also been obtained on configurations 9 to 12, and for the supersonic studies on configurations 11 and 12 store force data have been obtained for a large number of positions within the shaded area for several vertical store locations. For the subsonic studies (configurations 13 and 14), the local angularities in both the longitudinal and lateral planes and the local flow velocities were measured at various vertical locations beneath the wing and fuselage for the range of spanwise and chordwise locations indicated by the dashed line for the unswept wing and the shaded area for the swept wing. These configurations are similar to two of those used to measure store force data and therefore are useful not only in evaluating flow-field theories but also in evaluating methods of predicting store forces.

#### TYPICAL AERODYNAMIC CHARACTERISTICS

Inasmuch as the current operational problems are primarily associated with subsonic deliveries, the remainder of this paper will deal with the subsonic case.

Configuration 5 was chosen to illustrate some typical aerodynamic characteristics of a store in the carriage position and to show the effects of delivery conditions on release characteristics and is presented in figure 4. The pertinent geometric characteristics of the wing and the location of the store beneath the wing are indicated. This configuration was selected because of its similarity to configuration 14, for which complete flow-field surveys were available.

Before presenting the various aerodynamic characteristics of the store, a somewhat detailed look at the store normal-force and pitching-moment characteristics will be made to illustrate the order of magnitude of the various flow-field induced effects and to indicate the effectiveness of simplified theory for predicting the store forces and moments. The calculations are based on the application of the measured flow field (ref. 7) to body-fin theory and ignore the mutual interference effects between the wing and store. Figure 5 shows a comparison of the calculated and measured store normal-force coefficient with wing angle of attack for the body, the fins, and the body-fin combination. For the body alone it will be noted that the calculated buoyancy effect (shown by the short-dash line) associated with the wing-body-induced static-pressure gradient is rather large and produces a negative normal-force-curve slope and a large positive normal force at  $\alpha_w = 0^\circ$ . The positive force at  $\alpha_w = 0^\circ$  is, of course, associated with the wing-thickness-induced buoyancy and will increase with increasing wing thickness ratio. The wing for this case was 6 percent thick. The effect of the flow angularity on the body (indicated as the local  $\alpha$  effect)

includes both the induced-angle-of-attack and induced-camber effects determined by the method of reference 8 with the crossflow-separation effects accounted for by the method of reference 9. The sum of the buoyancy and local  $\alpha$  effects shown by the solid line indicates a positive value of normal force at  $\alpha_w = 0^\circ$  and is in fairly good agreement with the experimental data. The estimate of the fin increment accounting for the local angle-of-attack distribution, shown by the solid line in the lower left of figure 5, indicates a slope of about one-half of that predicted for the isolated fins and reasonably good agreement with experiment. The reduction in slope is, of course, associated with the wing-lift-induced downwash characteristics while the positive normal force at  $\alpha_w = 0^\circ$  is due to the thickness-induced upwash. The results for the body-fin combination, shown at the lower right of figure 5, also indicate fairly good agreement with the experiment.

The calculated and measured pitching-moment coefficients for the body, the fins, and the body-fin combination are shown in figure 6 as functions of wing angle of attack. The methods used were the same as those previously described in connection with the normal force. For the body alone, the buoyancy effect gives a stabilizing moment whereas the local angle-of-attack effect calculated by the methods of reference 4 gives an unstable slope. The sum of the buoyancy and local-angle-of-attack effect is shown by the solid line and indicates the same slope as the experiment over most of the angle-of-attack range; however, the magnitude of body pitching moment predicted is considerably higher. The estimate for the fin accounting for the local-angle-of-attack effect and shown on the lower left of figure 6 shows reasonable agreement at the lower values of  $\alpha_w$ ; however, at the higher value of  $\alpha_w$  this agreement deteriorates. The discrepancies between the calculated and experimental values of pitching-moment coefficient for both the body and the fin are additive so that the estimate for the body-fin combination gives, in general, poor agreement with the experiment. This figure serves to point out the need for more sophisticated theories to predict the store pitching-moment characteristics in the interference flow field.

Experimentally obtained aerodynamic characteristics for the example configuration (configuration 5) at a Mach number of 0.50 are shown in figure 7. The normal-force and pitching-moment curves are the same curves that were discussed on the two preceding figures and are presented here for completeness.

In the lateral plane, a positive value of side-force coefficient ( $C_Y$ ), indicating a force toward the fuselage, is obtained at  $\alpha_w = 0^\circ$ . As  $\alpha_w$  is increased, a change in sign of  $C_Y$  occurs. The significant point to be noted about the yawing moment is that the lateral center of pressure lies ahead of the store center of gravity for the complete wing angle-of-attack range shown, and, as a result, the nose of the store will be yawed in the direction of the side force. Figure 8 further illustrates the change in sign of side force with angle of attack and shows the experimental store pressure distributions measured on configuration 8 at  $\alpha_w = 0^\circ$  and  $\alpha_w = 8^\circ$ . The pressure distribution on the isolated store is also shown for reference. Note that at  $\alpha_w = 0^\circ$  high negative pressures are acting on the inboard side of the store whereas at  $\alpha_w = 8^\circ$  high positive pressures are obtained on the inboard side of the store.

## SEPARATION CHARACTERISTICS

Since all the curves shown in figure 7 are displaced at  $\alpha_w = 0^\circ$  and in the lateral case change sign with wing angle of attack, airspeed would be expected to have a large influence on the forces developed on the store at release. To illustrate the order of magnitude of this effect on the initial store trajectory, the linear accelerations acting on the store at release are shown in figure 9 for the example configuration.

On the left of figure 9, the effect of equivalent airspeed on the vertical acceleration at the store fin for a store at  $i_s = 0^\circ$  relative to the wing chord line, is shown for store weights of 180 and 960 pounds. The vertical acceleration at the store nose at  $i_s = -5^\circ$  is also shown as a function of airspeed for store weights of 180 and 960 pounds. As indicated by the arrows, positive acceleration is toward the airplane wing. The points on the store for which the acceleration is shown are the most critical points from contact consideration when both the store normal force and pitching moment are accounted for. The weights were taken to represent near minimum and maximum weights for this class of store. The wing angle-of-attack variation used in the calculation corresponds to the angle of attack required for steady level flight of the carrier airplane at a wing loading of 100 lb/ft<sup>2</sup> over the speed range and therefore decreases with increasing speed. For a wing loading of 100 lb/ft<sup>2</sup> this configuration gives an airplane weight of 18 650 pounds. For the lightweight store at  $i_s = 0^\circ$  the fin accelerates toward the wing and this acceleration increases rapidly with airspeed, and results, of course, from the buoyancy effect at  $\alpha_w = 0^\circ$ . When the store is mounted with  $-5^\circ$  incidence relative to the wing, the normal force at  $\alpha_w = 0^\circ$  is negative and this trend is reversed; that is, as speed is increased and store weight reduced, the store is accelerated away from the wing at a faster rate.

The curves on the right of the figure show that, as speed is increased, the lateral acceleration changes from an acceleration away from the fuselage to an acceleration toward the fuselage, as indicated by the variation of  $C_y$  and  $C_n$  with wing angle of attack in figure 7.

To account for the effect of dive angle on the store separation characteristics, a three-degree-of-freedom system of motion equations was used to calculate store trajectories in the longitudinal plane. This effect of dive angle is illustrated in figure 10 for a 960-pound store released at 530 knots.

On the left of figure 10 calculated trajectories are shown at a dive angle  $\gamma$  of  $0^\circ$  for initial store incidence angles of  $0^\circ$  and  $-5^\circ$ , and on the right of the figure at a dive angle of  $75^\circ$  also for initial store incidence angles of  $0^\circ$  and  $-5^\circ$ .

At zero dive angle the weight of the store is essentially normal to the aircraft reference and the initial acceleration corresponds to that shown in figure 9 by the dashed line at 530 knots. When the store is released contact does not occur. For a dive angle of approximately  $75^\circ$  the normal weight component is reduced by the cosine of the dive angle and a component of the weight

goes into thrust which accelerates the store relative to the carrier airplane. Since the store normal-force curves are displaced at  $\alpha_w = 0^\circ$ , the reduction in store normal force resulting from the change in  $\alpha_w$  required to maintain steady flight on the  $75^\circ$  flight path is insignificant relative to the reduction of the gravity component. As a result, for  $i_s = 0^\circ$ , the store normal force approximately equals its normal weight component and the nose-down pitch rotation combined with the forward acceleration of the store relative to the airplane causes the store fin to contact the trailing edge of the wing. However, at  $i_s = -5^\circ$ , contact is not indicated. Although the dive angle at which contact is shown for this store is large, a store having larger fins or located beneath a thicker wing section, where the buoyancy effect would be greater, would be expected to contact the wing at lower dive angles. The results of the calculated trajectories for the example configuration at  $i_s = 0^\circ$  are summarized in figure 11.

The lines or boundaries on the left of the figure represent the maximum dive angle for release of a 960-pound store without contact between the fin and airplane wing as a function of equivalent airspeed, under conditions of steady flight and imposed incremental load factors of -0.25 and -0.5. Contact is indicated on the hatched side of the boundary. The dashed line shows the boundary obtained if compressibility effects are neglected. (The compressibility effects are based on sea-level conditions.) For the store-airplane configuration illustrated here the reduction in store normal force and increase in drag associated with the higher Mach numbers opens the boundaries at the higher airspeeds. Data obtained on airplanes during attack missions indicate that at the instant of ordnance release the airplane is quite often in a pushover. For certain delivery techniques, a pushover is required to offset the horizontal drift associated with increases in speed during a dive. Figure 11 indicates that severe penalties in both maximum permissible dive angle and flight speed may be encountered if the store is released during a pushover.

On the right of the figure the effect of store weight on contact at release is shown as a function of equivalent airspeed for flight-path angles of  $0^\circ$  and  $60^\circ$ . The boundaries indicate the minimum weight at which the store can be released without contact over the speed range for the two dive angles. In this figure contact is indicated below the boundary.

#### CONCLUDING REMARKS

The available NACA and NASA data relating to the carriage and separation characteristics of external stores have been summarized. A comparison of calculated and measured store normal force and pitching moment has been presented to illustrate some of the subsonic interference origins and methods of combining experimental flow fields with theory to predict store forces and moments. This comparison indicates that additional work is required to develop completely satisfactory analytical methods of obtaining store moments in the interference flow field. Therefore, at present it appears that the best method is to measure the store characteristics in the wind tunnel. When the aerodynamic characteristics of a store in the wing flow field are known, the store trajectories can be calculated with reasonable accuracy. The effects of various combinations of speed, dive angle, airplane load factor, and store density on the separation characteristics are illustrated by using calculated store trajectories.

## REFERENCES

1. Matranga, Gene J.: Launch Characteristics of the X-15 Research Airplane as Determined in Flight. NASA TN D-723, 1961.
2. Faget, Maxime A.; and Carlson, Harry W.: Experimental Techniques for Predicting Store Motions During Release or Ejection. NACA RM L55L20b, 1956.
3. Sandahl, Carl A.; and Faget, Maxime A.: Similitude Relations for Free-Model Wind-Tunnel Studies of Store-Dropping Problems. NACA TN 3907, 1957.
4. Neihouse, Anshal I.; and Pepoon, Philip W.: Dynamic Similitude Between a Model and a Full-Scale Body for Model Investigation at Full-Scale Mach Number. NACA TN 2062, 1950.
5. Murphy, Glenn: Similitude in Engineering. The Ronald Press Co., 1950, pp. 17-41.
6. Alford, William J., Jr.; and Goodson, Kenneth W.: A Technique for Firing Dynamically Scaled Missile Models in Wind Tunnels and for Measuring Rocket-Motor Sound and Pressure Fluctuations. NASA TN D-224, 1960.
7. Alford, William J., Jr.; and King, Thomas J., Jr.: Experimental Investigation of Flow Fields at Zero Sideslip Near Swept- and Unswept-Wing—Fuselage Combinations at Low Speed. NACA RM L56J19, 1957.
8. Munk, Max M.: The Aerodynamic Forces on Airship Hulls. NACA Rept. 184, 1924.
9. Hopkins, Edward J.: A Semiempirical Method for Calculating the Pitching Moment of Bodies of Revolution at Low Mach Numbers. NACA RM A51C14, 1951.
10. Alford, William J., Jr.; and Silvers, H. Norman: Investigation at High Subsonic Speeds of Finned and Unfinned Bodies Mounted at Various Locations From the Wings of Unswept- and Swept-Wing—Fuselage Models, Including Measurements of Body Loads. NACA RM L54B18, 1954.
11. Johnson, Clinton T.: Flight Investigation of the Aerodynamic Forces on a Wing-Mounted External-Store Installation on the Douglas D-558-II Research Airplane. NACA RM H58B24, 1958.
12. Wornom, Dewey E.: Transonic Aerodynamic Characteristics of a  $45^\circ$  Swept-Wing—Fuselage Model With a Finned and Unfinned Body Pylon-Mounted Beneath the Fuselage or Wing, Including Measurements of Body Loads. NASA MEMO 4-20-59L, 1959.
13. Morris, Odell A.; Carlson, Harry W.; and Geier, Douglas J.: Experimental and Theoretical Determination of Forces and Moments on a Store and on a Store-Pylon Combination Mounted on a  $45^\circ$  Swept-Wing—Fuselage Configuration at a Mach Number of 1.61. NACA RM L57K18, 1958.

14. Hallissy, Joseph M., Jr.; and Kudlacik, Louis: A Transonic Wind-Tunnel Investigation of Store and Horizontal-Tail Loads and Some Effects of Fuselage-Afterbody Modifications on a Swept-Wing Fighter Airplane. NACA RM L56A26, 1956.
15. O'Bryan, Thomas C.: Flight Measurement of Aerodynamic Loads and Moments on an External Store Mounted Under the Wing of a Swept-Wing Fighter-Type Airplane. NACA RM L53G22, 1953.
16. Hamer, Harold A.; and O'Bryan, Thomas C.: Flight Measurements of the Loads and Moments on an External Store Mounted Under the Wing of a Swept-Wing Fighter-Type Airplane During Yawing and Rolling Maneuvers. NACA RM L55G22, 1955.
17. Hadaway, William M.: Aerodynamic Loads on an External Store Adjacent to an Unswept Wing at Mach Numbers Between 0.75 and 1.96. NACA RM L55L07, 1956.
18. Guy, Lawrence D.; and Hadaway, William M.: Aerodynamic Loads on an External Store Adjacent to a  $45^\circ$  Sweptback Wing at Mach Numbers From 0.70 to 1.96, Including an Evaluation of Techniques Used. NACA RM L55HL2, 1955.
19. Smith, Norman F.; and Carlson, Harry W.: The Origin and Distribution of Supersonic Store Interference From Measurement of Individual Forces on Several Wing-Fuselage-Store Configurations. III.- Swept-Wing Fighter-Bomber Configuration With Large and Small Stores. Mach Number, 1.61. NACA RM L55H01, 1955.
20. Smith, Norman F.; and Carlson, Harry W.: The Origin and Distribution of Supersonic Store Interference From Measurement of Individual Forces on Several Wing-Fuselage-Store Configurations. II.- Swept-Wing Heavy-Bomber Configuration With Large Store (Nacelle). Lateral Forces and Pitching Moments; Mach Number, 1.61. NACA RM L55E26a, 1955.
21. Smith, Norman F.: The Origin and Distribution of Supersonic Store Interference From Measurement of Individual Forces on Several Wing-Fuselage-Store Configurations. VI.- Swept-Wing Heavy-Bomber Configuration With Stores of Different Sizes and Shapes. NACA RM L55L08, 1956.
22. Carlson, Harry W.; and Geier, Douglas J.: The Origin and Distribution of Supersonic Store Interference From Measurement of Individual Forces on Several Wing-Fuselage-Store Configurations. V.- Swept-Wing Heavy-Bomber Configuration With Large Store (Nacelle). Mach Number 2.01. NACA RM L55K15, 1956.
23. Morris, Odell A.: The Origin and Distribution of Supersonic Store Interference From Measurements of Individual Forces on Several Wing-Fuselage-Store Configurations. IV.- Delta-Wing Heavy-Bomber Configuration With Large Store. Mach Number, 1.61. NACA RM L55I27a, 1955.
24. Alford, William J., Jr.; and King, Thomas J., Jr.: Experimental Investigation of Effects of Moderate Sideslip on the Flow Fields Near a  $45^\circ$  Swept-Wing-Fuselage Combination at Low Speed. NACA RM L57E10, 1957.

## BIBLIOGRAPHY

### Store Motions During Release

- Alford, William J., Jr.; and Goodson, Kenneth W.: A Technique for Firing Dynamically Scaled Missile Models in Wind Tunnels and for Measuring Rocket-Motor Sound and Pressure Fluctuations. NASA TN D-224, 1960.
- Carlson, Harry W.; Geier, Douglas J.; and Lee, John B.: Comparison and Evaluation of Two Model Techniques Used in Predicting Bomb-Release Motions. NACA RM L57J23, 1957.
- Carter, Howard S.; and Lee, John B.: Investigation of the Ejection Release of Several Dynamically Scaled Bluff Internal Stores at Mach Numbers of 0.8, 1.39, and 1.98. NACA RM L56H28, 1956.
- Faget, Maxime A.; and Carlson, Harry W.: Experimental Techniques for Predicting Store Motions During Release or Ejection. NACA RM L55L20b, 1956.
- Hinson, William F.: Investigation of a New Technique for Releasing an Externally Carried Fuel Tank at Subsonic and Supersonic Speeds Using a 1/40-Scale Model of a Supersonic Bomber Airplane. NASA TM X-462, 1961.
- Hinson, William F.: Investigation of the Subsonic and Supersonic Release Characteristics of an Externally Carried Fuel Tank From a 1/40-Scale Model of a Bomber Airplane. NASA TM X-354, 1961.
- Hinson, William F.: Transonic and Supersonic Ejection Release Characteristics of Six Dynamically Scaled External-Store Shapes From an 0.086-Scale Model of a Current Fighter Airplane. NASA TM X-128, 1959.
- Lee, John B.; and Carter, Howard S.: An Investigation of Ejection Releases of Submerged and Semisubmerged Dynamically Scaled Stores From a Simulated Bomb Bay of a Fighter-Bomber Airplane at Supersonic Speeds. NACA RM L56I10, 1956.
- Murphy, Glenn: Similitude in Engineering. The Ronald Press Co., 1950, pp. 17-41.
- Neihouse, Anshal I.; and Pepoon, Philip W.: Dynamic Similitude Between a Model and a Full-Scale Body for Model Investigation at Full-Scale Mach Number. NACA TN 2062, 1950.
- Rainey, Robert W.: A Wind-Tunnel Investigation of Bomb Release at a Mach Number of 1.62. NACA RM L53L29, 1954.
- Sandahl, Carl A.; and Faget, Maxime A.: Similitude Relations for Free-Model Wind-Tunnel Studies of Store-Dropping Problems. NACA TN 3907, 1957.

## Aerodynamic Characteristics of Stores in Carriage Position

- Alford, William J., Jr.: Experimental Static Aerodynamic Forces and Moments at Low Speed on a Canard Missile During Simulated Launching From the Midsemispan and Wing-Tip Locations of a  $45^\circ$  Sweptback Wing-Fuselage Combination. NACA RM L55A12, 1955.
- Alford, William J., Jr.: Theoretical and Experimental Investigation of the Subsonic-Flow Fields Beneath Swept and Unswept Wings With Tables of Vortex-Induced Velocities. NACA Rept. 1327, 1957. (Supersedes NACA TN 3738.)
- Alford, William J., Jr.; and King, Thomas J., Jr.: Experimental Static Aerodynamic Forces and Moments at High Subsonic Speeds on a Missile Model During Simulated Launching From the Midsemispan Location of a  $45^\circ$  Sweptback Wing-Fuselage-Pylon Combination. NACA RM L56J05, 1957.
- Alford, William J., Jr.; and Silvers, H. Norman: Investigation at High Subsonic Speeds of Finned and Unfinned Bodies Mounted at Various Locations From the Wings of Unswept- and Swept-Wing-Fuselage Models, Including Measurements of Body Loads. NACA RM L54B18, 1954.
- Alford, William J., Jr.; Silvers, H. Norman; and King, Thomas J., Jr.: Experimental Aerodynamic Forces and Moments at Low Speed of a Missile Model During Simulated Launching From the Midsemispan Location of a  $45^\circ$  Sweptback Wing-Fuselage Combination. NACA RM L54K11a, 1955.
- Alford, William J., Jr.; Silvers, H. Norman; and King, Thomas J., Jr.: Experimental Static Aerodynamic Forces and Moments at Low Speed on a Missile Model During Simulated Launching From the 25-Percent-Semispan and Wing-Tip Locations of a  $45^\circ$  Sweptback Wing-Fuselage Combination. NACA RM L55D20, 1955.
- Alford, William J., Jr.; Silvers, H. Norman; and King, Thomas J., Jr.: Preliminary Low-Speed Wind-Tunnel Investigation of Some Aspects of the Aerodynamic Problems Associated With Missiles Carried Externally in Positions Near Airplane Wings. NACA RM L54J20, 1954.
- Bobbitt, Percy J.; Carlson, Harry W.; and Pearson, Albin O.: Calculation of External-Store Loads and Correlation With Experiment. NACA RM L57D30a, 1957.
- Bobbitt, Percy J.; Malvestuto, Frank S., Jr.; and Margolis, Kenneth: Theoretical Prediction of the Side Force on Stores Attached to Configurations Traveling at Supersonic Speeds. NACA RM L55L30b, 1956.
- Geier, Douglas J.: An Investigation of Supersonic Store Interference in the Vicinity of a  $22^\circ$  Swept-Wing-Fuselage Configuration at Mach Numbers of 1.61 and 2.01. NACA RM L57L18, 1957.
- Geier, Douglas J.; and Carlson, Harry W.: Measurements of Static Forces on Externally Carried Bombs of Fineness Ratios 7.1 and 10.5 in the Flow Field of a Swept-Wing Fighter-Bomber Configuration at a Mach Number of 1.6. NACA RM L56K30, 1957.

- Guy, Lawrence D.: Loads on External Stores at Transonic and Supersonic Speeds. NACA RM L55E13b, 1955.
- Hallissy, Joseph M., Jr.; and Kudlacik, Louis: A Transonic Wind-Tunnel Investigation of Store and Horizontal-Tail Loads and Some Effects of Fuselage-Afterbody Modifications on a Swept-Wing Fighter Airplane. NACA RM L56A26, 1956.
- Johnson, Clinton T.: Flight Investigation of the Aerodynamic Forces on a Wing-Mounted External-Store Installation on the Douglas D-558-II Research Airplane. NACA RM H58B24, 1958.
- Kremzier, Emil J.; and Dryer, Murray: Aerodynamic Interference Effects on Normal and Axial Force Coefficients of Several Engine-Strut-Body Configurations at Mach Numbers of 1.8 and 2.0. NACA RM E52B21, 1952.
- Morris, Odell A.: Aerodynamic Forces and Moments on a Large Ogive-Cylinder Store at Various Locations Below the Fuselage Center Line of a Swept-Wing Bomber Configuration at a Mach Number of 1.61. NACA RM L56I25, 1957.
- Morris, Odell A.; Carlson, Harry W.; and Geier, Douglas J.: Experimental and Theoretical Determination of Forces and Moments on a Store and on a Store-Pylon Combination Mounted on a 45° Swept-Wing-Fuselage Configuration at a Mach Number of 1.61. NACA RM L57K18, 1958.
- O'Bryan, Thomas C.: Flight Measurement of Aerodynamic Loads and Moments on an External Store Mounted Under the Wing of a Swept-Wing Fighter-Type Airplane. NACA RM L53G22, 1953.
- Oehman, Waldo I.; and Turner, Kenneth L.: Aerodynamic Characteristics of a 45° Swept-Wing Fighter-Airplane Model and Aerodynamic Loads on Adjacent Stores and Missiles at Mach Numbers of 1.57, 1.87, 2.16, and 2.53. NACA RM L58C17, 1958.
- Robinson, Samuel W., Jr.; and Zlotnick, Martin: A Method for Calculating the Aerodynamic Loading on Wing-Tip-Tank Combinations in Subsonic Flow. NACA RM L53B18, 1953.
- Silvers, H. Norman; and O'Bryan, Thomas C.: Some Notes on the Aerodynamic Loads Associated With External-Store Installations. NACA RM L53E06a, 1953.
- Silvers, H. Norman; and King, Thomas J., Jr.: Investigation at High Subsonic Speeds of Bodies Mounted From the Wing of an Unswept-Wing-Fuselage Model, Including Measurements of Body Loads. NACA RM L52J08, 1952.
- Smith, Norman F.; and Carlson, Harry W.: Some Effects of Configuration Variables on Store Loads at Supersonic Speeds. NACA RM L55E05, 1955.
- Wornom, Dewey E.: Transonic Aerodynamic Characteristics of a 45° Swept-Wing-Fuselage Model With a Finned and Unfinned Body Pylon-Mounted Beneath the Fuselage or Wing, Including Measurements of Body Loads. NASA MEMO 4-20-59L, 1959.

## FORCE-MEASUREMENT METHODS

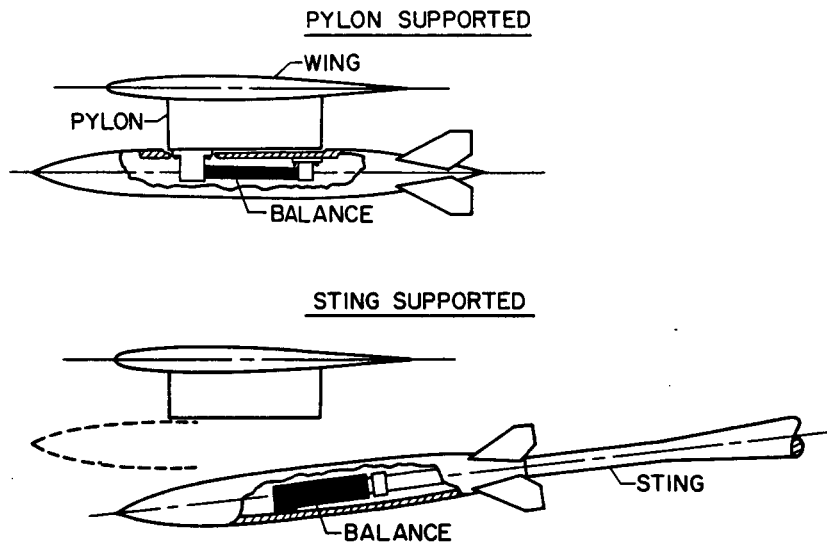


Figure 1

**CONFIGURATIONS STUDIED**  
PYLON SUPPORTED

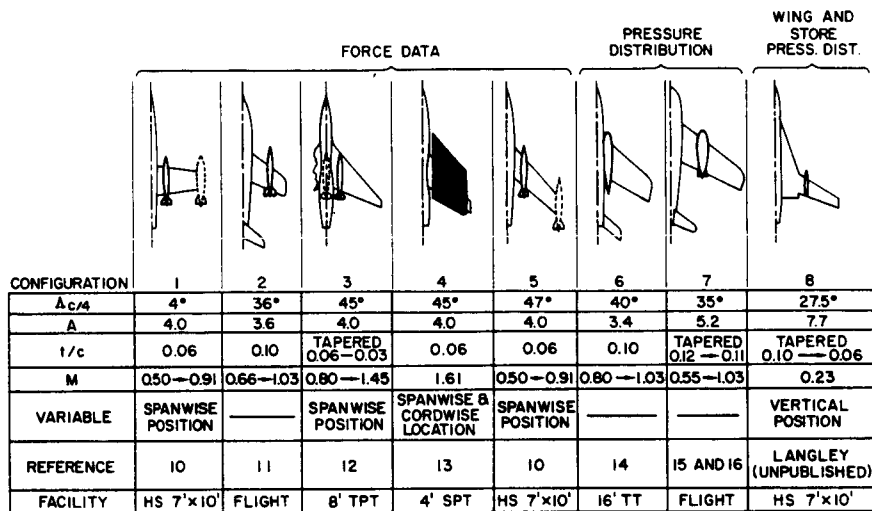


Figure 2

**CONFIGURATIONS STUDIED**  
STING SUPPORTED

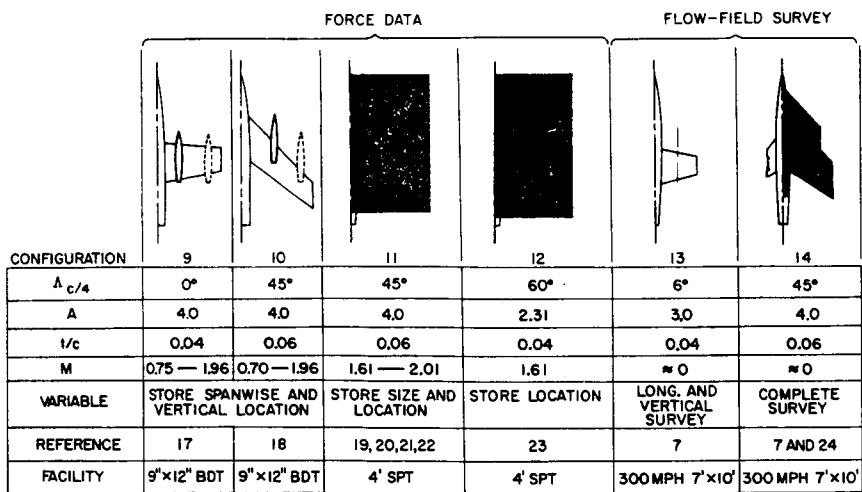


Figure 3

EXAMPLE CONFIGURATION

$A=4.0$ ;  $\lambda=0.6$ ;  $\Lambda_{c/4}=46.7^\circ$ ; 65A006; STORE FINENESS RATIO=9.34  
(CONFIG. 5)

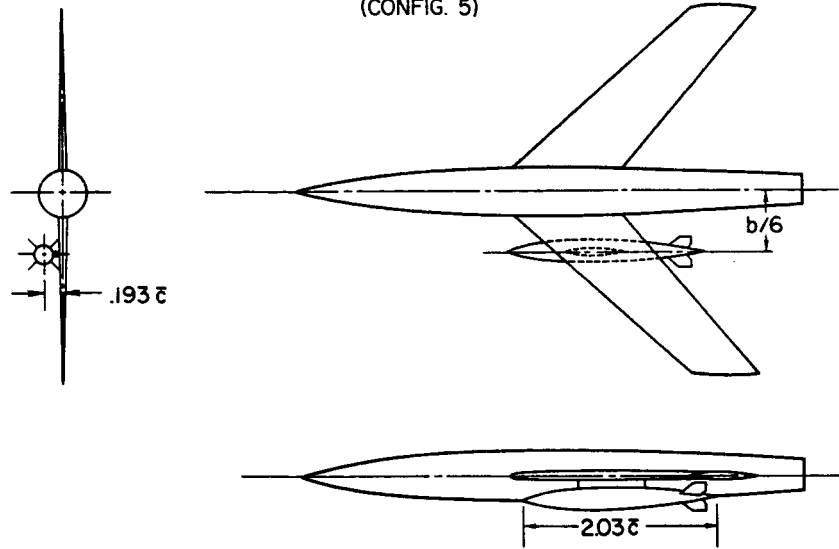


Figure 4

COMPARISON OF CALCULATED AND MEASURED NORMAL FORCE  
 $M=0.5$

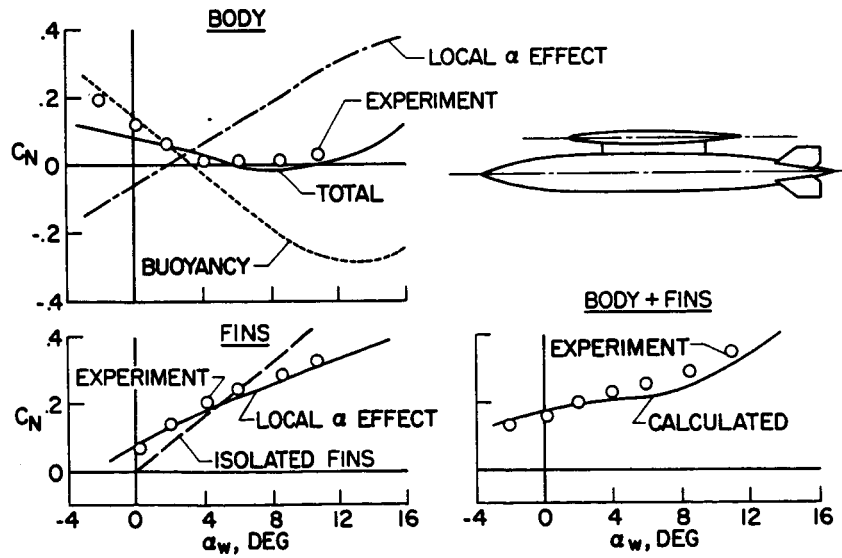


Figure 5

COMPARISON OF CALCULATED AND MEASURED  
PITCHING MOMENT

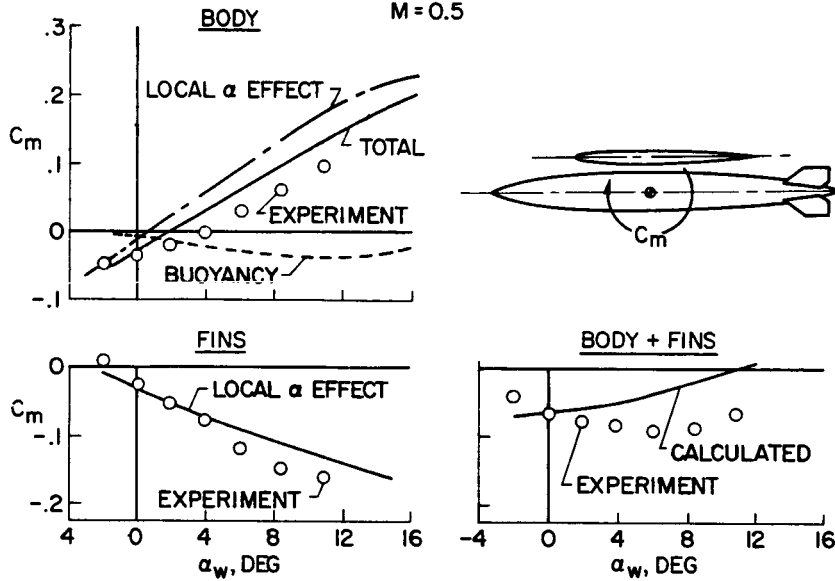


Figure 6

MEASURED CHARACTERISTICS OF STORE AT RELEASE; M=0.5

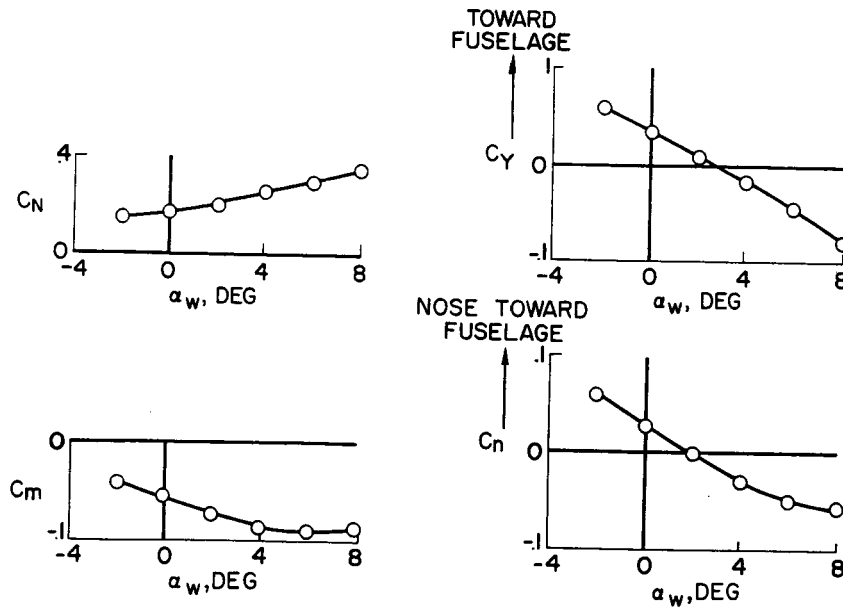


Figure 7

EXPERIMENTAL STORE PRESSURE DISTRIBUTION FOR  
CONFIGURATION 8

M=0.23

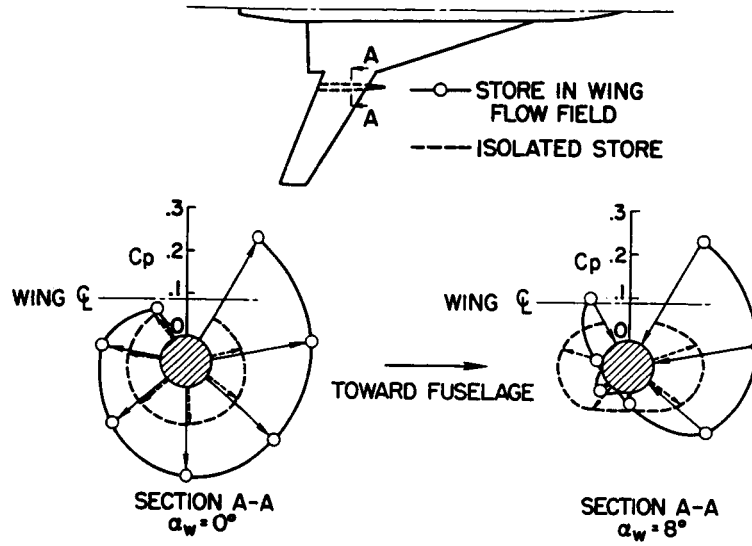


Figure 8

STORE ACCELERATIONS AT RELEASE

W/S = 100 LB/SQ FT; W = 18 650 LB

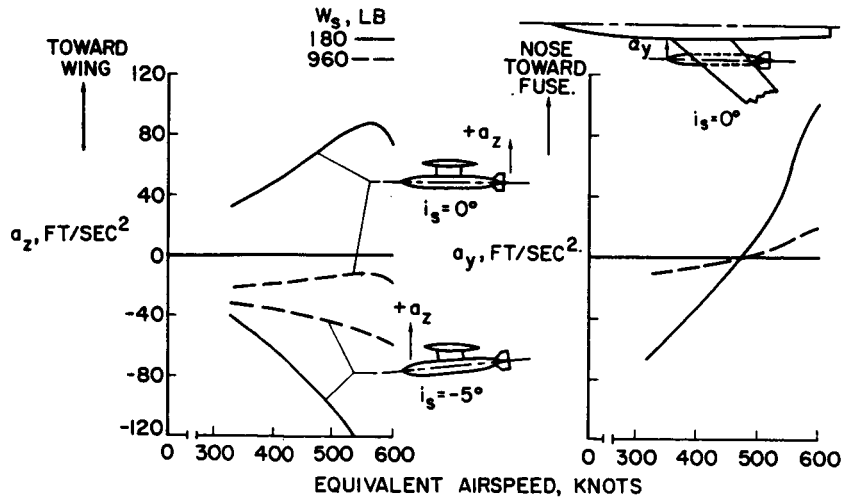


Figure 9

EFFECT OF DIVE ANGLE ON STORE TRAJECTORY  
 EAS = 530 KNOTS; W = 18 650 LB;  $W_s = 960$  LB

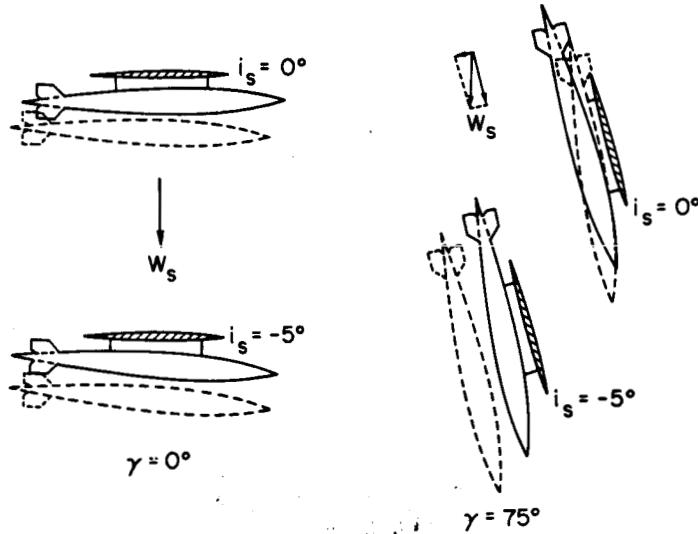


Figure 10

CONTACT BOUNDARIES  
 $W/S = 100$  LB/SQ FT;  $i_s = 0^\circ$ ; W = 18 650 LB

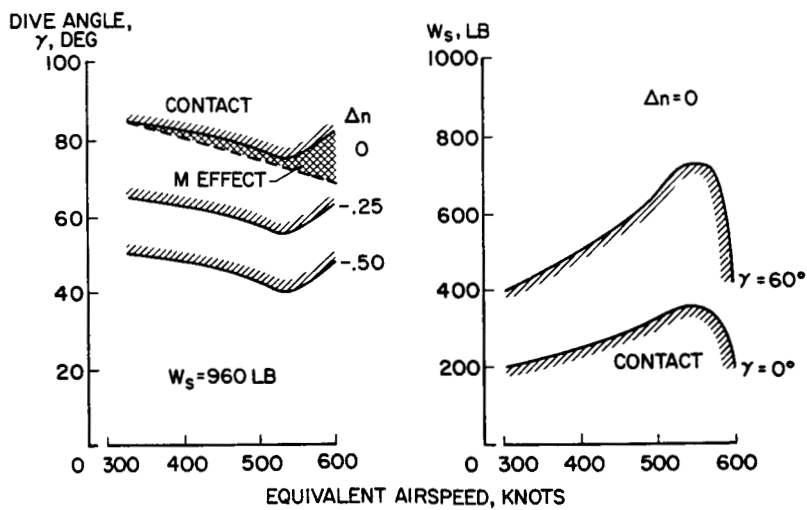


Figure 11

## 9. STUDY OF LOW-SPEED FLYING QUALITIES OF VERY LARGE AIRPLANES

### BY MEANS OF AN IN-FLIGHT SIMULATOR

By Robert O. Schade  
NASA Langley Research Center

and Richard F. Vomaske  
NASA Ames Research Center

#### SUMMARY

Very large jet transports such as the supersonic transport (SST) and the C-5 type airplanes now being considered introduce geometric and design features which can be expected to affect low-speed handling qualities adversely. As a result, the Langley and Ames Research Centers have recently conducted flight programs in which a large jet transport was used as an in-flight SST simulator to study the low-speed handling qualities of the SST and the C-5 type configurations.

Pilots found the initial pitch response to be sluggish, and they considered it a problem. Undesirable transient response characteristics were created by the low frequencies of the longitudinal short-period motion. For the configurations tested, it appears that some sort of stability augmentation will be necessary to correct the sluggish initial pitch response and the undesirable transient response caused by the low frequency of the longitudinal short-period motion. For the delta-type SST configuration, the speed-thrust instability did not present any appreciable problem for the particular pilot evaluation tasks used in these tests. However, more throttle activity and pilot workload were required to perform the same evaluation tasks. Roll-to-yaw coupling did not cause noticeable problems for the configurations and parameters tested. However, the C-5 type airplane may require some form of lateral-directional stability augmentation.

#### INTRODUCTION

Some of the future very large jet transports such as the SST's and the C-5's have mass and dimensional characteristics that are considerably different from those of present jet transports. A comparison of some of the mass characteristics of present jet transports with those of several generalized future large jet-transport configurations is shown in table I. The future large jet transports are a delta type SST, a variable-geometry type SST, and a C-5 type transport. The data presented represent parameter ratios of future jet transports to present jet transports, and the ratios of the weights are indicative of the large differences in size. It can be seen from the data that the pitch moments of inertia of future transports are at least

three to six times those of current jets and that the periods of the longitudinal short-period motion and Dutch roll motion are considerably longer.

These different characteristics tend to cause problems, particularly in low-speed flight. Some of the possible problems related to the size of these aircraft are: sluggish or low initial aerodynamic pitch response resulting from high pitch inertias; unusual dynamic or transient characteristics resulting from low frequencies of the longitudinal short-period and Dutch roll motions; and roll-to-yaw coupling resulting from unusual mass and aerodynamic characteristics.

There are other possible problems related to specific operating conditions for these types of very large jet transports. For example, operation with speed-thrust instability (or operation on the back side of the thrust-required curve) may cause a problem for the delta type SST configurations; these configurations operate in this condition because of the target approach speed recommended by the Federal Aviation Agency.

Since the geometric and design features of these very large jet transports appear to introduce characteristics which can adversely affect the low-speed flying qualities, an exploratory investigation of the possible problem areas was made to obtain some preliminary indications of criteria and requirements for this type of airplane. The best method to study these potential low-speed problems would be with an in-flight simulator; therefore, a contract was negotiated with the Boeing Company to modify a jet transport for in-flight simulation.

Presented in this report are the results of two flight-test programs in which the modified jet-transport airplane was used: tests conducted at the Langley Research Center of two simulated SST type configurations and tests conducted at the Ames Research Center of some parametric variations related to the C-5 type airplane. Because of the basic difference in the setup of the parameters of these two programs, the results will be discussed separately. However, the same general trends were noted in both sets of tests.

#### SYMBOLS

$\delta_c$	deflection of control column, in.
$\delta_w$	deflection of control wheel, deg
$\zeta$	damping ratio
$\zeta\omega_n$	Dutch roll damping parameter, 1/sec
$\ddot{\theta}$	pitching acceleration, rad/sec
$\ddot{\theta}/\delta_c$	longitudinal control sensitivity parameter, $\frac{\text{rad/sec}^2}{\text{in.}}$

$\dot{\phi}$	rolling velocity, deg/sec
$\dot{\phi}/\delta_w$	lateral control sensitivity parameter, 1/sec
$\omega_n$	undamped natural frequency, rad/sec
$\omega_n^2$	longitudinal short-period stability parameter, (rad/sec) <sup>2</sup>

## APPARATUS AND EQUIPMENT

The airplane that was used as an in-flight simulator is shown in figure 1; it is the Boeing 707 prototype (the 367-80 airplane). The nose boom shown in the figure has a vane at the forward end for sensing the angles of attack and sideslip.

Details of the method of simulation are described in reference 1, and the functions used are indicated in table II. As may be noted, the desired pitching, rolling, and yawing motions were obtained by conventional inputs to the elevator, lateral control, and rudder, respectively. The unique features of the system are the simulation of the lift and drag characteristics by modulating the spoilers and thrust reversers. Although the simulation of nonlinear ground effects by use of height information from the radar altimeter is another of the unique features of this system, ground-effect results will not be discussed in this paper.

## TEST PROCEDURES

For each of the tests, the low-speed flight characteristics were evaluated by using the simulated Instrument Flight Rules (IFR) approach illustrated in figure 2 as the basic evaluation task. The airplane intercepted the localizer at approximately 8 miles from the runway at an altitude of 1500 feet. At the intercept of the glide slope, approximately 5 miles from the runway, the pilot initiated the descent and attempted to fly the prescribed flight path as closely as possible down to approximately 200 feet and, if conditions were favorable, to continue visually to touchdown. The lateral-directional tests were made with the localizer offset 200 feet from the runway center line. After the simulated IFR breakout occurred at an altitude of 200 feet, the pilot performed a visual sidestep maneuver to line up with the runway.

## RESULTS AND DISCUSSION

### Longitudinal Aerodynamic Characteristics

Results of Langley Research Center tests.- Some of the more pertinent results of the Langley Research Center studies of the longitudinal aerodynamic

characteristics of generalized configurations of a delta type and a variable-geometry type SST in which the in-flight simulator was used are summarized in figures 3 to 7.

Because of the large values of the moment of inertia, the SST configurations exhibited sluggish initial pitch response, as illustrated in figure 3. In this figure, the changes in glide-path angle and pitching velocity with a step elevator input are compared for the two SST configurations and the present jet transport. Compared with present jet transports, the supersonic transport has a rather low and sluggish initial pitch response (or velocity). This response, along with the greater lift losses due to control for the short-coupled SST airplane, resulted in considerably longer times being required for small glide-path changes. These longer times made it difficult for the pilot to make quick and precise glide-path corrections and resulted in a higher pilot workload. The data of figure 3 show, however, that after this initial period the SST configurations had higher maximum pitching velocities than the present jet transport.

One method of relieving this sluggish-initial-response problem is the use of high initial control gearing fed through a stability-augmentation system. Shown in figure 4 are the variations of elevator deflection, pitching velocity, and change in angle of attack with time for the basic airplane and the airplane with such a stability-augmentation system. The curves for the basic airplane represent the response of a conventional airplane to a step elevator input.

The operation of the stability-augmentation system on the airplane is as follows: The high initial control gearing causes an increased pitch rate and angle-of-attack response, as shown in the figure; but, as both pitch rate and angle of attack build up, the augmentation system, which is also sensitive to these parameters, washes out the increased elevator gearing. As a result, the initial response is considerably improved without the already adequate steady-state response becoming overly sensitive.

Another problem encountered during the flight program, which the pilots called apparent low damping, is illustrated in figure 5. This figure, which is an illustrative example and not flight data, shows a comparison of the resulting pitching velocity following a step elevator input for present jet transports and for very large future jet transports. The solid curves illustrate the oscillatory motion, and the dashed curves illustrate the resulting motion with no oscillation. Both the oscillatory-motion curves have the same cycles to damp to half amplitude. Cycles to damp to half amplitude is normally used by the pilot as an indication of the damping. In this illustrative example, the SST period is double that of the present jet; therefore, the motion takes twice as long to damp. When the pilot applies control, the present jet transports generally respond as shown on the left side of the figure. However, for the SST (right side of fig. 5), the oscillatory motion continues into the part of the maneuver where it should have died out. This type of operation leads to problems in precision maneuvering. For example, when maneuvering the SST type configurations, the pilots would first apply more pitching moment or control than normally required in an effort to obtain better initial pitch response; this procedure was then followed by a control reversal

to minimize the large overshoot (apparent low damping) and still maintain the desired steady-state pitching velocity.

Shown in figure 6 is the evaluation of a stability-augmentation system that was used to correct this maneuvering problem. Plotted in the figure is the undamped natural frequency of the longitudinal short-period oscillation  $\omega_n$  as a function of the damping ratio  $\zeta$  for the basic and augmented SST type airplanes. The letters "P.R." next to the symbols indicate the average Cooper pilot ratings of two pilots for each condition. This numerical pilot rating system (ref. 2) is shown in table III. These numerical ratings suggest relative flight difficulties; for example, ratings of  $3\frac{1}{2}$  or less are satisfactory, ratings between  $3\frac{1}{2}$  and  $6\frac{1}{2}$  are unsatisfactory, and ratings above  $6\frac{1}{2}$  are unacceptable to catastrophic.

The data of figure 6 show that use of the final satisfactory stability-augmentation system in both configurations resulted in an increase in the natural frequency with essentially no change in the damping ratio. In order to determine the effect of increasing both the damping and the frequency, some flight-test data for an increased damping ratio of 0.94 with a moderate increase in frequency are also plotted in this figure. Although this change improved the basic condition, the pilots still were not entirely satisfied with the apparent damping characteristics of the airplane as shown by the poorer average pilot rating of  $3\frac{1}{2}$  as compared with a rating of 3 for the final stability-augmentation system.

A specific SST problem that was associated with the generalized delta configuration during the landing approach was operation of the aircraft on the back side of the thrust-required curve or with speed-thrust instability where increased power is required to fly slower. Illustrated in figure 7 are the effects of back side operation; two typical simulated IFR approaches are shown. The desired glide slopes with vertical offsets are indicated by the two sets of parallel lines. The vertical offsets were put into the glide slopes for these tests to establish an additional pilot task that would help evaluate the speed-thrust instability. The figure shows comparison data for a delta type SST with a value of speed-thrust instability (thrust weight ratio divided by velocity) of -0.0024 and a normal value of speed-thrust stability of 0.0005. For the airplane with speed-thrust stability, the airspeed that has decreased while the pilot restabilizes on the new glide slope starts to return to the original value; however, for the airplane with speed-thrust instability, the airspeed tends to decrease steadily until the pilot is required to use the throttle to prevent stalling. Even though the pilot, in this instance, was only attempting to evaluate the effects of back side operation with minimum use of throttles, it is apparent that his ability to change the glide slope was not appreciably affected by the speed-thrust instability for the particular evaluation tasks used in this investigation.

If the throttle had been used to compensate for changes in airspeed during these approaches, both sets of data would have shown improvements, particularly in airspeed accuracy, and the pilot's ability to fly the configuration would have been essentially the same for the speed-thrust instability and speed-thrust

stability conditions, except that more throttle activity and pilot workload would be required for the speed-thrust condition. Several pilots mentioned, however, that large values of speed-thrust instability did cause rapid speed bleed off or loss of altitude in turn maneuvers. Thus a fair amount of pilot attention was required to prevent high rates of descent from building up.

Results of Ames Research Center tests.- Some of the more pertinent results of the Ames parametric studies of the generalized C-5 type airplane are given in figures 8 and 9. The same in-flight simulator that was used in the SST studies at the Langley Research Center was employed for these tests. Data are presented for both ground-based and in-flight simulator results.

In figure 8, Cooper pilot rating is plotted as a function of the longitudinal stability parameter  $\omega_n^2$ . The term  $\omega_n^2$  is the square of the undamped natural frequency of the short-period oscillation. These data are for a limited variation of control sensitivity, that is, for values of pitching acceleration divided by column deflection  $\delta/\delta_c$  from 0.03 to 0.07. The damping ratio  $\zeta$  was 0.6 to 0.9, and the phugoid stability was positive. Reasonably fair agreement is obtained between the ground-based simulator results and the in-flight simulator results. The ground-based simulator is a moving-base simulator which used pitch and roll attitude cues during the tests. The satisfactory and unsatisfactory boundaries are related to the pilot rating scale. (See table III.) The trends of the data in figure 8 show that the pilot ratings are sensitive to variations in the longitudinal stability parameter for values less than about 1.2; however, the pilot ratings are relatively insensitive to variations for higher values of the parameter. The data also show that values of  $\omega_n^2$  less than about 0.8 appear to be unsatisfactory. The value of  $\omega_n^2$  for the generalized C-5 type airplane is approximately 0.5 and the value for present jet transports is approximately 1.4. The relatively low value of the parameter for the C-5 type airplane is caused by the high moments of inertia and low approach speeds.

Longitudinal control sensitivity is also an important parameter, as illustrated in figure 9. Pilot rating is plotted as a function of the control sensitivity parameter  $\delta/\delta_c$  (pitching acceleration divided by column deflection) for a restricted range of the longitudinal stability parameter  $\omega_n^2$  from 0.75 to 0.85 and for a minimum column deflection (required for maximum moment) of approximately 5 inches. The damping ratio and phugoid stability were the same as for figure 8. There is fair agreement between ground-based and in-flight data with the flight values having poorer pilot ratings. As would normally be expected, variations in the control sensitivity in the lower range cause large changes in pilot rating. It can be seen that values of  $\delta/\delta_c$  less than 0.02 are generally undesirable. Inasmuch as the values of this parameter for the C-5 type airplane fall in this general area, this airplane may encounter longitudinal control problems.

#### Lateral-Directional Aerodynamic Characteristics

Results of Langley Research Center tests.- The lateral-directional characteristics of the generalized SST type configurations investigated at the Langley

Research Center were satisfactory, and the effects of the different inertia ratios were not noticeable in the roll-to-yaw coupling of the Dutch roll motions at the approach speeds used.

The unaugmented Dutch roll characteristics of these airplanes are shown in figure 10. Shown in the figure are data for the marginally satisfactory, unaugmented present jet transports (pilot rating  $3\frac{1}{2}$  to  $4\frac{1}{2}$ ) and the unaugmented variable-geometry and delta type SST airplanes (pilot ratings of 3 and  $3\frac{1}{2}$ , respectively). The fact that the frequencies of the SST's are somewhat lower than those of the present jets indicates that the SST's would normally be given poorer pilot ratings. However, the increased damping ratio for the supersonic transports results in the satisfactory pilot ratings of 3 and  $3\frac{1}{2}$ . The delta type configuration was not rated higher than  $3\frac{1}{2}$  because the low damping characteristics of the rolling mode tended to cause the pilots to overshoot the desired roll angles when giving roll control.

Results of Ames Research Center tests. - Some of the Ames Research Center results related to lateral-directional parameters are given in figures 11 and 12. Figure 11 shows the variation of pilot rating with the Dutch roll damping parameter. The Dutch roll damping parameter ( $\zeta\omega_n$ ) is the damping ratio multiplied by the undamped natural frequency. There is good agreement between ground-based and in-flight simulator data. These data indicate that damping and frequency are important, particularly in the lower ranges where the pilot rating changes markedly for small changes in the damping parameter. The generalized C-5 type airplane and present jet transports both have Dutch roll damping parameters of approximately 0.1, and thus they would be in an area where Dutch roll problems could occur. As a result, augmentation may be required to improve the flight characteristics of the C-5 type airplane.

The effect of the variation of the lateral control sensitivity parameter  $\dot{\phi}/\delta_w$  (rolling velocity divided by wheel deflection) is shown in figure 12. In this figure, the pilot rating is plotted as a function of this parameter for configurations with good turn coordination and Dutch roll damping. For these data, roll-time constants from 0.5 to 0.75 were used, and the tests only considered wheel deflections required for a maximum rolling moment of between  $30^\circ$  and  $90^\circ$ . The sluggish and too-sensitive areas shown in the figure were established from ground-based simulator studies. Agreement between ground-based and in-flight simulator studies is good. The small crosshatched area in the lower right-hand side of the figure shows a single ground-based-simulator condition plotted to indicate what happens to pilot rating as lateral control becomes too sensitive. These data indicate that a value of the roll control sensitivity parameter  $\dot{\phi}/\delta_w$  between 0.6 and 0.7 would apparently be the optimum setting for aircraft of this size. The generalized C-5 type airplane is located on the lower side of this range, having a value of  $\dot{\phi}/\delta_w$  of approximately 0.4. For these tests, in which parameter variations were being studied, lateral-directional augmentation was used. The C-5 type airplane may also require some form of augmentation because of the roll-to-yaw coupling at the low approach

speeds. Results of tests related to this roll-to-yaw coupling problem are discussed in references 3 and 4.

In addition to the requirement for a minimum value of  $\dot{\phi}/\delta_w$ , the initial rolling response is important. Pilot opinion of initial roll response in terms of bank angle attained 1 second after control initiation is given in reference 5.

#### CONCLUDING REMARKS

The results of the in-flight simulation tests of very large jet transports can be summarized as follows:

1. Sluggish initial pitch response was apparent and was considered a problem by the pilots.

2. Undesirable transient response characteristics were created by the low frequencies of the longitudinal short-period motion.

3. For the configurations tested, it appears that some sort of stability-augmentation system will be necessary to correct the sluggish initial pitch response and the undesirable transient response caused by the low frequency of the longitudinal short-period motion.

4. For the delta type SST configuration, the speed-thrust instability did not present any appreciable problem for the particular pilot evaluation tasks used in these tests. However, more throttle activity and pilot workload were required to perform the same evaluation tasks.

5. In the tests of the C-5 type airplane conducted at the Ames Research Center, there was reasonable agreement between the ground-based and in-flight simulator studies.

6. Roll-to-yaw coupling did not cause any noticeable problems for the configurations and parameters tested. However, the C-5 type airplane may require some form of lateral-directional stability augmentation.

REFERENCES

1. Eldridge, William M.; and Crane, Harold L.: Use of a Large Jet Transport as an Inflight Dynamic Simulator. Presented to Flight Mechanics Panel of AGARD (Paris, France), May 10-11, 1966.
2. Cooper, George E.: Understanding and Interpreting Pilot Opinion. Aeron. Eng. Rev., vol. 16, no. 3, Mar. 1957, pp. 47-51, 56.
3. Quigley, Hervey C.; Vomasse, Richard F.; and Innis, Robert C.: Lateral-Directional Augmentation Criteria for Jet Swept-Wing Transport Airplanes Operating at STOL Airspeeds. Conference on V/STOL and STOL Aircraft, NASA SP-116, 1966, pp. 295-310.
4. McNeill, Walter E.; and Innis, Robert C.: The Effect of Yaw Coupling in Turning Maneuvers of Large Transport Aircraft. Conference on Aircraft Operating Problems, NASA SP-83, 1965, pp. 203-213.
5. Anderson, Seth B.: Considerations for Revision of V/STOL Handling Qualities Criteria. Conference on V/STOL and STOL Aircraft, NASA SP-116, 1966, pp. 229-247.

TABLE I

LARGE JET-TRANSPORT CHARACTERISTICS

FUTURE JET TRANSPORTS	DELTA TYPE SST 	VARIABLE- GEOM. TYPE SST 	C-5 TYPE TRANSPORT 
PARAMETER	FUTURE JET TRANSPORT PRESENT JET TRANSPORT		
LANDING WEIGHT	1.8	1.8	2.5
MOMENT OF INERTIA: PITCH ROLL YAW	3.6 .6 2.4	3.5 .8 2.4	6.0 4.9 5.3
DAMPED PERIOD: LONG.SHORT PERIOD DUTCH ROLL MOTION	2.3 1.2	1.3 1.5	1.3 1.4

TABLE II

## SST SIMULATION FUNCTIONS

FUNCTION	SYSTEM USED
PITCH AXIS	LONGITUDINAL CONTROL
ROLL AXIS	LATERAL CONTROL
YAW AXIS	DIRECTIONAL CONTROL
LIFT	MODULATED SPOILERS
DRAG	MODULATED THRUST REVERSERS
GROUND EFFECTS	RADAR ALTIMETER

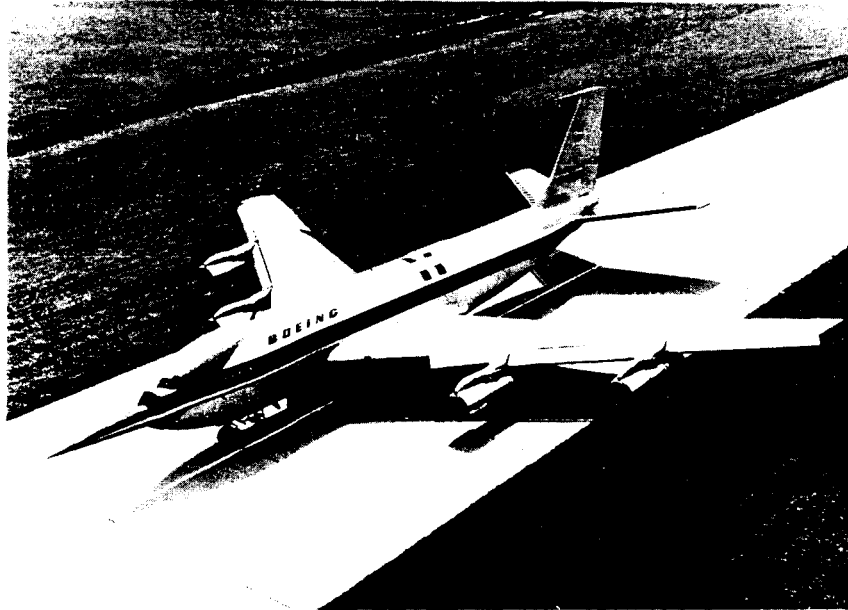
TABLE III

## COOPER PILOT RATING SYSTEM

OPER. COND.	ADJECTIVE RATING	NUMER. RATING	DESCRIPTION	PRIMARY MISSION ACCOMP.	CAN BE LANDED?
NORMAL OPER.	SATISFACTORY	1	EXCEL., INCLUDES OPT.	YES	YES
		2	GOOD, PLEASANT TO FLY	YES	YES
		3	SAT. BUT WITH SOME MILDLY UNPLEASANT CHARACTERISTICS	YES	YES
EMERG OPER.	UNSATISFACTORY	4	ACCEPTABLE, BUT WITH UNPLEASANT CHARACTERISTICS	YES	YES
		5	UNACCEPTABLE FOR NORMAL OPERATION	DOUBTFUL	YES
		6	ACCEPTABLE FOR EMERG. CONDITION ONLY*	DOUBTFUL	YES
NO OPER.	UNACCEPTABLE	7	UNACCEPTABLE EVEN FOR EMERG. COND.	NO	DOUBTFUL
	CATASTROPHIC	8	UNACCEPTABLE-DANGEROUS	NO	NO
		9	UNACCEPTABLE-UNCONTROLLABLE	NO	NO
		10	MOTIONS POSSIBLY VIOLENT ENOUGH TO PREVENT ESCAPE	NO	NO

\* FAILURE OF A STABILITY AUGMENTER.

# IN-FLIGHT SIMULATOR



L-2679-3

Figure 1

## BASIC EVALUATION TASK

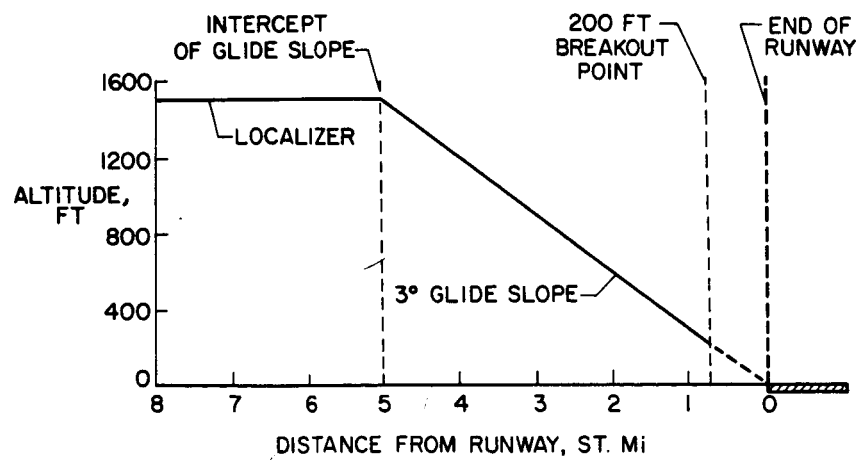


Figure 2

### COMPARISON OF RESPONSE CHARACTERISTICS

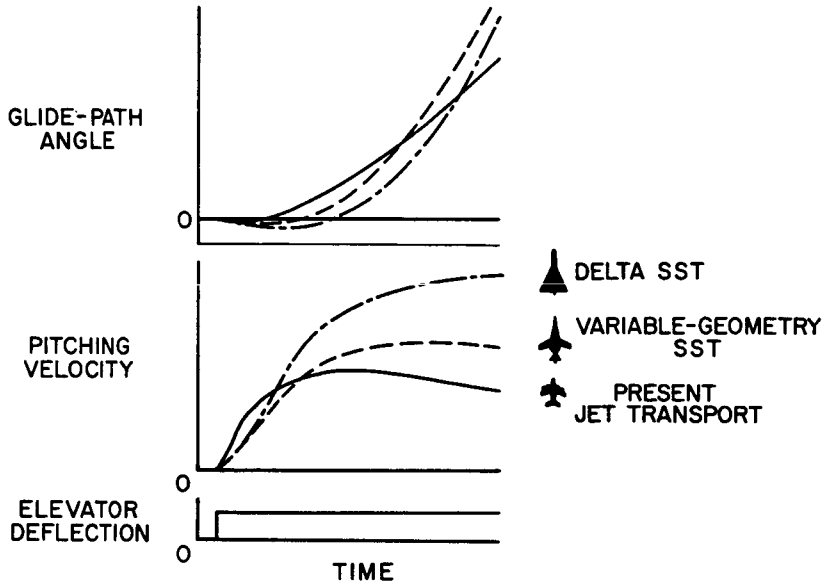


Figure 3

### AUGMENTED INITIAL RESPONSE SST TYPE

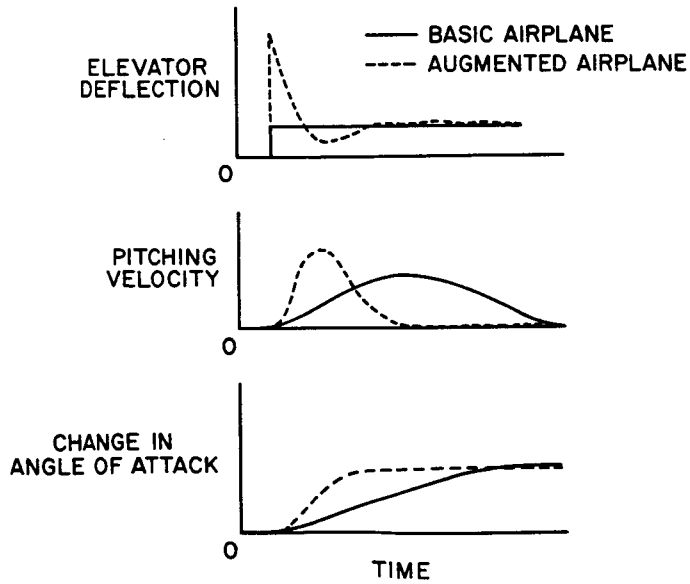


Figure 4

COMPARISON OF TRANSIENT - RESPONSE CHARACTERISTICS

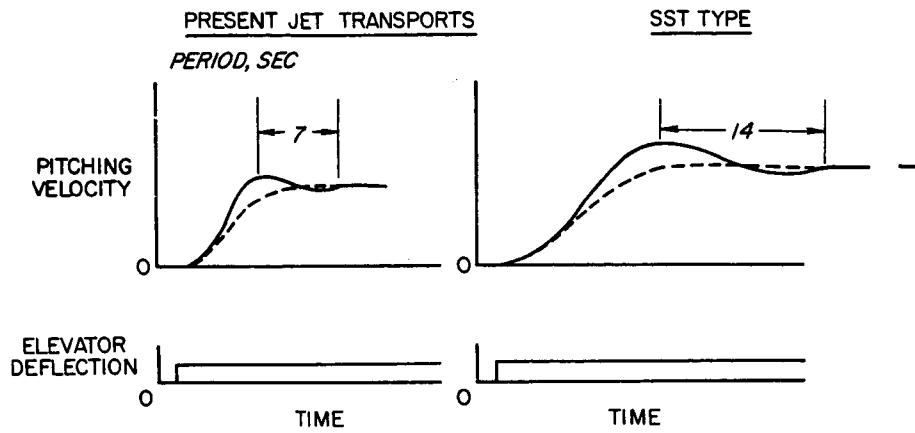


Figure 5

EFFECT OF AUGMENTATION ON LONGITUDINAL SHORT PERIOD SST TYPE

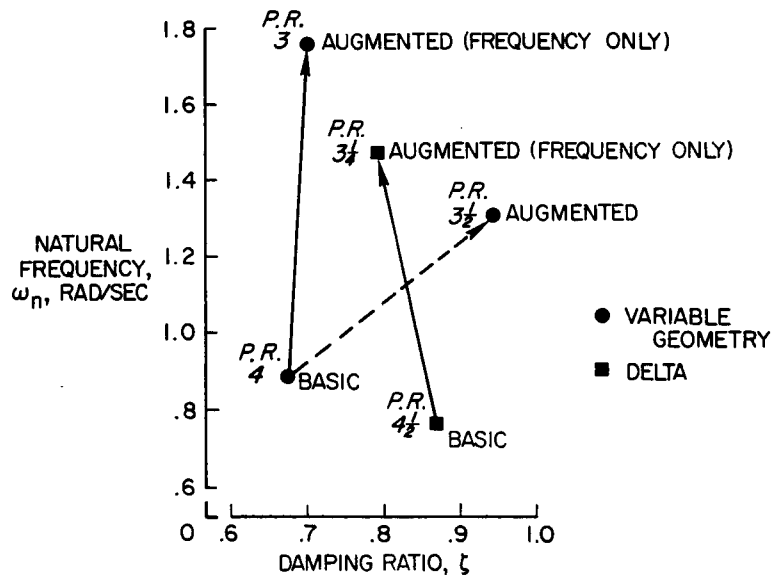


Figure 6

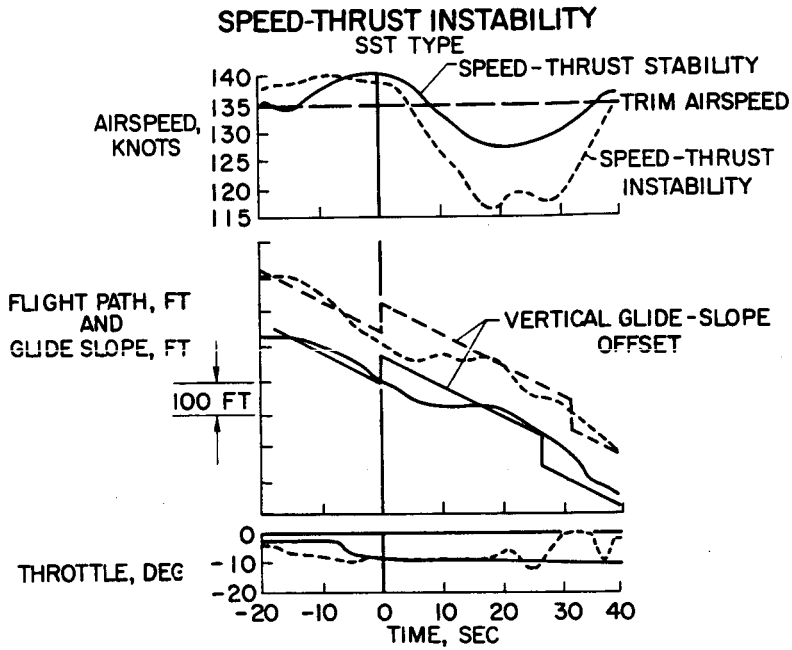


Figure 7

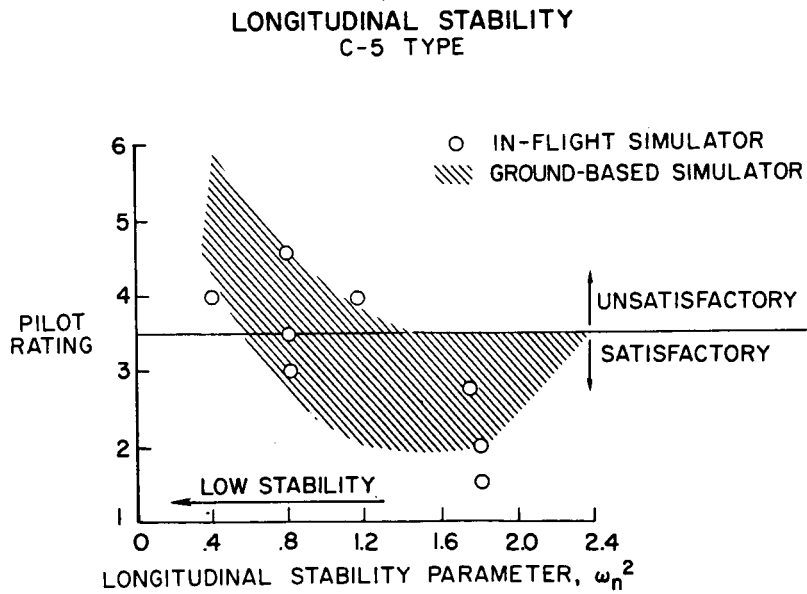


Figure 8

LONGITUDINAL CONTROL GEARING  
C-5 TYPE

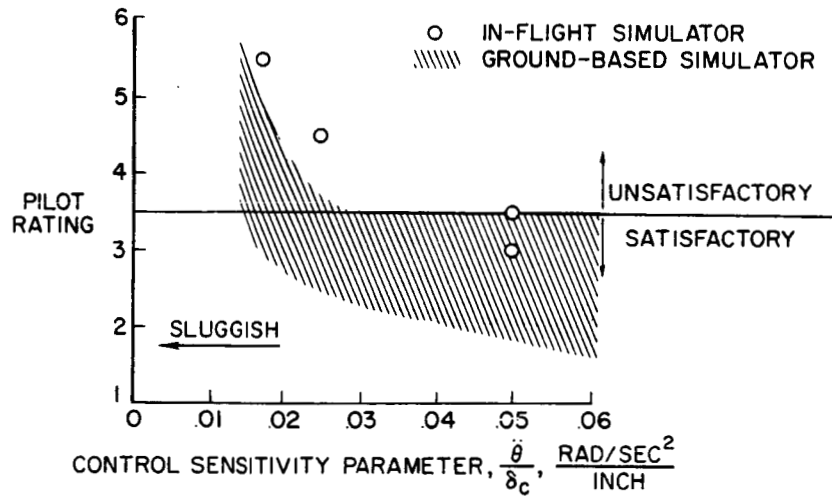


Figure 9

UNAUUGMENTED DUTCH ROLL CHARACTERISTICS  
SST TYPE

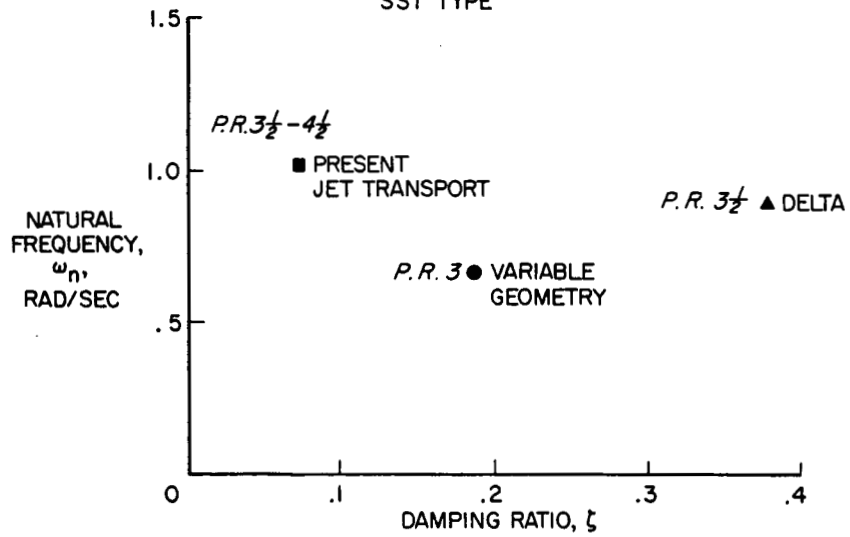


Figure 10

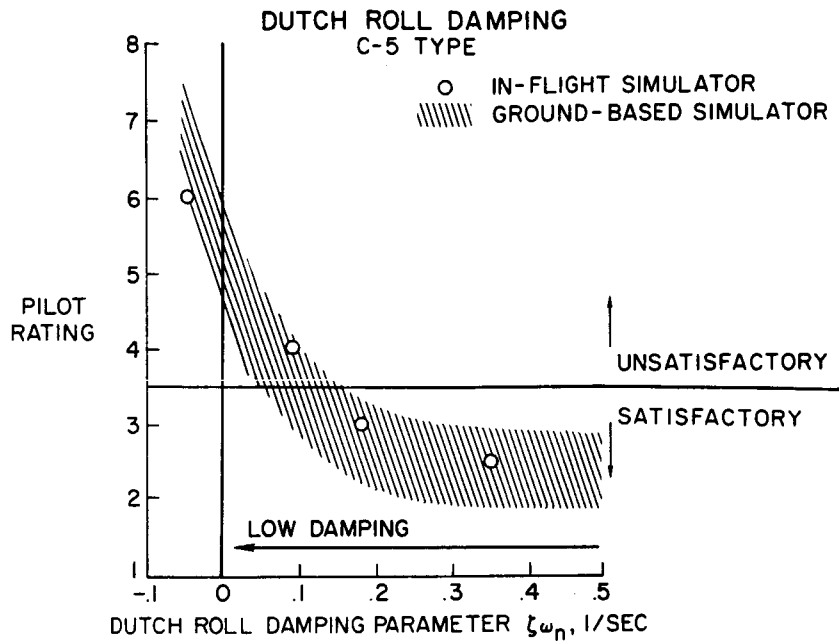


Figure 11

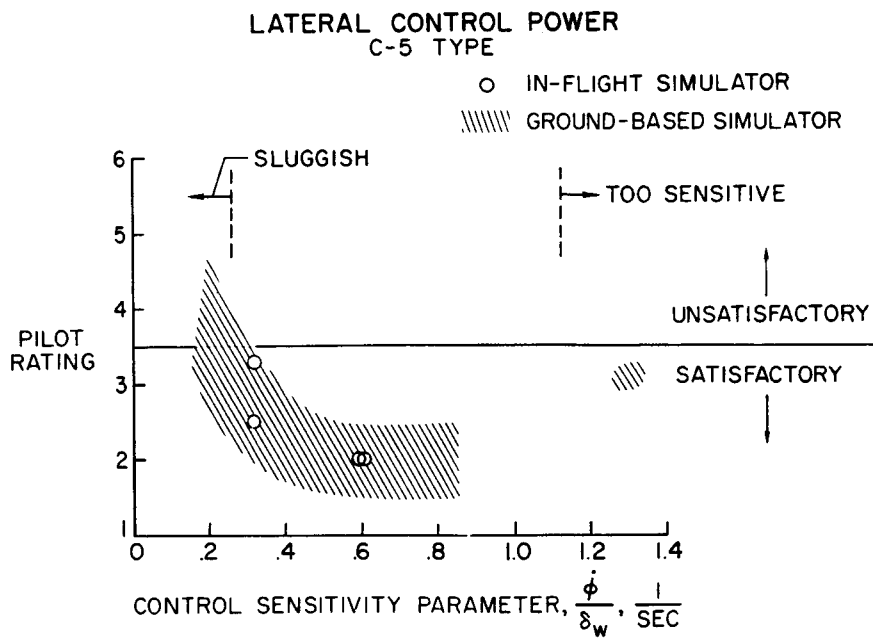


Figure 12

10. ASSESSMENT OF THE EFFECTS OF INLET SPILLAGE, BYPASS, AND  
BLEED AIR ON THE PERFORMANCE OF SUPERSONIC CRUISE AIRPLANES

By Lowell E. Hasel, Robert L. Weirich,  
and Vincent R. Mascitti  
NASA Langley Research Center

SUMMARY

The drags created by the overboard discharge of the excess inlet airflow during acceleration and of the inlet bleed air during cruise are critical factors in determining the performance of long-range supersonic cruise airplanes. Bypassing some of the excess air to the ejector during acceleration can reduce very significantly the excess air drag. Bleed drag reductions during cruise are attainable by tailoring of bleed and vortex-generator systems to increase the pressure recovery for a given bleed flow, by ducting flow to the ejector, and by surface injection to reduce the skin friction.

The cruise inlet pressure recovery which results in maximum airplane performance is strongly influenced by bleed drag. Unless the bleed drag can be made quite small, the potential performance benefits associated with operating the inlet at its maximum pressure recovery are not achievable.

INTRODUCTION

For long-range supersonic cruise airplanes such as the supersonic transport (SST) the payload is very sensitive to drag. Quite literally this situation has made it necessary to fight for every drag count and to examine closely potential methods of reducing each drag item. Such an examination must include the drags created by the discharge of the excess inlet and boundary-layer bleed air. In this paper these sources of drag are considered and known methods of reducing the associated performance penalties, either by optimization or drag reduction techniques, are reexamined. Few, if any, new concepts are suggested to those who are closely associated with the design of propulsion systems.

SYMBOLS

A	area, ft <sup>2</sup>
A <sub>c</sub>	inlet capture area, ft <sup>2</sup>
C <sub>v</sub>	nozzle velocity coefficient
D	drag, lb



F engine net thrust, lb  
 m airflow, lb/sec  
 M Mach number  
 $p_t$  total pressure, lb/ft<sup>2</sup>  
 q dynamic pressure, lb/ft<sup>2</sup>

Subscripts:

dis discharged air  
 2 engine face  
 $\infty$  free stream

INLET-ENGINE AIRFLOW MATCHING

As a starting point for this discussion the typical inlet-engine airflow matching characteristics for the supersonic transport are reviewed in figure 1. The ordinate is the conventional mass-flow ratio term in which the various airflow quantities, denoted by  $m$ , are referenced at each Mach number to  $m_{A_c}$ , the airflow in a stream tube with an area equal to the inlet area  $A_c$ . At the design Mach number of 2.7, the inlet is sized to satisfy the airflow requirements of the engine, cabin air-conditioning system (narrow unshaded strip), nozzle cooling, inlet boundary-layer bleed, and the bypass control system. At Mach numbers below the design value, the airflow requirements decrease significantly as shown by the lower heavy line. The amount of air delivered by the inlet also decreases, as indicated by the upper heavy line, because of the shock spillage ahead of the inlet lip. The inlet, however, supplies more air than the system requires and the excess air, which is called bypass in the figure, must be discharged overboard as illustrated in the left schematic sketch at the top of the figure.

Typical values of the drag coefficient which are created by discharging overboard the spillage, bypass, and inlet bleed air are shown in figure 2. The drag coefficient is based on the inlet area  $A_c$ . At cruise conditions,  $M_\infty = 2.7$ , most of the drag originates from the boundary-layer bleed air. At lower speeds, the drag coefficient is considerably larger and is primarily due to the spillage and bypass air. The drag level is equivalent to about 3 percent of the total airplane drag at cruise and to 8 or 9 percent at transonic speeds. If the bleed and bypass drag could be completely eliminated during the cruise portion of the flight, the total mission fuel consumption for a 500 000-pound SST airplane with typical aerodynamics would be reduced about 4500 pounds. This is a significant fuel saving when compared with the 40 000-pound payload. (A similar study is contained in ref. 1.) Elimination

of all the spillage, bypass, and bleed drag during the acceleration portion of the flight would reduce the fuel consumption by an additional amount of about 2000 pounds, or somewhat less than one-half of the 4500-pound cruise fuel increment. The acceleration fuel increment due to a given level of drag, such as that given in figure 2, can vary by large amounts, depending on the airplane and engine characteristics and the flight-path restrictions. The primary controlling factor is the thrust-minus-drag margin of the airplane. As the thrust-minus-drag margin decreases the fuel increment will increase. Generally, the acceleration fuel increment is small for the SST, but it can be large if the thrust-minus-drag margin becomes too small.

#### DRAG REDUCTION DURING ACCELERATION

Several approaches may be used to reduce the discharged-air drag during acceleration. (See refs. 2, 3, and 4.) At transonic speeds a trade-off is normally made between the amount of air spilled and bypassed so that the resultant drag is minimized. A primary problem here is the accurate assessment of the spillage drag because of the difficulty of determining the drag reduction due to suction forces on the lip and forward portion of the cowl. This subject is discussed in paper no. 12 by Anderson, Petersen, and Sorensen.

The excess-air drag may be significantly reduced by ducting a portion of the bypass air around the engine into the variable-area ejector nozzle. The reason that such an improvement can be achieved is shown in figure 3. The ordinate is an incremental force divided by the free-stream dynamic pressure and the free-stream tube area of the bypass air. When the air is discharged through a typical bypass nozzle, the drag coefficient indicated by the shaded area labeled "bypass nozzle" is produced. Analysis of data presented in reference 5 indicates that when the bypass air is discharged as secondary air through the engine ejector nozzle the nozzle performance may actually be improved and an increase in net thrust produced. The magnitude of the net thrust increase is indicated by the shaded area labeled "engine ejector nozzle." The net thrust-coefficient increment is largest at transonic speeds where the thrust-minus-drag margin is normally smallest. To illustrate the potential benefits of bypassing air to the nozzle, the discharged-air drag presented in figure 2 was recomputed for the case in which a portion of the bypass air (fig. 1) equal to 5 percent of the engine air was exhausted through the ejector nozzle. The lower drag level reduced the acceleration fuel consumption increment by about 40 percent.

Several comments should be made with regard to the use of the bypass air in the ejector nozzle. First, the amount of air which can be efficiently used in this manner will be determined by the nozzle pumping characteristics. At present only a limited amount of data is available for determining these characteristics for high-efficiency nozzles. Second, ducting the bypass air around the engine to the nozzle will probably require an increase in frontal area of the nacelle and an increase in nacelle weight. However, because of the favorable wing-nacelle interference effects which are known to be achievable during cruise, the increase of nacelle frontal area will not necessarily result in an adverse effect on overall performance.

## OPTIMIZATION OF INLET PERFORMANCE DURING CRUISE

It may be recalled from the previous discussion that during the cruise portion of the flight the total mission fuel increment attributable to bleed and bypass drag was about 4500 pounds. About three-fourths of this fuel increment, or 3400 pounds, is due to the bleed drag.

One approach to the bleed drag problem is to make a trade-off between inlet pressure recovery and bleed drag so that airplane performance is maximized. A thorough optimization of this type involves a complex procedure but the basic concept can be illustrated by the very simplified method outlined as follows (see also ref. 6):

Objective: Minimize fuel flow

$$\text{Fuel flow} = \text{Thrust} \times \text{Specific fuel consumption}$$

$$\text{Thrust} = D_{\text{basic airplane}} + D_{\text{bypass}} + D_{\text{bleed}}$$

$$\text{Specific fuel consumption} = f\left(\text{Thrust}, \frac{P_{t,2}}{P_{t,\infty}}\right)$$

Since the airplane is at cruising conditions the performance may be judged on the basis of fuel flow. Hence, the objective is to minimize the fuel flow. In other words, the product of thrust and specific fuel consumption must be minimized. Since thrust must equal drag the thrust is equal to the sum of the drag of the basic airplane (which does not change with pressure recovery) and the drag of the bleed and bypass flows. Specific fuel consumption is a function of the thrust and the inlet pressure recovery.

This procedure can be further understood by the use of the typical set of inlet-pressure-recovery data (fig. 4) which were obtained by the Ames Research Center at a Mach number of 3. Inlet pressure recovery is plotted as a function of inlet mass-flow ratio. The inlet is an axisymmetric design. The boundary-layer-bleed configuration consists of annular rows of holes located on the centerbody and cowl in the supersonic diffuser and at the inlet throat. The bleed air from the centerbody passes through struts to reach the external surface of the nacelle. Bleed mass-flow and pressure recovery were measured for each of these four sets of bleed holes concurrent with the inlet recovery and mass-flow measurements. The data presented in figure 4 indicate that as the pressure recovery decreases the bleed flow decreases. Hence the bleed drag and the required engine thrust decrease. On the other hand, the engine specific fuel consumption increases as pressure recovery decreases. Since the specific fuel consumption and thrust vary in opposite directions as the pressure recovery changes a minimization of the fuel flow may be possible.

It should be mentioned that in an optimization of this type the inlet size decreases as the pressure recovery decreases because the inlet is sized at each value of pressure recovery to match the decreasing airflow requirements of the engine, bleed system, and bypass control system (2 percent of inlet flow). For

example, in the optimization study which follows only the portion of the curve in figure 4 extending from pressure-recovery values of 0.923 to 0.887 is considered. The corresponding reduction in inlet capture area is 6.4 percent.

The drag created by discharging the bleed air depends on the exit nozzle configuration. (See appendix.) The drag values presented as a function of inlet pressure recovery in figure 5 were calculated by assuming that the air was discharged through four sonic nozzles with nozzle velocity coefficients of 0.985. The total pressure of the bleed air removed from the supersonic diffuser varied from 0.12 to 0.20 of the free-stream total pressure. The corresponding values for the air removed from the inlet throat region varied from about 0.24 to 0.43. The amount of bleed air was established by sizing the inlet to supply the air required by typical SST turbojet and turbofan engines operating at 65 000 feet. At the highest inlet pressure recovery the bleed drag is about 1130 pounds for the turbofan engine and 800 pounds for the turbojet. These values decrease about 20 percent when the design inlet pressure recovery decreases from 0.923 to 0.887.

The bypass-control-air drag was computed in a similar manner by assuming a pressure-recovery value of 0.95 of the inlet recovery. These drag values (not presented in fig. 5) are about 14 percent of the bleed-drag values at the highest pressure recovery and decrease slightly as the pressure recovery is reduced because of the decreasing inlet size.

The fuel flow variations for both engines are shown in figure 6. Fuel flow, expressed in pounds/hour/engine, is plotted as a function of inlet pressure recovery. The basic airplane drag, which does not vary with inlet pressure recovery, has been assumed to be equal to the minimum augmented or 10-percent augmented thrust output of each engine at an inlet pressure recovery of 0.923. The fuel flow of the turbofan engine is essentially constant over the range of inlet pressure recoveries considered. There is some increase in the turbojet fuel flow as pressure recovery decreases. This increase is larger for the 10-percent augmented case and amounts to about 220 pounds/hour/engine. The results of a complete optimization would account for other effects, such as inlet weight and skin-friction drag, spillage and bypass-air drag during acceleration, and nacelle-airframe wave-drag interference. Inclusion of these effects could very well alter the fuel-flow curves to favor, more than is shown in figure 6, the inlet designed for operation at the lower pressure recoveries. The point to be made from these curves is that a significant performance penalty does not necessarily result when the propulsion system is designed to operate at less than the maximum recovery attainable with a given inlet. Furthermore, other factors, such as internal-flow stability and hot-day operation, may be improved by the selection of the lower recoveries as the design point.

It is of interest to carry the study one step further and note the effect on fuel flow of increasing the inlet maximum pressure recovery (fig. 7) by reducing the back pressure on the throat boundary-layer bleed holes. The discussion thus far has been based on a configuration which attained a maximum pressure recovery of 0.923. Decreasing the back pressure increased the maximum pressure recovery to 0.934 and increased the amount of bleed at a given recovery.

The corresponding fuel-flow curves for the turbojet engine are shown in figure 8. At a given value of pressure recovery the fuel flow is less for the inlet which has the lower maximum recovery. This difference would be expected because of the lower bleed flows of this inlet. The most interesting point to note in figure 8 is that the minimum fuel flow of the higher recovery inlet exceeds that of the lower recovery inlet over most of the pressure recovery range considered. Admittedly the differences are small but the point can nevertheless be made that the best inlet for a cruise vehicle cannot be selected solely on the basis of maximum attainable pressure recovery. As will be emphasized later, one should not conclude from this analysis that the attainment of high pressure recovery is not an important inlet research goal. The research challenge is to obtain the high recoveries with low rates of bleed flow. This may be accomplished by such methods as detailed tailoring of the bleed system and of the vortex-generator patterns in the subsonic diffuser. This area of research is discussed in paper no. 11 by Sorensen, Anderson, Wong, and Smeltzer.

As is discussed more completely in the appendix, the slope and level of the fuel-flow curves (fig. 8) are dependent on the relationship between bleed drag and inlet pressure recovery. For example, if the bleed drag could be completely eliminated the fuel-flow level would be lower and the variation with pressure recovery would be greater than for the cases previously discussed. At the high recoveries the level is decreased by about 7 percent. A comparison of these curves emphasizes the importance of minimizing the bleed drag. Reduction of the bleed drag allows more of the potential benefits due to the higher inlet pressure recoveries to be realized.

#### DRAG REDUCTION DURING CRUISE

One potential method of reducing the bleed drag which is independent of inlet improvements is to duct the air around the engine and discharge it into the ejector nozzle. The associated drag penalty is shown in figure 9. In this figure the drag of the bleed air referenced to the free-stream dynamic pressure and the free-stream tube area of the bleed air is plotted as a function of bleed-air pressure recovery. The drag coefficient produced by discharging the air through a sonic nozzle is shown by the solid line. The shaded area indicates the drag which might result from discharging the air through the engine ejector nozzle. This area is bounded by the performance of two typical, high efficiency, SST nonafterburning nozzle configurations. (See ref. 5.) It appears possible that with a proper nozzle design the bleed air might be discharged with no significant drag penalty.

In paper no. 30, Peterson and Monta discuss injection of the bleed air into the nacelle boundary layer in such a manner that the nacelle skin friction is reduced. Based on the limited amount of data now available (ref. 7) the drag coefficient which results from using the air in this manner at a Mach number of 3 is about 0.2 to 0.3. The research conducted to date, however, has not been adequate to predict the maximum drag reductions attainable by this technique.

## CONCLUDING REMARKS

Critical drag items are the drag created by the overboard discharge of the excess airflow during acceleration and the discharge of the inlet bleed flow during cruise. If the bleed flow is discharged overboard in a conventional manner the associated total mission fuel consumption increment is about 3400 pounds for a typical SST configuration.

Bypassing air to the ejector during acceleration is an efficient method for disposal of the excess airflow. This method of drag reduction is of particular interest when the acceleration thrust-minus-drag margin is small.

The cruise inlet pressure recovery which results in maximum airplane performance is strongly influenced by bleed drag. Unless the bleed drag can be made quite small, the potential performance benefits associated with operating the inlet at its maximum pressure recovery are not achievable.

Bleed drag reductions during cruise are attainable by tailoring of bleed and vortex-generator systems to increase the pressure recovery for a given bleed flow, by ducting flow to the ejector, and by surface injection to reduce skin friction. All these approaches have merit, and use of them should result in improvements in overall airplane performance.

## APPENDIX

### INSTALLED DRAG OF DISCHARGED-AIR NOZZLES

The drag created by discharging air from various types of nozzles has been studied both theoretically and experimentally (refs. 8 to 13). References 8 and 9 consider the problem in detail and correlate the measured drags with drags predicted from pressure distributions calculated by the method of characteristics. By using the data presented in reference 8 and extending the method when necessary the drag characteristics of a series of representative nozzles have been calculated at  $M_{\infty} = 2.94$  and are presented in figure 10. The drag is referenced to the free-stream tube area of the air being discharged and is plotted as a function of the total pressure recovery of the discharged air. The local external flow was assumed to be at free-stream conditions. These drag characteristics include all the thrust and pressure forces acting on the nozzle surfaces and the pressure forces on the external surface of the door. The nozzle velocity coefficient was assumed to be 1 for all configurations. The flush and axial configurations have no door drag. The axial sonic and axial complete-expansion nozzles are included for reference purposes since, in the past, these configurations have been a convenient basis for determining discharged-air drag.

Two practical sonic nozzle configurations are considered in figure 10. For both the flush and external door designs the flow is discharged at a  $5^{\circ}$  angle and the sonic throat was assumed to be located at the lip which terminates the upper surface or door. Both of these nozzles result in drag levels which are higher than that of the axial sonic nozzle.

The partly submerged, complete-expansion nozzle discharging at a  $5^{\circ}$  angle is an optimum design for  $5^{\circ}$  fully expanded nozzles. At values of total pressure recovery less than 0.25 its drag is greater than that of the axial sonic nozzle. At high values of total pressure recovery use of this type of nozzle results in a drag level which is quite low.

The optimization study presented in figure 6 was based on the bleed and bypass drag generated by axial sonic nozzles with a nozzle velocity coefficient of 0.985. Most of the discharged-air drag is created by the bleed air which had pressure-recovery values from 0.12 to 0.43. Hence, the assumption of sonic nozzle drag is reasonable, although the resultant drags may tend to be somewhat too large.

Figures 11 and 12 have been prepared to indicate the effects which the assumptions regarding the bleed and bypass drags may have on the optimization results presented in figure 6. Figure 11 is a comparison of the bleed drag for the sonic and complete-expansion nozzles. (It should be noted that the complete-expansion nozzle underestimates the discharged-air drag and may therefore be thought of as a limit-type curve.) The assumption of a complete expansion nozzle decreases the bleed drag at the highest recovery by about 36 percent and also reduces the slope of the drag curve. The corresponding fuel-flow

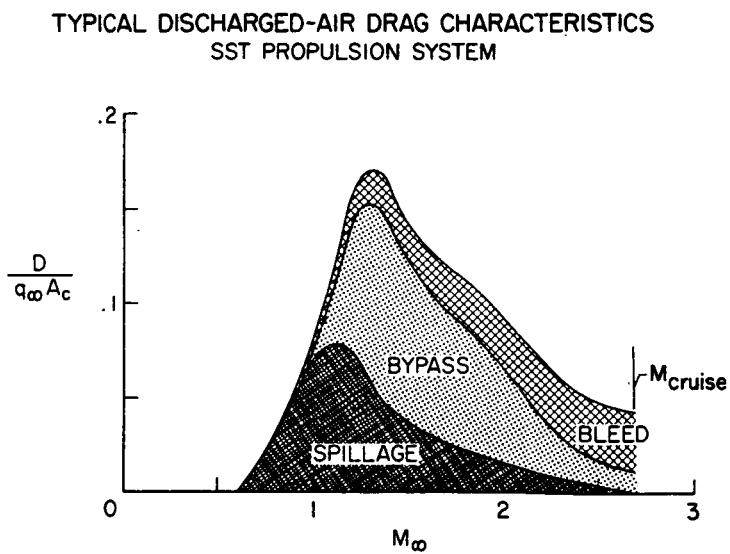
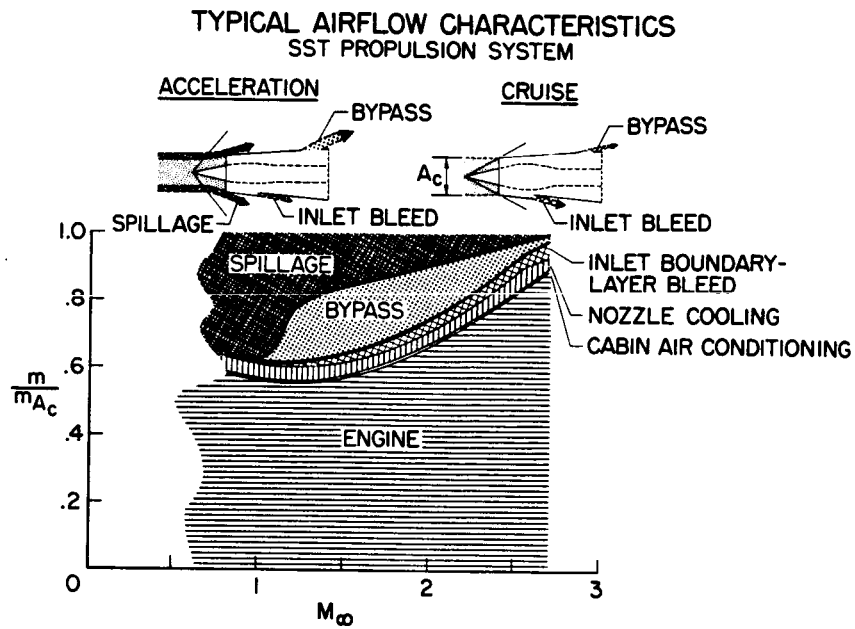
curves for the turbojet engine are compared in figure 12. The complete-expansion-nozzle assumption decreases the fuel flow at a given value of inlet pressure recovery, as would be expected, and the fuel flow increases at a more rapid rate as the design inlet pressure recovery is reduced.

Figure 12 indicates quite clearly that the slope and level of the fuel-flow curves are dependent on the relationship between bleed-air drag and inlet pressure recovery. As the bleed drag for a given inlet is reduced the slopes of the fuel-flow curves change in such a manner that the optimum recovery tends to approach the maximum value. It must be remembered, however, that when a complete optimization is made this trend may not be as definite as shown in figure 12.

## REFERENCES

1. Anderson, Warren E.; and Nelms, Walter P., Jr.: Performance and Control of Air-Induction Systems for a Commercial Supersonic Transport - Part I. Geometry and Steady-State Performance. Proceedings of the AIAA/ASD Meeting on Future Aerospace Vehicles - The Challenge to Interdisciplinary Concepts, ASD TDR 64-76, Apr. 1964, pp. 250-265.
2. Hearth, Donald P.; and Connors, James F.: A Performance Analysis of Methods for Handling Excess Inlet Flow at Supersonic Speeds. NACA TN 4270, 1958.
3. Hearth, Donald P.: Use of Main-Inlet Bypass To Supply Ejector Exhaust Nozzle at Supersonic Speeds. NACA RM E56K08, 1957.
4. Davis, Wallace F.; and Scherrer, Richard: Aerodynamic Principles for the Design of Jet-Engine Induction Systems. NACA RM A55F16, 1956.
5. Stofan, Andrew J.; and Mihalow, James R.: Performance of a Variable Divergent-Shroud Ejector Nozzle Designed for Flight Mach Numbers up to 3.0. NASA TM X-255, 1961.
6. Weber, Richard J.; and Luidens, Roger W.: A Simplified Method for Evaluating Jet-Propulsion-System Components in Terms of Airplane Performance. NACA RM E56J26, 1956.
7. Peterson, John B., Jr.; McRee, Donald I.; Adcock, Jerry B.; and Braslow, Albert L.: Further Investigation of Effect of Air Injection Through Slots and Porous Surfaces on Flat-Plate Turbulent Skin Friction at Mach 3. NASA TN D-3311, 1966.
8. Anderson, D. C.: Efficiency of Flush and Protruding Oblique Exhaust Nozzles With and Without External Flow. R-0955-22 (Contract NOa(s)55-133-c), Res. Dept., United Aircraft Corp., Oct. 1957.
9. Cossen, J. W.: Efficiency of Flush Oblique Nozzles Exhausting into Supersonic Streams Having Mach Numbers up to 4. R-1285-10 (Contract NOa(s) 55-133-c), Res. Dept., United Aircraft Corp., Sept. 1959.
10. Nelson, William J.; and Dewey, Paul E.: A Transonic Investigation of the Aerodynamic Characteristics of Plate- and Bell-Type Outlets for Auxiliary Air. NACA RM L52H20, 1952.
11. Dewey, Paul E.: A Preliminary Investigation of Aerodynamic Characteristics of Small Inclined Air Outlets at Transonic Mach Numbers. NACA TN 3442, 1955. (Supersedes NACA RM L53C10.)
12. Dewey, Paul E.; and Vick, Allen R.: An Investigation of the Discharge and Drag Characteristics of Auxiliary-Air Outlets Discharging Into a Transonic Stream. NACA TN 3466, 1955.

13. Vick, Allen R.: An Investigation of Discharge and Thrust Characteristics of Flapped Outlets for Stream Mach Numbers From 0.40 to 1.30. NACA TN 4007, 1957.



DRAG REDUCTION DURING ACCELERATION  
BYPASS AIR

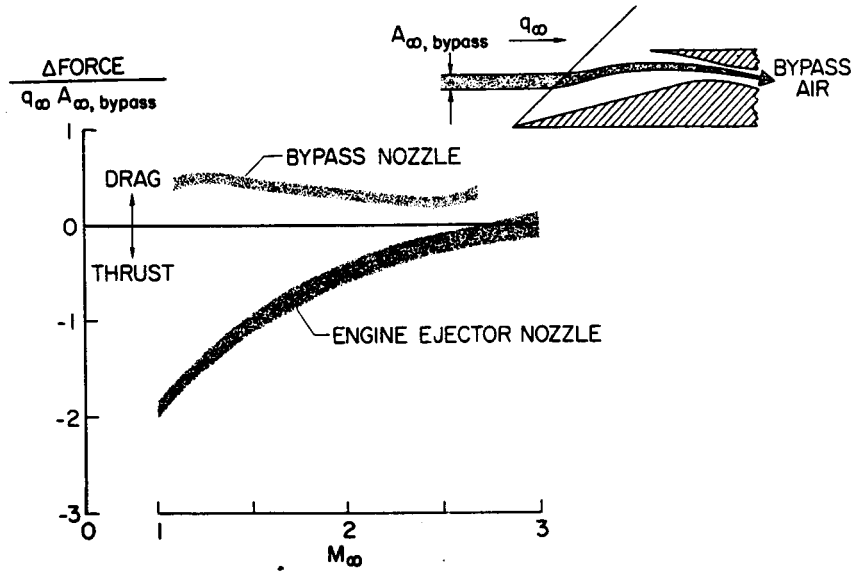


Figure 3

AXISYMMETRIC-INLET PERFORMANCE  
TYPICAL BLEED-HOLE CONFIGURATION;  $M_{\infty} = 3$

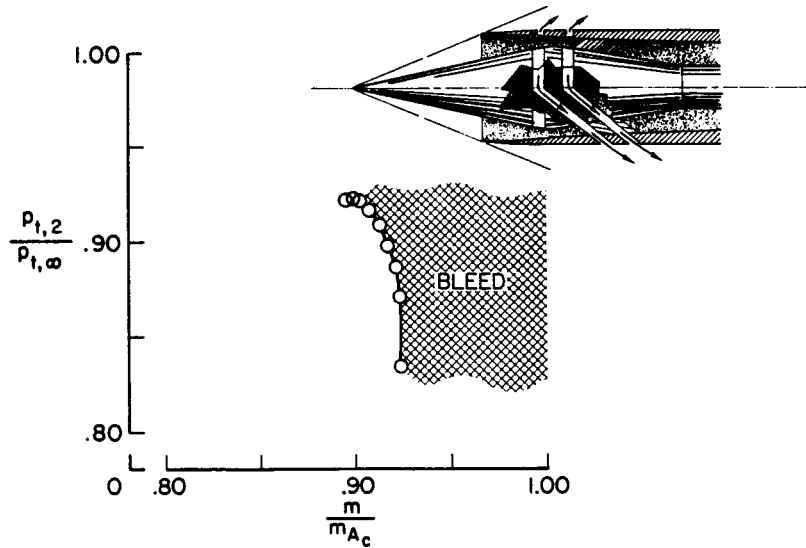


Figure 4

CALCULATED BLEED-AIR DRAG  
SONIC NOZZLE;  $C_v = 0.985$ ;  $M_\infty = 3$

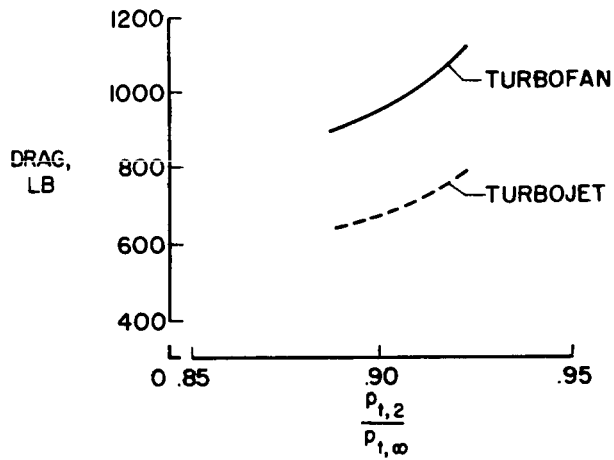


Figure 5

INLET OPTIMIZATION  
TYPICAL BLEED-HOLE CONFIGURATION;  
SONIC BLEED NOZZLE;  $C_v = 0.985$ ;  $M_\infty = 3$

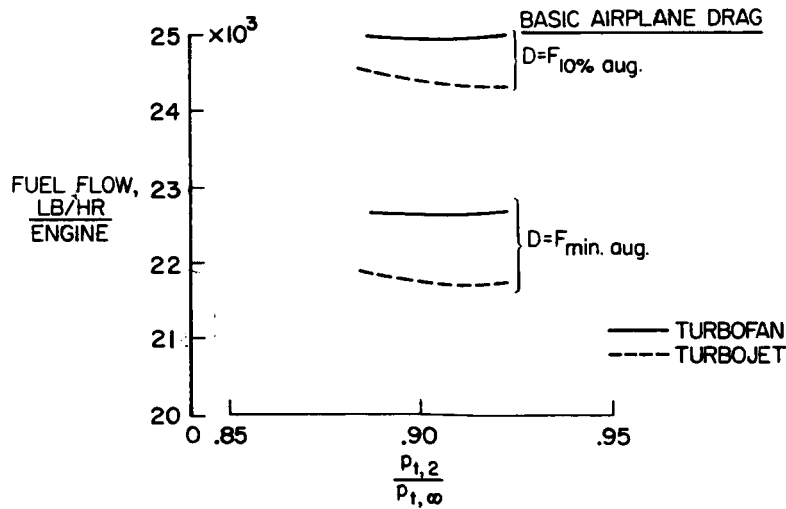


Figure 6

AXISYMMETRIC-INLET PERFORMANCE  
EFFECT OF BLEED-HOLE BACK PRESSURE;  $M_\infty=3$

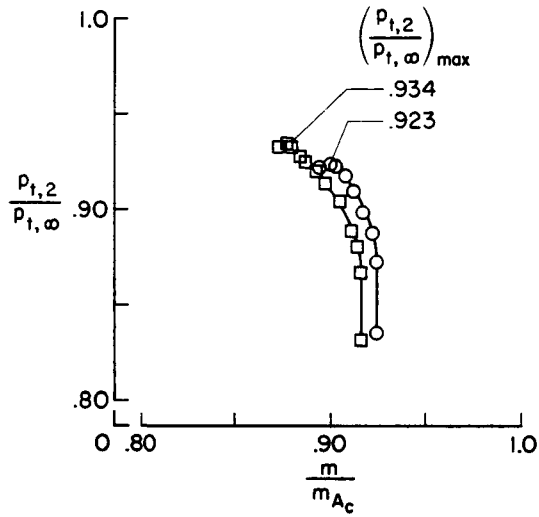


Figure 7 .

INLET OPTIMIZATION  
EFFECT OF BLEED-HOLE BACK PRESSURE; TURBOJET ENGINE;  
SONIC EXIT NOZZLE;  $C_V=0.985$ ;  $M_\infty=3$

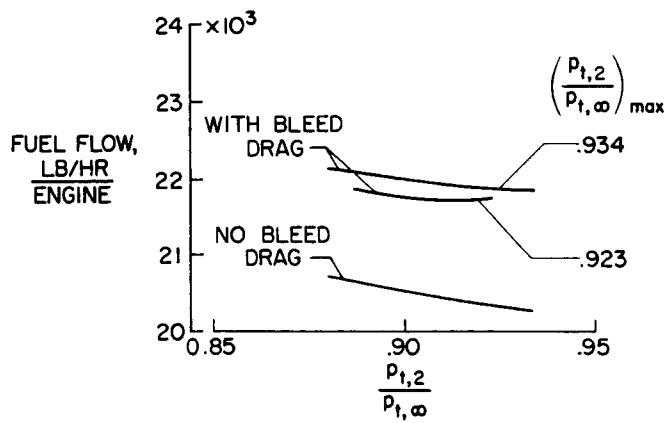


Figure 8

DRAG REDUCTION DURING CRUISE  
INLET BLEED AIR;  $M_\infty = 3$

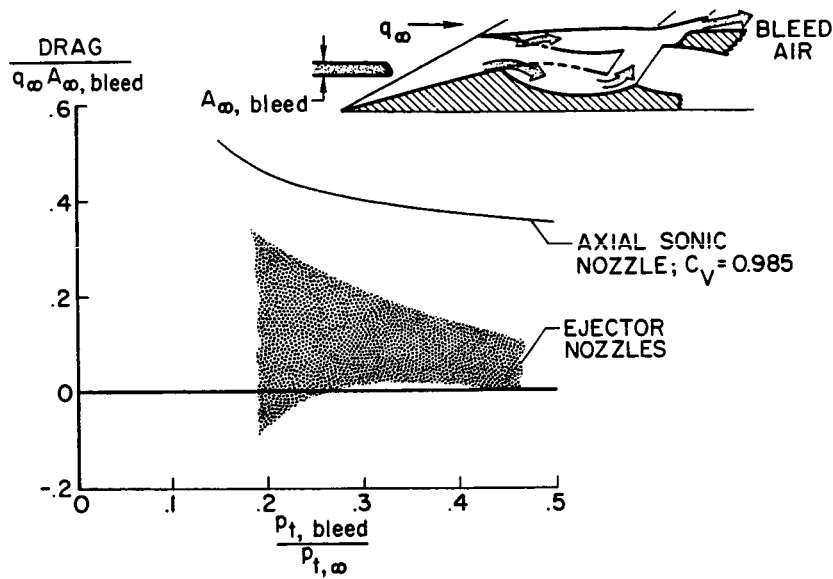


Figure 9

INSTALLED DRAG OF DISCHARGED-AIR NOZZLES  
 $M_\infty = 2.94$

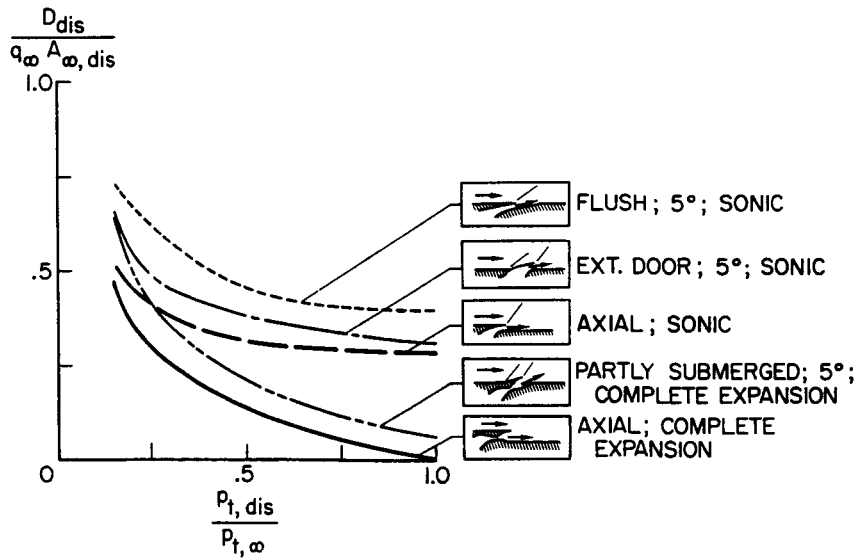


Figure 10

**CALCULATED BLEED-AIR DRAG**  
**EFFECT OF EXIT-NOZZLE CONFIGURATION;**  
**TURBOJET ENGINE;  $M_\infty=3$ ;  $C_v=0.985$**

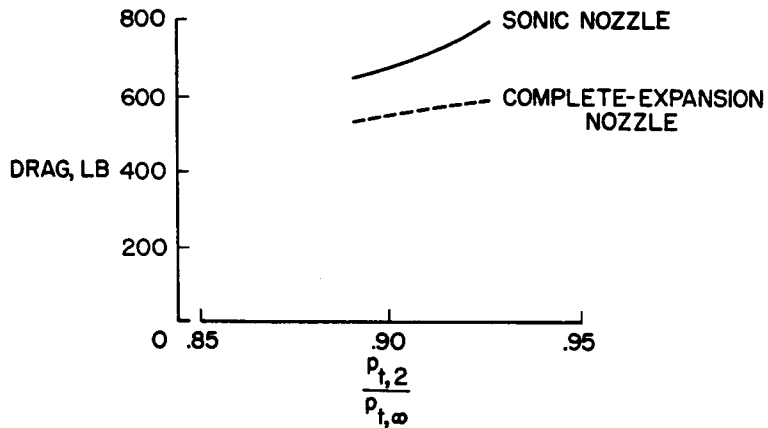


Figure 11

**INLET OPTIMIZATION**  
**EFFECT OF EXIT-NOZZLE CONFIGURATION;**  
**TURBOJET ENGINE;  $M_\infty=3$ ;  $C_v=0.985$**

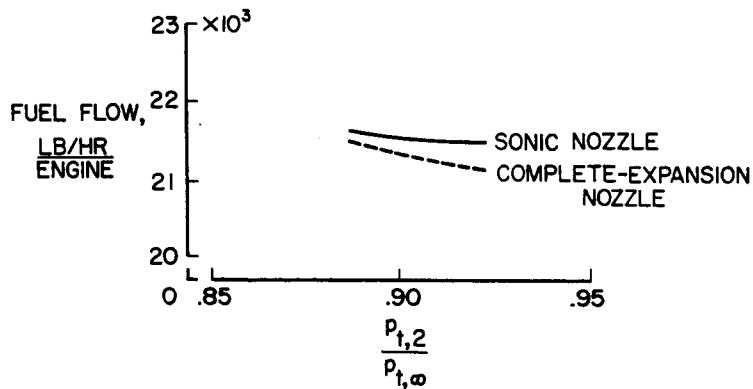


Figure 12

11. PERFORMANCE SUMMARY OF A TWO-DIMENSIONAL AND AN  
AXISYMMETRIC SUPERSONIC-INLET SYSTEM

By Norman E. Sorensen, Warren E. Anderson  
Norman D. Wong, and Donald B. Smeltzer  
NASA Ames Research Center

SUMMARY

The results of approximately three years of theoretical and experimental research effort are summarized for a large-scale two-dimensional and axisymmetric inlet system. A series of wind-tunnel tests have provided a background of experimental information showing the performance capabilities at Mach numbers from 0.6 to 3.2. The primary objectives were to investigate relatively short mixed-compression inlet systems with low external drag and to achieve high performance over the complete Mach number range with a minimum of engine-face distortion. The main conclusions are that the supersonic portion of the inlet system performed as predicted, and that the main difficulty in achieving high performance lay in the throat and subsonic diffuser. In addition, short subsonic diffusers appear practical when vortex generators are employed downstream of the throat.

INTRODUCTION

Air-induction system research and development programs at Ames Research Center have primarily supported the supersonic transport. The results, however, have a wide range of application to other supersonic aircraft. A series of wind-tunnel tests for large-scale two-dimensional and axisymmetric inlet systems have provided a background of experimental information showing the performance capabilities over most of the Mach number range up to 3.0. The present paper is intended as a brief summary of the results of approximately three years of theoretical and experimental research effort.

The programs were conceived to attain three major objectives. The first objective was to investigate mixed-compression inlet systems that were relatively short and had low external drag in an attempt to minimize the weight and drag while maintaining high internal performance. The second objective was to achieve high internal performance over the complete Mach number range, insuring maximum vehicle performance not only during cruise, but also during climb and acceleration. Because the engine-face distortion of short inlet systems is usually large, or unacceptable, the third objective was to investigate means for controlling the distortion to within acceptable levels.

Satisfactory performance of the supersonic transport has demanded propulsion systems with light-weight high-performance inlets. This has led to rather sophisticated designs which employ high internal contraction supersonic diffusers in combination with relatively short subsonic diffusers. Figure 1

shows the two-dimensional model mounted in the test section of the supersonic wind tunnel. It is designed for a Mach number of 3.0 and is capable of performing at off-design Mach numbers by opening the throat. The inlet is square, having a 14- by 14-inch capture area, and can be considered half of a complete inlet system feeding one engine. The external protuberances would not normally be present on an actual inlet and are peculiar to the ramp and boundary-layer-bleed control system of this model.

Figure 2 shows the axisymmetric model mounted in the test section of the transonic wind tunnel. It is also designed for Mach number 3.0. The model has a 20-inch capture diameter and is capable of performing at off-design Mach numbers by translating the centerbody. The small protuberances visible inside the inlet are vortex generators which have controlled the engine-face distortion. As mentioned for the two-dimensional model, the external protuberances are peculiar to this model and would not normally be present on an actual inlet. Both models are as large as practical for the test facility and can be considered 1/4 to 1/2 full scale. The models were tested in the wind tunnel primarily to determine the internal performance and bleed requirements from Mach number 0.6 to 3.2 at angles of attack and sideslip up to  $8^\circ$ . The Reynolds number per foot at Mach number 3.0 was about  $2 \times 10^6$  which corresponds to the Reynolds number per foot at 65,000 feet.

#### SYMBOLS

D	capture diameter, axisymmetric inlet
$m_{b2}$	bleed mass flow
$m_\infty$	free-stream mass flow
$M_\infty$	free-stream Mach number
$P_{t2}$	total pressure at engine face
$\bar{P}_{t2}$	area weighted average total pressure at engine face
$P_{t\infty}$	free-stream total pressure
$\alpha$	angle of attack
$\beta$	angle of sideslip

#### TWO-DIMENSIONAL RESULTS

Satisfactory comparisons of two-dimensional and axisymmetric inlets are difficult to make, and as a consequence each inlet will be discussed separately. Figure 3 is a sketch of the two-dimensional model. The variable ramp assembly is positioned by adjusting the height of the throat ramp which can be

differentially actuated for optimization of the area variation in the throat region. The angle of the initial ramp compression surface is fixed at  $7^\circ$ . The lower cowl surface can be translated aft, to the position indicated, for operation at Mach numbers lower than about 1.75. This translation provides for efficient external compression and spillage at low off-design Mach numbers. Perforated ramp and side-wall surfaces allow the boundary layer to bleed into three compartmented zones located above the ramps and then through ducts to controllable exit plugs. Bleed flows from the cowl and forward side wall are dumped directly to the outside airstream. Total pressure rakes are located at the simulated engine face. Vortex generators, which will be discussed subsequently, have been located in the throat region on the ramp and cowl surfaces, with eight on the cowl and eight on the ramp. The detailed design of the vortex generators follows the procedures of reference 1.

Initial tests were completed on the short subsonic diffuser, which represents an equivalent conical angle of about  $9^\circ$ . The maximum turning angle of the ramp surface was  $25^\circ$ . Design modifications, shown by the dashed lines, resulted in a subsonic diffuser which is equivalent to a  $7^\circ$  conical angle. With a slight increase in length, the ramp turning rates were reduced to a maximum of  $16^\circ$ .

Even though the off-design performance is important, the design performance is usually more important. Figure 4 indicates the supercritical performance at Mach number 3.0 and zero angle of attack and sideslip. Engine-face pressure recovery and distortion are plotted as a function of boundary-layer-bleed mass-flow ratio. The more usual abscissa for a supercritical plot is engine-face mass-flow ratio, which is merely the difference between 1 and the boundary-layer-bleed mass-flow ratio.

Initial tests of the two-dimensional inlet model utilizing the short subsonic diffuser indicated that flow along the ramp surface in the subsonic diffuser was separated. A total-pressure recovery of 87 percent was achieved with a bleed mass-flow ratio of about 13 percent with about 17-percent distortion. The modified system, as mentioned previously, had a subsonic diffuser with reduced turning angles on the ramp surface. The modification resulted in a peak pressure recovery of about 88 percent with about 14-percent bleed, but the distortion levels were high, 12 to 16 percent, because of flow separation on the subsonic ramp surface similar to that experienced with the shorter diffuser. Since a distortion of 10 percent is considered a nominal maximum, the forced mixing principle employing vortex generators was investigated for reducing the distortion. The test results show that adding four pairs of vortex generators across the width of the ramp side eliminated separated flow and reduced the distortion to 8 percent with a peak recovery of 90 percent. Placing vortex generators on both the cowl and ramp further reduced the distortion to 5 percent but increased mixing losses in the flow near the cowl surface, and resulted in a slight decrease in the maximum attainable recovery. The bleed mass-flow ratio for the bleed configuration used in this series of tests increased from about 11.5 percent to about 14.5 percent as a result of the terminal shock wave moving over the porous bleed surfaces in the throat. The dashed line is the envelope of peak performance for other bleed configurations. To avoid confusion the supercritical performance for all configurations was

not plotted, but the trade between peak performance and bleed appears to be about a 1-percent increase in pressure recovery for 1-percent increase in boundary-layer bleed.

The effect of vortex generators on engine-face distortion is further clarified in figure 5. This slide presents total-pressure ratio profiles at the engine face, measured by a vertical center-line rake, for the peak recovery conditions of the previous figure. Without vortex generators the profiles for both the short and modified inlet are highly distorted. Adding vortex generators on the ramp side eliminated separation and improved the profile mostly near the ramp side, leaving the distortion near the cowl side much as it was. The addition of generators on the cowl side improved the profile to the point where the distortion was reduced to about 5 percent. The vortex generator tests were limited, and further improvements might be possible.

The performance at angles of attack and sideslip has shown some interesting results. Figure 6 shows the peak pressure recoveries at Mach numbers 3.0 and 2.5 for the short and modified inlets. As is expected the peak recovery at angle of attack is different from the recovery at angle of sideslip, the latter, shown by the dashed curves, having the lower recoveries. Two interesting results are to be noted. One is that the difference in recovery at angle of attack and sideslip is considerably greater at Mach number 3.0 than at 2.5. The other point is that the inlet with the short subsonic diffuser performs about as well as the one with the modified diffuser at Mach number 2.5, but is considerably poorer at Mach number 3.0 by 3 to 6 percent. This appears to be a result of the previously mentioned separated flow in the subsonic diffuser which persists or is aggravated with increase in angle of attack and sideslip. At Mach number 2.5 or less the flow is attached. This accounts for the better results shown for Mach number 2.5.

The final data plot for the two-dimensional inlet is shown in figure 7. Pressure recovery and distortion for peak operating conditions are plotted for a range of Mach numbers from 0.6 to 3.0. A break in the curves occurs at a Mach number of 1.3 because of test facility restrictions which limited boundary-layer bleed to about 2 percent at the transonic Mach numbers. At the higher Mach numbers from 1.55 to 3.0 the bleed varied from about 7 to 14 percent. Note that the cowl was retracted for Mach numbers below 1.75 and the inlet operated as an all external compression system, which probably accounts for the change in trend of the distortion in this Mach number range. The use of vortex generators on the ramp reduced distortion about 2 to 4 percent throughout the Mach number range without significantly affecting engine-face pressure recovery. A similar effect will be shown later for the axisymmetric inlet.

#### AXISYMMETRIC RESULTS

Figure 8 shows quarter section sketches of three of the inlet systems that have been tested. The upper quarter section shows two of the systems while the lower section shows the third system. In the upper quarter section one system is a rather long 1.86 diameter system measured from the lip to the engine face;

the other is a medium system 1.57 diameters long. Since the supersonic diffuser is the same for both of these systems, the subsonic diffuser accounts for the difference in length. The short inlet system in the lower quarter section is 1.40 diameters long. The upper and lower supersonic diffusers are almost the same length but differ in their theoretical efficiencies by about 3 percent. The upper inlet is capable of a theoretical throat recovery of 96.3 percent and represents an earlier design. Subsequent work revealed that a diffuser could be designed with 99.3 percent theoretical recovery if both the cowl contours and the forward portion of the centerbody were curved from  $10^\circ$  to  $15^\circ$  instead of being a straight  $12.5^\circ$  cone as in the earlier inlet mentioned above. The main problem in both supersonic diffusers has been to avoid boundary-layer separation due to shock-wave impingements. This requirement tended to establish a lower limit on inlet length of about that shown. Both supersonic diffusers were designed with the aid of a computer program (ref. 2) employing the method of characteristics. It has proved to describe accurately the flow field. An important consideration in a translating centerbody design is providing enough capture mass flow for the engine at off-design Mach numbers. These inlets supply about 40-percent mass-flow ratio at Mach number 1.0 and satisfy the demand of a selected turbofan engine. This type of inlet could satisfy a wide range of engines if a collapsible centerbody were employed.

The model has provision for removing the boundary layer through four porous bleed areas, two on the cowl and two on the centerbody. The porous areas are composed of holes drilled normal to the surface for a maximum porosity of about 40 percent. The porous pattern required by each inlet could be altered by filling some of the holes. Each of the four areas has a separate and controllable exit. The exits for the cowl bleed are illustrated in figure 8; those for the centerbody are further downstream and are not visible in the figure. By opening or closing these exits, the bleed mass flow could be varied for a given bleed configuration.

With these supersonic diffuser lines, three subsonic diffusers were designed. The basic area distributions follow a linear rate of change of Mach number from the end of the throat region to the engine face. The throat region which is two throat heights long has about a  $2^\circ$  divergence between the cowl and the centerbody. This method of design has proved effective in preventing boundary-layer separation in this portion of the inlet, something which was not accomplished in initial tests (1963) employing a linear area variation from the beginning of the throat region to the engine face. The equivalent conical angles of these diffusers (measured from the beginning of the throat region to the engine face) are about  $11^\circ$ ,  $15^\circ$ , and  $20^\circ$  for the long, medium, and short inlet systems, respectively. Also shown in the figure are vortex generators located just downstream of the throat of the short and medium inlet systems. The long inlet was not tested with vortex generators. Tests of several generator heights showed that the optimum height was about 20 percent of the throat height. For the short inlet, 50 generators were located on the centerbody and 60 on the cowl. Additional details of the generators for the medium inlet are presented in reference 3.

Figure 9 compares the peak performance attained at various bleed mass-flow ratios for the three inlet systems just described at the design Mach

number of 3.0 and at  $0^\circ$  angle of attack. For the initial tests a peak recovery of 86 percent with 13-percent bleed was attained with about 10-percent engine-face distortion. As mentioned previously, this inlet system employed a subsonic diffuser with a linear area variation. Since recoveries as high as 97 percent were measured in the throat, the main losses in performance lay in the subsonic diffuser. This diffuser had an initial rate of expansion that was too rapid causing separation and preventing attainment of higher recoveries. This led to the design shown for the long inlet whereby the initial rate of expansion was reduced preventing separation. This improved the performance to the point where a little over 90-percent recovery with about 11-percent bleed was attained. The engine-face distortion was about 10 percent and was the lowest distortion that could be attained with this diffuser which did not employ vortex generators. With the medium inlet employing vortex generators, not only was the distortion lowered to about 6 or 7 percent, but the level of recovery increased approximately 1 percent so that 91-percent recovery was attained with about 11-percent bleed. This latter result is attributable to the better distribution of the flow energy induced by the vortex generators. With the short inlet with the shortest subsonic diffuser but with a 3 percent more efficient supersonic diffuser, the recovery level increased about 2 percent over the bleed range indicated so that almost 93-percent recovery with 11-percent bleed resulted. However, the distortion level was about 3 percent higher than for the medium length inlet, probably because of the shorter subsonic diffuser.

Because the high levels of recovery shown for the short inlet have heretofore been unknown at a Mach number of 3.0, the supercritical performance was examined carefully and is shown in figure 10. Note that the scales for recovery and distortion have been reduced about 50 percent. Three levels of bleed flow are represented, an open, intermediate, and restricted bleed. The bleed through the two areas in the supersonic diffuser was held constant at 3.5 percent, and the total level of bleed was therefore regulated entirely by the adjustment of the two throat bleed exit settings. (The "unstart" angle of attack indicated on the recovery plot is explained in the next paragraph.) This inlet system is capable of recoveries of 93, 92, and 90 percent with bleed mass flow of about 12, 9.5, and 7.5 percent, respectively. Notice that limiting the throat bleed progressively limits the supercritical bleed mass-flow range from about 4 percent for the open bleed to about 1.5 percent for the restricted bleed. In addition, the distortion remains at or below about 10 percent over the useful supercritical range. The knee of the recovery curves represents the point where the terminal shock wave leaves the bleed area in the throat region and further movement downstream does not change the bleed mass flow. The distortion under these conditions can be quite high, 40 percent or greater.

Most axisymmetric mixed-compression inlets have been sensitive to small angle-of-attack changes caused by disturbances, such as gusts; that is, the inlets unstart easily with small changes in flow angle. This is not necessarily true for these inlets. Examples of the unstart sensitivity to flow angle at various operating points are shown on the curve for the intermediate bleed setting. With the shock wave in its most forward position, and without changing the inlet geometry, the inlet can be pitched only  $1/2^\circ$  before it unstarts, but if the performance is degraded 2 or 3 percent, as it would normally be for a practical operating condition,  $2^\circ$  or  $3^\circ$  of flow angle can be tolerated. This is with the inlet centerbody in the position for which the throat Mach number

is about 1.2. With higher throat Mach numbers more tolerance is expected. It should be noted that the performance indicated at the operating points does not represent the performance at the unstart angles of attack. The performance is always something less at angle of attack. This is shown in figure 11 where comparable peak recoveries and the distortion are plotted as functions of flow angle for the three inlet systems. Each system exhibits its own peculiarities and a trend is not clear from the results. The short inlet, for instance, produces the highest recovery at  $5^\circ$  and  $8^\circ$ , a result which one might not expect. In addition, the distortion, even though it is high, is no worse than the medium length inlet at these same angles, and perhaps the generally lower distortion of the long inlet can be attributable to its longer length. The recovery for the short inlet, however, drops more rapidly from  $0^\circ$  to  $2^\circ$  than either of the other two systems sharing the same supersonic diffuser. This would seem to indicate the supersonic diffuser has an important influence on the angle-of-attack performance.

The three inlet systems have performed well over the complete Mach number range. Critical recovery and the accompanying distortion are shown in figure 12 to be comparable from Mach number 0.6 to 3.2. The results from Mach number 0.6 to 1.2 are optimum for a selected turbofan engine; that is, the net thrust minus the additive drag has been optimized to provide realistic as well as comparable results. The long and medium systems have shown about the same recovery capabilities but the distortion of the medium length inlet is generally lower. This indicates that the vortex generators are effective throughout the Mach number range even when (at other than the design Mach number) they are much displaced from the design position in which the cowl and centerbody generators are opposite one another. The short inlet shows a similar trend of recovery but at several percent increase at the higher Mach numbers. The distortion is generally lower than that of the long inlet. The peculiar dip in recovery at Mach number 2.9 for the short inlet is difficult to explain. This was not detected in the tests of the other two configurations but may also have been present. The points at  $M_\infty = 3.2$  are overspeed conditions for the inlets; that is, the results at  $M_\infty = 3.2$  were obtained with the Mach number 3.0 geometry settings, which accounts for the rapid deterioration of the distortion and recovery.

#### CONCLUDING REMARKS

The main conclusions to be drawn from the present summary for the two-dimensional and axisymmetric inlet systems are that the supersonic portion of the inlet systems performed as predicted, and that the main difficulty in achieving high performance lay in the proper design of the throat and subsonic diffuser. Also, short subsonic diffusers appear feasible when vortex generators are employed downstream of the throat. In addition, it appears that in order to achieve the highest performance a nearly isentropic supersonic diffuser must be employed which requires complete contouring of both the cowl and centerbody.

## REFERENCES

1. Taylor, H. D.: Summary Report on Vortex Generators. UAC Research Department Rep. R-05280-9, March 7, 1950.
2. Sorensen, Virginia L.: Computer Program for Calculating Flow Fields in Supersonic Inlets. NASA TN D-2897, 1965.
3. Sorensen, Norman E., and Smeltzer, Donald B.: Study and Development of an Axisymmetric Supersonic Inlet. AIAA Propulsion Joint Specialist Conference, Colorado Springs, Colorado. June 14-18, 1965. NASA TM X-56977.

TWO-DIMENSIONAL INLET MODEL

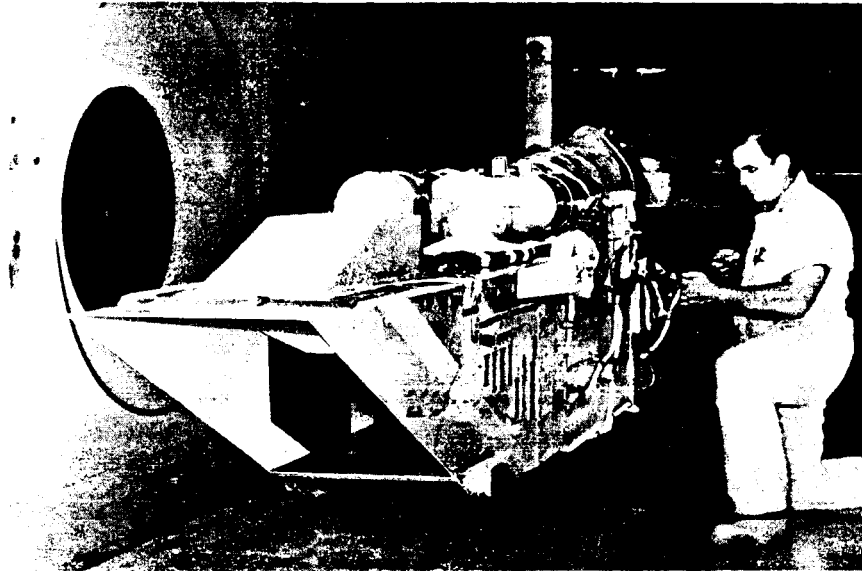


Figure 1

A-32238.1

AXISYMMETRIC INLET MODEL

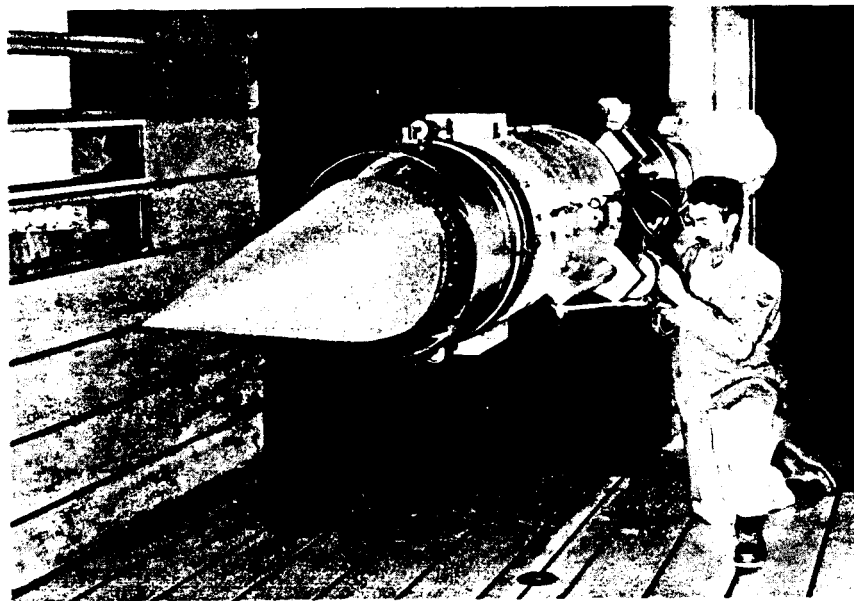


Figure 2

A-34092.1

## TWO-DIMENSIONAL INLETS

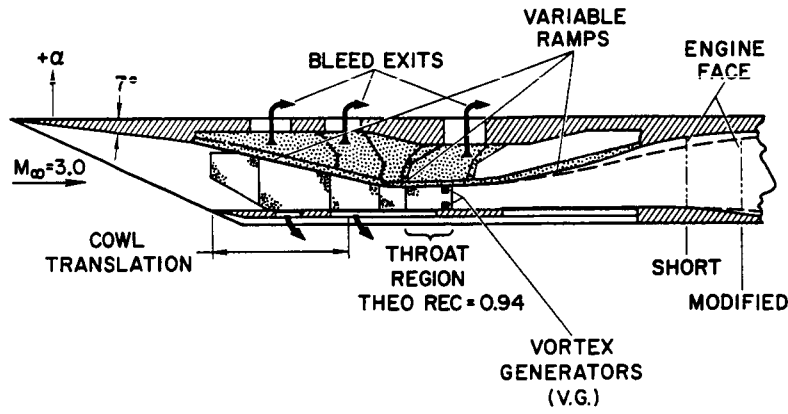


Figure 3

## TWO-DIMENSIONAL INLETS, SUPERCRITICAL PERFORMANCE $M_\infty = 3, \alpha = \beta = 0^\circ$

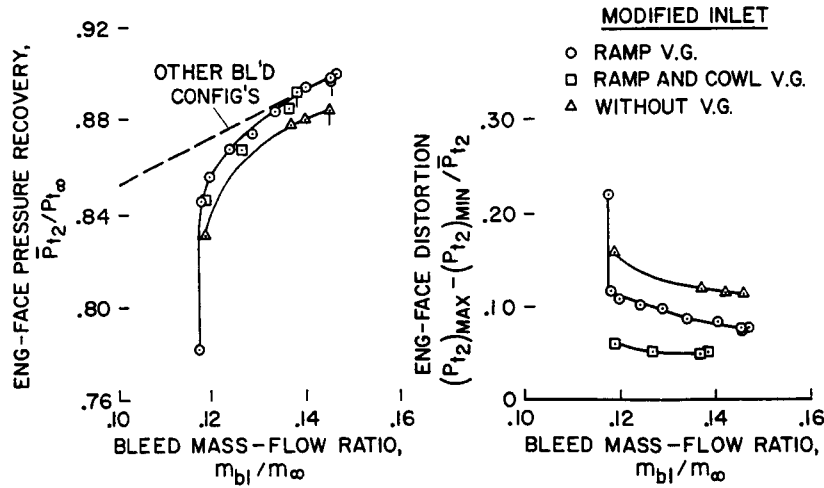


Figure 4

TWO-DIMENSIONAL INLETS, EFFECT OF VORTEX GENERATORS  
 $M_\infty=3, \alpha=\beta=0^\circ$

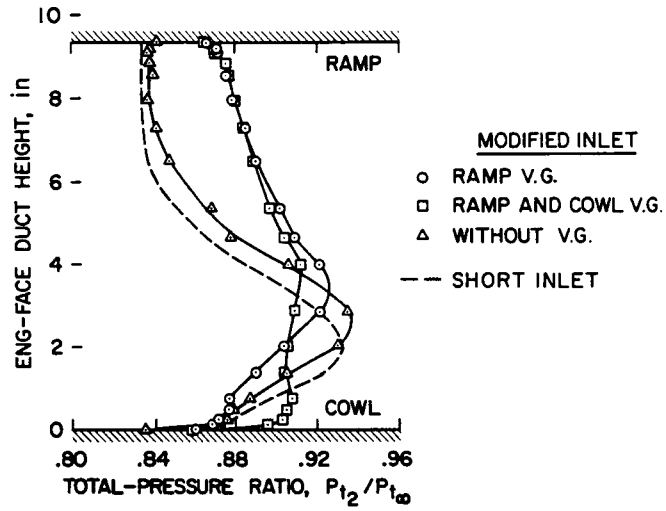


Figure 5

TWO-DIMENSIONAL INLETS, PEAK PERFORMANCE WITH FLOW ANGLE

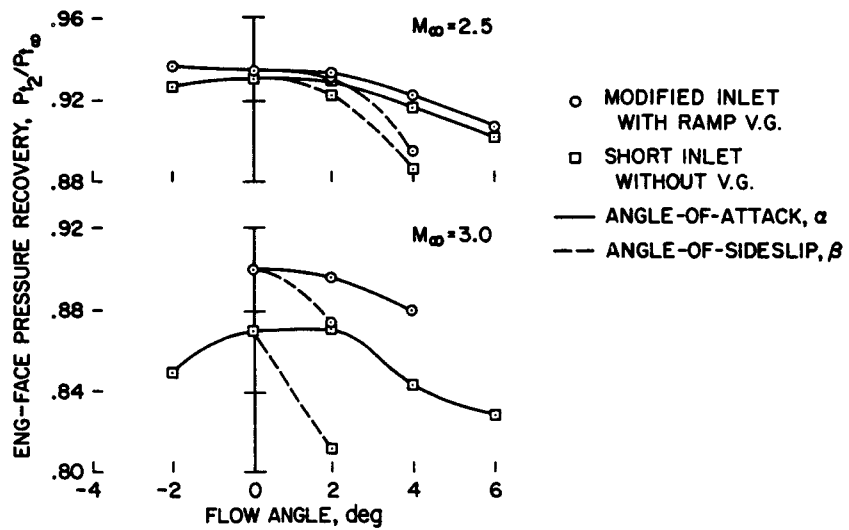


Figure 6

TWO-DIMENSIONAL INLETS, OFF-DESIGN PERFORMANCE  
 $\alpha = \beta = 0^\circ$

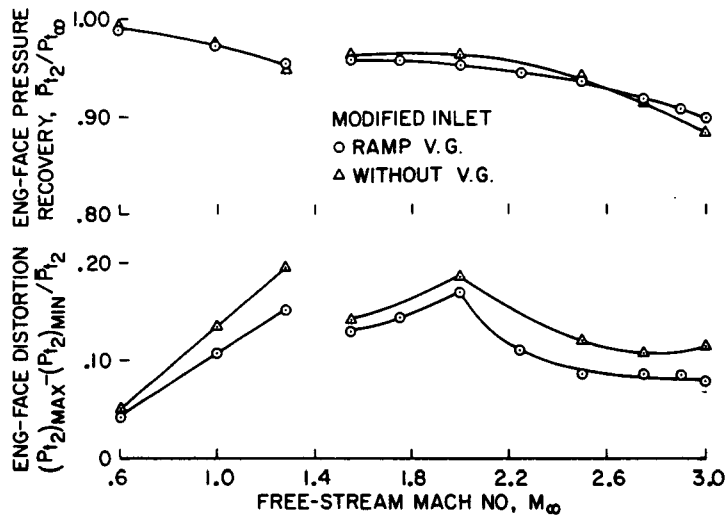


Figure 7

AXISYMMETRIC INLETS

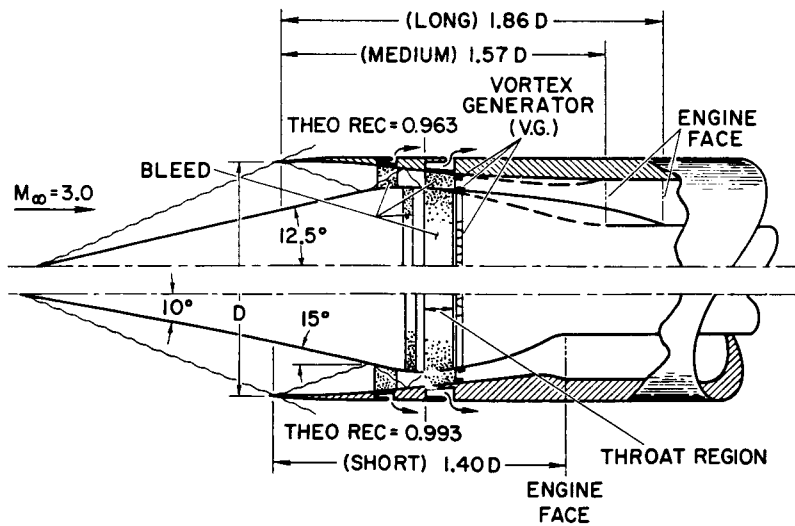


Figure 8

AXISYMMETRIC INLETS, PEAK PERFORMANCE  
 $M_\infty = 3, \alpha = 0^\circ$

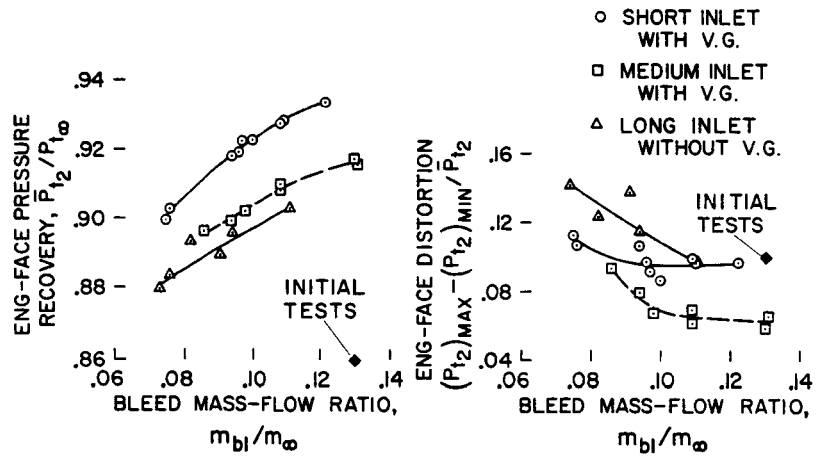


Figure 9

SHORT AXISYMMETRIC INLETS, SUPERCRITICAL PERFORMANCE  
 $M_\infty = 3, \alpha = 0^\circ$

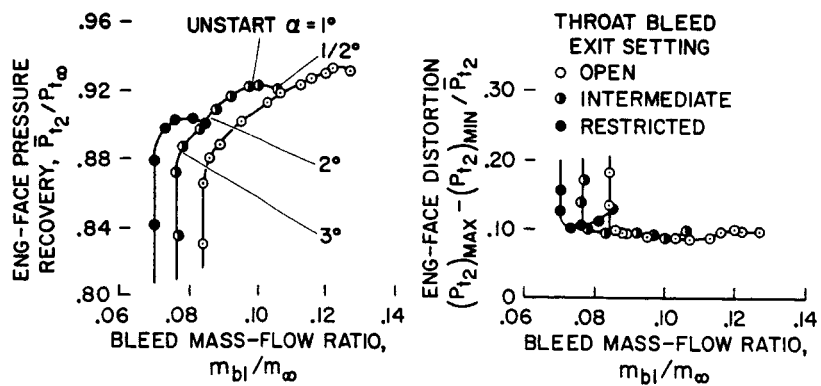


Figure 10

AXISYMMETRIC INLETS, PEAK PERFORMANCE WITH FLOW ANGLE  
 $M_\infty = 3$

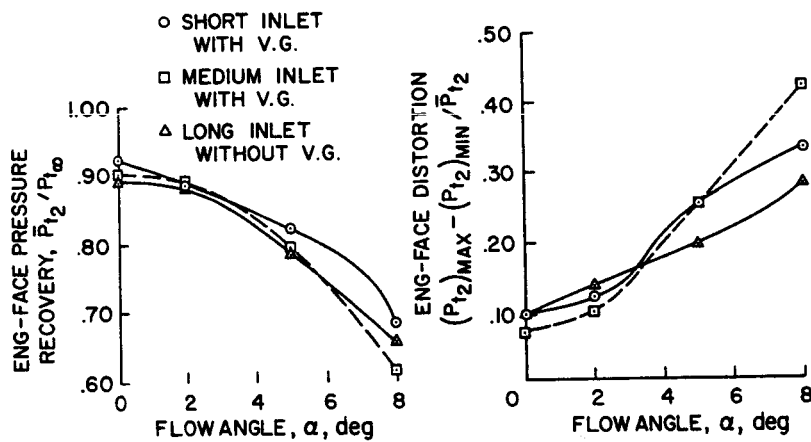


Figure 11

AXISYMMETRIC INLETS, OFF-DESIGN PERFORMANCE  
 $\alpha = 0$

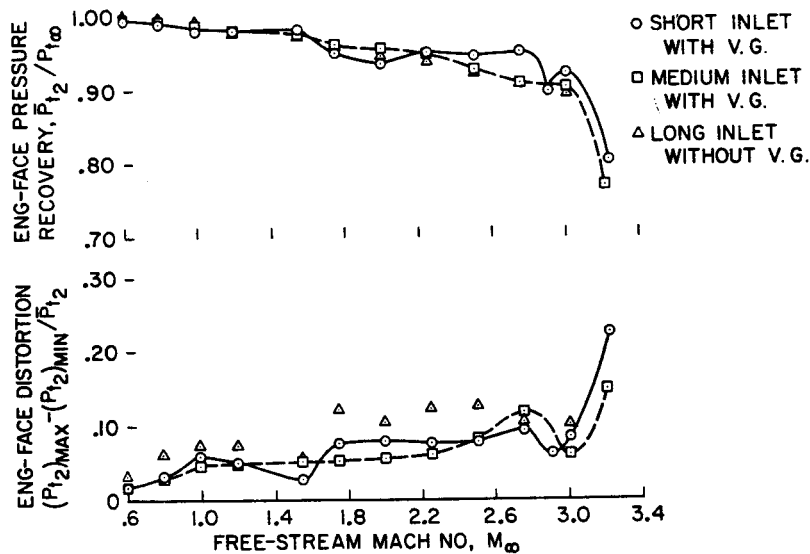


Figure 12

12. AN EVALUATION OF TRANSONIC SPILLAGE DRAG BASED ON  
TEST RESULTS FROM LARGE-SCALE INLET MODELS

By Warren E. Anderson, Martine W. Petersen<sup>1</sup>,  
and Norman E. Sorensen  
NASA Ames Research Center

SUMMARY

Transonic spillage drag is evaluated on the basis of test results of three experimental inlet research programs. The additive-drag component of spillage drag was calculated from experimental measurements on both axisymmetric and two-dimensional type inlet models. In both cases, the theoretical prediction of additive drag required a precise knowledge of the pressure distribution on the compression surface.

Cowl lip suction force, which acts to cancel a portion of the additive drag, was measured on a two-dimensional spillage-drag model. The effects of a wide variety of geometric factors were studied on this model. It was found, for example, that a significant cancellation (large cowl lip suction force) occurred subsonically for a wide range of cowl lip shapes, whereas the effect at higher supersonic Mach numbers was small.

INTRODUCTION

In recent years the development of high-performance aircraft has focused attention on the propulsion penalties associated with inlet-engine matching requirements. During off-design operation, one penalty of major importance is inlet spillage drag, particularly in the transonic Mach number range where effects on vehicle performance can be large.

Recently, three experimental inlet research programs have been in progress at the Ames Research Center. Two of the programs involve large-scale axisymmetric and two-dimensional models being tested in support of the supersonic transport. These models have provided data for the two spillage-drag components, additive drag and cowl lip suction force. A third program was an Air Force supported contractual study of spillage drag in two-dimensional inlets. This study involved investigation of a wide variety of inlet geometries and directed considerable attention to both additive drag and lip forces on the cowl and side wall.

This paper will present representative test results from all three models within the Mach number range from 0.6 to 1.3. Some comparisons with available theoretical predictions are also included.

---

<sup>1</sup>Propulsion and Thermo Analysis Engineering Specialist - North American Aviation, Inc., Los Angeles Division

## SYMBOLS

A	area
$C_D$	drag coefficient, $\frac{\text{drag}}{qA}$
$D_a$	additive drag
$D_{c_0}$	reference cowl drag
$\Delta D_c$	cowl suction force
$D_c$	cowl drag
$D_{cs}$	compression surface drag
$D_E$	inlet system external drag
$D_{\text{SPILLAGE}}$	$D_a - \Delta D_c$
$K_{\text{ADD}}$	incremental additive-drag correction factor, $\frac{\Delta D_{\text{SPILLAGE}}}{\Delta D_a}$
$m_i$	inlet mass flow
$\frac{m_i}{m_\infty}$	inlet mass-flow ratio
$M_\infty$	free-stream Mach number
P	static pressure
$P_{t_\infty}$	free-stream total pressure
$\bar{P}_{t_2}$	area weighted average total pressure at engine-face station
q	dynamic pressure
V	velocity
$\delta$	angle, deg

### Subscripts

c	capture
i	inlet
o	initial conditions in stream tube

REF reference  
X station  
 $\infty$  free stream

## DISCUSSION

The concepts basic to an understanding of the spillage drag are discussed in many publications (e.g., refs. 1 through 5). The following paragraphs, therefore, cover the basic descriptions and definitions only in rather broad and simplified terms.

Inlet system drag definitions are presented in figure 1 together with an illustration showing the effect of inlet mass-flow ratio on the drag components. The term  $D_{c_0}$  is the cowl drag at a reference mass-flow ratio (operating condition) and includes the external-cowl pressure and friction drag chargeable to the propulsion system. The variation of cowl pressure drag with mass-flow ratio,  $\Delta D_c$ , is negative and is referred to as the cowl lip suction force. The spillage drag by definition is equal to  $D_a - \Delta D_c$ .

Additive drag,  $D_a$ , is a force correction which is applied in equating internal thrust and external drag for purposes of evaluating vehicle performance; it is a bookkeeping item for making the definition of thrust and drag compatible and is not a force felt on the vehicle surface. However, it represents a performance factor which the propulsion aerodynamicist can control. The influence of additive drag on mission performance is analyzed in reference 1.

The general expression for additive drag is developed in figure 2 with the aid of a simplified sketch of an inlet flow field. The net force on the entering stream tube element, indicated by the dashed lines, is equal to the momentum change within the element. A summation of forces and rearrangement of terms yields an equation which states that the additive drag is equal to the momentum change plus the inlet pressure force plus the compression surface drag. Finally, the additive drag coefficient is referenced to the inlet capture area,  $A_c$ , as shown. The equation for additive drag differs for different inlet geometries; an open nose inlet requires only the first two terms or total-momentum change, whereas a two-dimensional inlet with side walls requires a fourth term similar to that for the ramp compression surface, to account for the side-wall pressure and friction drag.

## EXPERIMENTAL RESULTS

### Additive-Drag Measurements

Transonic additive-drag measurements were made on two large-scale inlet models. One of the models was axisymmetric with a capture diameter of 20.0 inches. The other inlet model was two-dimensional with a capture height and width of 14.0 inches. Both models are described in reference 6.

Additive-drag values were obtained from a momentum balance as shown in figure 2. In the axisymmetric inlet, total and static-pressure rakes were installed on the centerbody at the maximum diameter station. These rakes were used to measure the inlet total-momentum change and inlet mass-flow ratio. The centerbody was instrumented with static-pressure orifices (area weighted) from which the centerbody pressure drag was computed. Figure 3 shows typical additive-drag values and the corresponding total-pressure recovery at the engine face for several Mach numbers and a range of inlet mass-flow ratios. For these tests, the centerbody was a  $12.5^\circ$  half-angle cone and the cowl lip was positioned at the maximum diameter. Near the maximum mass-flow ratio, inlet choking caused a large reduction in pressure recovery and little decrease in additive drag. Reducing mass-flow ratio produced the characteristic increase in additive drag at all Mach numbers. Data obtained with the cowl lip at more forward positions indicated similar families of curves, but with higher values of additive drag and total-pressure recovery.

Figure 4 shows the minimum additive-drag coefficients measured for three centerbody shapes at transonic Mach numbers. The lower curve is for the  $12.5^\circ$  half-angle cone. The two upper curves are for isentropic surfaces that had initial cone angles of  $5^\circ$  and  $10^\circ$  and curved to a total compression of  $15^\circ$ . The minimum additive drag has a peak at  $M_\infty = 1.1$  for all three centerbody shapes. A computer program employing the method of characteristics was used to calculate the supersonic additive-drag curve for the  $12.5^\circ$  cone. Although an extrapolation of this curve to transonic Mach numbers would fair into the peak measured value of minimum additive drag for the  $12.5^\circ$  cone, the drag at low supersonic Mach numbers is overestimated. The experimental results show that the total-momentum change (represented by the first two terms of the additive-drag equation) is nearly zero at high mass-flow ratios and the additive drag is almost equal to the centerbody drag (the filled symbols). Measured static-pressure ratio distributions used to calculate the centerbody drag for Mach numbers 0.8 and 1.0 are presented in figure 5. The pressures are seen to change rapidly near the maximum centerbody diameter; to calculate additive drag theoretically, the theory must be able to predict the pressures in this region to an exact degree.

Figure 6 shows the total-pressure recovery at the engine face and the corresponding values of additive-drag coefficient computed for optimized<sup>2</sup> operating conditions of a supersonic transport engine. These values are compared with the minimum measured values of additive drag and the corresponding total-pressure recoveries. For optimized operating conditions the cowl lip was slightly forward of the maximum centerbody diameter and the additive drag was substantially higher than the minimum values.

In summary, the momentum-balance method appears to be satisfactory for experimentally evaluating the transonic additive drag of axisymmetric type inlets. Nearly all the additive drag at full flow conditions is centerbody pressure drag. For theoretical predictions of additive drag, it is therefore necessary to have accurate knowledge of the centerbody pressure distribution.

---

<sup>2</sup>The optimum inlet-engine operating condition is at the maximum value of net thrust minus additive drag.

The additive drag at the optimized engine-inlet operating conditions is substantially higher than the minimum measured values.

The two-dimensional inlet model was instrumented in a manner similar to the axisymmetric model. Measurements of static pressure at the cowl lip station and of inlet mass-flow ratio permitted calculation of the momentum terms of the additive-drag equation. The ramp and side-wall drag values were obtained from static-pressure measurements on these surfaces. Figure 7 shows the variation of engine-face total-pressure recovery and inlet additive-drag coefficient with inlet mass-flow ratio. Included in the figure is a sketch of the inlet showing the cowl lip located slightly forward of the minimum throat station. Also indicated are other geometric features of the configuration, that is, ramp, sharp cowl lip, and extended side walls. Results are shown for tests with and without boundary-layer bleed on the ramp and side-wall surfaces in the throat region. The bleed increased the total-pressure ratio and the maximum mass-flow ratio considerably at Mach numbers of 1.0 and 1.275. Losses at a Mach number of 1.275 remain relatively high, however, and suggest that substantial friction effects were present. Note that the use of boundary-layer bleed does not change the basic curves of additive-drag coefficient. This should be expected since the bleed surfaces are downstream of the lip station; the data indicate consistency in the additive-drag measurements.

The ability to calculate additive drag theoretically is valuable for inlet design and vehicle performance studies. Figure 8 presents results from theoretical and semiempirical calculations of minimum additive-drag coefficients compared to the experimental values. In this case, the theory is based on the assumption of one-dimensional flow relationships from the free stream to the cowl-lip station and considers theoretical shock losses only. To calculate ramp drag, the ramp pressure was assumed to vary linearly from either free-stream or downstream shock-wave conditions at the ramp leading edge to the inlet conditions at the cowl lip. The basic theoretical curve is in fair agreement with experiment at Mach numbers below 1.0, but agreement is poor at other Mach numbers. However, if experimental ramp and side-wall drag is used in place of that calculated from the assumed linear pressure distribution, agreement is greatly improved. Also, another unrealistic assumption in the basic theory was that only shock losses affect the momentum balance. Figure 7 indicates that the two-dimensional inlet configuration had substantial friction losses at  $M_{\infty} = 1.275$  because of the long perforated ramp and side-wall surfaces forward of the lip station. If these losses are accounted for in the theoretical calculation of conditions at the lip station, the results shown compare reasonably well with those obtained experimentally.

The Ames tests of additive drag on a two-dimensional inlet are summarized as follows. Experimental techniques provide accurate measurements of additive drag. Theoretical predictions of two-dimensional additive drag are excessively high at supersonic Mach numbers unless the ramp drag and total-pressure losses at the inlet lip station are accurately determined.

## Spillage-Drag Measurements

Force-balance measurements of spillage drag on large-scale complete inlet models generally provide only qualitative results. It is inherently difficult to obtain accurate values since the basic model drag forces are large relative to the spillage-drag increments of interest. A model was therefore specially designed and constructed for measuring spillage drag accurately. The tests were conducted so as to ensure maximum accuracy of the results. A photograph of the model mounted in the wind tunnel is shown in figure 9. The test program studied a wide variety of geometric factors affecting the spillage drag of rectangular (two-dimensional) supersonic inlets. Several cowls, side walls, and fixed initial ramps could be interchanged on the model. The second ramp was variable from  $5^\circ$  to  $12^\circ$  relative to the free-stream vector. The model and test results are completely described in reference 5.

One feature of this spillage-drag investigation was the determination of external pressure drag for the cowl plus side wall. Only meager information exists on this important component of the total external drag of two-dimensional inlets. The incremental change in external pressure drag when mass flow is reduced from a reference mass-flow ratio<sup>3</sup> is, of course, the lip suction force which was discussed earlier. Six of the cowl shapes which were instrumented for static-pressure measurements are described in figure 10. Cowls 1, 2, and 3 had circular-arc external surfaces, whereas the remaining three were straight external angle cowls. Cowl and side-wall external pressure drag characteristics for cowls 1, 2, 4, and 6 are shown in figure 11 for a range of mass-flow ratios at Mach numbers 0.84 and 1.29. The ramp angle and the side-wall external angle were held fixed for this comparison at  $5^\circ$  and  $6^\circ$ , respectively. In addition, the side-wall leading edge was cut back at an angle coincident with the initial ramp compression shock wave at a free-stream Mach number of 3.0. All of the cowl shapes yield suction forces which would allow partial cancellation of the additive drag at reduced mass-flow conditions. It is interesting that the drag becomes negative and these surfaces actually produce thrust at mass-flow ratios somewhat less than the reference value. At subsonic conditions ( $M_{\infty} = 0.84$ ) circular-arc cowls 1 and 2 have lowest drag at high mass-flow ratios and straight cowl 6 has the best lip suction capabilities. The curves for Mach number 1.29 indicate that low angle cowls 1 and 4 provide the best performance. At higher supersonic speeds, cowl 4 with the lowest cowl angle provided the best drag characteristics.

Force-balance measurements of total external drag were obtained for various geometric configurations of the spillage-drag model. The incremental change in external drag as the mass-flow ratio is reduced below the reference value is, in effect, the increment in spillage drag (see fig. 1). (This change differs from the incremental change in additive drag by the amount of the lip suction force.) The increment in spillage drag, measured by a force balance, divided by the corresponding change in additive drag is defined as  $K_{ADD}$ , the incremental additive-drag correction factor. The amount of additive drag change which appears as a change in spillage drag is indicated by  $K_{ADD}$  as follows.

---

<sup>3</sup>Reference mass-flow ratio is defined in this case as a value equal to the inlet area,  $A_i$ , divided by the capture area,  $A_c$ .

$$D_{\text{SPILLAGE}} = \Delta D_{\text{SPILLAGE}} + D_{a\text{-REF}}$$

$$D_{\text{SPILLAGE}} = K_{\text{ADD}} \Delta D_a + D_{a\text{-REF}}$$

Figure 12 presents curves of  $K_{\text{ADD}}$  based on theoretically computed values of  $\Delta D_a$  as a function of mass-flow ratio for cowls 4 and 6 (agreement between measured and theoretically computed  $\Delta D_a$  was good for all cowls tested). The figure shows additive-drag corrections at  $M_\infty = 0.84$  are greater (numerically lower), and are affected less by mass-flow ratio than those at  $M_\infty = 1.29$ . Also, these corrections are affected more by Mach number than by the cowl lip shape.

In addition to the results presented, the tests of the spillage-drag model provided the following information.

1. Lower spillage drag was obtained by rotating the external ramp of the inlet, to deflect excess airflow, than by rotating the cowl. However, the combined rotation of both cowl and ramp would provide the lowest spillage drag.

2. Blunting the leading edge of a  $10^\circ$  circular-arc cowl with 0.040-inch and 0.100-inch radii had little effect upon additive-drag cancellation but increased total external drag chargeable to the inlet.

3. Ramp pressure drags and cowl plus side-wall external drag measured for a number of configurations are useful in determining total inlet drag penalties.

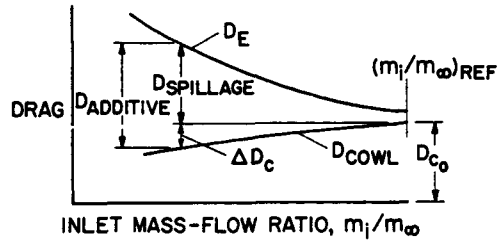
4. Mathematical models for computation of theoretical additive drag, that were devised and programmed for computer usage, were confirmed by the test results.

#### REFERENCES

1. Mount, Joseph S.: The Effect of Additive Drag Upon Aircraft Performance. Paper No. 64-599, Am. Inst. Aeron. Astronaut., Aug. 1964.
2. Davis, Wallace F.; and Scherrer, Richard: Aerodynamic Principles for the Design of Jet-Engine Induction Systems. NACA RM A55F16, 1956.
3. Sibulkin, Merwin: Theoretical and Experimental Investigation of Additive Drag. NACA Rept. 1187, 1954. (Supersedes NACA RM E51B13.)
4. Davis, Wallace F.; and Gowen, Forrest E.: The Change With Mass-Flow Ratio of the Cowl Pressure Drag of Normal-Shock Inlets at Supersonic Speeds. NACA RM A56C06, 1956.

5. Petersen, Martine W., and Tamplin, Gordon C.: Experimental Review of Transonic Spillage Drag of Rectangular Inlets. AFAPL-TR-66-30, U.S. Air Force, May 1966.
6. Sorensen, Norman E., Anderson, Warren E., Wong, Norman D., and Smeltzer, Donald B.: Performance Summary of a Two-Dimensional and an Axisymmetric Supersonic-Inlet System. Paper No. 11, NASA Conference on Aircraft Aerodynamics, May 1966.

### INLET SYSTEM DRAG DEFINITIONS



THE EXTERNAL DRAG OF AN INLET SYSTEM IS  $D_E$

$$D_E = D_{COWL} + D_{ADDITIVE} = D_c + D_a$$

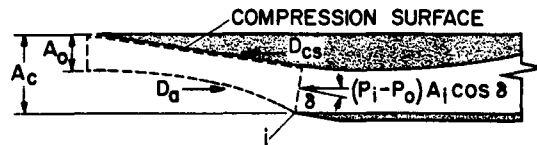
$$D_c = D_{c_0} - \Delta D_c$$

$$D_E = D_{c_0} - \Delta D_c + D_a$$

$$D_{SPILLAGE} = D_a - \Delta D_c$$

Figure 1

### ADDITIVE DRAG



CONSIDERING THE ENTERING STREAM TUBE ELEMENT

NET FORCE = MOMENTUM CHANGE

$$D_a - (P_i - P_0) A_i \cos \delta - D_{cs} = m_i (V_i \cos \delta - V_0)$$

TOTAL MOMENTUM

$$D_a = m_i (V_i \cos \delta - V_0) + (P_i - P_0) A_i \cos \delta + D_{cs}$$

$$C_{D_a} = \frac{D_a}{q_0 A_c}$$

Figure 2

AXISYMMETRIC INLET PERFORMANCE

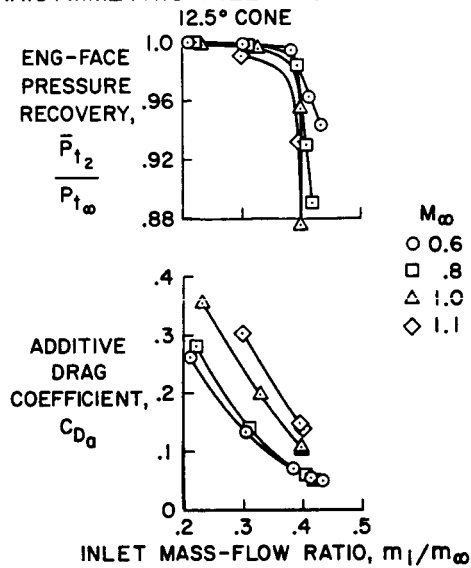


Figure 3

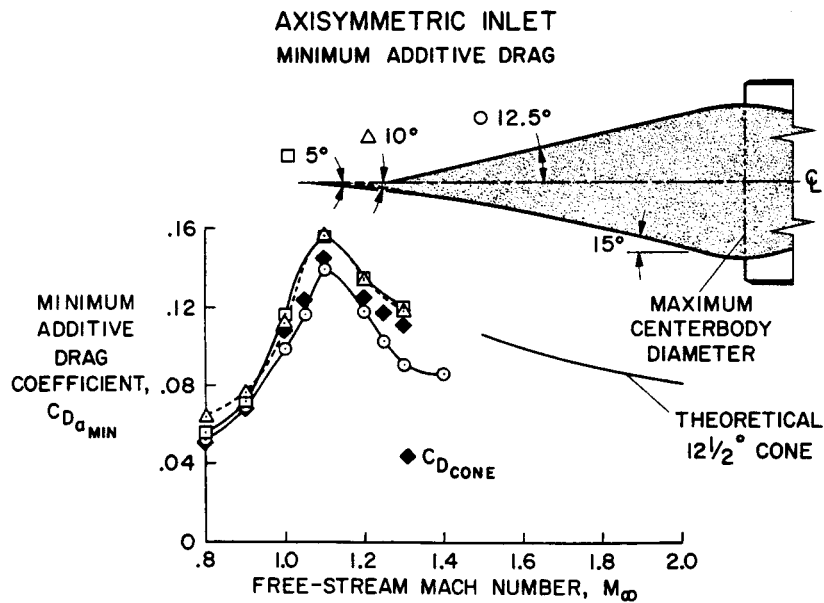


Figure 4

AXISYMMETRIC INLET  
TYPICAL CONE STATIC-PRESSURE RATIOS

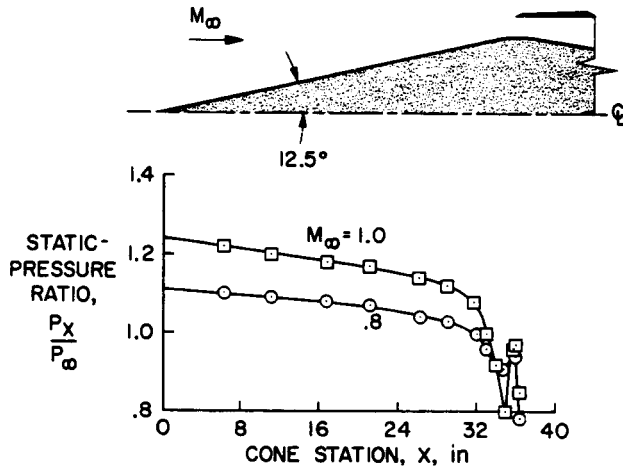


Figure 5

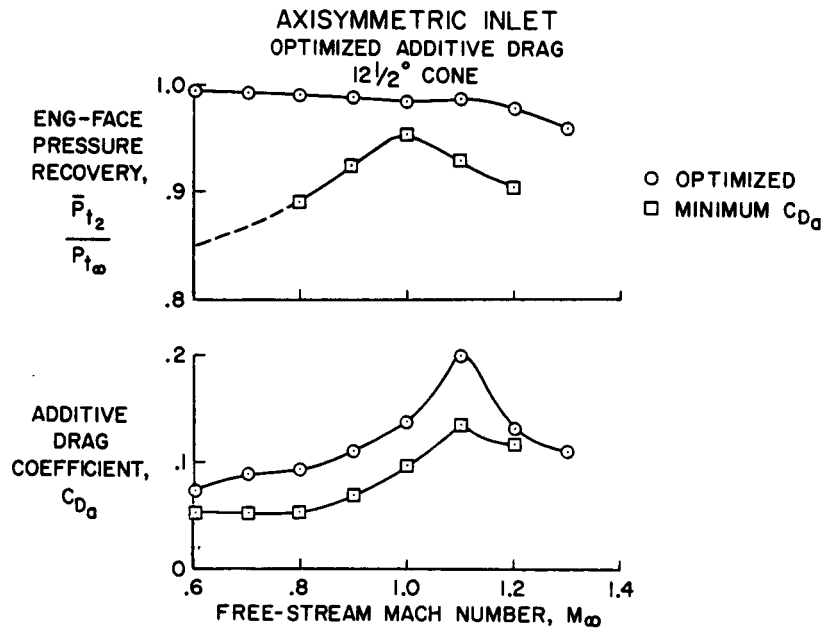


Figure 6

TWO-DIMENSIONAL INLET PERFORMANCE

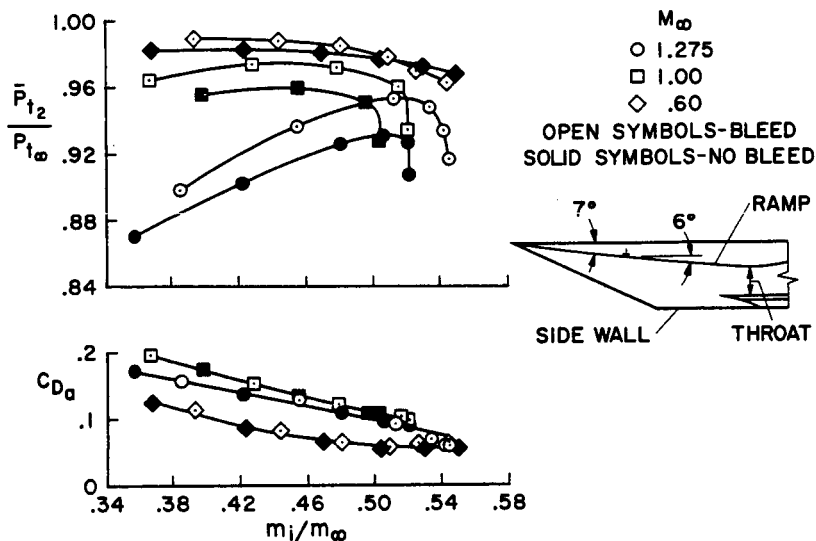


Figure 7

TWO-DIMENSIONAL INLET  
THEORETICAL ADDITIVE DRAG

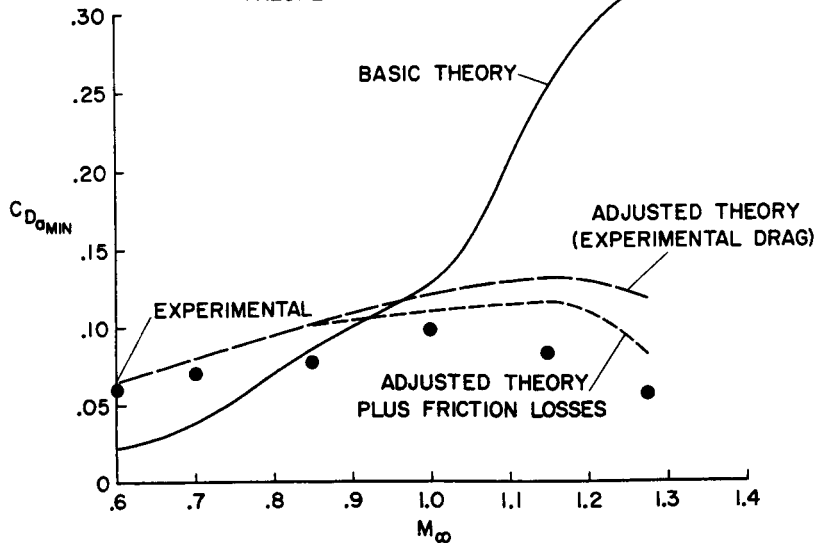


Figure 8

SPILLAGE-DRAG MODEL  
INSTALLATION

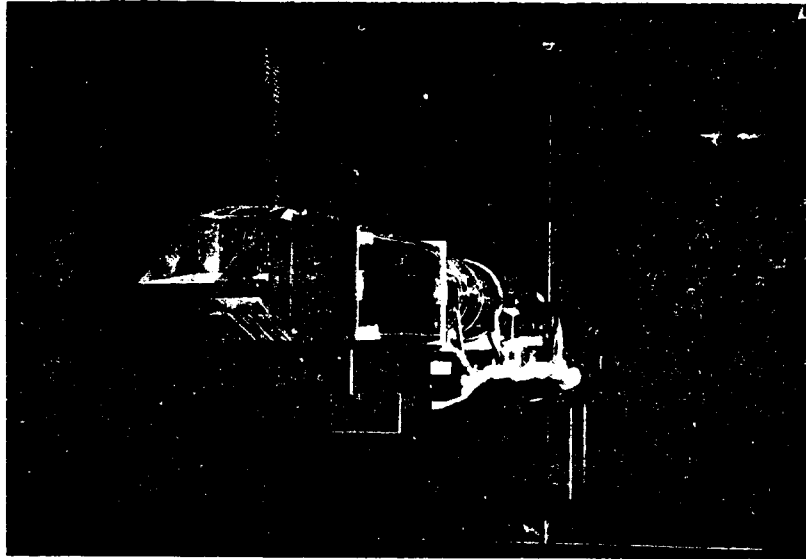
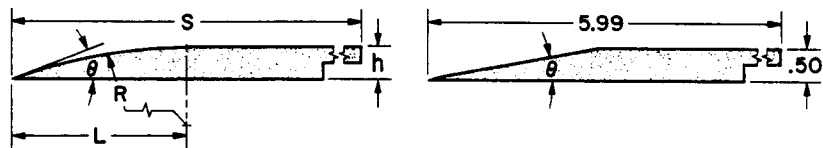


Figure 9

A-35112

SPILLAGE-DRAG MODEL  
COWL LIP SHAPES



COWL	L	R	$\theta$	S	h
C1	5.71	32.9	10°	5.99	0.50
C2	3.79	14.7	15°	5.99	.50
C3	7.95	29.3	15°	7.99	1.00

COWL	$\theta$
C4	6°
C5	10°
C6	15°

ALL DIMENSIONS IN INCHES

Figure 10

SPILLAGE-DRAG MODEL  
COWL PLUS SIDEWALL PRESSURE DRAG

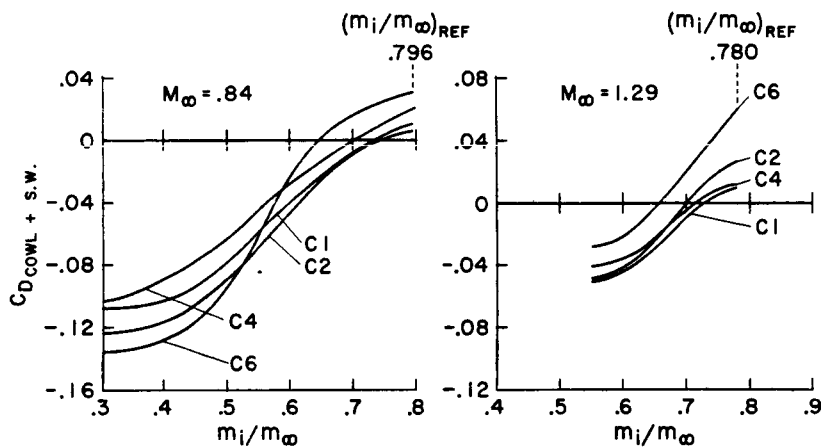


Figure 11

SPILLAGE-DRAG MODEL  
INCREMENTAL ADDITIVE DRAG CORRECTION FACTOR

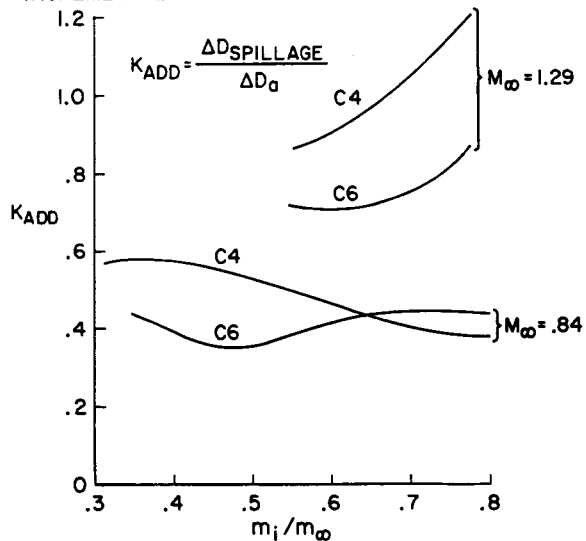


Figure 12

### 13. INITIAL FLIGHT EXPERIENCE WITH THE XB-70 AIR-INDUCTION SYSTEM [U]

By Ronald H. Smith and William G. Schweikhard  
NASA Flight Research Center

#### SUMMARY

The preliminary results and developmental problems from flight tests of the XB-70 air-induction system are briefly reviewed. The system is generally satisfactory, is adequately matched to the engine flow requirements, and can be controlled for the various flight ranges. Inlet unstarts at cruise Mach number constitute a new problem for high supersonic aircraft seriously affecting the dynamics of the inlet and airframe.

#### INTRODUCTION

The two XB-70 airplanes have been flying for many months. Even though many flights have been conducted for the purpose of developing and demonstrating the airplane systems, a significant amount of research data has been obtained. The importance of inlet performance and its direct influence on overall vehicle performance has been very apparent during the early XB-70 experience as it surely will be on future airplanes incorporating similar air-induction systems.

Future air-breathing aircraft cruising at Mach numbers of 2.2 and greater will very likely incorporate mixed compression inlets for better propulsive efficiencies. The XB-70 air-induction system is one of the first of this type to reach flight status. The initial experiences with the performance and operation of the inlet are reviewed in the present paper. This paper presents some of the operational experience with the air-induction system of the XB-70 airplanes acquired during their initial flights. The physical characteristics and principles of operation of the inlet are described, and the test ranges in regard to vehicle and inlet configuration are given. A summary of the inlet performance achieved to date is presented. Finally, there is a brief discussion of inlet problems, many of which have resulted as a part of the early effort to investigate the operating envelope of the inlet and to check out its control system.

#### DISCUSSION

Figure 1 is a photograph of one of the XB-70 airplanes in low Mach number flight alongside a chase plane. Note the proportion of the XB-70 integrated inlet-engine system to total airplane volume. The length of the inlet from the leading edge to the compressor face is about 90 feet. The primary duct is large enough for a man to walk upright almost to the engines.

A large number of supersonic flight hours have been flown with the two XB-70 airplanes. Both have flown to Mach number 3 with the number two airplane flying most of the high supersonic flights. The more significant flight hours from the inlet viewpoint are those obtained at speeds above Mach number 2 where the inlet is started, which means that supersonic flow exists in the forward part of the duct and a normal shock exists downstream of the inlet throat. In this region the operation of the inlet system becomes more critical in that it affects not only the efficiency of the propulsion system but also the dynamics of the airplane. Thus, a preponderance of inlet testing has been done in this region as evidenced in figure 2. The enclosed area is the envelope of overall flight experience to date. Symbols are used to represent major planned and unplanned inlet events as follows: unstart, a rapid expulsion of the internal normal shock; duct buzz, an unstable cyclic flow variation associated with an unstarted condition; engine compressor stalls; and miscellaneous events attributed to the air-induction control system and affecting the vehicle or engines. An example of the latter would be a rapid inadvertent opening of the main bypass doors resulting in a compressor stall. The majority of the unstart data points shown have been intentionally induced as part of the testing and development of the air-induction system.

As would be expected, most of the data points designating inlet events lie between Mach numbers 2 and 3, where most inlet testing has been done. The lower Mach number areas have been investigated in many previous airplanes and have not been the concern of the present program. Some of the data points may be grouped together into a series of related events which occurred sequentially during a single flight. For example, the events that are connected by the line were initiated when a piece of structure was ingested into the duct at Mach number 2.6 and an altitude of 62 000 feet, resulting in multiengine stalls, engine shutdown, unstart, and sustained buzz. The events extended over 6 minutes after which the vehicle was stabilized at Mach number 1.7 and an altitude of 45 000 feet. Inlet airflow interrelationships with engines and airplanes become important in the integrated XB-70 air-induction system as illustrated in figure 3. Shown are details of the left inlet airflow system. At cruise Mach number, about 81 percent of the airflow which enters the inlet is channeled as primary flow and actually enters the engines. About 16 percent is bled off by the extensive boundary-layer control system which rejects the undesired air in three ways. Boundary-layer plenums I and II reject air overboard directly behind the nose-wheel-well fairing, reducing the base drag in that region. Plenum IV air is rejected overboard through a fixed set of louvers. Plenum III air is channeled far aft into the engine region and is used for engine cooling or is rejected into the base region, reducing base drag. About 3 percent of the primary inlet air passes into the bypass plenum region through large perforations in the duct walls and is rejected through nozzles formed by the bypass doors in the upper wing surface or is ducted aft and used for engine cooling. The flow system exemplifies the sophistication required of the inlet to match airflow requirements of the engine, to remove boundary layer efficiently, and to reduce inlet drag.

The requirements for efficient shock-system control are illustrated in figure 4, a top schematic view of the left inlet. The vertical two-dimensional inlet achieves compression by means of a series of interacting oblique shock

waves in the external and forward internal regions of the inlet duct, designating it a mixed compression inlet. The flow, reduced in Mach number by the shock system, traverses the inlet throat and becomes subsonic on passing through a normal shock. The strength of this normal shock, which is closely associated with the shock position, has a direct effect on performance of the inlet.

In order to maintain the desired shock system, a series of controlled movable ramps are positioned for optimum inlet performance. The bypass door areas are controlled to match the airflow requirements of the engines and to position the terminal shock by varying the duct back pressure. As the shock is positioned farther forward toward the throat, higher total-pressure recovery is achieved with resultant higher engine performance. However, a stability limit is approached at which the inlet may unstart. In some unstart cases, duct buzz may also occur. In either event, the performance of the inlet is reduced and, in addition, the effect of the inefficient and transient spillage of air may result in additional drag and require vehicle control inputs by the pilot. To avoid such events the inlet may be configured in a lower performance but more stable mode, with the shock farther downstream. When the inlet is started, the inlet throat height varies automatically with Mach number in accordance with a schedule which may be deviated to a low, intermediate, or high setting. The bypass-door control senses a pressure ratio in the throat region and controls the shock to a low, intermediate, or high performance setting which corresponds roughly to an aft, mid, or forward shock position. Many recent flights have been in the upper intermediate range and a few have been attempted at high performance. Some stabilized flight points are shown in figure 5 in relation to the unstart and restart boundaries experienced during wind-tunnel tests. The unstart margin is a function of both throat and bypass door settings. The unstart line shown in the figure is for throat-induced unstarts or the throat choking limit. These margins are being investigated in flight. The center line is the center of the intermediate flight operating range. The deviation of the points from the inlet throat schedule indicates the range of testing that has been conducted to explore the inlet flight envelope. Most of the points are well away from the unstarted region and reflect the general trade off which has been taken to insure stable operation. The degree to which this stability margin results in a reduction in inlet performance is illustrated in figure 6.

Shown are flight points of total-pressure recovery, primarily in the range for a started inlet. The main point to be drawn from these preliminary flight data points, achieved under essentially steady-state conditions, is that a wide range of performance is possible. In order to avoid inlet problems, a conservative approach was taken in the early developmental program by operating in the lower performance modes. These earlier flight points fall mostly below the shaded intermediate region. As flight experience is gained, higher performance points are being obtained.

At this interim point in the program it is not possible to state with confidence just what the maximum practical pressure recovery will be for cruise conditions. The predicted cruise goal is shown as a solid symbol in figure 6. (See ref. 1.) The data at the moment appear to be somewhat short of the predicted values, but it should be remembered that systematic tests to determine the inlet performance limits have not been accomplished. Furthermore, many of

the systems of measurement on which inlet data depend are not as thoroughly calibrated and checked out as they will be later in the research phase of the program.

Finally, it should be noted that the flight data are taken only at engines 1 and 3, whereas the wind-tunnel data are taken at all three engine positions. (See refs. 2 to 4.) Quarter-scale wind-tunnel tests indicate higher pressure recoveries at the center engine position than at the other two. However, at a Mach number of 3 the differences are small and the correlation with flight is insufficient to permit an estimation of flight conditions for the center area with any degree of confidence.

The comparison between the wind-tunnel test and aircraft operating levels of recovery illustrates the importance of the inlet performance to stability trade off. Higher recovery has been achieved recently in flight in the high performance mode, but the time at Mach number 3 has been limited. These recent attempts to approach the better recovery at high settings have been accompanied by a greater incidence of unstart and some engine stalls. As these problems are resolved higher operational recoveries are anticipated.

Figure 7 presents another measure of inlet performance - distortion, which is defined as the difference between the highest and lowest total pressures at the engine compressor face divided by the average total pressure. Shown as shaded area is an envelope of distortions for the steady-state flight test points to date. Two typical flights are shown within the envelope. The distortion is, in general, low for high supersonic airplanes today which possibly accounts for the rather low incidence of compressor stall experienced with the XB-70 engines. The engine limit lines specified earlier in the program are shown for reference purposes. The presently used limit lines are defined by a different weighting method than shown here.

The general distortion trends suggest some areas for investigation. The high transonic peak may be associated with the initial inlet shock attachment point or the early bypass door movements. The bypass door schedule probably influences distortion and recovery in the region of the second peak above Mach number 2 when first controlling shock position. The distortion above Mach number 2 is influenced by such things as diffuser exit Mach number, boundary-layer interactions in the duct, and a diminishing bypass area as Mach number 3 is approached. These effects will be investigated in flight by a series of carefully controlled tests.

Most of the in-flight performance described in the previous figures had been predicted by the extensive series of wind-tunnel tests, but many of the installation and operational effects did not come forth until the inlet was incorporated into the full-scale flight vehicle.

Foreign-object damage (FOD), always a problem for air-breathing airplanes, has been unusually severe for the XB-70. FOD on such an inlet can become a more serious problem than just engine damage. An example was given earlier in which FOD triggered a series of events.

A different type of problem with foreign material was uncovered as a result of a recent flight to Mach number 3 at an altitude of approximately 70 000 feet in which both inlets unstarted. After the flight, the bleed holes in the boundary-layer removal areas on the throat ramps were found to be clogged. Apparently, compound used for polishing the inlet had filled portions of the porous surfaces containing bleed holes as small as three-hundredths of an inch. Resultant bleed flow blockage was a contributor to the instability of shock position which led to a double unstart at Mach number 3.

In spite of the fact that engine stalls have not been a problem with the XB-70, there is concern over the possibility of stalls in mixed compression inlets, particularly short inlets, because they can cause unstarts to occur.

Engine-induced stalls have not been as frequent as those caused by the inlet disturbances. Increased distortion as a result of an improper bypass door operation has been cited as the cause of stall in one case. Another more surprising stall occurred with the engine well within the stable operating region. It is suspected that noise associated with inlet duct internal turbulence as a result of a low performance inlet setting triggered the stall. Turbulence such as this is being investigated by the engine and airframe manufacturers to better understand and interpret the effects on the engine and its control system. Some spurious control signals have been experienced. The buzz indicator, which senses a pressure far downstream in the duct, is presently deactivated from the inlet control system. The reason is that during stable inlet operation the inlet cycled for a restart because the buzz sensor interpreted something incorrectly as inlet buzz. The control system commanded the large bypass doors to open in order to restart the supposedly buzzing inlet. Such bypass movements have produced effects on the vehicle nearly as pronounced as true unstarts. Restart cycles of the inlet control system have also happened when there were no unstarts. The cause of a series of spurious restart cycles was traced to a transient voltage which induced a signal to the inlet control system resulting in the restart cycle. Spurious control signals, whether aerodynamically, electrically, or mechanically induced, are a problem.

Of particular interest, are the effects of unstart and the corrective action of the inlet control system on the vehicle. Inlet unstart, and subsequent restart cycle, is as serious a problem to the control of the airplane as it is to the performance of the inlet. In figure 8 is shown a double unstart that occurred during a turn at Mach number 3. The left duct unstarted 2 seconds after the start of the time history and the right duct unstarted 11 seconds later. The change in pressures under the left wing caused by the expulsion of the normal shock forward of the inlet lip combines with the opening of the bypass doors, which act essentially as elevons, to produce an increase in the normal acceleration. The pilot counters this pitching motion with a longitudinal control input of approximately 3° nose-down elevon. Without this input the airplane would have pitched to a higher load factor. Likewise, loss of thrust, increased spillage drag, and the opening of the bypass during the restart cycle caused a longitudinal deceleration of approximately 0.1g. Perhaps even more significant than the steady-state deceleration is its rate of onset, or jerk, which is very nearly a 0.1g step function. The unstart and door movements also affect the lateral control of the airplane causing it to

roll toward the side that has unstarted. The pilot's corrective action prevents the roll rate from becoming large but there is a noticeable change in bank angle. There have been a number of false unstarts with similar effects on the airplane. It has been suggested that this unstart was caused by foreign material in the boundary-layer bleed holes but recent experiences with additional double unstarts at Mach numbers from 2.7 to 3.0 have shown this to be only a partial answer.

#### CONCLUDING REMARKS

The XB-70 air-induction system is generally satisfactory, is adequately matched to the engine flow requirements, and can be controlled for the various flight ranges. The large size of the duct and the arrangement of the engines probably contribute to the unusual amount of foreign-object damage experienced. Flow distortion at the compressor face is well within the permissible range and has been insufficient to cause engine performance loss at most flight conditions. Inlet unstarts at cruise Mach number constitute a new problem for high supersonic aircraft seriously affecting the dynamics of the inlet and airframe. The noise, like a muffled explosion, and the aircraft gyrations are unacceptable for pilot and crew.

The allowable in-flight margins between inlet stability and optimum performance in flight including effects of turbulence, passing shocks, and other disturbances will be evaluated and compared with wind-tunnel experience, theoretical predictions, and computer simulations in a joint NASA/USAF XB-70 program.

#### REFERENCES

1. Wolfe, J. E.: Propulsion System Performance Substantiation Report for the XB-70A Air Vehicle (YJ93-GE-3 Engines). NA-64-674 (Contract AF33(600)-42058), North Am. Aviation, Inc., [1964].
2. Bowditch, David N.; and Anderson, Bernhard H.: Investigation of the Performance and Control of a Mach 3.0, Two-Dimensional, External-Internal-Compression Inlet. NASA TM X-470, 1961.
3. Chew, W. L.; and Daniel, B. R.: Wind Tunnel Investigation of the 0.577-Scale B-70 Inlet. AEDC-TDR-62-244, U.S. Air Force, Jan. 1963.
4. Butler, C. B.; Graham, F. J.; Hartin, J. P.; and Daniel, B. R.: Investigation of the 0.25-Scale B-70 Variable-Geometry Inlet at Mach Numbers From 0.60 to 1.40. AEDC-TN-61-72, U.S. Air Force, July 1961. (Available from DDC as AD 324 192.)

# XB-70 IN FLIGHT

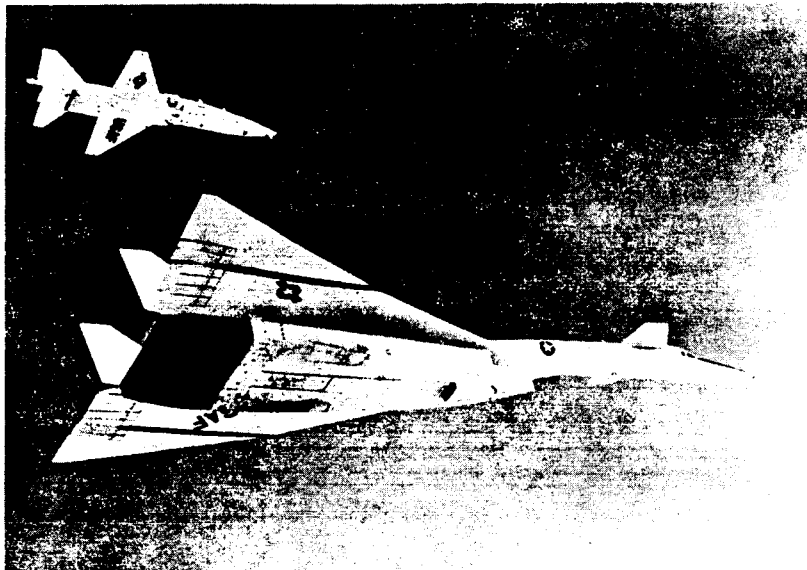


Figure 1

## AIR-INDUCTION-SYSTEM EVENTS

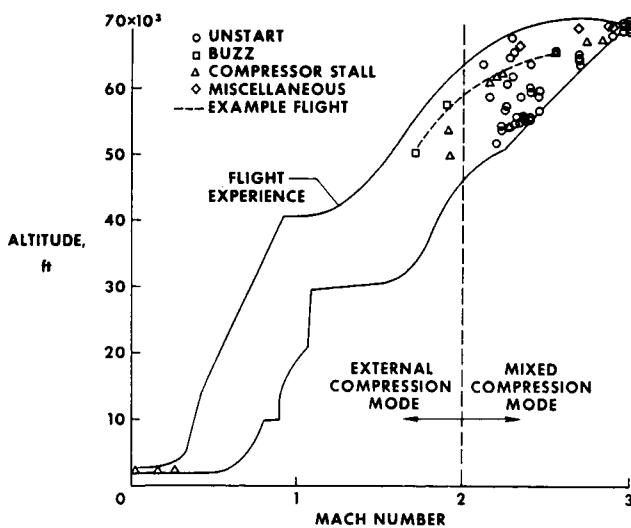


Figure 2

### AIRFLOW SYSTEM LEFT INLET

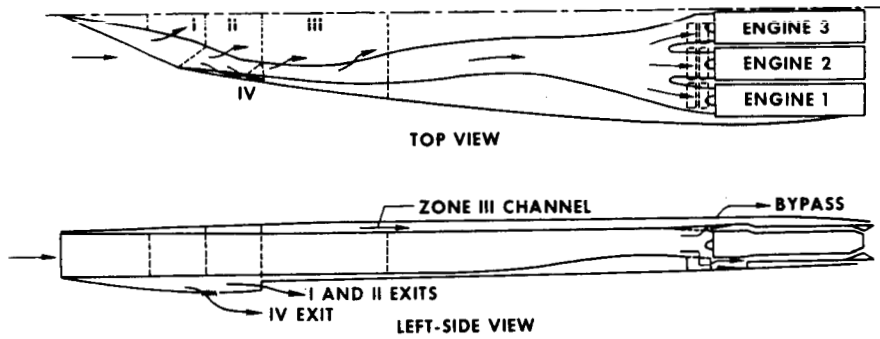


Figure 3

### XB-70 INLET SCHEMATIC TOP VIEW, LEFT SIDE

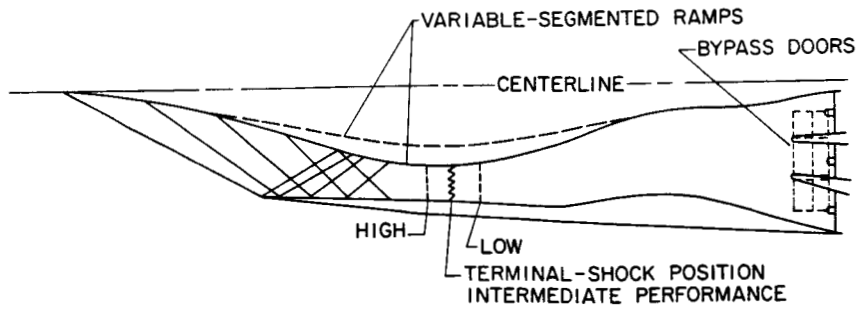


Figure 4

### INLET OPERATING REGIONS

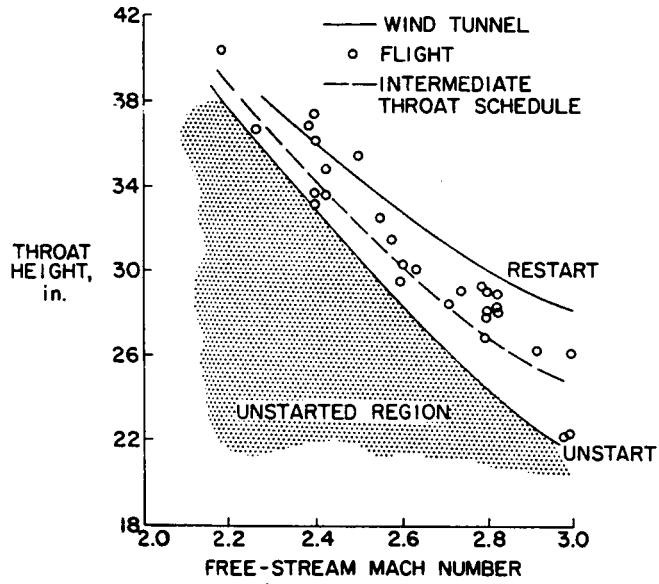


Figure 5

### TOTAL-PRESSURE RECOVERY AS A FUNCTION OF MACH NUMBER

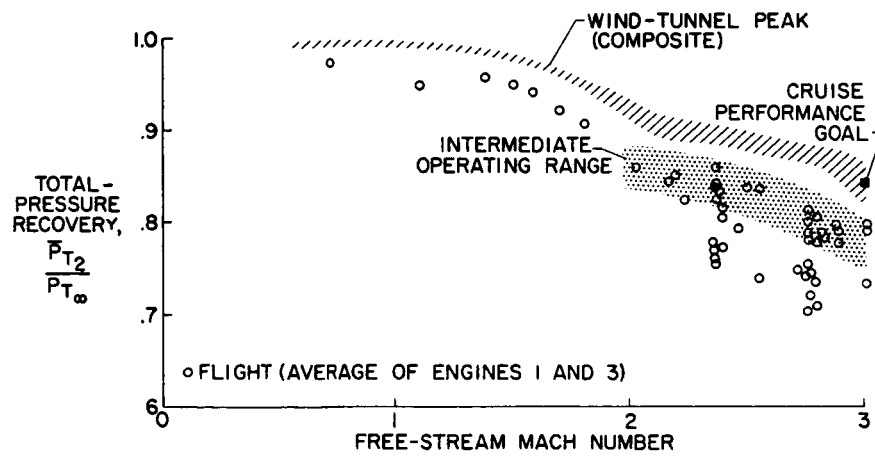


Figure 6

**DISTORTION**  
AVERAGE OF ENGINES 1 AND 3

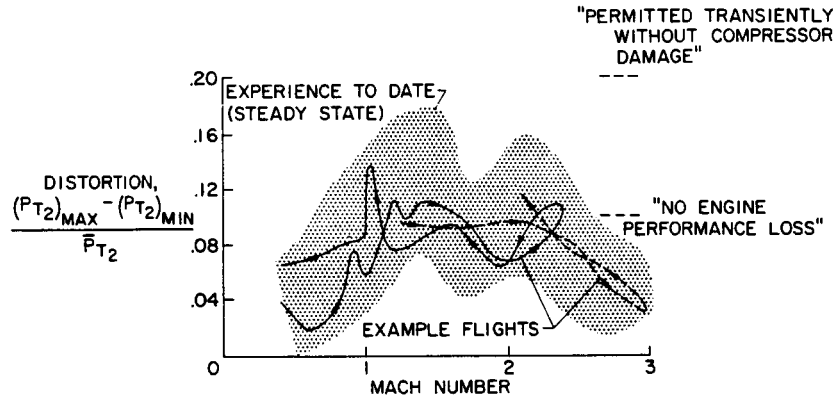


Figure 7

**MACH 3 DOUBLE UNSTART**

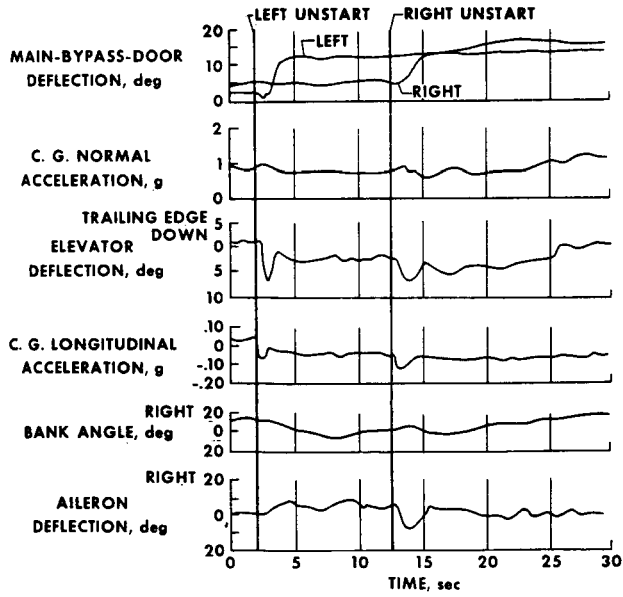


Figure 8

14. A STUDY OF THE PROBLEMS OF CONTROL OF  
A SUPERSONIC INLET

By John J. Gawienowski, and John L. Benson<sup>1</sup>  
NASA Ames Research Center

SUMMARY

A major problem in operating internal contraction inlets on supersonic aircraft is preventing inlet unstart due to terminal shock instability. Factors contributing to this problem, such as the dynamic response of an inlet to internal and external disturbances and performance characteristics of inlet controllers, were investigated. The results of the investigation showed that for the given inlet design and its idealized control system, a stability margin corresponding to less than 1-percent reduction of pressure recovery would prevent inlet unstart by the simulated disturbances, and that the dynamic and static characteristics of the current state-of-the-art inlet controllers would adequately meet the requirements of a control system for a supersonic mixed-compression inlet. A comparison of an analytical inlet model with experimental results showed very good agreement.

INTRODUCTION

A major problem in the operation of a mixed compression inlet on a supersonic aircraft is inlet unstart due to terminal shock instability. To achieve high efficiency of the propulsion system it is necessary to maintain the terminal shock close to the inlet's aerodynamic throat. The necessary stability margin, the distance from the throat at which the terminal shock must be positioned to prevent unstarting, is a function of the amplitude and frequency of the flow disturbances, the dynamic characteristics of the inlet, and the response and static accuracy of the control system. To examine each of these factors, a research program was undertaken by Ames through a contract with the Lockheed-California Company. The program objectives are presented in figure 1. The research effort was divided into three major areas: the wind-tunnel testing of a controlled axisymmetric inlet to determine the response of the terminal shock when subjected to simulated internal and external disturbances; the bench testing of representative state-of-the-art inlet controllers to determine their performance characteristics; and finally, a comparison of the response of an analytical representation of the inlet system with experimental data. A detailed description of the test equipment, procedure, and results is presented in reference 1.

---

<sup>1</sup>Lockheed-California Company.

## SYMBOLS

$m_2/m_{\infty}$	engine-face mass-flow ratio
$M_{\infty}$	free-stream Mach number
$P_{12}$	static pressure, on centerbody aft of throat
$P_{t_2}/P_{t_{\infty}}$	engine-face total-pressure recovery
$\alpha$	angle of attack

## DESCRIPTION OF MODEL

The axisymmetric mixed-compression inlet model tested is shown in figure 2. The inlet incorporates three boundary-layer-bleed plenums on the centerbody and two on the cowl, and is instrumented with 45 dynamic pressure transducers and 281 static pressure orifices. The cowl sleeve can be translated to vary contraction ratio and the aft sleeve can be translated to regulate exit mass flow. Probes were located at the cowl lip to measure local Mach number. The measured steady-state performance of the inlet shown in figure 3 is representative of the current  $M = 3.0$  inlet state of the art. The maximum pressure recovery is 88 percent with a bleed mass-flow ratio of approximately 8-1/2 percent.

Figure 4 is a schematic drawing of the inlet and its controls. The model is equipped with a variable bypass valve located at the simulated engine face station and a variable aft-exit valve. Both valves can be scheduled to perform various time-dependent displacements controlled from a small analog computer or a signal generator. The analog computer also served as an idealized inlet controller in a closed-loop shock position control system in which static pressure orifice  $P_{12}$  provided the control signal. For this control mode, the switches in figure 4 are closed. During this phase of the investigation, the bypass valve responded to an error signal proportional to the difference between the steady state and the disturbed shock position. The flow disturbances were generated internally by the aft exit valve and externally by the disturbance airfoil.

Figure 5 is a photograph of the airfoil installed in the Ames 8- by 7-foot wind tunnel. The airfoil has a rectangular planform which spans the test section. It is supported at the center by a strut mounted from the tunnel ceiling and at each tip by journal bearings which permit rotation in angle of attack. The airfoil is located far enough upstream for the inlet to operate in the "far" field produced by the airfoil when it is oscillated through angle of attack. The mechanism for oscillating the airfoil operates through the center strut.

## DESCRIPTION OF DISTURBANCES

Figure 6 lists the internal and external disturbances investigated in the test program. The internal disturbances considered were: simulated engine disturbances, such as a throttle advance or afterburner blowout, and sinusoidal oscillations of the exit mass flow. These engine transients were chosen to be investigated because of their relatively large amplitudes and short periods. The time history variations of engine airflow were obtained from the General Electric Company. The external disturbances investigated were: a simulated atmospheric gust, a simulated shock wave from passing supersonic aircraft, and sinusoidal oscillations of the disturbance airfoil. The gust was investigated because it is believed to be the most common atmospheric disturbance, and because it is known to cause occasional large perturbations. It was treated as a discrete phenomenon with a cosine variation of Mach number representing a 1.5-percent change in local Mach number. Because it was not possible to vary wind-tunnel temperatures rapidly gusts due to free-stream temperature changes could not be simulated. The passing shock wave was investigated because it was believed to present the strongest probable external disturbance. The time history variation of external pressure, which represented a  $\pm 1$  percent change in local static pressure, was determined from sonic boom measurements.

To obtain the inlet's dynamic characteristics the response of the inlet's terminal shock to sinusoidal oscillations of the exit plug or of the disturbance airfoil was determined before the engine and atmospheric disturbances were simulated. Data were obtained for exit plug frequencies from 1 to 30 cps and disturbance airfoil frequencies from 1 to 20 cps, with the inlet control in both open and closed loop modes.

Test results showed that for both internal and external sinusoidal disturbances the response characteristic of the inlet terminal shock was approximately linear up to 10 cps.

## RESPONSE TO THROTTLE ADVANCE

Figure 7 shows the response of the inlet model to an engine throttle disturbance for both open and closed loop modes. This disturbance was simulated by a reduction in diffuser exit mass flow as shown in the upper plot. The open-loop control mode, with the bypass valve inoperative, is shown as a solid line; the closed-loop mode, with the bypass valve operative is shown as a dashed line. The resulting change in signal pressure,  $P_{12}$ , in pounds per square foot, is shown in the next plot. The response of the terminal shock position, in inches aft of the spike vertex, indicates that the closed-loop mode caused a significant reduction in terminal shock motion compared with the open-loop mode. All the simulated disturbance tests were made with the terminal shock initially positioned to prevent unstart in the open-loop mode. This procedure was adopted because earlier tests had indicated that the location of the boundary-layer-bleed system, relative to the terminal shock, could appreciably affect the terminal shock motion. Therefore, it is

probable that the shock movement in the closed-loop tests is less than it would be if the initial shock position were closer to the aerodynamic throat. (The inlet aerodynamic throat, or forward limit of stable shock position, was located 38-3/4 inches aft of the spike vertex.) The bottom plot presents the total pressure recovery variation with time. This plot was derived by taking points on the shock position curve and assuming that the corresponding pressure recovery was that for steady-state conditions with the same shock position. From this plot a stability margin is determined which is defined as the difference in pressure recovery between the initial or steady shock position and the pressure recovery which is indicated at the farthest forward shock position. For the open-loop mode, a stability margin of approximately 1.5 counts of pressure recovery is required to prevent unstart and under closed-loop conditions about 0.1 count is required. These wind-tunnel disturbance tests do not include all the factors that may influence the terminal shock stability margin during actual flight conditions. Because of a lack of data, no provisions were made to simulate engine and structure noise, forebody turbulence, or controller time constants.

The afterburner blowout test results showed that the open-loop mode requires a stability margin of 1.2 counts of pressure recovery and the closed-loop mode requires a stability margin of about 0.4 count.

#### RESPONSE TO ATMOSPHERIC GUST

Figure 8 shows the response characteristics of the inlet model for both open- and closed-loop modes when the model is subjected to a simulated atmospheric gust. Note that the time scale has been considerably expanded. In the first plot, airfoil angle of attack represents the simulated atmospheric gust disturbance. This scheduled variation of airfoil angle corresponds to the measured steady-state change in local Mach number. The variation in the signal pressure,  $P_{12}$ , and the terminal shock position are shown in the next two plots. In comparing the terminal shock travel for both control modes, it will be noted that the shock motion is greater in the closed-loop mode than in the open loop. This is due to the high phase lag of the closed-loop system of which the major contributing factor is the dynamic characteristics of the bypass exit plenum. The bottom plot presents the derived pressure recovery. For this disturbance the stability margin required for both the open- and closed-loop modes is approximately 0.3 count of pressure recovery. The stability margin requirement is small because of the high frequency of this disturbance. The pressure recovery shows a large momentary decrease in recovery because of the shock passing downstream of the boundary-layer-bleed system into a high Mach number region with the attendant stronger shock — boundary-layer interaction. The downstream movement would be expected to increase the diffuser exit distortion, which, in an actual installation, might result in compressor stall. A large downstream shock movement was experienced during the afterburner blowout disturbance in the open-loop mode, which also would cause an increase in distortion.

The results of the test of a passing shock wave indicate a stability margin requirement of about 0.6 count of pressure recovery for the open-loop mode and 0.4 count for the closed-loop mode.

#### DESCRIPTION OF BENCH TEST SIMULATION

The second objective of the test program was to determine the dynamic and static characteristics of pressure ratio computers which might be used as inlet shock position controllers. A schematic diagram of the dynamic bench test simulation is shown in figure 9. The upper half of the diagram shows the mechanical equipment portion of the simulation which includes a pneumatic function generator to produce the desired signal pressures, a reference pressure, an actual inlet controller, the bypass actuator from the inlet model, and a simulated load on the actuator. The actuator position was transmitted to the analog computer, represented in the lower half of the diagram. This analog representation included the bypass plenum dynamics, simulated engine disturbances, the diffuser dynamics, the resultant shock position output, simulated external disturbances, and signal pressure nonlinearities. The output of the analog computer was directed into the pneumatic function generator to complete the system. Besides the dynamic characteristics of the controllers which were determined in the bench test simulation, various static characteristics were determined, such as gain, linearity, hysteresis, threshold, repeatability, saturation limits, temperature sensitivity, drift, and noise. All these measured static characteristics proved to be satisfactory and, to some degree, similar.

Significant test results obtained are shown in figure 10. The three typical controllers, designated according to their method of computing pressure ratio, are A, an electromechanical unit, B, a hydromechanical unit, and C, a hydropneumatic unit. The chart presents the ratio of closed-loop to open-loop shock travel for the three controllers for the various internal and external disturbances. The shock travel used in the ratios was the minimum travel attainable without causing an inlet unstart. Since the bench-test simulation was performed prior to the wind-tunnel test, it did not incorporate an exact representation of the inlet dynamic characteristics. In addition, a difference in initial steady-state shock position and disturbance periods contributed to the bench test shock travel distances being generally larger than those observed in the wind-tunnel test. The results shown in this chart are, therefore, indicative only of the comparative performances of the controllers. For the internal disturbances the chart shows that the performance of the three controllers was similar and generally satisfactory. The one exception, unit B during the afterburner blowout test, was due to the controller becoming saturated and thereby limiting the velocity of the bypass door. For the external disturbances, units B and C, with slower response rates than A, could not respond to the very rapid disturbances and thereby did not influence the shock travel. The ratios shown for units B and C are greater than 1.0 because the open-loop shock travel distance is very small, about the same order of magnitude as the noise in the system. Unit A, with a relatively fast response, attempted to compensate for the disturbance but only aggravated the condition because it was 180° out of phase at the disturbance frequency. This problem

can easily be rectified; however, it should be recognized that such events can occur. In this case it was advantageous to have a low response controller. It should be mentioned here that these controller units were adaptations of existing hardware and additional modifications can be made to improve their response rates.

#### CORRELATION OF MATHEMATICAL MODEL WITH EXPERIMENTAL DATA

The final objective of the test program was to prepare a mathematical model for an analog simulation of the closed-loop wind-tunnel-test control system. This simulation was similar to that employed in the closed-loop bench test, except that all the wind-tunnel inlet model characteristics were programmed into the analog computer. The simulation was composed of an analytical model of the inlet aerodynamics and the previously measured dynamic characteristics of the bypass, controller, and signal pressure. The bypass dynamics could not be predicted purely on a theoretical basis because of the complex aerodynamic passages of the bypass exhaust system of the model used in this study; the dynamics of the controller were determined from the bench tests because they also are too complex to predict analytically; and the signal pressure dynamic characteristics from a previous wind-tunnel test were used because the analytical model could not predict the observed nonlinearities. Figure 11 shows a comparison between the results from the analog simulation and the wind-tunnel test for a closed-loop control system subjected to a throttle advance. As noted, agreement between simulated results and experiment for this case is very good. Similar results were obtained for the other internal disturbance, indicating the feasibility of conducting accurate analytical studies prior to the fabrication and test of a complete system.

#### CONCLUSIONS

The results obtained from this investigation indicate that for this inlet design and its idealized control system, a stability margin corresponding to a loss of less than one count of pressure recovery would prevent inlet unstart initiated by the simulated disturbances; that the dynamic and static characteristics of the current state-of-the-art inlet controllers would adequately meet the requirements of a control system for a supersonic mixed compression inlet; and analytical models can be developed which will closely correlate with experimental data.

While many useful results were obtained in this study, the need for additional research in certain areas is evident. The most important of these include:

1. Further research to better define the time history variations of pressure, temperature, and velocity in gusts and other types of atmospheric disturbances.

2. Additional research to determine the effects of dynamic inlet flow distortions on engine operation including the modeling of engine stall.

3. Additional testing of an integrated inlet-engine-exhaust system with realistic controls to further define problem areas and substantiate mathematical modeling techniques.

#### REFERENCE

1. Lockheed-California Company: Investigation of Supersonic Transport Engine Inlet Configuration. LR-19014, Lockheed-California Co., Sept. 30, 1965. (Prepared for NASA under Contract NAS2-2363.)

## PROGRAM OBJECTIVES

- INLET DYNAMIC TESTS
- CONTROLLER BENCH TESTS
- COMPARISON OF ANALYTIC METHODS WITH RESULTS

Figure 1

## INLET CONTROLS MODEL

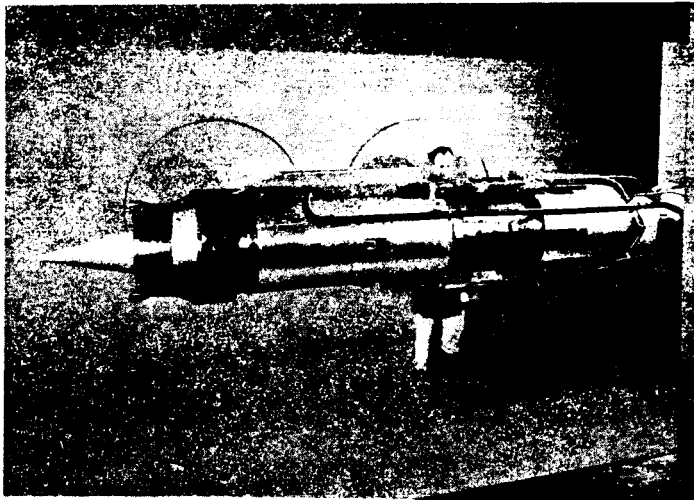


Figure 2

AAA115-2

PRESSURE RECOVERY VERSUS MASS FLOW RATIO

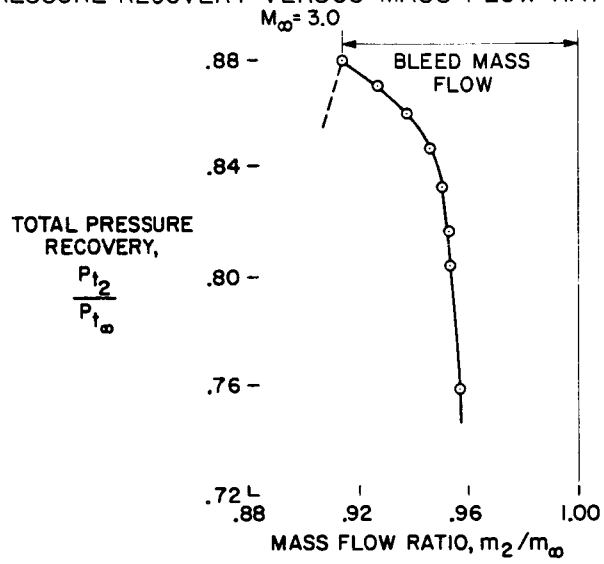


Figure 3

INLET MODEL CONTROL SCHEMATIC

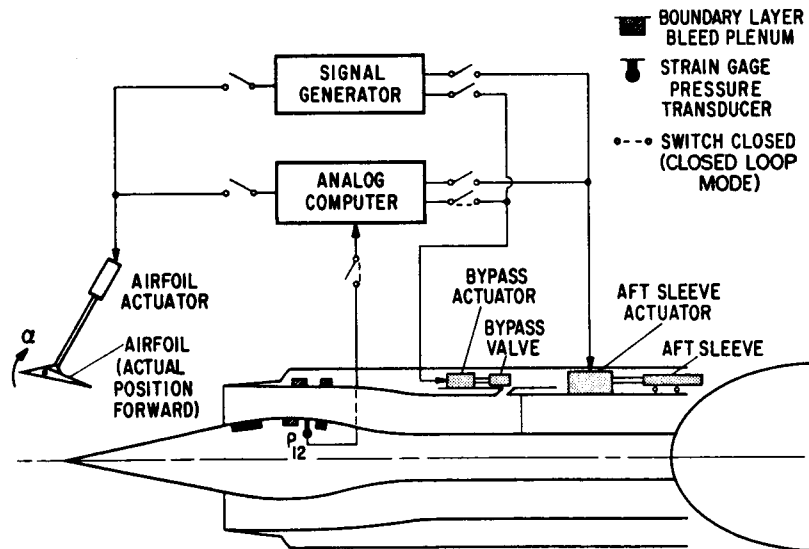


Figure 4

DISTURBANCE AIRFOIL INSTALLED IN  
8x7-ft WIND TUNNEL

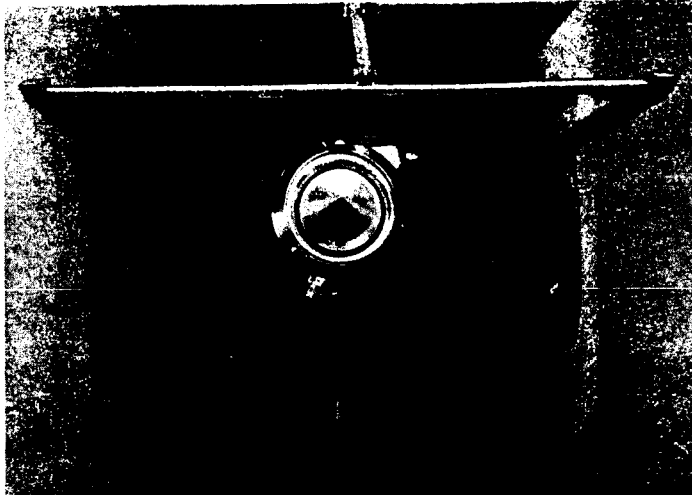


Figure 5

AAA115-5

DISTURBANCES EXAMINED

- INTERNAL DISTURBANCES
  - THROTTLE ADVANCE
  - AFTERBURNER BLOWOUT
  - SINUSOIDS — VARIOUS FREQUENCIES AND AMPLITUDES
  
- EXTERNAL DISTURBANCES
  - ATMOSPHERIC GUST
  - PASSING SHOCK WAVES
  - SINUSOIDS — VARIOUS FREQUENCIES AND AMPLITUDES

Figure 6

RESPONSE CHARACTERISTICS OF INLET MODEL  
TO THROTTLE ADVANCE

$M_\infty = 3.0$

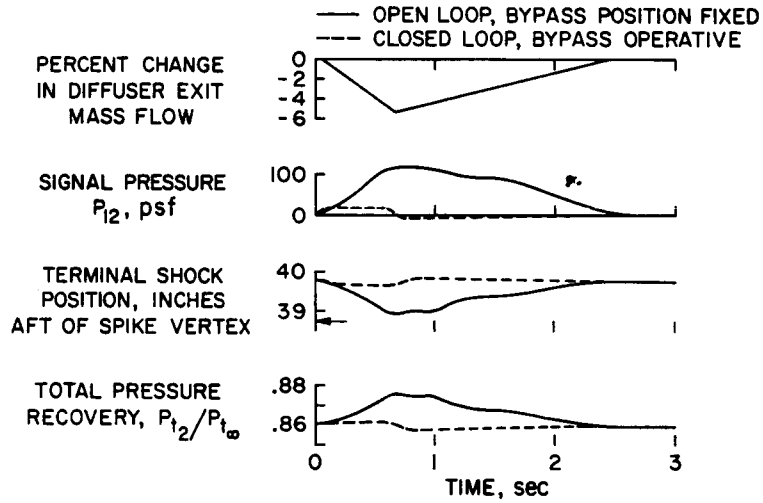


Figure 7

RESPONSE CHARACTERISTICS OF INLET MODEL  
TO ATMOSPHERIC GUST

$M_\infty = 3.0$

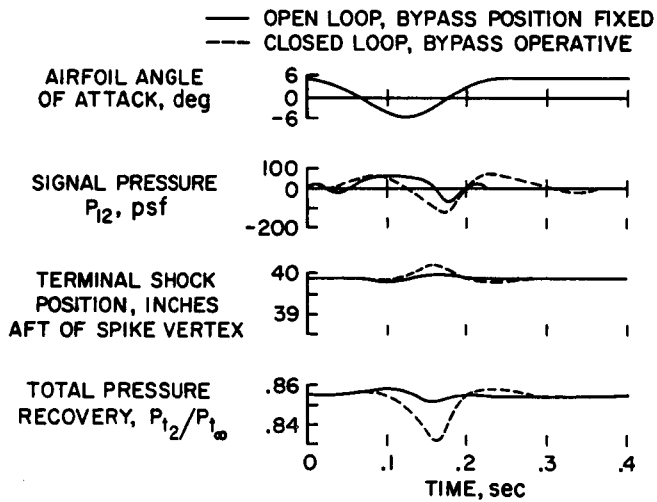


Figure 8

### BENCH TEST SCHEMATIC

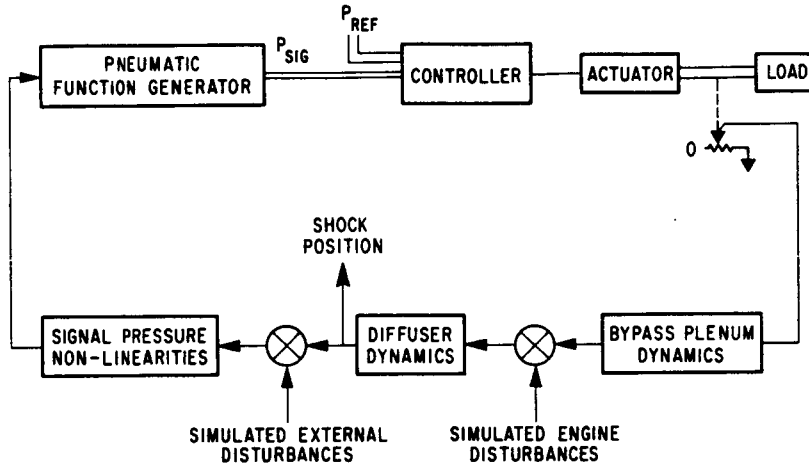


Figure 9

### BENCH TEST RESULTS

DISTURBANCE	SHOCK TRAVEL CLOSED LOOP			
	SHOCK TRAVEL OPEN LOOP			
	A	B	C	
INTERNAL	THROTTLE ADVANCE	.6	.8	.8
	AFTER BURNER BLOW OUT	.5	1.1	.6
EXTERNAL	PASSING SHOCK WAVE	6.0	1.0	2.1
	ATMOSPHERE GUST	9.5	1.4	1.3
	ELECTRO-MECHANICAL	HYDRO-MECHANICAL	HYDRO-PNEUMATIC	

Figure 10

COMPARISON OF WIND TUNNEL DATA AND ANALYTICAL  
SIMULATION RESULTS

$M_\infty = 3.0$

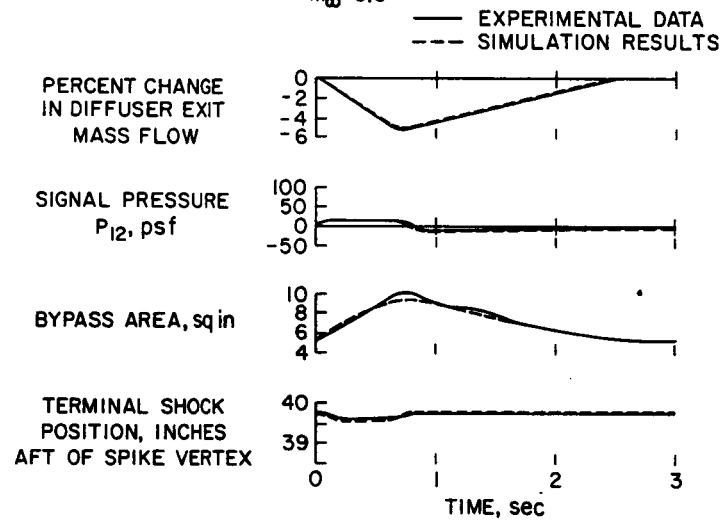


Figure 11

## 15. SUMMARY OF RESEARCH ON JET-EXIT INSTALLATIONS

By Blake W. Corson, Jr., and James W. Schmeer  
NASA Langley Research Center

### SUMMARY

A review is made of recent NASA research on performance of propulsive exhaust nozzles and jet-airframe interference. The importance of off-design performance and nozzle-installation effects is emphasized. Extensive reference is made to papers describing specific research.

### INTRODUCTION

As early as a decade ago, the NACA had made comprehensive studies of aircraft jet-engine exhaust-nozzle performance for nozzles of conventional type such as convergent-divergent ejectors and isentropic spike nozzles. Although the performance penalties associated with off-design operation and jet-airframe interference were recognized problems, primary attention had been directed toward achievement of maximum performance at specified design operating conditions. Representative papers on early research on exhaust nozzles are cited in references 1 to 4.

More recently, development of the variable-sweep concept for aircraft wings and increasing interest in tactical fighter and supersonic transport aircraft have revived general interest in aircraft propulsion, especially in the off-design performance of exhaust nozzles, and in the mutual influence between the propulsion system and the airframe. Research on aircraft propulsion stemming from these interests has produced a sizable volume of information, some of which has not received wide distribution. It is the purpose of this paper to present a brief résumé of recent NASA research on exhaust nozzles and jet effects.

### SYMBOLS

D	drag of external airstream on nozzle components, plus ram drag of nozzle secondary flow
F	nozzle gross thrust
$F_i$	ideal gross thrust of exhaust gases, isentropically expanded to ambient static pressure
L/D	lift-drag ratio

Preceding page blank

M free-stream Mach number  
 $\Delta R$  increment in range  
 $\theta$  discharge angle

## DISCUSSION

### Performance Sensitivity to Critical Parameters

Figure 1 illustrates the importance of exhaust-nozzle performance in relation to other factors which determine overall aircraft performance. The chart is based on a 3500-nautical-mile mission for a 450 000-pound supersonic transport aircraft cruising at a Mach number of 2.7. Increment in range is shown as a function of percentage change in a specified parameter. The parameters considered are: inlet pressure recovery, propulsion package weight, airframe lift-drag ratio, and nozzle gross thrust coefficient. For example, a 1-percent improvement in nozzle gross thrust coefficient will increase the range by 100 nautical miles, in this case by about 3 percent. It is obvious also that nozzle performance has much more influence on aircraft range than the other factors considered. (See ref. 5.)

### Supersonic Transport Fuel Usage

Fuel usage for a typical supersonic transport mission is shown in figure 2. Inasmuch as one-half of the fuel is used in cruise at  $M = 2.7$ , the highest possible nozzle performance must be achieved at that design condition. Note, however, that 35 percent of the fuel (and perhaps the 15-percent reserve fuel) is used in the off-design conditions of take-off, climb, acceleration, letdown, and loiter, so that high performance of the nozzle in off-design operation is also of prime importance and should be achieved without compromising cruise performance.

The expression "off-design" is used herein to indicate values of airspeed and nozzle pressure ratio considerably different from those for which the nozzle design is optimized. For supersonic transport nozzles, "off-design" frequently implies operation at subsonic and transonic speeds. In this sense, much of the exhaust-nozzle research at Langley has been directed toward study of off-design performance.

### Partial Scope of Research on Isolated Nozzles

Figure 3 indicates the scope of some recently completed and current NASA research on isolated exhaust nozzles. The principal types of propulsive nozzles, classified broadly as "open" and "plug," are indicated in this figure along with special features having general application. Any of these nozzles which can provide for efficient expansion of the exhaust gases at high pressure

ratio can be designed to give good performance at a specified design condition. The merit of any particular nozzle type, however, frequently depends upon its ability to operate efficiently at conditions other than design. This quality usually requires variable geometry. Research on terminal fairings for exhaust nozzles is treated in references 6 to 11. In this paper, no attempt is made to summarize the research on noise suppressors (see refs. 12 to 16) or on thrust reversers (see refs. 17 to 27).

### Research Models

Figures 4 and 5 present composite photographs of jet-exit research models investigated in the Langley 16-foot transonic tunnel. Each model incorporated a hydrogen-peroxide gas generator to produce a hot jet properly scaled to simulate the engine exhaust. (See refs. 28 to 30.) Each investigation pertained to the effects of jet operation on afterbody pressures and drag, on aircraft stability and control, and, in some cases, on temperature of airframe components washed by the jet. Description of work conducted with these models is presented in the references as follows: F-11F, references 11, 21, 31, and 32; F-101, references 33 to 35; A-2F(A-6), references 36 and 37; wing-nacelle jet, reference 38; isolated nacelle, reference 39; and clustered jet exits, reference 40. The nozzle types indicated in figure 3 are representative of many configurations which have been investigated on test rigs similar to the isolated nacelle shown in figure 5.

### Convergent-Divergent Ejector Nozzles

In the field of aircraft propulsion, the convergent-divergent ejector nozzle is sometimes regarded as a standard by which other nozzles may be evaluated. In figure 6, the thrust efficiency of a convergent-divergent nozzle is presented as a function of flight Mach number. Thrust efficiency is defined as the ratio of nozzle gross thrust minus external drag to ideal thrust. (The drag term also includes the ram drag of secondary air.) The shaded region in this figure represents the band of efficiency within which convergent-divergent nozzles for the supersonic transport can be designed to operate. (See ref. 41.) At design conditions near a Mach number of 3.0, the nozzle afterbody can be made cylindrical, in which case there is no pressure drag, skin friction drag is small, and thrust-minus-drag performance is near ideal. To achieve high performance over a wide range of speeds, the nozzle must incorporate variable geometry as indicated in the sketches and have the ability to vary expansion ratio from a value of unity at low speeds to about 4.0 at a Mach number of 3.0. At off-design conditions, however, especially at subsonic cruise or loiter and for transonic acceleration, the boattail angle (and, therefore, drag) is large, and thrust-minus-drag performance is reduced accordingly. Even though the variable-geometry convergent-divergent ejector nozzle will operate with high efficiency over a wide range of speeds, this type of nozzle, in general, is mechanically complex and heavy. Results of research on miscellaneous convergent-divergent and ejector nozzles are presented in references 2, 3, 39, and 41 to 61. Boattail and afterbody drag pertinent to variable-geometry convergent-divergent nozzles is discussed in references 62 to 70.

## Blow-In-Door Ejector Nozzle

Features of the blow-in-door exhaust nozzle system, which makes use of base ventilation to improve off-design performance, are illustrated in figure 7. The name is derived from the free-floating flaps, or blow-in doors, which are located just upstream of the ejector shroud. At subsonic and transonic speeds where the jet total-pressure ratio is low, the doors are forced inward by the higher external pressure. External air flows into the ejector and reduces the overexpansion of the primary exhaust. At higher Mach numbers, the higher pressure inside the shroud forces the doors to a closed position and the system functions as a convergent-divergent ejector. Because these doors or auxiliary inlets are upstream of the nozzle exit, it might be expected that this type of nozzle would be sensitive to installation effects or to unsymmetrical external flow.

The solid-line curve in figure 7 presents subsonic and transonic data obtained with an isolated nozzle operating in axisymmetric external flow (ram drag of secondary air not included in performance parameter). The dashed-line curve shows performance of a nozzle of the same design when installed as a twin cluster in an aircraft configuration and operating in the aircraft flow field. A comparison of nozzle performance for the isolated and installed cases shows that the performance for the installed nozzles is lower than that for the isolated nozzle by about 2 percent. A small part of this loss was internal and was caused by lower pressures in the secondary air passage which forms an internal base. Most of the loss, however, is due to increased external drag. The severe drop in performance at transonic speeds for both the isolated and installed nozzles is due to rapid increase in drag on the doors and shrouds in this speed range. At higher Mach numbers, the doors close; the performance improves and has been shown to fall within the shaded band. The curves showing performance at subsonic and transonic speeds are data for a specific engine operating at specified values of pressure ratio. The shaded band showing supersonic performance is intended to indicate general capability of the blow-in-door type of nozzle. Performance of several blow-in-door nozzle designs is presented in references 71 to 73, and data pertinent to auxiliary inlets for supplying nozzle secondary air flow are given in reference 74.

## Plug Nozzle With Terminal Fairings

Typical performance for an isentropic plug nozzle with and without terminal fairings is presented in figure 8. An isentropic plug nozzle can generally be designed to give good performance at any specified operating condition. For example, the nozzle without terminal fairings shown in the upper left-hand side of figure 8 was designed for a pressure ratio of 10 corresponding to operation of a turbojet at Mach 1.8. At speeds near this value the performance of this nozzle is good, as shown by the solid-line curve. Because the basic design of an isentropic plug nozzle requires rather abrupt curvature of the outer lip, lip drag is high, especially at transonic speeds, and performance is correspondingly low. At speeds above the design value, the nozzle is underexpanded and performance suffers.

One approach toward improving the off-design operation is through the use of terminal fairings as illustrated in the upper right-hand side of figure 8. The terminal fairings are streamlined bodies which fair into the rearward-facing surface of the nozzle outer lip and effectively reduce afterbody boat-tail angle. These fairings reduce lip drag, permit venting of the base at low speed, and provide additional expansion surface for the jet at high speeds. The performance of the  $M = 1.8$  design nozzle with the terminal fairings is shown by the dashed line. Subsonic and transonic performance is improved through reduction of lip drag; peak performance is at about the same level, but design speed and pressure ratio have been increased because the effective expansion ratio has been increased. The performance of plug and other type nozzles with and without terminal fairings is presented in references 6 to 11, and 75 to 82.

#### Long-Cone Plug Nozzle

The long-cone plug nozzle, illustrated in the sketches in figure 9, attacks the problem of lip drag by removing most of the lip. The essential elements of the nozzle are a more or less cylindrical shroud surrounding a relatively long straight conical plug. The upper left-hand sketch in the figure shows the nozzle in the off-design or subsonic configuration. The shroud lip has a very shallow boattail angle and terminates near the maximum diameter of the plug. Subsonic performance of the nozzle with full length plug as shown by the solid line is excellent. The plug length can be reduced by one-half (short-dash line) with only a small penalty. Further reduction in plug length results in rather drastic losses. The performance of this subsonic configuration is generally poor at speeds greater than a Mach number of 1.0 because of reduced pressure on the plug (ref. 83).

For transonic and supersonic operation, this type of plug nozzle must incorporate a translating shroud as indicated in the upper right-hand sketch so that the configuration becomes an annular convergent-divergent nozzle. With translation of the shroud scheduled to provide expansion ratio appropriate to Mach number and pressure ratio, the performance at supersonic speeds is competitive with that of a convergent-divergent nozzle. Although good performance can be obtained over a wide range of Mach number, the cone plug nozzle poses a mechanical design problem when variation of nozzle throat area is required, as for afterburning.

#### Concave-Plug Nozzle

Figure 10 presents typical performance of a concave-plug nozzle. This nozzle design concept represents an extreme approach to weight reduction in a plug-type nozzle, in that most of the plug is eliminated. The central plug base is contoured to promote a vortex-ring type of recirculating flow. This recirculating flow acts as a gas plug which is pressurized by the converging flow of the annular jet. Pressure acting on the concave-plug base increases with discharge angle  $\theta$  and with increasing total pressure of the jet.

In the lower part of figure 10, performance is shown for two schedules of jet total-pressure ratio. The higher values correspond to the operating pressure-ratio schedule for a turbojet engine, the lower values are for a turbofan. When used with a turbojet engine, the concave-plug nozzle is at least competitive with other type nozzles. Performance is generally poor at transonic speeds and low pressure ratio, the loss being associated with partial entrainment of the recirculating base flow by the annular jet which results in reduced base pressure. Performance can be improved by the use of terminal fairings. The performance of various concave-plug nozzles is presented in references 8 and 84 to 87.

#### Clustered Jet Exits

In multiengine airplane configurations, it may be advantageous sometimes to install the engines in one package rather than place individual pods along the fuselage or on the wings. One of the models used to study afterbody drag and jet interference effects of clustered jet exits is shown in figures 5 and 11. This model represents a side-by-side cluster of four engines having convergent-divergent nozzles with  $5^\circ$  boattail angle. In figure 11 some of the results obtained with this model are compared with those from an isolated nozzle. The solid-line curve shows performance for the inline clustered jets, the short-dash curve is for the staggered jets, and the long-short-dash curve is for an isolated nozzle. The external drag of the in-line clustered jet afterbody was found to be about double that of four isolated nacelle nozzles throughout the Mach number range of the tests. This increase in external drag reduced performance by as much as 3 percent. Staggering the two inboard engines had a slight beneficial effect at supersonic speeds because of the favorable interference from the outboard jet exhaust on the boattail of the inboard nozzles. In making a choice between the use of clustered or isolated engines, the rather considerable increase in afterbody drag for the clustered engines would have to be weighed against the possible advantages of this arrangement. Data pertinent to clustered jet-exit arrangements are presented in references 40 and 88 to 93. Related information on jet-airframe interference is given in references 94 to 102.

#### CONCLUDING REMARKS

A brief review of some of the recent NASA research on exhaust nozzles and jet effects has been presented. In summary, there are several points to be emphasized. Although isolated nacelle investigations are valuable in studies of the effects on nozzle performance of the external flow field and of parametric changes, the ultimate evaluation of exhaust-nozzle performance should be made with nozzles incorporated in the aircraft configuration. Furthermore, in the selection of an exhaust system, performance at off-design operating conditions as well as at design cruise must be considered. Compromises between these performance characteristics and both exhaust system weight and complexity of operation must be evaluated in order to optimize airplane performance.

## REFERENCES

1. Valerino, Alfred S.; Zappa, Robert F.; and Abdalla, Kaleel L.: Effects of External Stream on the Performance of Isentropic Plug-Type Nozzles at Mach Numbers of 2.0, 1.8, and 1.5. NASA MEMO 2-17-59E, 1959.
2. Beheim, Milton A.: Off-Design Performance of Divergent Ejectors. NACA RM E58G10a, 1958.
3. Greathouse, William K.; and Beale, William G.: Performance Characteristics of Several Divergent-Shroud Aircraft Ejectors. NACA RM E55G21a, 1955.
4. Cortright, Edgar M., Jr.; and Kochendorfer, Fred D.: Jet Effects on Flow Over Afterbodies in Supersonic Stream. NACA RM E53H25, 1953.
5. Nichols, Mark R.: Aerodynamics of Airframe-Engine Integration of Advanced Supersonic Aircraft. NASA TN D-3390, 1966.
6. Norton, Harry T., Jr.; and Swihart, John M.: Effect of Terminal Fairings on the Performance of a Plug-Type Exhaust Nozzle in Quiescent Air and at Mach Numbers of 1.62, 1.93, 2.55, and 3.05. NASA TM X-463, 1961.
7. Norton, Harry T., Jr.; and Keith, Arvid L., Jr.: Effect of Base Bleed and Terminal Fairings on the Performance of Exhaust-Nozzle-Afterbody Combinations at Mach Numbers of 1.93, 2.55, and 3.05. NASA TN D-539, 1960.
8. Mercer, Charles E.; and Salters, Leland B., Jr.: Performance of a Plug Nozzle Having a Concave Central Base With and Without Terminal Fairings at Transonic Speeds. NASA TN D-1804, 1963.
9. Willis, Conrad M.; and Norton, Harry T., Jr.: Effect of Afterbody Terminal Fairings on the Performance of Plug-Type Exhaust Nozzles at Transonic Speeds. NASA TM X-762, 1963.
10. Willis, Conrad M.; and Mercer, Charles E.: Effect of Afterbody Terminal Fairings on the Performance of a Pylon-Mounted Turbojet-Nacelle Model. NASA TM X-215, 1960.
11. Swihart, John M.; Norton, Harry T., Jr.; and Schmeer, James W.: Effect of Several Afterbody Modifications Including Terminal Fairings on the Drag of a Single-Engine Fighter Model With Hot-Jet Exhaust. NASA MEMO 10-29-58L, 1958.
12. Coles, Willard D.; Mihaloew, John A.; and Swann, William H.: Ground and In-Flight Acoustic and Performance Characteristics of Jet-Aircraft Exhaust Noise Suppressors. NASA TN D-874, 1961.
13. Schmeer, James W.; Salters, Leland B., Jr.; and Cassetti, Marlowe D.: Transonic Performance Characteristics of Several Jet Noise Suppressors. NASA TN D-388, 1960.

14. Coles, Willard D.; Mihalow, John A.; and Callaghan, Edmund E.: Turbojet Engine Noise Reduction With Mixing Nozzle-Ejector Combinations. NACA TN 4317, 1958.
15. Ciepluch, Carl C.; North, Warren J.; Coles, Willard D.; and Antl, Robert J.: Acoustic, Thrust, and Drag Characteristics of Several Full-Scale Noise Suppressors for Turbojet Engines. NACA TN 4261, 1958.
16. North, Warren J.: Transonic Drag of Several Jet-Noise Suppressors. NACA TN 4269, 1958.
17. Tolhurst, William H., Jr.; Hickey, David H.; and Aoyagi, Kiyoshi: Large-Scale Wind-Tunnel Tests of Exhaust Ingestion Due to Thrust Reversal on a Four-Engine Jet Transport During Ground Roll. NASA TN D-686, 1961.
18. Kelly, Mark W.; Greif, Richard K.; and Tolhurst, William H., Jr.: Full-Scale Wind-Tunnel Tests of a Swept-Wing Airplane With a Cascade-Type Thrust Reverser. NASA TN D-311, 1960.
19. Sutton, Fred B.; and Brownson, Jack J.: The Effects of Thrust Reversal at Mach Numbers up to 0.86 on the Longitudinal and Buffeting Characteristics of a Typical Jet-Transport Airplane Configuration. NASA TN D-136, 1960.
20. Anderson, Seth B.; Cooper, George E.; and Faye, Alan E., Jr.: Flight Measurements of the Effect of a Controllable Thrust Reverser on the Flight Characteristics of a Single-Engine Jet Airplane. NASA MEMO 4-26-59A, 1959.
21. Swihart, John M.: Effect of Target-Type Thrust Reverser on Transonic Aerodynamic Characteristics of a Single-Engine Fighter Model. NACA RM L57J16, 1958.
22. Kohl, Robert C.; and Algranti, Joseph S.: Investigation of a Full-Scale, Cascade-Type Thrust Reverser. NACA TN 3975, 1957.
23. Povolny, John H.; Steffen, Fred W.; and McArdle, Jack G.: Summary of Scale-Model Thrust-Reverser Investigation. NACA Rept. 1314, 1957. (Supersedes NACA TN 3664.)
24. McArdle, Jack G.: Performance Characteristics of Ring-Cascade-Type Thrust Reversers. NACA TN 3838, 1956.
25. Steffen, Fred W.; and McArdle, Jack G.: Performance Characteristics of Cylindrical Target-Type Thrust Reversers. NACA RM E55I29, 1956.
26. Steffen, Fred W.; McArdle, Jack G.; and Coats, James W.: Performance Characteristics of Hemispherical Target-Type Thrust Reversers. NACA RM E55E18, 1955.

27. Steffen, Fred W.; Krull, H. George; and Ciepluch, Carl C.: Preliminary Investigation of Several Target-Type Thrust-Reversal Devices. NACA RM E53L15b. 1954.
28. Runckel, Jack F.; and Swihart, John M.: A Hydrogen Peroxide Hot-Jet Simulator for Wind-Tunnel Tests of Turbojet-Exit Models. NASA MEMO 1-10-59L, 1959.
29. Runckel, Jack F.; Willis, Conrad M.; and Salters, Leland B., Jr.: Investigation of Catalyst Beds for 98-Percent Concentration Hydrogen Peroxide. NASA TN D-1808, 1963.
30. Willis, Conrad M.: The Effect of Catalyst-Bed Arrangement on Thrust Buildup and Decay Time for a 90 Percent Hydrogen Peroxide Control Rocket. NASA TN D-516, 1960.
31. Norton, Harry T., Jr.; and Swihart, John M.: Effect of a Hot-Jet Exhaust on Pressure Distributions and External Drag of Several Afterbodies on a Single-Engine Airplane Model at Transonic Speeds. NACA RM L57J04, 1958.
32. Swihart, John M.; and Mercer, Charles E.: Investigation at Transonic Speeds of a Fixed Divergent Ejector Installed in a Single-Engine Fighter Model. NACA RM L57L10a, 1958.
33. Lee, Edwin E., Jr.; Foss, Willard E., Jr.; and Runckel, Jack F.: Jet Effects on the Base, Afterbody, and Tail Regions of a Twin-Engine Airplane Model With High and Low Horizontal-Tail Locations. NASA TM X-2, 1959.
34. Lee, Edwin E., Jr.; and Salters, Leland B., Jr.: Effects of Afterbody Shape and Hot Jet Exhausts on Pressures, Temperatures, and Drag of a Twin-Engine Fighter-Airplane Model Having an Overhanging Fuselage. NASA MEMO 12-29-58L, 1959.
35. Foss, Willard E., Jr.; Runckel, Jack F.; and Lee, Edwin E., Jr.: Effects of Boattail Area Contouring and Simulated Turbojet Exhaust on the Loading and Fuselage-Tail Component Drag of a Twin-Engine Fighter-Type Airplane Model. NACA RM L58C04, 1958.
36. Mercer, Charles E.; Salters, Leland B., Jr.; and Capone, Francis J.: Afterbody Temperatures, Pressures, and Aerodynamic Characteristics Resulting From Extension of Speed-Brake Configurations Into the Exhaust Jets of a Twin-Engine Attack-Type-Airplane Model. NASA TM X-517, 1961.
37. Lee, Edwin E., Jr.; and Mercer, Charles E.: Jet Interference Effects on a Twin-Engine Attack-Type-Airplane Model With Large Speed-Brake, Thrust-Spoiler Surfaces. NASA TM X-454, 1961.
38. Lee, Edwin E., Jr.; and Swihart, John M.: Tabulated Pressure Data for a 60° Delta-Wing-Body-Tail Model With a Hot Jet Exhausting From a Pylon-Mounted Nacelle. NACA RM L57J22, 1958.

39. Norton, Harry T., Jr.; Runckel, Jack F.; and Pendergraft, Odis C., Jr.: Transonic Performance of Two Convergent-Divergent Ejector Nozzles Designed for Corrected Secondary Flows of 3 and 9.4 Percent. NASA TM X-909, 1964.
40. Kirkham, Frank S.; Lee, Edwin E., Jr.; and Lauer, Rodney F., Jr.: Afterbody Drag of Several Clustered Jet-Exit Configurations at Transonic Speeds. NASA TM X-1216, 1966.
41. Runckel, Jack F.: Review of NASA Exhaust Nozzle Research. Proceedings of NASA Conference on Supersonic-Transport Feasibility Studies and Supporting Research - September 17-19, 1963, NASA TM X-905, 1963, pp. 315-332.
42. Mercer, Charles E.; and Schmeer, James W.: Transonic Performance of Ejector Nozzles Having Zero Boattail Angle and an Internal Base. NASA TM X-1104, 1965.
43. Norton, Harry T., Jr.; and Pendergraft, Odis C., Jr.: Transonic Performance of a Convergent-Divergent Ejector Nozzle Designed for a Corrected Secondary-Weight-Flow Ratio of 0.07. NASA TM X-974, 1964.
44. Mihalow, James R.: Internal-Performance Evaluation of Two Fixed-Divergent-Shroud Ejectors. NASA TN D-763, 1961.
45. Mihalow, James R.; and Stofan, Andrew J.: Internal-Performance Evaluation of a Two-Position Divergent Shroud Ejector. NASA TN D-762, 1961.
46. Stofan, Andrew J.; and Mihalow, James R.: Performance of a Variable Divergent-Shroud Ejector Nozzle Designed for Flight Mach Numbers up to 3.0. NASA TM X-255, 1961.
47. Stofan, Andrew J.: Effects of Nozzle-Shroud Misalignment on Performance of a Fixed-Shroud Divergent Ejector. NASA TM X-97, 1960.
48. Norton, Harry T., Jr.; Cassetti, Marlowe D.; and Mercer, Charles E.: Transonic Off-Design Performance of a Fixed Divergent Ejector Designed for a Mach Number of 2.0. NASA TM X-165, 1959.
49. Klann, John L.; and Huff, Ronald G.: Characteristics of Five Ejector Configurations at Free-Stream Mach Numbers From 0 to 2.0. NASA TM X-23, 1959.
50. Swihart, John M.; Mercer, Charles E.; and Norton, Harry T., Jr.: Effect of Afterbody-Ejector Configurations on the Performance at Transonic Speeds of a Pylon-Supported Nacelle Model Having a Hot-Jet Exhaust. NASA TN D-1399, 1962. (Supersedes NASA MEMO 1-4-59L, 1959.)
51. Runckel, Jack F.: Preliminary Transonic Performance Results for Solid and Slotted Turbojet Nacelle Afterbodies Incorporating Fixed Divergent Jet Nozzles Designed for Supersonic Operation. NASA MEMO 10-24-58L, 1958.

52. Trout, Arthur M.; Papell, S. Stephen; and Povolny, John H.: Internal Performance of Several Divergent-Shroud Ejector Nozzles With High Divergence Angles. NACA RM E57F13, 1957.
53. Hearth, Donald P.: Use of Main-Inlet Bypass To Supply Ejector Exhaust Nozzle at Supersonic Speeds. NACA RM E56K08, 1957.
54. Krull, H. George; and Beale, William T.: Internal Performance Characteristics of Short Convergent-Divergent Exhaust Nozzles Designed by the Method of Characteristics. NACA E56D27a, 1956.
55. Valerino, Alfred S.; and Yeager, Richard A.: External-Stream Effects on Gross Thrust and Pumping Characteristics of Ejectors Operating at Off-Design Mach Numbers. NACA RM E56C14, 1956.
56. Steffen, Fred W.; Krull, H. George; and Schmiedlin, Ralph F.: Effects of Several Geometric Variables on Internal Performance of Short Convergent-Divergent Exhaust Nozzles. NACA RM E54L09, 1955.
57. Steffen, Fred W.; Krull, H. George; and Schmiedlin, Ralph F.: Effect of Divergence Angle on the Internal Performance Characteristics of Several Conical Convergent-Divergent Nozzles. NACA RM E54H25, 1954.
58. Hearth, Donald P.; and Valerino, Alfred S.: Thrust and Pumping Characteristics of a Series of Ejector-Type Exhaust Nozzles at Subsonic and Supersonic Flight Speeds. NACA RM E54H19, 1954.
59. Kochendorfer, Fred D.: Note on Performance of Aircraft Ejector Nozzles at High Secondary Flows. NACA RM E54F17a, 1954.
60. Guentert, Eleanor Costilow; and Neumann, Harvey E.: Design of Axisymmetric Exhaust Nozzles by Method of Characteristics Incorporating a Variable Isentropic Exponent. NASA TR R-33, 1959.
61. Farley, John M.; and Campbell, Carl E.: Performance of Several Method-of-Characteristics Exhaust Nozzles. NASA TN D-293, 1960.
62. Beheim, Milton A.; Klann, John L.; and Yeager, Richard A.: Jet Effects on Annular Base Pressure and Temperatures in a Supersonic Stream. NASA TR R-125, 1962.
63. Beheim, Milton A.: Flow in the Base Region of Axisymmetric and Two-Dimensional Configurations. NASA TR R-77, 1960.
64. Cabbage, James M., Jr.: Effect of Convergent Ejector Nozzles on the Boat-tail Drag of a  $16^\circ$  Conical Afterbody at Mach Numbers of 0.6 to 1.26. NACA RM L58G25, 1958.
65. Nelson, William J.; and Scott, William R.: Jet Effects on the Base Drag of a Cylindrical Afterbody With Extended Nozzles. NACA RM L58A27, 1958.

66. Baughman, L. Eugene; and Kochendorfer, Fred D.: Jet Effects on Base Pressures of Conical Afterbodies at Mach 1.91 and 3.12. NACA RM E57E06, 1957.
67. Cabbage, James M., Jr.: Jet Effects on the Drag of Conical Afterbodies for Mach Numbers of 0.6 to 1.28. NACA RM L57B21, 1957.
68. Silhan, Frank V.; and Cabbage, James M., Jr.: Drag of Conical and Circular-Arc Boattail Afterbodies at Mach Numbers From 0.6 to 1.3. NACA RM L56K22, 1957.
69. Henry, Beverly Z., Jr., and Cahn, Maurice S.: Pressure Distributions Over a Series of Related Afterbody Shapes as Affected by a Propulsive Jet at Transonic Speeds. NACA RM L56K05, 1957.
70. Henry, Beverly Z., Jr.; and Cahn, Maurice S.: Additional Results of an Investigation at Transonic Speeds To Determine the Effects of a Heated Propulsive Jet on the Drag Characteristics of a Series of Related Afterbodies. NACA RM L56G12, 1956.
71. Schmeer, James W.; Mercer, Charles E.; and Kirkham, Frank S.: Effect of Bypass Air on the Performance of a Blow-In-Door Ejector Nozzle at Transonic Speeds. NASA TM X-896, 1963.
72. Kirkham, Frank S.; and Schmeer, James W.: Performance Characteristics at Mach Numbers Up to 1.29 of a Blow-In-Door Ejector Nozzle With Doors Fixed in Full-Open Position. NASA TM X-830, 1963.
73. Migdal, David; and Horgan, John J.: Thrust Nozzles for Supersonic Transport Aircraft. Paper No. 63-AHGT-73, Am. Soc. Mech. Engrs., 1963.
74. Hearth, Donald P.; and Cubbison, Robert W.: Investigation at Supersonic and Subsonic Mach Numbers of Auxiliary Inlets Supplying Secondary Air Flow to Ejector Exhaust Nozzles. NACA RM E55J12a, 1956.
75. Krull, H. George; Beale, William T.; and Schmiedlin, Ralph F.: Effect of Several Design Variables on Internal Performance of Convergent-Plug Exhaust Nozzles. NACA RM E56G20, 1956.
76. Krull, H. George; and Beale, William T.: Comparison of Two Methods of Modulating the Throat Area of Convergent Plug Nozzles. NACA RM E54L08, 1955.
77. Krull, H. George; and Beale, William T.: Effect of Outer-Shell Design on Performance Characteristics of Convergent-Plug Exhaust Nozzles. NACA RM E54K22, 1955.
78. Krull, H. George; and Beale, William T.: Effect of Plug Design on Performance Characteristics of Convergent-Plug Exhaust Nozzles. NACA RM E54H05, 1954.

79. Hearth, Donald P.; and Gorton, Gerald C.: Investigation of Thrust and Drag Characteristics of a Plug-Type Exhaust Nozzle. NACA RM E53L16, 1954.
80. Ciepluch, Carl C.; Krull, H. George; and Steffen, Fred W.: Preliminary Investigation of Performance of Variable-Throat Extended-Plug-Type Nozzles Over Wide Range of Nozzle Pressure Ratios. NACA RM E53J28, 1954.
81. Cubbison, Robert W.: Asymmetric "Penshape" Nozzles in Jet-Canard Configurations for Attitude Control. NASA TN D-1561, 1963.
82. Beale, William G.; and Povolny, John H.: Internal Performance of Two-Dimensional Wedge Exhaust Nozzles. NACA RM E56K29b, 1957.
83. Schmeer, James W.; Kirkham, Frank S.; and Salters, Leland B., Jr.: Performance Characteristics of a  $10^\circ$  Conical Plug Nozzle at Mach Numbers up to 1.29. NASA TM X-913, 1964.
84. Corson, Blake W., Jr.; and Mercer, Charles E.: Transonic Thrust and Drag Characteristics of an Annular Nozzle Having a Semitoroidal Concave Plug. NASA TM X-958, 1964.
85. Mercer, Charles E.; and Simonson, Albert J.: Effect of Geometric Parameters on the Static Performance of an Annular Nozzle With a Concave Central Base. NASA TN D-1006, 1962.
86. Corson, Blake W., Jr.; and Mercer, Charles E.: Static Thrust of an Annular Nozzle With a Concave Central Base. NASA TN D-418, 1960.
87. Baker, Von D.; Johnson, Richard A.; Brasket, Richard G.; and Lamb, Owen P.: Experimental Results With Lift Engine Exhaust Nozzles. Paper No. 65-574, Am. Inst. Aeron. Astronaut., June 1965.
88. Weidner, John P.; and Cabbage, James M.: Base Pressures and Convective Heat-Transfer Coefficients for Clustered Sonic Nozzles With Emphasis on Choked Exhaust Backflow. NASA TN D-2929, 1965.
89. Norton, Harry T., Jr.; Foss, Willard E., Jr.; and Swihart, John M.: An Investigation of Modified Clustered Jet-Exit Arrangements at Supersonic Speeds. NASA TM X-540, 1961.
90. Stitt, Leonard E.; and Cubbison, Robert W.: External Drag of Multijet Exit Configuration With and Without Base Flow at Mach Numbers From 2.0 to 3.0. NASA TM X-103, 1960.
91. Cabbage, James M., Jr.: Effect of Multiple-Jet Exits on the Base Pressure of a Simple Wing-Body Combination at Mach Numbers of 0.6 to 1.27. NASA TM X-25, 1959.
92. Swihart, John M.; and Keith, Arvid L., Jr.: An Investigation of Clustered Jet-Exit Arrangements at Supersonic Speeds. NASA MEMO 5-11-59L, 1959.

93. Swihart, John M.; and Nelson, William J.: Performance of Multiple Jet-Exit Installations. NACA RM L58E01, 1958.
94. Runckel, Jack F.; Lee, Edwin E., Jr.; and Simonson, Albert J.: Sting and Jet Interference Effects on the Afterbody Drag of a Twin-Engine Variable-Sweep Fighter Model at Transonic Speeds. NASA TM X-755, 1963.
95. Henry, Beverly Z., Jr.: Interference Effects at Transonic Speeds of Jets Exhausting From the Hull Step of a Model of a Large, Water-Based Airplane. NASA TM X-218, 1960.
96. Swihart, John M.; and Crabill, Norman L.: Steady Loads Due to Jet Interference on Wings, Tails, and Fuselages at Transonic Speeds. NACA RM L57D24b, 1957.
97. Bressette, Walter E.; and Leiss, Abraham: Effects on Adjacent Surfaces From the Firing of Rocket Jets. NACA RM L57D19a, 1957.
98. Leiss, Abraham; and Bressette, Walter E.: Pressure Distribution Induced on a Flat Plate by a Supersonic and Sonic Jet Exhaust at a Free-Stream Mach Number of 1.80. NACA RM L56I06, 1957.
99. Cornette, Elden S.; and Ward, Donald H.: Transonic Wind-Tunnel Investigation of the Effects of a Heated Propulsive Jet on the Pressure Distributions Along a Fuselage Overhang. NACA RM L56A27, 1956.
100. Bressette, Walter E.: Some Experiments Relating to the Problem of Simulation of Hot Jet Engines in Studies of Jet Effects on Adjacent Surfaces at a Free-Stream Mach Number of 1.80. NACA RM L56E07, 1956.
101. Bressette, Walter E.; and Leiss, Abraham: Investigation of Jet Effects on a Flat Surface Downstream of the Exit of a Simulated Turbojet Nacelle at a Free-Stream Mach Number of 1.39. NACA RM L55L13, 1956.
102. Salmi, Reino J.; and Klann, John L.: Interference Effects at Mach 1.9 on a Horizontal Tail Due to Trailing Shock Waves From an Axisymmetric Body With an Exiting Jet. NACA RM E55J13a, 1956.

PERFORMANCE SENSITIVITY TO CRITICAL PARAMETERS  
3500 N. Mi. MISSION; M = 2.7 CRUISE

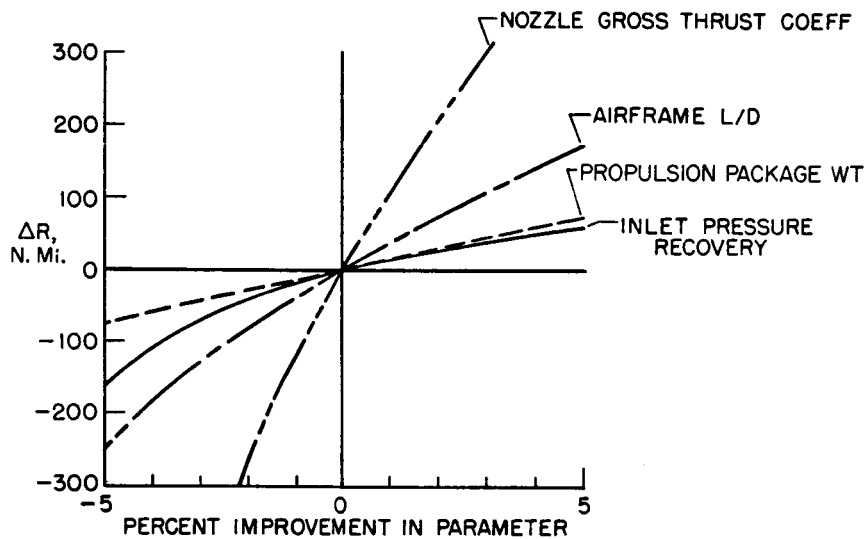


Figure 1

SUPERSONIC TRANSPORT FUEL USAGE

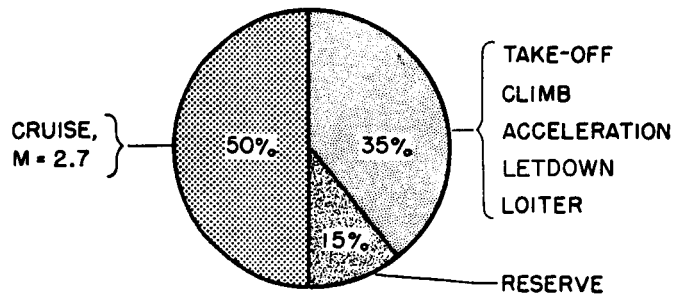


Figure 2

### EXHAUST-NOZZLE RESEARCH

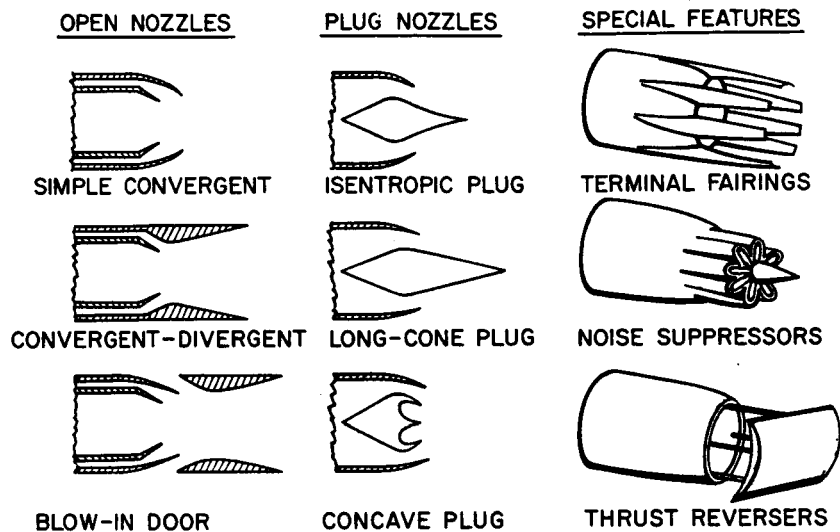


Figure 3

### JET-EFFECTS AIRCRAFT MODELS

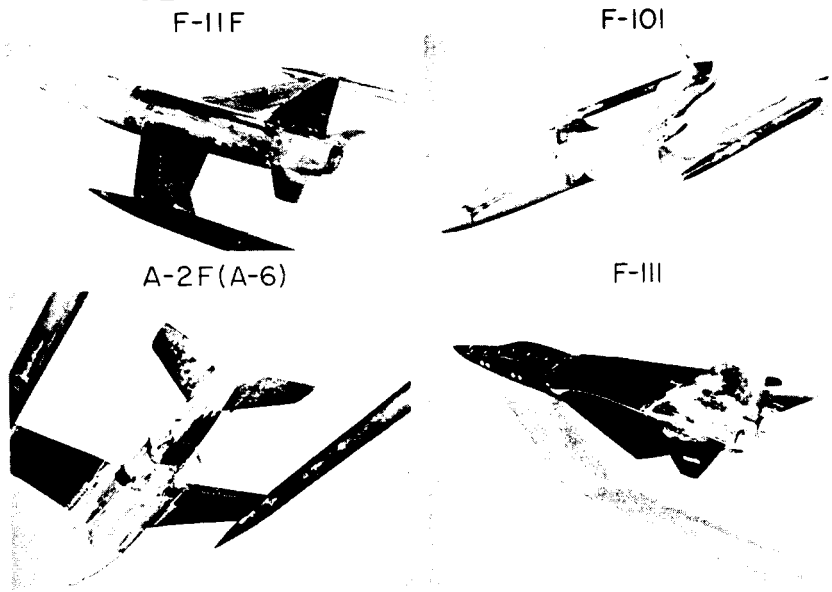


Figure 4

L-2680-4

## V/STOL AND RESEARCH MODELS

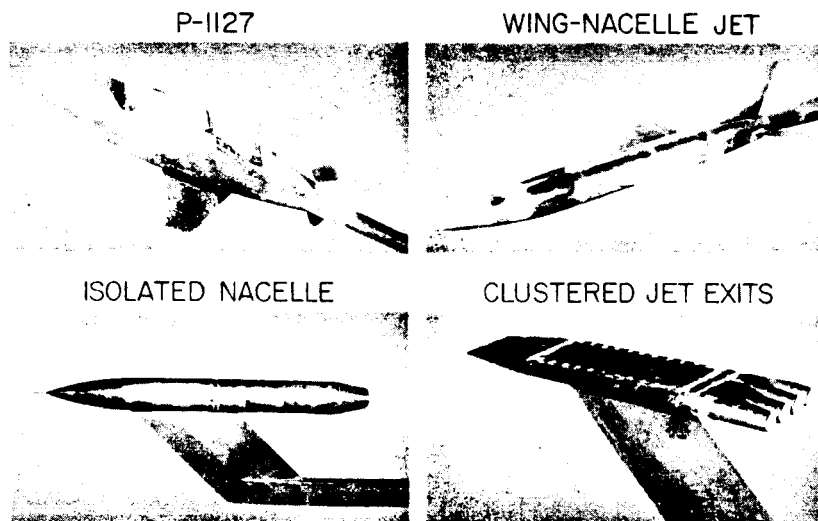


Figure 5

L-2680-5

## PERFORMANCE OF CONVERGENT-DIVERGENT EJECTOR NOZZLES

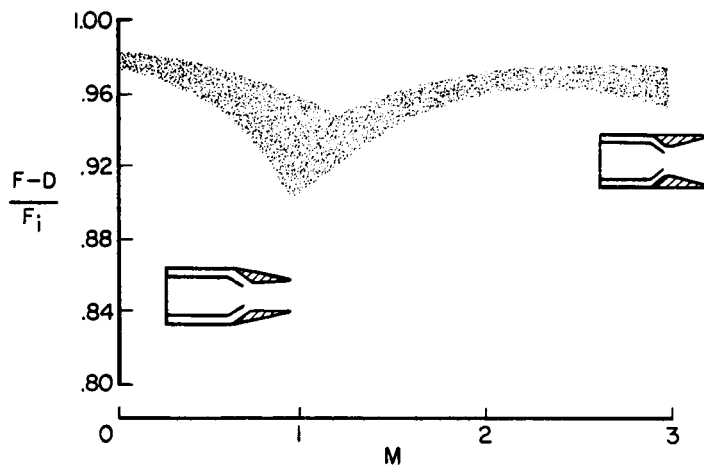


Figure 6

### BLOW-IN-DOOR EJECTOR NOZZLE

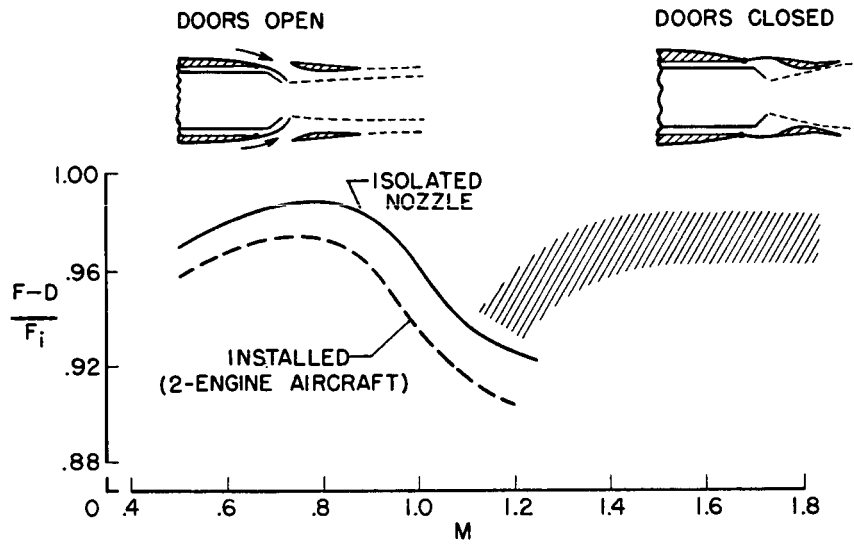


Figure 7

### PLUG NOZZLE WITH TERMINAL FAIRINGS

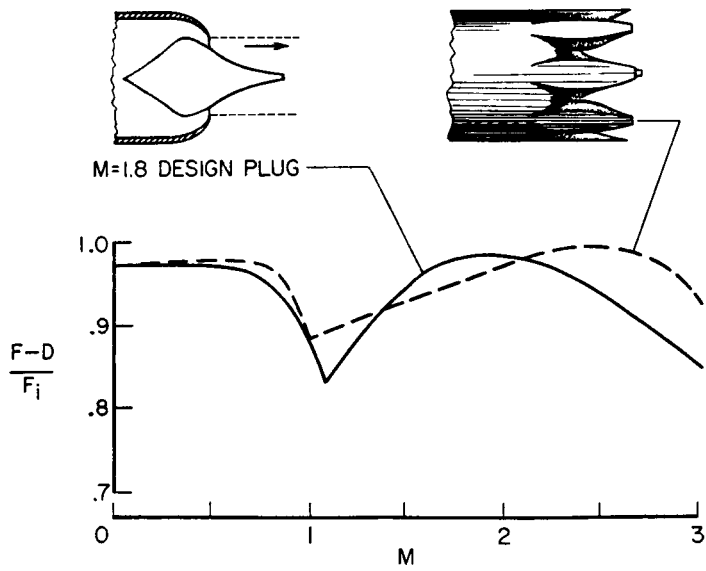
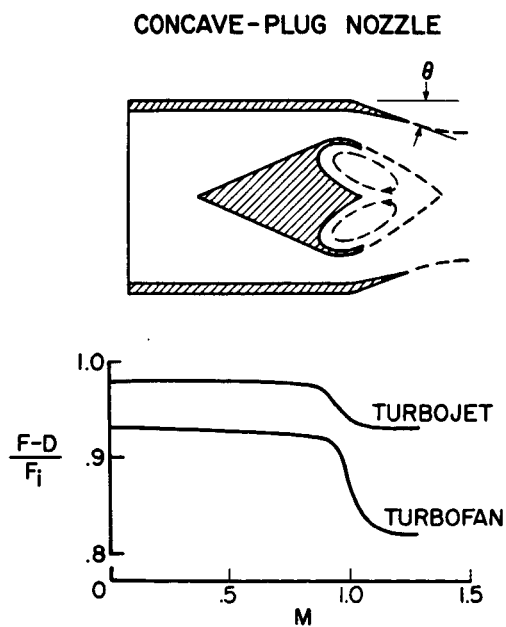
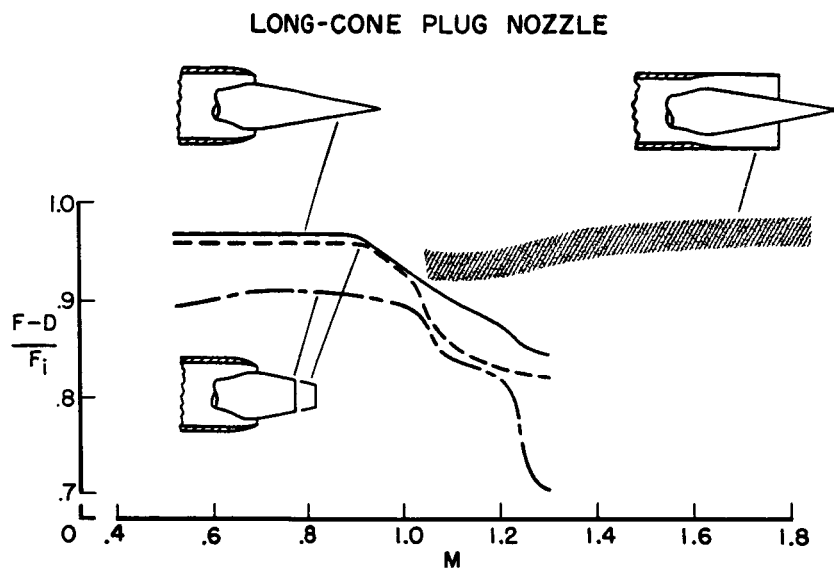


Figure 8



### CLUSTERED JET EXITS

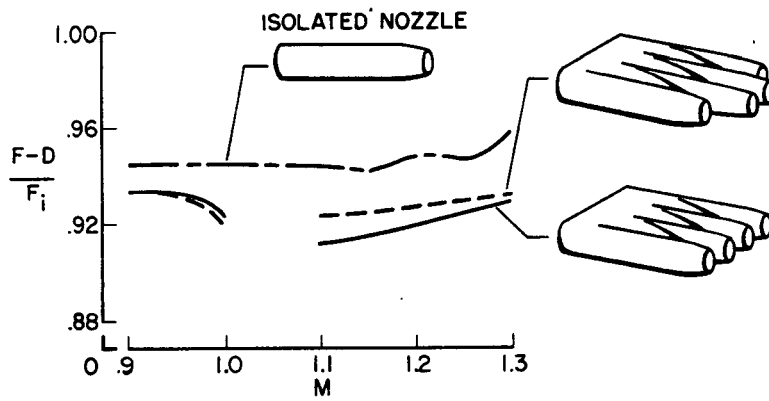


Figure 11

## 16. JET-EXIT AND AIRFRAME INTERFERENCE STUDIES ON TWIN-ENGINE-FUSELAGE

### AIRCRAFT INSTALLATIONS

By Jack F. Runckel  
NASA Langley Research Center

### SUMMARY

Jet interference effects on the drag and on the nozzle-afterbody performance of twin-engine-fuselage aircraft configured for a Mach number 1.2 mission are discussed. A detailed tailoring of the afterbody with the nozzles is required to obtain the best afterbody thrust-minus-drag performance. Performance improvements were obtained for a model of an aircraft under development by increasing the afterbody length relative to the jet exits by the addition of volume between and around the jet exhausts.

### INTRODUCTION

In paper no. 15, Corson and Schmeer presented the off-design problems of isolated nozzles and indicated that sizable nozzle performance penalties are associated with the installation of the exhaust system in an airplane. The present paper is concerned with the combined nozzle-afterbody performance of twin-engine-fuselage aircraft specifically designed to operate at a Mach number of 1.2; such aircraft might be required for a high-speed sea-level dash.

Jet exits on single-engine-fuselage airplanes are usually located at the end of the afterbody, and jet interference effects are usually confined to a small region near the jet exhaust. Corson and Schmeer in paper no. 15 referred to several jet-airframe interference studies on single-engine airplane models. Twin-engine aircraft can have the jet exits located either at the terminal section of the fuselage (refs. 1 to 6) or forward on the fuselage (refs. 7 to 13). In either instance, the arrangement used to provide aft-end closure of the fuselage ahead of and between the engines determines the magnitude of jet-airframe interference and has an appreciable effect on the configuration drag (refs. 9, 10, and 13 to 15). The jet exhausts can also affect the airplane stability (refs. 8 to 13), the local loading and skin temperatures (refs. 7 to 13), and the base pressures (paper no. 15 and refs. 1 to 3, 6, 8 to 11, and 13).

## SYMBOLS

$C_p$	pressure coefficient
$D$	drag
$D/q$	drag coefficient based on unit wing area
$d_e$	diameter of nozzle shroud exit
$d_p$	diameter of primary nozzle
$F$	total gross thrust force
$\frac{F - D}{F_i}$	ratio of total gross thrust minus drag aft of separation line to ideal thrust of both primary nozzles
$F_i$	ideal isentropic thrust of both primary nozzles
$M$	free-stream Mach number
$P_{t,j}$	jet total pressure
$p_\infty$	free-stream static pressure
$q$	free-stream dynamic pressure
$x$	distance from primary-nozzle or shroud exit

## DISCUSSION

### Afterbody Drag

It is known that a large amount of the total drag can occur on the afterbody (ref. 16). This situation is particularly serious at transonic speeds where the boattail drag and base drag coefficients are usually maximum (refs. 2, 6, and 17 to 21). Two examples of twin-engine configurations will be discussed to illustrate the magnitude of afterbody drag on this type of aircraft.

A technique for measuring the afterbody drag of aircraft models with jet-power simulation was developed in the Langley 16-foot transonic tunnel (ref. 22). The main features of this system can be examined in figure 1. The photograph shows a research model supported by an underneath sting and a thin strut attached to the forebody to minimize support-system interference. The forebody and wings, which were swept back  $108^\circ$ , provided the correct simulated flow field over the afterbody and propulsion system. The wing tips overlapped but did not touch the afterbody. The model was separated just ahead of the horizontal tails (66-percent-length station) and sealed, and the rear section including the tails

was attached to an internal strain-gage balance. The long engine interfairing was designed to improve the area progression at the rear of the model (refs. 13, 14, and 23).

A powered model of an aircraft under development, which was supported in a similar manner, is shown in figure 2. The wings were swept back  $72.5^\circ$ , and the engine interfairing terminated near the jet exits. Horizontal-tail fairings were located adjacent to both engine nozzles. The separation line was again directly ahead of the horizontal tails at 74 percent of the model length. Force and pressure measurements were obtained on the rear section of the model, with primary and secondary flows in the ejector nozzles and bleed flow at a step exit on the afterbody boattail being controlled variables. Nozzle-afterbody thrust-minus-drag performance will be presented in a subsequent section. It should be noted that the performance ratio used in this paper includes the drag of the afterbody, tails, and nozzle surfaces; therefore, the values of the performance parameter in the present paper are lower than those presented by Corson and Schmeer in paper no. 15.

Both the research and the development models had the inlets faired over. Separate investigations were conducted to determine the effect of fairing over the inlets (ref. 22, for example), and the interference on the afterbody was found to be negligible. The engine exhausts were simulated with hot jets by using the technique described in reference 24.

Comparisons of the afterbody drag of the two configurations (figs. 1 and 2) relative to the drag coefficient of the complete models are presented in figure 3 for a Mach number of 1.2 at sea level and adjusted for full-scale Reynolds numbers. The afterbody of the research model, shown crosshatched, comprised about one-third of the the body length and contained about 36 percent of the total wetted area. The bar next to this model represents the drag coefficient of the entire configuration based on unit area. With the jets operating at a typical turbofan pressure ratio at a Mach number of 1.2, the afterbody drag was 41 percent of the total drag.

The afterbody of the development model comprised only one-fourth of the complete model length but had about 39 percent of the total wetted area. The afterbody drag, for the same operating conditions, was 46 percent of the complete model drag. These results show that a large percentage of the total drag occurs on a relatively small portion of the afterbody of twin-engine aircraft configurations.

#### Afterbody Closure

Several areas on twin-engine-fuselage airplanes are known to be sensitive to jet interference effects. Among these are the afterbody boattail (refs. 9 and 13), tail surfaces (refs. 10 and 11), and fuselage bases (refs. 2, 5, 6, and 10). Inasmuch as the afterbody of an aircraft may be a region of high local drag, an examination of the afterbody of a twin-engine aircraft was made to determine whether detailed tailoring would render better performance. A basic difference in the two configurations of figures 1 and 2 is the way the body

between the engine nozzles is designed. This terminal section is called the engine interfairing.

Pressure distributions on the interfairings of the two configurations are shown in figure 4. The nozzle exits, indicated by the diameter  $d_e$ , are located at the reference station 0 on the abscissa. The axial distance  $x$  from the exit is given in exit diameters. Pressure measurements are shown for the row of orifices closest to the center line of the exhaust nozzles.

The research model had a long interfairing extending downstream of the jet exits. The results obtained with the jets off indicate a gradual pressure recovery from low pressures near the engine base region. With the jets on, the interference was generally favorable, increasing the pressures to a positive value and causing thrust on part of the interfairing (ref. 22).

The wedge-shape interfairing on the development model was mostly ahead of the jet exit station. The interfairing pressures of this model were lower than those of the research model with the jets off. Jet operation produced a relatively small increase in pressure, an indication that the region between the engines remains an effective base drag area.

These results prompted an investigation of the flow field behind the aft end of the development model. An axial static probe was extended downstream of the model along the center line to measure pressures behind the model. The results are given in figure 5. The pressures obtained with the jets both off and on again show low pressures on the interfairing; however, an abrupt rise which occurred in pressure directly behind the model indicates that extending the fuselage volume into this greater-than-free-stream pressure field would probably reduce afterbody drag.

#### Engine-Interfairing Studies

Past work has shown that configurations with jets exhausting alongside aft-sloping fuselage surfaces have had favorable jet interference effects on drag; that is, jet operation increased the local pressures in the regions adjacent to and downstream of the jet exits (paper no. 15 and refs. 8 to 13). Usually, excess low-energy internal air is available near the nozzle, and this dumped air can provide a cooling film between the hot exhaust and the fuselage skin (refs. 5 and 10). The results of reference 15 indicate that axial-force reduction by interference between a jet and a neighboring afterbody would be large at supersonic speeds. In addition, an extension of the interfairing would improve the area progression (refs. 4, 14, and 23) and probably would reduce the wave drag.

The rest of this paper will be concerned with only the development model, and the discussion will be confined to performance at a Mach number of 1.2. The first attempt to improve the afterbody performance involved an increase in interfairing length and a volume addition, as is shown in figure 6. A blow-in-door nozzle which had the doors closed next to the interfairing and tail fairings was utilized to allow for maximum volume between the nozzles. The

nozzle-afterbody performance parameter  $\frac{F - D}{F_i}$  is the ratio of the total gross thrust minus the drag aft of the line of separation to the ideal thrust of the two primary nozzles. This ratio includes changes in both nozzle performance and afterbody drag due to interfairing differences and jet interference effects. The performance of the two configurations is plotted as a function of jet pressure ratio for identical internal and external flow conditions. These and all subsequent data are presented for zero secondary airflow and a corrected bleed-flow ratio of about 8 percent.

The gain in performance for the configuration with the extended interfairing is about 5 percent. This performance gain is equivalent to about a 30-count decrease in drag coefficient for the airplane model. It is apparent that major gains in performance are possible by working on the nozzle-afterbody region of twin-engine-fuselage aircraft.

The initial improvement in performance obtained with an extended interfairing led to further work to explore this concept. An investigation was conducted to determine the effect of engine interfairing and aft-end changes on the performance of the model with a short, small-diameter nozzle shroud. The results are presented in figure 7. Incremental nozzle-afterbody performance gains are plotted as a function of interfairing length in primary-nozzle diameters. The primary-nozzle diameter was constant for these and subsequent data and corresponded to the scaled nozzle area required for the 1.2 Mach number sea-level dash. The jet pressure ratio was about 3.4 for all configurations. Shown in figure 7 are interfairings of short (① and ⑥), medium (② and ④), and long (③ and ⑤) extensions.

The interfairing-length differences are shown in the photographs in figure 8. The basic short interfairing is shown in the picture on the left, the medium extension of the interfairing is presented in the center photograph, and the long interfairing is shown on the right. The performance of these configurations (fig. 7), indicated by numbers ①, ②, and ③, respectively, shows that a medium extension of the interfairing (configuration ②) produced a performance gain of over 2 percent. A further increase in length to the long interfairing (configuration ③) gave an additional gain of 1 percent. The increase in performance with increasing interfairing length indicates that adding length downstream of the jet exits can provide performance improvements due to better closure, a more favorable flow field, and more favorable jet interference effects.

The numbers ④ and ⑤ in figure 7 represent configurations having the same medium and long interfairings as those indicated by the numbers ② and ③, respectively. The differences in these configurations are shown in the photographs in figure 9. Additional volume was added around the nozzles by installing larger tail fairings which house the horizontal-tail mechanism. The small tail fairings on the medium- and long-interfairing configurations are shown in the bottom pictures and the large tail fairings on the same configurations are shown in the photographs at the top.

The larger tail fairings provided further substantial increases in performance, as shown by the data points for configurations ④ and ⑤ in figure 7.

The use of tail fairings to reduce transonic drag through favorable jet interference and application of the area rule are discussed in reference 14.

A different approach was also tried by using a concave-base interfairing concept based on the concave-base plug nozzle (ref. 25). Figure 10 shows the concave-base interfairing concept. The long interfairing shown on the left was cut-off at about the same length as the basic interfairing (right photograph), and the base was recessed, as shown in the center (configuration ⑥). The cut-off interfairing is essentially a volume addition relative to the basic interfairing since it brings the interfairing surfaces closer to the jet exits. The performance of this configuration, shown by the number ⑥ in figure 7, was equal to that of the model with the long interfairing (configuration ③). Although the cut-off configuration was about the same length as the basic configuration, the pressure coefficients on the sides and base of the concave-base interfairing (configuration ⑥) were higher than those of the wedge-shape interfairing (configuration ①) and, therefore, the effective base drag of the cut-off configuration was lower.

The results presented in figure 7 indicate that adding length to and/or volume between the short, small-diameter nozzles provided performance improvements relative to the model with the basic interfairing. The main benefits are believed to be caused by more favorable jet interference effects and lower slopes on the afterbody between the engines for the altered configurations. Of course, there are compensating problems, such as weight and balance, added skin friction, and high local skin temperatures, which must be considered in making aft-end changes.

#### Nozzle-Afterbody Integration

Other work on nozzle sizing indicated that nozzles having larger diameters than those previously discussed would provide better performance. Models designed to integrate a large-diameter shroud with a long interfairing were investigated and the results are compared in figure 11. The performance and length parameters are the same as those of figure 7. The reference level of performance is again that of the short, small-diameter nozzle with the basic interfairing, indicated by the solid circle (configuration ①). The open symbols represent the large-diameter shrouds. The squares represent configurations with long, large-diameter nozzles, such as those shown in figure 2.

Some of the large-diameter nozzle-afterbody combinations are shown in figure 12. The long nozzle with the basic interfairing is shown in the left picture. This configuration had almost 2-percent better performance than the reference nozzle, as indicated by the square directly above the solid symbol in figure 11.

The addition of a long interfairing to the long nozzle (square symbol at  $x/d_p = 3.25$ ) provided a gain in performance of about 1 percent. Shortening the nozzle with the same long interfairing provided an additional gain, as indicated by the diamond-shape symbol. This configuration is shown in the center photograph of figure 12. These results are consistent with those shown in figure 7

since shortening the nozzle with the same length interfairing exposes a greater portion of the interfairing to favorable jet interference effects.

The terminal-fairing nozzle shown in the right photograph in figure 12 represents a more complete integration of the nozzle with the afterbody. This concept (ref. 26) has been discussed by Corson and Schmeer in paper no. 15. The terminal-fairing nozzle maintained the diameters and blow-in-door features of the large nozzle, but had a short, fixed shroud. A photograph of the terminal-fairing nozzle configuration is presented on the right-hand side of figure 12. This nozzle-afterbody combination had a large-volume interfairing and utilized the interfairing (refs. 27 and 28) and tail fairing (ref. 14) as part of the nozzle surface. The nozzle had eight terminal bodies, and the open spaces between the terminal fairings allowed ventilation between the jet and the free stream.

The performance of the terminal-fairing configuration is shown by the triangle-shape symbol in figure 11. This combination produced the highest nozzle-afterbody performance at Mach 1.2 of the large-shroud-nozzle-afterbody models investigated. The data presented by Corson and Schmeer in paper no. 15 and the results of reference 15, which indicate favorable jet interference effects at supersonic speeds, indicate that the supersonic performance of this configuration would also be good. (See ref. 27.)

#### CONCLUDING REMARKS

The results presented indicate that a relatively large amount of the total drag, of the order of 40 to 50 percent, occurs on the aft end of twin-engine-fuselage aircraft at transonic speeds. The performance of configurations with jet exits at the rear of the afterbody may be improved by increasing the afterbody length relative to the jet exits by the addition of volume between and around the jet exhausts. A detailed tailoring of the afterbody with the nozzles is required to obtain the best afterbody thrust-minus-drag performance. Of course, there are compensating problems, such as weight and balance, added skin friction, and high local skin temperatures, which must be considered in making aft-end changes. The cutoff large-volume interfairing represents a possible compromise.

## REFERENCES

1. Salmi, Reino J.; and Klann, John L.: Investigation of Boattail and Base Pressures of Twin-Jet Afterbodies at Mach Number 1.91. NACA RM E55C01, 1955.
2. Leiss, Abraham: Free-Flight Investigation of Effects of Simulated Sonic Turbojet Exhaust on the Drag of Twin-Jet Boattail Bodies at Transonic Speeds. NACA RM L56D30, 1956.
3. Rustemeyer, A. H.; and Twomey, E. J.: Thrust and Drag Characteristics of Several Turbojet Exhaust Models at Supersonic and High-Subsonic Mach Numbers. R-0922-16 (Contract NOa(s)55-134-c), Res. Dept., United Aircraft Corp., June 1957.
4. Reyn, J. W.: On the Optimum Body Shape at the Base With an Application to a Fuselage With Jet Engine Tail Pipes at Transonic Speeds. Rept. VTH-101, Tech. Hogeschool Delft Vliegtuigbouwkunde, Nov. 1958.
5. Bottorff, Marion R.: Wind Tunnel Tests at Mach Numbers From .82 to 2.05 of a 4.2% Scale A3J-1 Base Drag Model Using Hydrogen-Air Combustors for Jet Simulation. USCEC Rept. 65-7, Aerodyn. Test Lab., NMC, Univ. of Southern California, Nov. 2, 1959.
6. Langfelder, Helmut: Low-Drag Installation of Twin Propulsion Nozzles in the Rear of the Fuselage for Transonic and Supersonic Flight. Aerodynamics of Power Plant Installation, Pt. I, AGARDograph 103, Oct. 1965, pp. 195-216.
7. Swihart, John M.; and Crabill, Norman L.: Steady Loads Due to Jet Interference on Wings, Tails, and Fuselages at Transonic Speeds. NACA RM L57D24b, 1957.
8. Mitcham, Grady L.: A Summary of the Longitudinal and Lateral Stability and Control Characteristics Obtained From Rocket-Model Tests of a Swept-Wing Fighter-Type Airplane at Mach Numbers From 0.5 to 1.9. NACA RM L56K19, 1957.
9. Lee, Edwin E., Jr.; and Salters, Leland B., Jr.: Effects of Afterbody Shape and Hot Jet Exhausts on Pressures, Temperatures, and Drag of a Twin-Engine Fighter-Airplane Model Having an Overhanging Fuselage. NASA MEMO 12-29-58L, 1959.
10. Lee, Edwin E., Jr.; Foss, Willard E., Jr.; and Runckel, Jack F.: Jet Effects on the Base, Afterbody, and Tail Regions of a Twin-Engine Airplane Model With High and Low Horizontal-Tail Locations. NASA TM X-2, 1959.
11. Lee, Edwin E., Jr.; and Mercer, Charles E.: Jet Interference Effects on a Twin-Engine Attack-Type-Airplane Model With Large Speed-Brake, Thrust-Spoiler Surfaces. NASA TM X-454, 1961.

12. Mercer, Charles E.; Salters, Leland B., Jr.; and Capone, Francis J.: Afterbody Temperatures, Pressures, and Aerodynamic Characteristics Resulting From Extension of Speed-Brake Configurations Into the Exhaust Jets of a Twin-Engine Attack-Type-Airplane Model. NASA TM X-517, 1961.
13. Foss, Willard E., Jr.; Runckel, Jack F.; and Lee, Edwin E., Jr.: Effects of Boattail Area Contouring and Simulated Turbojet Exhaust on the Loading and Fuselage-Tail Component Drag of a Twin-Engine Fighter-Type Airplane Model. NACA RM L58C04, 1958.
14. Ballinger, J. G.; and Horn, R. C.: Final Report - Afterbody Drag Reduction by Application of the Area Rule Accounting for Jet Exhaust. WADC Tech. Rept. 57-634, ASTIA Doc. No. AD 142335, U.S. Air Force, Dec. 1957.
15. Pitts, William C.; and Wiggins, Lyle E.: Axial-Force Reduction by Interference Between Jet and Neighboring Afterbody. NASA TN D-332, 1960.
16. Stoney, William E., Jr.: Some Experimental Effects of Afterbody Shape on the Zero-Lift Drag of Bodies for Mach Numbers Between 0.8 and 1.3. NACA RM L53I01, 1953.
17. Henry, Beverly Z., Jr.; and Cahn, Maurice S.: Additional Results of an Investigation at Transonic Speeds To Determine the Effects of a Heated Propulsive Jet on the Drag Characteristics of a Series of Related Afterbodies. NACA RM L56G12, 1956.
18. Cabbage, James M., Jr.: Jet Effects on the Drag of Conical Afterbodies for Mach Numbers of 0.6 to 1.28. NACA RM L57B21, 1957.
19. Hargis, Calvin B., Jr.; Davison, P. H.; and Savage, S. B.: Methods for Estimating Base Pressures on Aircraft Configurations. WADC Tech. Note 57-28, ASTIA Doc. No. AD 110742, U.S. Air Force, July 1957.
20. Swihart, John M.; and Nelson, William J.: Performance of Multiple Jet-Exit Installations. NACA RM L58E01, 1958.
21. Cabbage, James M., Jr.: Effect of Multiple-Jet Exits on the Base Pressure of a Simple Wing-Body Combination at Mach Numbers of 0.6 to 1.27. NASA TM X-25, 1959.
22. Runckel, Jack F.; Lee, Edwin E., Jr.; and Simonson, Albert J.: Sting and Jet Interference Effects on the Afterbody Drag of a Twin-Engine Variable-Sweep Fighter Model at Transonic Speeds. NASA TM X-755, 1963.
23. Bielat, Ralph P.; Robins, A. Warner; and Alford, William J., Jr.: The Transonic Aerodynamic Characteristics of Two Variable-Sweep Airplane Configurations Capable of Low-Level Supersonic Attack. NASA TM X-304, 1960.
24. Runckel, Jack F.; and Swihart, John M.: A Hydrogen Peroxide Hot-Jet Simulator for Wind-Tunnel Tests of Turbojet-Exit Models. NASA MEMO 1-10-59L, 1959.

25. Corson, Blake W., Jr.; and Mercer, Charles E.: Transonic Thrust and Drag Characteristics of an Annular Nozzle Having a Semitoroidal Concave Plug. NASA TM X-958, 1964.
26. Runckel, Jack F.: Preliminary Transonic Performance Results for Solid and Slotted Turbojet Nacelle Afterbodies Incorporating Fixed Divergent Jet Nozzles Designed for Supersonic Operation. NASA MEMO 10-24-58L, 1958.
27. Weir, John: Aircraft Performance Problems Associated With Engine and Intake Installation. Aerodynamics of Power Plant Installation, Pt. I, AGARDograph 103, Oct. 1965, pp. 173-194.
28. Connors, James F.; and Meyer, Rudolph C.: Investigation of an Asymmetric "Penshape" Exit Having Circular Projections and Discharging Into Quiescent Air. NACA RM E56K09a, 1957.

RESEARCH MODEL

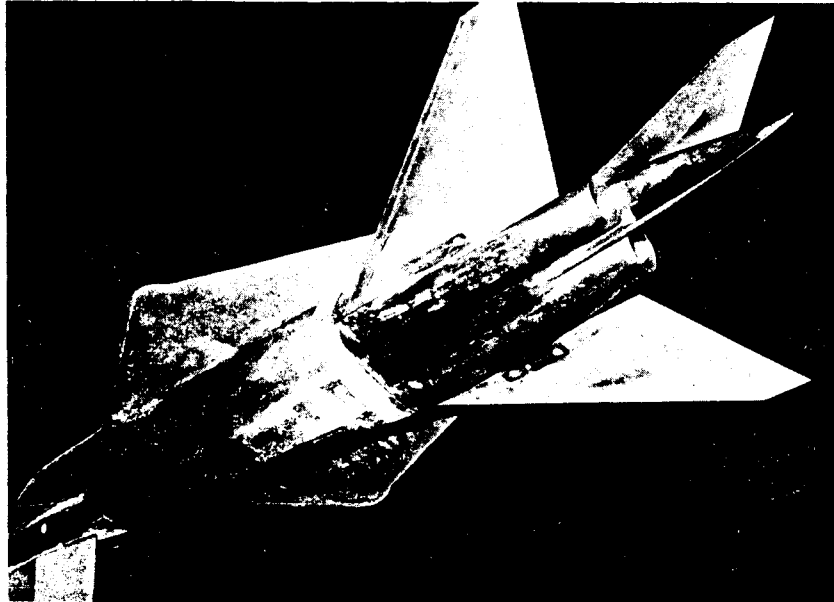


Figure 1

L-2681-1

DEVELOPMENT MODEL

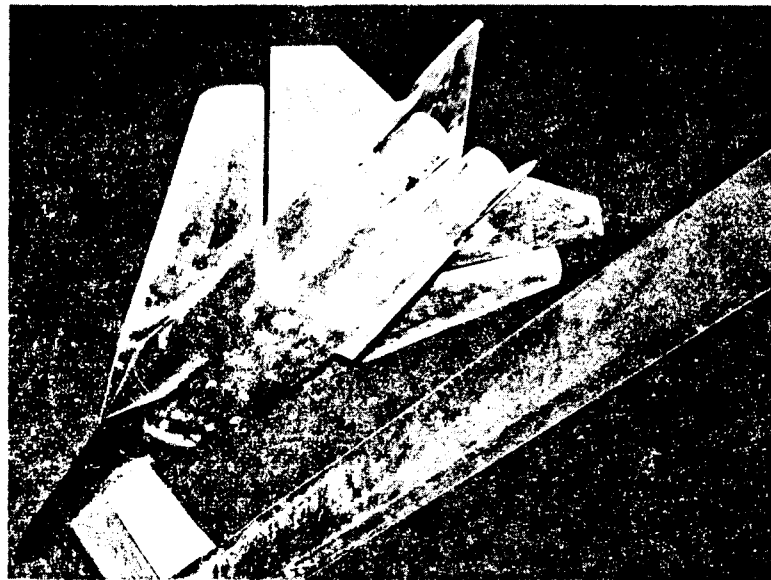


Figure 2

L-2681-2

COMPARISON OF TOTAL AND AFT-END DRAG

M = 1.2 AT SEA LEVEL

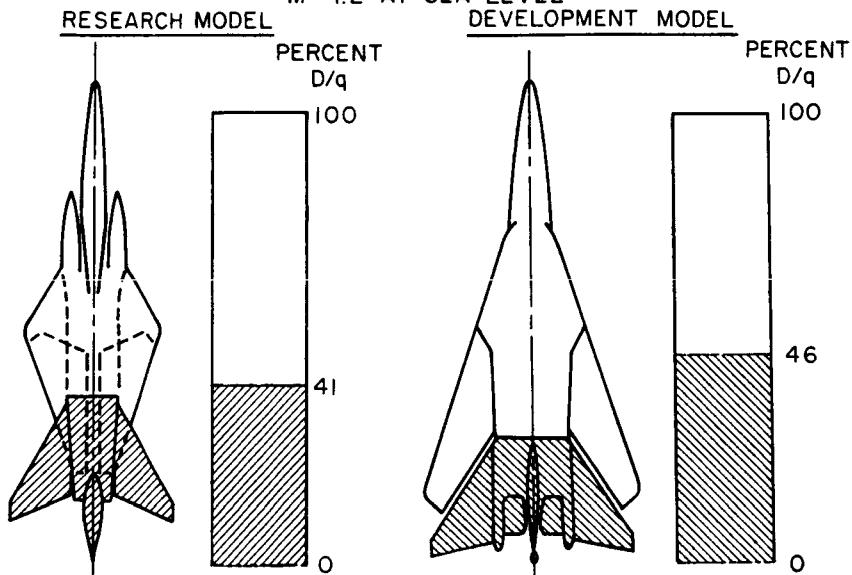


Figure 3

ENGINE INTERFAIRING PRESSURE DISTRIBUTIONS

M = 1.2

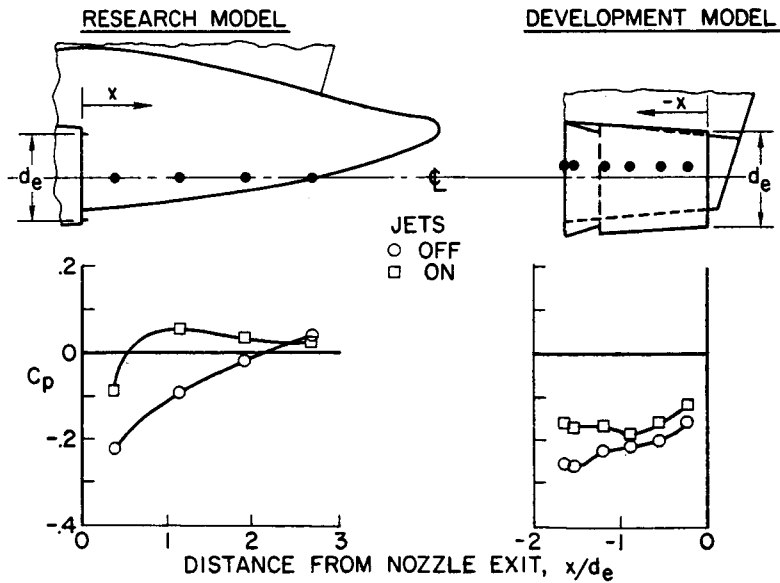


Figure 4

FLOW-FIELD STATIC-PRESSURE DISTRIBUTIONS  
M = 1.2

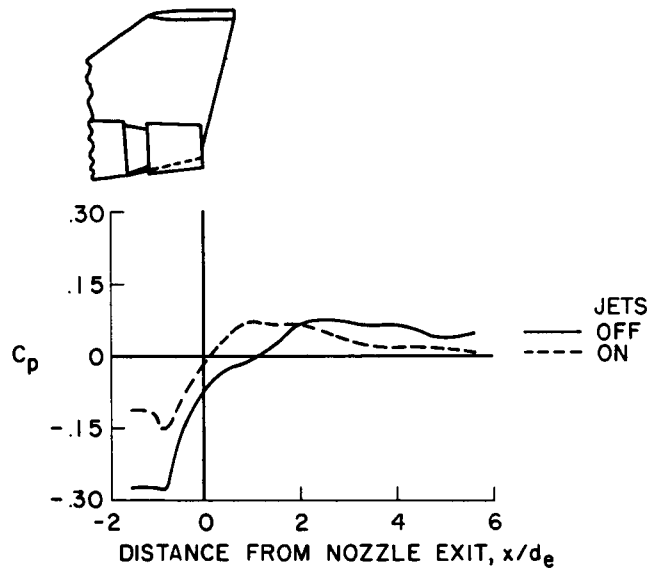


Figure 5

PERFORMANCE OF  
BASIC- AND EXTENDED-INTERFAIRING CONFIGURATIONS  
M=1.2

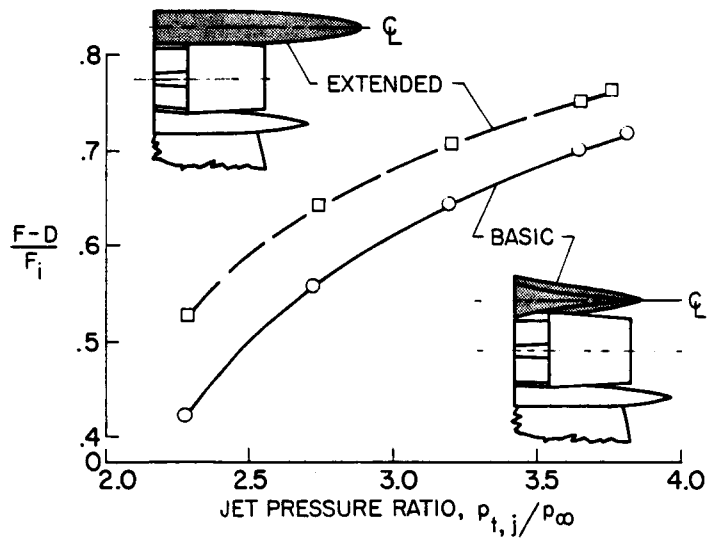


Figure 6

EFFECT OF AFTERBODY LENGTH AND VOLUME  
M=1.2; SHORT SMALL-DIAMETER NOZZLE SHROUD

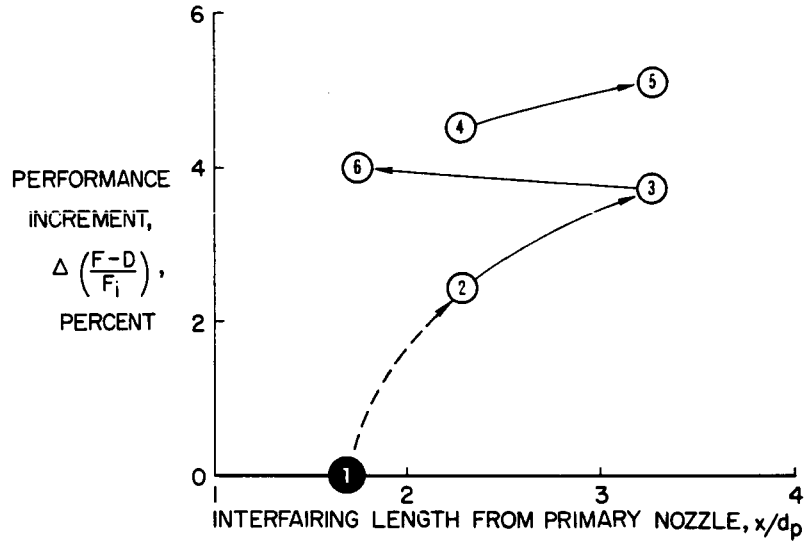


Figure 7

INTERFAIRING EXTENSIONS

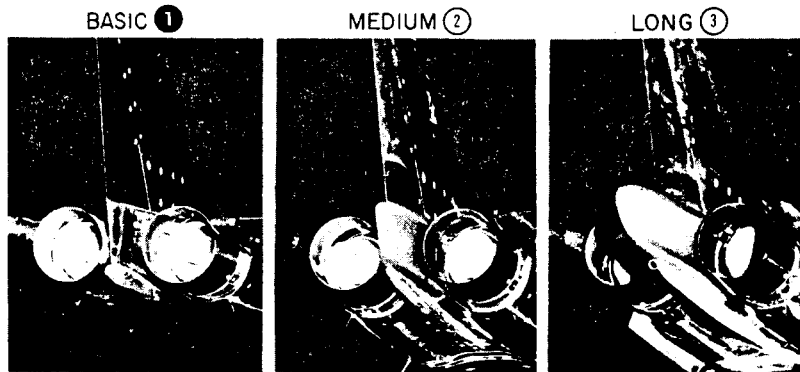
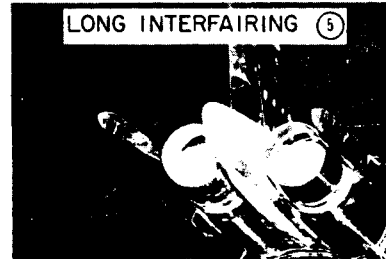
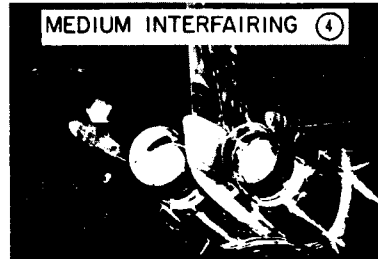


Figure 8

L-2681-8

## TAIL FAIRINGS

LARGE



SMALL

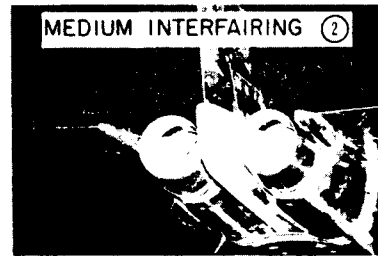


Figure 9

L-2681-9

## INTERFAIRINGS

LONG ③



CUT-OFF ⑥



BASIC ①

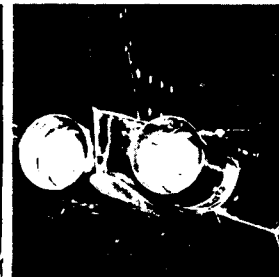


Figure 10

L-2681-10

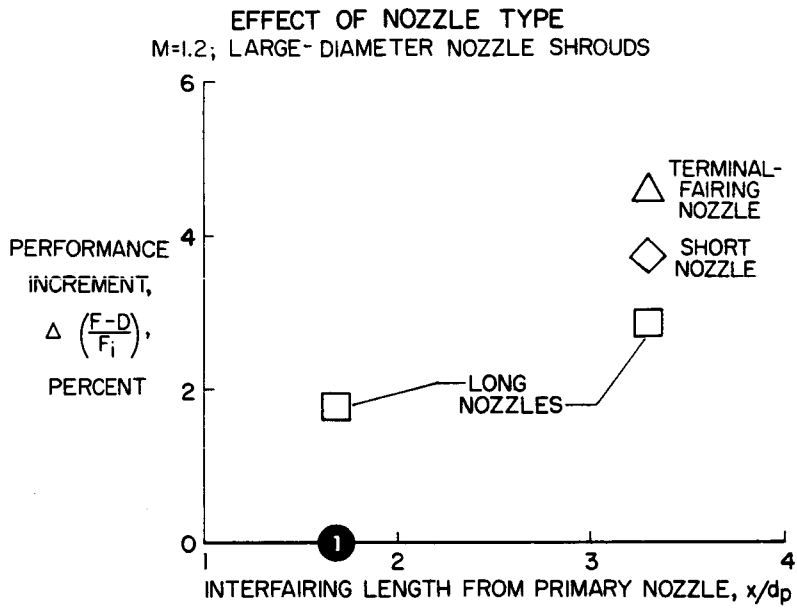


Figure 11

**LARGE-DIAMETER NOZZLE SHROUDS**

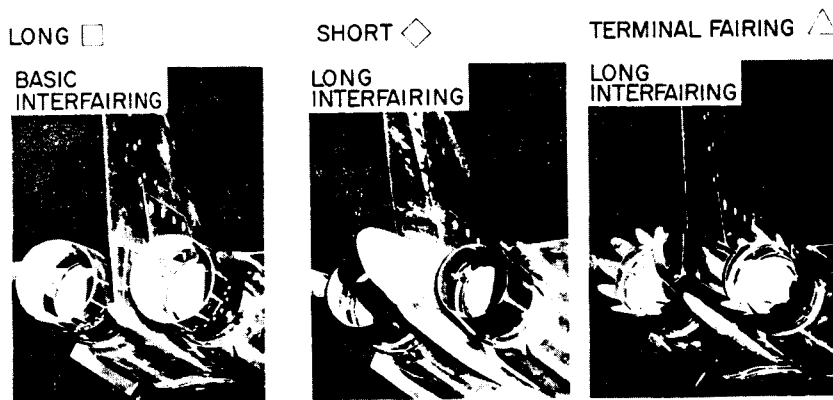


Figure 12

L-2681-12

17. STATIC-TEST RESULTS FROM EXHAUST NOZZLES WITH NOVEL  
FEATURES FOR SUPERSONIC-AIRCRAFT APPLICATIONS

By Fred W. Steffen and Donald L. Bresnahan  
NASA Lewis Research Center

SUMMARY

The effects of some geometric variations on the static internal performance and pumping characteristics of plug, auxiliary-inlet ejector, and variable-flap ejector nozzles are presented. The data were obtained in the nozzle static-test facility at the Lewis Research Center. It was concluded that, even though all the exit types can, in principle, provide satisfactory performance over a wide range of nozzle pressure ratios, all the exit types are mechanically complex. The effects of some mechanical simplifications on performance are shown. It was also concluded that ejector nozzles can generally obtain the amount of secondary air anticipated for adequate film cooling from ram air whereas some plug-nozzle film-cooling schemes may require engine-cycle air.

INTRODUCTION

Many types of exits have been proposed for supersonic-aircraft applications. An infinite number of modifications can be made to each of the basic types in an attempt to optimize the performance, pumping, and stability characteristics over the wide range of conditions presented by the supersonic-airplane environment. During the past several years, three types of exits - namely, the plug nozzle, the auxiliary-inlet ejector nozzle, and the variable-flap ejector nozzle - have been tested in the nozzle static-test facility at the Lewis Research Center. These three types of exits are shown in figure 1. In this paper, the effects of a few geometric variables on the internal performance and pumping characteristics of these nozzles are presented.

Internal static performance does not, of course, include external flow effects. At transonic flight conditions, where exits are boattailed and internal flows may be overexpanded, the overall installed performance obtained with external flow would be expected to differ from the internal static performance. However, at takeoff conditions, where external flow velocities are low, and at supersonic cruise conditions, where boattail angles are reduced to zero and internal flows are fully expanded, the internal performance obtained at static conditions would closely approximate the overall installed performance.

## SYMBOLS

F	measured gross thrust
$F_i$	ideal gross thrust
$p_o$	ambient static pressure
$p_t$	total pressure
$T_t$	total temperature
w	weight-flow rate
$w_t$	tertiary weight-flow rate

### Subscripts:

p	primary flow
s	secondary flow

## FACILITY

The static-test facility used to obtain nozzle data is shown in figure 2. Its principal components include a mounting pipe suspended from flexure rods within a vacuum tank, a pair of vented labyrinth seals to separate the high pressure of the supply air from the low pressure in the vacuum tank, and a load cell to measure axial force on the mounting pipe and experimental nozzle. Secondary air enters the system through a flexible hose with zero axial momentum. Both primary air and secondary air are at room temperature. The nozzle gross thrust is determined from an algebraic summation of primary-flow inlet momentum, pressure-area forces, and load cell force.

The systematic error in the performance coefficients measured in the facility is essentially determined by the systematic error incurred in calibrating the facility flow measuring station with a nozzle made to ASME (American Society of Mechanical Engineers) specifications. The flow coefficient of the calibrating nozzle is known with an accuracy of  $\pm 1/2$  percent. Therefore, systematic error in the flow measurement, which directly affects nozzle efficiency, is  $\pm 1/2$  percent. It is clear that for some supersonic aircraft, where nozzle performance should be known to within 0.1 percent, a more accurate flow calibration method is desirable.

The random error incurred in obtaining an individual value of a performance coefficient (one data point) is about  $\pm 1/2$  percent. This relatively low value is achieved by minimizing friction forces in the suspension system and making multiple pressure measurements. Further reductions in random error can

be obtained by averaging measured flow coefficients and exit momenta (taken at operating conditions where these would be expected to remain constant) and computing performance coefficients based on the average value of these parameters. In this manner, the random error can be reduced to infinitesimally small values and small changes in performance can be detected. Data presented have been averaged and each point represents an average of at least five data points.

## PLUG NOZZLE

An exit type which has long been considered for supersonic aircraft is the plug nozzle. A mechanically variable plug nozzle and its internal performance are shown in figure 3. The internal performance is represented by the thrust coefficient which is defined as the ratio of the measured gross thrust to the ideal gross thrust. The basic unshrouded plug nozzle concept provides for a free jet boundary so that the jet can adjust to ambient conditions. An unshrouded plug nozzle design approach is to tilt the throat plane so that, at design pressure ratio, an expansion around the shroud exit will result in axial jet flow. At a subsonic cruise pressure ratio of 6, for example, a throat tilt angle of  $22^\circ$  would be required. With external flow, the large boattail angle and plug angle associated with the  $22^\circ$  tilt angle will cause high boattail drag and overexpansion on the plug surface. In the unshrouded configuration shown in figure 3, a throat tilt angle of  $7^\circ$  and a plug surface angle of  $15^\circ$  are used with the intention of minimizing external flow effects at transonic Mach numbers. For acceleration to supersonic cruise, the plug is collapsed to permit operation of the afterburner (as opposed to other designs which may use a translating plug) and a divergent shroud is fully extended. The divergent shroud has an internal shroud angle of  $9^\circ$ . When cruise conditions are reached, the afterburner is shut down and the plug is expanded to its original position. The divergent shroud, which has a cylindrical exterior and therefore presents no boattail pressure drag, is left in the extended position.

As shown in figure 3, the performance of the takeoff and subsonic cruise configuration decreases with increasing pressure ratio, indicating that regions of local overexpansion on the plug surface are increasing in this pressure-ratio range. At a pressure ratio of 6, the afterburner (A/B) is assumed to be turned on. If only the plug were collapsed, the performance shown by the dashed curve would be obtained. Extension of the divergent shroud enables the acceleration performance shown by the solid curve to be realized. At cruise conditions, afterburner off, expansion occurs along the divergent shroud and plug surface and a high level of cruise performance results. With mechanical variation then, the internal performance of a plug nozzle, as indicated in figure 3, can be maintained at an acceptably high level over a wide range of flight conditions. It should be noted, however, that external flow effects will reduce the performance from that shown at transonic flight conditions.

The effects of some geometric variations on the supersonic cruise performance of the supersonic cruise configuration are shown in figure 4. In figure 4(a), increasing the shroud angle from  $5^\circ$  to  $12^\circ$  decreases the cruise performance by about 1.4 points. In figure 4(b), the effect of plug angle on cruise performance is shown to be very small for plug angles between  $10^\circ$  and

15°. Figure 4(c) shows the effect of reducing plug length by plug truncation. The supersonic cruise performance is decreased a negligible amount as the plug length, measured downstream from the nozzle throat, is decreased from 100 percent to 50 percent but is decreased significantly as the plug length is further decreased. The effects of some of these same geometric variations on the takeoff performance of the takeoff configuration are shown in figure 5. In figure 5(a), the effect of changing the plug angle from 10° to 15° is shown to affect the performance of the takeoff configuration only slightly. Truncation of the plug of the takeoff configuration to about 27 percent of its full length is shown, in figure 5(b), to decrease the performance from  $1\frac{1}{2}$  to 3 points, depending on nozzle pressure ratio.

The plug nozzle just shown was designed for a pressure-ratio range from 3.2 to 26.0. Plug nozzles intended for smaller pressure-ratio ranges can be somewhat simplified. A plug nozzle designed for a pressure-ratio range from 2.0 to 12.5 and its performance are presented in figure 6. Although this nozzle design retains the collapsing plug feature for throat area control, the shroud does not translate but contracts for area-ratio variation. This nozzle has small amounts of secondary air introduced through a plug slot for simulated plug cooling flow. The performance of this and succeeding nozzles which have secondary flow is defined as the ratio of the measured gross thrust to the ideal gross thrust of both the primary and secondary flows.

The divergent shroud was considered to be either actuated or freely floating. Floating positions were considered to be limited by stops to an inward angle of 10.5° and an outward angle of 3°. To obtain the performance shown in figure 6, several models with different fixed divergent-shroud positions were run at each pressure ratio. The best performance obtained at each pressure ratio is shown by the solid line. The solid line, therefore, represents the performance that could be obtained if the shroud were held by actuators at optimum expansion conditions. The internal-pressure distribution data obtained during these tests, together with an assumed uniform external pressure, made it possible to calculate the floating position that the shroud would assume at each pressure ratio. The performance of the fixed models with shroud positions set at the calculated floating positions is shown by the dashed line. The dashed line, therefore, represents the reduced performance that would be obtained if the floating-shroud concept is used. Additional calculations showed that, with external flow, typical boattail pressure distributions (as opposed to a uniform static pressure) would not significantly change the floating positions. The reduced boattail pressure would affect the expansion along the plug surface, however, and the performance would be further reduced. It appears, therefore, that the elimination of divergent-shroud actuators from this particular nozzle design would result in some reduction in performance at transonic pressure ratios.

The plug surface in a plug nozzle must be cooled, possibly by film cooling. In figure 7, the measured film-cooling pressure requirements of a particular plug nozzle model are presented as a function of plug flap angle. In the upper part of the figure, the cooling slot arrangement used to obtain these data is also shown. There are two circumferential slots, one at the nozzle throat and another at about 40 percent of the full plug length. It can be seen that to

obtain 6-percent corrected secondary flow (an amount which might be required with the afterburner on) at low flap angles (which would exist at these conditions), a secondary total pressure greater than the primary total pressure would be required. Even the minimum secondary-to-primary total-pressure ratio shown in this figure is as high as 0.31. Ram air would not reach this level below a flight Mach number of 1.2. Therefore, this particular plug film-cooling scheme would require air from the engine cycle below this Mach number.

#### AUXILIARY-INLET EJECTOR

A second type of exit that has been considered is the auxiliary-inlet ejector. The auxiliary-inlet-ejector concept is shown in figure 8. At supersonic cruise flight conditions, an auxiliary-inlet ejector operates as a standard ejector nozzle, with a small amount of secondary air being introduced for cooling. To optimize performance at these conditions, the leading-edge section of the divergent shroud is hinged so that only a small gap exists between the primary and secondary nozzles. At transonic flight conditions, the primary nozzle is mechanically opened for afterburner operation and the leading-edge section of the shroud is mechanically retracted to increase the amount of secondary flow. At subsonic flight conditions, with the afterburner off, internal and external pressure forces are expected to be such that doors on the outside of the nacelle will open and trailing-edge flaps will close, without any need for mechanical actuation. The large amount of tertiary flow which enters the auxiliary inlet is intended to prevent overexpansion of the primary nozzle stream. The last sketch in figure 8 shows the incorporation of a retractable multiple-chute noise suppressor, similar in shape to that used on subsonic engines, into the auxiliary-inlet-ejector design. It was found that chutes of this type, which in this case were probably immersed in supersonic flow, seriously reduced the takeoff performance.

The auxiliary-inlet-ejector design could be somewhat simplified if the mechanically actuated leading-edge section of the divergent shroud could be removed and replaced with a fairing fixed in the retracted position. The effects of removing this section on the cruise performance of a particular configuration are shown in figure 9. Removing the leading-edge section reduced the thrust coefficient by 0.4 of a point while the secondary-to-primary total-pressure ratio required to provide 2-percent cooling flow was essentially unchanged. A thrust coefficient decrement of 0.4 of a point at supersonic cruise conditions may be important for some applications.

#### VARIABLE-FLAP EJECTOR

A third type of exit is the variable-flap ejector. A schematic view of a variable-flap ejector is shown in figure 10. Fixed models of variable-flap-ejector components are shown in figure 11. The primary nozzle is considered to be actuated whereas the divergent shroud can be actuated or freely floating. Each flap in the divergent shroud is a link in a four-bar linkage. The forward

pivot point in the linkage is attached to the primary nozzle so that the leading edge of the divergent shroud can follow the movements of the primary nozzle. Each flap of the divergent shroud may have several slots to promote detachment and stability of the primary jet at low area ratios and low pressure ratios. These slots can be seen in the divergent-shroud model shown in figure 11(a). Some models of this ejector had star-shaped primary nozzles. A model of a star-shaped primary nozzle is shown in figure 11(b). The star-shape design permits the leaves to fold upon one another for primary-nozzle area variation. The performance of a variable-flap ejector with a star-shaped primary nozzle and slotted flaps is shown in figure 12. Both the cruise and take-off thrust coefficients are acceptably high. The available and required secondary-to-primary total-pressure ratios are also shown in this figure. The available secondary pressure is considered to be the total pressure available at the engine face. At supersonic cruise, the secondary-to-primary total-pressure ratio required for 2-percent corrected secondary cooling flow was well below the available amount. To obtain the takeoff thrust coefficient shown in this figure, almost all the secondary-to-primary total-pressure ratio available must be used. This result suggests that the secondary flow for takeoff, which amounts to about 4 percent of the primary flow, would have to be taken aboard through inlets located close to the ejector to minimize duct losses.

#### CONCLUSIONS

The effects of some geometric variables on the internal performance of plug nozzles, auxiliary-inlet ejectors, and variable-flap ejectors have been presented. It is concluded that:

1. All the exit types discussed can, in principle, meet the performance requirements of supersonic aircraft.
2. All the exit types are mechanically complex.
3. The ejector nozzles can generally obtain the amount of secondary air anticipated for adequate film cooling from ram air whereas some plug-nozzle film-cooling schemes may require engine-cycle air.

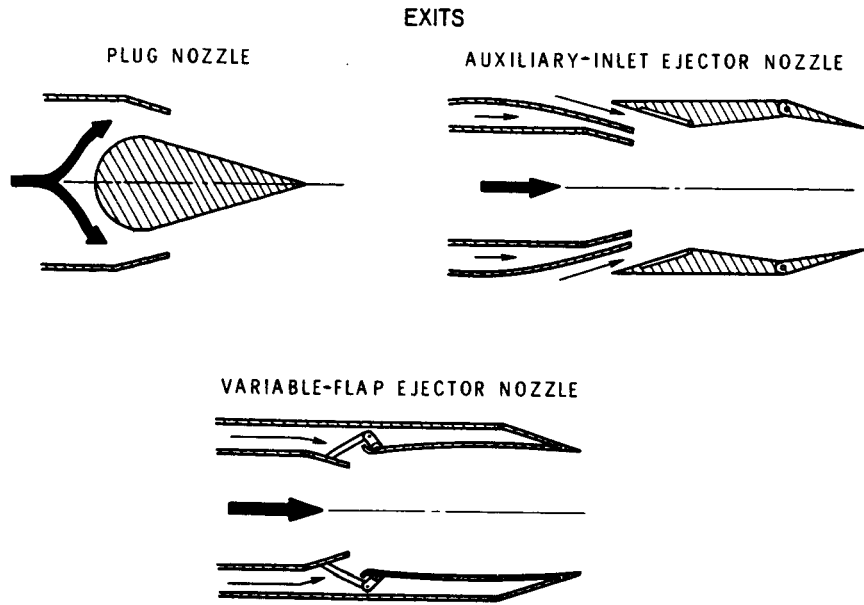


Figure 1

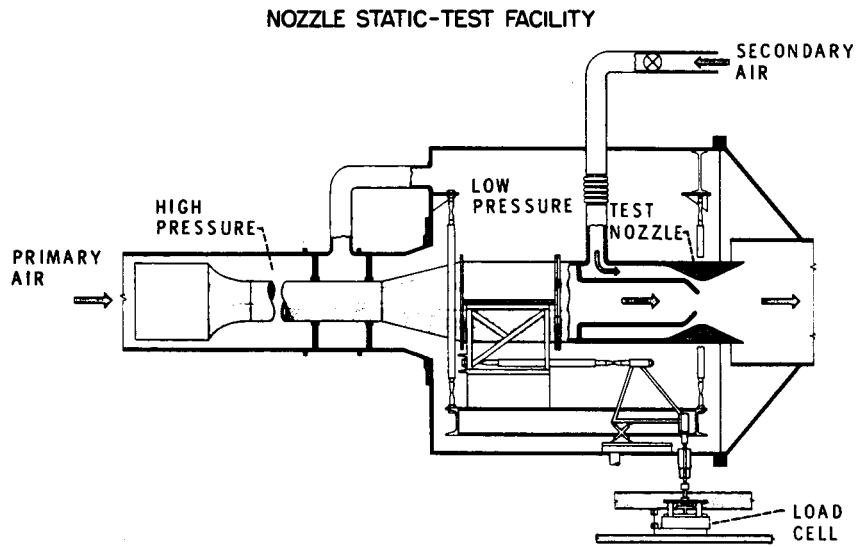


Figure 2

MECHANICALLY VARIABLE PLUG NOZZLE  
INTERNAL PERFORMANCE

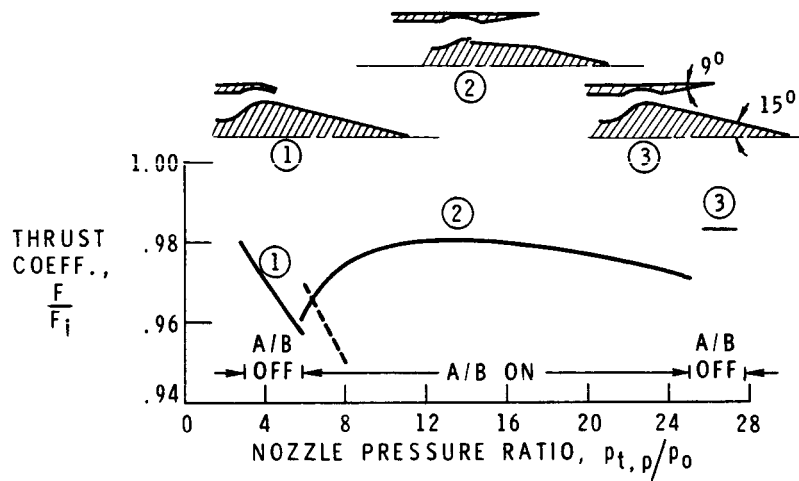


Figure 3

EFFECT OF GEOMETRIC VARIABLES ON PLUG NOZZLE PERFORMANCE  
CRUISE PRESSURE RATIO OF 26.0

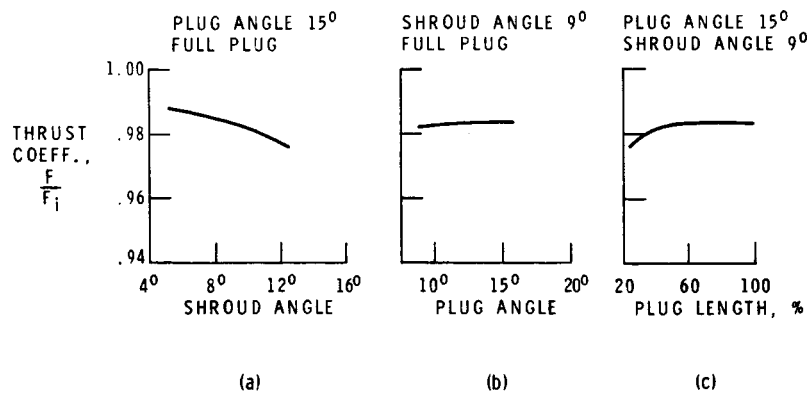


Figure 4

EFFECT OF GEOMETRIC VARIABLES ON  
PLUG NOZZLE PERFORMANCE

TAKEOFF PRESSURE RATIOS

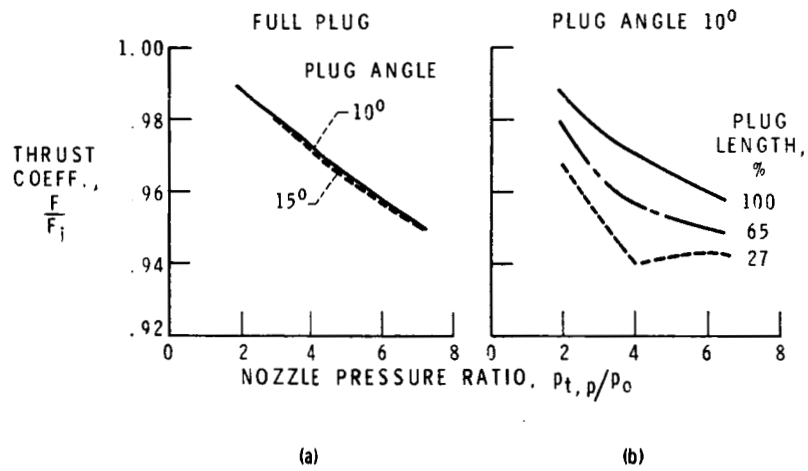


Figure 5

FLOATING SHROUD VARIABLE PLUG NOZZLE PERFORMANCE

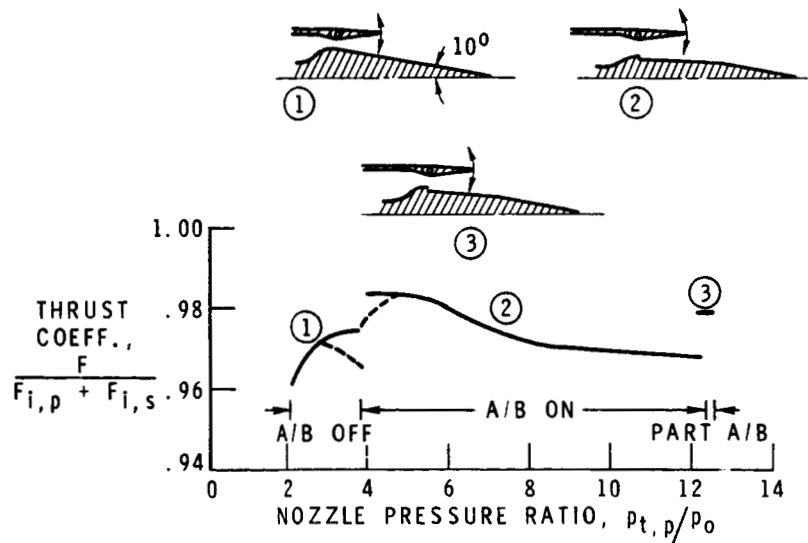


Figure 6

PRESSURE REQUIREMENTS FOR PLUG FILM COOLING

$$P_{t,p}/P_0 > 3.0$$

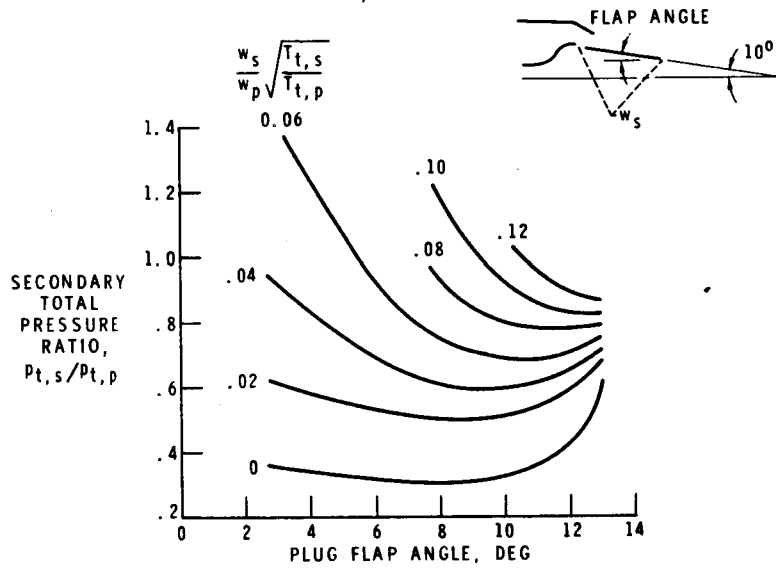
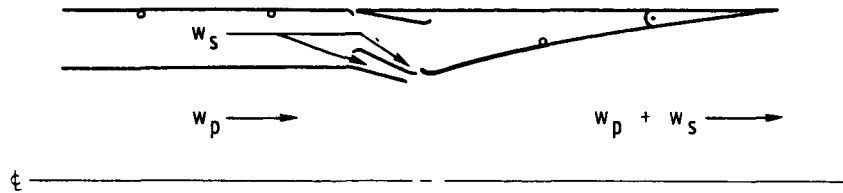
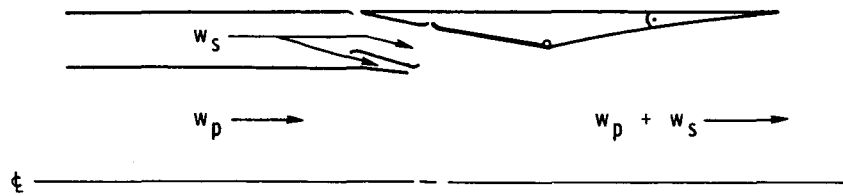


Figure 7

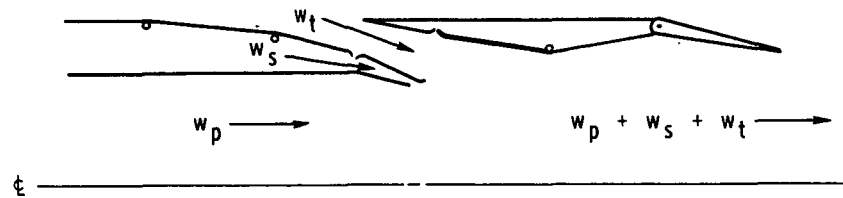
SCHMATIC VIEW OF AUXILIARY-INLET EJECTOR  
SUPERSONIC



TRANSONIC



SUBSONIC



TAKEOFF WITH NOISE SUPPRESSION CHUTES

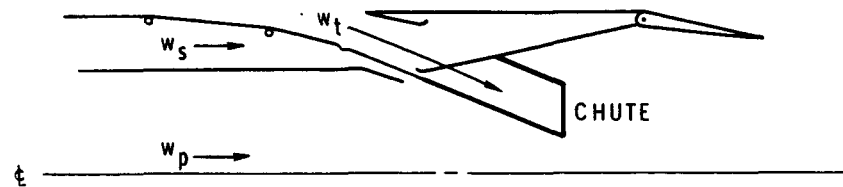


Figure 8

CRUISE PERFORMANCE AND PUMPING CHARACTERISTICS  
OF AN AUXILIARY-INLET EJECTOR

A-ACTUATED  
DIVERGENT SHROUD

B-LOCKED OPEN  
DIVERGENT SHROUD



$$\frac{w_s \sqrt{T_{t,s}}}{w_p \sqrt{T_{t,p}}} = 0.02$$

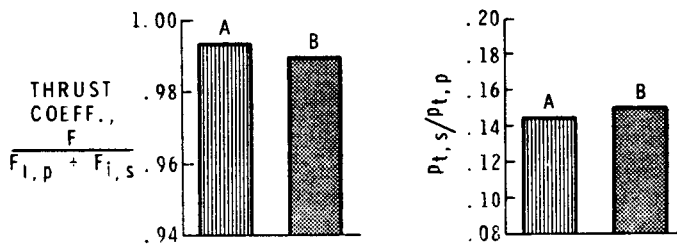


Figure 9

SCHEMATIC VIEW OF VARIABLE-FLAP EJECTOR

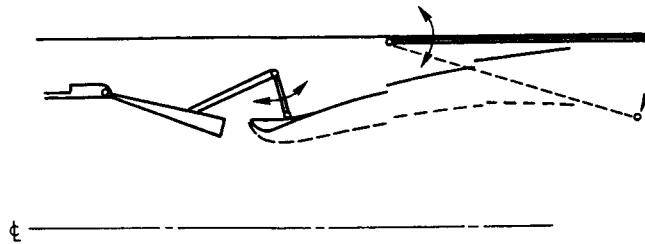


Figure 10

SLOTTED DIVERGENT SHROUD MODEL

STAR-SHAPED PRIMARY MODEL

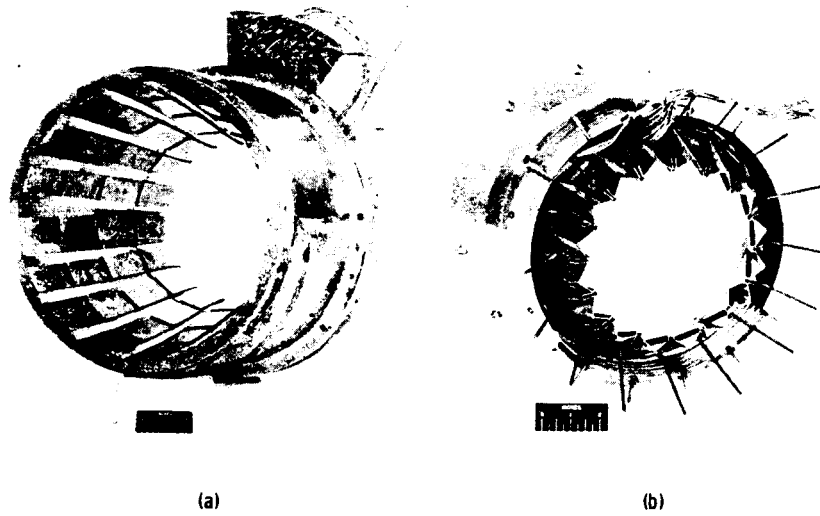


Figure 11

PERFORMANCE OF A VARIABLE-FLAP EJECTOR  
STAR-SHAPED PRIMARY NOZZLE AND  
SLOTTED SECONDARY FLAPS

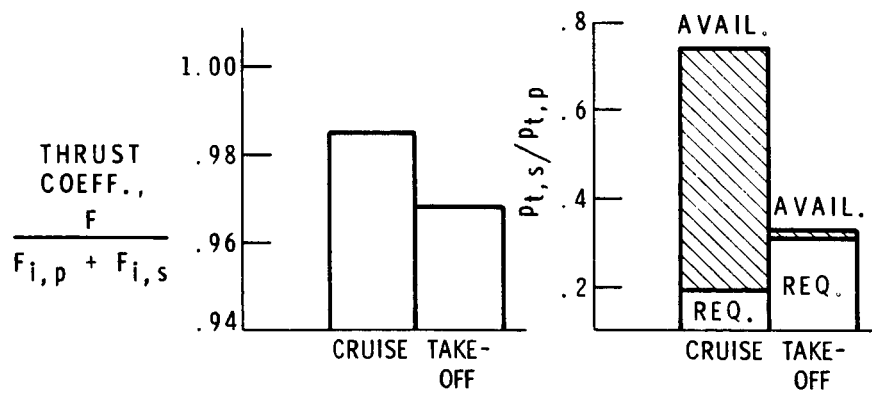


Figure 12

## 18. WIND-TUNNEL STUDIES OF NACELLE INTERFERENCE DRAG

AT HIGH SUBSONIC SPEEDS INCLUDING

THE EFFECT OF POWERED JETS

By James C. Patterson, Jr.  
NASA Langley Research Center

### SUMMARY

Experimental wind-tunnel investigations have been conducted recently by the National Aeronautics and Space Administration to determine the aerodynamic interference associated with engine-pylon installations. The studies included the effects of powered jets. Tests were conducted on an aft-fuselage-mounted nacelle configuration over a Mach number range from 0.665 to 0.82 at Reynolds numbers of  $2.74 \times 10^6$  to  $3.94 \times 10^6$  based on the mean geometric chord of 3.2 inches. Tests were also conducted on a semispan model of a cargo-type logistic transport configuration with an underwing pylon-mounted powered-engine nacelle and on a 0.0576-scale semispan model of the Lockheed C-5A transport configuration. The effects of powered fan-jet model engines were included. These tests were conducted over a Mach number range from 0.70 to 0.825 at Reynolds numbers of  $6.10 \times 10^6$  to  $7.13 \times 10^6$  based on the mean geometric chord of 21.158 inches.

The results of these investigations indicate that favorable interference drag may be obtained by detailed tailoring of the engine nacelles and pylons to the airplane itself. The effect of the powered jet on aerodynamic interference is such that the favorable interference noted at the cruise Mach number was doubled throughout the higher lift-coefficient range of this investigation.

### INTRODUCTION

One important fact to be considered in the design of airplanes of today is aerodynamic interference. Investigations to determine aerodynamic interference resulting from engine-pylon installations have been conducted recently by the NASA on a small transport configuration having aft-fuselage-mounted nacelles and on the more familiar underwing pylon-mounted nacelle configurations. The studies of the underwing configurations included the effects of a powered model of a fan-jet engine.

The ability to simulate the full-scale engine and nacelle aerodynamic and geometric effects in the wind tunnel is unique and offers the potential of obtaining engine-jet-stream interference effects which could very possibly result in new engine-installation methods.

ceding page blank

## SYMBOLS

$C_D$	drag coefficient, $Drag/qS$
$\Delta C_D$	interference drag coefficient
$C_L$	lift coefficient
$\Delta C_p$	incremental pressure coefficient
$M$	Mach number
$P_{t,e}$	engine fan exit total pressure
$P_{t,\infty}$	free-stream total pressure
$q$	free-stream dynamic pressure
$R_{\bar{c}}$	Reynolds number based on mean geometric chord
$S$	wing area
$x/l$	ratio of longitudinal distance from powered-engine leading edge to total length of powered engine

## DISCUSSION

### Aft-Fuselage-Mounted Nacelle Configuration

A sting-supported model of a small transport configuration with engine nacelles pylon-mounted on the rear of the fuselage is shown in figure 1. Tests were conducted on this configuration with the engine nacelles mounted in various longitudinal locations, with the engine-nacelle incidence angle and cant angle varied to align the engines with the local flow, and with the pylons and engine nacelles extended chordwise (as shown by the dashed nacelle-pylon outline in fig. 1) in an attempt to improve the area distribution in the vicinity of the engine nacelles. The test Mach number ranged from 0.665 to 0.82.

The results of this investigation are presented as interference drag coefficient  $\Delta C_D$  for the various configurations tested. These interference-drag values are obtained from the difference between the drag level of the basic airplane configuration and that of the basic configuration less pylons and engine nacelles plus the calculated skin-friction drag of the pylons and engine nacelles throughout the Mach number range for a lift coefficient of 0.25. (See fig. 2.)

The interference-drag results obtained for the four previously mentioned configurations tested - engine longitudinal location, nacelle incidence angle,

cant angle, and engine and pylon extension - are shown in figure 3. The interference-drag results of the basic configuration are shown in each of the four plots for reference. The negative values of  $\Delta C_D$  represent favorable interference whereas the positive values represent interference drag. The results obtained for the basic configuration indicate interference drag in the lower Mach number range and favorable interference above a Mach number of 0.79.

The optimum longitudinal nacelle location, determined from tests conducted on a series of chordwise nacelle locations, was obtained by moving the nacelle-pylon combination rearward 27 percent of the wing mean aerodynamic chord from its original position on the basic configuration. The interference-drag results obtained for the improved longitudinal location indicate a reduction in interference drag coefficients over that obtained for the original location throughout the Mach number range with an increase in the favorable interference at the higher test Mach numbers.

To aline the engine nacelles with the local flow, tests were conducted through a nacelle-incidence-angle range from approximately  $0^\circ$  to  $4^\circ$ . The lowest interference drag results were obtained at an incidence angle of  $2.5^\circ$ . The effect of this incidence angle is shown in the lower left-hand plot of figure 3; throughout the Mach number range, the interference drag coefficient is reduced.

A cant angle of  $3.5^\circ$  was investigated (nacelle inlet directed outward), which resulted in a slight decrease in drag in the lower Mach number range, followed by a reduction in the favorable interference at higher Mach numbers. Since only one cant angle was investigated, it is possible that further improvement may very well be obtained at other cant angles.

The rearward chordwise engine nacelle and pylon extension, of approximately 25 percent of the nacelle length, increases the favorable interference from a Mach number of 0.775 to a Mach number of 0.82 as a result of an improvement in the local area distribution.

Unfortunately, tests were not conducted with the nacelle-pylon configuration in its most favorable location, but the configuration changes investigated are such that their contributions to interference drag may very possibly be additive. Nevertheless, the data presented indicate that the aerodynamic interference can be reduced and a favorable interference produced in many cases as a result of tailoring the nacelle-pylon combination to the airplane itself by taking into consideration the area distributions and local flow conditions.

#### Underwing Pylon-Mounted Engine Nacelles Including Power Effect

Investigations including the effects of the fan-jet flow on the aerodynamic interference have also been made of the more familiar underwing pylon-mounted engine configuration. With the development of the current high-bypass fan-jet engines, the exact effect that the fan-jet flow has on aerodynamic interference has become very important. An investigation to determine this power

effect has recently been conducted with the use of a semispan model of a cargo type airplane configuration. Figure 4 shows this model installed in the Langley 8-foot transonic pressure tunnel. The fuselage is mounted directly on the tunnel wall while the wing is mounted directly on the force balance. A powered model of a fan-jet engine is pylon-mounted under the wing. The force results were obtained for the wing-pylon-engine combination and included the influence of the presence of the fuselage on these components.

The interference drag coefficient  $\Delta C_D$  for the powered-model test was obtained by reducing the total drag measured with the force balance by the computed thrust and by the drag of the three individual components of the model: wing, engine, and pylon. This procedure is shown by the following equation:

$$\Delta C_D = (C_D)_{\text{total}} + C_F - (C_D)_{\text{wing}} - (C_D)_{\text{engine}} - (C_{D,f})_{\text{pylon}}$$

where

- $(C_D)_{\text{total}}$  total measured wing-pylon-engine drag coefficient, obtained from wall-mounted strain-gage force balance
- $C_F$  engine net thrust coefficient based on wing area, computed from total-pressure and static-pressure measurements taken in fan inlet, fan exit, turbine inlet, and turbine exit
- $(C_D)_{\text{wing}}$  wing-drag coefficient, obtained from wall-mounted strain-gage force balance during tests made with the engine and pylon removed
- $(C_D)_{\text{engine}}$  measured drag coefficient less pylon drag coefficient and less engine net thrust coefficient for the engine alone
- $(C_{D,f})_{\text{pylon}}$  pylon skin-friction drag coefficient, calculated by using skin-friction values from the Sommer and Short 'T' method (see ref. 1)

The engine-alone measurements were obtained during tests of the engine mounted on an elongated pylon that was mounted directly on the balance. The pylon drag was measured during tests performed with the engine removed from this configuration. The engine net thrust was obtained from the same type of pressure measurements and computing method used during the complete-configuration test.

Fan-jet engine.- The general outline of the full-scale fan-jet engine which is to be used on the C-5A logistic transport is shown in figure 5. The engine is approximately 25 feet long and has a maximum fan-cowl diameter of 9 feet. Eighty-five percent of the maximum thrust of 41 000 pounds is produced by this fan. With a bypass ratio of 8.1, approximately 1335 lb/sec of the total engine weight flow of 1500 lb/sec passes through the fan, whereas 165 lb/sec of air enters the primary discharge nozzle.

An effort was made during the design of this engine to maintain an area distribution which would be compatible to that of the overall area buildup of the C-5A type airplane configuration. This effort has resulted in a smooth total area distribution for the engine-airplane combination.

Model engine.- A cross-sectional view of the powered model of the C-5A engine used during this investigation is shown in figure 6. The two-stage fan is connected directly to the nitrogen-driven three-stage turbine. This model engine was designed to produce the same mass-flow ratio and exit-pressure ratio as the actual full-scale engine. At the maximum design speed of 45 000 rpm, the model engine, which has a maximum diameter of 5.9 inches and an overall length of 18 inches, develops approximately 130 horsepower.

Total-pressure rakes and static-pressure taps were located in the fan inlet, in the fan exit, and in the turbine exit to obtain the measurements to be used in computing thrust. A total of 276 pressures were recorded during this investigation and included surface pressures on the fan cowl, turbine, turbine exit plug, pylon surfaces, and wing upper and lower surfaces in the vicinity of the wing-pylon juncture.

Jet effects.- The effect of the powered fan-jet engine on the aerodynamic interference is shown in figure 7 as the interference drag coefficient  $\Delta C_D$  plotted against lift coefficient for fan-exit pressure ratios of 1.0 and 1.47. A pressure ratio of 1.0 is obtained with the engine operating just fast enough to overcome the internal losses of the engine, and zero thrust is produced. A pressure ratio of 1.47 is obtained for the maximum design speed, where maximum thrust is produced. The data indicate that with power on, the favorable interference is increased throughout the lift-coefficient range, with a maximum increase of approximately 10 drag counts at the highest lift coefficient.

A possible explanation for the increase in favorable interference may be that with the engine operating at the zero thrust condition, there is a tendency for the pressure to become equalized on the inboard and outboard sides of the pylon. This balance of pylon pressure is believed to be caused by a pressure leakage that takes place between the fan cowl and the turbine cowl, as shown by the arrow in the cutaway oblique view of the engine in figure 7. The change in pressure coefficient ( $\Delta C_p$ ) between the inboard side and the outboard side of the pylon measured along the nacelle-pylon juncture is presented in the lower plot of figure 7 as a function of nacelle length.

The pressure difference is small for the zero thrust condition; however, with the engine producing maximum thrust, the fan exit is choked and the pressure leakage from the inboard side to the outboard side of the pylon cannot occur. This is shown in figure 7 as an increase in the difference in pressure coefficient. This increase in pylon normal force is believed to be a result of an increase in the end-plate effectiveness of the engine nacelle with the fan exit choked plus the effect of the increase in the fan-jet flow over the rear portion of the pylon. This pylon normal force, when reduced to a lift vector perpendicular to the local flow, results in a thrust vector in the stream direction, because of the direction of this local flow associated with the

swept wing. This induced thrust may possibly account, in part, for the favorable interference obtained with power on.

C-5A logistics transport.- Further investigations have been made by using a semispan model of the C-5A logistics transport configuration mounted in the Langley 8-foot transonic pressure tunnel. Again, the fuselage was mounted directly on the tunnel wall and the wing was mounted directly on the force balance. Two powered fan-jet engines were pylon-mounted under the wing of the C-5A model as shown in figure 8. A total of 552 surface pressures and total rake pressures were measured during this two-engine investigation.

Engine position.- The results obtained from an investigation of engine position are shown as interference drag plotted against Mach number in figure 9 for the basic engine position, for the engine moved rearward, and for the engine moved rearward and vertically upward. The data indicate that the greatest favorable interference effect is obtained with the engine in the most forward position. These results substantiate results obtained previously (not shown herein) for the one-engine test where it was also found that with the engine in the foremost longitudinal and lowest vertical position the most favorable interference results were obtained.

The data in figure 9 indicate that interference drag is very sensitive to engine position. With the engine moved rearward approximately 10 percent of the engine length, favorable interference is obtained in the lower Mach range; before the cruise Mach number is reached, however, the interference drag coefficient becomes unfavorable. The reduction in pylon leading-edge sweep associated with this rearward movement of the engine from  $77.5^\circ$  to  $74^\circ$  results in an increase in pylon side force which may possibly account for the favorable interference obtained for this configuration at the lower Mach numbers. The unfavorable interference drag obtained in the higher Mach number range would result from the change in the area distribution caused by this change in engine position. As the engine is moved closer to the wing, the interference drag is increased even further and, in fact, no favorable effects occur throughout the Mach number range. These results, in the lower Mach number range, may be attributed to the increase in pylon leading-edge sweep and the associated loss in side force; in the higher Mach number range, they may be attributed to a magnification of the already unfavorable effects associated with the change in area distribution as the engine is moved even closer to the wing.

Pylon leading-edge extension.- The effect of pylon leading-edge extension was also investigated. Figure 10 shows the two pylon configurations tested. The first pylon has a leading edge sweep of  $74^\circ$  and is attached to the lower surface of the wing, just behind the wing leading edge, as proposed for the C-5A airplane. The second pylon, having the same sweep, has its leading edge extended forward approximately 10 percent of the pylon chord. This extension results in the pylon leading edge extending over the wing, as shown by the dashed outline on the sketch in the upper part of the figure.

The data indicate that the configuration having the originally proposed pylon configuration provided favorable interference at the cruise Mach number. The extended-eylon configuration produced approximately zero interference drag

in the lower Mach number range, becoming unfavorable at the higher test Mach numbers. Further wind-tunnel investigations will be necessary before an explanation can be given for this difference in interference drag resulting from this change in pylon extension.

#### CONCLUSIONS

Wind-tunnel studies of nacelle interference drag at high subsonic speeds including the effect of powered jets have been presented. The data indicate that the aerodynamic interference resulting from nacelle-eylon installation may be minimized or even made favorable by properly locating the engine nacelles and by detailed tailoring of the engine-eylon configuration. It has also been shown that the effect of the powered jet is such that the favorable interference noted in this investigation was doubled throughout the higher lift-coefficient range. Inasmuch as only a few possible engine installations have been studied herein, it should be emphasized that more extensive wind-tunnel investigations will be required before the exact effect that the powered jets have on interference drag can be fully understood.

#### REFERENCE

1. Peterson, John B., Jr.: A Comparison of Experimental and Theoretical Results for the Compressible Turbulent-Boundary-Layer Skin Friction With Zero Pressure Gradient. NASA TN D-1795, 1963.

AFT-FUSELAGE-MOUNTED NACELLES  
 WING AREA, 51.5 SQ IN.; MEAN AERODYNAMIC CHORD, 3.2 IN.;  
 $R_{\xi} = 2.74 \text{ TO } 3.94 \times 10^6$

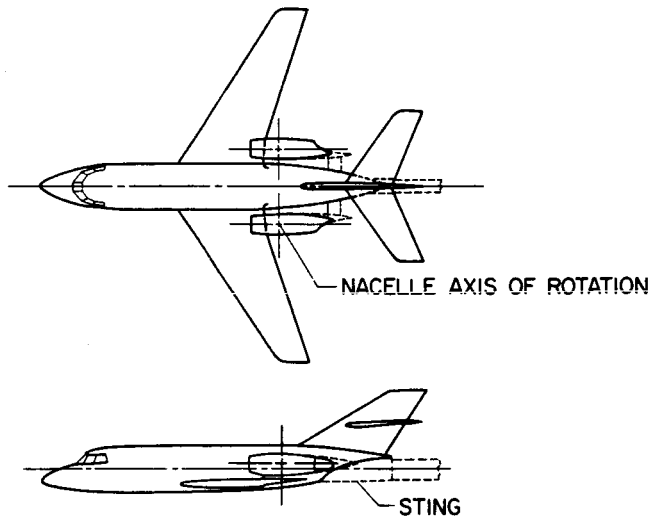


Figure 1

ENGINE NACELLE-PYLON DRAG  
 $C_L = 0.25$

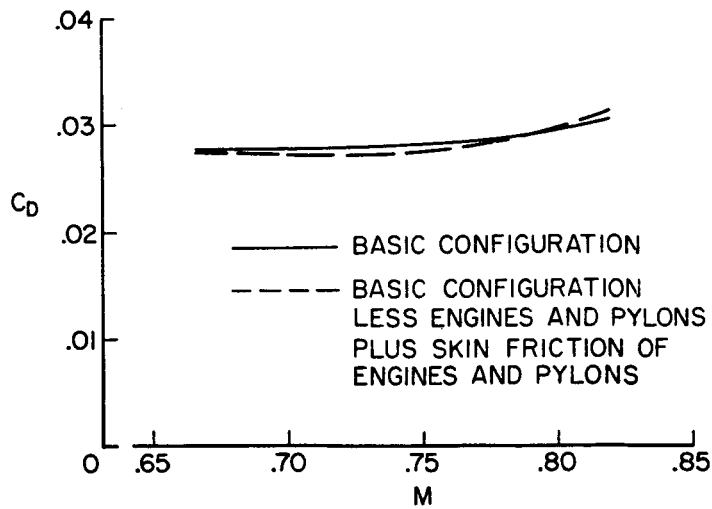


Figure 2

# INTERFERENCE DRAG

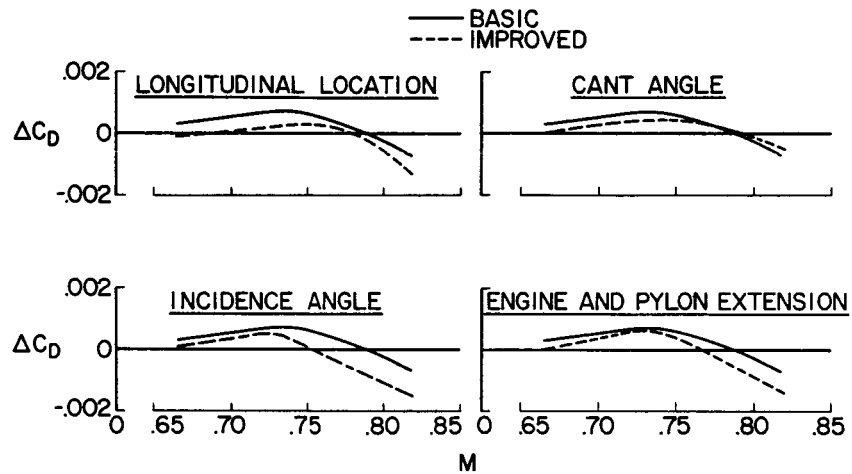


Figure 3

## CARGO-TYPE AIRPLANE MODEL WITH POWERED ENGINE

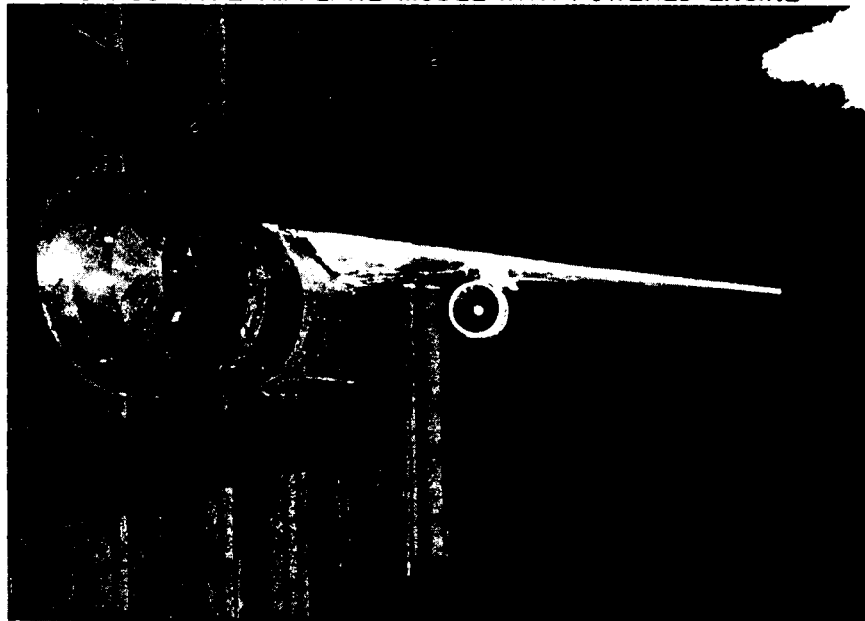


Figure 4

L-2683-6

### CONFIGURATION OF C-5A FAN-JET ENGINE

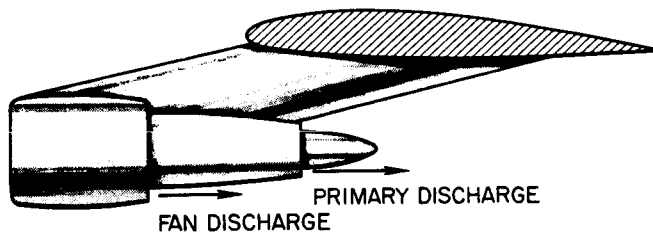


Figure 5

### MODEL-ENGINE CROSS SECTION

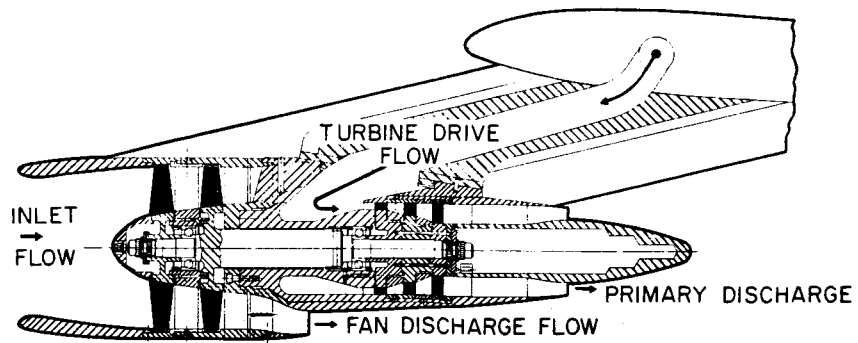


Figure 6

ENGINE-JET EFFECT  
M=0.78

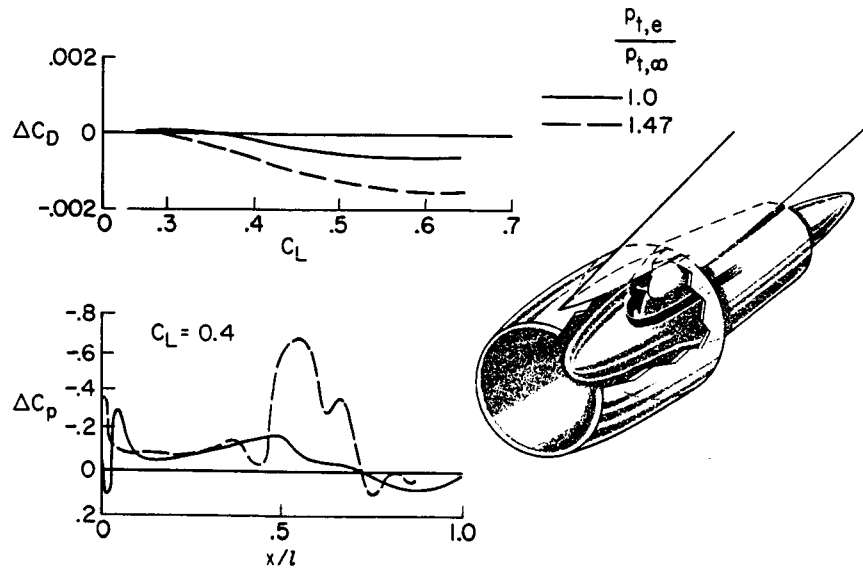


Figure 7

C-5A MODEL WITH POWERED ENGINES



Figure 8

L-2683-5

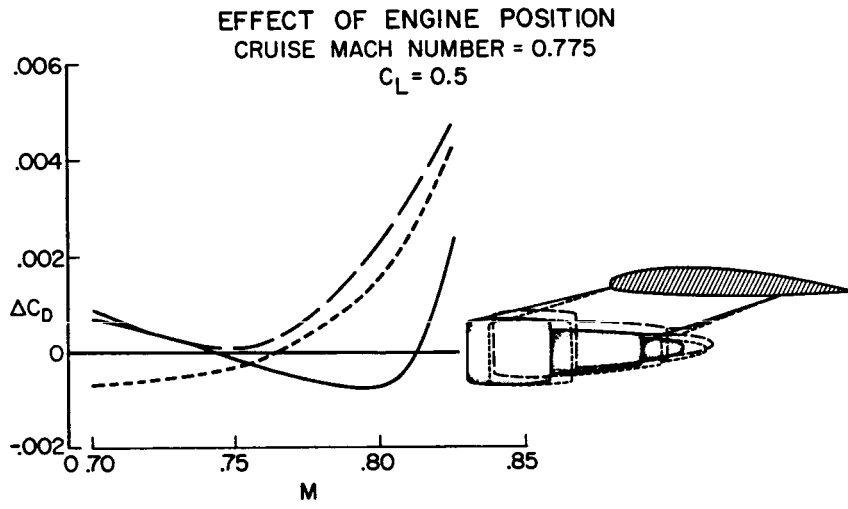


Figure 9

**EFFECT OF PYLON LEADING-EDGE EXTENSION**  
**CRUISE MACH NUMBER = 0.775**  
 $C_L = 0.5$

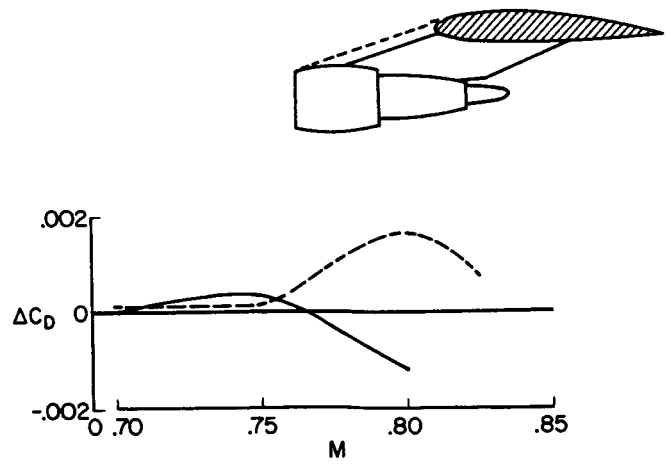


Figure 10

## 19. GROUND EFFECTS RELATED TO LANDING OF AIRPLANES

### WITH LOW-ASPECT-RATIO WINGS

By William B. Kemp, Jr., Vernard E. Lockwood,  
and W. Pelham Phillips  
NASA Langley Research Center

#### SUMMARY

Some results of a study of the influence of ground-induced aerodynamic effects on the landing maneuver of airplanes with low-aspect-ratio wings are presented. The fundamental mechanism of ground induction is reviewed and a simplified landing-flare analysis is used to illustrate the significance of the ground-induced pitching moment, the load factor just before touchdown, and the ground effects on the elevator characteristics. Some effects of wing planform and airplane size are shown by use of dynamic calculations of airplane motions during the landing flare. A constant-pitch-attitude landing flare is shown to be possible for some large airplanes with low-aspect-ratio wings.

#### INTRODUCTION

Many airplane designs proposed for supersonic missions have employed low-aspect-ratio delta-related wing planforms. The achievement of appropriate lift coefficients for landing with these wings requires angles of attack so high that provision of adequate ground clearance is a serious problem and may possibly necessitate lower wing loadings or longer landing gears than would be desirable otherwise. Some wind-tunnel measurements on low-aspect-ratio wings have indicated that the effects of ground proximity may allow the angle of attack at a landing touchdown to be several degrees less than that required to obtain the same lift coefficient away from the ground, and thus may significantly alleviate the ground-clearance problem. Furthermore, since this angle-of-attack change due to ground proximity may be of the same order of magnitude as the flight-path angle in a normal landing approach, the execution of a landing-flare maneuver without changing airplane attitude appears within the realm of possibility. The constant-attitude flare is viewed in some quarters as being considerably easier and therefore safer than a conventional landing-flare maneuver.

With these considerations in view, a study has been initiated at the NASA Langley Research Center using wind-tunnel experiments and theoretical procedures to determine the influence of several configuration parameters on the ground effects on low-aspect-ratio wings. It is the purpose of this paper to present some highlights of the findings to date as they relate to the landing maneuver.

## SYMBOLS

A	wing aspect ratio
$\bar{c}$	wing mean aerodynamic chord, ft
$c_e$	elevator chord, ft
$C_L$	lift coefficient
$C_D$	drag coefficient
$C_m$	pitching-moment coefficient
$C_{L\delta}$	rate of change of lift coefficient with elevator angle at constant angle of attack, per degree
$C_{m\delta}$	rate of change of pitching-moment coefficient with elevator angle at constant angle of attack, per degree
h	height above ground of a point on the wing chord plane at the longitudinal location of the center of gravity, ft
$h_{lg}$	height of landing gear above ground, ft
n	normal load factor
S	wing area, sq ft
t	time, sec
V	airplane velocity, knots
W	airplane weight, lb
$\alpha$	angle of attack, deg
$\delta$	elevator angle, deg
$\Delta C_{i,G}$	ground-induced increment in any coefficient $C_i$
$\Delta\alpha_F$	angle-of-attack change during the flare, deg
$\Delta\delta_F$	elevator-angle change during the flare, deg
$\gamma$	flight-path angle, deg
$\theta$	airplane pitch attitude, deg

Subscripts:

- A conditions in free-air approach
- G conditions at ground contact

DISCUSSION

Comparison of Conventional- and Delta-Wing Airplanes

The first two figures compare the ground effects on two airplane configurations having widely different aspect ratios. Figure 1 illustrates the ground effects measured on a wind-tunnel model typical of a conventional subsonic jet transport with an aspect-ratio-6 wing. Drag coefficient, angle of attack, and pitching-moment coefficient are shown as functions of lift coefficient. The solid curves represent the characteristics in free air and the dashed curves correspond to the wheels touching the ground.

At the lower lift coefficients, the ground effect produces a small increase in lift at a given angle of attack. The maximum lift coefficient, however, is significantly reduced by proximity to the ground. These trends are typical of the ground effects observed on configurations with wings of moderate to high aspect ratio. For comparison, figure 2 shows the corresponding characteristics of a model having a  $55^\circ$  clipped delta wing with an aspect ratio of 2.26. Again, the drag coefficient, angle of attack, and pitching-moment coefficient are plotted against lift coefficient for free air and for a height representative of a wheel touchdown condition. Since the low-aspect-ratio wing does not exhibit a true stall, the ground effects on maximum lift coefficient need not be considered. Lift coefficients appropriate for a landing approach are indicated for each configuration. Observe that at the approach lift coefficient, the ground effects on the low-aspect-ratio wing allow a reduction in angle of attack of more than  $3^\circ$  from free air to touchdown, whereas the corresponding angle-of-attack reduction for the subsonic jet configuration is only about  $1/2^\circ$ .

Both configurations show significant drag reductions in ground effect. Although these drag reductions would affect the speed bleed-off in a landing flare, further analysis of the ground effects on drag is beyond the scope of this paper.

The pitching-moment characteristics show that both configurations experience a modest increase in static stability in proximity to the ground, with a resultant increase in nose-down moment at the approach lift coefficient. The effect of trimming out this moment change is discussed in a subsequent section. The data of figures 1 and 2 show that the angle-of-attack increment produced by ground proximity is of greatest interest for the low-aspect-ratio configuration. The present study has, therefore, emphasized the low aspect ratios.

## Mechanism of Ground Induction

Consider an airplane flying in close proximity to the ground (fig. 3). The effect of the ground is to prevent the existence of any vertical air velocity at the ground plane. If the ground is replaced by an inverted mirror-image airplane flying under the ground, all vertical velocities induced by the airplane and its image are canceled at the plane of symmetry. Thus, the effects of the image airplane are identical to the effects of a ground plane. Figure 4 shows the airplane in side view with a typical chordwise distribution of lift due to angle of attack. The aerodynamic center is at the centroid of this distribution. This same distribution of lift is represented on the image airplane as a system of lifting and trailing vortices. The image vortex system induces upwash velocities in the wing chord plane that may be distributed somewhat as shown in the middle sketch. The induced upwash over the region of the wing has an average value which is equivalent to an angle-of-attack change and a gradient which is equivalent to a camber change. The equivalent camber would induce a lift whose center would be near the rear of the wing. The combined ground-induced lift may be distributed as shown by the lower sketch and its center of pressure would be expected to lie behind the aerodynamic center and produce a nose-down ground-induced pitching moment.

The present ground-effects study utilizes both theoretical and experimental procedures. In a theoretical computer program currently being developed to implement the principles shown in figure 4 a vortex lattice type of lifting-surface aerodynamic theory is used so that the effects of the chordwise distribution of the lift and the ground-induced velocities can be accounted for adequately.

## Experimental Program

The experimental program recognized the importance of the ground-induced pitching moment by placing some emphasis on the configuration of the elevators used to trim out the moment. Figure 5 illustrates two of the wind-tunnel models used. The wings were of delta planform with clipped tips and had leading-edge sweep angles of  $55^\circ$  and  $70^\circ$ . Some data obtained on this  $55^\circ$  wing were shown in figure 2. Elevators having chords of about 10 percent and 20 percent of the wing mean aerodynamic chord were examined. The models were tested in a wind tunnel at various heights above a ground plane. A moving-belt ground plane was used to remove uncertainties even though a correlation discussed by Alexander D. Hammond in paper no. 22 indicates that the moving belt was unnecessary for these models.

The ground effects measured on these two models are compared in figure 6. The ground-induced increments in lift and pitching moment at zero elevator deflection, and the ground-induced increments in the elevator lift and moment parameters, are shown as functions of height above the ground. The ground-induced increments were measured at a constant angle of attack of  $12^\circ$ . The lift increment and the increments of the elevator parameters are each normalized by their respective free-air values.

For the  $55^\circ$  wing, shown by the solid curves, all of the parameters increase continuously with decreasing height. For the  $70^\circ$  wing, the lift at zero elevator and the lift due to elevator deflection also increase continuously but the two moment parameters show a reversal in the ground-effect trend at the lowest height. Although this trend reversal is not fully understood at present, it may be associated with the formation of an effective venturi throat between the ground and the wing trailing edge that may cause negative pressures on the underside of the wing near the trailing edge. It is possible that the  $55^\circ$  wing may also have shown some tendency toward trend reversal if it had been tested closer to the ground. The lowest points shown for each wing, however, represent heights that are appropriate for wheel touchdown. The ground-induced lift increment at touchdown is seen to be nearly the same for both wings.

### Simplified Landing-Flare Analysis

In order to assess the importance of these ground effects on the landing maneuver, the analysis procedure illustrated in figure 7 was used. Two flight conditions are assumed. The first is a steady-state landing approach glide out of ground effect on a straight descending flight path. The second represents the conditions at the instant of wheel contact with the ground. The flight path here may be curved and is usually at a flight-path angle less than that in the approach.

The curvature of the flight path requires a normal load factor somewhat greater than 1. The normal load factor at ground contact may be expressed approximately as the ratio of the lift coefficient at ground contact to that in the steady-state approach. Now if the approach lift coefficient is known and a value for normal load factor is assumed, the lift coefficient at ground contact may be determined. The wind-tunnel data may then be used to find the trimmed angle of attack in the approach and at ground contact corresponding to the appropriate lift coefficients and ground heights. The change in angle of attack during the flare is denoted by the symbol  $\Delta\alpha_F$  and is a sort of ground-effect figure of merit as determined in the wind tunnel.

The significance of this parameter is indicated by the second equation of figure 7, which was derived by using the angle relationships shown in the sketches. For a smooth landing, the flight-path angle at ground contact should be nearly zero. Thus, for any given value of the approach flight-path angle, the change in airplane attitude required to achieve this change in flight-path angle is determined by  $\Delta\alpha_F$ . If, for example, the value of  $\Delta\alpha_F$  were  $-2\frac{1}{2}^\circ$ , a very reasonable landing flare could be achieved with no change in airplane attitude. The change in elevator angle during the flare can also be determined from the wind-tunnel data and is a measure of the required pilot activity.

Application of this analysis procedure to the data for the  $55^\circ$  delta wing yields the results given in figure 8. The angle-of-attack increment  $\Delta\alpha_F$  and the corresponding increment in elevator angle are given as functions of the approach lift coefficient with the normal load factor at ground contact as a

parameter. For the untrimmed case, an angle-of-attack reduction in the flare in excess of  $3^\circ$  is indicated for an assumed approach lift coefficient of 0.65. If the airplane is trimmed with an elevator having a chord of about 20 percent of the wing mean aerodynamic chord, the elevator must be pulled up nearly  $4^\circ$  and the resulting negative lift reduces the angle-of-attack increment to about  $-2^\circ$  even if no increase in load factor is assumed. Of course, some increase in load factor is necessary if the flight-path angle is to be reduced in the flare. If the load factor at ground contact is as high as 1.1, the beneficial increment in angle of attack is reduced to only  $-0.6^\circ$ .

It is of interest, therefore, to understand more fully the mechanism by which these potentially beneficial ground effects are being rendered unavailable. In figure 9 the same  $55^\circ$  delta wing is assumed to be trimmed with the same 20-percent-chord elevator to a load factor of 1.1 at ground contact. The ground effects, however, are now represented by successive superposition of three major components: the ground effect on the variation of lift with angle of attack, the ground effect on the variation of pitching moment with angle of attack, and the ground effect on the lift and moment associated with elevator deflection. The angle-of-attack increment in the flare and the elevator-angle increment are again plotted as functions of approach lift coefficient. If the only ground effects considered are those that influence the variation of lift with angle of attack, the short-dash lines show that at an assumed approach  $C_L$  of 0.65, the angle-of-attack increment is again about  $-3^\circ$  and the elevator-angle change is only that required to pull the additional 0.1 load factor. The additional inclusion of the ground effects on the variation of pitching moment with angle of attack, as indicated by the long-dash curves, required an additional  $5^\circ$  of elevator-angle change and reduced the angle-of-attack increment to about  $-1.3^\circ$ . As indicated by the solid lines, the inclusion of the ground effects on the elevator characteristics further reduced the angle-of-attack increment to  $-0.6^\circ$  but required a somewhat smaller elevator-angle change. The reason for this last effect can be explained by reference to figure 6. For the  $55^\circ$  wing, the ground effect at touchdown has increased the elevator moment effectiveness by 17 percent, and thereby reduced the elevator angle required to trim out the ground-induced moment. The elevator lift parameter, however, has increased 35 percent, and this negative lift has a detrimental effect on  $\Delta\alpha_F$  in spite of the smaller elevator angle. It is apparent that the ground effects on the elevator lift and moment characteristics are an important part of the whole ground-effect picture and must be accounted for in analysis or in simulation of ground effects if the results obtained are to be meaningful.

It is logical to ask whether some change in the elevator configuration would allow the potential benefit of the ground effect to be realized more fully. Figure 10 illustrates the effect of reducing the chord of these full-span elevators from 20 percent to about 10 percent of the wing mean aerodynamic chord for the case of a load factor of 1.1 at ground contact. When the model was trimmed with the smaller chord elevator, an angle-of-attack reduction in the flare of about  $1.1^\circ$  was achieved at the assumed approach lift coefficient, compared with only  $0.6^\circ$  when the model was trimmed with the larger elevator. The elevator-angle increment in the flare shown on the right of the figure is slightly greater for the small-chord elevator because the basic elevator effectiveness is lower than that of the large-chord elevator. The beneficial effect

of reducing elevator chord is due partly to the longer moment arm of the small elevator which allows a given moment change to be trimmed out with less loss in lift, and partly to the more rearward location of the center of pressure of the ground-induced lift associated with elevator deflection.

### Dynamic Motion Calculations

In the preceding discussion, the ground effects have been examined by comparing the initial and final conditions in a landing flare with an assumed value for the touchdown load factor. The actual load factor can be determined from calculations using the dynamic equations of motion through complete landing-flare maneuvers. Several examples of such calculations are given in figure 11. This figure presents the variation of rate of descent, elevator angle, and normal load factor with height of the landing gear above the ground, calculated for landing flares assumed to be made at constant pitch attitude. For all cases the small-chord elevator, an approach speed of 131 knots, and an approach flight-path angle of  $-2.75^\circ$  were assumed. The first two curves compare the  $70^\circ$  and  $55^\circ$  wings on airplanes having a wing area representative of a fixed-wing supersonic transport airplane. The wing loadings were selected to give approach lift coefficients appropriate for the respective wing planforms. These airplanes first enter the ground-effect region at a height of about 60 feet, and the ground effects reduce the rate of descent from an initial value of 10.6 feet per second to touchdown values of 5 feet per second for the  $70^\circ$  wing and  $6\frac{1}{2}$  feet per second for the  $55^\circ$  wing. Observe that although both airplanes reached about the same value of load factor at touchdown, the load factor during most of the landing flare was somewhat higher for the  $70^\circ$  wing. This higher load factor resulted in a greater reduction in rate of descent.

The short-dash curves show a landing flare for an airplane assumed to be a 1/3-scale model of the large one with a  $55^\circ$  delta wing. The wing loading and the initial conditions are the same as those for the large airplane. The small airplane enters ground effect at a height of about 20 feet, and although the load factor reaches a peak value considerably higher than that for the large airplane, the high load factors exist for a much shorter duration and result in much less reduction in rate of descent. This finding implies that the importance of the ground effects on a large airplane cannot be directly inferred from observations made in flight of a small airplane.

The results shown here for the  $70^\circ$  wing indicate a rate of descent at touchdown which is almost low enough for a smooth landing. The data used in these calculations were obtained on a wind-tunnel model without camber or twist. There are preliminary indications that wing twist in the direction of washout at the tips can provide further reductions in the rate of descent at touchdown. Thus, a successful constant-attitude landing flare can probably be achieved. Notice, however, that the elevator angle must be changed during the flare by about  $7^\circ$ . Thus, an automatic flare - that is, one requiring no pilot action - has not been achieved.

## CONCLUDING REMARKS

The study described has indicated that a meaningful analysis of wind-tunnel ground-effect data or a realistic simulation of ground effects must utilize a complete description of the ground effects on the lift and pitching-moment characteristics due to angle of attack and elevator deflection. In addition, it was shown that the ground effects on low-aspect-ratio wings can produce significant reductions in the pitch attitude at ground contact, and constant-attitude landing flares may be possible for some large airplane configurations. The truly automatic landing flare requiring no change in elevator angle, however, is difficult to achieve.

GROUND EFFECT ON SUBSONIC JET  
TRANSPORT CONFIGURATION

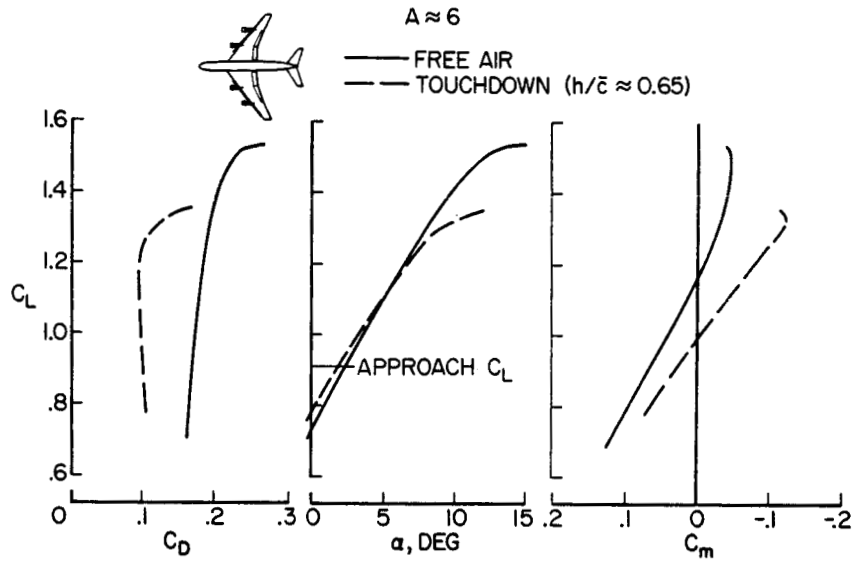


Figure 1

GROUND EFFECT ON 55° DELTA CONFIGURATION

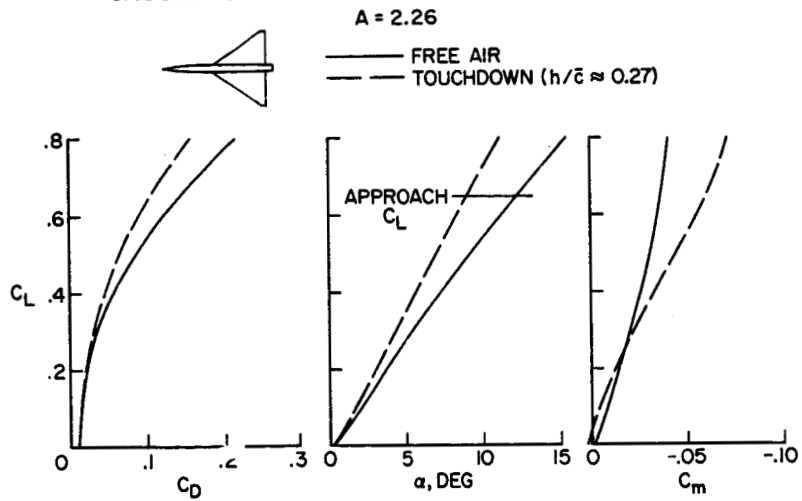


Figure 2

### IMAGE REPRESENTATION OF GROUND

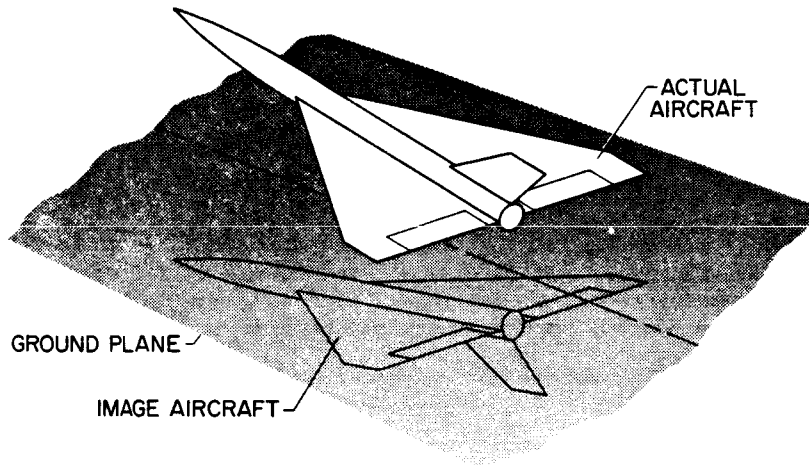


Figure 3

### MECHANISM OF GROUND INDUCTION

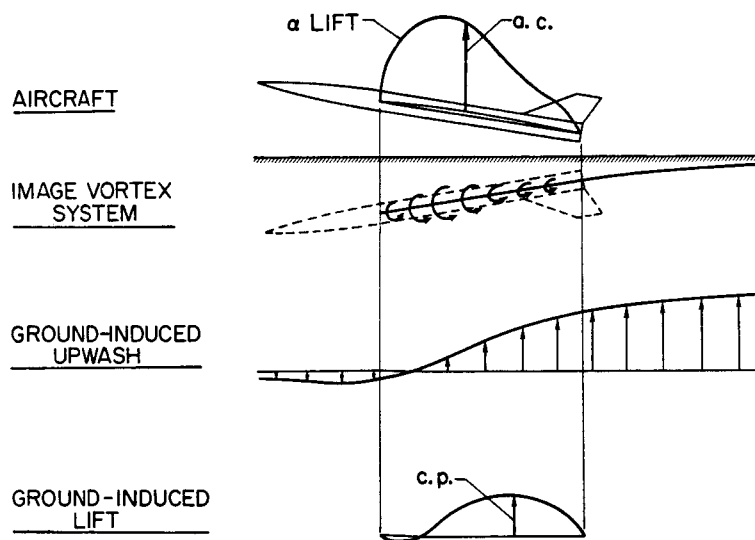


Figure 4

# MODELS USED IN WIND-TUNNEL INVESTIGATION

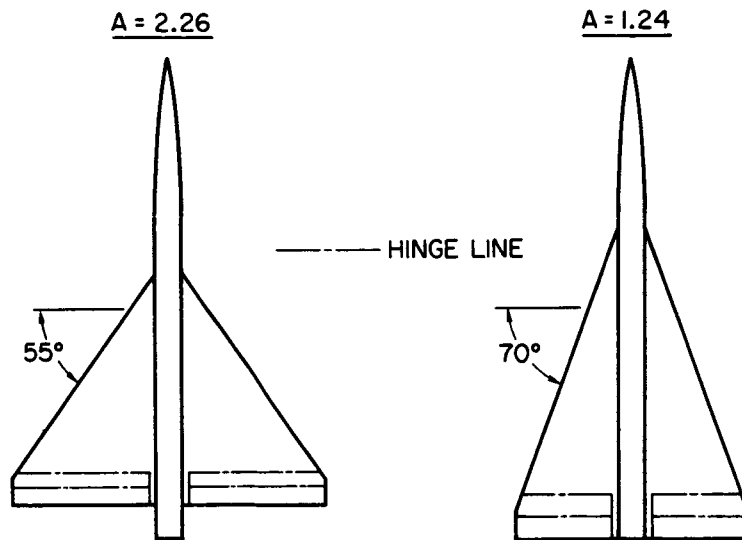


Figure 5

## GROUND EFFECT ON DELTA WINGS

$\alpha = 12^\circ; c_e \approx 0.2\bar{c}$

L.E. SWEEP, DEG

—○— 55  
 —□— 70

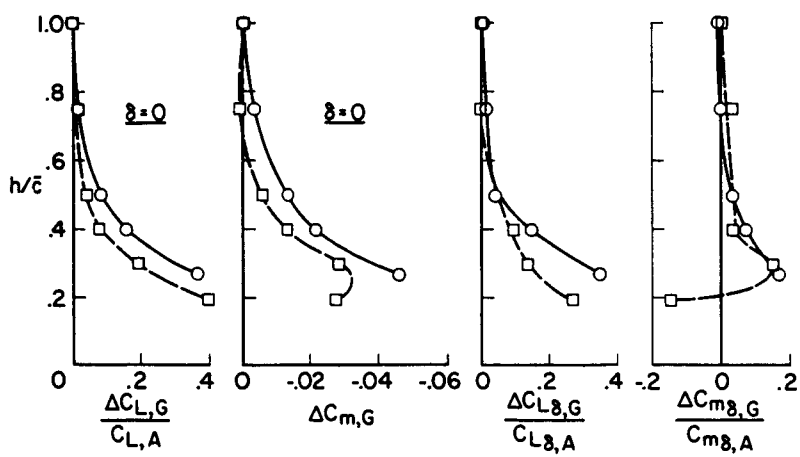


Figure 6

## BASIS OF DATA ANALYSIS

$$n_G \approx \frac{C_{L,G}}{C_{L,A}}$$

$$\Delta\alpha_F = \alpha_G - \alpha_A = (\theta_G - \theta_A) + (\gamma_A - \gamma_G)$$

$$\Delta\delta_F = \delta_G - \delta_A$$

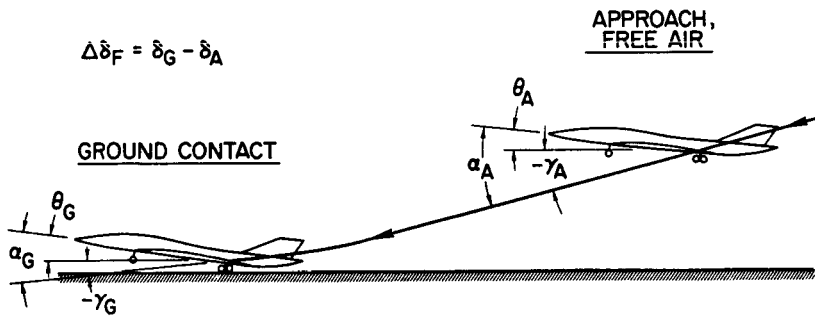


Figure 7

### EFFECT OF TRIMMING AND FLARE LOAD FACTOR 55° DELTA WING ; $c_e \approx 0.2 \bar{c}$

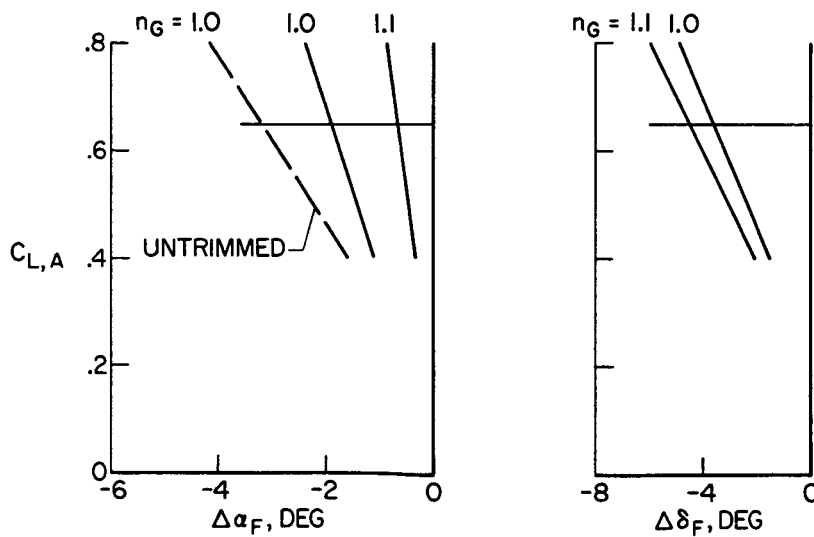


Figure 8

COMPONENT BUILDUP OF GROUND EFFECT  
 55° DELTA WING ; TRIMMED ;  $n_G = 1.1$

GROUND EFFECT INCLUDED IN :

- $C_L(\alpha)$
- $C_L(\alpha), C_m(\alpha)$
- $C_L(\alpha, \delta), C_m(\alpha, \delta)$

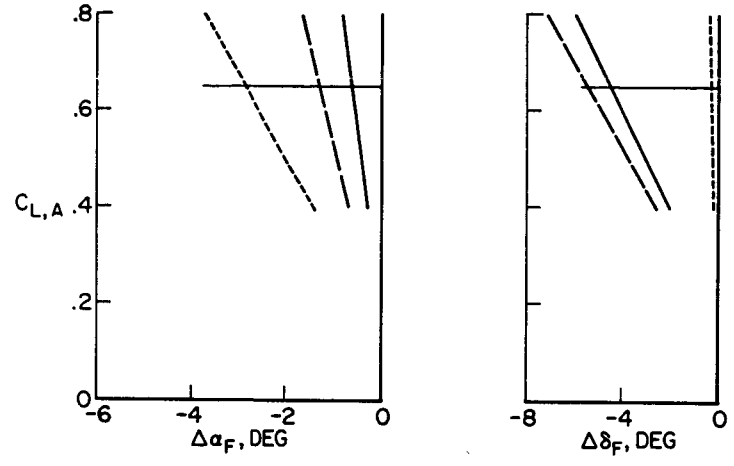


Figure 9

EFFECT OF ELEVATOR CHORD  
 55° DELTA WING ;  $n_G = 1.1$

- $c_e/\bar{c}$  0.2
- $c_e/\bar{c}$  0.1

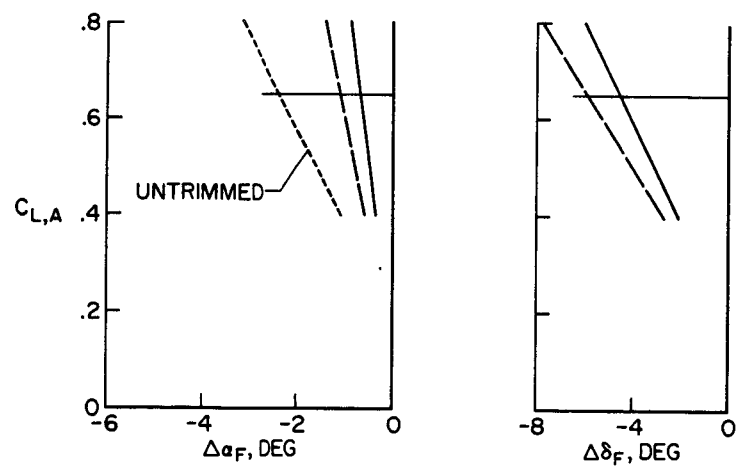


Figure 10

### CONSTANT-ATTITUDE LANDING FLARES

$c_e \approx 0.18$ ;  $V_A = 131$  KNOTS;  $\gamma_A = -2.75^\circ$

L.E. SWEEP, DEG	WING AREA, SQ FT	W/S, LB/SQ FT
70	8000	35
55	8000	40
55	889	40

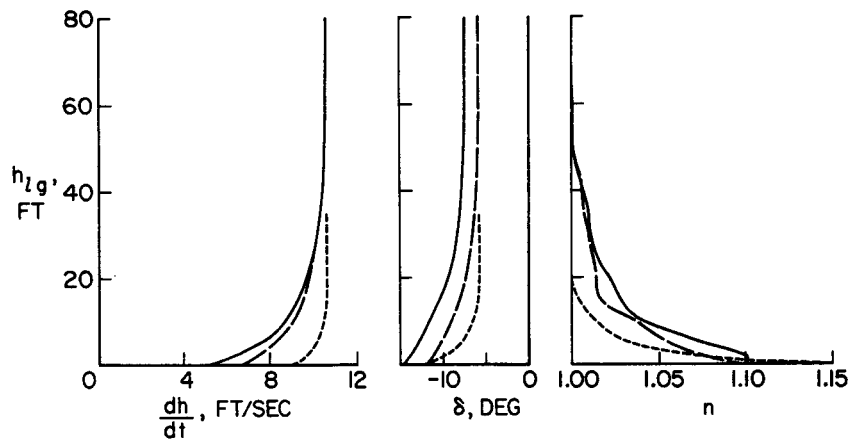


Figure 11

## 20. FLIGHT STUDIES OF GROUND EFFECTS ON AIRPLANES

### WITH LOW-ASPECT-RATIO WINGS

By L. Stewart Rolls, C. Thomas Snyder,  
Ames Research Center  
and William G. Schweikhard  
Flight Research Center

#### SUMMARY

The ground effects on two aircraft with low-aspect-ratio delta wings, the F5D-1 and the XB-70A, were measured in flight tests. In a companion program, both small and full-scale models and several wind tunnels were used to document the ground effects for the F5D-1. These flight tests indicated ground effects were not a problem in landing either of these vehicles. The limited wind-tunnel program indicated that scale effects were not of first-order importance in defining ground effects, and that wind-tunnel tests provide reasonable agreement with the values in flight. A simulation study, using a fixed-cockpit projection-type simulator, performed in conjunction with these studies indicated levels of moment and lift changes which would be unsatisfactory from the pilot's viewpoint; however, some possible alleviating features were noted.

#### INTRODUCTION

For low-aspect-ratio wing designs the effect of ground proximity on longitudinal aerodynamics is becoming recognized as contributing significantly to take-off and landing characteristics. The increase in lift due to the ground effect helps to reduce the long ground rolls associated with the high take-off speeds of these aircraft. But on the other hand, the pitching-moment changes due to these ground effects may adversely affect the pilot's ability to make an accurate flare during landing or the rotation maneuver during take-off. For example, preliminary fixed-cockpit simulation studies of the landing characteristics of a large, low-aspect-ratio aircraft indicated that the pilots had difficulty in making precise landings when the anticipated ground effects were programed into the simulation. The fact that the simulator study indicated a control problem while none has been encountered in low-aspect-ratio aircraft currently flying suggests the need for further investigation of the problem. Several possible sources of the difference have been suggested. One is the possibility that Reynolds number significantly affects small-scale wind-tunnel measurements of ground effect. Second is the possibility that the pilot cannot make realistic assessments from fixed-base simulations in which motion is lacking and the resolution in the visual display is limited.

Flight-test programs on two low-aspect-ratio delta-wing aircraft were extended to measure the ground effect on each. These aircraft are the F5D-1, equipped with an oggee planform, being flown at the Ames Research Center, and the XB-70A, which is currently undergoing joint Air Force and NASA flight testing at Edwards Air Force Base. In addition, comprehensive tests with both small and full-scale models were conducted in several wind tunnels to document the characteristics of the F5D-1 aircraft.

This paper will present the ground effect data measured on the XB-70A and the F5D-1 aircraft in flight, will compare wind-tunnel and flight data, and will indicate, on the basis of piloted simulator studies, the manner in which various magnitudes of ground effect influence the precision of the landing.

#### SYMBOLS

$C_L$	lift coefficient, $L/qS$
$C_{Ltrim}$	lift coefficient in trim
$C_{L\infty}$	lift coefficient out of ground effect
$C_D$	drag coefficient, $D/qS$
$\bar{c}$	mean aerodynamic chord, ft
$D$	drag, lb
$g$	acceleration due to gravity, $ft/sec^2$
$h$	distance from reference point on aircraft to ground, ft
$L$	lift, lb
$q$	dynamic pressure, $lb/sq\ ft$
$S$	wing area, $sq\ ft$
$T$	thrust, lb
$W$	weight, lb
$\delta_E$	elevon deflection, deg
$\delta_{Etrim}$	elevon deflection required for trim, deg
$\gamma$	flight-path angle, deg

$(\Delta C_L)_{GE}$  change in lift coefficient due to ground effect

$(\Delta C_m)_{GE}$  change in pitching-moment coefficient due to ground effect

## TEST AIRCRAFT AND TEST TECHNIQUES

### Test Aircraft

Figures 1 and 2 are photographs of the two aircraft for which ground effects were measured in flight. Figure 1 shows the F5D-1 aircraft, constructed by the Douglas Aircraft Company with a wing modified to an Ogee planform. This aircraft has an aspect ratio of 1.70, a wing area of 661 square feet, and a mean aerodynamic chord of 22.6 feet. Figure 2 shows the XB-70A aircraft, a multijet, supersonic bomber built by North American Aviation. This aircraft has an aspect ratio of 1.75, a wing area of 6300 square feet, and mean aerodynamic chord of 78.5 feet. It is apparent that there is a large difference in the size of the two aircraft.

### Test Techniques

Ground effect on the XB-70A was measured during the landing approach while the aircraft was making a steady descent at a constant angle of attack and power setting. The increase in lift coefficient was determined from the resultant flare as the aircraft approached the ground. In addition, the change in elevon position determined the pitching moment due to ground effect. The equations for determining the lift changes from the measured quantities are shown in figure 3. In this case, the Askania Tracking System of the Air Force Flight Test Center's take-off and landing facility was used to measure the changes in rate of descent and flight path, while onboard instrumentation recorded angle of attack and elevon position.

The data for the F5D-1 aircraft were obtained during level "fly-by" runs at various heights and at several speeds. Figure 4 shows the aircraft during one of these runs along the runway. (The white shadow across the base of the vertical surface is a condensation trail caused by the strong vortex at the root leading edge of the ogee wing.) This method relied upon the onboard measurements of aircraft accelerations, thrust, attitude, and height to permit the calculation of the parameters significant to ground effect. The methods for reducing these measured quantities to lift and drag coefficients are presented in reference 1. A Lockheed Location Orientation Recording Instrument (LORI) was mounted vertically on the lower surface of the fuselage. This system measured aircraft height above the runway, rate of change in height, ground speed, and pitch angle.

The wind-tunnel program conducted in conjunction with the flight tests of the ogee wing F5D-1 aircraft included tests in three wind tunnels and afforded the opportunity to evaluate scale effects as well as to compare tunnel and

flight measured results. For the full-scale data the actual aircraft was used as a model in the Ames 40- by 80-foot wind tunnel and for the small-scale data a properly modified 0.15-scale model of the F5D-1 aircraft was tested in the Lockheed 8- by 12-foot wind tunnel and the Langley 7- by 10-foot wind tunnel. Tests in the Langley tunnel were conducted with both a moving and stationary ground plane.

## RESULTS AND DISCUSSION

Figure 5 shows a set of data measured on the XB-70A aircraft. Briefly, the measured data, in the form of the rate of descent and elevon angle to trim, are plotted as a function of the height parameter or the height divided by the mean aerodynamic chord. The change in the rate of descent as the vehicle nears the ground is used to calculate the resultant increase in lift coefficient. During this flight maneuver, elevon motion is used to maintain the prescribed flight path. Thus, to obtain the actual lift coefficient increase due to ground effect, it is necessary to correct the measured lift increment to zero elevon angle as shown on this figure. For this particular aircraft the elevon movement nearly cancels the increase in lift due to the ground effect. Also on this figure two symbols indicate the amount of ground effect measured in a wind tunnel. The wind-tunnel data are too limited for definitive conclusions as to agreement, but testing is continuing.

The effect of the ground proximity on the aerodynamic properties of the F5D-1 aircraft is presented on figure 6, which shows the variations of angle of attack, drag coefficient, and elevon angle for trim as a function of lift coefficient. The shaded area on each curve shows the ranges covered during the flight tests. One boundary curve represents the characteristics out of ground effect while the other boundary represents the characteristics at touchdown and there are progressive variations with height between these curves. Thus, the difference between these two curves is the magnitude of the ground effect for each quantity.

Comparisons of the flight and wind-tunnel measured ground effect on the F5D-1 ogee configuration are presented on figures 7 and 8. Figure 7 presents the lift data and figure 8 the moment data in terms of the elevon angle required for trim. For simplicity of presentation, only the lift and moment comparisons are presented, and they are presented at only the highest and lowest height for which comparative data are available. The aircraft touchdown occurs at an  $h/\bar{c}$  of 0.28. A more complete comparison is presented in reference 2. The curves are identified with each wind tunnel, while the data points are the flight data. The Langley tests in the 7- by 10-foot wind tunnel showed no difference between the data for the ground plane moving or stationary and the lift data from all sources agree well. The moment data show a difference between the flight and wind-tunnel data equivalent to about 2-percent mean aerodynamic chord uncertainty in the location of the centers of rotation or a shift in the moment at zero lift equal to about  $1^\circ$  of elevon angle. The cause of these discrepancies has not been established, but in any case they are small enough to be of little concern. In general, it appears

from this limited comparison that scale effect is not of first-order importance in defining ground effect, and that wind-tunnel tests provide reasonable agreement with values determined in flight.

The measured effects of the ground proximity on the aerodynamic characteristics of the aircraft were used to calculate the landing characteristics illustrated in figure 9. These data from analog computed landings show the rate of descent at various heights and indicate that the ground effect depends on how the pilot controls the aircraft. The data on the left side of the figure are for a constant pitch attitude approach and illustrate that there is a large reduction in the rate of descent at touchdown. In essence, the data indicate what the response would be if the pilot were completely successful in counteracting the effect of the pitching-moment change on the aircraft's attitude, thus permitting the lift increment to assist in arresting the rate of descent. The required elevon angle variation does, however, reduce the ground effect lift increment as was noted in the case of the XB-70A. The right side of the figure shows the approach with constant elevon control. Here, the pitching moment has a predominant effect on the rate of descent near the ground as evidenced by the increase in rate of descent at touchdown. Also these figures show that the low approach angle is generally beneficial except that for the constant attitude case the aircraft actually did not touch down, but ballooned.

While it is beyond the scope of this paper to go into detail regarding the simulator study, it is considered apropos to make some mention of these results. To provide some confidence to the simulation, a considerable amount of time was spent in simulating characteristics of aircraft (the F5D-1 and the DC-8) with which the pilots had some flight experience or knowledge. After the pilots gained confidence in the simulation, they rated the landing characteristics of a large low-aspect-ratio delta-wing aircraft with various combinations of lift and moment changes due to ground effect. Their ratings are summarized on figure 10. It should be emphasized that these data are preliminary and are presented simply to indicate trends -- not to establish boundaries. The ordinate is the change in lift coefficient due to ground effect divided by the lift coefficient out of ground effect and the abscissa is the change in pitching moment due to ground effect divided by the lift coefficient out of ground effect. The combinations of lift and moment changes due to ground effect which were investigated on the simulator fall within the shaded areas. The adjective pilot rating is listed beside each test configuration. The pilots rated the conditions on the right side of the figure as unsatisfactory because of the difficulty in controlling the large pitch-down tendencies; they rated those in the upper region as only marginally satisfactory because of the additional effort necessary to control the floating tendencies; and they rated those in the lower left area as satisfactory. These tests also indicated the pilots reacted more to small changes in the pitching moment than to small changes in the lift. An incidental point of interest is that these simulator studies indicated an improvement in the pilots' ratings if the lift increment "leads" the pitching-moment change (i.e., starts to increase at heights higher than those where the pitching moment starts to change). It was also observed generally that if the moment change occurs after the pilot has started his flare maneuver, the effect of

the pitching moment tends to be obscured; this suggests one reason why the unfavorable pitching-moment changes have not been significant for the smaller aircraft. The moment and lift changes for the F5D-1 and the XB-70A aircraft fall in the area considered satisfactory by the pilot.

#### CONCLUDING REMARKS

Flight tests on two low-aspect-ratio delta-wing aircraft indicated that the ground effect was not a problem in landing either vehicle. A limited wind-tunnel program indicated that scale effects were not of first-order importance in defining ground effect, and that wind-tunnel tests provide reasonable agreement with values in flight. Simulator studies indicated the levels of moment and lift changes due to ground effect which would be unsatisfactory from the pilot's standpoint; however, some possible alleviating features were noted.

#### REFERENCES

1. Rolls, L. Stewart; and Wingrove, Rodney C.: An Investigation of the Drag Characteristics of a Tailless Delta-Wing Airplane in Flight, Including Comparison With Wind-Tunnel Data. NASA MEMO 10-8-58A, 1958.
2. Rolls, L. Stewart; and Koenig, David G.: Flight Measured Ground Effect on a Low-Aspect-Ratio Ogee Wing Including a Comparison With Wind-Tunnel Results. NASA TN D-3431, 1966.

F5D-1 AIRCRAFT

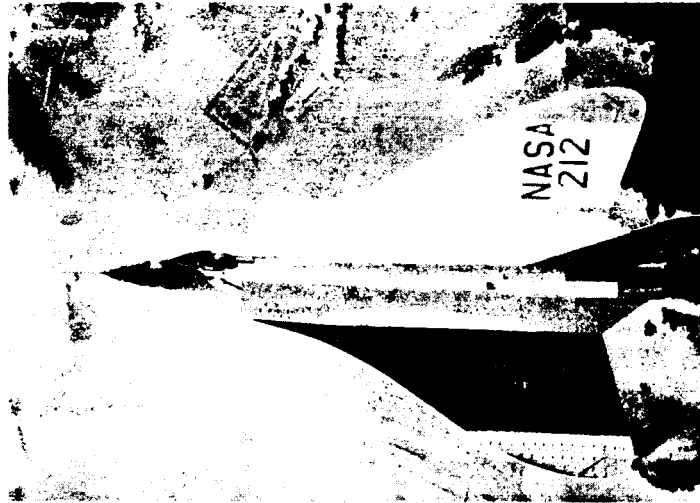


Figure 1

A-33500-3

XB-70A AIRCRAFT

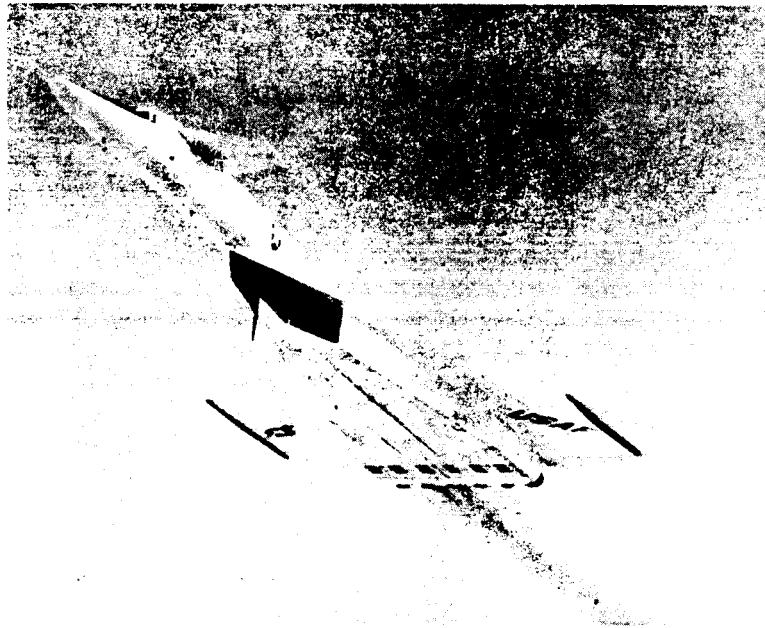
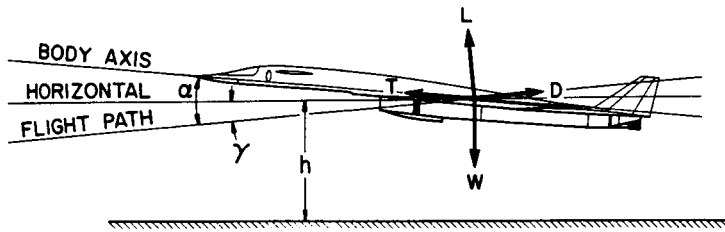


Figure 2

A-36987

### LIFT EQUATION, XB-70A METHOD



EQUATING VERTICAL FORCES

$$L \cos \gamma + D \sin \gamma - W + T \sin(\alpha - \gamma) = \frac{W}{g} \frac{d^2h}{dt^2}$$

ASSUMING:  $\gamma$  IS SMALL ( $3^\circ$  OR LESS) &  $T \sin(\alpha - \gamma)$  IS SMALL

THEN: 
$$L \cos \gamma - W = \frac{W}{g} \frac{d^2h}{dt^2}$$

Figure 3

### F5D-1 DURING LEVEL RUN ALONG RUNWAY

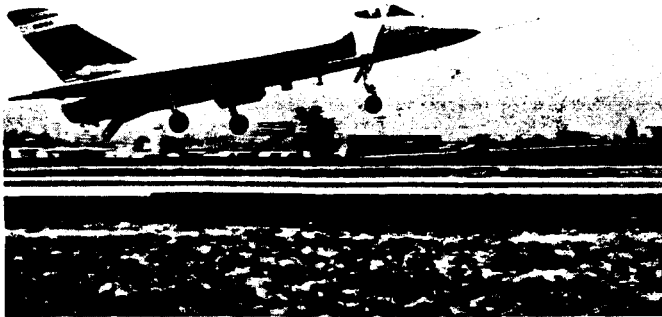


Figure 4

A-35650-2

XB-70 FLIGHT DATA

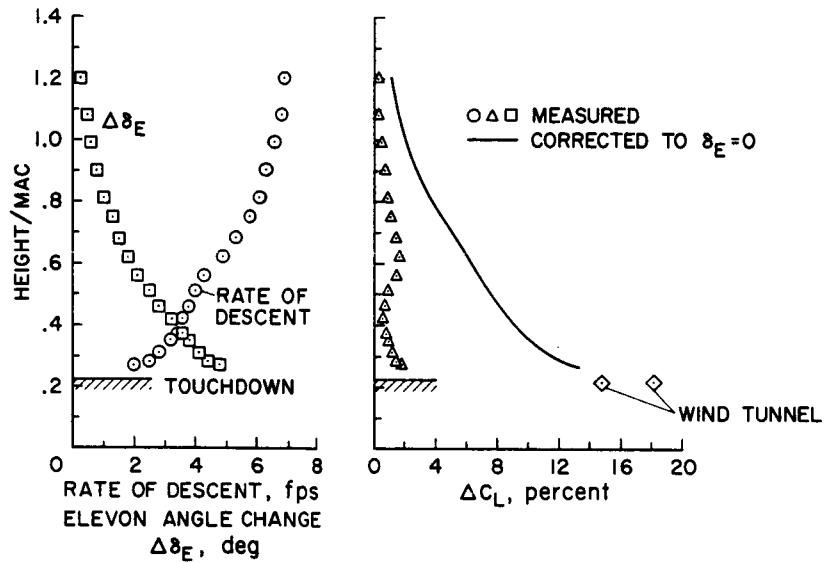


Figure 5

GROUND EFFECT ON F5D-1 FLIGHT CHARACTERISTICS

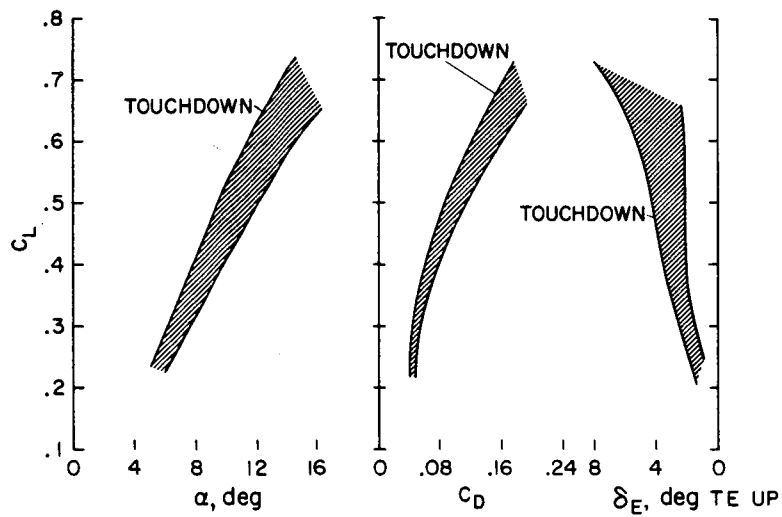


Figure 6

COMPARISON OF FLIGHT AND WIND TUNNEL DATA  
LIFT CHARACTERISTIC

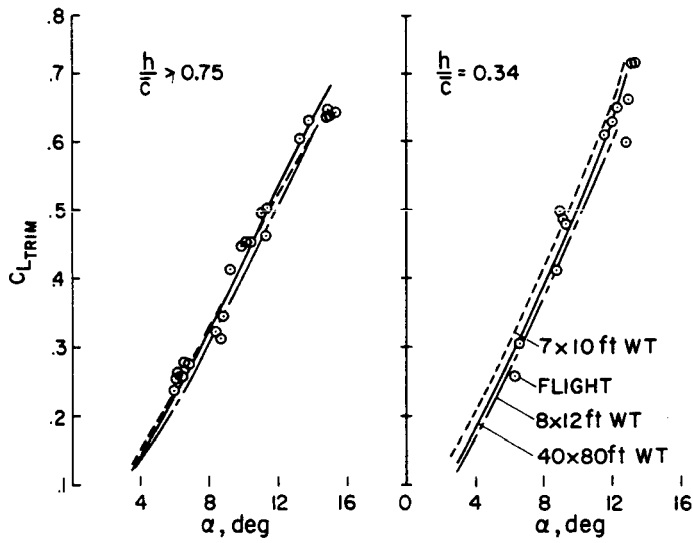


Figure 7

COMPARISON OF FLIGHT AND WIND TUNNEL DATA  
ELEVON ANGLE FOR TRIM

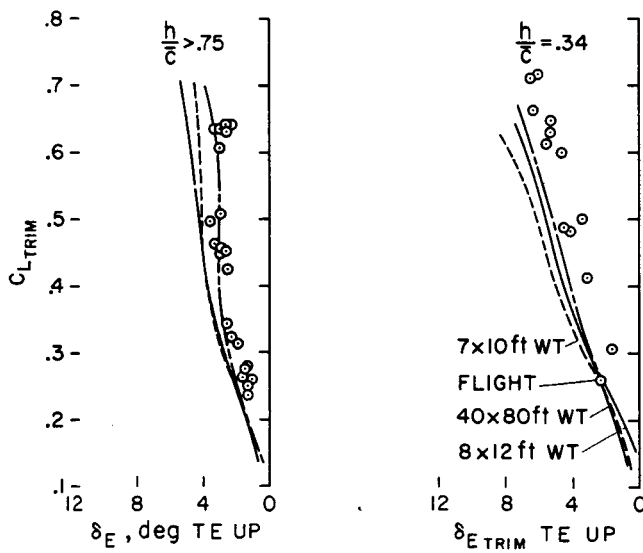


Figure 8

### LANDING CHARACTERISTICS WITH GROUND EFFECT

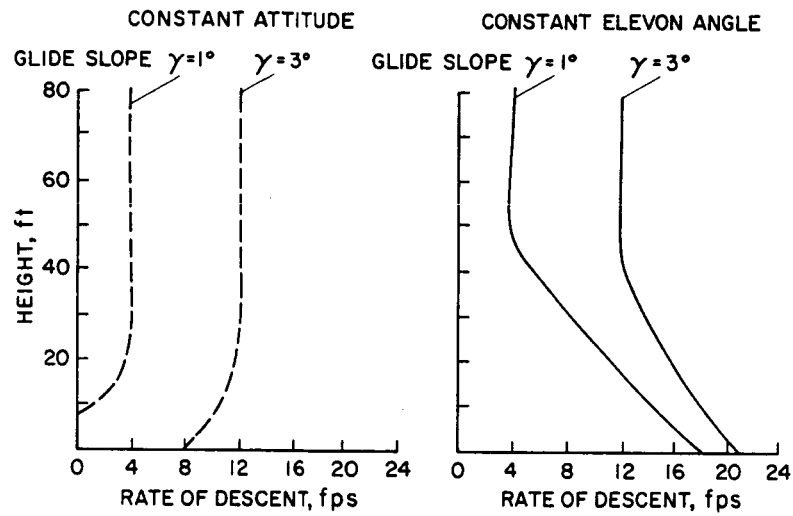


Figure 9

### PILOT RATING OF GROUND EFFECT SIMULATOR STUDIES

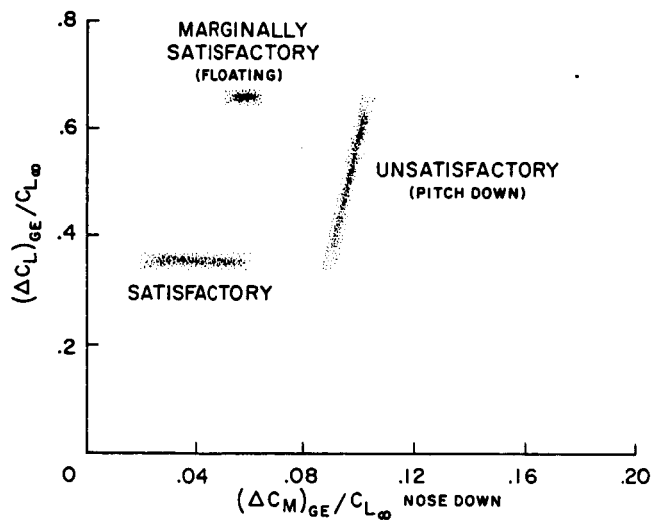


Figure 10

## 21. EXPERIMENTAL AND THEORETICAL STUDIES

## OF WING-LEADING-EDGE VORTEX FLOW

By Mark W. Kelly, Victor R. Corsiglia,  
and David G. Koenig  
NASA Ames Research Center

## SUMMARY

This paper presents a review of experimental and theoretical studies of leading-edge vortex flow on low-aspect-ratio wings. The experimental results show that such flow significantly increases lift-curve slope, reduces drag due to lift, and reduces static longitudinal stability at high values of lift coefficient. These results also show that the magnitude of these effects is increased by the use of wing planforms having high sweepback over the inboard portion of the wing.

Flow visualization studies of a low-aspect-ratio wing with the leading-edge swept  $77^\circ$  on the inboard portion of the wing and  $59^\circ$  on the outboard portion revealed the existence of two strong vortex cores. One of these originated at the intersection of the wing leading edge with the fuselage. The other originated in the vicinity of the discontinuity of leading-edge sweep angle. These two vortices interacted to produce a nonconical flow over the aft portion of the wing.

A brief review is presented of some of the existing theoretical methods for predicting the effects of vortex flow on the aerodynamic characteristics of wings. Two main deficiencies of these theoretical methods are that they do not allow for vortex interaction and that they are restricted to conical flows. A new theoretical approach which eliminates these deficiencies is described, and preliminary results obtained from this theory are compared with those obtained from other theories and with experimental results. This comparison indicates that the new theory holds promise for predicting the effects of vortex flow on low-aspect-ratio wings. However, additional work is required on the key problem of establishing the strength of the vorticity shed from the wing as a function of wing geometry and angle of attack.

## INTRODUCTION

The subject of vortex flow on low-aspect-ratio wings has challenged researchers in aerodynamics for many years. For example, in 1939 Bollay presented a theoretical study of vortex flow on low-aspect-ratio rectangular wings (ref. 1). This was followed more recently by theoretical studies of vortex flow on triangular wings (e.g., refs. 2 and 3) and by many experimental studies (e.g., ref. 4). However, vortex flow still is not sufficiently well understood to allow reliable quantitative predictions of its effects on aerodynamic characteristics for use in wing design. In addition, many wing

planforms of current interest, such as double-delta and variable-sweep wings, show strong effects of vortex flow. Therefore, additional studies are of interest and are required.

The type of vortex flow to be considered in this paper is illustrated on figure 1 for both a variable-sweep wing and a low-aspect-ratio wing. For variable-sweep wings a high-energy vortex flow is generated by the highly swept inboard fixed portion of the wing. As discussed in paper no. 5 by Ray, Lockwood, and Henderson, this vortex flow contributes to a loss of static longitudinal stability at high angles of attack. Therefore, the designer attempts to suppress the development of this vortex flow on variable-sweep wings by using appropriate flow-control devices. Typical effects achieved by such devices are presented in paper no. 5 and will not be considered further herein. For low-aspect-ratio wings the leading-edge vortex flow has the favorable effect of increasing the lift-curve slope, in addition to the unfavorable effect of reducing longitudinal stability at high angles of attack. Therefore, a quantitative understanding of the effects of vortex flow on low-aspect-ratio wings is required to achieve a trade-off between these favorable and unfavorable effects.

This paper presents the results of experimental and theoretical studies of vortex flow on low-aspect-ratio wings. The subjects to be discussed are summarized in figure 2. First, results of experimental studies to determine the longitudinal aerodynamic characteristics of a family of low-aspect-ratio double-delta wings are summarized. Second, flow visualization studies to determine the origin and development of the vortex flow pattern are presented and discussed. Finally, some of the existing theories for predicting the effects of vortex flow are briefly reviewed and a new theoretical approach, which eliminates some of the assumptions and constraints of past theoretical methods, is described.

#### MODEL AND APPARATUS

The model used in the experimental portion of this investigation is shown in figure 3. The basic wing had a trapezoidal planform with an aspect ratio of 1.69, a taper ratio of 0.12, and a leading-edge sweep angle of  $59^\circ$ . Various double-delta planforms were obtained by adding various sizes of strakes to this basic planform. These strakes had a leading-edge sweep angle of  $77^\circ$ . This model was tested in the Ames 40- by 80-foot wind tunnel at a Reynolds number of about 15 million.

#### REDUCTION OF DATA

The data from this investigation were reduced to coefficients based on the total wing area and mean aerodynamic chord of the equivalent delta wing. The equivalent delta wing was selected to have the same exposed wing area and

span as that of the particular double-delta wing under construction. The reference dimensions of the equivalent delta planforms and those of the total theoretical planforms are listed in table I.

## DISCUSSION OF RESULTS

### Experimental Studies

The effects of changing the wing planform by adding various strakes to the basic wing are shown in figure 4 which presents lift coefficient as a function of angle of attack. These results show that, at low lift coefficients, the addition of the strakes reduced lift-curve slope, as would be expected since adding the strakes reduced the aspect ratio of the wing. However, adding the strakes also caused a significant increase in the lift-curve slope at high values of lift coefficient. At lift coefficients greater than 0.6 planforms with strakes require less angle of attack than the basic wing to obtain a given lift coefficient. Thus, at high angles of attack, the favorable effects of the strakes on the nonlinear portion of the lift (which is due to leading-edge vortex flow) more than offset the unfavorable effect on lift-curve slope due to the reduction in aspect ratio. It should be noted that the wing with the small strake produced slightly higher lift coefficients at high angles of attack than did the configuration with the large strake. Thus, it appears that there is an optimum strake configuration as far as improving lift-curve slope is concerned.

The effects of the strakes on the variation of pitching moment with lift coefficient are shown in figure 5. These results show that the intensified leading-edge vortex flow caused by the addition of the strakes reduced the static longitudinal stability at lift coefficients greater than 0.6. This illustrates a key problem in wing design, that is, how to obtain the favorable effects of the strakes on lift without suffering an unacceptable loss in longitudinal stability.

The effect of the strakes on the drag characteristics of the model are shown on figure 6. These results show that the strakes reduced the drag due to lift for lift coefficients above 0.6. This reduction, of course, results from the increased lift-curve slope due to the strakes discussed previously. Thus, the increased vortex flow promoted by the strakes reduced the drag due to lift at high lift coefficients by an amount which more than offset the increase in drag due to lift caused by the reduction in aspect ratio.

Since leading-edge vortex flow is associated with flow separation from the wing leading edge, it would be expected that the use of flow control devices on the wing leading edge should have a significant effect on the aerodynamic characteristics due to vortex flow. The effects of using a full span nose flap on the wing planform employing the small strake (aspect ratio equal to 1.49) are shown on figure 7. These results show that the nose flaps suppressed the formation of leading-edge vortex flow, and thus extended the linear portion of the lift curve to higher angles of attack and significantly reduced the magnitude of the nonlinear lift.

The effect of the nose flaps on pitching moment is shown in figure 8. These results show that the suppression of the vortex flow by the nose flaps alleviated the reduction in longitudinal stability at lift coefficients above 0.6.

The effect of the nose flaps on the variation of drag with lift is presented in figure 9, which shows that the use of the nose flaps produced a reduction in the drag due to lift. This reduction is contrary to what might be expected since, as previously discussed, the nose flaps reduced the lift-curve slope. However, the deflected nose flaps provided a forward-facing surface which allowed the realization of enough leading-edge suction to more than compensate for this reduction in lift-curve slope.

In order to gain some insight into the fundamental aspects of the flow producing these results, and also to serve as a guide in setting up theoretical models able to predict these results, various flow visualization studies were made. The results of one of these studies is shown in figure 10. This photograph shows the vortex flow over a small-scale double-delta wing body configuration installed in the Ames 7- by 10-foot wind tunnel. (This model was geometrically similar to the large-scale 1.49 aspect-ratio wing configuration tested in the 40- by 80-foot wind tunnel described previously.) The vortices shown in figure 9 were made visible by the natural condensation of the water vapor in the air in the wind tunnel as it flowed over the wing leading edge. One vortex originated at the juncture of the leading edge of the strake with the fuselage. The other vortex formed in the vicinity of the juncture of the strake leading edge with the basic wing leading edge. Vorticity, of course, is being shed from the full length of the wing leading edge. The portions of this flow which are visible in figure 10 are only those where the temperatures induced by this vorticity were low enough to condense the water vapor in the wind-tunnel air. It should be noted that there is a strong interaction between the two vortices over the aft portion of the wing, and that the resulting flow is nonconical.

From these flow visualization studies it appears that the following factors must be considered in any complete theoretical treatment of leading-edge vortex-flow phenomena. First, the theory must not be restricted to conical flows, since for many wing planforms of current interest, the flow is nonconical over large portions of the wing. Second, the interaction of the various vortices with each other must be allowed for. And, third, some means must be attained for establishing the strength of the vortex shed from the various portions of the wing leading edge.

#### Theoretical Studies

Some of the better-known methods for predicting vortex lift are summarized in figure 11. As shown in the upper left-hand corner of this figure, the flow is separated into two parts for theoretical treatment; a linear part which is predicted by conventional lifting surface theory; and a nonlinear part which is due to the leading-edge vortex flow (termed vortex lift). One of the oldest and easiest methods of predicting vortex lift is that of crossflow theory (ref. 5). The flow model used for this theory is shown in the upper right-

hand corner of figure 11. To estimate the magnitude of the vortex lift this method treats the flow in the crossflow plane as that around a flat plate with an assumed drag coefficient. The advantage of this method is that it is simple and easy to use. The disadvantages are that it depends on the assumed crossflow drag coefficient, and that it is not adequate for handling the effects of vortex interaction. Another well-known theoretical method for predicting the effects of leading-edge vortex flow is that of Brown and Michael (ref. 3). The mathematical model used by Brown and Michael is shown in the lower left-hand corner of figure 11. This model is composed of the wing, two vortex lines above the wing leading edge, and two flat vortex sheets which connect the wing and the vortex lines. The strength and position of the vortex sheets and the vortex lines are determined by applying the Kutta condition to the flow at the wing leading edge, and requiring that the total force on the vortex system be zero. The advantage of the Brown and Michael approach over that of crossflow theory is that it does not depend on any empirical or arbitrary constants. However, it overpredicts the vortex lift by about a factor of 2. In addition, the vortex configuration is assumed at the start, so that subjects such as vortex interaction or the dependence of the vortex system on wing leading-edge geometry cannot be treated. Another theoretical method for predicting the effects of vortex lift is that due to Mangler and Smith. The mathematical model used by Mangler and Smith is shown in the lower right-hand corner of figure 11. This model is considerably more representative of the actual vortex flow over simple delta wings than that of Brown and Michael; consequently, the results are in better agreement with experiment so far as simple delta wings are concerned. However, the method of Mangler and Smith is restricted to conical flow, and, further, is mathematically complex and difficult to extend to nonconical flows.

Because of the inadequacies and restrictive nature of the various existing theories, Ames Research Center contracted the Vidya Division of Itek Corporation to develop a theory for predicting the lift and pitching moment due to vortex flow on low-aspect-ratio wings of arbitrary planform. This theory is still being developed and therefore, the discussion to follow is more in the nature of a progress report than a presentation of a completed work. Some of the basic elements of the mathematical model used in this theory are shown in figure 12. The mathematical model is called the N-vortex flow model because the theory has been based on an arbitrary number of vortices being shed from the wing leading edge as indicated by the sketch on figure 12. As shown by this sketch, the basic idea of this theory is that the vortices will be shed at each of N chordwise stations along the wing leading edge. Once shed, these vortices will be allowed to interact or roll up with each other in any way that is required to maintain a completely force-free vortex system. Some of the basic assumptions of this theory are listed in figure 12. The vortex strength, initial position, and initial velocity are determined by an analysis in the crossflow plane as indicated by the sketch in the lower left-hand corner of figure 12. Thus, this portion of the analysis inherently assumes the restrictions of slender body theory. The vortex is shed so as to satisfy the Kutta condition at the wing leading edge. This, of course, includes consideration of the combined effect of all of the vortices present at that particular wing station. Some of the advantages of this theoretical approach are that (1) it distributes the vorticity along the wing leading edge in a quasi-sheet, (2) it allows the vortices to interact and roll up as they do in the

real flow, and (3) it is not restricted to conical flow. Thus, this theory should prove useful for studying the effects of wing geometry changes on vortex-flow phenomena. Some of the disadvantages of this theoretical method are as follows: (1) the method is numerically complex (however, it has been programmed for solution by digital computers, so this is not a serious problem), (2) the Kutta condition is satisfied only at discrete points (i.e., only at the chordwise stations where the vortices are shed), and (3) the determination of the strength of the vorticity being shed along the wing leading edge is difficult. This latter shortcoming, however, is common to all of the theoretical methods, and is considered to be the key problem to be resolved in future work. In particular, for general application of the theory it is necessary to be able to establish the strength of the vorticity being shed along the wing leading edge as a function of wing leading-edge geometry, that is, angle of sweepback, leading-edge radius, leading-edge camber (such as provided by nose flaps), etc.

Figure 13 presents some preliminary results obtained from the N-vortex theory along with theoretical results obtained by the methods of Brown and Michael and Mangler and Smith. Also shown on figure 13 are experimental results obtained by Bartlett and Vidal. These results were obtained for a simple delta wing with sharp leading edges and with an aspect ratio of 1.50. The total normal-force curves shown for the various theoretical methods were obtained by adding the normal force predicted by the various theories for the leading-edge vortex flow to the normal force predicted by the linear lifting surface theory of Lawrence (ref. 6) for the unseparated flow. The N-vortex theory used in these calculations employed 48 vortex elements. This comparison shows that the results obtained from the N-vortex theory agree with those obtained by the method of Mangler and Smith, and that both of these methods show better agreement with experiment than does the method of Brown and Michael. However, both the N-vortex and the Mangler and Smith theoretical results overpredict the lift by about 20 percent.

The variation of pitching moment with angle of attack predicted by these same theoretical methods is shown in the lower right-hand corner of figure 13, along with the experimental results of Bartlett and Vidal. As was the case for the normal-force characteristics just discussed, the various theoretical methods overpredict the effects of vortex flow on pitching moment. However, much closer agreement of theory with experiment is obtained when pitching-moment coefficient is plotted as a function of normal-force coefficient. Thus it appears that the main discrepancy in the prediction of pitching moment is due to errors in predicting normal force as a function of angle of attack rather than to errors in the distribution of the normal force over the wing surface. This discrepancy is believed to be due to errors in estimating the strength of the vorticity shed from the wing leading edge in the theoretical methods. As noted previously, this is considered to be the key problem in all of the theoretical methods. Additional work is required to establish the strength of vorticity shed from the wing leading edge in order to improve and extend the theoretical methods. This work should include the effects of the fuselage, wing leading-edge sweep, and wing leading-edge radius on vortex strength, since it is known that these effects are large. Further,

many aircraft designs of current interest (e.g., hydrogen-fueled hypersonic aircraft) will have large fuselages relative to the wing, and blunt wing leading edges.

#### CONCLUDING REMARKS

In summary, these studies have shown that vortex flow effects are important on a variety of modern wing configurations. It should be noted that, while this discussion has treated only longitudinal characteristics, it is well-known that vortex-flow phenomena have powerful effects on lateral directional characteristics, and further, that these effects are generally more difficult to predict than the longitudinal effects. While existing theories predict the correct trends, they are overly restrictive in their assumptions as to the mathematical model assumed to represent the vortex flow and generally are not accurate enough for design purposes. The new N-vortex theory appears promising, but additional work is required to establish the strength of the vorticity shed from the wing leading edge as a function of airplane geometry.

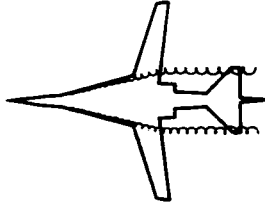
#### REFERENCES

1. Bollay, William: A Non-Linear Wing Theory and Its Application to Rectangular Wings of Small Aspect Ratio. Z. Angew. Math. Mech. Bd. 19, Nr. 1, Feb. 1939, pp. 21-35.
2. Mangler, K. W.; and Smith, J. H. B.: Calculation of the Flow Past Slender Delta Wings With Leading Edge Separation. Rept. No. Aero.2593, British R.A.E., May 1957.
3. Brown, Clinton E.; and Michael, William H., Jr.: On Slender Delta Wings With Leading-Edge Separation. NACA TN 3430, 1955.
4. Bartlett, G. E.; and Vidal, R. J.: Experimental Investigation of Influence of Edge Shape on the Aerodynamic Characteristics of Low Aspect Ratio Wings at Low Speeds. J. Aeron. Sci, vol. 22, no. 8, Aug. 1955, pp. 517-533, 588.
5. Betz, A.: Applied Airfoil Theory. Vol. IV of Aerodynamic Theory, div. J, ch. III, sec. 7, W. F. Durand, ed., Julius Springer (Berlin), 1935 (reprinted by Durand Reprinting Committee, 1943), pp. 69-72.
6. Lawrence, H. R.: The Lift Distribution on Low Aspect Ratio Wings at Subsonic speeds. J. Aeron. Sci., vol. 18, no. 10, Octo. 1951, pp. 683-695.

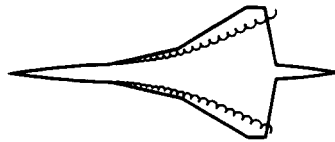
TABLE I. - WING PLANFORM REFERENCE DIMENSIONS

<b>Basic wing</b>	
Theoretical planform	
Total wing area, ft <sup>2</sup> . . . . .	439
Exposed wing area, ft <sup>2</sup> . . . . .	333
Span, ft . . . . .	27.3
Mean aerodynamic chord, ft . . . . .	19.4
Aspect ratio . . . . .	1.69
Taper ratio . . . . .	0.123
Equivalent delta planform	
Total wing area, ft <sup>2</sup> . . . . .	461
Exposed wing area, ft <sup>2</sup> . . . . .	333
Span, ft . . . . .	27.3
Mean aerodynamic chord, ft . . . . .	22.5
Aspect ratio . . . . .	1.62
Taper ratio . . . . .	0
<b>Basic wing plus small strake</b>	
Theoretical planform	
Total wing area, ft <sup>2</sup> . . . . .	512
Exposed wing area, ft <sup>2</sup> . . . . .	358
Span, ft . . . . .	27.3
Mean aerodynamic chord, ft . . . . .	25.4
Aspect ratio . . . . .	1.46
Taper ratio . . . . .	0.082
Equivalent delta planform	
Total wing area, ft <sup>2</sup> . . . . .	501
Exposed wing area, ft <sup>2</sup> . . . . .	358
Span, ft . . . . .	27.3
Mean aerodynamic chord, ft . . . . .	24.5
Aspect ratio . . . . .	1.49
Taper ratio . . . . .	0
<b>Basic wing plus large strake</b>	
Theoretical planform	
Total wing area, ft <sup>2</sup> . . . . .	555
Exposed wing area, ft <sup>2</sup> . . . . .	387
Span, ft . . . . .	27.3
Mean aerodynamic chord, ft . . . . .	28.3
Aspect ratio . . . . .	1.34
Taper ratio . . . . .	0.075
Equivalent delta	
Total wing area . . . . .	542
Exposed wing area . . . . .	387
Span, ft . . . . .	27.3
Mean aerodynamic chord, ft . . . . .	26.4
Aspect ratio . . . . .	1.38
Taper ratio . . . . .	0

## EFFECT OF LEADING-EDGE VORTEX FLOW



- VARIABLE-SWEEP WINGS  
1. REDUCES LONGITUDINAL STABILITY



- LOW-ASPECT-RATIO WINGS  
1. INCREASES LIFT-CURVE SLOPE  
2. REDUCES LONGITUDINAL STABILITY

Figure 1

## SUBJECTS TO BE DISCUSSED

- EFFECTS OF VORTEX FLOW ON AERODYNAMIC CHARACTERISTICS
- FLOW VISUALIZATION STUDIES
- THEORETICAL TREATMENT OF VORTEX FLOW

Figure 2

LOW-ASPECT-RATIO WING MODEL

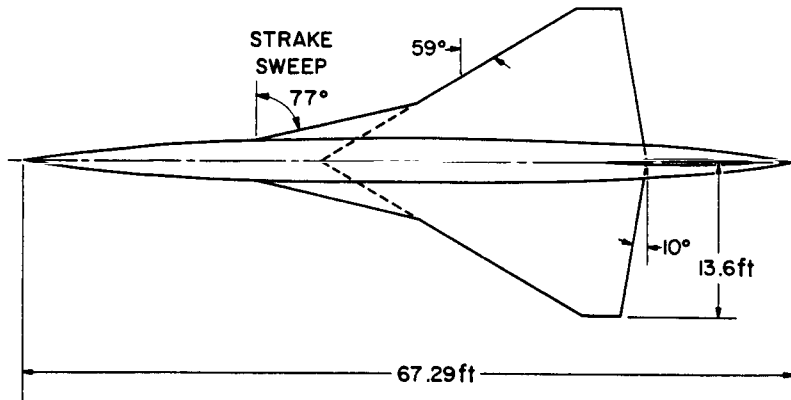


Figure 3

EFFECT OF PLANFORM ON LIFT

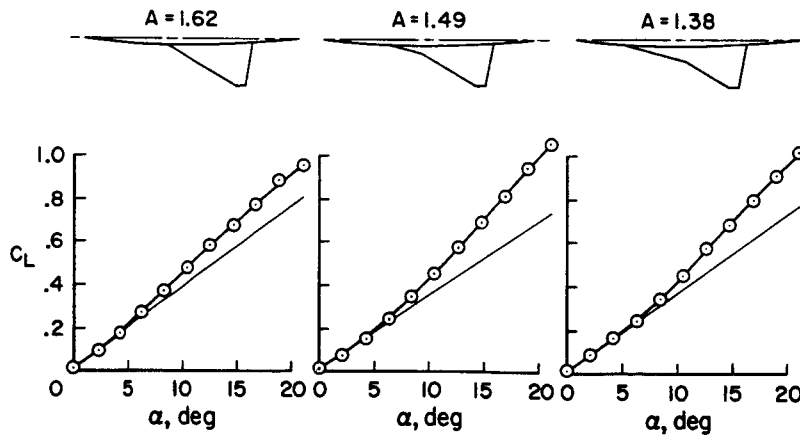


Figure 4

EFFECT OF PLANFORM ON PITCHING MOMENT

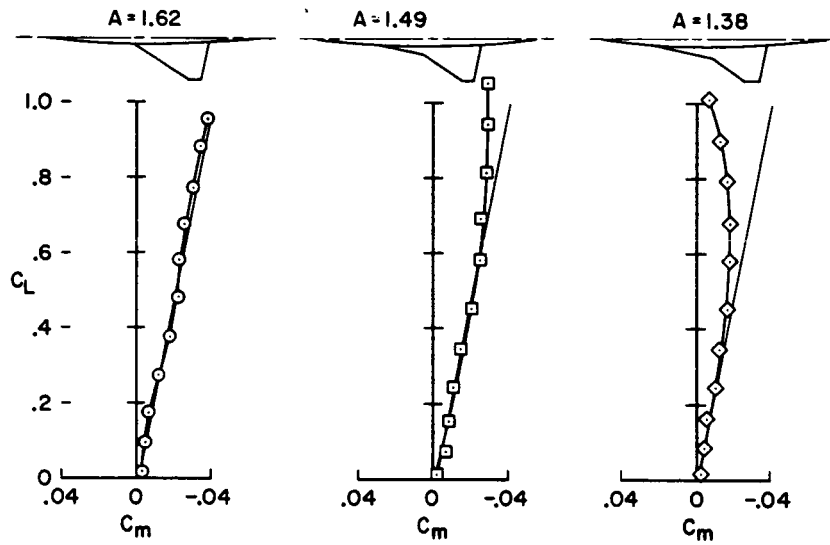


Figure 5

EFFECT OF PLANFORM ON DRAG

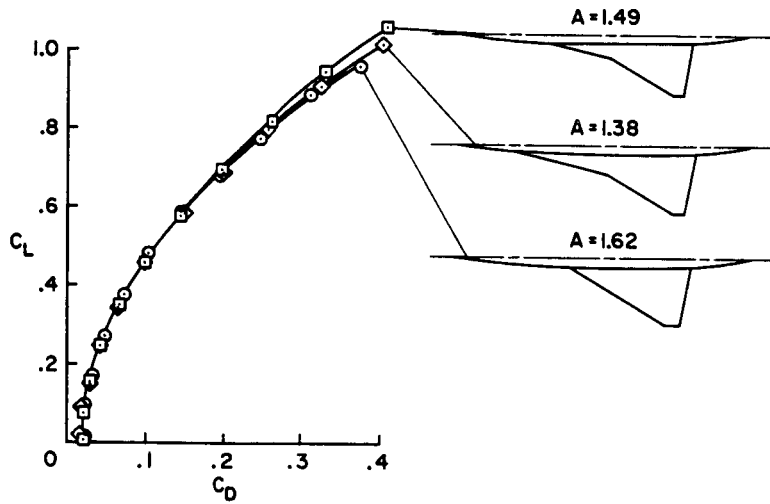


Figure 6

### EFFECT OF NOSE FLAPS ON LIFT

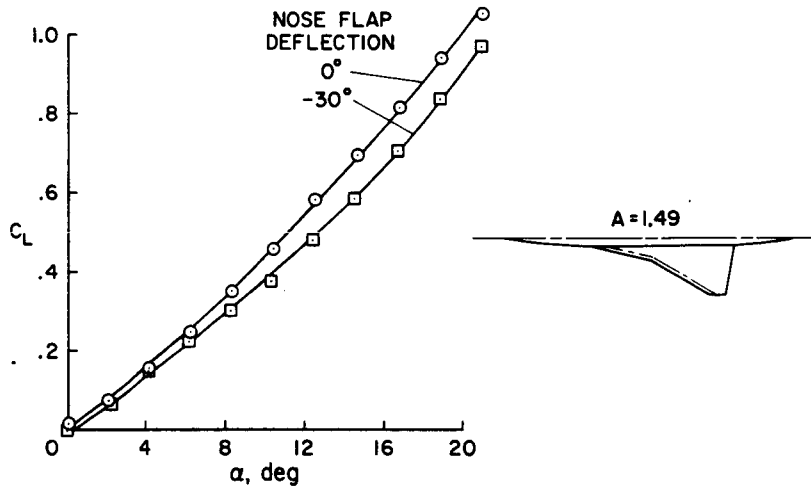


Figure 7

### EFFECT OF NOSE FLAPS ON PITCHING MOMENT

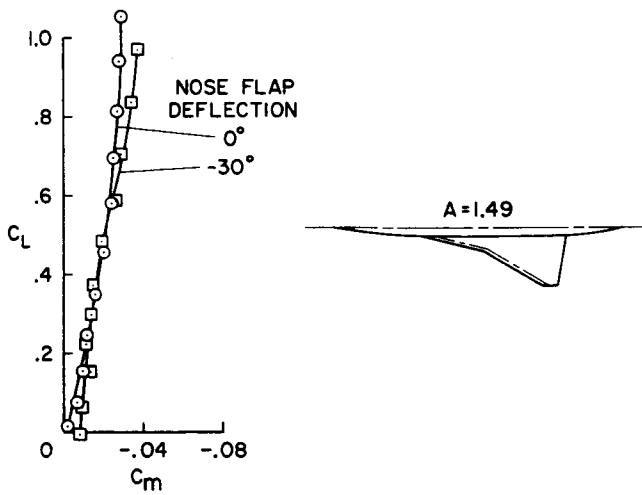


Figure 8

### EFFECT OF NOSE FLAPS ON DRAG

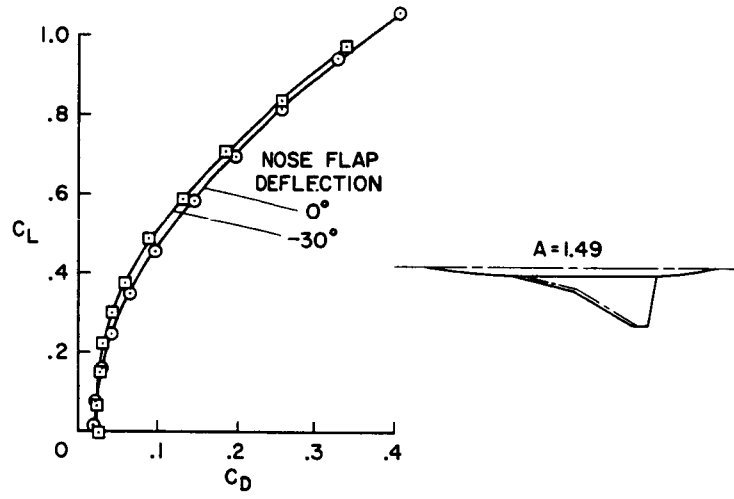


Figure 9

### VORTEX FLOW ON DOUBLE-DELTA WING



Figure 10

AAA112-9

SUMMARY OF EXISTING METHODS FOR PREDICTING VORTEX LIFT

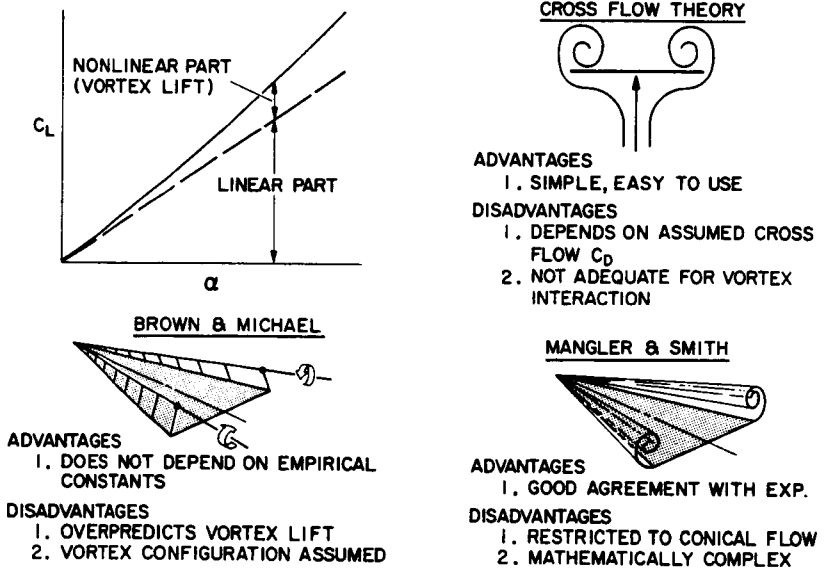


Figure 11

N-VORTEX FLOW MODEL

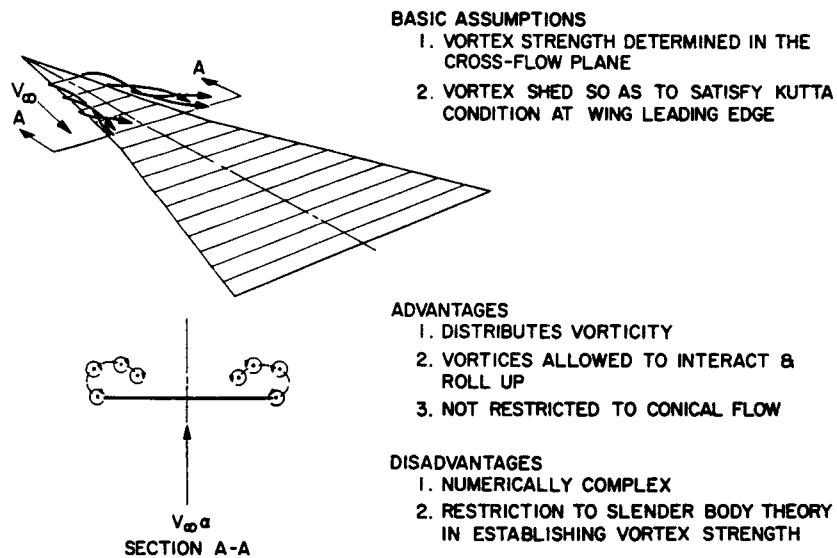


Figure 12

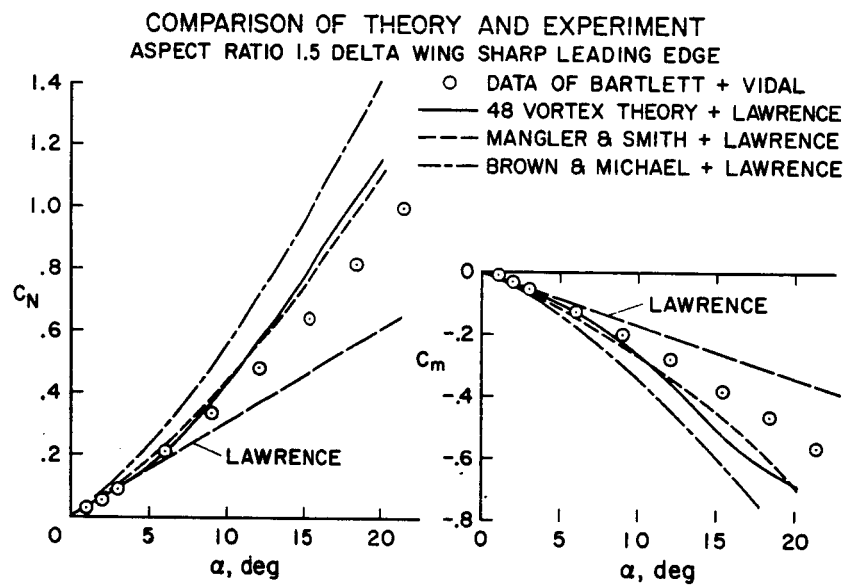


Figure 13

## 22. SOME RECENT STUDIES OF HIGH-LIFT FLAPS

### ON COMPOSITE WING PLANFORMS

By Alexander D. Hammond  
NASA Langley Research Center

22

#### SUMMARY

Over the years techniques for generating very high lift have been developed by NACA, NASA, and other research establishments. Work on mechanical flap systems to achieve high lift resulted in the development of the double-slotted flap which, in a full-span configuration, is capable of achieving lift coefficients up to 3 and 4.

The purpose of this paper is to present the results of some recent investigations which show the application of the previously developed double-slotted-flap systems to attain high lift on the newer composite wing planforms such as the variable-sweep wing.

The application of double-slotted-flap systems to composite wing planforms results in configurations capable of efficiently developing high lift if careful attention is paid to the details of the design of the system. It is shown herein that leading-edge slats are an essential part of the high-lift system. A moderate sized wing glove was found to have negligible effect on the lift and drag of an efficient high-lift system but was detrimental insofar as the longitudinal stability is concerned.

Adequate determination of flow separation effects on wings with high-lift devices, especially near maximum lift, requires that tests be made at Reynolds numbers as high as possible. The necessity for testing over a moving-belt ground board to determine the ground effects depends on the lift developed by the high-lift system and the height of the lifting system above the ground plane.

#### INTRODUCTION

Over the years techniques for generating very high lift have been developed and demonstrated by NACA, NASA, and other research establishments. Work on mechanical flap systems to achieve high lift resulted in the development of the single-slotted and double-slotted flaps capable of achieving lift coefficients up to 3 and 4. (See refs. 1 to 8.) The purpose of this paper is to present the results of some recent investigations which show the application of the previously developed double-slotted-flap systems to attain high lift on the newer composite wing planforms such as the variable-sweep wing.

Preceding page blank

## SYMBOLS

$C_L$	lift coefficient, $\frac{\text{Lift}}{qS}$
$C_D$	drag coefficient, $\frac{\text{Drag}}{qS}$
$C_m$	pitching-moment coefficient, $\frac{\text{Pitching moment}}{qS\bar{c}}$
$C_{m, \bar{c}/4}$	pitching-moment coefficient referred to quarter-chord point of wing mean aerodynamic chord, $\frac{\text{Pitching moment}}{qS\bar{c}}$
$A$	wing aspect ratio, $b^2/S$
$b$	wing span, inches
$c$	wing chord, inches
$\bar{c}$	wing mean aerodynamic chord, inches
$h$	height of wing chord plane above the ground, inches
$i_t$	tail incidence angle, degrees
$\Delta p$	increment in static pressure between wing upper surface and wing lower surface, pounds/foot <sup>2</sup>
$q$	free-stream dynamic pressure, pounds/foot <sup>2</sup>
$R$	free-stream Reynolds number per foot
$S$	wing area, feet <sup>2</sup>
$x$	chordwise distance from wing leading edge, inches
$\alpha$	wing angle of attack, degrees
$\delta_f$	flap deflection, degrees
$\delta_{\text{slat}}$	slat deflection, degrees
$\Lambda$	leading-edge sweep angle, degrees
$\Lambda_{c/4}$	sweep of wing quarter-chord line, degrees

## DISCUSSION

### Review of Fundamentals

Figure 1 shows sketches of a double-slotted flap in the retracted and deflected positions. A large-chord flap, a vane, and a leading-edge slat can be stored within the contour of a relatively thin airfoil as indicated by the cross section drawing for a typical wing station. When the high-lift system is deflected as shown in the lower sketch, it is desirable to have a smooth upper-surface contour with the camber distributed over the entire wing chord insofar as possible. For this reason, it is desirable to have a large-chord flap, from 30 to 40 percent of the wing chord, and a vane with a chord of about half the flap chord, so that the flap can be extended as far as possible. This chord extension increases the wing area and also provides for a smooth camber line. Flow through the slots provides some boundary-layer control on the flap and vane. It is important for the slots to be convergent, that is, for the minimum area to occur at the slot exit. Although the flap illustrated is a double-slotted flap, the rear flap can be divided into two parts with another slot between them to form a triple-slotted flap to attain higher usable flap deflections.

The leading-edge slat has a chord of about 15 percent of the wing chord and there is a gap between the slat and the wing leading edge to provide boundary-layer control. Most high-lift systems need leading-edge devices as is illustrated by the chordwise load distributions shown in figure 2. The plot on the left of figure 2 illustrates the typical chordwise load distribution as the result of angle of attack with the peak load at the leading edge of the airfoil. When the double-slotted flap is deflected to  $35^\circ$ , the flap load distribution is added to the angle-of-attack distribution. High pressure peaks occur at the flap and vane leading edges and the peak at the wing leading edge would also be increased. However, because of the increase in the adverse pressure gradient that would accompany this increase in the leading-edge peak pressure, separation often occurs, and the increase in leading-edge pressure is not realized. When a slat is deflected in front of the wing, the leading-edge separation is alleviated and the lift peak on the front part of the airfoil is restored. Higher lift is obtained as a result of the alleviation of the separation effects and the chord extension provided by the slat.

### Composite Wing Configurations

Sketches of the composite wing configurations used in a recent high-lift investigation at the Langley Research Center are shown in figure 3. The tests were made in the 17-foot test section of the Langley 300-MPH 7- by 10-foot tunnel. The basic wing configuration shown here had an unswept wing with a span of 120 inches and an aspect ratio of 10; it was equipped with a double-slotted-flap high-lift system shown in figure 3. The double-slotted flap was full span and extended from wing tip to wing tip even underneath the fuselage. The configuration was tested with and without the  $70^\circ$  swept-wing glove shown by the shaded area. When the glove was in place, the leading-edge slat extended from

the intersection of the wing and glove to the wing tips. Without the glove, the slat extended from the fuselage to the wing tip. The high-lift devices with and without the wing glove were also tested at wing sweeps of  $15^\circ$  and  $25^\circ$ . Although the wing span was greater for the swept wings, the aspect ratio of all three wings was approximately the same. The coefficients for each wing configuration are based on the geometry of each wing without the wing glove.

The effect of the leading-edge slat on the  $15^\circ$  swept-wing configuration is shown in figure 4. The maximum lift for the wings with the leading-edge slat on is higher for both flap deflections. It can also be seen that the onset of separation for the  $40^\circ$  flap deflection, indicated by a decrease in lift-curve slope at an angle of attack of about  $1^\circ$ , is delayed to a higher angle of attack with the leading-edge slat on.

The data for the basic wing without the high-lift devices were used to compute the envelope drag polar shown by the dashed curve in figure 4. That is, the basic wing-span efficiency factor of 0.89 and the zero-lift drag of a symmetrical airfoil of the same thickness were used to compute the curve. It can be seen that the full-span high-lift system has about the same span efficiency as the basic wing, since the drag data for the high-lift devices are tangent to the envelope drag curve at high lift coefficients.

The effect of wing sweep for the wings with  $40^\circ$  flap deflection and leading-edge slats is shown in figure 5. As the wing sweep is increased, the lift decreases and the induced drag becomes larger. However, it should be pointed out that the flap span on the  $25^\circ$  swept wing extended only from the wing-fuselage junction to the wing tip and that part of the lift loss shown results from the flap span effects. In fact, if the loss of lift resulting from sweep is calculated by the method of reference 9, the lift at zero angle of attack for the  $25^\circ$  swept wing would fall at the tick mark. The calculated loss of lift due to the reduction in flap span then reduces the lift further so that the increment between the unswept wing and the  $25^\circ$  swept wing at zero angle of attack agrees with the total computed loss. The lift loss shown for the  $15^\circ$  swept wing is almost all due to wing sweep since this wing has nearly a full-span flap.

The data shown in figure 6 indicate that there is very little, if any, effect of the wing glove on either the lift or drag for any of the wing sweeps and further indicate that, for a glove this size, a composite wing can develop the same lift as the basic wing without the glove. However, the distribution of this lift will change as indicated by the pitching-moment data shown in figure 7. The pitching-moment coefficients for the same flap configuration are shown for the  $0^\circ$ ,  $15^\circ$ , and  $25^\circ$  swept wings. There is a forward shift of the lift load with the leading-edge glove on as indicated by the change in slope of the pitching-moment curves between the glove-off and glove-on curves. However, there is very little change in the variation of the pitching moment with angle of attack for a glove this size.

The results of some tests reported in reference 10 on a variable-sweep model for which the sweep of the glove leading edge was varied from  $60.4^\circ$  to  $70^\circ$  and then to  $75^\circ$  are shown in figure 8. The glove area increased as the glove sweep increased. The wing was equipped with a double-slotted flap deflected to  $50^\circ$  in combination with a leading-edge slat that extended across

the outer wing panel. Again there is very little effect of the glove on the lift and drag characteristics. There is, however, a definite destabilizing effect of the glove on the pitching-moment characteristics. The previous pitching-moment data (fig. 7) were for a tail-off configuration and these data are for a tail-on configuration. However, the data for this model with the tail off show the same destabilizing pitching-moment trends as are shown for the tail-on configuration, although the trends were not as pronounced - an indication that there are some changes in the flow at the tail as a result of the glove. This destabilizing effect of the wing glove with the high-lift configuration has also been shown for the unflapped wing at low lift coefficients by Ray, Lockwood, and Henderson in paper no. 5.

### Reynolds Number Effects

In any discussion of the results of high-lift investigations, the effects of Reynolds number must always be considered. Shown in figure 9 are some results from an investigation of a model of a current fighter in the Ames 12-foot pressure tunnel at the Reynolds numbers shown. The data are for a complete model with a slat deflection of  $45^\circ$ , a flap deflection of  $40^\circ$ , and for a tail incidence of  $-10^\circ$ . The data for a Reynolds number of  $1.89 \times 10^6$  indicate a very low maximum lift as well as premature separation as shown by the high drag and the early breaks in the slopes of the lift-coefficient and pitching-moment curves. The data for a Reynolds number of  $3.21 \times 10^6$  do not attain a maximum lift as high as the data for  $5.97 \times 10^6$ , but do, however, show the same initial lift-curve and pitching-moment breaks. These results emphasize that tests should be made at Reynolds numbers high enough to determine the flow separation effects adequately, especially near maximum lift.

### Ground Simulation

One other subject relating to testing techniques involved with high-lift investigations is the proper ground simulation to determine the ground effects. The significance of the ground effect has been discussed in paper no. 19 by Kemp, Lockwood, and Phillips and in paper no. 20 by Rolls, Snyder, and Schweikhard. The use of the moving-belt ground board for determining ground effects is presented in reference 11, and results for configurations with double-slotted flaps are summarized in figures 10 and 11.

Figure 10 shows the effect of ground simulation on the lift, drag, and pitching-moment characteristics of the double-slotted flaps on the unswept-wing configuration discussed previously. The out-of-ground-effect data are compared with data taken at  $h/b = 0.06$  above a fixed ground plane and at the same height over a moving ground plane. The point here is not to show the ground effects as such but to show that, up to a lift coefficient of about 1.6, both methods of ground simulation give the same results. However, at lift coefficients above 1.6, at this ground height, the fixed-ground-board method of ground simulation shows too large an effect of ground. These data indicate that, at this height, tests can be made on configurations developing lift coefficients up to 1.6 without the need for a moving ground plane. Other data for this lifting system at different heights indicate the same general trend. A

correlation of lift coefficient and ground height was made in reference 11 for this configuration and other full-span flap systems (with aspect ratios from 6 to 10), to show when it is necessary to have a moving ground plane. The conditions requiring moving ground board for proper ground simulation are shown in figure 11. The symbols represent data points used to establish the boundary shown. For lift coefficients attained at ground heights that fall above the boundary, a conventional ground board is adequate. If the lift coefficient attained for a given ground height falls below the boundary, a moving ground plane would be needed to determine the effects of the ground properly. The lift coefficients developed by low-aspect-ratio wings at the minimum heights allowed for by the landing gear generally fall in the area above the boundary where a conventional fixed ground board would provide adequate ground simulation.

#### CONCLUDING REMARKS

The application of previously developed mechanical high-lift systems to composite wing planforms resulted in configurations capable of efficiently developing high lift, if careful attention is paid to details of the design of the system. It has been shown that leading-edge slats are an essential part of the high-lift system.

The effect of a moderate sized wing glove was found to be negligible on the lift and drag of an efficient high-lift system but is detrimental insofar as the longitudinal stability is concerned.

Tests of high-lift devices should be made at Reynolds numbers as high as possible in order to determine adequately the effects of flow separation on the high lift characteristics, especially near maximum lift.

The necessity for testing over a moving ground board to determine the ground effects depends on the lift developed by the high-lift system and the height of the lifting system above the ground plane.

## REFERENCES

1. Abbott, Ira H.; and Von Doenhoff, Albert E.: Theory of Wing Sections. Dover Publ., Inc., 1959.
2. Cahill, Jones F.: Summary of Section Data on Trailing-Edge High-Lift Devices. NACA Rept. 938, 1949. (Supersedes NACA RM L8D09.)
3. Young, A. D.: The Aerodynamic Characteristics of Flaps. R. & M. No. 2622, British A.R.C., Feb. 1947.
4. Riebe, John M.: A Correlation of Two-Dimensional Data on Lift Coefficient Available With Blowing-, Suction-, Slotted-, and Plain-Flap High-Lift Devices. NACA RM L55D29a, 1955.
5. Schwartzberg, Milton A.; and Burch, John L.: Lifting Capabilities of Wings With and Without High-Lift Devices. Eng. Rept. No. 8055 (Contract NOa(s)55 655-c), The Glenn L. Martin Co., Apr. 1956.
6. Dike, D. J.; Dunn, H. S.; Hazen, D. C.; and Lehnert, R. F.: A Study of the Low Speed Aerodynamic Characteristics of High-Lift Flow Controlled Profiles and Wings. Rept. No. 349 (Contract No. Noas 55-583-d), Dept. Aeron. Eng., Princeton Univ., May 1958.
7. Naeseth, Rodger L.; and Davenport, Edwin E.: Investigation of Double Slotted Flaps on a Swept-Wing Transport Model. NASA TN D-103, 1959.
8. Henderson, William P.; and Hammond, Alexander D.: Low-Speed Investigation of High-Lift and Lateral Control Devices on a Semispan Variable-Sweep Wing Having an Outboard Pivot Location. NASA TM X-542, 1961.
9. Lowry, John G.; and Polhamus, Edward C.: A Method for Predicting Lift Increments Due to Flap Deflection at Low Angles of Attack in Incompressible Flow. NACA TN 3911, 1957.
10. Lockwood, Vernard E.: High-Lift Characteristics of a Variable-Sweep Supersonic Transport Model With a Blended Engine-Fuselage and Engine-Mounted Horizontal Tails. NASA TM X-1199, 1966.
11. Turner, Thomas R.: Endless-Belt Technique for Ground Simulation. Conference on V/STOL and STOL Aircraft, NASA SP-116, 1966, pp. 435-446.

# DOUBLE-SLOTTED FLAP AND SLAT

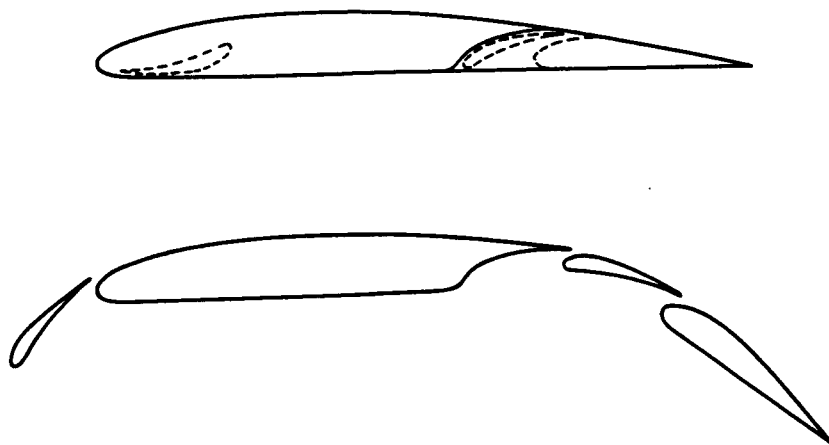


Figure 1

## CHORDWISE LOAD DISTRIBUTION

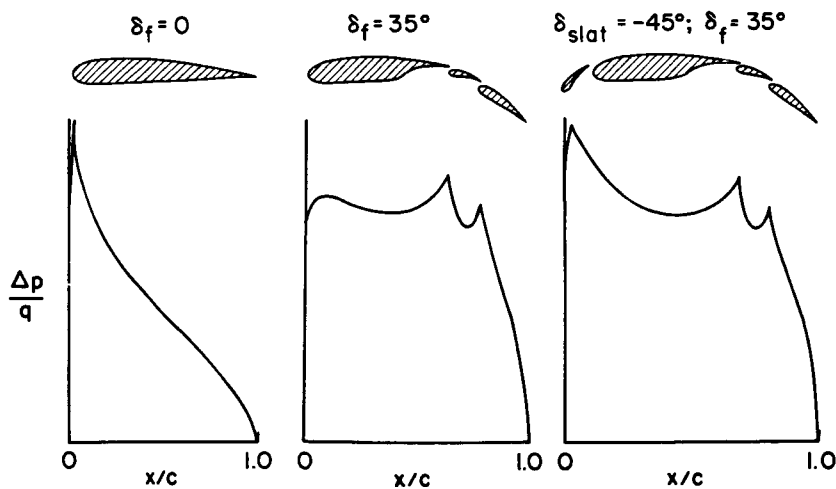


Figure 2

COMPOSITE WING CONFIGURATIONS  
HIGH-LIFT INVESTIGATION

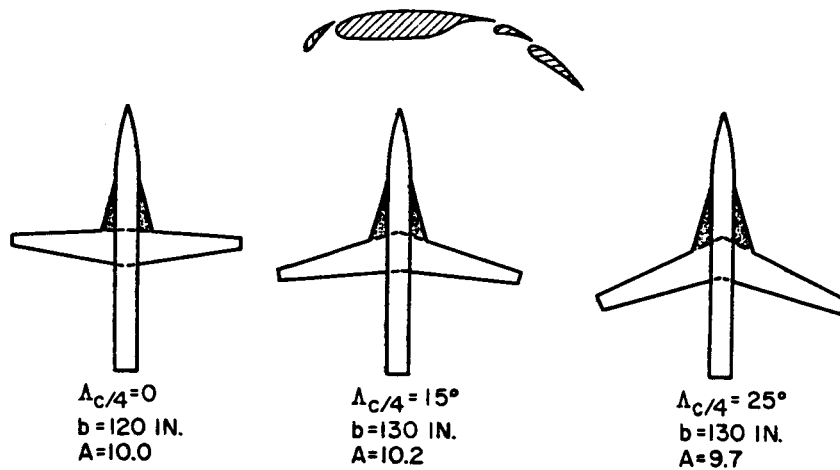


Figure 3

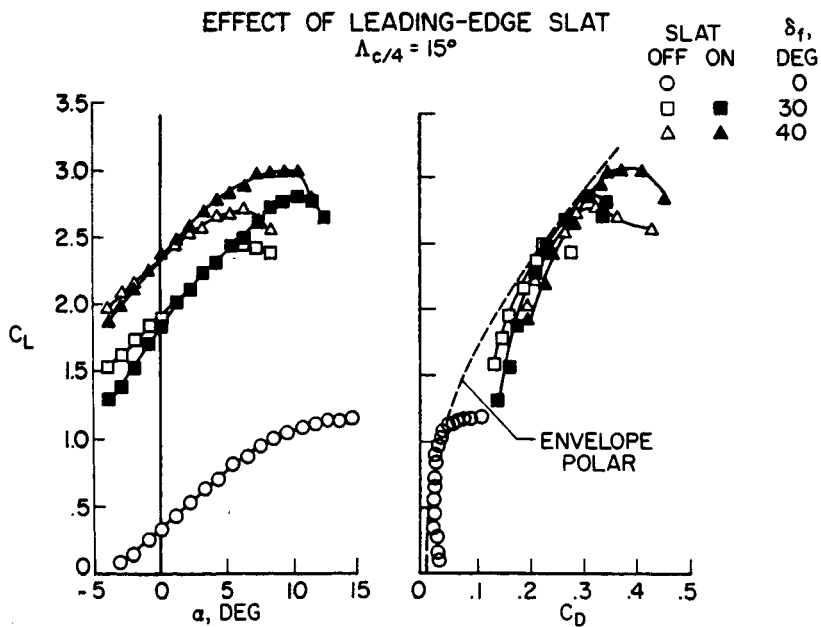


Figure 4

EFFECT OF WING SWEEP  
 $\delta_f = 40^\circ$ ; SLAT ON

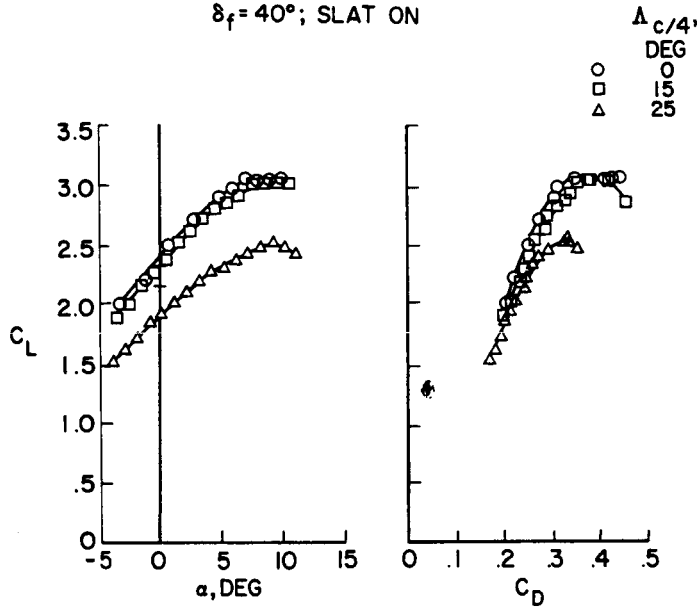


Figure 5

EFFECT OF LEADING-EDGE GLOVE  
 $\delta_f = 40^\circ$ ; SLAT ON

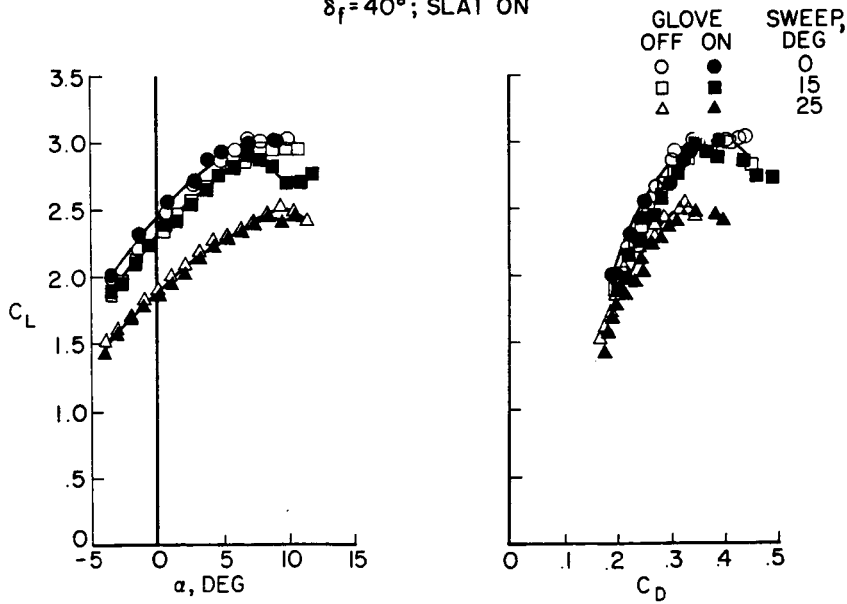


Figure 6

EFFECT OF LEADING-EDGE GLOVE  
 $\delta_f = 40^\circ$ ; SLAT ON

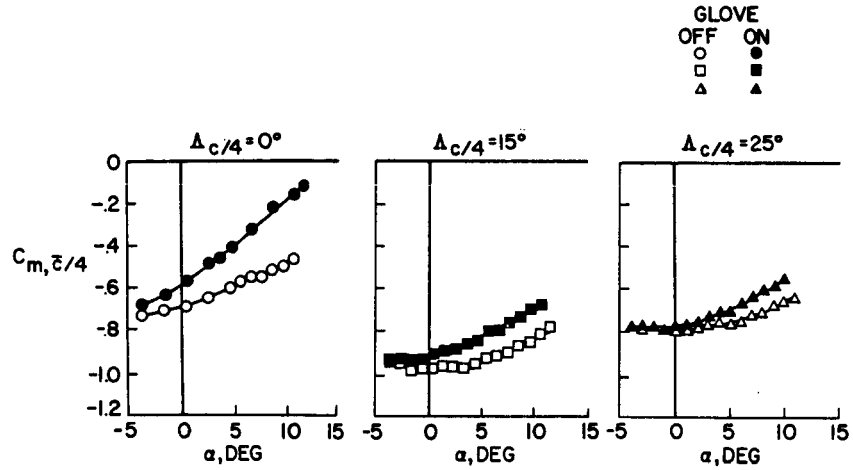


Figure 7

EFFECT OF GLOVE SWEEP  
 $\delta_f = 50^\circ$ ;  $i_t = -10^\circ$

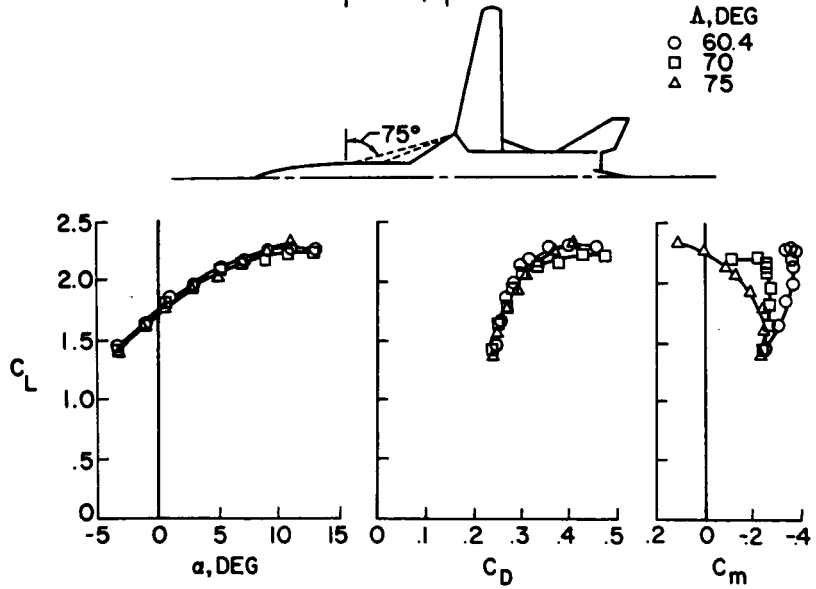


Figure 8

### EFFECT OF REYNOLDS NUMBER

$\delta_{slat} = -45^\circ; \delta_f = 40^\circ; i_f = -10^\circ$

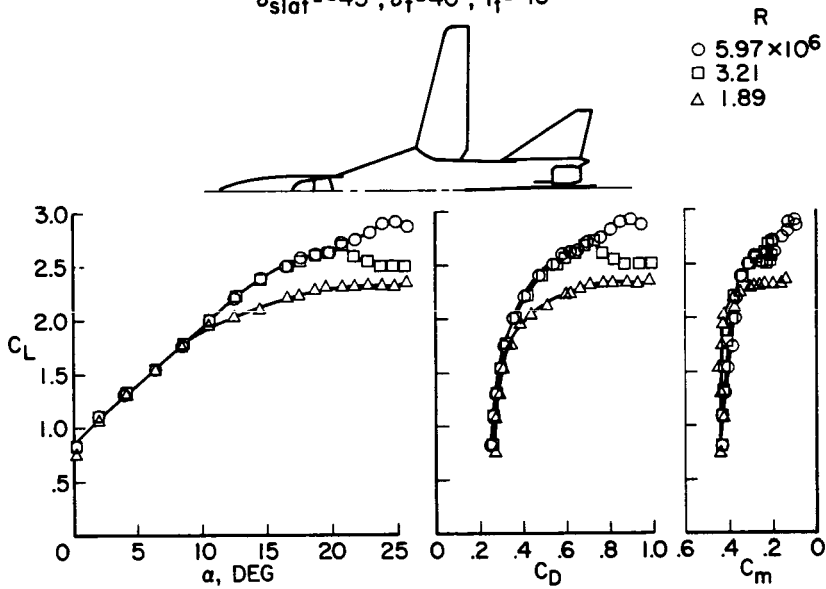


Figure 9

### EFFECT OF GROUND SIMULATION

$h/b$   
 $\circ$   $\infty$   
 $\square$  .06 FIXED BOARD  
 $\triangle$  .06 MOVING GROUND

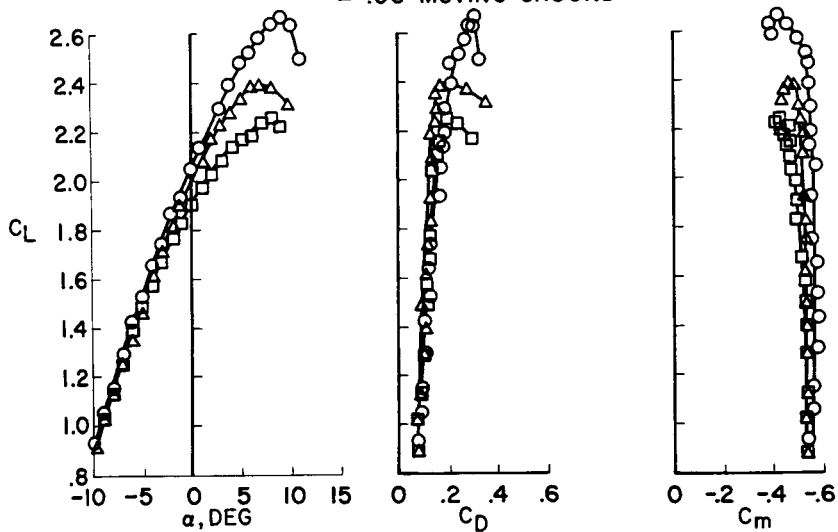


Figure 10

CONDITIONS REQUIRING MOVING GROUND BOARD  
FULL-SPAN HIGH-LIFT DEVICES

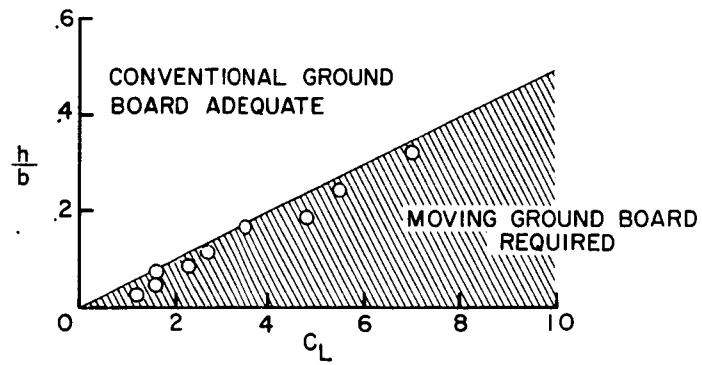


Figure 11

## 23. STUDIES OF VARIOUS FACTORS AFFECTING

### DRAG DUE TO LIFT AT SUBSONIC SPEEDS

By William P. Henderson  
NASA Langley Research Center

#### SUMMARY

Studies of various factors affecting the subsonic drag due to lift of thin highly swept wings indicate that wings having sharp leading edges exhibit low values of leading-edge suction, and no significant change in the suction is evident with increasing Reynolds number. Wings incorporating leading-edge radii exhibit 90-percent suction at Reynolds numbers (based on leading-edge radius) above 20 000. The suction developed by highly swept wings falls off considerably with lift coefficient even at relatively high Reynolds numbers, and realistic drag estimates should include this effect. Additional systematic studies are needed to assess the effects of Mach number on leading-edge suction.

#### INTRODUCTION

Because of the highly swept and relatively sharp leading edges for wing designs of interest for supersonic aircraft such as the proposed supersonic transport, a knowledge of the various factors affecting the drag due to lift at subsonic speeds is becoming increasingly necessary. In view of this interest, an investigation was conducted to determine the effects of Reynolds number, lift coefficient, and wing leading-edge radius on the drag due to lift of a series of thin, highly swept, low-aspect-ratio wing-body configurations. The purpose of this discussion is to review some of the results of this investigation.

#### SYMBOLS

A	aspect ratio
b	wing span
c	wing chord
$\bar{c}$	mean geometric chord
$C_D$	drag coefficient
$\Delta C_D$	drag due to lift
$C_{D,i}$	induced drag coefficient
$C_{D,o}$	drag coefficient at zero lift

Preceding page blank

$C_{D,p}$	profile drag coefficient due to lift
$\frac{\partial C_{D,i}}{\partial C_L^2}$	drag-due-to-lift parameter
$C_L$	lift coefficient
$C_{L,opt}$	optimum lift coefficient
$C_N$	normal-force coefficient
$C_s$	suction force coefficient
$F$	resultant force vector
$(L/D)_{max}$	maximum lift-drag ratio
$M$	Mach number
$R_{\bar{c}}$	Reynolds number based on $\bar{c}$ , $\rho V \bar{c} / \mu$
$R_{r,e}$	Reynolds number based on $r$ , $\rho V_n r / \mu$
$r$	average leading-edge radius
$s$	leading-edge-suction parameter
$V$	free-stream velocity
$V_n$	velocity component measured normal to wing leading edge, $V \cos \Lambda$
$y$	spanwise coordinate
$\alpha$	angle of attack
$\alpha_i$	induced angle of attack
$\Gamma$	circulation strength
$\delta_f$	leading-edge flap deflection (positive leading edge up), deg
$\Lambda$	wing leading-edge sweep angle, deg
$\mu$	coefficient of viscosity
$\rho$	density

## DISCUSSION

### Scope of Investigation

The scope of this wind-tunnel investigation is shown in figure 1. The test conditions provide for Mach numbers less than 0.3 and Reynolds numbers (based on the wing mean-geometric chord) ranging from about  $1 \times 10^6$  to  $20 \times 10^6$ . The wings, which were tested in combination with a fuselage, vary in leading-edge sweep from  $49^\circ$  to  $74^\circ$  and the aspect ratio varies from 4.02 to 1.33. All these wings had symmetrical airfoil sections; the  $74^\circ$  swept wing had, in addition, a 15-percent-chord leading-edge flap and a warped section designed for supersonic cruise. The first series of wings had standard 63A and 65A airfoil sections, whereas the second series of wings had flat-plate sections. In this second series of wings, the wings shown in figure 1 on the center right were obtained by removing a portion of the trailing edge from the wings shown on the center left. A portion of the leading edge of these wings could also be changed in order to vary the leading-edge sweep, the leading-edge profile shape, and the wing aspect ratio. The leading-edge profile shape was varied from sharp to nearly round. The thickness for these wings varied between 3 and 5 percent chord.

The wind-tunnel studies were made in the Langley low-turbulence pressure tunnel. Because of tunnel limitations, the Mach numbers were limited to 0.30. As a result, only a brief discussion of Mach number effects is included herein.

### Boundary-Layer Transition

For the purpose of insuring turbulent flow on these wings, transition strips were placed on the upper and lower surface of each wing panel. The size and location of the transition particles needed to provide fully turbulent flow rearward of the strips were determined by the methods discussed previously in paper no. 2 by Braslow, Hicks, and Harris.

The significance of fixing transition on a wing surface as regards the drag due to lift is illustrated in figure 2. The variations of the drag with Reynolds number, at lift coefficients of 0 and 0.3, are presented for a wing with fixed and free transition. The transition strips were added near the leading edge of this wing so as to obtain the correct value of drag at zero lift. The transition strip, of course, would not be expected to affect leading-edge separation. These data show that at zero lift and low Reynolds numbers the wing with free transition exhibits a lower value of drag than the wing with fixed transition. As the Reynolds number is increased, the point of natural transition moves forward on the wing with the result that the difference in drag is considerably reduced. At the higher lift coefficient the point of natural transition is presumed to be near the nose of the wing inasmuch as values of drag for this wing are the same as for the wing with fixed transition.

It is evident from these data that the wings with fixed and free transition will exhibit values of drag due to lift which are somewhat different. Therefore, if correct values of drag due to lift are to be obtained, care must

be taken to select transition particles of proper size to provide fully turbulent flow over the wing. (See ref. 1.)

### Leading-Edge-Suction Parameter

Of the several parameters available for drag-due-to-lift analyses, the one to be used in this paper is the effective leading-edge suction. The definition of this parameter and reasons for its choice are demonstrated in figure 3. This parameter is referred to as "effective leading-edge suction" because, for the highly swept thin wings under consideration, the departure from the full suction theory is associated primarily with leading-edge separation. It should be noted that the subsequent use herein of an effective suction includes all the profile drag due to lift  $C_{D,p}$ . The drag-coefficient variation with lift coefficient is presented for two flat-plate wings with identical leading-edge shape but of different aspect ratio and taper ratio. The wing on the right of the figure was obtained from the wing on the left by removing a portion of the wing trailing edge.

In both plots, the upper curve is for zero percent suction, and the lower curve is for 100 percent suction. The experimental data are shown by the circular test points. As indicated by the force diagram, the zero percent suction curve corresponds to the condition when the resultant-force vector is normal to the chord, as a result of extensive separation at the wing leading edge. The drag-due-to-lift coefficient for this condition is  $C_L \tan \alpha$ . For 100 percent suction, the drag-due-to-lift coefficient is the potential flow induced vortex drag and is indicated as  $C_{D,i}$  in the vector diagram. The drag-due-to-lift coefficients for 100 percent suction were determined from a modified Multhopp subsonic lifting surface theory. For an elliptically loaded wing this value would be the classic  $C_L^2 / \pi A$ .

The effective leading-edge-suction parameter  $s$  is defined as the experimentally measured suction in percent of the total theoretical suction; that is, it locates the experimental data relative to the two theoretical boundaries and is given by the following equation:

$$s = \frac{C_L \tan \alpha - (C_D - C_{D,o})}{C_L \tan \alpha - A \int_{-1}^1 \Gamma \alpha_1 d\left(\frac{y}{b/2}\right)} \times 100$$

For these wings, the effective suction level is approximately 18 percent and indicates that for these wings with identical leading-edge shape the suction parameter  $s$  is independent of aspect ratio and taper ratio.

Another method of analysis based on use of the coefficient of profile drag due to lift  $C_{D,p}$  does not show this independence of aspect ratio and taper

ratio, as is illustrated in figure 3, where at  $C_L = 0.3$ , the wing on the right had a  $C_{D,p}$  that is 30 drag counts higher than the wing on the left.

Because the leading-edge-suction parameter tends to eliminate the effects of aspect ratio and taper ratio, this parameter  $s$  was chosen to analyze the drag-due-to-lift characteristics presented. For the warped wings of this investigation the suction parameter was determined by using a value of  $C_{D,o}$  from an equivalent flat wing, whereby camber drag was eliminated from the analysis.

### Sharp-Leading-Edge Wings

For supersonic speeds, the requirement for acceptable performance dictates the use of thin highly swept wings, and for a wing with a supersonic leading edge, use of a sharp leading-edge section. A sharp leading edge, of course, is not conducive to low values of drag due to lift at subsonic speeds, as is illustrated in figure 4. The variation of leading-edge suction is presented as a function of Reynolds number for a  $67^\circ$  swept wing in the left plot, and the variation of suction with wing sweep for several sharp-edge wings is shown in the right plot. The values of  $s$  shown in this figure and in most of the following figures were taken at the lift coefficient for  $(L/D)_{\max}$  and are designated  $C_{L,opt}$ .

These data show that the  $67^\circ$  swept wing exhibits low values of suction, and only a slight increase with Reynolds number is evident. All the sharp-edge wings of the present study, shown as the circular symbols on the right of figure 4, exhibited the same trend of only slight variations of  $s$  with Reynolds number that is shown by the data for the  $67^\circ$  swept wing on the left. As a result, the suction parameter can be plotted as a function of wing sweep angle independent of Reynolds number. The data for the  $67^\circ$  swept wing presented on the left of this figure is also included on the right as the solid symbol. The data shown by the square symbols were obtained from references 2 to 5. These data again show that sharp-edged highly swept wings exhibit low values of suction. Even for low values of wing sweep, suction values no higher than about 50 percent are evident.

### Configuration Modifications

Several features that can increase the effective suction can be incorporated into a wing design. Two of these features are shown in figure 5. This figure shows the effect of leading-edge flaps and wing warp on the variation of the leading-edge suction with Reynolds number for a  $74^\circ$  swept wing configuration. These data show that both leading-edge flaps and wing warp increase the values of suction over that obtained on the symmetrical, sharp-leading-edge wing. Although an increase in suction was obtained, still only a slight increase with Reynolds number is evident. The suction obtained for the warped wing shows a value of about 40 percent. Since the warping of this wing was designed from supersonic rather than subsonic considerations, values of suction

substantially less than 100 percent are not surprising. Further increases in the effective suction can possibly be obtained on the warped wing by incorporating a leading-edge flap; however, the total increment shown for the symmetrical wing may not be obtained for the warped wing.

A third feature that provides increases in the leading-edge suction is use of a wing leading-edge radius. Figure 6 presents the variation of  $s$  and  $(L/D)_{\max}$  with Reynolds number for a highly swept wing with a sharp and a round leading edge. These data indicate that the wing with the round leading edge exhibits large variations of  $s$  with Reynolds number, whereas the wing with the sharp leading edge results in relatively constant values of  $s$ . The significance of this result in terms of the variation of  $(L/D)_{\max}$  with Reynolds number for these two wings is shown in the right-hand plot of this figure. The dashed lines represent lines of constant drag due to lift. For the wing with invariant suction the change in  $(L/D)_{\max}$  with Reynolds number is the result of the change in skin-friction drag. However, for the wing with the round leading edge only about 1/3 of the increase in  $(L/D)_{\max}$  can be attributed to the reduction in skin-friction drag and the other 2/3 to the reduction in drag due to lift. Tests at supersonic speeds on a wing of sufficient sweep to have the leading edge swept behind the Mach line (i.e., a subsonic leading edge) have indicated that a leading-edge radius of approximately the same percentage of the wing chord as shown in this figure could be added without imposing a loss in performance (ref. 6).

The previous discussion has shown that using the leading-edge-suction parameter tended to eliminate some of the effects of planform in an analysis of the drag due to lift, as long as the conditions at the leading edge of the wing are the same. This result suggests that in attempts to correlate the wind-tunnel data use might be made of a parameter which considers only the leading-edge conditions. The parameter used in this analysis is a Reynolds number based on the velocity component and an average leading-edge radius, both measured normal to the leading edge of the wing. A correlation of the wind-tunnel data by use of this Reynolds number is shown in figure 7. In this figure, the suction parameter  $s$  is presented as a function of the leading-edge Reynolds number  $R_{\lambda e}$ . The data shown are for the symmetrical wings shown in figure 1. These wings have thickness ratios between 3 and 5 percent chord and leading-edge sweep angles between  $49^\circ$  and  $73^\circ$ . These data indicate that about 90 percent suction can be obtained on highly swept thin wings at Reynolds numbers (based on leading-edge radius) above 20 000.

Earlier correlations obtained by using transition-free data have shown somewhat different results, especially in the low Reynolds number range. (See ref. 7.)

#### Effect of Lift Coefficient and Mach Number

The preceding summary figures have shown the effects of some configuration variables on the leading-edge suction taken at  $C_{L,\text{opt}}$  and at low Mach numbers.

Several other effects should be considered. The first, which is shown in figure 8, is the variation of suction with lift coefficient for  $45^\circ$  and  $62^\circ$  swept wings at several Reynolds numbers. The data for the  $45^\circ$  swept wing, which were obtained from reference 1, show that increasing the Reynolds number results in an increase in the suction at  $C_{L,opt}$ , and these high values of suction can be maintained to significantly higher lift coefficients before separation effects cause the suction to diminish. However, for the  $62^\circ$  swept wing, leading-edge separation occurs at relatively low lift coefficients so that even at the higher Reynolds numbers, high values of suction can be maintained over only a small lift-coefficient range. Simple sweep theory would indicate the same effects shown by these data; that is, separation effects causing losses in suction would occur at significantly lower lift coefficients for the highly swept wing. It should be emphasized that because of the large variations of suction with lift coefficient exhibited by these wings, the use of a constant value of suction (for example, the value obtained at  $C_{L,opt}$ ) in defining the entire drag polar would give dangerously optimistic results.

In paper no. 3 of this conference, D. L. Loving suggested that the location of the transition strips can significantly affect the separation characteristics behind the strip. However, for these thin wings at low speeds the large loss of effective suction at the higher lift coefficients is primarily associated with leading-edge separation, and it is not expected that the position of the transition strips would significantly affect these results.

Another effect to be considered is that of Mach number on the leading-edge suction, as shown in figure 9. A search of the literature indicated that data are very scarce from systematic investigations, in the high-subsonic-speed range, of the effects of leading-edge radius, Reynolds number, and wing planform for highly swept wing-body configurations which have transition fixed at the leading edge of the wing. Therefore, only a limited analysis of the Mach number effects, based on the data presented in this figure, is possible. These data were obtained from reference 1. In this figure, the suction parameter is given as a function of Mach number for  $45^\circ$  and  $63^\circ$  swept wings, both wings having 5-percent-thick symmetrical and conically cambered airfoil sections. These data show that the suction varies very slightly with Mach number for the symmetrical wings. However, for the conically cambered  $45^\circ$  swept wing, although substantial improvement is provided at low speeds, losses in suction appear at Mach numbers above 0.7 until at a Mach number near 1.0 the cambered and symmetrical  $45^\circ$  swept wings have nearly the same value of  $s$ . For the delta wing, the benefits of camber are maintained to the highest Mach number of the tests because of the high critical Mach number associated with the higher leading-edge sweep angle. The limited results shown are applicable only to these wings, in that changes in the airfoil section or wing planform could significantly alter these results. Additional systematic results are needed to complete this study.

With regard to these Mach number dependent data, it should be noted that for higher lift coefficients, if shock stall is encountered, the method of fixing transition utilized in this study may not provide reliable aerodynamic data, as has been pointed out previously in paper no. 3 by Loving.

## CONCLUSIONS

Studies of various factors affecting the subsonic drag due to lift of thin, highly swept wings indicated the following conclusions:

1. Wings having sharp leading edges exhibit low values of leading-edge suction, and no significant change in the suction with increasing Reynolds number is evident.

2. Wings incorporating leading-edge radius exhibit approximately 90 percent suction at Reynolds numbers (based on leading-edge radius) above 20 000.

3. The suction developed by highly swept wings is considerably reduced as lift coefficient is increased, even at relatively high Reynolds numbers; and realistic drag estimates should include this effect.

4. Additional systematic studies are needed for a more comprehensive understanding of the effects of Mach number on leading-edge suction.

## REFERENCES

1. Boyd, John W.; Migotsky, Eugene; and Wetzell, Benton E.: A Study of Conical Camber for Triangular and Sweptback Wings. NACA RM A55G19, 1955.
2. Carter, C. Robert: Effect of Rearward Body Strakes on the Transonic Aerodynamic Characteristics of an Unswept-Wing Fighter Aircraft. NASA TN D-3011, 1965.
3. Blackwell, James A., Jr.; and Kelly, Thomas C.: Effects of Configuration Geometry on the Transonic Aerodynamic Characteristics of Canard Airplane Configurations. NASA TN D-2465, 1964.
4. Ray, Edward J.; and Taylor, Robert T.: Transonic Aerodynamic Characteristics of a Tailless Fixed-Wing Supersonic Transport Model. NASA TM X-1214, 1966.
5. Holdaway, George H.; and Mellenthin, Jack A.: Investigation at Mach Numbers of 0.20 to 3.50 of Blended Wing-Body Combinations of Sonic Design With Diamond, Delta, and Arrow Plan Forms. NASA TM X-372, 1960.
6. Morris, Odell A.; and Fournier, Roger H.: Aerodynamic Characteristics at Mach Numbers of 2.30, 2.60, and 2.96 of a Supersonic Transport Model Having a Fixed, Warped Wing. NASA TM X-1115, 1965.
7. Frost, Richard C.; and Rutherford, Robbie: Subsonic Wing Span Efficiency. AIAA J., vol. 1, no. 4, Apr. 1963, pp. 931-933.

### SCOPE OF WIND-TUNNEL PROGRAM

$M < 0.30$ ;  $R_{\bar{c}} = 1 \times 10^6$  TO  $20 \times 10^6$

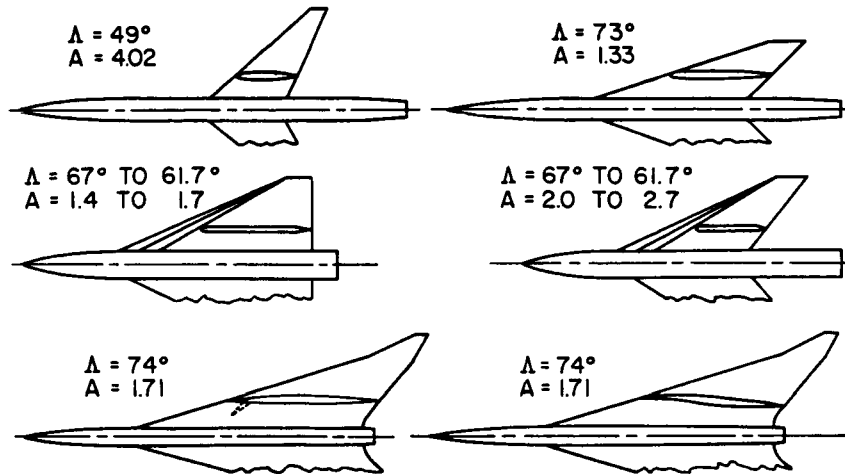


Figure 1

### THE EFFECT OF TRANSITION SHARP LEADING EDGE; $M < 0.30$

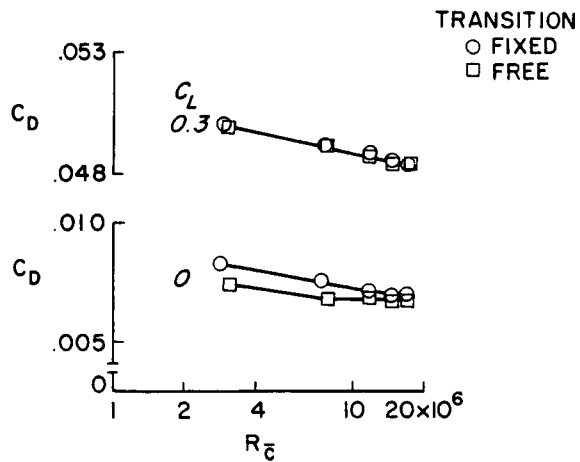


Figure 2

CHOICE OF PARAMETERS  
 $s = \text{MEASURED } C_s \text{ IN \% OF THEORETICAL } C_s ; M < 0.30$

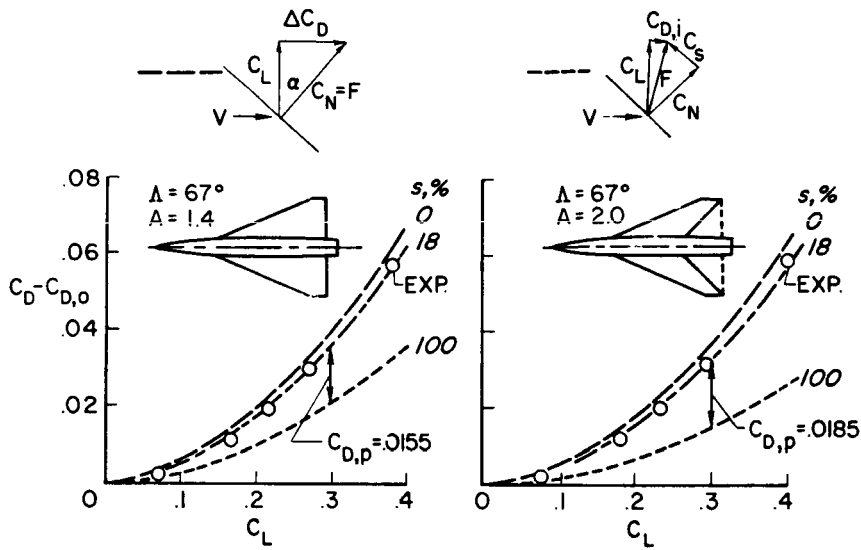


Figure 3

VARIATION OF  $s$  WITH  $R_{\bar{c}}$  AND  $\Lambda$   
 SHARP LEADING EDGES;  $C_{L,opt}$ ;  $M < 0.30$

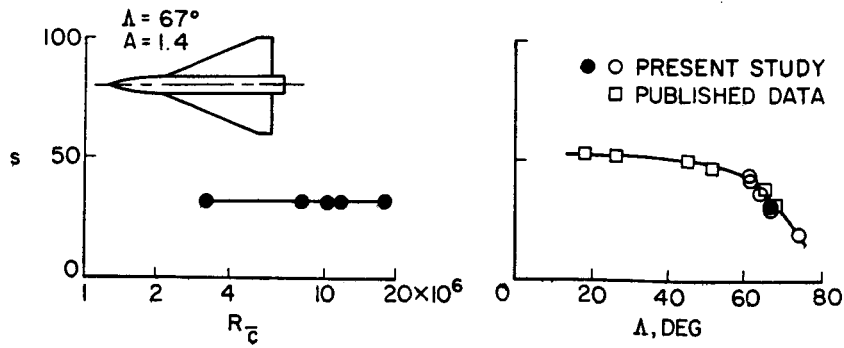


Figure 4

### EFFECT OF LEADING-EDGE FLAPS AND WING WARP

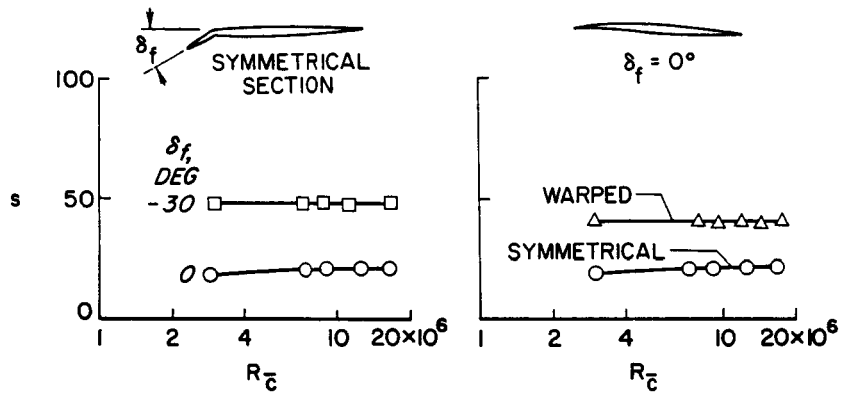
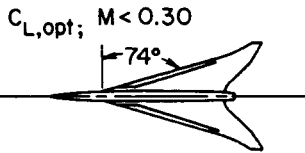


Figure 5

### EFFECT OF LEADING-EDGE SHAPE

$C_{L,opt}; M < 0.30$

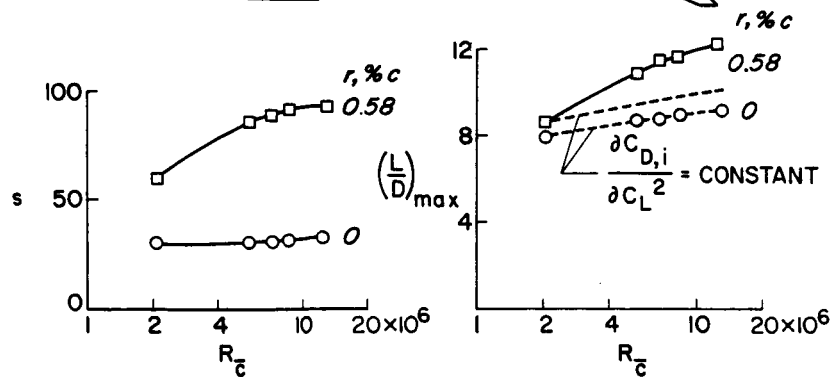
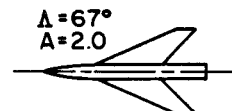
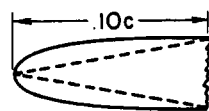


Figure 6

CORRELATION OF  $s$   
 SYMMETRICAL WINGS;  $\Delta = 49^\circ$  TO  $73^\circ$ ;  $C_{L,opt}$ ;  $M < 0.30$

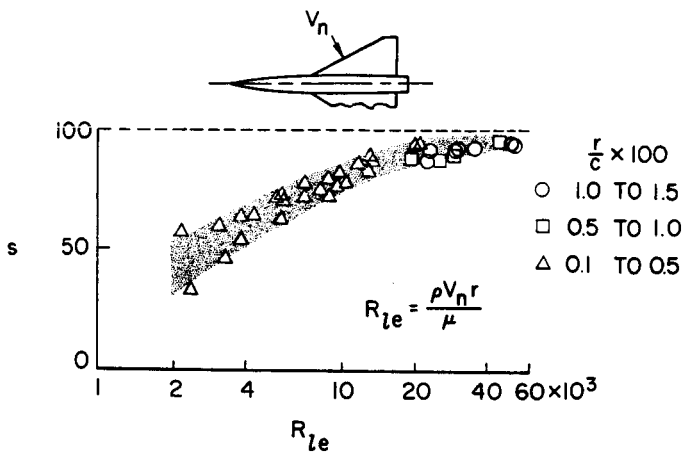


Figure 7

VARIATION OF  $s$  WITH LIFT COEFFICIENT

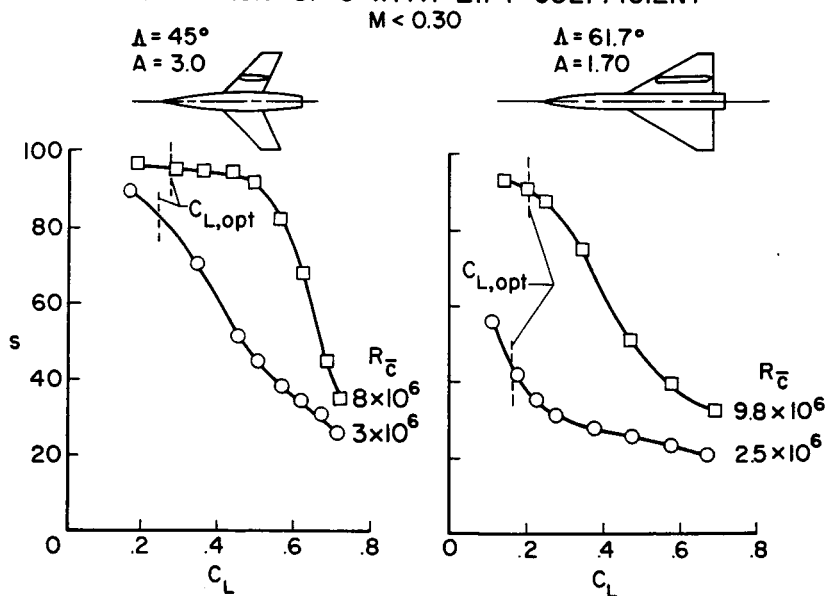


Figure 8

VARIATION OF  $s$  WITH MACH NUMBER

$C_{L,opt}$  ;  $R_c = 2.9 \times 10^6$  ;  $\frac{t}{c} = 0.05$

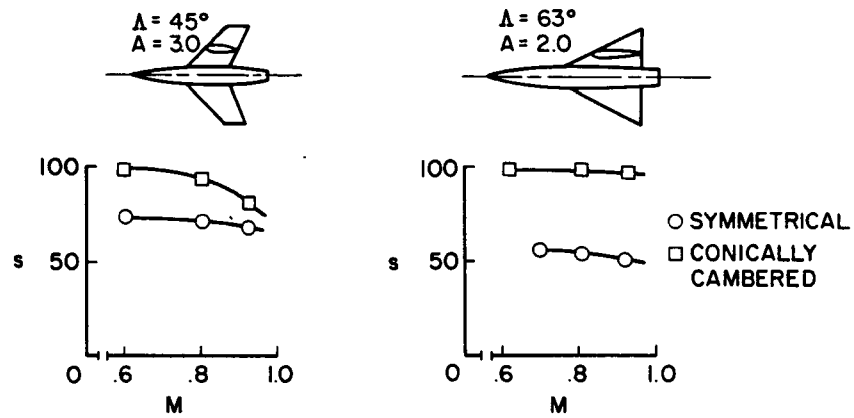


Figure 9

## 24. SUMMARY OF EXTERNAL-STORE DRAG

By Barrett L. Shroust and Thomas C. Kelly  
NASA Langley Research Center

### SUMMARY

The drag problems associated with the addition of external stores to airplanes are reviewed. Current analytic techniques for estimating drag penalties associated with the addition of stores in both subsonic and supersonic flight are discussed. In subsonic flight, the drag penalty caused by the addition of external stores is shown to be a function of the type of store installation. In supersonic flight, the drag is shown to be a function of the type of store installation and also of the location of the store installation with respect to the rest of the airplane components. Special store arrangements and attention to the design of the store itself can reduce the drag penalty of the store installation.

### INTRODUCTION

The current trend in military airplanes is toward carrying a large variety of external stores in the form of bombs, rockets, rocket launchers, and fuel tanks. The essence of the problem associated with these external stores is that the aerodynamicist designs the airplane to be essentially "clean" as shown in figure 1, while the airplane will probably fly in some less clean configuration, as shown in figure 2. The addition of external stores in various combinations and by various methods of attachment can lead to precipitous increases in drag and perhaps compromise the mission of the airplane. In figure 2 are shown only a few of the possible arrangements of stores - it has been estimated that there are roughly 17 million store combinations possible on one currently operational Navy airplane.

A great quantity of data on external stores has been published in the past 15 years by the NACA, the NASA, and other research organizations. A rather extensive bibliography which covers such problem areas as store effects on performance, store characteristics, and configuration and interference effects is included herein. A parallel bibliography, covering store separation characteristics and store loads, is contained in paper no. 8 by McKinney and Polhamus.

The present paper is concerned with the drag characteristics of the store-airplane configuration. Selected data from some of the reports in the bibliography are presented and some general conclusions regarding store drag are made. A directory of the bibliography is included in table I as a convenience to the reader in locating specific information.

Preceding page blank

## SYMBOLS

$C_D$	drag coefficient
$D$	diameter of store
$M$	Mach number
$r$	store nose radius
$\Delta$	increment

### Subscripts:

$lp$	last pair
meas	measured
min	minimum
o	zero lift
store	isolated store

## DISCUSSION OF ANALYTIC TECHNIQUES

The discussion of analytic techniques is limited to some of the fundamental problems associated with the drag of external stores or of the store-airplane combination. The basic factors which must be considered in estimating the zero-lift drag of the airplane with external stores in the subsonic region are skin-friction drag, base drag, form drag, and interference drag. Estimates can be readily made for the skin-friction drag, base drag, and form drag by using well-documented techniques, as all these drag components are essentially the drag components of the isolated store. Interference effects, particularly store-store interference where stores are mounted in close proximity, may lead to a significant drag increase. Some limited data on these effects exist and are included in the bibliography.

Factors to be evaluated in the supersonic region are skin-friction drag, base drag, asymmetry and interference drag, and wave drag. Skin-friction and base drag can be estimated by using well-known techniques, asymmetry drag and interference effects can be estimated by using techniques described in paper no. 26 by Carlson and McLean, and the wave drag, which must be estimated for the store and airplane in combination, can be calculated by using a method programed for an electronic computer. This zero-lift wave-drag program is described in part in paper no. 27 by Harris.

It should be pointed out that, although great quantities of wind-tunnel external-store data exist, in many cases insufficient knowledge of the nature of the boundary layer leads to inaccuracies in skin-friction estimation and extrapolation to full-scale values.

Within the supersonic region, the accuracy of the drag estimates also depends on how closely the configuration satisfies the assumptions of linearized theory upon which the computer programs are based. Numerous close correlations have been made by using these estimating techniques on various versions of supersonic transport configurations. These designs are generally long and slender with thin wing sections and with all components integrated to produce a low-drag configuration. The average fighter airplane, however, is not likely to be slender; the wing elements may be relatively thick; and, the external stores may be added with little regard to favorable interference effects. Figure 3 shows the correlation between theory and experiment obtained for a current fighter airplane in the transonic and supersonic flight regimes. Zero-lift drag is plotted against Mach number. The configuration is a variable-sweep airplane with the wings swept fully aft. The experimental data are from references 1 and 2. The stores are pylon mounted beneath the wing - four stores for the transonic region and two stores for the supersonic region. The level of drag for the stores-off configuration is predicted very well in the subcritical Mach number range, and the increment due to the addition of stores is also predicted very closely.

In the supersonic region, the estimated drag for the stores-off configuration is less than that for the experiment. The increment between the stores-on data and stores-off data is predicted reasonably well by the analytic methods. It appears that some further refinement of the analytic techniques would be useful in making more accurate quantitative estimates of the drag characteristics of configurations such as this.

#### DISCUSSION OF EXPERIMENTAL DATA

The remainder of this paper is concerned with a number of particular store installations. Most of these store arrangements are typical of those found on current fighter airplanes.

Analysis of the data in figure 4 gives an idea of the subsonic drag penalty associated with several types of store installations. The data in figures 4 and 5 were taken from a number of the reports in the bibliography. The ordinate is the increment in experimental zero-lift drag due to the addition of the store or stores. The abscissa is the drag of the isolated store multiplied by the number of stores in the installation. All coefficients are based on the wing area of the particular configuration. No attempt was made to predict the drag increment of the store support system; thus, the experimental value is the total drag penalty of the store and installation. The solid line represents equality between the experimental drag increment and the isolated store drag. Examples of the more common installations are the pylon-mounted single store, the pylon-mounted multiple rack, and the tangent-mounted store,

where the store is mounted flush with the aircraft surface. Less common perhaps is the semisubmerged installation. It is not surprising that this semi-submerged installation shows low values of measured drag compared with the isolated store drag since roughly half the wetted area is submerged within the airplane.

In general, for stores carried completely external to the aircraft, the tangent mount and the pylon-mounted single store lead to only small drag penalties, while the pylon-mounted multiple-rack installation causes a fairly sizable drag penalty.

Figure 5 illustrates the same type of analysis for the supersonic Mach number range. Again, the total measured increase in zero-lift drag due to the installation of the store or stores is plotted against a simple multiple of the isolated-store drag. Here again the coefficients are based on the wing area for the particular configuration. The Mach number range is from about 1.4 to 2.5. Figure 6 shows sketches of the various installations keyed to the data points in figure 5. Data point ① is for a model of a current fighter airplane with four Falcon missiles. The increment of installation drag is due in part to the skin friction of the rather large end-plate installation. It should be noted that some decrease in the store drag increment occurred at lift. Data point ② represents the same type of configuration but with two Falcon missiles. The deviation from the line of equality is somewhat less for this installation than for installation ①. However the decrease in the drag increment at lift for installation ② is negligible. Installation ③ is a rather unique mounting system; that is, the six missiles were sting mounted on the leading edge of the wing. A portion of the drag reduction is undoubtedly due to the elimination of missile base drag by the support system. Installation ④ is for the underwing installation of the same six missiles. A significant increase in drag over that for the leading-edge installation is apparent; however the departure from the line of equality can be attributed in part to the increased skin-friction drag of the pylon installations.

Installations ⑤ and ⑥, for a research model, indicate the large influence of store location on drag. In this particular case, the forward location led to a very high drag level compared with that for the rearward location. Installations ⑦ to ⑩ are for a model of a current fighter airplane with a variety of Sparrow installations. The two fuselage mounts (⑦ and ⑩) show considerably less drag penalty than the corresponding store wing mounts ⑧ and ⑨, respectively. Installations ⑪ and ⑫ are pylon mounts on the engine nacelles and on the fuselage. The fuselage mount ⑫ shows an appreciably smaller drag penalty than the nacelle mount ⑪.

It can be seen that, for the supersonic range in particular, not only the type of installation but also its location on the aircraft can considerably affect the magnitude of the drag. For the supersonic range, consideration of the store in the design of the aircraft using area-rule techniques would certainly be of benefit.

Some of the installations mentioned are perhaps worthy of further comment. Figure 7 presents experimental results for a tangent-mounted store installation and a pylon-mounted installation. The increment of drag for the tangent-mounted store is approximately the estimated amount for skin-friction and base drag. The added increment for the pylon is, however, considerably more than can be attributed to skin-friction drag. The reason for these phenomena is, at present, unknown, although it is probably associated with the amount of the store submerged within the boundary layer.

Figure 8 shows data from reference 3 for a current fighter airplane with a large store semisubmerged in the fuselage. Data are presented for the clean configuration, that is, with the cavity faired, for the configuration with the store installed, and for the configuration with the open cavity after ejection of the store. Of particular interest is the drag of the cavity with the store removed. For this particular installation, in the high subsonic and low supersonic speed ranges, the cavity drag penalty is as much or more than that for the installed store. Although this is not always the case, it is a point to be evaluated when considering a store installation of this type.

Figure 9 presents data for a tandem store installation consisting of two rows of three tandem-mounted stores. On the left side of the figure is shown the gross drag increment for the one, two, and three store pair installations over the Mach number range from 0.6 to 0.9. On the right side of the figure is shown the increment in drag due to the addition of the last store pair for various Mach numbers. It can be seen that the increment in drag for each additional pair decreases. For a blunt-nosed, blunt-based store, this type of installation should be of considerable benefit.

Figure 10 is concerned more with individual stores than with store installations. The data are from reference 4. The installation consists of 16 stores, 9 in the free stream and 7 tandem mounted. The drag increment of the installation is quite large; however, a significant increase is noted for a change in corner radius of the stores. This increment remained relatively constant over the Mach number range of the tests.

This figure illustrates the basis of the store drag problem, that is, if it is necessary to hang a multitude of stores from the aircraft, then a large drag penalty will likely exist. In this case, the drag of the configuration was more than doubled by the addition of stores.

## CONCLUDING REMARKS

Analytic methods have been shown to give a reasonably good estimate of the drag increment due to the addition of external stores. The drag penalty due to the addition of stores in the subsonic speed range has been shown to depend in part on the type of installation; the lowest drag penalty is associated with a semisubmerged installation and the largest drag penalty with a multiple-rack installation. At supersonic speeds, the drag of the store depends not only on the type of installation but also on the store location. Use of the analytic methods through area-rule considerations offers promise of drag reduction in the supersonic flight regime. Other factors to be considered in the reduction of store drag are tandem store arrangements and the effects of the shape of the store itself.

## REFERENCES

1. Ayers, Theodore G.: Transonic Aerodynamic Characteristics of a Variable-Wing-Sweep Tactical Fighter Model - Phase 4. NASA TM X-1237, 1966.
2. Shaw, David S.; and Babb, C. Donald: Supersonic Investigation of the Static Stability, Performance, and Control of a Variable-Sweep Tactical Fighter Model - Phase 4. NASA TM X-1143, 1965.
3. Wainwright, John B.; and Rubinstein, Marvin: Report on the Aerodynamic Effects of External Stores on a Wind Tunnel Model XF8U-1 Airplane in the Mach Number Range 0.8 to 1.4. USCEC Rept. 32-1-5, Aerodyn. Test Div., NAMTC, Univ. of Southern California, Apr. 28, 1955.
4. Ferris, James C.: Effects of External Stores on Performance and Stability of a Supersonic Fighter-Bomber Airplane. NASA TM X-1218, 1966.

## BIBLIOGRAPHY

1. Silvers, H. Norman; and Vogler, Raymond D.: Résumé of Wind-Tunnel Data on the Effect of External Stores on Stability of Models of Military Airplanes. NACA RM L6K08, 1946.
2. Boddy, Lee E.; and Morrill, Charles P., Jr.: The Aerodynamic Effects of Rockets and Fuel Tanks Mounted Under the Swept-Back Wing of an Airplane Model. NACA RM A7J03, 1948.
3. Silvers, H. Norman; and Spreemann, Kenneth P.: Correlation of Wind-Tunnel and Flight Determinations of the Buffet Speed of an Airplane Equipped With External Stores. NACA RM L7E20, 1948.
4. Silvers, H. Norman; and Spreemann, Kenneth P.: Wind-Tunnel Investigation of a Wing-Fuselage Combination With External Stores. NACA RM L7K20, 1948.
5. Hart, Roger G.; and Katz, Ellis R.: Flight Investigations at High-Subsonic, Transonic, and Supersonic Speeds To Determine Zero-Lift Drag of Fin-Stabilized Bodies of Revolution Having Fineness Ratios of 12.5, 8.91, and 6.04 and Varying Positions of Maximum Diameter. NACA RM L9I30, 1949.
6. Silvers, H. Norman; and Spreemann, Kenneth P.: Effect of Airfoil Section and Tip Tanks on the Aerodynamic Characteristics at High Subsonic Speeds of an Unswept Wing of Aspect Ratio 5.16 and Taper Ratio 0.61. NACA RM L9J04, 1949.
7. Spreemann, Kenneth P.; and Silvers, H. Norman: Experimental Investigation of Various Wing-Mounted External Stores on a Wing-Fuselage Combination Having a Sweptback Wing of Inverse Taper Ratio. NACA RM L9J06, 1950.
8. Silvers, H. Norman; and Spreemann, Kenneth P.: Experimental Investigation of Various External-Store Configurations on a Model of a Tailless Airplane With a Sweptback Wing. NACA RM L9K25, 1950.
9. Welsh, Clement J.; and Morrow, John D.: Effect of Wing-Tank Location on the Drag and Trim of a Swept-Wing Model as Measured in Flight at Transonic Speeds. NACA RM L50A19, 1950.
10. May, Ellery B.; Jr.: Investigation of the Aerodynamic Effects of an External Store in Combination With 60° Delta and Low-Aspect-Ratio Tapered Wings at a Mach Number of 1.9. NACA RM L50K03, 1951.
11. Spreemann, Kenneth P.; and Alford, William J., Jr.: Investigation of the Effects of Geometric Changes in an Underwing Pylon-Suspended External-Store Installation on the Aerodynamic Characteristics of a 45° Sweptback Wing at High Subsonic Speeds. NACA RM L50L12, 1951.

12. Hoffman, Sherwood: Comparison of Zero-Lift Drag Determined by Flight Tests at Transonic Speeds of Pylon, Underslung, and Symmetrically Mounted Nacelles at 40 Percent Semispan of a  $45^\circ$  Sweptback Wing and Body Combination. NACA RM L51D26, 1951.
13. Pepper, William B., Jr.; and Hoffman, Sherwood: Comparison of Zero-Lift Drags Determined by Flight Tests at Transonic Speeds of Symmetrically Mounted Nacelles in Various Chordwise Positions at the Wing Tip of a  $45^\circ$  Sweptback Wing and Body Combination. NACA RM L51F13, 1951.
14. Silvers, H. Norman; King, Thomas J., Jr.; and Pasteur, Thomas B., Jr.: Investigation of the Effect of a Nacelle at Various Chordwise and Vertical Positions on the Aerodynamic Characteristics at High Subsonic Speeds of a  $45^\circ$  Sweptback Wing With and Without a Fuselage. NACA RM L51H16, 1951.
15. Dugan, James C.: External Store Development. Mem. Rept. No. WCNSR-43019-1-1, Wright Air Develop. Center, U.S. Air Force, Aug. 13, 1951.
16. Tamburello, V.; and Burgan, Elmer: Exploratory Wind-Tunnel Tests of External Stores Mounted in Various Locations on the Wing of a 0.17-Scale Model Jet-Fighter Type Airplane. Rept. C-453 Aero 806, David W. Taylor Model Basin, Navy Dept., Sept. 1951.
17. Hasel, Lowell E.; and Sevier, John R., Jr.: Aerodynamic Characteristics at Supersonic Speeds of a Series of Wing-Body Combinations Having Cambered Wings With an Aspect Ratio of 3.5 and a Taper Ratio of 0.2 - Effect at  $M = 1.60$  of Nacelle Shape and Position on the Aerodynamic Characteristics in Pitch of Two Wing-Body Combinations with  $47^\circ$  Sweptback Wings. NACA RM L51K14a, 1952.
18. Kremzier, Emil J.; and Dryer, Murray: Aerodynamic Interference Effects on Normal and Axial Force Coefficients of Several Engine-Strut-Body Configurations at Mach Numbers of 1.8 and 2.0. NACA RM E52B21, 1952.
19. Silvers, H. Norman; and King, Thomas J., Jr.: A Small-Scale Investigation of the Effect of Spanwise and Chordwise Positioning of an Ogive-Cylinder Underwing Nacelle on the High-Speed Aerodynamic Characteristics of a  $45^\circ$  Sweptback Tapered-in-Thickness Wing of Aspect Ratio 6. NACA RM L52J22, 1952.
20. Hoffman, Sherwood: Transonic Flight Tests To Compare the Zero-Lift Drags of Underslung Nacelles Varied Spanwise on a  $45^\circ$  Sweptback Wing and Body Combination. NACA RM L52D04a, 1952.
21. Driver, Cornelius: Aerodynamic Characteristics at Supersonic Speeds of a Series of Wing-Body Combinations Having Cambered Wings With an Aspect Ratio of 3.5 and a Taper Ratio of 0.2 - Effect at  $M = 2.01$  of Nacelle Shape and Position on the Aerodynamic Characteristics in Pitch of Two Wing-Body Combinations With  $47^\circ$  Sweptback Wings. NACA RM L52F03, 1952.

22. Scallion, William I.: Low-Speed Investigation of the Effects of Nacelles on the Longitudinal Aerodynamic Characteristics of a  $60^\circ$  Sweptback Delta-Wing—Fuselage Combination With NACA 65A003 Airfoil Sections. NACA RM L52F04, 1952.
23. Jacobsen, Carl R.: Effects of Systematically Varying the Spanwise and Vertical Location of an External Store on the Aerodynamic Characteristics of an Unswept Tapered Wing of Aspect Ratio 4 at Mach Numbers of 1.41, 1.62, and 1.96. NACA RM L52F13, 1952.
24. Bielat, Ralph P.; and Harrison, Daniel E.: A Transonic Wind-Tunnel Investigation of the Effects of Nacelle Shape and Position on the Aerodynamic Characteristics of Two  $47^\circ$  Sweptback Wing-Body Configurations. NACA RM L52G02, 1952.
25. Jacobsen, Carl R.: Effects of the Spanwise, Chordwise, and Vertical Location of an External Store on the Aerodynamic Characteristics of a  $60^\circ$  Delta Wing at Mach Numbers of 1.41, 1.62, and 1.96. NACA RM L52H29, 1952.
26. Silvers, H. Norman; and King, Thomas J., Jr.: Investigation at High Subsonic Speeds of Bodies Mounted From the Wing of an Unswept-Wing—Fuselage Model, Including Measurements of Body Loads. NACA RM L52J08, 1952.
27. Smith, Willard G.: Wind-Tunnel Investigation at Subsonic and Supersonic Speeds of a Model of a Tailless Fighter Airplane Employing a Low-Aspect-Ratio Swept-Back Wing - Effects of External Fuel Tanks and Rocket Packets on the Drag Characteristics. NACA RM A52J31, 1953.
28. Jacobsen, Carl R.: Effects of the Spanwise, Chordwise, and Vertical Location of an External Store on the Aerodynamic Characteristics of a  $45^\circ$  Sweptback Tapered Wing of Aspect Ratio 4 at Mach Numbers of 1.41, 1.62, and 1.96. NACA RM L52J27, 1953.
29. Jacobsen, Carl R.: Effects of Size of External Stores on the Aerodynamic Characteristics of an Unswept and a  $45^\circ$  Sweptback Wing of Aspect Ratio 4 and a  $60^\circ$  Delta Wing at Mach Numbers of 1.41, 1.62, and 1.96. NACA RM L52K20a, 1953.
30. Mitcham, Grady L.; and Blanchard, Willard S., Jr.: Low-Lift Drag and Stability Data From Rocket Models of a Modified-Delta-Wing Airplane With and Without External Stores at Mach Numbers From 0.8 to 1.36. NACA RM L53A27, 1953.
31. Wallskog, Harvey A.; and Hart, Roger G.: Investigation of the Drag of Blunt-Nosed Bodies of Revolution in Free Flight at Mach Numbers From 0.6 to 2.3. NACA RM L53D14a, 1953.
32. Rainey, Robert W.: Effect of Variations in Reynolds Number on the Aerodynamic Characteristics of Three Bomb or Store Shapes at a Mach Number of 1.62 With and Without Fins. NACA RM L53D27, 1953.

33. Carmel, Melvin M.; and Fischetti, Thomas L.: A Transonic Wind-Tunnel Investigation of the Effects of Nacelles on the Aerodynamic Characteristics of a Complete Model Configuration. NACA RM L53F22a, 1953.
34. Mason, Homer P.: Effects of External Store Mounting on the Buffet, Trim, and Drag Characteristics of Rocket-Powered Fuselage and Store Combinations Between Mach Numbers of 0.7 and 1.4. NACA RM L53J22, 1953.
35. Alexander, S. R.: The Influence of External and Internal Stowage of Sparrow II on the Performance of a Transonic Day Fighter Configuration. NAVAER Rept. No. DR-1484, Bur. Aeron., Aug. 1953.
36. Judd, Joseph H.: Flight Investigation of Engine Nacelles and Wing Vertical Position on the Drag of a Delta-Wing Airplane Configuration From Mach Number 0.8 to 2.0. NACA RM L53L21, 1954.
37. Silvers, H. Norman; King, Thomas J., Jr.; and Alford, William J., Jr.: Wind-Tunnel Investigation at High Subsonic Speeds of the Effects of Wing-Mounted External Stores on the Loading and Aerodynamic Characteristics in Pitch of a 45° Sweptback Wing Combined With a Fuselage. NACA RM L54A21, 1954.
38. Alford, William J., Jr.; and Silvers, H. Norman: Investigation at High Subsonic Speeds of Finned and Unfinned Bodies Mounted at Various Locations From the Wings of Unswept- and Swept-Wing—Fuselage Models, Including Measurements of Body Loads. NACA RM L54B18, 1954.
39. Henning, Allen B.: The Effects of Wing Mounted External Stores on the Trim, Buffet, and Drag Characteristics of a Rocket-Propelled Model Having a 45° Sweptback Wing. NACA RM L54B19, 1954.
40. Hoffman, Sherwood; and Wolff, Austin L.: Effect on Drag of Longitudinal Positioning of Half-Submerged and Pylon-Mounted Douglas Aircraft Stores on a Fuselage With and Without Cavities Between Mach Numbers of 0.9 and 1.8. NACA RM L54E26, 1954.
41. Smith, Norman F.: Exploratory Investigation of External Stores on the Aerodynamic Characteristics of a 1/16-Scale Model of the Douglas D-558-II Research Airplane at a Mach Number of 2.01. NACA RM L54FO2, 1954.
42. Mason, Homer P.; and Henning, Allen B.: Effects of Some External-Store Mounting Arrangements and Store Shapes on the Buffet and Drag Characteristics of Wingless Rocket-Powered Models at Mach Numbers From 0.7 to 1.4. NACA RM L54I20a, 1954.
43. Gapcynski, John P.; and Carlson, Harry W.: A Pressure-Distribution Investigation of the Aerodynamic Characteristics of a Body of Revolution in the Vicinity of a Reflection Plane at Mach Numbers of 1.41 and 2.01. NACA RM L54J29, 1955.

44. Ballentine, Donald C.: Wind-Tunnel Investigation of a 0.15-Scale Model F3H-2N Airplane Equipped With an Adjustable Leading-Edge Slot and Various External Stores. Aero Rept. 871, David W. Taylor Model Basin, Navy Dept., Oct. 1954.
45. Alford, William J., Jr.; Silvers, H. Norman; and King, Thomas J., Jr.: Experimental Aerodynamic Forces and Moments at Low Speed of a Missile Model During Simulated Launching From the Midsemispan Location of a 45° Sweptback Wing-Fuselage Combination. NACA RM L54K11a, 1955.
46. Alford, William J., Jr.: Experimental Static Aerodynamic Forces and Moments at Low Speed on a Canard Missile During Simulated Launching From the Midsemispan and Wing-Tip Locations of a 45° Sweptback Wing-Fuselage Combination. NACA RM L55A12, 1955.
47. Smith, Norman F.; and Carlson, Harry W.: The Origin and Distribution of Supersonic Store Interference From Measurement of Individual Forces on Several Wing-Fuselage-Store Configurations. 1.- Swept-Wing Heavy-Bomber Configuration With Large Store (Nacelle). Lift and Drag; Mach Number, 1.61. NACA RM L55A13a, 1955.
48. Sleeman, William C., Jr.; and Alford, William J., Jr.: Low-Speed Investigation of the Effects of Wing Tanks and Speed Brakes on the Static Stability of a Model Having a 40° Swept Wing. NACA RM L55C17, 1955.
49. Silvers, H. Norman; and King, Thomas J., Jr.: Investigation at High Subsonic Speeds of the Effects of Various Underwing External-Store Arrangements on the Aerodynamic Characteristics of a 1/16-Scale Model of the Douglas D-558-II Research Airplane. NACA RM L55D11, 1955.
50. Alford, William J., Jr.; Silvers, H. Norman; and King, Thomas J., Jr.: Experimental Static Aerodynamic Forces and Moments at Low Speed on a Missile Model During Simulated Launching From the 25-Percent-Semispan and Wing-Tip Locations of a 45° Sweptback Wing-Fuselage Combination. NACA RM L55D20, 1955.
51. Mason, Homer P.: Effects of Wing-Mounted Tank-Type Stores on the Low-Lift Buffeting and Drag of a Swept-Wing Airplane Configuration Between Mach Numbers of 0.8 and 1.3. NACA RM L55D27, 1955.
52. Smith, Norman F.; and Carlson, Harry W.: The Origin and Distribution of Supersonic Store Interference From Measurement of Individual Forces On Several Wing-Fuselage-Store Configurations. II.- Swept-Wing Heavy-Bomber Configuration With Large Store (Nacelle). Lateral Forces and Pitching Moments; Mach Number, 1.61. NACA RM L55E26a, 1955.
53. Smith, Norman F.; and Carlson, Harry W.: The Origin and Distribution of Supersonic Store Interference From Measurement of Individual Forces on Several Wing-Fuselage-Store Configurations. III.- Swept-Wing Fighter-Bomber Configuration With Large and Small Stores. Mach Number, 1.61. NACA RM L55H01, 1955.

54. Kelly, Thomas C.: Transonic Wind-Tunnel Investigation of the Effects of External Stores and Store Position on the Aerodynamic Characteristics of a 1/16-Scale Model of the Douglas D-558-II Research Airplane. NACA RM L55I07, 1955.
55. Morris, Odell A.: The Origin and Distribution of Supersonic Store Interference From Measurement of Individual Forces on Several Wing-Fuselage-Store Configurations. IV.- Delta-Wing Heavy-Bomber Configuration With Large Store. Mach Number, 1.61. NACA RM L55I27a, 1955.
56. Hart, Roger G.: Flight Investigation at Mach Numbers From 0.8 to 1.5 To Determine the Effects of Nose Bluntness on the Total Drag of Two Fin-Stabilized Bodies of Revolution. NACA TN 3549, 1955. (Supersedes NACA RM L50I08a.)
57. Wainwright, John B.; and Rubinstein, Marvin: Report on the Aerodynamic Effects of External Stores on a Wind Tunnel Model XF8U-1 Airplane in the Mach Number Range 0.8 to 1.4. USCEC Rept. 32-1-5, Aerodyn. Test Div., NAMTC., Univ. of Southern California, Apr. 28, 1955.
58. Carlson, Harry W.; and Geier, Douglas J.: The Origin and Distribution of Supersonic Store Interference From Measurement of Individual Forces on Several Wing-Fuselage-Store Configurations. V.- Swept-Wing Heavy-Bomber Configuration With Large Store (Nacelle). Mach Number 2.01. NACA RM L55K15, 1956.
59. Smith, Norman F.: The Origin and Distribution of Supersonic Store Interference From Measurement of Individual Forces on Several Wing-Fuselage-Store Configurations. VI.- Swept-Wing Heavy-Bomber Configuration With Stores of Different Sizes and Shapes. NACA RM L55L08, 1956.
60. Robinson, Ross B.: Longitudinal Characteristics of an Unswept-Wing Fighter-Type Model With External Stores at a Mach Number of 1.82 and Some Effects of Horizontal-Tail and Yaw-Damper Deflection on the Sideslip Derivatives. NACA RM L55L26, 1956.
61. Hallisy, Joseph M., Jr.; and Kudlacik, Louis: A Transonic Wind-Tunnel Investigation of Store and Horizontal-Tail Loads and Some Effects of Fuselage-Afterbody Modifications on a Swept-Wing Fighter Airplane. NACA RM L56A26, 1956.
62. Foster, Gerald V.; and Driver, Cornelius: Effects of External Stores on the Static Longitudinal and Lateral Aerodynamic Characteristics of a Model of a 45° Swept-Wing Fighter Airplane at Mach Numbers of 1.61 and 2.01. NACA RM L56F15a, 1956.
63. Spearman, M. Leroy; and Driver, Cornelius: Longitudinal and Lateral Stability Characteristics of a Low-Aspect-Ratio Unswept-Wing Airplane Model at Mach Numbers of 1.82 and 2.01. NACA RM L56H06, 1957.

64. Morris, Odell A.: Aerodynamic Forces and Moments on a Large Ogive-Cylinder Store at Various Locations Below the Fuselage Center Line of a Swept-Wing Bomber Configuration at a Mach Number of 1.61. NACA RM L56I25, 1957.
65. Alford, William J., Jr.; and King, Thomas J., Jr.: Experimental Static Aerodynamic Forces and Moments at High Subsonic Speeds on a Missile Model During Simulated Launching From the Midsemispan Location of a  $45^\circ$  Swept-back Wing-Fuselage-Pylon Combination. NACA RM L56J05, 1957.
66. Hill, P. R.; and Hoffman, S.: Preliminary Evaluation of the Wing Leading Edge as a Missile-Mounting Location. NACA RM L56J12, 1957.
67. Geier, Douglas J.; and Carlson, Harry W.: Measurement of Static Forces on Externally Carried Bombs of Fineness Ratios 7.1 and 10.5 in the Flow Field of a Swept-Wing Fighter-Bomber Configuration at a Mach Number of 1.6. NACA RM L56K30, 1957.
68. Hoffman, Sherwood: Zero-Lift Drag of a Large Fuselage Cavity and a Partially Submerged Store on a  $52.5^\circ$  Sweptback-Wing-Body Configuration as Determined From Free-Flight Tests at Mach Numbers of 0.7 to 1.53. NACA RM L56L21, 1957.
69. Nugent, Jack: Effect of Wing-Mounted External Stores on the Lift and Drag of the Douglas D-558-II Research Airplane at Transonic Speeds. NACA RM H57E15a, 1957.
70. Gapcynski, John P.; and Carlson, Harry W.: The Aerodynamic Characteristics of a Body in the Two-Dimensional Flow Field of a Circular-Arc Wing at a Mach Number of 2.01. NACA RM L57E14, 1957.
71. Polhamus, Edward C.: Effect of Nose Shape on Subsonic Aerodynamic Characteristics of a Body of Revolution Having a Fineness Ratio of 10.94. NACA RM L57F25, 1957.
72. Pearson, Albin O.: Transonic Investigation of Effects of Spanwise and Chordwise External Store Location and Body Contouring on Aerodynamic Characteristics of  $45^\circ$  Sweptback Wing-Body Configurations. NACA RM L57G17, 1957.
73. Hoffman, Sherwood: Free-Flight Investigation of the Drag of a Model of a  $60^\circ$  Delta-Wing Bomber With Strut-Mounted Siamese Nacelles and Indented Fuselage at Mach Numbers From 0.80 to 1.35. NACA RM L57G29, 1957.
74. Church, James D.: Effects of Components and Various Modifications on the Drag and the Static Stability and Control Characteristics of a  $42^\circ$  Swept-Wing Fighter-Airplane Model at Mach Numbers of 1.60 to 2.50. NACA RM L57K01, 1957.

75. Geier, Douglas J.: An Investigation of Supersonic Store Interference in the Vicinity of a  $22^\circ$  Swept-Wing—Fuselage Configuration at Mach Numbers of 1.61 and 2.01. NACA RM L57L18, 1957.
76. Cook, Martin L.: Static Longitudinal Characteristics of a Semispan Delta-Wing Airplane Model With a Pylon-Mounted 0.500-Scale Model XASM-N-8 Corvus Missile. Aero Rept. 920, David W. Taylor Model Basin, Navy Dept., June 1957.
77. Brindle, C. Carl: Longitudinal Characteristics at Supersonic Speeds of a Winged and a Wingless 0.08-Scale Half Model Sparrow I Missile at Angles of Attack up to  $180^\circ$ . Aero Rept. 931, David W. Taylor Model Basin, Navy Dept., Dec. 1957.
78. Reese, David E., Jr.: A Wind-Tunnel Investigation of Several Wingless Missile Configurations at Supersonic Speeds. NACA RM A57J22, 1958.
79. Gnos, A. Vernon; and Kurkowski, Richard L.: Static Longitudinal and Lateral Stability and Control Characteristics of a Model of a Swept-Wing Fighter-Bomber-Type Airplane With a Top Inlet at Mach Numbers From 1.6 to 2.35. NACA RM A57K20, 1958.
80. Hoffman, Sherwood: Free-Flight Investigation at Mach Numbers From 0.8 to 1.5 of the Effect of a Fuselage Indentation on the Zero-Lift Drag of a  $52.5^\circ$  Sweptback-Wing—Body Configuration With Symmetrically Mounted Stores on the Fuselage. NACA RM L57L04, 1958.
81. Morris, Odell A.: Effects of External Store-Pylon Configuration and Position on the Aerodynamic Characteristics of a  $45^\circ$  Swept Wing-Fuselage Combination at a Mach Number of 1.61. NACA RM L58C13, 1958.
82. Oehman, Waldo I.; and Turner, Kenneth L.: Aerodynamic Characteristics of a  $45^\circ$  Swept-Wing Fighter Airplane Model and Aerodynamic Loads on Adjacent Stores and Missiles at Mach Numbers of 1.57, 1.87, 2.16, and 2.53. NACA RM L58C17, 1958.
83. Robinson, Robert C.: The Effect of Lower Surface Spoilers on the Transonic Trim Change of a Wind-Tunnel Model of a Fighter Airplane Having a Modified Delta Wing. NASA MEMO 12-27-58a, 1959.
84. Hoffman, Sherwood: Free-Flight Investigation of the Drag of a  $60^\circ$  Delta-Wing Configuration With Large Stores Mounted Below the Indented Fuselage at Mach Numbers Between 0.8 and 1.6. NASA MEMO 10-9-58L, 1958.
85. Margolis, Kenneth; Malvestuto, Frank S., Jr.; and Maxie, Peter J., Jr.: Theoretical Calculations of Supersonic Wave Drag at Zero Lift for a Particular Store Arrangement. NACA TN 4120, 1958.

86. Appich, W. H., Jr.; Oehman, Waldo I.; and Gregory, Donald T.: Aerodynamic Characteristics of Three Versions of a Supersonic Airplane Model With a  $45^\circ$  Sweptback Midwing at Mach Numbers of 1.57 and 2.01. NASA MEMO 12-6-58L, 1959.
87. Bielat, Ralph P.: A Transonic Wind-Tunnel Investigation of the Performance and of the Static Stability and Control Characteristics of a Model of a Fighter-Type Airplane Which Embodies Partial Body Indentation. NASA MEMO 12-13-58L, 1959.
88. White, Maurice D.; and Innis, Robert C.: A Flight Investigation of the Low-Speed Handling Qualities of a Tailless Delta-Wing Fighter Airplane. NASA MEMO 4-15-59A, 1959.
89. Carmel, Melvin M.; and Gregory, Donald T.: Preliminary Investigation of the Static Longitudinal and Lateral Stability Characteristics of a Model of a  $45^\circ$  Swept Wing Airplane at Mach Numbers of 1.59, 1.89, and 2.09. NASA MEMO 3-30-59L, 1959.
90. Wornom, Dewey E.: Transonic Aerodynamic Characteristics of a  $45^\circ$  Swept-Wing—Fuselage Model With a Finned and Unfinned Body Pylon-Mounted Beneath the Fuselage or Wing, Including Measurements of Body Loads. NASA MEMO 4-20-59L, 1959.
91. Drougge, Georg (with appendix by Sune B. Berndt and Lars O. A. Hilding): An Experimental Investigation of the Interference Between Bodies of Revolution at Transonic Speeds With Special Reference to the Sonic and Supersonic Area Rules. FFA Rept. 83, Aeron. Res. Inst. Swed., 1959.
92. Pitts, William C.; and Wiggins, Lyle E.: Axial-Force Reduction by Interference Between Jet and Neighboring Afterbody. NASA TN D-332, 1960.
93. Fischetti, Thomas L.; and Eaton, Peter T.: Investigation of the Effects of the Corvus Missile on the A4D-2 Airplane at High Subsonic Speeds. Aero Rept. 987, David W. Taylor Model Basin, Navy Dept, July 1960.
94. Anon.: Aircraft Bombs, Fuzes and Associated Components. NAVWEPS OP 2216, Vol. 1, Dept. Navy, Aug. 1, 1960.
95. Pivirotto, Thomas J.: Aerodynamic Test of the 0.16-Scale Model of the Hughes Model 50 Missile. WT 20-355, Jet Propulsion Lab., California Inst. Technol., Aug. 21, 1960.
96. Brown, A. E.; deLancey, L. M.; and Meeker, R. E.: Studies of the Side-winder 1C Aeromechanics - Part 1. Aerodynamics NAVWEPS Rept. 6596, Pt. 1, U.S. Naval Ord. Test Station, Oct. 24, 1960.
97. Fischetti, Thomas L.; and Eaton, Peter T.: Wind-Tunnel Investigation of the Effects of Externally Installed Missiles on an Aircraft Configuration at High Subsonic Speeds. Aero Rept. 995, David W. Taylor Model Basin, Navy Dept., Dec. 1960.

98. Luoma, Arvo A.: Transonic Wind-Tunnel Investigation of the Static Longitudinal Stability and Performance Characteristics of a Supersonic Fighter-Bomber Airplane. NASA TM X-513, 1961.
99. Robinson, Ross B.; and Spearman, M. Leroy: Static Lateral and Directional Stability and Control Characteristics of a 1/40-Scale Model of a 60° Delta Wing Bomber Configuration at a Mach Number of 1.99. NASA TM X-537, 1961.
100. Bielat, Ralph P.; and Robins, A. Warner: Stability and Control Characteristics at Transonic Speeds of Two Variable-Sweep Airplane Configurations Differing in Wing-Pivot Locations. NASA TM X-559, 1961.
101. Luoma, Arvo A.: Transonic Wind-Tunnel Investigation of the Static Stability and Control Characteristics of a Supersonic Fighter-Bomber Airplane. NASA TM X-591, 1961.
102. Brindle, C. Carl: Wind-Tunnel Investigation of the Drag Characteristics of a Pylon-Mounted Missile. Aero Rept. 1010, David W. Taylor Model Basin, Navy Dept., June 1961.
103. Eaton, Peter T.: Wind-Tunnel Investigation of the Effects of Multiple External Stores on the Longitudinal Aerodynamic Characteristics of the Douglas A4D Airplane. Aero Rept. 1009, David W. Taylor Model Basin, Navy Dept., Sept. 1961.
104. Brindle, C. Carl: Wind-Tunnel Investigation of External Store Arrangements To Reduce Wave Drag. Aero Rept. 1016, David W. Taylor Model Basin, Navy Dept., Nov. 1961.
105. Landrum, Emma Jean: Static Lateral and Directional Stability and Control Characteristics of a 1/40-Scale Model of a 60° Delta Wing Bomber Configuration at a Mach Number of 1.61. NASA TM X-748, 1963.
106. Foster, Gerald V.; and Kyle, Robert G.: Aerodynamic Characteristics of a 1/22-Scale Model of a Fighter Airplane With an Extended Forebody and Other Modifications at Mach Numbers of 1.57 and 2.01. NASA TM X-833, 1963.
107. Eaton, Peter T.; and Swinney, Charles S.: Incremental Lift and Drag of an External Aircraft Store - Phase I. Test Rept. AL 20, David Taylor Model Basin, Dept. Navy, July 1965.
108. Shaw, David S.; and Babb, C. Donald: Supersonic Investigation of the Static Stability, Performance, and Control of a Variable-Sweep Tactical Fighter Model - Phase 4. NASA TM X-1143, 1966.
109. Ferris, James C.: Effects of External Stores on Performance and Stability of a Supersonic Fighter-Bomber Airplane. NASA TM X-1218, 1966.

110. Ayers, Theodore G.: Transonic Aerodynamic Characteristics of a Variable-Wing-Sweep Tactical Fighter Model - Phase 4. NASA TM X-1237, 1966.
111. Landrum, Emma Jean: Effect of Nacelle Orientation on the Aerodynamic Characteristics of an Arrow Wing-Body Configuration at Mach Number 2.03. NASA TN D-3284, 1966.
112. Norris, John D.; and McGhee, Robert J.: Effects of Bluntness on the Subsonic Drag of an Elliptical Forebody. NASA TN D-3388, 1966.

TABLE I.- BIBLIOGRAPHY CROSS-REFERENCE

Bibliography number containing results related to -				
Effects of variations in store location	Various stores in combination; multiple installations	Partially-submerged store installations	Isolated-store characteristics	Store-configuration variations; interference effects
3	2	4	5	18
7	27	17	14	31
8	30	21	18	40
9	39	34	30	41
10	40	40	31	52
11	57	57	32	53
13	60	68	34	55
14	63	74	39	56
16	72	79	40	58
17	82	89	42	59
19	86		45	62
20	93		46	71
21	97		47	91
22	103		50	92
23	107		51	109
25	108		64	111
26	109		66	112
28			67	
29			77	
34			80	
35			84	
36			95	
37			96	
38			102	
40				
42				
47				
53				
54				
57				
66				
72				
75				
81				
97				
100				
104				
107				
108				
109				

CLEAN CONFIGURATION

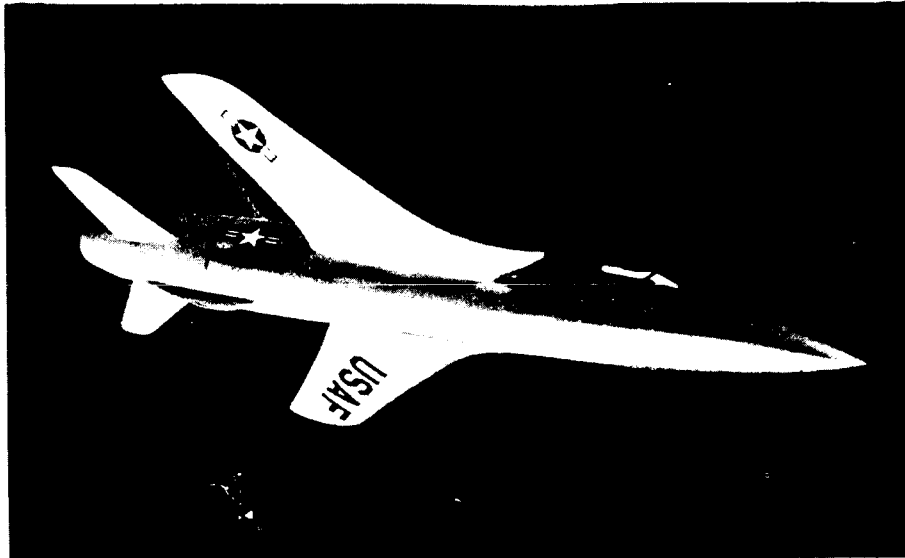


Figure 1

L-2694-1

CONFIGURATION WITH STORES



Figure 2

L-2694-8

### ANALYSIS AND CORRELATION

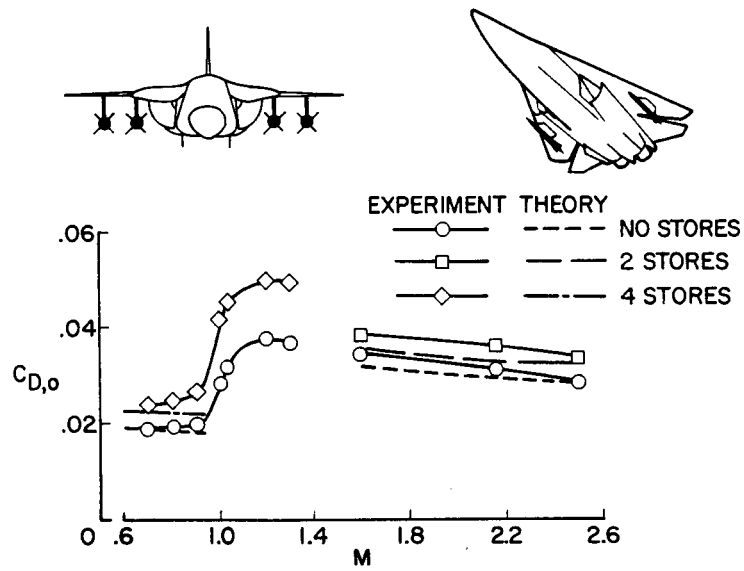


Figure 3

### INCREMENTAL STORE-INSTALLATION DRAG SUBSONIC

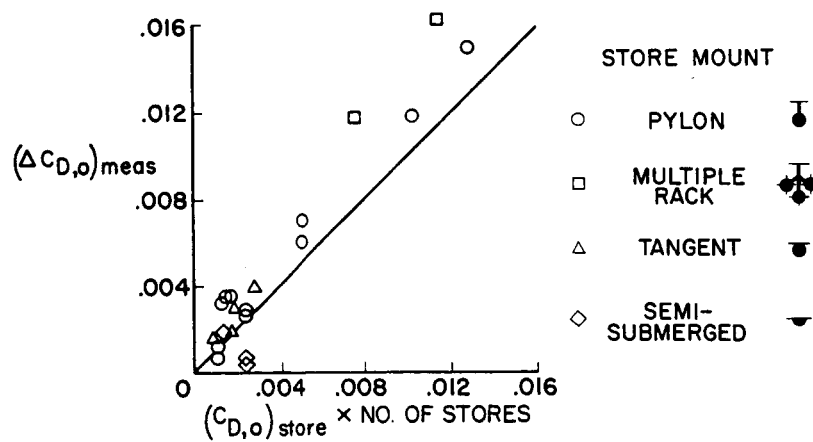


Figure 4

INCREMENTAL STORE-INSTALLATION DRAG  
SUPERSONIC

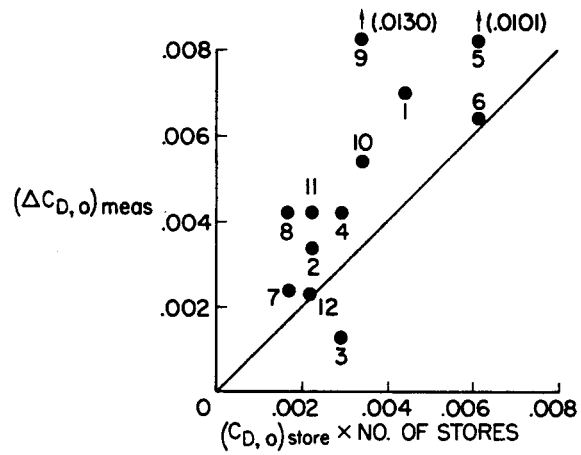


Figure 5

STORE INSTALLATIONS

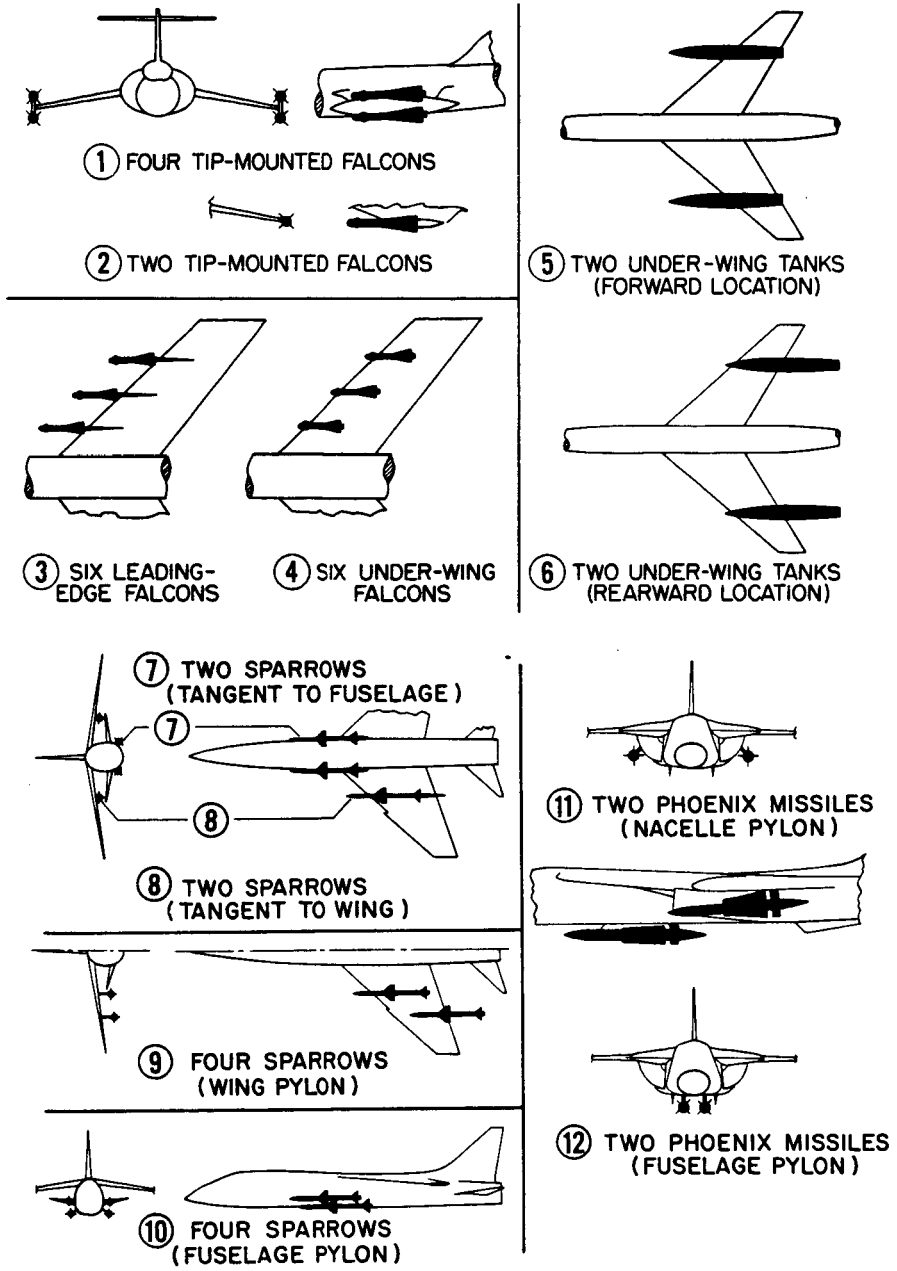


Figure 6

### TANGENT AND PYLON INSTALLATIONS

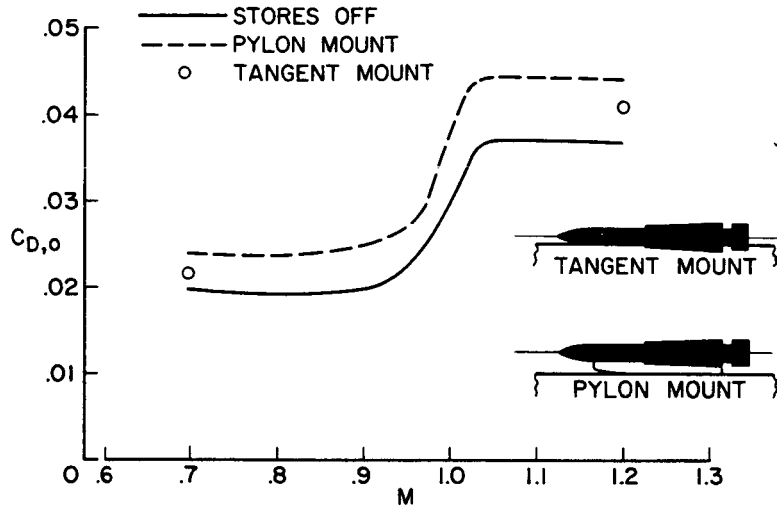


Figure 7

### SEMISUBMERGED STORE INSTALLATION

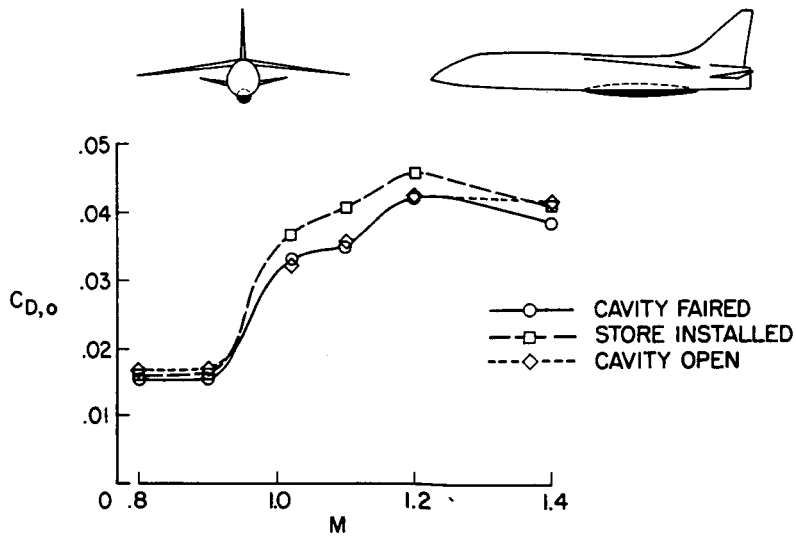


Figure 8

### TANDEM STORE INSTALLATION

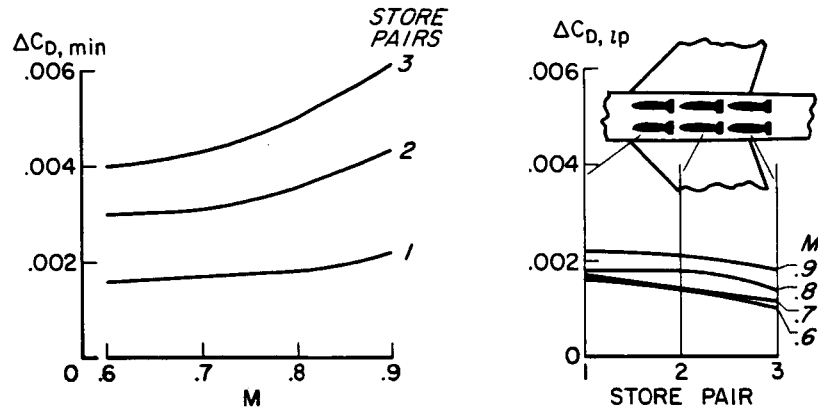


Figure 9

### EFFECTS OF STORE CORNER RADIUS

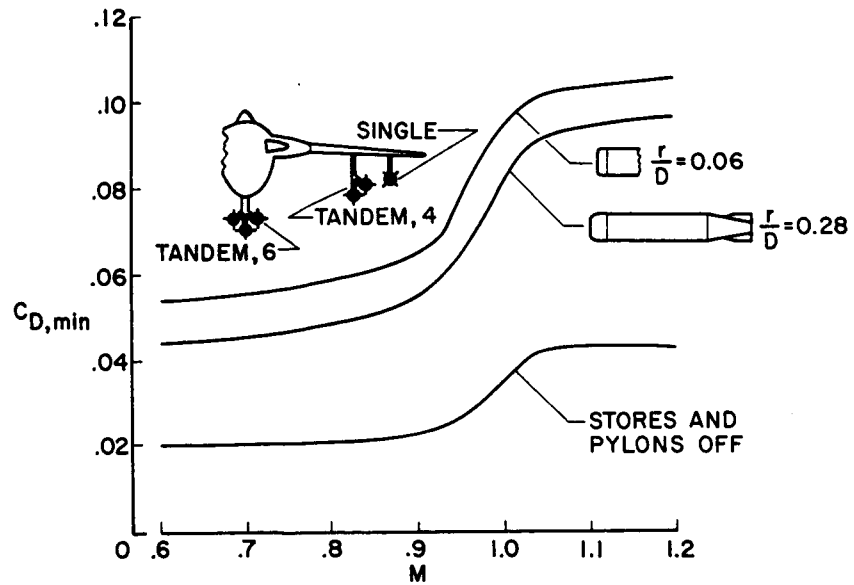


Figure 10

## 25. STATUS OF RESEARCH ON A SUPERCRITICAL WING

By Richard T. Whitcomb and James A. Blackwell, Jr.  
NASA Langley Research Center

### SUMMARY

A drastic modification of airfoil shape for high subsonic cruise airplanes is proposed which substantially increases the drag rise Mach number. The airfoil incorporates a slot between the lower and upper surfaces near the trailing edge with negative camber on the airfoil ahead of the slot and substantial positive camber rearward of the slot. A wing-fuselage configuration incorporating the proposed airfoil has been investigated. The wing of this model has  $35^\circ$  of sweepback of the quarter-chord and an aspect ratio of 10.

Presently, a cruise Mach number of approximately 0.90 has been achieved with the supercritical-wing—fuselage configuration. The drag at the cruise condition is about .5 percent lower than that for comparable conventional configurations. Also, the new supercritical airfoil appears to afford a substantial improvement in high lift stability and buffeting.

### INTRODUCTION

The Air Force C-5 program and the more recent considerations of a new generation of subsonic jet transports has stimulated a renewed interest in means of improving the performance of cruise airplanes at high subsonic speeds. The principal factor limiting the performance of such airplanes is the drag rise which occurs at about a Mach number of 0.8 for the current generation of jet transports. This drag rise not only limits the speed of the airplane but also reduces the lift-drag ratio at the cruise point. Both factors adversely affect airplane operating costs.

The most widely used means for delaying the drag rise is wing sweepback; however, excessive wing sweepback results in a reduction in the aerodynamic aspect ratio for a given structural panel aspect ratio, an increase in the severity of the pitch-up problem, and a reduction in the lift coefficient for landing and take-off. Because of these problems, the sweep utilized in the current generation of transports and in several recent cargo-type configurations has been limited to  $35^\circ$  at the quarter-chord. More recently, several U.S. aircraft companies and the British, particularly Pearcey (ref. 1), have developed refinements in essentially conventional airfoil shapes to provide moderate delays in the drag rise. These refinements have been incorporated in the several recent cargo-type configurations.

In the present paper, a drastic change in airfoil shape, which results in substantially greater delays in drag rise than those previously achieved, is discussed. This airfoil shape incorporates a slot between the lower

surface and the upper surface near the trailing edge with negative camber in the airfoil ahead of the slot and substantial positive camber rearward of the slot. Because the flow over a substantial portion of this airfoil is supercritical at the cruise condition, it is referred to as a supercritical airfoil. It should be emphasized that the research on this concept is continuing on an intensive basis, and the present paper should be considered a status report rather than a final summary.

#### SYMBOLS

$b$	span
$C_D$	drag coefficient
$C_L$	lift coefficient
$C_m$	pitching-moment coefficient, referred to $\bar{c}$
$C_p$	pressure coefficient
$C_{p,sonic}$	pressure coefficient corresponding to local Mach number of 1.0
$c$	wing chord
$\bar{c}$	wing mean aerodynamic chord
$c_d$	section drag coefficient
$c_m$	section pitching-moment coefficient, referred to $0.25c$
$c_n$	section normal-force coefficient
$M$	Mach number
$t$	wing thickness
$y$	spanwise distance

#### FLOW PHENOMENA

In order to illustrate the basic flow phenomena for conventional airfoils (NACA 64A-series) and the new supercritical airfoil, schematic illustrations of the flow fields and chordwise surface pressure distributions, based on wind-tunnel measurements, are presented in figure 1. The flow phenomena for the conventional airfoil are shown at a Mach number of 0.69 which is higher than

that for the initiation of drag rise ( $M = 0.67$ ), and those for the new supercritical airfoil are shown at a Mach number of 0.79 which is slightly lower than that for the initiation of drag rise ( $M = 0.80$ ). (See fig. 2.)

When a subsonic cruise airplane approaches the speed of sound, a local region of supersonic flow develops above the wing. (See sketch in the upper left of fig. 1.) This supersonic flow is decelerated to subsonic flow through a shock wave. The shock wave produces some energy loss and thus a drag increase. More importantly, the shock wave usually causes separation of the boundary layer on a conventional airfoil. Most of the drag rise is associated with this separation. The separation is a result of the boundary layer having insufficient momentum to traverse the total pressure rise of the shock wave and the normal subcritical pressure recovery. (See the pressure distribution in the lower left of fig. 1.)

In the new supercritical airfoil, a slot between the lower and upper surfaces is placed at an intermediate point in the combined pressure rise. (See schematic drawing in upper right of fig. 1.) (The part of the airfoil ahead of the slot is referred to herein as the fore component, that behind the slot as the aft component.) With such an arrangement, the boundary layer on the upper surface of the fore component of the airfoil and the second boundary layer on the upper surface of the aft component both experience a pressure rise less than the total rise on a conventional airfoil; therefore, the tendency toward boundary-layer separation is reduced. Ideally, the airfoil is shaped to provide only the pressure rise due to the shock wave on the fore component whereas the pressure recovery that follows is concentrated on the aft component.

When boundary-layer separation is reduced or eliminated, the severe drag rise is delayed to a higher Mach number. At the higher Mach number, the drag due to shock losses increases. This drag increment is an order of magnitude less than that associated with the separation; however, for subsonic-cruise-type airplanes any drag rise is unacceptable. Therefore, the supercritical airfoil has been reshaped to reduce the drag associated with the shock losses. The energy losses in a shock wave are lessened by reducing the extent of the shock wave and diminishing the Mach number ahead of the wave. Both of these effects are accomplished in the supercritical airfoil by reducing the curvature and slope of the upper surface of the fore component. With such a reshaping, the supersonic region is as shown in the sketch in the upper right of figure 1. The extent of this region reaches a maximum and then decreases ahead of the shock wave. In contrast, for a conventional airfoil shape the supersonic region continually expands to the shock as shown in the sketch in upper left of figure 1. Also, as indicated by the pressure distributions, the Mach number ahead of the shock wave on the supercritical airfoil is substantially less than that on a conventional airfoil.

With the reduced curvature of the upper surface, the lower surface of the wing must have additional curvature for a wing with a given thickness ratio. For the fore component of the new supercritical airfoil, the camber is effectively negative. Obviously, an airfoil with negative camber and low angle of attack produces very little lift; the required lift for cruise is achieved by incorporating substantial positive camber into the aft component of the airfoil.

Because of the increase in Mach number provided by the airfoil and the increased curvature of the lower surface, supercritical flow and a shock wave develop on the lower surface of the fore component at the probable cruise condition (fig. 1). In addition, a large pressure rise occurs on the lower surface of the airfoil at the point of reversal of the camber line. The addition of the pressure rise of the shock wave to the pressure rise associated with camber reversal gives a total pressure rise approximately equal to that on the upper surface of a conventional airfoil at supercritical conditions. Without the slot, this pressure rise would undoubtedly cause boundary-layer separation. However, the presence of the slot greatly reduces the tendency toward such separation in an action similar to that on the upper surface. The boundary layer on the fore component experiences only part of the total rise before being accelerated in the slot. The rest of the pressure rise occurs near the leading edge of the aft component where the boundary layer is very stable and can traverse the rise. Again, as for the upper surface, the lower surface should be shaped so that the pressure rise on the fore component is limited to that associated with the shock wave whereas the rest of the rise is concentrated on the aft component. Thus, the slot is necessary to control boundary-layer separation on the lower surface as well as on the upper surface.

A more complete discussion of the flow phenomena associated with the proposed supercritical airfoil is presented in reference 2.

#### TWO-DIMENSIONAL INVESTIGATION

In order to evaluate and develop the supercritical airfoil shape, a two-dimensional airfoil model was investigated in the Langley 8-foot transonic pressure tunnel (ref. 2). The model completely spanned the tunnel with the two solid side walls of the tunnel acting as large end plates. The normal force and pitching moment of the airfoil were determined by pressure distributions; drag was determined from wake survey measurements. The airfoil utilized had a thickness of  $13\frac{1}{2}$  percent chord. As a basis for reference, an NACA 64A-series airfoil which is representative of the airfoil shapes on current jet airplanes was also investigated.

Variations of drag coefficient with Mach number at a normal-force coefficient of 0.65 for the supercritical airfoil and for the NACA 64A-series airfoil are shown in figure 2. The 64A-series airfoil experienced a drag rise at about a Mach number of 0.67. The more recent airfoil shapes mentioned in the introduction would probably experience a similar drag rise at a Mach number of 0.70. The supercritical airfoil has a gradual increase in drag to a Mach number of about 0.78. This gradual rise is associated with small amounts of shock loss. Between  $M = 0.78$  and 0.79 the drag decreases somewhat, and then it increases sharply. This abrupt increase in drag is associated with a movement of the shock wave to a point rearward of the slot exit. For such a condition, the entire pressure rise of the shock plus the normal pressure recovery occur on the aft component with a resulting flow separation on the upper surface. Thus, the effectiveness of the new airfoil shape in delaying drag rise is limited.

The dip in the drag variation between  $M = 0.78$  and  $0.79$  is real. The schlieren photographs, wake surveys, and pressure distributions all indicate that the shock wave disappears. The exact reasons for this complete disappearance of the shock wave are not fully understood. A discussion of a possible reason is given in reference 2. However, from a practical standpoint, the most important characteristic of the airfoil is the relatively low drag increments due to shock losses for Mach numbers up to  $0.79$ .

The variations of pitching-moment coefficient with Mach number at a normal-force coefficient of  $0.65$  for the supercritical airfoil and for the reference 64A-series airfoil are presented in figure 3. The supercritical airfoil has a large negative pitching moment. This moment is the result of the large load on the aft component. (See pressure distribution in lower right of fig. 1.) For an unswept wing, the drag associated with trimming such a moment would probably be prohibitive; however, for a sweptback wing, this negative pitching moment is not necessarily a problem as is discussed in the section "Results and Discussion."

Additional aerodynamic characteristics obtained from the two-dimensional investigation are presented in reference 2.

### THREE-DIMENSIONAL INVESTIGATION

#### Configuration

In order to determine whether the delay in drag rise achieved for the relatively simple two-dimensional situation can be attained for the much more complex three-dimensional case, an investigation of a swept-wing—fuselage model incorporating the supercritical airfoil was made. The wing-fuselage configuration utilized for the three-dimensional investigation is shown in figures 4 and 5. The wing of the model has  $35^\circ$  of sweep at the quarter-chord; this sweep angle is the same as that for most current jet airplanes and several recent cargo-type configurations. The wing also has an aspect ratio of 10, a value significantly higher than the wing aspect ratio for current transports. However, the thickness ratios for the various sections of the wings are greater than those currently used; therefore, the wing bending structural problem is not significantly different from that for current designs. The use of a higher aspect ratio and greater section thickness ratios needs some explanation. An analysis of the characteristics of the new airfoil suggested that the maximum overall performance to be gained through the use of the new airfoil could be achieved if only part of the effectiveness of the shape is utilized to increase speed whereas the rest of the effectiveness is utilized to increase the cruise lift-drag ratio.

The wing was investigated with  $4^\circ$  of twist. To simplify model construction, the actual model had no twist. The twist was effectively achieved by rotating the flow in the wind tunnel into two circulation patterns symmetrically displaced with respect to the vertical center plane of the tunnel.

The shapes of the airfoils at various stations along the semispan of the wing are shown in figure 6. These airfoil shapes were not arrived at by mathematical calculations. The flow fields are highly nonlinear. The maximum Mach number on the upper surface was about 1.6 and the minimum Mach number on the lower surface was about 0.6. Further, the favorable influence of the supercritical airfoil on drag rise superimposed on the favorable effect of sweepback results in a probable cruise Mach number approaching the speed of sound. At these higher subsonic Mach numbers, the lateral disturbances produced by the various elements of the configuration expand rapidly so that a strong mutual interference exists between the flow fields about the several elements. No available theory can predict the required surface shapes for such three-dimensional, nonlinear conditions. Instead, on the basis of pressure distributions, surface oil films, and schlieren photographs, deviations from the desired flow fields were determined experimentally for the initial configuration. Then, on the basis of these measurements and the fundamental laws governing mixed flow, the initial shape was modified progressively to arrive at the final desired flow fields.

As shown in figure 4, the slot does not extend along the entire span of the wing. The load on the tip section is relatively low compared with that on the inboard sections; the thickness ratio of the tip is also relatively small. Therefore, the slot was believed not to be needed to control the flow on this less critical region. The surface oil film measurements indicate that the flow moves smoothly over this tip region.

The fuselage of the configuration was specially shaped and a thick glove was added to the forward region of the inboard sections of the wing to provide a longitudinal area development for the configuration approaching that for an ideal transonic body. The glove was necessary in order to allow satisfactory contours of the fuselage.

#### Results and Discussion

The variation of drag coefficient with Mach number at a lift coefficient of 0.5 for the configuration incorporating the supercritical airfoil is shown by the solid line in figure 7. For comparison, the average of similar results obtained for two recent cargo-type configurations (hereinafter referred to as reference) having the same sweep angle as the present model - that is,  $35^\circ$  of the quarter-chord - are presented as the dashed line labeled "recent technology." The investigations of the present and reference configurations were made in the Langley 8-foot transonic pressure tunnel with the same balance and support sting. The ratio of wing span (approximately 5 ft) to tunnel width was the same. The Reynolds number for the present investigation was approximately one-half that for the investigations of the reference configurations.

For the reference configurations, boundary-layer transition strips were placed near the leading edge on the upper surface and lower surface of the wing and on the fuselage. For the supercritical configuration, similar strips were placed on the upper surface of the wing and on the fuselage. However, the strip

on the lower surface was moved rearward to approximately the 50-percent-chord station to provide a ratio of boundary-layer thickness to slot height in the slot, which approximates that probably present in the slot on a full-scale airplane. Such a procedure for simulating a full-scale boundary-layer thickness is described in paper no. 3 by Loving. Boundary-layer strips were also placed on the upper surface of the aft component of the airfoil.

The drag results for the several configurations have been adjusted to provide results for the same relative fuselage volume to wing area and a closed fuselage aft end. The drag results obtained for the supercritical configuration have been adjusted upward to provide the drag level which would have been associated with a transition-strip location similar to that for the reference configurations. All results have been adjusted, on the basis of the usual variation of turbulent skin friction with Reynolds number, to a condition approximating that for an airplane of the C-5 size operating at an altitude of 35 000 feet. Such an adjustment provides a more realistic comparison of the results for the supercritical configuration and those obtained for the reference configuration. The slot, aft component struts support, glove, and the greater induced velocities on the surface of the supercritical configuration all increase the skin friction compared with that of the reference configurations. Thus, a comparison of the drag results at wind-tunnel Reynolds numbers would show a penalty for the supercritical configuration substantially greater than that for full-scale Reynolds numbers.

The curve for the reference configurations shows an abrupt drag rise at a Mach number slightly higher than 0.82. The supercritical configuration experienced a similar rise at a Mach number slightly higher than 0.9; thus, the drag rise has been delayed approximately 0.08 Mach number or 10 percent. The drag at a Mach number of 0.9 for the supercritical configuration is approximately 5 percent less than that for the reference configurations at a Mach number of 0.82. An analysis of the several differences between the supercritical configuration and the reference configurations indicates that the increased aspect ratio should result in a 9-percent reduction in drag and that the added skin friction should increase the drag approximately 4 percent. The delay in drag rise provided by the supercritical configuration for a substantial lift-coefficient range above and below 0.50 is approximately equal to that shown in figure 7; however, at very low lift coefficients, the delay is reduced because of separation on the lower surface of the supercritical configuration.

The pressure distributions measured at a Mach number of 0.9 for a lift coefficient of 0.50 are shown in figure 8. These pressure distributions indicate no severe wave drag problems. The surface oil films for the same condition indicate no significant regions of separation. A small bubble of separation occurs on the outboard region of the lower surface at the entrance to the slot just aft of the negative pressure peaks noted in the pressure distributions. Further refinements in the shape in this region should eliminate the pressure peak and the associated separation bubble.

The pressure distributions for a Mach number of 0.92 at a lift coefficient of 0.48, as presented in figure 8, indicate that the drag rise present at this Mach number is caused by a sudden rearward shift of the shock wave on the

outboard region of the upper surface to a position near the slot. The surface oil films indicate that this shock caused separation on the aft component and on a small region of the fore component. This separation pushed the shock wave forward in this region, as indicated by the pressure distributions. A discussion of the effect of separation on shock position is presented in paper no. 3 by Loving. The pressure distributions shown in figure 8 and the surface oil films for the same condition indicate no separation and insignificant shock losses on the entire inboard region of the configuration at  $M = 0.92$ . Similar detailed flow measurements indicate no severe problems in this inboard region until a Mach number of 0.95 is exceeded. Thus, it appears that, to obtain further delays in the drag rise Mach number, the rapid rearward movement of the shock wave on the outboard region of the wing must be retarded. A study of several means for accomplishing this action is being planned.

To date, no investigations of the effects of adding nacelles to the configuration have been made but such an investigation is planned. During this investigation, a detailed analysis of the flow phenomena associated with the favorable pylon-nacelle-wing interference described by Patterson in paper no. 18 will be made, with the intent, of course, of increasing this favorable interference.

A limited comparison of the trim, stability, and buffet characteristics for the supercritical configuration with those based on the reference configurations (labeled "recent technology") are shown in figure 9. The results shown for the supercritical configuration are for a Mach number of 0.85 which is 0.05 less than the probable cruise Mach number. The reference results are presented for a corresponding Mach number of 0.77. At a lift coefficient of 0.5, the results for the reference configurations show a pitching moment of approximately -0.05. Such a negative pitching moment causes no severe trim problem. The supercritical configuration had a near zero pitching moment at the same lift coefficient. Thus, in contrast to the very large negative pitching moment for the two-dimensional supercritical airfoil, as discussed in the section "Two-Dimensional Investigation," the swept wing with such an airfoil has a less negative pitching moment than wings with conventional airfoils. The glove added to the leading edge of the inboard sections and the wing twist required to obtain the desired span load distribution at the cruise condition provided a positive pitching-moment increment which offset the negative pitching moments of the sections.

The results presented in figure 9 indicate that the supercritical configuration experienced an increase in stability beyond a lift coefficient of approximately 0.6. No abrupt decrease in stability was observed to a lift coefficient of 0.95 at which moderate buffeting occurred. Because of the inadequacy of the stiffness of the support system during the investigation of the supercritical configuration, no attempt was made to obtain data after buffeting occurred. The results for the reference configurations show a decrease in stability at  $C_L \approx 0.7$ .

An indication of the possible influence of the new airfoil shape on buffet characteristics was also obtained during the investigation. It is realized that a quantitative indication of buffeting can be obtained only in flight or

with a dynamically similar model in a wind tunnel. The models of the supercritical configuration and the reference configurations are not dynamically similar to airplanes. However, a qualitative comparison of the buffet characteristics for the supercritical configuration and for the reference configurations is provided by model buffeting or shake. For the reference configurations initial model buffeting occurred at  $C_L \approx 0.7$ , the lift coefficient at which the abrupt decrease in stability occurred. (See fig. 9.) The model of the supercritical configuration buffeted at a lift coefficient of about 0.95, a value one-third higher than that for the reference configurations. These limited stability and buffet results suggest that the flow through the slot and the shape of the supercritical airfoil probably provide a strong favorable effect on boundary-layer separation at high lift coefficients as well as the design condition.

Thus far no results have been obtained which define the landing and take-off characteristics at low speeds for the configuration with the supercritical airfoil. However, as shown in figure 6, the present model has very large leading-edge radii ( $0.027c$ ). The favorable influence of such radii on the low-speed, high-lift characteristics should more than offset any adverse effect of the negative camber of the fore component. Thus, there appears to be no obvious reason for the characteristics at low speeds being any worse than those for configurations with conventional airfoils. The aft component of the supercritical airfoil can probably be incorporated into the low-speed landing-flap system and, thus, should not materially increase the complexity of an already complex airplane.

The determination of the influence of the new airfoil on wing weight will require a very comprehensive analysis. However, one factor controlling this weight is discussed here briefly. At the cruise condition, the aft component produces approximately 40 percent of the lift of the wing. However, the structure of the airplane configuration is usually designed on the basis of the higher maneuver lifts. When the angle of attack is increased to produce these higher lifts, the load on the aft component remains approximately constant and the fore component produces the additional lift. Therefore, the proportion of the load on the aft component at these conditions is substantially less than that at the cruise condition. Thus, it might be expected that the structural weight penalty associated with the loads on the aft component would not be as great as indicated by the load distributions obtained at the cruise lift coefficient.

#### CONCLUDING REMARKS

Presently, with a swept-wing configuration incorporating the proposed supercritical airfoil, a subsonic cruise Mach number of 0.90 has been achieved. This Mach number is approximately 10 percent higher than that for the most recent comparable configurations with essentially conventional airfoils. The drag at near the cruise condition is about 5 percent lower than that for the comparable conventional configurations. Also, it appears that the supercritical airfoil affords a significant improvement in high lift stability and buffeting.

Further research may reveal insurmountable problems. On the other hand, it is likely that the research will indicate further advantages for the new airfoil shape. For the present, the results presented indicate that the proposed concept has interesting practical promise.

#### REFERENCES

1. Pearcey, H. H.: Shock-Induced Separation and Its Prevention by Design and Boundary Layer Control. Boundary Layer and Flow Control, Vol. 2, G. V. Lachmann, ed., Pergamon Press, 1961, pp. 1166-1344.
2. Whitcomb, Richard T.; and Clark, Larry R.: An Airfoil Shape for Efficient Flight at Supercritical Mach Numbers. NASA TM X-1109, 1965.

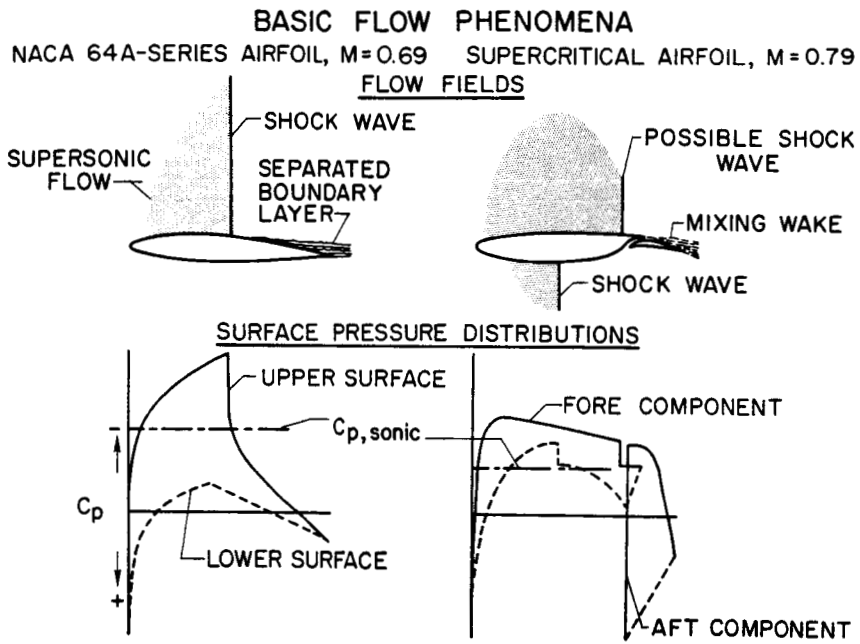


Figure 1

DRAG COMPARISON AT  $c_n = 0.65$   
 $1/c = 0.135$

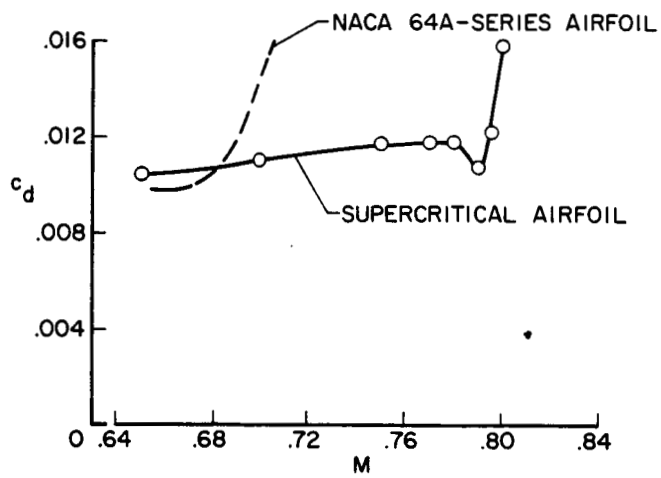


Figure 2

PITCH COMPARISON AT  $c_n = 0.65$

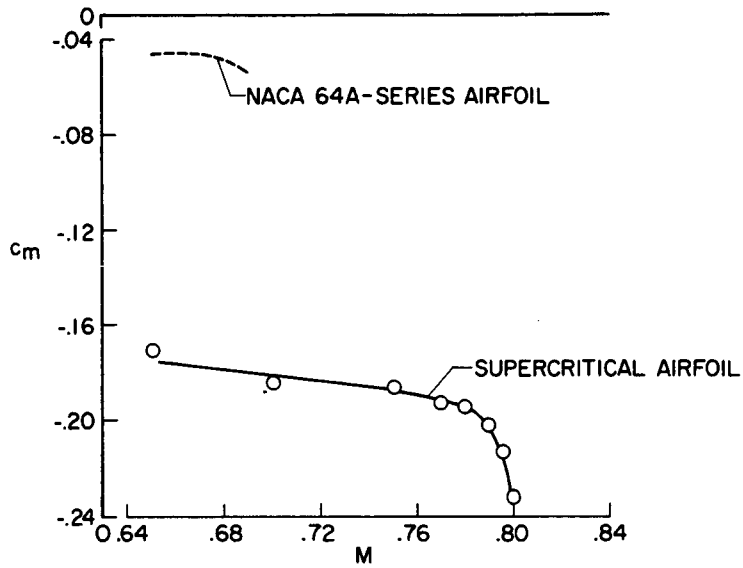


Figure 3

PLAN VIEW OF CONFIGURATION INCORPORATING SUPERCRITICAL AIRFOIL

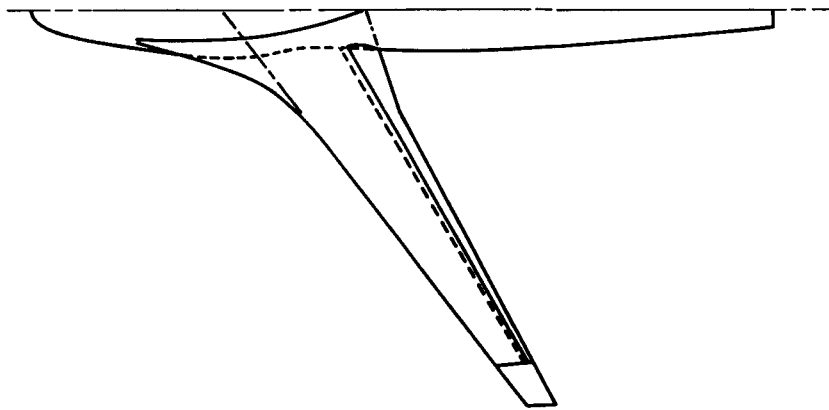


Figure 4

CONFIGURATION INCORPORATING SUPERCRITICAL AIRFOIL

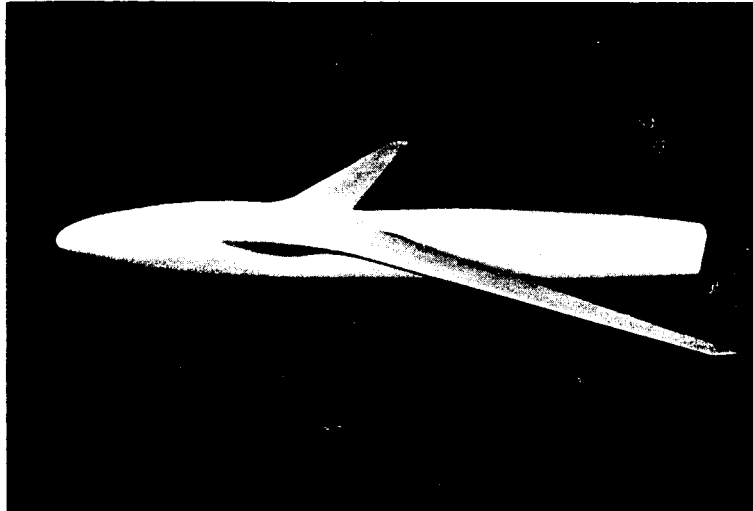


Figure 5

L-66-4086

AIRFOIL SHAPES FOR SUPERCRITICAL WING

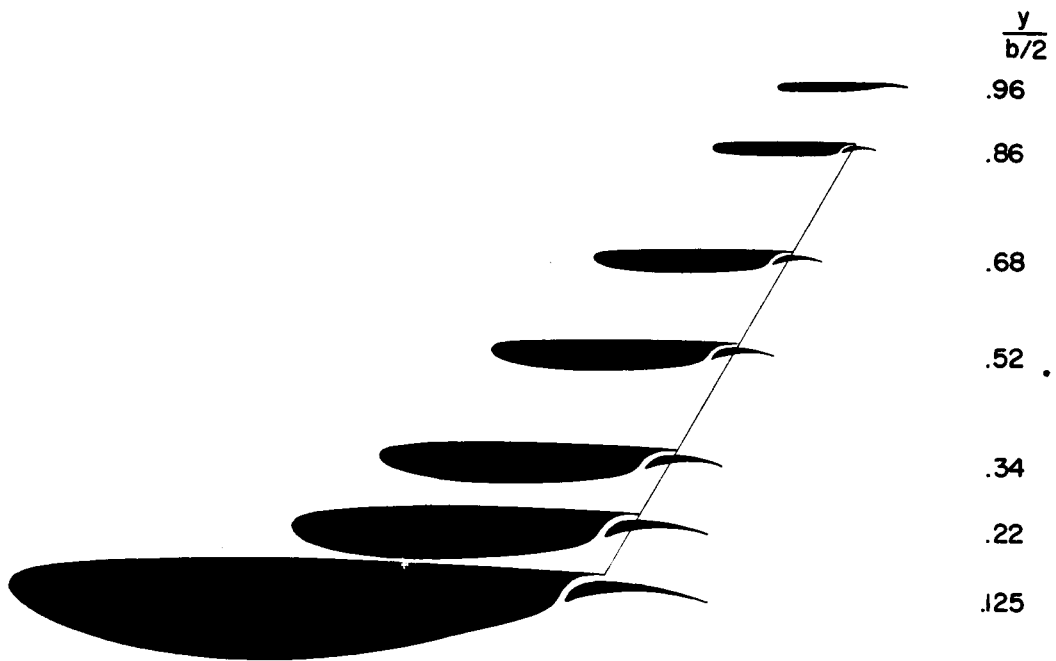


Figure 6

COMPARISON OF WING-FUSELAGE DRAG  
 $C_L = 0.50$

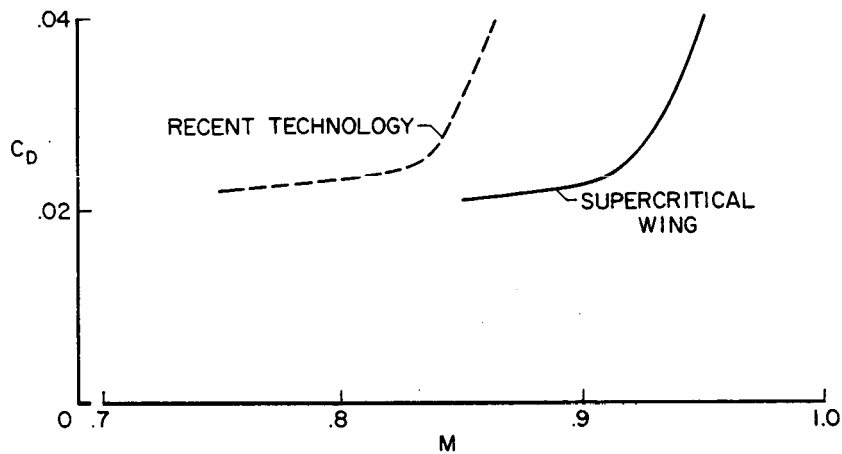


Figure 7

PRESSURE DISTRIBUTIONS ON SUPERCritical WING

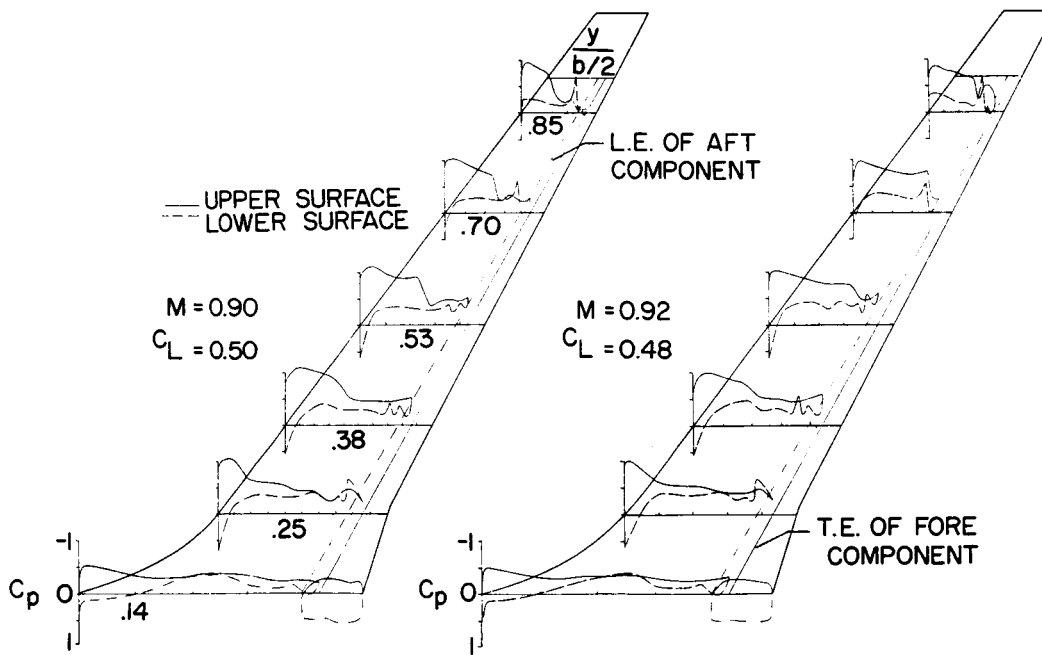


Figure 8

COMPARISON OF WING-FUSELAGE PITCHING MOMENTS

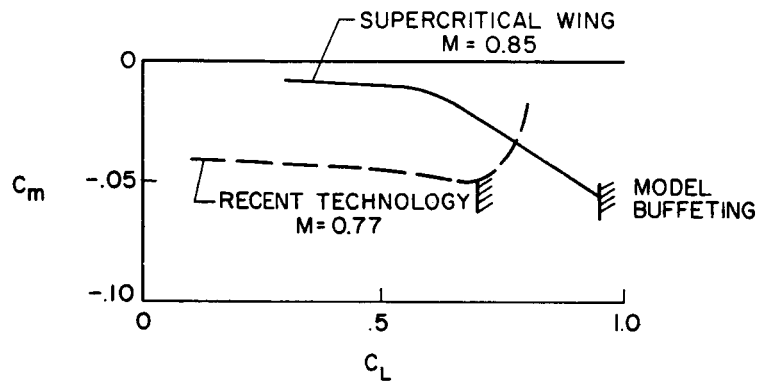


Figure 9

## 26. CURRENT METHODS FOR PREDICTION AND MINIMIZATION OF

### LIFT-INDUCED DRAG AT SUPERSONIC SPEEDS

By Harry W. Carlson and F. Edward McLean  
NASA Langley Research Center

#### SUMMARY

The current state of the art of predicting and minimizing lift-induced drag at supersonic speeds as practiced at the Langley Research Center is reviewed. Numerical methods of implementing the linearized theory for use on high-speed electronic computers are outlined, and applications of the methods to wings, wing-body combinations, and complete configurations are studied. It is concluded that the techniques are generally applicable in the supersonic speed range at least up to a Mach number of 3 for configurations employing slender bodies and thin, moderately cambered wings, as represented by current supersonic-transport designs.

#### INTRODUCTION

In the past few years, a significant part of the theoretical drag-reduction potential of warped supersonic wings (refs. 1 to 3) has been achieved in wind-tunnel experiments (refs. 4 and 5). Successful application of the theoretical concepts has been due in part to the imposition of experimentally determined restraints on camber surface severity (refs. 4 and 6). Experimental studies (refs. 7 to 9) have also shown the manner in which wing warp may be incorporated into complete airplane configurations so as to preserve and enhance the benefits of the wing design. Another recent development has been the implementation of the theory by numerical methods programed for high-speed computers (refs. 10 to 12). These programs provide a versatile set of tools for rapid estimation and optimization of wing aerodynamic characteristics. The purpose of this paper is to review the nature of the theory and numerical methods of implementation and to discuss the findings of experimental studies regarding the applicability of the methods to wings alone, to wing-body combinations, and to complete configurations.

#### SYMBOLS

$C_D$	drag coefficient
$\Delta C_D$	incremental drag coefficient due to lift
$C_L$	lift coefficient

$C_{L,des}$	lift coefficient for which the warped wing surface is designed to produce a minimized drag
$C_{L,opt}$	lift coefficient yielding maximum lift-drag ratio for a theoretically optimum surface
$C_m$	pitching-moment coefficient about the $0.45\bar{c}$ station
$C_{m,0}$	pitching-moment coefficient at zero lift
$C_p$	pressure coefficient
$C_Y$	side-force coefficient
$c_r$	root chord
$\bar{c}$	mean aerodynamic chord
$(L/D)_{max}$	maximum lift-drag ratio
$M$	Mach number
$R_{\bar{c}}$	Reynolds number based on mean aerodynamic chord
$w$	upwash velocity
$x^*$	wing shear parameter (see fig. 6)
$z$	camber-surface ordinate
$\alpha$	angle of attack

## DISCUSSION

### Numerical Analysis of Lifting Surfaces

An illustration of the representation of a wing in the numerical analysis is given in figure 1. A simplified analysis may be made for the pair of lifting elements shown at the left of the figure. In generating lift, the forward element of the pair creates a downwash field between trailing tip vortices and an upwash field in the remainder of the Mach cone region. Lift generated by the rearward element depends on its attitude relative to the upwash created by the forward element. Linearized theory provides a solution for the lifting characteristics of an element in the flow field created by one or more forward elements, each generating a given lift. The upwash field at the element is related directly to the lift of the forward element and only indirectly to the angle of attack required for that lift; thus, the case in which the required angle is related to a specified load is termed the direct solution. A complete wing represented as an array of elements is shown at the right of figure 1. This

drawing is schematic; in actual practice, many more elements would be used. In the direct solution, lifting pressures are assigned to each of the elements and the required surface slopes are found. In the inverse solution, the surface slopes are specified and the resulting lifting pressures are found. The inverse solution is more complex but may be handled numerically, provided the calculations are made by following a precise routine - that is, by working from the forward to the rearward elements.

It may be observed that the greatest benefits of warping are derived for wings with leading edges swept behind the Mach line. The leading-edge elements, acting in the upwash field of the forward elements, generate fairly large amounts of lift on a forward-facing slope, and thus produce a thrust component rather than a drag component. However, even for planforms for which the drag reduction is small, the use of twist and camber is worthy of investigation, since it can help reduce the problem of the supersonic aerodynamic-center shift.

Figures 2 and 3 illustrate the design and analysis tools provided by the numerical solutions of the theory. An example of the direct problem is shown in figure 2. A planform and a desired loading distribution (represented by the arrows) are specified, and a surface which will support that loading is determined. Symbols on the plot represent wing forces, and inset sketches show the corresponding shapes of the camber surfaces as determined by use of the method of reference 10. The circular symbol represents a solution for the surface required to yield an arbitrarily selected distribution of load at a specified lift coefficient. The somewhat unusual loading distribution selected is only one of many possible distributions.

By determining the solutions for three or more specific load distributions and by using a numerical evaluation of the mutual interference of loadings and surfaces, an optimum combination of loadings for minimum drag is obtained. The square symbol represents the solution for a surface defined by an optimum combination of three loadings. The solid line shows the variation of drag increment with lift for a wing which is allowed to assume the optimum shape at all lift coefficients. Since a real wing must have a fixed surface shape, this curve forms a lower-bound envelope of possible drag reduction for a given planform.

Because of necessary departures from the idealized optimum camber surfaces in airplane design, it is advantageous to have a means of evaluating arbitrarily selected shapes for use in trade studies. In figure 3 is shown an example of the inverse problem treated in references 11 and 12. A planform and a cambered surface shape are given, and the lift loading and the resultant forces are determined. The circular symbol represents the machine solution for a wing of specified shape at a reference attitude of  $0^\circ$ , and the corresponding inset sketch shows the distribution of lifting pressures. A special case of camber surface shape is a flat plate. The solution for the lifting pressures and forces on a flat wing having the same planform as the wing of specified shape is represented by the dashed line. These two solutions may be combined to define the pressures and drag for the cambered wing of specified shape as the angle of attack and lift coefficient are varied. The solid line represents

the combined solution and the inset sketches along this line illustrate the variations in wing loading with lift coefficient.

The computer programs thus serve the following purposes:

(1) To define a lower bound of possible drag reduction and describe the theoretical lower-bound shapes

(2) To define the loadings and lift-drag characteristics of arbitrarily selected wing shapes

(3) To describe the loadings and lift-drag characteristics of flat wings having the same planform as the wings of specified shape, the lift-drag characteristics being a base point for judging the benefits of twist and camber

In current configuration analyses, the lifting effects for an infinitely thin wing calculated by use of these programs are added directly to the effects of thickness evaluated independently by use of machine programs based on supersonic-area-rule concepts (ref. 13). Thus, the possibility of mutual interaction between lift and volume is not considered. In addition, no account is taken of the leading-edge suction forces which, although important at subsonic speeds, have not been found to exist to any appreciable extent at supersonic speeds. The presence of a detached leading-edge vortex flow, which could influence to some degree the loadings and forces at supersonic speeds, is similarly neglected.

#### Application of Analysis Methods

Application to wings alone. - An example of the use of wing warp to provide a reduction in drag at lifting conditions and an improvement in trim characteristics is shown in figure 4. An investigation of the semispan wing shown at the upper left of the figure was conducted at a Mach number of about 2 and a Reynolds number of  $4.4 \times 10^6$  in the Langley 4- by 4-foot supersonic pressure tunnel (ref. 4). A warped wing and a flat wing of the same planform were investigated. The experimental results are compared with theoretical curves for these two wings and with a theoretical curve for a wing defined by an optimum combination of loadings. The drag of the warped wing is somewhat higher than that of the flat wing at zero lift, but is significantly lower than that of the flat wing at the higher lift coefficients. The fact that the experimental results fail to achieve the theoretical drag levels for the optimum surface is to be expected, inasmuch as an infinite incidence at the root chord is unrealistically assumed for the theoretically optimum surface. Although the optimum loading theory indicates a maximum lift-drag ratio for a lift coefficient of about 0.16, it was found that a wing designed for a theoretically minimum drag at that lift coefficient actually performed little better than the flat wing. Experimental evidence has shown that better results are obtained when the lift for maximum lift-drag ratio is due in part to the warped surface and in part to the angle of attack of that surface. The particular warped wing surface shown in this figure was designed to produce a lift coefficient of 0.08. In addition, the wing employed restrictions in incidence of the root chord and in

local loading (ref. 6). The inverse program may be used to assure that these departures from the theoretically optimum surface introduce no large penalties. Figure 4 also shows that, in addition to providing for reduced drag, the wing warping results in a more positive pitching-moment coefficient which permits more efficient trimming of the configuration.

The necessity for realistic restraints on the severity of camber surfaces is illustrated in figure 5. Measured and predicted maximum lift-drag ratio and pitching-moment coefficient at zero lift are shown for a series of three wings (from ref. 4) differing only in the degree of warping, which is dictated by the design lift coefficient. The design lift coefficient  $C_{L,des}$  is referred to the lift coefficient giving maximum lift-drag ratio for the theoretically optimum wing surface  $C_{L,opt}$ . Inset sketches show the increasing severity of the wing surface with increases in the design lift coefficient. The highest lift-drag ratio obtained experimentally is lower than the theoretical maximum and occurs for a value of  $C_{L,des}$  about half as large as that required for the theoretical maximum. This result is probably due to the increasing inapplicability of the linearized theory as the surface becomes more highly warped. It should not be assumed that a ratio of  $C_{L,des}$  to  $C_{L,opt}$  of 0.5 is to be used in all instances. The choice of design lift coefficient will be influenced by the planform and the Mach number and by moment considerations as well. It should be noted that, as shown at the right of the figure, the beneficial pitching-moment coefficient at zero lift increases steadily as the value of  $C_{L,des}/C_{L,opt}$  is increased from 0 to 1.0.

The linearized theory, on which the methods of twisted and cambered wing design are based, sets specific requirements for the surface slope with respect to the flight direction but imposes no restrictions on the slope with respect to the lateral direction. Results from a recent experimental investigation which illustrate the importance of lateral-slope considerations are shown in figure 6. The models were variations of the basic wing shown in figure 4, which had a design lift coefficient of 0.08. The wings have been sheared to produce a flat lateral section at various stations  $x^*$  along the root chord of the wing, as shown in the inset sketch at the upper right. The variation of measured  $(L/D)_{max}$  with the shear parameter  $x^*/c_r$  is shown, along with sketches of the side views of the semispan wings. The experimental data indicate that maximum performance is attained for values of  $x^*/c_r$  near 0.5. It would appear that best results are obtained when the surface is arranged to lie in as nearly a single plane as possible without changing the streamwise slopes. The results of an experimental study in which wing dihedral is the variable (ref. 14) lead to a similar conclusion.

Application to wing-bodies.- An important consideration in the application of twisted and cambered wing design is the manner in which wing and fuselage are combined. Reference 7 gives maximum lift-drag ratios for wing-fuselage combinations employing the basic cambered wing of figure 4, and these data are presented in figure 7. Also, for reference purposes, data are presented for a combination in which the uncambered or flat wing is used. It was previously believed that a fuselage aligned with the free stream would be beneficial in

that it would cover up the troublesome inboard wing region having large surface slopes. Experimental data for the first of the warped-wing—fuselage configurations in figure 7 indicate, however, that the combination with a fuselage so aligned has a maximum lift-drag ratio only slightly larger than that of the flat-wing—body configuration. Another possible way of combining the wing and fuselage is to align the fuselage with the wing root chord. As shown in figure 7, the maximum lift-drag ratio for this combination is considerably larger than that for the flat-wing—body configuration. The final configuration in this figure employs a fuselage which is aligned with the root chord but which has a reflex at the wing apex and at the root-chord trailing edge. In effect, the thickness of this configuration, both wing and fuselage, is displaced symmetrically about the camber surface defined for the wing planform. For the design condition of  $C_L = 0.08$  the fuselage ahead of and behind the wing surface is aligned with the free stream and carries little or no lift. This wing-body combination produced the highest maximum lift-drag ratio of the test configurations; the ratio was about 1.1 larger than for the uncambered- or flat-wing—body configuration. It would appear that such an arrangement of the configuration volume preserves the distribution of wing loading prescribed by the wing theory. Theoretical maximum lift-drag ratios evaluated by use of the mean-camber-surface concept, which is discussed in the following paragraph, predict reasonably well the performance gains of the last two configurations in figure 7 but fail to assess properly the penalties associated with the streamwise fuselage alignment.

The concept of a mean camber surface is quite useful in analyzing the characteristics of a wing-body configuration with appreciable thickness. An application of this kind of analysis to the prediction of interference effects for a delta-wing—wedge-body model at  $M = 2.0$  (ref. 15) is shown in figure 8. Lift-drag polars and curves for angle of attack as a function of lift coefficient are shown for a high-wing and a low-wing configuration. The lift characteristics have been estimated from program calculations for a warped surface formed by the locus of points midway between the upper and lower model surfaces. Since the numerical solution cannot work with discontinuous slopes, it is necessary in this example to approximate the mean camber surface with a surface that varies gradually from element to element. The step in the surface is thus replaced by a series of ramps extending over a number of grid elements. It is also necessary to tax the machine storage capacity in order to obtain a good approximation of this model surface, obviously an extreme case of a warped wing surface. The data show that the high-wing configuration has lower drag at lifting condition than does the low-wing configuration and that the theory correctly predicts this drag. It should be noted that the mean camber surface used to represent the high-wing model more nearly corresponds to the surface required for an optimum combination of loads. The use of favorable-interference concepts, as exemplified by the high-wing model, is in a sense a special case of twist and camber. As shown at the right of the figure, the theory somewhat overestimates the influence of the wedge in the generation of interference lift, perhaps because in real flow the body pressure field extends some distance ahead of the theoretically sonic leading-edge wing.

Since a mean camber surface may be used to represent the lifting effects of a wing-body combination, it would be expected that, conversely, lifting

effects for a theoretically determined mean camber surface would be best retained with a symmetrical distribution of thickness above and below that surface.

Positioning of engine nacelles or stores has an important influence on configuration aerodynamic characteristics. Fairly large variations in wave drag at zero lift can result from variations of nacelle location relative to the wing-fuselage. As illustrated in figure 9, nacelle alignment also influences the drag. This figure presents data from reference 8 and shows the variation of  $\Delta C_D$  for the wing-nacelle combination with alignment or cant angle at  $C_L = 0.16$ . By definition, the drag increment is zero for zero cant angle. As shown in the inset sketch, a nacelle-pylon installation experiences a side force due to the flow angularity produced by the wing. A component of this force acts in the drag direction. When the nacelle is aligned with the local flow, there is no side force and no drag component. When the nacelle is aligned with the airplane axis or the free stream, there is a side force normal to the nacelle but the drag component is zero. For a cant angle larger than the flow angle, the side-force vector reverses and considerable drag can result. Also, for negative cant angles, the drag penalties can become large. It is interesting to note that a thrust, not a drag, is indicated for cant angles between the free stream and the local flow, with the maximum thrust halfway between the two. Setting a nacelle-pylon combination at such an angle results in somewhat higher drag at zero lift but produces, as does a twisted or cambered wing, a reduction in drag at design conditions. Calculations of local-flow angle is not now a part of the machine programs, but may be handled by a graphical integration of pressures to obtain velocity potential and a subsequent differentiation to obtain surface velocities. When calculated surface angles are used to optimize nacelle-pylon alignment, some correction should be made for the tendency to overestimate flow angularity off the wing surface at the pylon location. In the example given here the measured flow angle at the nacelle was only about two-thirds of the predicted surface angles. These considerations are also applicable to any vertical surfaces displaced from the airplane axis (e.g., outboard vertical fins). This rather simplified analysis of a complex situation has proved effective in obtaining drag reduction.

Application to complete configurations.- The individual elements of design philosophy as applied to airplane components have been discussed. In this section of the paper the integration of these elements into complete-configuration design is considered. The supersonic-transport design of reference 9 shown in figure 10 has been derived in part from skin-friction and wave-drag considerations which tend to minimize drag at zero lift. It also employs to some degree all the design considerations previously discussed - that is, the restricted design lift coefficient for the wing surface, the shear consideration, the nacelle and fin alignment, and the symmetrical distribution of thickness about the wing camber plane. In addition, for that region of the wing influenced by the nacelle thickness pressures (the shaded area and the lower cross section) the computed wing surface has been altered in order that the net lift distribution on the wing surface including the nacelle-induced pressures would be the same as that specified by the wing theory. The wing loading due to the nacelle pressure field has been calculated and the wing mean camber surface has been

reflexed to introduce a compensating loading. Detailed interference considerations discussed in reference 16 lead to the same design procedure.

Shown in figure 11 are the lift-drag characteristics of the optimized configuration at a Mach number of 2.6 for a tunnel Reynolds number of  $4.5 \times 10^6$ . Data on the left side of the figure are for the wing-fuselage combinations alone. Measured and calculated lift-drag polars are plotted for the warped-wing-body and for a similar configuration without wing warp. For the higher lift coefficients considered, the warped-wing-body is seen to provide a significant reduction in drag. On the right side of the figure, the lift-drag polar for the complete configuration shows the effect of the nacelles and vertical fins added in accordance with the previously outlined design concepts. Although there is a sizable increase of drag at zero lift, favorable-interference considerations and wing reflex have nearly compensated for the additional nacelle and fin wave drag and skin-friction drag for practical values of lift coefficient. Furthermore, the tunnel  $(L/D)_{\max}$  of 7.9 is for a complete configuration which has substantial pitching moment at zero lift and which would be expected to have little or no trim drag penalty. Extrapolation to full-scale cruise flight conditions yields a value of  $(L/D)_{\max}$  of about 9.5.

The benefits of the wing twist and camber and favorable-interference considerations are not confined to a specific design point, but have been found to extend over wide ranges of Mach number and lift coefficient, as shown in references 9 and 17.

#### CONCLUDING REMARKS

The design and estimation techniques discussed herein have been shown to be applicable in the supersonic range at least up to a Mach number of 3.0 for configurations employing slender bodies and thin, moderately cambered wings. Thus, if a configuration meets the requirements for efficient supersonic cruise (a necessity for supersonic-transport designs), the methods may be used with some confidence in estimating and optimizing the aerodynamic characteristics. With configurations for which supersonic cruise efficiency is not a major consideration (e.g., supersonic dash vehicles), there may be some question as to the applicability of methods based on linearized theory.

## REFERENCES

1. Jones, Robert T.: Theoretical Determination of the Minimum Drag of Airfoils at Supersonic Speeds. *J. Aeron. Sci.*, vol. 19, no. 12, Dec. 1952, pp. 813-822.
2. Grant, Frederick C.: The Proper Combination of Lift Loadings for Least Drag on a Supersonic Wing. *NACA Rept. 1275*, 1956. (Supersedes *NACA TN 3533*.)
3. Brown, Clinton E.; and McLean, Francis E.: The Problem of Obtaining High Lift-Drag Ratios at Supersonic Speeds. *J. Aero/Space Sci.*, vol. 26, no. 5, May 1959, pp. 298-302.
4. Carlson, Harry W.: Aerodynamic Characteristics at Mach Number 2.05 of a Series of Highly Swept Arrow Wings Employing Various Degrees of Twist and Camber. *NASA TM X-332*, 1960.
5. McLean, F. Edward; and Fuller, Dennis E.: Effects of Thickness on Supersonic Performance of a Wing-Body Configuration Employing a Warped Highly Swept Arrow Wing. *NASA TN D-3034*, 1965.
6. Brown, Clinton E.; McLean, F. E.; and Klunker, E. B.: Theoretical and Experimental Studies of Cambered and Twisted Wings Optimized for Flight at Supersonic Speeds. *Advan. in Aeron. Sci.*, vol. 3, Pergamon Press, 1961, pp. 415-431.
7. Carlson, Harry W.: Longitudinal Aerodynamic Characteristics at Mach Number 2.02 of a Series of Wing-Body Configurations Employing a Cambered and Twisted Arrow Wing. *NASA TM X-838*, 1963.
8. Landrum, Emma Jean: Effect of Nacelle Orientation on the Aerodynamic Characteristics of an Arrow Wing-Body Configuration at Mach Number 2.03. *NASA TN D-3284*, 1966.
9. Morris, Odell A.; and Fournier, Roger H.: Aerodynamic Characteristics at Mach Numbers 2.30, 2.60, and 2.96 of a Supersonic Transport Model Having a Fixed, Warped Wing. *NASA TM X-1115*, 1965.
10. Carlson, Harry W.; and Middleton, Wilbur D.: A Numerical Method for the Design of Camber Surfaces of Supersonic Wings With Arbitrary Planforms. *NASA TN D-2341*, 1964.
11. Middleton, Wilbur D.; and Carlson, Harry W.: A Numerical Method for Calculating the Flat-Plate Pressure Distributions on Supersonic Wings of Arbitrary Planform. *NASA TN D-2570*, 1965.
12. Middleton, Wilbur D.; and Carlson, Harry W.: Numerical Method of Estimating and Optimizing Supersonic Aerodynamic Characteristics of Arbitrary Planform Wings. *J. Aircraft*, vol. 2, no. 4, July-Aug. 1965, pp. 261-265.

13. Harris, Roy V., Jr.: An Analysis and Correlation of Aircraft Wave Drag. NASA TM X-947, 1964.
14. Middleton, Wilbur D.; and Carlson, Harry W.: Supersonic Longitudinal Aerodynamic Characteristics of Two Wing-Body Configurations Employing Warped Arrow Wings of Varying Dihedral. NASA TM X-897, 1963.
15. Morris, Odell A.: Aerodynamic Characteristics in Pitch at a Mach Number of 2.01 of Several Wing-Body Combinations With Wedge-Shaped Bodies Located Above and Below a  $54.5^\circ$  Swept Delta Wing. NASA TN D-1823, 1963.
16. Robins, A. Warner; Morris, Odell A.; and Harris, Roy V., Jr.: Recent Research Results in the Aerodynamics of Supersonic Vehicles. Paper No. 65-717, Am. Inst. Aeron. Astronaut., Nov. 1965.
17. Middleton, Wilbur D.; and Sorrells, Russell B.: Off-Design Aerodynamic Characteristics at Mach Numbers 1.61 and 2.20 of a Series of Highly Swept Arrow Wings Designed for Mach Number 2.0 Employing Various Degrees of Twist and Camber. NASA TN D-1630, 1963.

## LIFTING-SURFACE REPRESENTATION

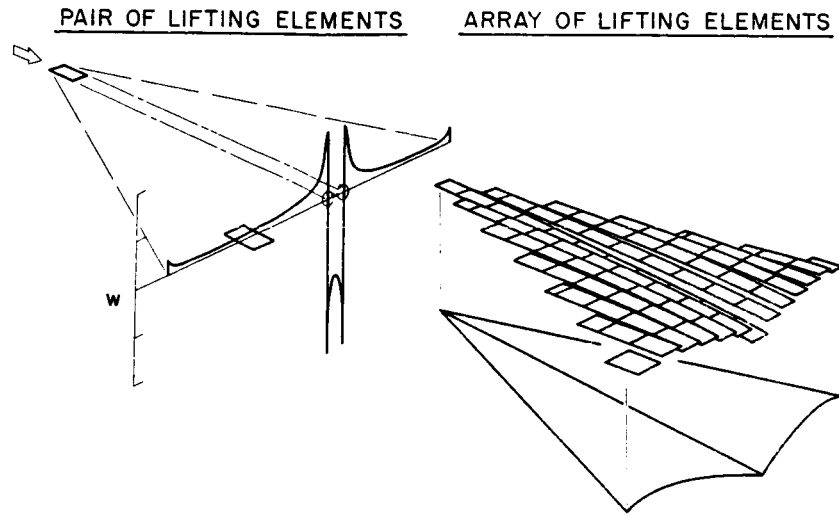


Figure 1

## DESIGN METHODS

WING SHAPE AND CORRESPONDING DRAG FOR SPECIFIED LOADING

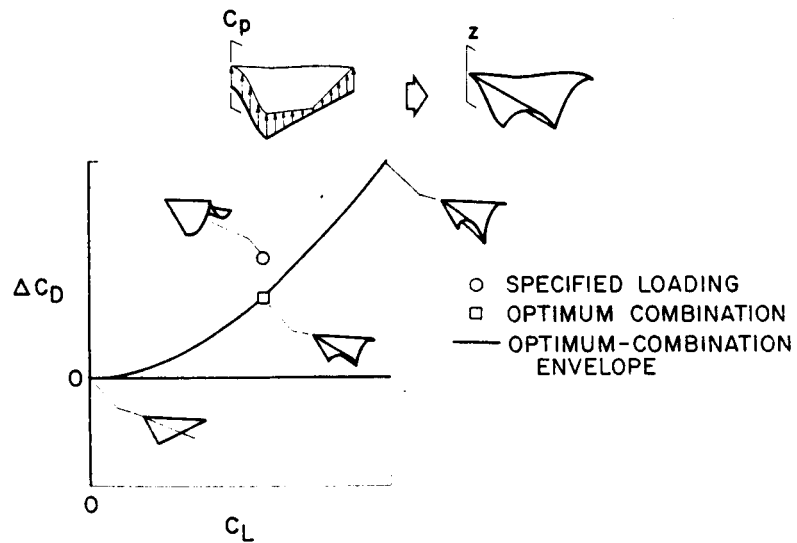


Figure 2

## ESTIMATION METHODS

### LOADING AND CORRESPONDING DRAG FOR SPECIFIED SHAPE

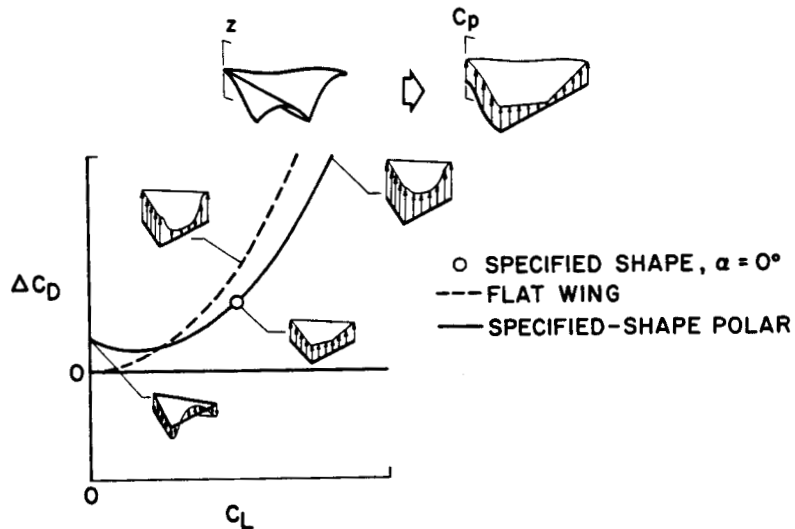


Figure 3

### AN EXAMPLE OF THE USE OF WING WARP

$M=2$

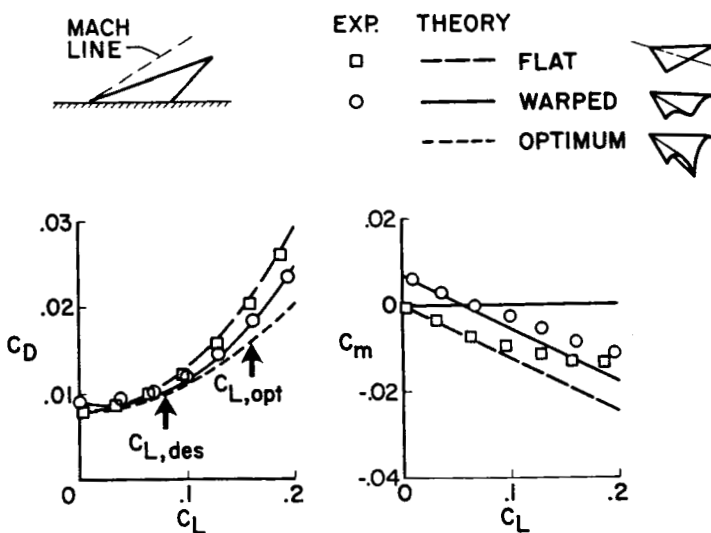


Figure 4

### EFFECT OF DESIGN LIFT COEFFICIENT

M=2

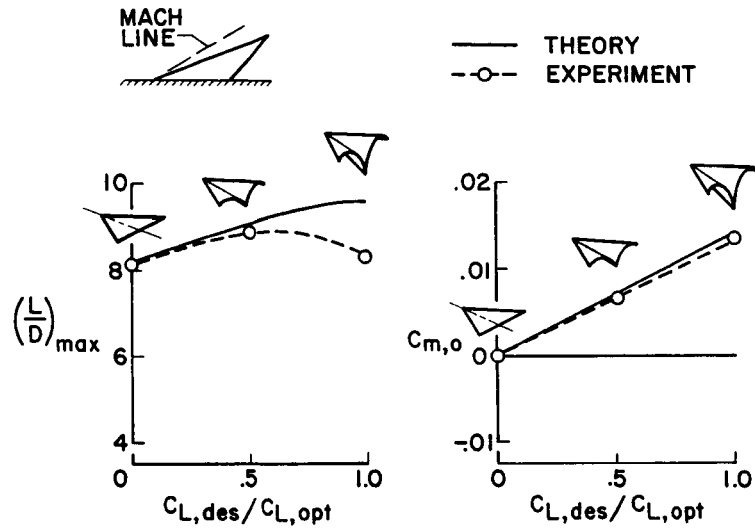


Figure 5

### EFFECT OF WING SHEAR EXPERIMENT; M=2

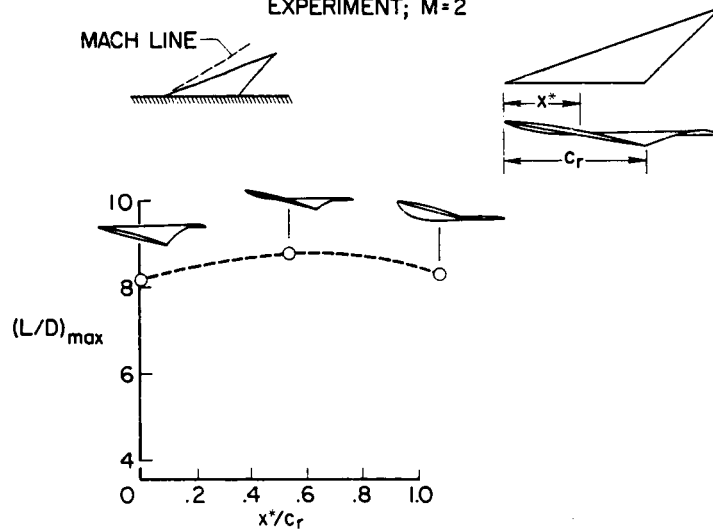


Figure 6

# EFFECT OF FUSELAGE ALINEMENT

M=2

EXPERIMENT  
THEORY

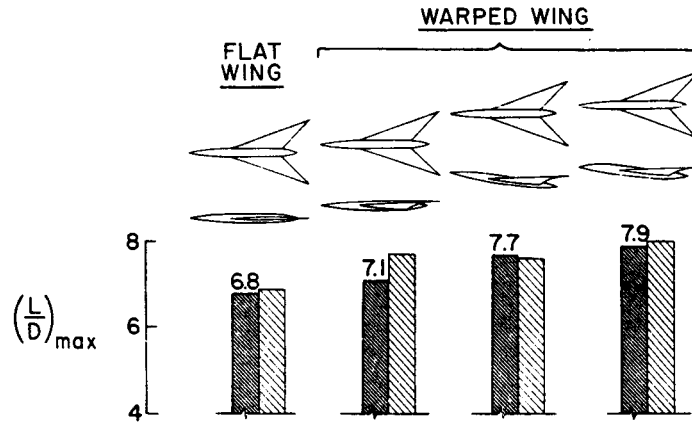


Figure 7

# CONCEPT OF MEAN CAMBER SURFACE

M = 2

EXP. THEORY

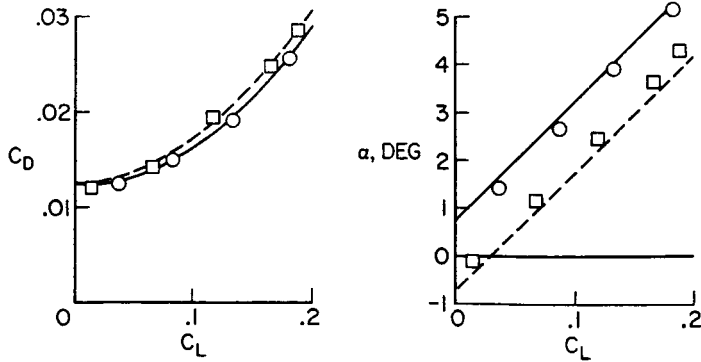
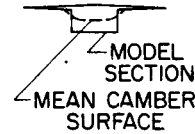
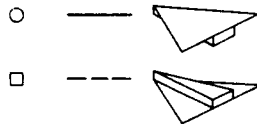


Figure 8

### EFFECT OF NACELLE ALINEMENT

$M=2; C_L=0.16$

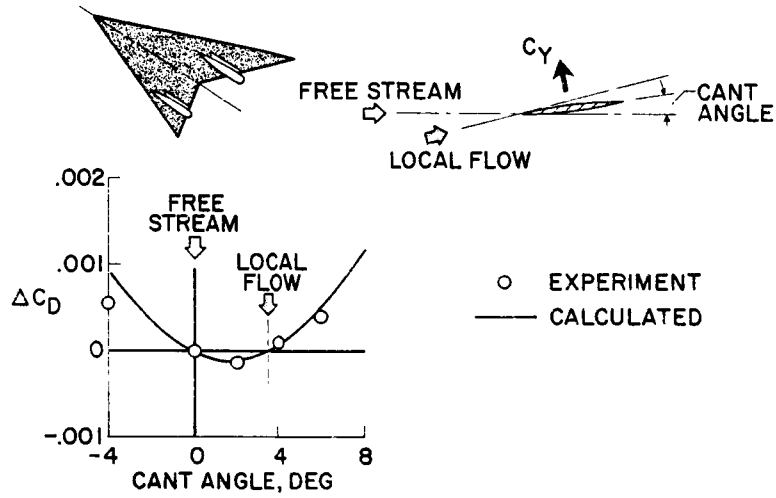


Figure 9

### A CONFIGURATION EMPLOYING OPTIMIZED LIFT DESIGN FEATURES

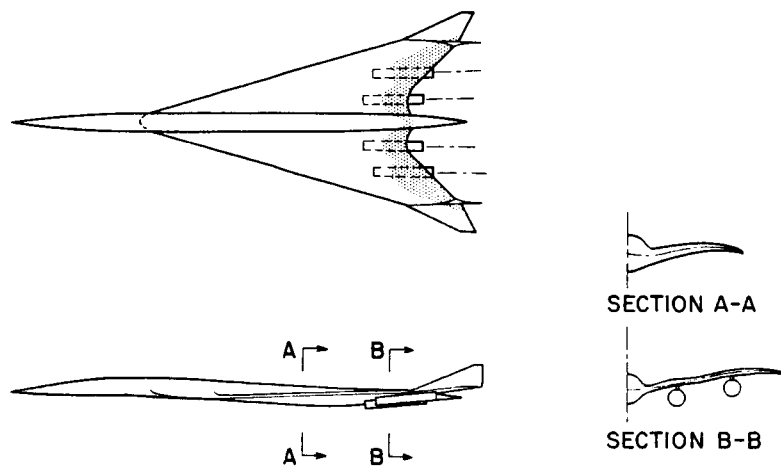


Figure 10

LIFT AND DRAG OF OPTIMIZED CONFIGURATION  
 $M=2.6; R_{\bar{c}}=4.5 \times 10^6$

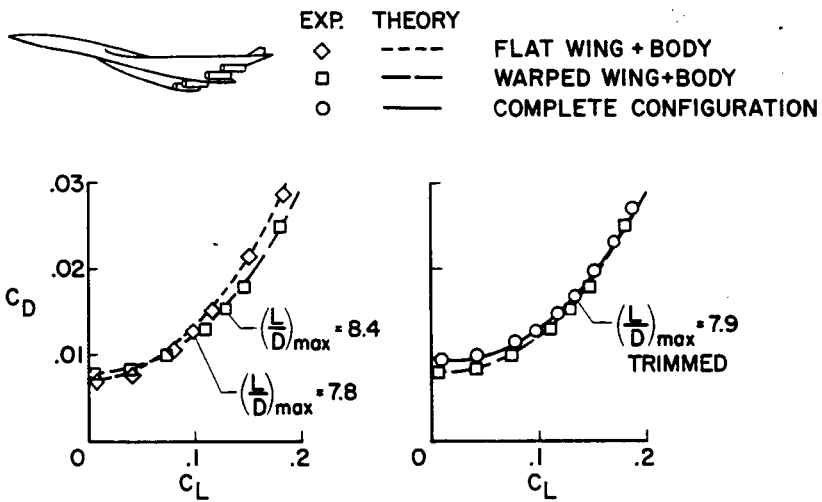


Figure 11

## 27. A NUMERICAL TECHNIQUE FOR ANALYSIS

### OF WAVE DRAG AT LIFTING CONDITIONS

By Roy V. Harris, Jr.  
NASA Langley Research Center

#### SUMMARY

A numerical technique for an application of the far-field linear theory is presented. This technique, when adapted to the high-speed electronic digital computer, provides a practical means for analyzing the total wave drag of an airplane at lifting conditions. An indication of the accuracy of the method at lifting conditions is shown by comparing measured pressure signatures at various azimuth angles about an airplane model with those predicted by theory. Calculations are made to illustrate some effects of configuration variables on the total wave drag of an airplane at lifting conditions.

#### INTRODUCTION

The recent development of numerical techniques for estimating and optimizing the lift-drag characteristics of supersonic cruise vehicles has led to significant improvements in aerodynamic performance at supersonic speeds (ref. 1). Most of these techniques have resulted from applications of existing theories to the high-speed electronic digital computer. As a result, analytical approaches which once were considered too complex for practical application can now be used to conduct aerodynamic trade studies in time to affect the preliminary design of airplanes.

Two approaches to the analytical drag buildup of an airplane at supersonic speeds are illustrated in figure 1. On the left of the figure is an illustrative drag polar for a supersonic-cruise vehicle with the cruise lift coefficient indicated by the solid symbol. For purposes of analysis, the drag is usually considered to be composed of skin-friction drag, zero-lift wave drag (or wave drag due to volume), and drag due to lift. This approach to the drag calculation was used in paper no. 26 by Harry W. Carlson and F. Edward McLean. It should be noted, however, that the drag due to lift consists of part vortex drag and part wave drag due to lift, and that the approach utilized by Carlson and McLean neglects any interference effects between the wave drag due to lift and that due to volume. A more fundamental approach, as illustrated by the bar graph on the right, is to consider the drag to be composed of its three basic elements, friction drag, total wave drag (including that due to lift), and vortex drag. Some aspects of the techniques for calculating skin-friction drag are discussed in paper no. 30. by John B. Peterson, Jr., and William J. Monta and in paper no. 31 by K. R. Czarnecki. The calculation of vortex drag at supersonic speeds for the condition of 100 percent leading-edge suction is the same as the

calculation of induced drag at subsonic speeds and depends only on the spanwise load distribution (ref. 2). For the more realistic condition in which little or no leading-edge suction is achieved at supersonic speeds, the problem is more complex and no suitable numerical technique presently exists. A numerical technique has been developed for the analysis of airplane wave drag at lifting conditions, and the purpose of this paper is to present this new application of the far-field linear theory which, when adapted to the high-speed electronic digital computer, provides a practical means for analyzing the total wave drag of an airplane at lifting conditions.

#### SYMBOLS

- A            equivalent-body area due to volume
- $C_D$         total-drag coefficient
- $C_{D,wave}$     wave-drag coefficient
- $C_L$         lift coefficient
- D            wave drag
- $l$            component of section lift along intercept of airplane and the Mach cutting plane, taken in direction of  $\theta$
- L            length of equivalent body
- M            Mach number
- p            reference static pressure
- $\Delta p$        incremental pressure due to flow field of airplane or model
- q            dynamic pressure
- S            total equivalent-body area
- x,y,z        coordinates along X, Y, and Z axes
- X,Y,Z        axis system of airplane or model
- $\beta = \sqrt{M^2 - 1}$
- $\theta$          azimuth angle referred to control cylinder, as shown in figure 2
- $\mu$          Mach angle

Primes are used to indicate derivatives with respect to x.

## DISCUSSION

### Calculation of Wave Drag at Lifting Conditions

The far-field linear-theory approach to supersonic flow is illustrated in figure 2. Consider an airplane in a steady supersonic stream and the cylindrical control volume suggested by Hayes in reference 2. Define the azimuthal angle  $\theta$  to be such that  $\theta$  is zero to the side of the airplane, with negative values below the airplane and positive values above it. Consider next a point on the surface of the control volume below the airplane and between the forward and rearward trailing Mach cones. The upstream Mach forecone from this point represents a surface of coincident signals in that all disturbances which lie in this plane arrive at the point simultaneously. It is possible, therefore, to determine a linear distribution of singularities that produce the same pressure disturbances as the airplane at the surface of the control volume. If the dimensions of the control volume are allowed to become infinitely large, the surfaces of coincident signals become planes in the vicinity of the airplane, and the linear source-sink distribution can be related to an equivalent-body area distribution (shown in fig. 2), which is determined by the intercepts of the planes of coincident signals (referred to as the "Mach cutting planes") and the airplane. The dotted lines shown in the area-distribution sketches indicate the equivalent-body area distribution due to volume and the solid lines indicate the total equivalent-body area distribution including the effects of lift.

The mathematical basis for the concept of equivalent area due to lift can be determined from the following equation for airplane wave drag (refs. 2 and 3) that was derived by use of the far-field linear-theory approach:

$$\frac{D}{q} = \frac{-1}{4\pi^2} \int_0^{2\pi} \int_0^L \int_0^L \left[ A''(x_1, \theta) - \frac{\beta}{2q} \lambda'(x_1, \theta) \right] \left[ A''(x_2, \theta) - \frac{\beta}{2q} \lambda'(x_2, \theta) \right] \log_e |x_1 - x_2| dx_1 dx_2 d\theta$$

This equation shows that the ratio of the wave drag to the free-stream dynamic pressure is a function of the second derivative of the equivalent-body area distribution due to volume  $A(x, \theta)$  and is also a function of a term that is proportional to the first derivative of the longitudinal distribution of lift  $\lambda(x, \theta)$ , as determined by the Mach cutting planes. If the term  $S(x, \theta)$  is so defined that

$$S''(x, \theta) = A''(x, \theta) - \frac{\beta}{2q} \lambda'(x, \theta)$$

then

$$S(x, \theta) = A(x, \theta) - \frac{\beta}{2q} \int_0^x \lambda(x, \theta) dx$$

It can thus be seen that  $S(x,\theta)$  is equal to the equivalent-body area distribution due to volume minus a term which has units of area and is a function of the longitudinal lift distribution as determined by the Mach cutting planes. This term is defined as the equivalent-body area due to lift. As illustrated in figure 2, the equivalent-body area due to lift varies from positive values below the airplane to negative values above the airplane. To the side of the airplane, the area due to lift becomes zero since there is no component of lift in this direction. It should be noted that the pressures that occur below the airplane cause the sonic boom along the ground track. Also, the equivalent-body area distribution corresponding to  $\theta = -90^\circ$  is used in the calculation of sonic-boom signatures. This subject is treated subsequently in paper no. 29 by McLean, Carlson, and Hunton.

An illustration of the procedure that has been programmed for determining the equivalent-body area distributions of an airplane at lifting conditions is presented in figure 3. The left side of the figure illustrates the procedure for determining the area due to volume and the right side of the figure illustrates the procedure used to determine the area due to lift. For calculation of the equivalent-body area due to volume, a mathematical representation of the airplane in terms of the  $x$ ,  $y$ , and  $z$  coordinates is used as input to the computer. The computer then solves for the normal projection of the area intercepted by the Mach cutting planes and thus defines the equivalent-body area due to volume  $A(x,\theta)$ . For calculation of the equivalent-body area due to lift, the wing camber surface in terms of  $x$ ,  $y$ , and  $z$  coordinates is used as input to the computer, and the lifting-surface pressure distribution is determined by the method which was described in paper no. 26 by Carlson and McLean. The computer then solves for the intercept of the Mach cutting planes and the wing camber surface and integrates the lifting pressures along this line to determine the component of force normal to the free stream and in the  $\theta$  direction. This component of force  $l(x,\theta)$  is then used to define the equivalent-body area due to lift. Finally, the computer sums the area due to volume and the area due to lift and solves for the total wave drag.

Direct comparisons between measured and computed wave drag at lifting conditions cannot be made because of the difficulty in determining the supersonic vortex drag. Numerous correlations at zero lift, however, have shown good agreement with the theory (ref. 4). An indication of the accuracy of the equivalent-body concept at lifting conditions can be made by comparing the measured pressure signatures at various azimuth angles about an airplane model with those predicted from its equivalent bodies. Such a comparison is made in figure 4. These data were taken at a Mach number of 1.4 and a lift coefficient of 0.10 for the configuration shown in the sketch. The upper three plots show the equivalent-body area distributions for the azimuth angle of  $-90^\circ$  (which is directly below the model), the azimuth angle of  $0^\circ$  (which is to the side), and the azimuth angle of  $90^\circ$  (which is above the model). The dashed lines indicate the area due to volume and the solid lines indicate the total equivalent-body area including the effects of lift. The three corresponding lower plots show a comparison between the pressure signatures predicted by theory and those measured in the wind-tunnel tests. The classic far-field type of pressure signature was not achieved in these tests because of the dimensional restraints imposed by the wind tunnel. The near-field effects have been included,

however, in the theoretical predictions (ref. 5). The good agreement between the measured and predicted pressure signatures at the various azimuth angles indicates that good agreement for the wave drag at lift should be expected.

Calculations of the wave drag at several lifting conditions have been made for the configuration shown in figure 4 at a Mach number of 2.7, and some of the results are shown in figure 5. The upper plots show the equivalent-body area distributions for lift coefficients of 0 and 0.08. The lower plots show the corresponding ratio of the equivalent-body wave drag to dynamic pressure as a function of the azimuth angle. The dashed lines indicate the integrated average and, hence, the total wave drag of the airplane. Consider, first, the results at zero lift for which the entire equivalent-body area is due to volume and, therefore, only positive areas exist. This portion of the figure is simplified by showing only selected area distributions for positive values of the azimuth angle. Comparing the shape of each equivalent-body area distribution with its corresponding drag contribution in the lower plot indicates that the equivalent bodies having the lowest fineness ratios and the steepest slopes make the largest contribution to the wave drag. For example, the equivalent body for an azimuth of  $90^\circ$  has the largest maximum area and the shortest length and, therefore, the largest contribution to the wave drag of the airplane. At a lift coefficient of 0.08, the area due to lift significantly alters the shape of the equivalent-body area distributions. The equivalent body for an azimuth of  $90^\circ$ , for example, although having the same length as the zero-lift condition, now has a much larger area change occurring over that length and therefore makes a much larger contribution to the airplane wave drag. Thus, a direct relationship can be established between the wave drag of an airplane at any given lift coefficient and its equivalent-body area distributions.

#### Configuration Effects on Wave Drag at Lifting Conditions

A comparison of the wave drag of two similar configurations at a Mach number of 2.0 and a lift coefficient of 0.10 is shown in figure 6. Both wing-body combinations were symmetrical, employed the same body, and had wings of equal area, equal span, and equal thickness ratio. One configuration, however, had a wing of delta planform, whereas the other had a wing of arrow planform. Comparing the equivalent-body area distributions at azimuth angles of  $-90^\circ$ ,  $0^\circ$ , and  $90^\circ$  indicates that the effect of spreading the lift over a greater length with the arrow wing is to reduce the rate of area growth of the equivalent bodies. The effect on the airplane wave drag is shown in the lower plots, where the total wave drag of the arrow-wing configuration is about 30 percent less than that of the delta-wing configuration.

Up to this point, all configurations that have been considered would be expected to have little or no interference between wave drag due to lift and wave drag due to volume. An example for which interference effects do exist between wave drag due to lift and that due to volume is shown in figure 7. Consider the arrow-wing-body configuration shown in figure 6, again at a Mach number of 2.0 and a lift coefficient of 0.10, but now with a high wing position as shown at the left in figure 7 and with a low wing position as shown at the right. The equivalent-body area distribution for  $\theta = 0^\circ$  (which is to the

side of the airplane) is unaffected by changes in the vertical position of the wing and, thus, is the same for both configurations. The Mach cutting planes intercept the high-wing configuration in such a manner that the area due to lift is shifted forward to the center line for the azimuth angle of  $90^\circ$  and is shifted rearward for the azimuth angle of  $-90^\circ$ . For the low-wing configuration, the reverse is true. The area due to lift is shifted rearward for an azimuth angle of  $90^\circ$  and forward for an azimuth angle of  $-90^\circ$ . The effects of interference between lift and volume on the total wave drag can be seen in figure 8. The bar graph shows a comparison of total wave-drag coefficient based on wing area for the low-wing, midwing, and high-wing configurations. For this example, the low-wing arrangement results in a 7.5 percent higher wave drag than the high-wing arrangement.

#### CONCLUDING REMARKS

A numerical technique has been presented for an application of the far-field linear theory. This technique, when adapted to the high-speed electronic digital computer, provides a practical means for analyzing the total wave drag of an airplane at lifting conditions. Numerous correlations at zero lift have shown good agreement with the theory. An indication of the accuracy of the method at lifting conditions was shown by comparing measured pressure signatures at various azimuth angles about an airplane model with those predicted by theory. The good agreement between the measured and predicted pressure signatures indicates that good agreement for the wave drag at lifting conditions should be expected. Results from a limited number of calculations showed some effects of differences in configuration on the total wave drag of airplanes at lifting conditions.

#### REFERENCES

1. Robins, A. Warner; Morris, Odell A.; and Harris, Roy V., Jr.: Recent Research Results in the Aerodynamics of Supersonic Vehicles. Paper No. 65-717, Am. Inst. Aeron. Astronaut., Nov. 1965.
2. Hayes, Wallace D.: Linearized Supersonic Flow. Rept. No. AL-222, North American Aviation, Inc., June 18, 1947.
3. Lomax, Harvard: The Wave Drag of Arbitrary Configurations in Linearized Flow as Determined by Areas and Forces in Oblique Planes. NACA RM A55A18, 1955.
4. Harris, Roy V., Jr.: An Analysis and Correlation of Aircraft Wave Drag. NASA TM X-947, 1964.
5. Middleton, Wilbur D.; and Carlson, Harry W.: A Numerical Method for Calculating Near-Field Sonic-Boom Pressure Signatures. NASA TN D-3082, 1965.

## TWO APPROACHES TO ANALYTICAL DRAG BUILDUP

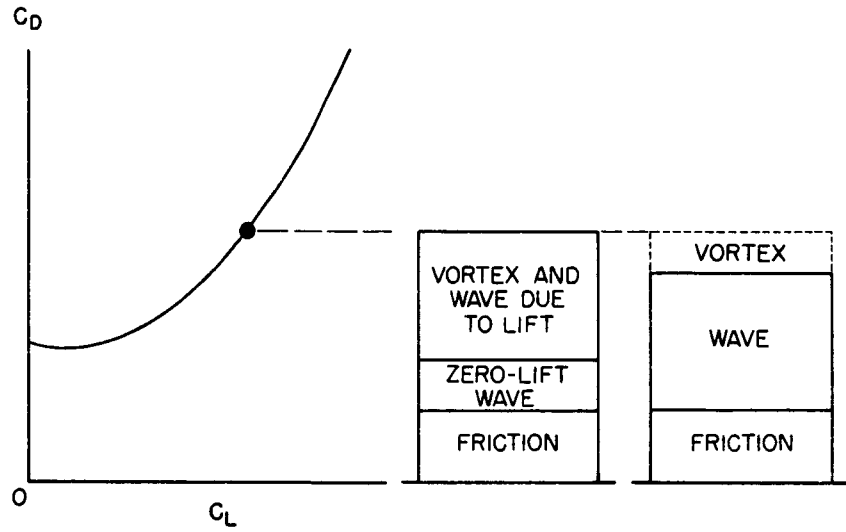


Figure 1

## ILLUSTRATION OF FAR-FIELD LINEAR-THEORY APPROACH

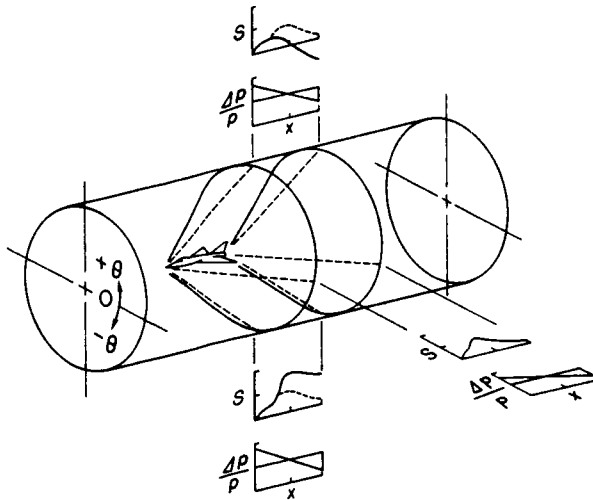


Figure 2

ILLUSTRATION OF MACHINE COMPUTING PROCEDURE

AREA DUE TO VOLUME =  $A(x, \theta)$

AREA DUE TO LIFT =  $\frac{\beta}{2q} \int_0^x l(x, \theta) dx$

MATHEMATICAL MODEL OF AIRPLANE

WING CAMBER SURFACE

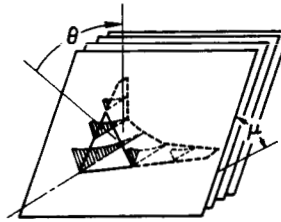
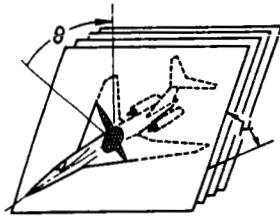
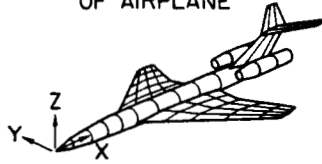


Figure 3

EXPERIMENTAL VERIFICATION OF EQUIVALENT-BODY CONCEPT

$M = 1.4; C_L = 0.10$

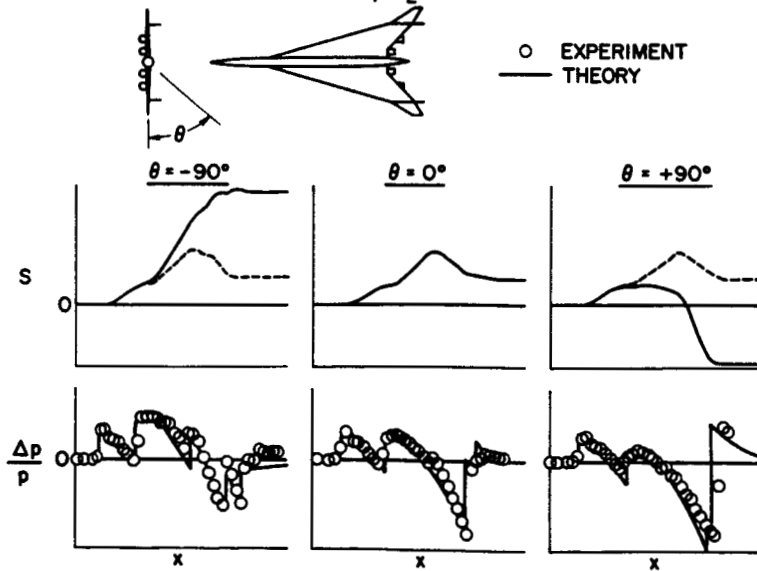


Figure 4

RELATIONSHIP BETWEEN WAVE DRAG AND EQUIVALENT-BODY AREA  
 $M = 2.7$

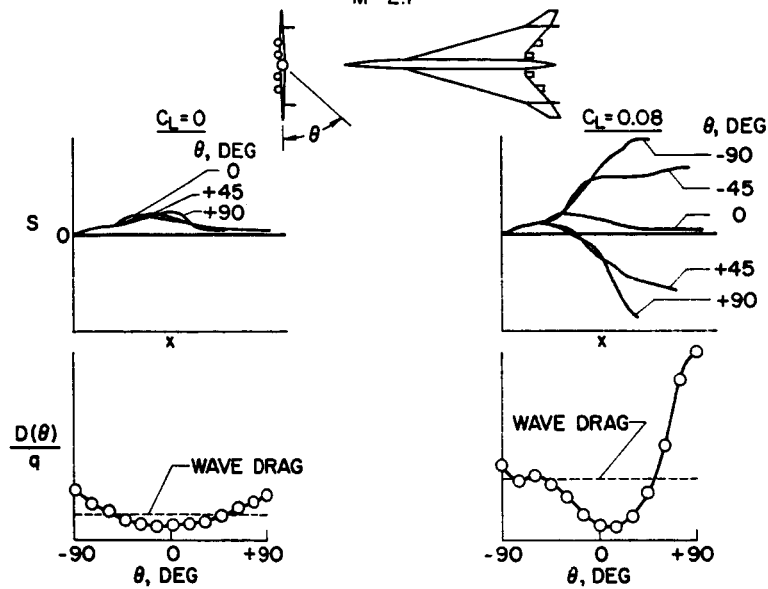


Figure 5

CONFIGURATION EFFECTS ON WAVE DRAG AT LIFT  
 $M = 2.0; C_L = 0.10$

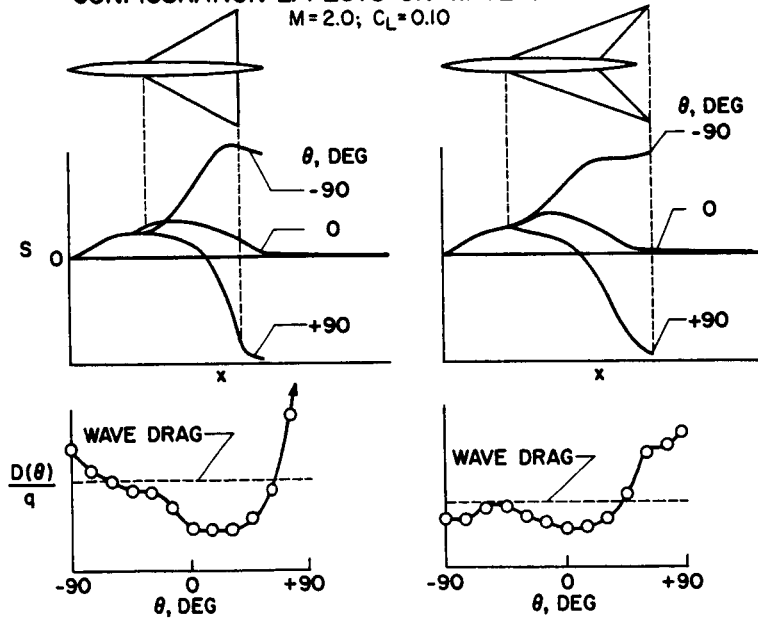


Figure 6

INTERFERENCE EFFECTS BETWEEN LIFT AND VOLUME  
 AREA DISTRIBUTIONS AT  $M=2.0$  AND  $C_L=0.10$

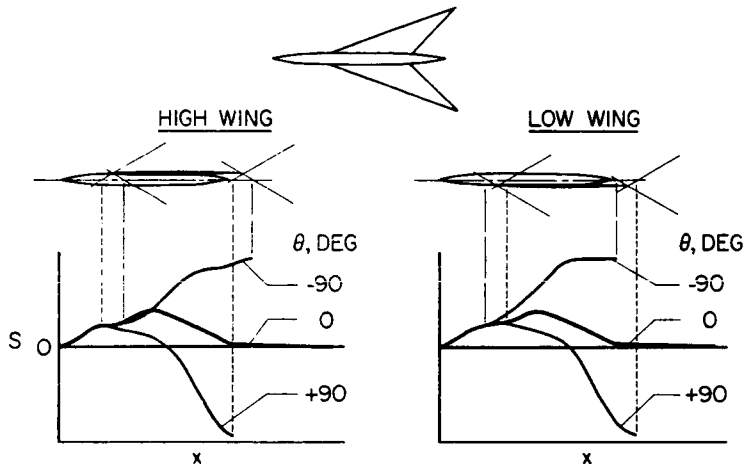


Figure 7

INTERFERENCE EFFECTS BETWEEN LIFT AND VOLUME  
 WAVE DRAG AT  $M=2.0$  AND  $C_L=0.10$

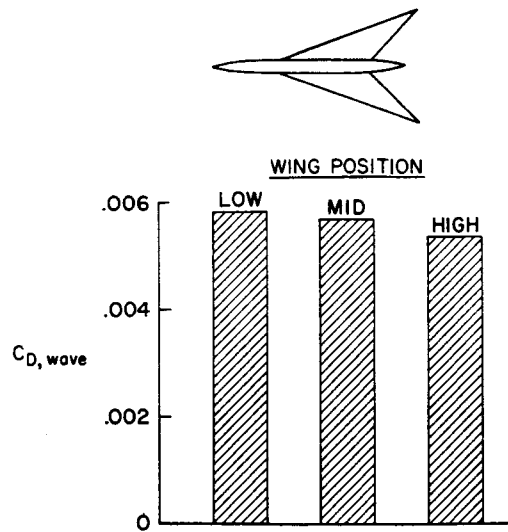


Figure 8

28. AN INTEGRATED APPROACH TO THE ANALYSIS AND DESIGN OF WINGS  
AND WING-BODY COMBINATIONS IN SUPERSONIC FLOW

By Ralph L. Carmichael, and Frank A. Woodward<sup>1</sup>  
NASA Ames Research Center

SUMMARY

A numerical procedure has been developed for analyzing wings and wing-body combinations and for designing optimum wing camber surfaces in the presence of a body. The method is very general and applies to wings of arbitrary planform and bodies of arbitrary cross section and camber. The procedure has been programmed for automatic computation and considerable effort has been made to allow the user to analyze a great variety of configurations with relatively simple input data.

For a given wing or wing-body combination, five classes of problems may be solved:

- (1) Wing warp required to support a given loading on the wing
- (2) Wing loading for a given wing warp
- (3) Pressures on the upper and lower surfaces of a warped wing of small but finite thickness
- (4) Minimum drag wing shape for a given lift constraint
- (5) Minimum drag wing shape for a given lift and moment constraint

The validity of the method has been confirmed by comparison with exact solutions to the linearized flow equation for several simple wings and wing-body combinations. In addition theoretical and experimental results have been compared for more complex configurations.

INTRODUCTION

The work described in this paper has been undertaken in an effort to develop a procedure for designing wing-body combinations with low drag at supersonic speeds.

Several methods have been published which enable one to compute the camber surface of minimum drag for an isolated wing at a given lift. None

---

<sup>1</sup>The Boeing Company

of these methods, however, considers the effect of the flow disturbance generated by the body on the shape of the optimum camber surface. The new method used in this work enables one to determine the lifting surface of minimum drag for a given value of lift in the presence of a body which may be at incidence relative to the free stream. In addition to this computation, the lift and drag of a configuration of given geometry may be determined, thereby providing the wing-body interference for configurations of arbitrary planform and camber. By using this procedure, one can assess the effects of such modifications as wing and body camber and incidence on the lift, drag, and moment characteristics of a given wing-body configuration.

The numerical procedure has been programed for automated computation for a great variety of configurations.

The theoretical analysis and the computer program used for the numerical computations in this paper were developed by the Aerodynamic Research Unit of the Airplane Group of The Boeing Company under NASA contract NAS2-2282. (See refs. 1 and 2.)

#### SYMBOLS

AR	aspect ratio
b	span
c	chord
$C_{L\alpha}$	slope of lift curve, $dC_L/d\alpha$ , per radian
$C_L$	lift coefficient
$C_m$	pitching-moment coefficient
$C_{m_0}$	pitching moment at zero lift
$\Delta C_p$	difference in pressure coefficient between upper and lower surfaces of wing
d	body diameter
L/D	lift-drag ratio
M	Mach number
P	difference between pressure coefficient at given angle of attack and pressure coefficient at zero angle of attack

r	body radius
$U_{\infty}$	free-stream velocity
x,y,z	Cartesian coordinates
x'	distance from the leading edge
$\alpha$	angle of attack
$\beta = \sqrt{M^2 - 1}$	
$\Lambda$	leading-edge sweep angle

#### METHOD OF ANALYSIS

The actual wing-body combination is replaced by distributions of singularities, which satisfy the linearized equation of supersonic flow, whose strengths are adjusted to satisfy the boundary conditions required by the geometry of the particular configuration. The wing warp and incidence are represented by distributions of vorticity corresponding to pressure differences across the wing. The wing thickness effect is given by sources and sinks located over the wing reference plane. The body thickness, camber, and incidence are simulated by line sources and doublets placed along the body reference axis. Finally, the interference effects of the wing on the body are cancelled by a distribution of vorticity on the surface of the body.

A typical wing-body combination is represented in figure 1. A grid which conforms to the general geometry of the configuration subdivides the wing and body into a large number of small panels. Each panel is a region over which a particular singularity strength is held constant. In this way, the continuous distribution of singularities representing the actual wing and body is approximated by simple functions with a finite range of values. Associated with each panel is a control point for matching the boundary conditions. At each control point, the flow must be tangential to the panel surface. In contrast to the wing-alone programs in common use which usually match only the downwash, the normal vector to the panel surface is used in this computation. The resultant normal velocity at each panel control point may now be expressed as a system of linear equations in terms of the singularity strengths. The coefficients of this system of equations are computed and stored as a matrix of aerodynamic influence coefficients. Then, for a given camber shape or pressure distribution, the various singularity strengths which satisfy all the boundary conditions are computed, and from these, the pressure distribution, lift, drag, and moment on the wing and body may be computed.

This method differs from that of Harris discussed in paper no. 27 in that the forces are computed by integration of the local pressures over the surface of the configuration. This method may be referred to as a near-field theory,

whereas that of Harris may be called a far-field theory. Of course, the results of the two methods will be identical except for the leading-edge suction force (on subsonic leading edges) which is not included in the surface-integration method.

Since the lift and drag of the configuration are functions of a finite number of real variables, the determination of the surface of minimum drag for a given lift constraint can now be solved by the Lagrange multiplier method.

A complete description of the theory and programing details is contained in references 1 and 2.

## RESULTS AND DISCUSSION

### Pressures and Forces on Flat Wings

The accuracy of the technique for computing pressures and forces on isolated wings is indicated in figures 2, 3, and 4. In each case, planforms have been selected for which exact solutions are known to the linearized equation of supersonic flow.

In figure 2, the program results are compared with exact conical flow theory for delta wings. Examples are shown for both subsonic and supersonic leading-edge wings. The symbols represent the pressures given by the program for wing chords located at 15, 45, and 75 percent of the semispan. The solid curves were computed from conical flow theory and may be found as solutions 3 and 6 in reference 3. The results agree quite well except at the sharp ridges of the supersonic solution. This rounding of the pressures computed by this program occurs because the pressures shown are actually average pressures over a wing panel.

The next example, illustrated in figure 3, is a test of the ability of the method to predict tip effect and to account for a subsonic trailing edge. The planform is a constant chord wing with  $\beta AR = 1.92$ . The leading and trailing edges are subsonic with  $\beta \cot \Lambda = 0.6$ . The program results along four different wing chords at 25, 50, 75, and 95 percent of the semispan are given by the symbols. The solid lines are the results given in reference 4 which were computed by the technique of superposing conical flows. As in the previous example, the program results agree very well except in the regions where the pressure distributions vary rapidly. Along the chords where the analytic solution varies rapidly, the program results underpredict the pressures in front of a sharp pressure drop and overpredict those behind the drop with the result that the integrated loadings are quite close to those of the analytic solution. This can be seen by the results shown in figure 4. The integrated loadings for a delta wing with  $60^\circ$  of leading-edge sweep are shown by the symbols. The solid curve is the well-known exact conical flow solution for a delta wing.

## Wing-Body Loadings

To confirm the accuracy of the method for calculating wing-body interference, a configuration whose loading has been measured was studied. A sketch of the configuration is presented as figure 5. The rectangular wing of aspect ratio 3 is mounted in the midwing position on a cylindrical body with an ogival nose. The wind-tunnel model was constructed with pressure taps along  $0^\circ$  and  $45^\circ$  meridian lines on the body and along several chords on the wing. The pressures measured at a Mach number of 1.48 and reported in reference 5 are compared with the program results in figure 6. The parameter  $P$  represents the value of pressure coefficient at angle of attack less the pressure coefficient at zero angle of attack. The predicted pressures agree quite well with those measured experimentally at  $\alpha = 2^\circ$ . As the angle of attack increased, the agreement was less satisfactory.

The examples shown and other test cases studied provide confidence in the ability of the method to predict loadings, forces, and moments to a degree of accuracy well within the requirements of engineering design.

## Prediction of the Effect of Wing and Body Camber

All the preceding results are accessible by established methods and serve to provide confidence in the method. The results to be shown in this section are not within the scope of any of the well-known methods.

The aerodynamic characteristics of a wing-body combination are sensitive to modifications, such as wing incidence relative to the body, wing or body camber, etc. In fact, it is precisely through modifications such as these that the characteristics of an airplane are brought in line with the design requirements. This computational method enables the designer to make accurate estimates of the effect of these changes to the basic configurations.

As reported in reference 6, a study was made of a series of wing-body wind-tunnel models employing various combinations of wing and body warps. The wing was arrow shaped with a leading-edge sweep angle of  $70^\circ$  and an aspect ratio of 2.24. Configuration 1 consisted of a flat wing on the uncambered body. Configuration 2 was made up of a cambered wing mounted on the uncambered body such that the body axis was at zero incidence when the wing was at the design condition; namely,  $C_L = 0.08$  and  $M = 2$ . Configuration 3 had the same cambered wing but the axis of the body was aligned with the root chord of the wing; also, the nose of the body was drooped and the rear portion of the body was swept upward.

The effects of these variations in model geometry are illustrated in figure 7. The symbols represent the experimental data reported in reference 6 and the curves are the program results. Since the theoretical method described in this paper does not include viscous effects, it was necessary to estimate the skin-friction drag in order to compare theoretical and experimental drag values. For this study, the skin friction was taken to be the difference between the experimental drag and the theoretical wave drag of the symmetrical

configuration at zero lift. This drag increment was then added to all the theoretical results to obtain the curves of theoretical lift-drag ratio as a function of lift coefficient. As predicted theoretically, none of the modifications changed the slope of the lift or moment curves. However, there were significant differences in the angle of attack at zero lift, pitching moment at zero lift, and maximum lift-drag ratio of the three configurations. As can be seen in figure 7, this method provides very accurate estimates of these quantities.

The characteristics of these wing-body combinations are somewhat different from those of the isolated wing, as can be seen in figure 8. The wing referred to in this figure is the cambered and twisted wing of reference 7 used in configurations 2 and 3 and the wing-body is configuration 2 of figure 7. One may observe that the wing alone has a  $C_{m_0}$  of approximately 0.01, whereas the body in combination with this wing has virtually no pitching moment at zero lift. In a similar manner, the lift curves of the two configurations are displaced. This indicates the importance of the body on the overall properties of wing-body combinations and may help to explain some of the discrepancies which have occurred between theory and experiment on wing-body combinations designed by wing-alone computing programs.

#### Effect of Body Size on Shape of the Minimum Drag Wing

One of the unique features of this computing procedure is the ability to compute the surface of minimum drag for a given wing planform in the presence of a body which may be at incidence relative to the wind. To illustrate the importance of the body flow field a study has been made of the minimum drag shape of a given wing with different size bodies. The basic wing planform is a simple delta wing with  $\beta \cot \Lambda = 0.3$  which corresponds to a leading-edge sweep of  $73.3^\circ$  at a Mach number of  $\sqrt{2}$ . The shape of the isolated wing with minimum drag for a fixed lift is illustrated in figure 9. Five sections are shown through this wing constructed with the leading edge in the x-y plane. The straight reference lines are the intersection of the section plane with the x-y plane. The same wing was then analyzed in combination with bodies of various sizes, one of which is shown in figure 10. The shape of the wing in the presence of this small body is similar to the shape of the isolated wing. This confirms the intuitive conclusion that a small body should have a small effect on the optimum wing shape. As the ratio of body diameter to wing span was increased, the shape of the minimum drag camber surface for the wing-body combination varied considerably from the shapes shown in figures 9 and 10. The effect on this shape of such variables as nose length and shape, incidence of the body relative to the free stream, and location of the wing on the body has not been adequately investigated at this time. For this reason, the shapes of these wings are not presented.

The theoretical model upon which these calculations are based assumes inviscid flow. For this reason, these shapes should be viewed cautiously as far as actual experimental performance is concerned.

## CONCLUDING REMARKS

The computational method whose results are described in this paper provides the designer with the ability to predict the longitudinal characteristics of wing-body combinations of arbitrary planform, camber, twist, and thickness. By this procedure one may accurately estimate many important performance parameters which are not available by the older techniques now in use. The technique is rapid and straightforward enough to be used in engineering design studies of families of configurations. The program is written for the class of computers in wide use by the aviation industry today. With the optimization capability built into the program it should be possible to calculate low-drag wing-body combinations to be used as the basis for designing efficient aerodynamic vehicles.

## REFERENCES

1. Woodward, F. A.; and Larson, J. W.: A Method of Optimizing Camber Surfaces for Wing-Body Combinations at Supersonic Speeds. Part I - Theory and Application. Doc. D6-10741, Pt. I, The Boeing Co., 1965. (Prepared for NASA under contract NAS2-2282.)
2. Brown, J. E.; Kawaguchi, A. S.; and LaRowe, Eugene: A Method of Optimizing Camber Surfaces for Wing-Body Combinations at Supersonic Speeds. Part II Digital Computer Program Description. Doc. D6-10741, Pt. II, The Boeing Co., 1965. (Prepared for NASA under contract NAS2-2282.)
3. Jones, Robert T.; and Cohen, Doris: High Speed Wing Theory. Princeton Univ. Press, 1960, pp. 156-157.
4. Cohen, Doris: Formulas for the Supersonic Loading, Lift and Drag of Flat Swept-Back Wings With Leading Edges Behind the Mach Lines. NACA Rept. 1050, 1951.
5. Nielsen, Jack N.: Quasi-Cylindrical Theory of Wing-Body Interference at Supersonic Speeds and Comparison With Experiment. NACA Rept. 1252, 1955. (Supersedes NACA TN 2677 by Nielsen and Pitts and NACA TN 3128 by Pitts, Nielsen, and Gionfriddo.)
6. Carlson, Harry W.: Longitudinal Aerodynamic Characteristics at Mach Number 2.02 of a Series of Wing-Body Configurations Employing a Cambered and Twisted Arrow Wing. NASA TM X-838, 1963.
7. Carlson, Harry W.: Aerodynamic Characteristics at Mach Number 2.05 of a Series of Highly Swept Arrow Wings Employing Various Degrees of Twist and Camber. NASA TM X-332, 1960.

TYPICAL PANEL LAYOUT FOR WING-BODY COMBINATION

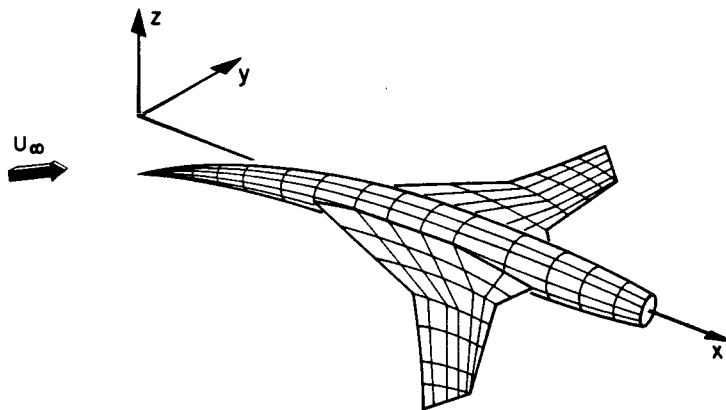


Figure 1

COMPARISON BETWEEN EXACT LINEAR THEORY AND PROGRAM RESULTS FOR DELTA WINGS

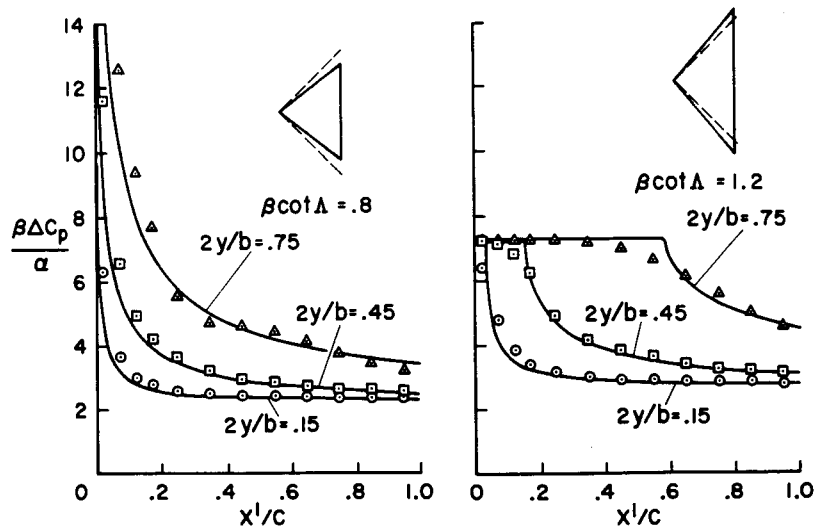


Figure 2

COMPARISON BETWEEN EXACT LINEAR THEORY AND PROGRAM RESULTS FOR A SWEEPED WING  
 $\beta R = 1.92; \beta \cot \Delta = .6$

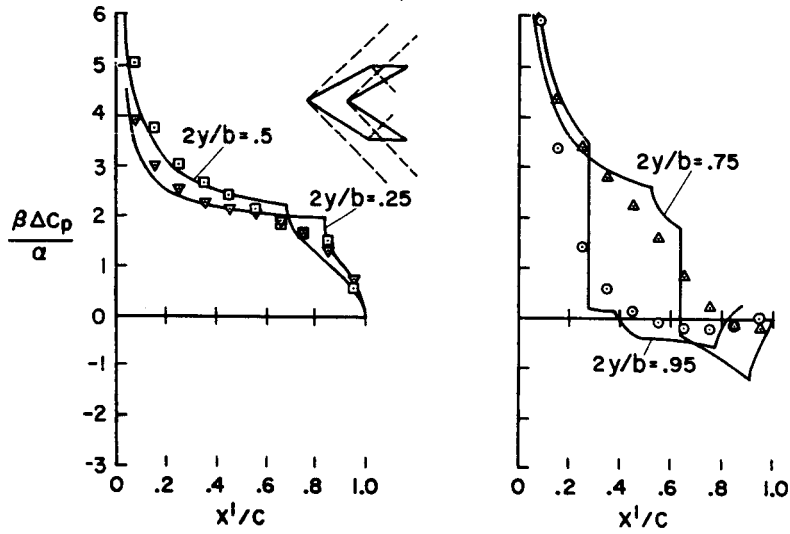


Figure 3

LIFT-CURVE SLOPE OF DELTA WING,  $\Delta = 60^\circ$

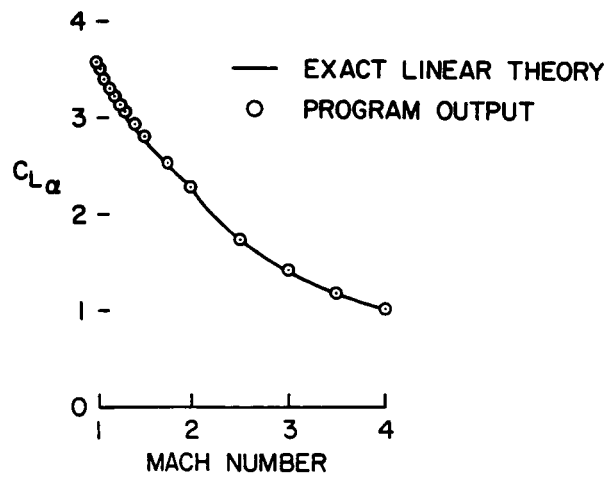


Figure 4

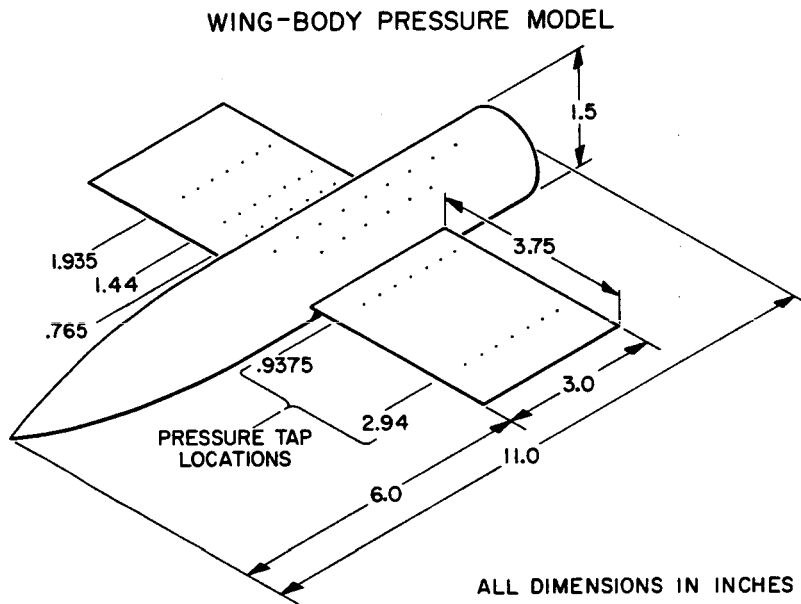


Figure 5

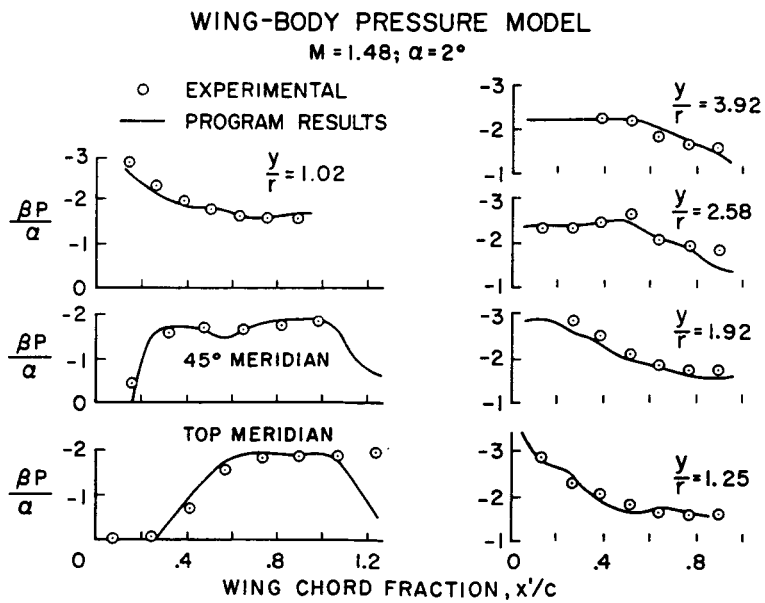


Figure 6

EFFECT OF WING AND BODY CAMBER AT M=2

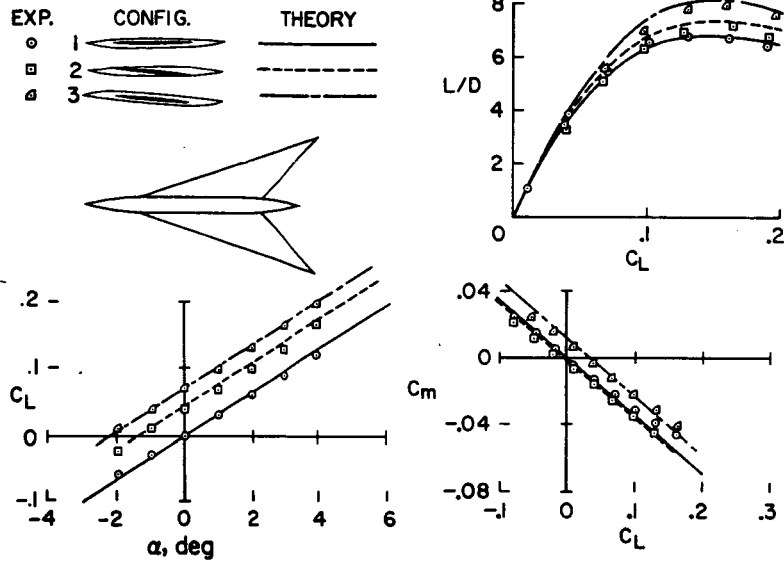


Figure 7

WING-ALONE AND WING-BODY CHARACTERISTICS AT M=2

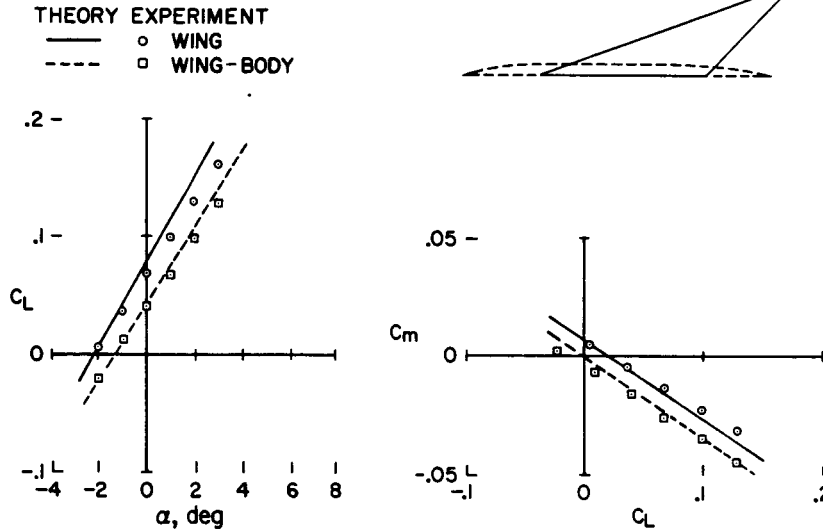


Figure 8

WING-ALONE OPTIMUM CAMBER SURFACE

$$\beta \cot \Delta = 3$$

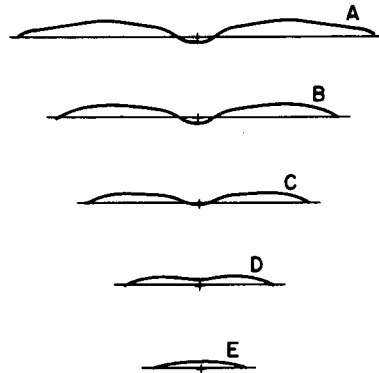
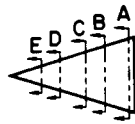
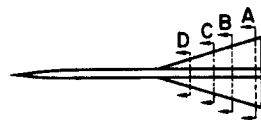


Figure 9

EFFECT OF BODY ON OPTIMUM CAMBER SURFACE



$$d/b = 0.1$$

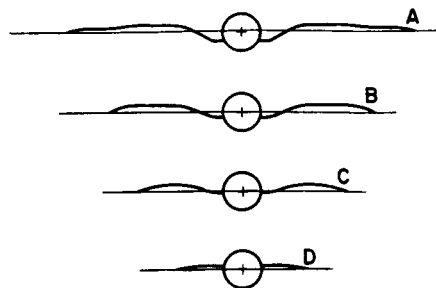


Figure 10

## 29. SONIC-BOOM CHARACTERISTICS OF PROPOSED SUPERSONIC AND HYPERSONIC AIRPLANES

By F. Edward McLean, Harry W. Carlson,  
NASA Langley Research Center

and Lynn W. Hunton  
NASA Ames Research Center

Existing theoretical methods of sonic-boom estimation have been used to determine the sonic-boom profiles of representative supersonic and hypersonic airplanes of the future. The sonic-boom characteristics of these future airplanes have been related to the sonic-boom characteristics of current supersonic airplanes. In the supersonic climb and cruise phases of flight, where the sonic-boom overpressure and impulse levels are relatively high, the use of near-field effects to modify the sonic-boom disturbance of these large future airplanes has been considered. The near-field investigation indicates that some reduction in overpressure and impulse might be possible.

### INTRODUCTION

Consideration was given to the aerodynamic drag problem associated with the pressure disturbances about a supersonic airplane in paper no. 27 by Harris. As the pressure disturbances generated beneath the airplane propagate to the ground they give rise to another problem - the problem of sonic boom. The noise and structural excitations which can result from sonic boom have raised serious questions as to the acceptability of routine flights of future supersonic and hypersonic airplanes over populated areas. Since these routine flights would be desirable from an economic standpoint, sonic boom has thus become a major consideration in the design and projected operation of these proposed airplanes.

During the course of research on the sonic-boom problem, theoretical methods have been developed which can be used to relate the sonic-boom disturbance to the characteristics of the airplane (refs. 1 to 4). These methods are based on the equivalent-body principles discussed in paper no. 27. Procedures have also been developed to account for the propagation of the sonic-boom disturbance from the airplane to the ground (ref. 5). The purpose of the present paper is to utilize these existing methods to relate the predicted sonic-boom characteristics of the large, heavy supersonic and hypersonic airplanes of the future to those of currently operational supersonic airplanes. Another purpose is to explore some means which might be used to modify the sonic-boom disturbances associated with these proposed airplanes.

## SYMBOLS

$A_e$	effective cross-sectional area due to a combination of volume and lift
$C_L$	lift coefficient
$h$	airplane altitude or perpendicular distance from model to measuring probe
$I$	positive impulse of pressure signature, $\int \Delta p \, dt$
$l$	length of airplane or model
$M$	Mach number
$p$	reference pressure
$\Delta p$	incremental pressure due to flow field of airplane or model
$\Delta p_{\max}$	maximum positive value of $\Delta p$
$t$	time
$t_r$	time required for pressure disturbance to rise from zero overpressure ( $\Delta p = 0$ ) to maximum overpressure ( $\Delta p = \Delta p_{\max}$ ) (see fig. 1)
$W$	airplane weight
$x$	distance measured along longitudinal axis of airplane or model
$\Delta x$	distance measured parallel to longitudinal axis of model from point in undisturbed stream to point on pressure signature
$\alpha$	varies as

## DISCUSSION

### Some Aspects of the Sonic-Boom Problem

A number of factors characterize the sonic-boom ground pressure disturbance. Figure 1 can be used to illustrate some of these factors which are considered in the present paper.

General signature characteristics.- Some important general characteristics of the ground pressure signature are illustrated in the upper portion of figure 1. In the signature at the upper left, which is drawn for the case of no atmospheric distortion,  $\Delta p_{\max}$  is the maximum rise in ground pressure due to the flow field of the airplane. Impulse is the time integral of the positive overpressure as indicated by the shaded portion of the signature. In some

manner, both of these signature characteristics influence the response of people and structures to sonic boom. During the early phases of the supersonic transport competition, concern over sonic boom led to the establishment of tentative upper limits on  $\Delta p_{\max}$  of 2.0 pounds per square foot in climb and 1.5 pounds per square foot in cruise.

The possible effects of random atmospheric disturbances on the sonic-boom signature are illustrated in the upper right portion of figure 1. As indicated, these atmospheric disturbances can either spike the signature and lead to higher values of overpressure than expected or round the signature and lead to lower values of overpressure than expected. In this paper only the nominal or averaged values of overpressure are considered, with the realization that random atmospheric distortions can lead to overpressures above and below the nominal.

Specific signature characteristics.- Some specific signature characteristics which may be important are illustrated in the lower portion of figure 1. A typical far-field N-wave is shown in the lower left of the figure. A far-field condition is said to exist when shocks from the individual airplane components have merged at the ground and have formed this N-wave pattern.

For some normal operating conditions of a large supersonic airplane, the ground pressure disturbance retains some features of the shock pattern from individual airplane components (ref. 6). In this near-field situation, the character of the pressure signature depends directly on the effective shape of the airplane. A typical twin-peaked near-field signature is illustrated in the lower center of figure 1.

Because of the dependence of the near-field pressure signature on the arrangement and operating condition of the airplane, a variety of near-field signatures is possible. Two near-field signatures discussed in this paper are the plateau signature and the signature with finite rise time, which are illustrated in the lower right of figure 1. It can be noted that the finite rise-time signature is characterized by a gradual buildup in overpressure. If the buildup in overpressure can be extended over an appreciable rise time  $t_r$  on the order of 10 to 15 milliseconds, the sonic-boom disturbance might be more acceptable than the typical disturbance which has an instantaneous pressure jump.

Although not an extremely important sonic-boom consideration, it can be noted that the pressures at the tail-shock portion of the signatures of figure 1 do not return to ambient conditions within the time shown in the figure. This feature of the sonic-boom disturbance is characteristic of the general solution of sonic-boom theory and has been observed in flight investigations.

The aspects of the sonic-boom problem which are illustrated in figure 1 do not represent all the factors which characterize the sonic-boom disturbance. Such factors as the energy spectrum of the pressure wave are also important. As yet, research has not conclusively established which of the several characteristics of the ground pressure disturbance governs human and structural response to sonic boom.

## Sonic-Boom Characteristics of Current Supersonic Airplanes

Flights of operational supersonic airplanes have provided valuable information for preliminary assessment of the sonic-boom problem of future airplanes. In addition to public- and structural-response data, these flights have provided a means for evaluating sonic-boom prediction methods. Correlations of measured and theoretical sonic-boom characteristics are presented in figure 2 for three current supersonic airplanes, the F-104 fighter, the medium B-58 bomber, and the large, heavy B-70 bomber. On the left side of the figure, the variation of maximum ground overpressure with altitude is shown for the three airplanes. The impulse characteristics are similarly shown on the right side of the figure. For both overpressure and impulse the theoretical predictions are represented as a band of values to account for differences in operating weight and Mach number at a given altitude. As indicated in the figure, the larger and more flexible the airplane, the wider the band of possible values of overpressure and impulse.

Three important points can be made with the results presented in figure 2. First, existing theoretical estimation methods provide a good assessment of the nominal overpressure and impulse characteristics of these three airplanes, which vary widely in size and general arrangement. Secondly, there are substantial increases in overpressure and impulse with increased airplane size. These increases in overpressure and impulse are due principally to increased weight, which varies from 27 000 pounds for the F-104 to approximately 100 000 pounds for the B-58 and to about 450 000 pounds for the B-70 airplane. The third important indication of the results presented in figure 2 is the near-field influence on the overpressure characteristics of the large B-70, as represented by the shaded band in the upper left of the figure. In the operating region where these near-field effects are present, the maximum ground overpressures of the B-70 are not much greater than those of the smaller B-58 airplane.

Selected ground pressure signatures from the large B-70 airplane can be used to illustrate the types of sonic-boom disturbance that can be expected from future supersonic and hypersonic airplanes. These signatures, which have minimal atmospheric distortions, are presented in figure 3. The measured and theoretical ground pressure signatures at the top of the figure illustrate the natural near-field tendencies of a large supersonic airplane which is operating at relatively low altitude, in this case, at an altitude of 31 000 feet. A typical near-field signature such as this would be expected during the early supersonic climb stages of flight of the large supersonic and hypersonic airplanes of the future.

The measured and theoretical B-70 ground pressure signatures at the bottom of figure 3, which are for a Mach number of 2.6 and a flight altitude of 66 000 feet, approach the typical far-field N-wave pattern. This type of ground pressure disturbance would be expected during the cruise flight of future supersonic airplanes and during the midclimb and cruise flight of future hypersonic vehicles.

For both flight conditions illustrated in figure 3, the major disagreement between theory and flight measurements is in the tail-shock portion of the

signature where the wake conditions and engine exhaust plume are difficult to define.

### Sonic-Boom Characteristics of Future Supersonic and Hypersonic Airplanes

Correlations such as those shown in figures 2 and 3 give some confidence that current theoretical methods can be used to analyze the sonic-boom characteristics of future airplanes in the supersonic speed regime. The scarcity of sonic-boom information at extremely high speeds gives somewhat less assurance as to the applicability of these methods at hypersonic speeds. On the basis of some preliminary studies of hypersonic configurations, however, it is believed that the present methods are adequate to illustrate the trends of sonic boom at hypersonic speeds.

The predicted sonic-boom overpressure and impulse characteristics of two research configurations, which have been chosen to illustrate the sonic-boom problem of proposed supersonic and hypersonic airplanes, are presented in figure 4. The supersonic configuration, represented by the solid curve, has a cruise Mach number of 2.7 and a design range of 3480 nautical miles. The hypersonic airplane, represented by the dashed curve, has a cruise Mach number of 6.0 and a design range of 5000 nautical miles. The predicted maximum ground overpressure and impulse of the two configurations are shown as they vary with range or distance from take-off.

The sonic-boom profiles indicate that both airplanes would generate relatively high ground overpressure and impulse during the early climb and acceleration phases of flight. In this flight regime, the natural near-field characteristics of these large airplanes serve to reduce the overpressures some 10 to 15 percent below the levels which would be expected on the basis of the far-field assumptions of sonic-boom theory. At cruise conditions, which are represented by the flat portions of the profiles, the overpressure and impulse would be at reduced levels. The cruise values would be expected to lie between the levels measured during high-altitude flights of the current B-58 and B-70 airplanes. As the two airplanes approach their destination and descend toward the ground, the overpressure and impulse would be expected to increase from the cruise values. In this descent phase of flight the near-field effects would also be present.

The basic factor which leads to the relatively high values of overpressure and impulse in the early stages of the two flight profiles shown in figure 4 is the initiation of supersonic climb and acceleration at relatively low altitudes. This low-altitude initiation of supersonic flight is an economic consideration based on the desire for minimum block time and for minimum propulsion-system and airplane weight. Although other configurations might produce variations from the sonic-boom profiles used in this illustration, the economic factors would tend to dictate similar trends in sonic-boom characteristics.

As indicated in figure 4, the regions of relatively high overpressure and impulse are limited in range to some 200 to 400 nautical miles in climb and to some similar range in descent. Although this range of relatively high sonic-boom exposure is limited, it might be desirable to alter the shape and magnitude of the sonic-boom disturbance in these flight regimes. The rest of the present paper considers the possibility of such an alteration.

### Near-Field Considerations

A possible means for altering the shape and magnitude of the sonic-boom disturbance from a large airplane is to make use of the natural near-field characteristics of such an airplane. Two important factors which influence the near-field characteristics are the area distribution of the airplane due to combined volume and lift effects and the length of the airplane. The supersonic airplane considered in figure 4 is used to illustrate these area and length effects.

The influence of effective area distributions  $A_e$  on the character of the sonic-boom disturbance is illustrated in figure 5(a). The effective area distribution and predicted ground-track pressure signature corresponding to a typical climb condition of the original design are shown at the top of the figure. The predicted sonic-boom disturbance is a twin-peaked near-field signature. A modification of the original effective area distribution to the shape shown in the lower right of figure 5(a) would theoretically alter the pressure disturbance to the plateau shape at the bottom of the figure with considerably reduced overpressures.

The effect of airplane length on near-field characteristics is illustrated in figure 5(b). The area distribution at the upper right of the figure corresponds to the original area distribution with the length increased from 230 to 280 feet. This extension of length induces more near-field effects in the signature and reduces the maximum overpressure. The effective area distribution and signature at the bottom of figure 5(b) show the combined effects of increased length and area modification on the near-field signature. For this illustrative example, the resultant maximum overpressure is less than half of the original value. Although no attempt has been made to modify the tail shock, note that, for this particular application, the pressure jump at the aft portion of the signature is no greater than the modified bow pressure rise.

Airplane modification for plateau pressure.- If the near-field characteristics of the original and modified area distributions are determined for a number of airplane lengths, the design requirements for a plateau pressure signature of a given maximum overpressure can be established.

Figure 6 presents the results of such a study for a typical supersonic airplane climb condition of  $M = 1.4$ ,  $W = 400\ 000$  pounds, and  $h = 40\ 000$  feet. In this figure the circular symbol represents the maximum overpressure of approximately 2.2 pounds per square foot for the original design area distribution and design length of 230 feet. The curves indicate the variation of maximum ground overpressure with airplane length for the original effective area

distribution (dashed curve) and for a modified area distribution which varies as  $x^{3/2}$  to provide a plateau pressure distribution (solid curve). The manner in which the original and modified pressure signatures vary with length is indicated by the inset sketches.

The obvious point to be made from the results is that, for this typical climb condition, modification of the airplane effective area distribution can lead to substantial reductions in maximum overpressure both within the airplane design length of 230 feet and at greater lengths. At a given airplane length, the area modification also resulted in a 6- to 7-percent decrease in impulse. Airplane weight, of course, influences the overpressure levels shown. For example, an increase in climb weight from 400 000 to 500 000 pounds would require a 25- to 30-foot extension in length to maintain a given overpressure level.

At altitudes and Mach numbers associated with the cruise conditions of a large supersonic airplane, the design requirements for near-field effects would be more stringent than at climb conditions. The higher altitudes and Mach numbers increase the lift contribution to the effective area distribution which leads to a more rapid approach to far-field conditions. These factors are illustrated in figure 7 for a typical cruise Mach number of 2.7, a weight of 350 000 pounds, and an altitude of 65 000 feet. For these conditions, the predicted ground pressure disturbance for the original design condition of the supersonic airplane (represented by the circular symbol) would be a typical far-field N-wave with a maximum overpressure of about 1.55 pounds per square foot. As indicated in the figure, within the original design length of 230 feet, for these cruise conditions, the plateau pressure disturbance cannot be generated. As airplane length is increased, however, near-field effects are induced in the original configuration, as indicated by the inset pressure signatures. At airplane lengths greater than about 260 feet, it is once again possible to modify the configuration so as to produce a plateau pressure disturbance with reduced maximum overpressure and impulse.

Wind-tunnel investigation of airplane modification for plateau pressure.- To investigate the applicability of the plateau pressure modification previously discussed, small 4-inch complete models of the original and modified supersonic configuration have been tested in the Langley 4- by 4-foot supersonic pressure tunnel. The airplane models were designed to simulate the typical climb condition considered in figure 6. Some results of the wind-tunnel investigation are presented in figure 8.

Plan views of the original and modified configurations are presented at the top of the figure. The rather modest changes in effective area distribution which were theoretically required to produce the plateau pressure disturbance can best be seen in the effective area distribution plots in the middle of the figure. The purpose of the area modification was to smooth the original distribution and reduce the rate of change of area with longitudinal distance.

The measured and theoretical signatures at the bottom of figure 8, which correspond to a station 10 body lengths below the models, indicate that the desired effect of replacing the twin-peaked signature of the original

configuration with a plateau pressure disturbance was essentially accomplished. Differences between the measured and theoretical signatures of the modified model could be attributed to slight differences between the actual and specified models.

It should be pointed out that the sonic-boom disturbance along the ground track of a supersonic airplane depends only on a particular effective area distribution. The wave drag, on the other hand, depends on the averaged contributions of a number of equivalent bodies corresponding to all orientations of the airplane. (See paper no. 27 by Harris.) Consideration of the near-field modification discussed would depend on a complete analysis of the consequences of the modification on other aspects of the airplane performance. For the particular modification considered in this figure, the wave drag of the configuration was reduced at the climb Mach number of 1.4 with little or no penalty for other flight conditions. This effect would not necessarily hold for some other configuration.

Airplane modification for finite rise time.- As mentioned earlier, a sonic-boom disturbance with an appreciable rise time might be more desirable than the typical disturbance which has an instantaneous pressure rise. Accordingly, a near-field investigation of the supersonic airplane of the previous discussion was made to determine the design requirements for such a finite rise-time signature. This design requirement would increase the chances for a substantial rise time. Small rise times have been measured during flights of current airplanes.

The results of the rise-time investigation for a typical supersonic climb condition are shown in figure 9. The variation of maximum overpressure with length of the original configuration is once again represented by the dashed curve. The area development  $x^{5/2}$ , which is one requirement for finite rise time, is represented by the solid curve. The results indicate that even for this climb condition some extension in airplane length is required to generate the signature with gradual pressure rise and that some increases in maximum overpressure and impulse appear to be necessary to achieve this type of pressure disturbance. With lengths above about 260 feet, however, appreciable rise times appear to be possible. The variation of rise time from the cutoff point to the maximum length is from 0 to 160 milliseconds.

Figure 10 shows the results of a similar analysis of the finite rise-time signature for typical supersonic cruise conditions. The results indicate that the design requirements for gradual pressure rise in this cruise speed regime are too stringent to be met within practical airplane lengths and weights.

The foregoing near-field analyses of a large supersonic airplane suggest that substantial modifications of the shape and magnitude of the sonic-boom disturbances may be possible at typical climb conditions. Less substantial, but perhaps important modifications can be made in the sonic-boom signatures of long airplanes at supersonic cruise flight conditions. Similar analyses of a typical hypersonic configuration show similar possibilities for signature modification in these flight regimes. At hypersonic speeds, however, near-field effects are not to be expected.

## CONCLUDING REMARKS

Existing theoretical methods of sonic-boom estimation have been used to determine the sonic-boom profiles of representative supersonic and hypersonic airplanes of the future. The sonic-boom characteristics of these future airplanes have been related to the sonic-boom characteristics of current supersonic airplanes. In the supersonic climb and cruise phases of flight, where the sonic-boom overpressure and impulse levels are relatively high, the use of near-field effects to modify the sonic-boom disturbance of these large future airplanes has been considered. The near-field investigation indicates that some reduction in overpressure and impulse might be possible.

## REFERENCES

1. Whitham, G. B.: The Flow Pattern of a Supersonic Projectile. Commun. Pure Appl. Math., vol. V, no. 3, Aug. 1952, pp. 301-348.
2. Walkden, F.: The Shock Pattern of a Wing-Body Combination, Far From the Flight Path. Aeron. Quart., vol. IX, pt. 2, May 1958, pp. 164-194.
3. Carlson, Harry W.: Correlation of Sonic-Boom Theory With Wind-Tunnel and Flight Measurements. NASA TR R-213, 1964.
4. Middleton, Wilbur D.; and Carlson, Harry W.: A Numerical Method for Calculating Near-Field Sonic-Boom Pressure Signatures. NASA TN D-3082, 1965.
5. Friedman, Manfred P.; Kane, Edward J.; and Sigalla, Armand: Effects of Atmosphere and Aircraft Motion on the Location and Intensity of a Sonic Boom. AIAA J., vol. 1, no. 6, June 1963, pp. 1327-1335.
6. McLean, F. Edward: Some Nonasymptotic Effects on the Sonic Boom of Large Airplanes. NASA TN D-2877, 1965

# SOME ASPECTS OF THE SONIC-BOOM PROBLEM

## GENERAL SIGNATURE CHARACTERISTICS



## SPECIFIC SIGNATURE CHARACTERISTICS

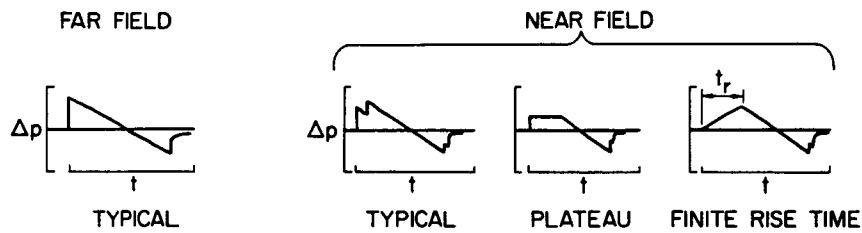


Figure 1

## SONIC-BOOM CHARACTERISTICS OF CURRENT SUPERSONIC AIRPLANES

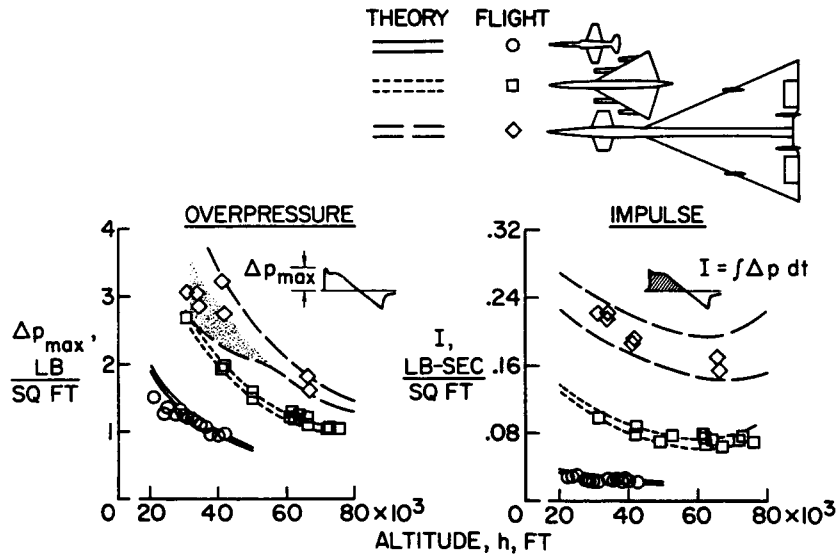


Figure 2

### CHARACTERISTIC PRESSURE SIGNATURES OF LARGE SUPERSONIC AIRPLANE

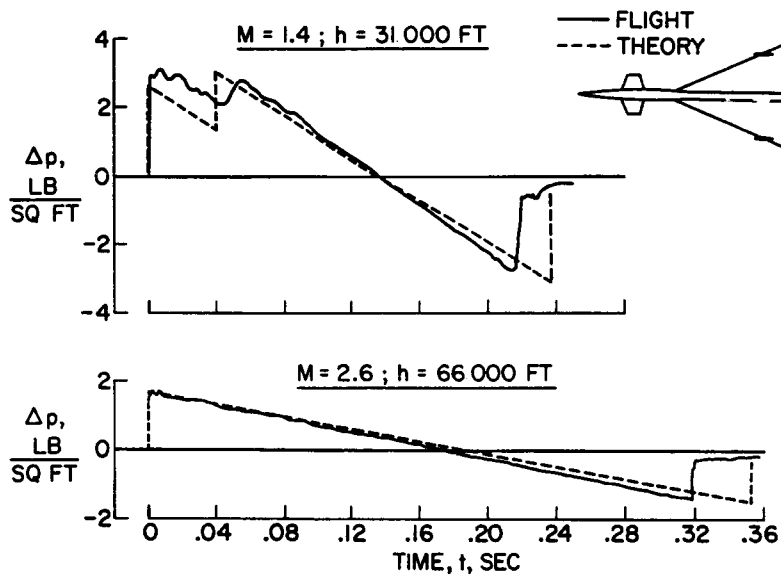


Figure 3

### SONIC-BOOM PROFILES OF LARGE SUPERSONIC AND HYPERSONIC AIRPLANES

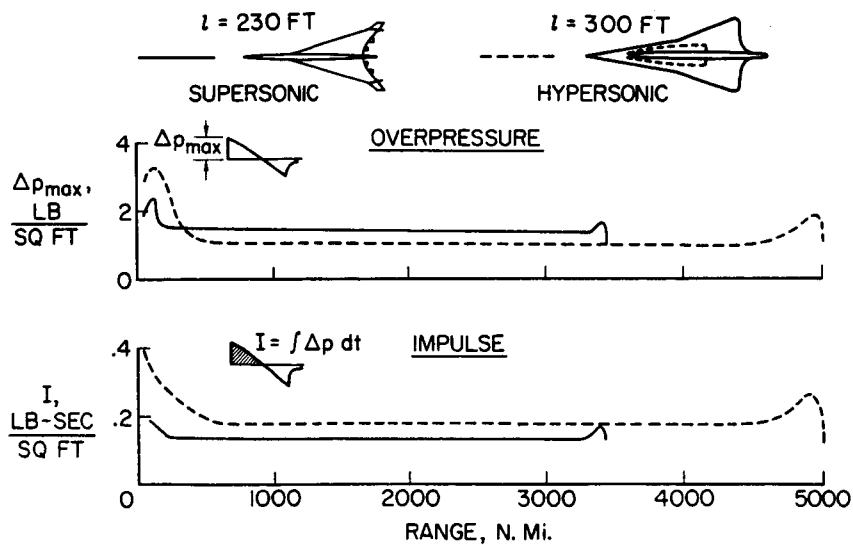


Figure 4

**NEAR-FIELD CONSIDERATIONS**  
 INFLUENCE OF AIRPLANE EFFECTIVE AREA DISTRIBUTION ;  $l = 230$  FT

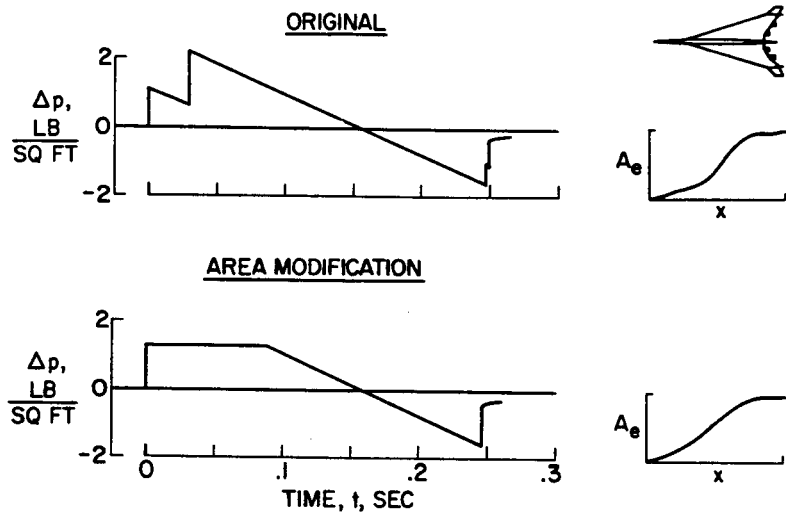


Figure 5(a)

**NEAR-FIELD CONSIDERATIONS**  
 INFLUENCE OF AIRPLANE LENGTH ;  $l = 280$  FT

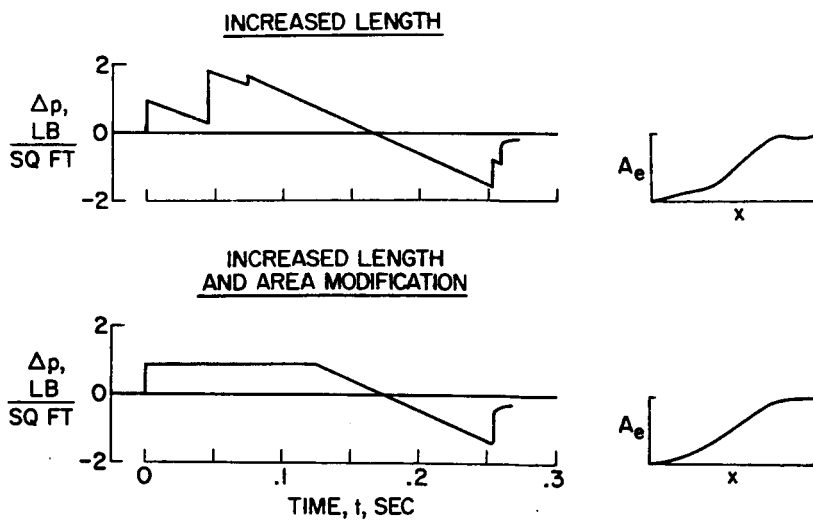


Figure 5(b)

AIRPLANE MODIFICATION FOR PLATEAU PRESSURE SIGNATURE  
 CLIMB;  $M=1.4$ ;  $W=400\ 000\ \text{LB}$ ;  $h=40\ 000\ \text{FT}$

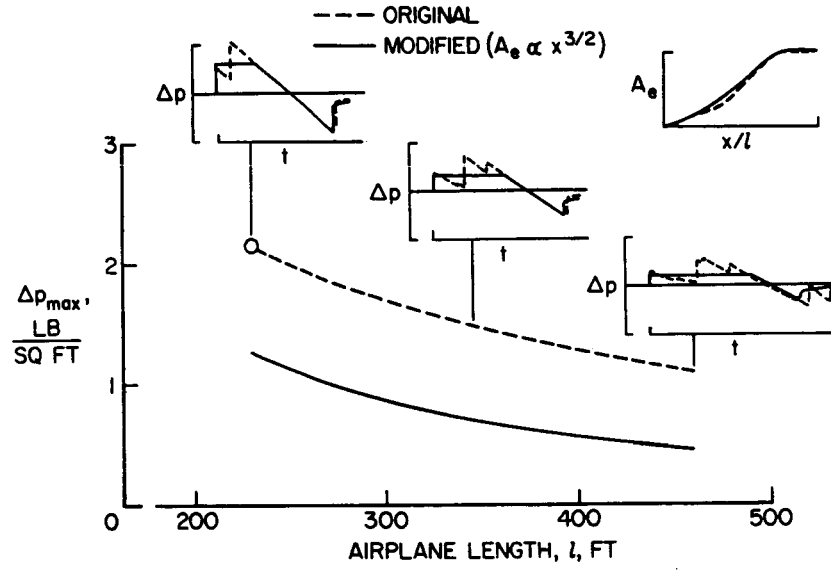


Figure 6

AIRPLANE MODIFICATION FOR PLATEAU PRESSURE SIGNATURE  
 CRUISE;  $M=2.7$ ;  $W=350\ 000\ \text{LB}$ ;  $h=65\ 000\ \text{FT}$

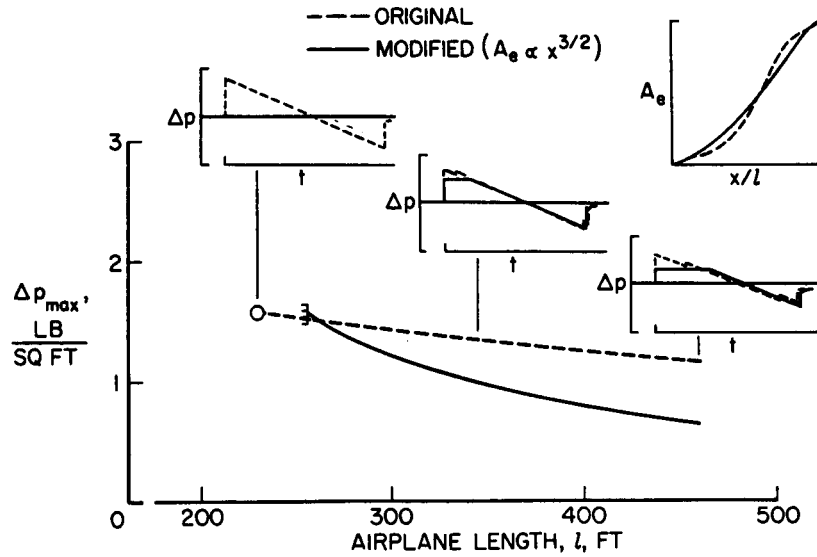


Figure 7

RESULTS OF COMPLETE-MODEL TESTS OF AIRPLANE MODIFICATION

$M=1.41$  ;  $C_L=0.1$  ;  $h/l=10$

○ EXPERIMENT  
— THEORY

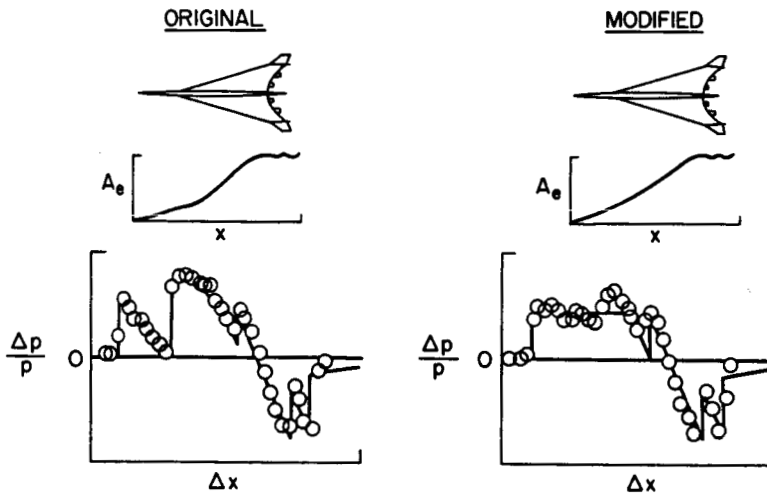


Figure 8

AIRPLANE MODIFICATION FOR SIGNATURE WITH FINITE RISE TIME CLIMB ;  $M=1.4$  ;  $W=400\ 000\ \text{LB}$  ;  $h=40\ 000\ \text{FT}$

--- ORIGINAL  
— MODIFIED ( $A_e \propto x^{5/2}$ )

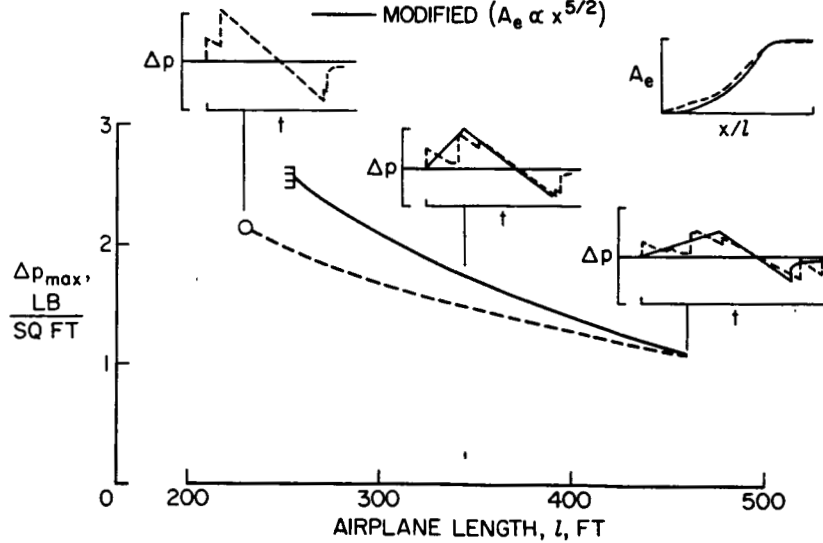


Figure 9

AIRPLANE MODIFICATION FOR SIGNATURE WITH FINITE RISE TIME  
 CRUISE ; M = 2.7 ; W = 350 000 LB ; h = 65 000 FT

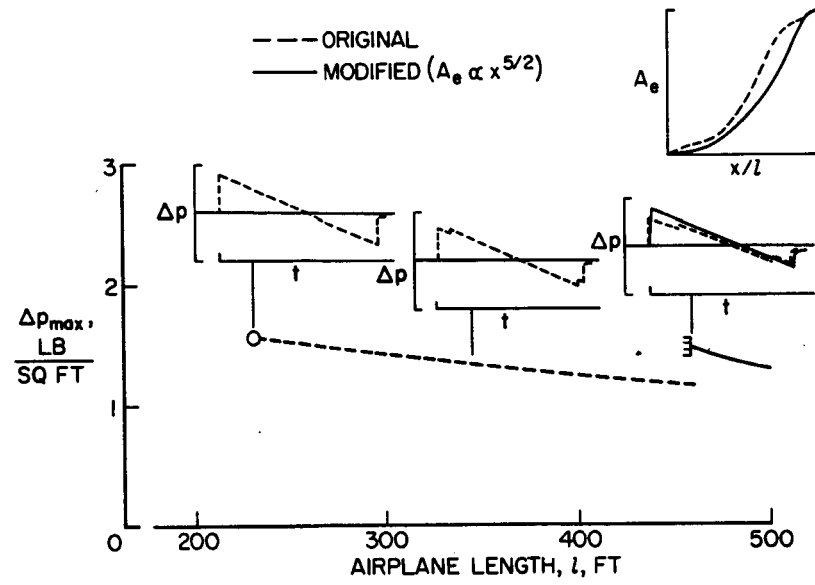


Figure 10

30. CONSIDERATIONS REGARDING THE EVALUATION AND REDUCTION  
OF SUPERSONIC SKIN FRICTION

By John B. Peterson, Jr., and William J. Monta  
NASA Langley Research Center

SUMMARY

A comparison is made between previously published experimental data for supersonic turbulent boundary-layer skin friction and the skin-friction predictions obtained by using the Sommer and Short T' and Spalding and Chi methods. Also, various methods for reducing skin friction on the supersonic transport are discussed.

INTRODUCTION

Although the wave drag and the drag due to lift of the proposed supersonic transport configurations have been greatly reduced as the design has progressed, the skin-friction drag has remained relatively constant. Because the skin-friction drag of a typical supersonic transport is a large part of the total drag, reduction of the skin-friction drag is potentially a good means of obtaining drag reductions.

Figure 1 shows a breakdown of the drag of a typical supersonic transport cruising at a Mach number of 2.7 and an altitude of 65 000 ft. As can be seen, skin friction accounts for about 40 percent of the total drag. Since a typical transport has about 100 counts of total drag at cruise, the skin-friction drag is about 40 counts. For each count that the drag can be reduced, the lift-drag ratio can be increased by about 0.1.

Several methods which can be used to reduce the skin-friction drag on a supersonic transport will be reviewed in this paper. In addition, methods for calculating skin-friction drag will be reviewed.

SYMBOLS

b	wing span
c	wing chord
$C_D$	drag coefficient
$C_{D,F}$	drag coefficient due to skin friction

$\Delta C_{D,F}$	increment in drag coefficient due to skin friction
$C_F$	average skin-friction coefficient
$C_{F,aw}$	adiabatic wall average skin-friction coefficient
$C_{F,injection}$	average skin-friction coefficient with air injection
$C_{F,no injection}$	average skin-friction coefficient without air injection
$C_{F,n=0}$	average skin-friction coefficient for $n = 0$
$c_f$	local skin-friction coefficient
$c_{f,i}$	incompressible local skin-friction coefficient (see section "Methods of Evaluating Skin Friction")
$h$	altitude
$M$	Mach number
$\dot{m}$	injection-air mass-flow rate
$n$	planform exponent (see fig. 10)
$R_l$	Reynolds number based on distance from leading edge
$R_x$	Reynolds number based on distance from virtual origin of turbulent boundary layer
$S$	reference surface area
$T_{aw}$	adiabatic wall temperature
$T_w$	wall temperature
$V_\infty$	free-stream air velocity
$w$	injection-air weight-flow rate
$y$	distance from center line in spanwise direction
$\eta_r$	recovery factor
$\rho_\infty$	free-stream air density

Subscripts:

exp                                    experimental value  
theor                                   theoretical value

DISCUSSION

Methods of Evaluating Skin Friction

Several years ago, a comparison between the various theories of supersonic skin friction in use at that time and the available experimental data showed that the Sommer and Short T' method generally gave the best prediction of compressible turbulent boundary-layer skin friction (ref. 1). A new method for the prediction of compressible turbulent skin friction has since been developed by Spalding and Chi (ref. 2). Also, some new experimental data for supersonic skin friction at high Reynolds numbers have extended the range of Reynolds numbers over which experimental results are available (refs. 3 to 9). In all of these references except reference 9, local skin friction was measured. Therefore, comparisons herein will be made by using local rather than average skin-friction measurements.

Figures 2 to 7 show comparisons between presently available experimental data and the skin-friction predictions of Sommer and Short (figs. 2, 4, and 6) and Spalding and Chi (figs. 3, 5, and 7). (The experimental data presented in the figures were obtained from references 3 to 8 and 10 to 12.) The skin friction is presented in the form of the ratio  $\frac{c_f}{c_{f,i}}$ , where the value of  $c_{f,i}$  is predicted by the method involved. As will be shown, neither method gives completely satisfactory results over the entire range of Reynolds numbers.

In figures 2 and 3 are shown the experimental variations of  $\frac{c_f}{c_{f,i}}$  with M for a value of  $R_x$  of  $10 \times 10^6$  compared with the predictions of Sommer and Short (fig. 2) and Spalding and Chi (fig. 3). The curves and data shown are all for adiabatic wall temperatures. There is some scatter in the experimental data, but generally the Sommer and Short T' prediction agrees slightly better with the data at this Reynolds number than the Spalding and Chi prediction.

When the new experimental data for skin friction at higher Reynolds numbers of  $50 \times 10^6$  and  $100 \times 10^6$  are used in the same type of comparison, the results are not the same, as shown in figures 4 and 5. (The data of Hopkins and Keener were obtained for a Reynolds number based upon momentum thickness. These data are converted in figures 4 and 5 to values for  $R_x$  by using the method of reference 1.) For these conditions, the data agree better with the Spalding and Chi prediction and lie above the Sommer and Short T' prediction curve.

The reason for the agreement of the data with the Sommer and Short T' prediction at low Reynolds numbers and with the Spalding and Chi prediction at high Reynolds numbers can be shown by plotting the skin-friction ratio as a function of Reynolds number for a constant Mach number. The Sommer and Short T' curve is shown in figure 6 and the Spalding and Chi curve is shown in figure 7. The data were all obtained for Mach numbers between 2.20 and 2.95 and transformed to values for a Mach number of 2.7 by using the equation

$$\frac{c_f}{c_{f,i}} = \left( \frac{c_{f,exp}}{c_{f,theor}} \right)_{M_{exp}} \left( \frac{c_{f,theor}}{c_{f,i}} \right)_{M=2.7}$$

The values obtained for  $\frac{c_f}{c_{f,i}}$  by using this equation are not the same for the two methods since the parameter  $c_{f,theor}$  is dependent upon the particular method involved. Therefore, the values of the ratio  $\frac{c_f}{c_{f,i}}$  are slightly different in figures 6 and 7. However, this procedure allows a direct comparison to be made between the data and the predicted curves by preserving the relation of experimental values to predicted values. It appears from these data that the skin-friction ratio is almost independent of Reynolds number. Both methods predict some variation of the skin-friction ratio with Reynolds number and, therefore, neither prediction curve matches the data over the entire range of Reynolds numbers. In order to predict the average skin friction, it is important that the method give accurate results for the local skin-friction level at all Reynolds numbers up to the Reynolds number of interest, since the average is obtained by integrating the local values. Therefore, even though the Spalding and Chi method gives accurate results for the local skin friction at high Reynolds numbers, it does not necessarily give accurate results for the average skin friction at these Reynolds numbers. There is also some doubt as to the validity of the Spalding and Chi method for use at the high temperature levels encountered on a supersonic transport, since the constants in this method were obtained by comparison with wind-tunnel data and no provision was made to account for the effect of temperature level on the viscosity ratio of air. Most other methods of predicting skin friction, including the Sommer and Short T' method, do have such a provision.

As can be seen, only a limited amount of experimental data is available for the very high Reynolds numbers encountered by a supersonic transport. More data are needed to increase confidence in the prediction of skin friction at high Reynolds numbers.

The effect of wall temperature on the average skin friction at  $M = 3.0$  and  $R_x = 94 \times 10^6$  is shown in figures 8 and 9 for an ogive-cylinder body of revolution (ref. 9). The variations of  $\frac{C_F}{C_{F,aw}}$  with  $\frac{T_w}{T_{aw}}$  are presented for experiment and theory, where  $T_{aw}$  is based on a recovery factor  $\eta_r$  of 0.89 and the value of  $C_{F,aw}$  is obtained by extrapolating the experimental values to adiabatic conditions. A comparison of these figures shows that the Sommer

and Short T' method better predicts the effect of wall temperature on skin friction at Mach 3. However, the heat-transfer correlations in reference 13 indicate that the Spalding and Chi method is more accurate at hypersonic speeds.

It is apparent that there is much room for improvement in the accuracy of predictions of turbulent skin-friction drag. However, the Sommer and Short T' method is considered to provide the best predictions of skin friction under conditions encountered by the supersonic transport. Therefore, this method is used to calculate skin friction in the rest of this paper.

### Methods of Reducing Skin Friction

Most of the methods discussed in this paper for reducing the skin friction on a supersonic transport have been presented before in various conference papers and NASA reports. These methods are presented herein without regard to the design considerations involved, or the effects they might have on other characteristics of the aircraft. Application to a supersonic transport will require careful and ingenious design in order to obtain favorable overall results.

Configuration changes and blending.- One way to reduce skin friction is to take advantage of the fact that skin friction is low at high Reynolds numbers. (See ref. 14.) Figure 10 illustrates the changes in skin friction which occur as the wing planform is changed so as to remove areas from the tips and add areas in the center, where they will be in high Reynolds number flows. The skin friction was calculated at a Mach number of 2.7 and an altitude of 65 000 ft for a wing with a planform area of 8000 ft<sup>2</sup> and an aspect ratio of 1.7. The wing chord was determined by a power-law formula, and the midchord sweep of the wing was held constant at 50°. As can be seen, the areas near the tips are progressively moved toward the center of the wing. This process results in a reduction in the total skin friction, even though the total area and the aspect ratio of the wing remain the same.

Another obvious way of reducing skin friction is decreasing the wetted area of the aircraft. The method used to decrease the wetted area, which is called blending, is accomplished by deforming the aircraft into a shape that is as close as possible to a body of revolution. Such a shape, of course, would have the least surface area for a given volume distribution. Although this type of blending is used to reduce skin friction only, it is not incompatible with the type of blending which can be used to reduce wave drag and structural weight.

An example of a configuration shape which resulted from blending and changing the planform of a delta-wing type supersonic transport is shown in figure 11. The wing planform has been changed to remove areas near the tips and add areas near the center in such a way that the total area and the wing aspect ratio are constant. The wing and tail have been blended into the fuselage with large fillets; the nacelles have been blended together and a splitter plate used to separate the inlets. The data of reference 15 show that a

splitter plate prevents mutual interference between inlets when they are unstarted. The nacelle inlets have not been blended into the wing because such blending would have produced problems of diverting the wing boundary layer around the inlets.

The skin-friction-drag reductions that might be obtained by these configuration changes are shown in table I. The reductions due to planform changes result only from removing areas in low Reynolds number flows and replacing them in high Reynolds number flows. There is no change in the total wetted area. The skin-friction-drag reductions due to blending result from changes in the total wetted area which occur as the components of the aircraft are blended. Changes in the skin friction caused by three-dimensional effects in the corners were neglected in these calculations. Although each individual increment is small, the total increment can be a significant reduction in the skin-friction drag. For an aircraft with 40 counts of skin-friction drag, the total reduction shown in table I amounts to about 2 counts.

Effects of emissivity on wall temperature and skin friction.- As shown before, the wall-temperature ratio has a large effect on skin friction. Both the theory and the experimental data showed that the skin friction increased as the wall-temperature ratio decreased. This trend is shown in figure 12, where the skin-friction drag is plotted as a function of the wall-temperature ratio for a typical supersonic transport flying at a Mach number of 2.7 and an altitude of 65 000 ft. Also shown in the figure are vertical dashed lines at the temperature ratios corresponding to the equilibrium wall temperatures for various wall emissivities. (See also ref. 16.) The range of emissivities being considered for presently proposed supersonic transports is shown as the crosshatched region. As is well known, radiation of heat from the wall caused by high emissivities reduces the wall temperature. For this particular configuration, an emissivity of 0.5 reduces the wall-temperature ratio to about 0.95, and an emissivity of 1.0 reduces it to about 0.91. It can be seen that increasing the emissivity reduces the wall temperature but increases the skin-friction drag. Low emissivities have the opposite effect of increasing the wall temperature and reducing the skin-friction drag. Therefore, low values of the emissivity, which can be controlled to a certain extent by the choice of paint or surface coating used, reduce the skin-friction drag of a supersonic transport. Determination of the best wall emissivity to use will depend on the exact configuration and structural design chosen.

Boundary-layer control.- The ideal way to reduce the skin friction on a supersonic transport, of course, would be with laminar-flow control. Research on laminar-flow control, however, is still continuing and very little practical experience has been obtained so far. Therefore, laminar-flow control does not appear feasible for the first-generation supersonic transport.

Theoretically, it is possible to obtain about 2 feet of natural laminar flow on unswept leading edges, such as the engine nacelles, and about 1.2 feet of natural laminar flow on swept leading edges, such as the wing and tail (ref. 17). With these amounts of laminar flow, the skin-friction drag could be reduced by about 3 percent. However, large extents of natural laminar flow on the supersonic transport appear unlikely, since this condition would require very

accurate construction, extensive maintenance, and some method of avoiding insect contamination during service.

There is, however, a method of reducing the turbulent skin-friction drag. It has been shown experimentally that the turbulent skin friction can be reduced by injecting air into the boundary layer through rearward-inclined flush slots in the surface (refs. 18 and 19). The effect of air injection on the drag is shown in figure 13, in which the model drag coefficient is plotted as a function of the injection mass-flow parameter. The lower curve presents the variation of the measured values of  $C_D$  with the rate of air injection through a rearward-inclined flush slot at  $M = 3.0$ . These measured values of  $C_D$  include the reduction in skin friction as well as the thrust recovered from the injected air. The upper curve represents the calculated values of  $C_D$  that could be obtained if the momentum thrust of the same air were recovered with a convergent nozzle. The difference in the levels of the two curves indicates that a reduction in skin friction occurred. The physical process behind this skin-friction reduction is not yet fully understood.

A possible application of air injection to one of the supersonic transport configurations is presented in figure 14. The abscissa is the injection-air weight-flow rate through inclined flush slots. The air for injection can be obtained from the inlet bleed air, which is already available for use onboard the airplane. The ordinate is the ratio of the average airplane skin-friction coefficient with air injection to the average skin-friction coefficient without air injection. The flow rate of the inlet bleed air is estimated to be about 80 lb/sec. With this amount of air, the skin friction can be reduced by 5 percent.

Recently published boundary-layer surveys behind flush slots (ref. 19) have suggested that perhaps even larger reductions in skin friction could be obtained from two or three slots distributed along the surface, instead of one slot near the leading edge. This hypothesis requires experimental verification, however, before it can be used. The feasibility of using air injection to reduce skin friction depends upon many considerations. The point to be made, however, is that the skin-friction reductions shown in figure 14 indicate that further study of the use of air injection on the supersonic transport is warranted.

#### CONCLUDING REMARKS

In summary, a comparison between theory and the latest experimental results for compressible turbulent skin friction shows that more data are needed to increase confidence in the prediction of skin friction at supersonic speeds and high Reynolds numbers.

Planform changes and configuration blending can significantly change the total skin-friction drag of a supersonic transport. Also, the wall emissivity of a supersonic transport can have a large effect on the skin-friction drag.

The reduction in turbulent skin friction obtainable with air injection through rearward-inclined flush slots indicates that further study is warranted.

## REFERENCES

1. Peterson, John B, Jr.: A Comparison of the Experimental and Theoretical Results for the Compressible Turbulent-Boundary-Layer Skin Friction With Zero Pressure Gradient. NASA TN D-1795, 1963.
2. Spalding, D. B.; and Chi, S. W.: The Drag of a Compressible Turbulent Boundary Layer on a Smooth Flat Plate With and Without Heat Transfer. J. Fluid Mech., vol. 18, pt. 1, Jan. 1964, pp. 117-143.
3. Jackson, Mary W.; Czarnecki, K. R.; and Monta, William J.: Turbulent Skin Friction at High Reynolds Numbers and Low Supersonic Velocities. NASA TN D-2687, 1965.
4. Monta, William J; and Allen, Jerry M.: Local Turbulent Skin-Friction Measurements on a Flat Plate at Mach Numbers From 2.5 to 4.5 and Reynolds Numbers up to  $69 \times 10^6$ . NACA TN D-2896, 1965.
5. Aircraft Div., Douglas Aircraft Co., Inc.: Investigation of Skin Friction Drag on Practical Construction Surfaces for the Supersonic Transport. FDL TDR 64-74, U.S. Air Force, Aug. 1964.
6. Moore, D. R.; and Harkness, J.: Experimental Investigations of the Compressible Turbulent Boundary Layer at Very High Reynolds Numbers. AIAA J., vol. 3, no. 4, Apr. 1965, pp. 631-638.
7. Hopkins, Edward J.; and Keener, Earl R.: Experimental Investigation of Surface Pitot Tubes for Measuring the Local Turbulent Skin Friction at Supersonic Mach Numbers on Adiabatic Flat Plates. NASA TN D-3478, 1966.
8. Winter, K. G.; Smith K. G.; and Gaudet, L.: Measurements of Turbulent Skin Friction at High Reynolds Numbers at Mach Numbers of 0.2 and 2.2. Recent Developments in Boundary Layer Research, Pt. I, AGARDograph 97, May 1965, pp. 97-124.
9. Czarnecki, K. R.; Jackson, Mary W.; and Monta, William J.: Studies of Skin Friction at Supersonic Speeds. NASA Conference on Supersonic-Transport Feasibility Studies and Supporting Research. NASA TM X-905, 1963, pp. 177-189.
10. Matting, Fred W; Chapman, Dean R.; Nyholm, Jack R.; and Thomas, Andrew G.: Turbulent Skin Friction at High Mach Numbers and Reynolds Numbers in Air and Helium. NASA TR R-82, 1961.
11. Coles, Donald: Measurements in the Boundary Layer on a Smooth Flat Plate in Supersonic Flow. III. Measurements in a Flat-Plate Boundary Layer at the Jet Propulsion Laboratory. Rept. No. 20-71 (Contract No. DA-04-495-Ord 18), Jet Propulsion Lab., California Inst. Technol., June 1, 1953.

12. Shutts, W. H.; Hartwig, W. H.; and Weiler, J. E.: Final Report on Turbulent Boundary-Layer and Skin-Friction Measurements on a Smooth, Thermally Insulated Flat Plate at Supersonic Speeds. DRL-364, CM-823 (Contract NOrd-9195), Univ. of Texas, Jan. 5, 1955.
13. Bertram, Mitchel H.; and Neal, Luther, Jr.: Recent Experiments in Hypersonic Turbulent Boundary Layers. Presented to the AGARD Specialists Meeting on Recent Developments in Boundary-Layer Research (Naples, Italy), May 10-14, 1965.
14. Robins, A. Warner; Harris, Roy V., Jr.; and Jackson, Charlie M., Jr.: Characteristics at Mach Number of 2.03 of a Series of Wings Having Various Spanwise Distributions of Thickness Ratio and Chord. NASA TN D-631, 1960.
15. Moseley, George W.; Peterson, John B., Jr.; and Braslow, Albert L.: An Investigation of Splitter Plates for the Aerodynamic Separation of Twin Inlets at Mach 2.5. NASA TN D-3385, 1966.
16. Allen, Jerry M.; and Czarnecki, K. R.: Effects of Surface Emittance on Turbulent Skin Friction at Supersonic and Low Hypersonic Speeds. NASA TN D-2706, 1965.
17. Jillie, Don W.; and Hopkins, Edward J.: Effects of Mach Number, Leading-Edge Bluntness, and Sweep on Boundary-Layer Transition on a Flat Plate. NASA TN D-1071, 1961.
18. McRee, Donald I.; Peterson, John B., Jr.; and Braslow, Albert L.: Effect of Air Injection Through a Porous Surface and Through Slots on Turbulent Skin Friction at Mach 3. NASA TN D-2427, 1964.
19. Peterson, John B., Jr.; McRee, Donald I.; Adcock, Jerry B.; and Braslow, Albert L.: Further Investigation of Effect of Air Injection Through Slots and Porous Surfaces on Flat-Plate Turbulent Skin Friction at Mach 3. NASA TN D-3311, 1966.

TABLE I

CALCULATED SKIN-FRICTION-DRAG REDUCTIONS  
 DUE TO CONFIGURATION CHANGES  
 M=2.7; h = 65 000 FT

	$\frac{\Delta C_{D,F}}{C_{D,F}}$
<u>PLANFORM CHANGES</u>	
WING.....	-0.5 %
TAIL .....	-0.1 %
	<u>TOTAL -0.6 %</u>
<u>BLENDING</u>	
WING-FUSELAGE JUNCTURE.....	-3.1 %
VERTICAL-TAIL-FUSELAGE JUNCTURE .....	-0.3 %
NACELLES.....	-1.3 %
	<u>TOTAL -4.7 %</u>
TOTAL CHANGE IN SKIN-FRICTION DRAG DUE TO CONFIGURATION CHANGES.....	<u><u>-5.3 %</u></u>

DRAG BREAKDOWN OF A TYPICAL SUPERSONIC TRANSPORT  
 $M=2.7$ ;  $h=65\ 000\ \text{FT}$

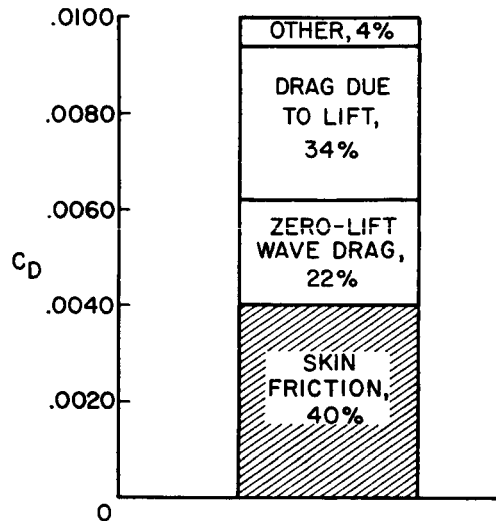


Figure 1

EFFECT OF MACH NUMBER ON TURBULENT SKIN FRICTION  
 SOMMER AND SHORT T' METHOD;  $T_w/T_{aw}=1.0$

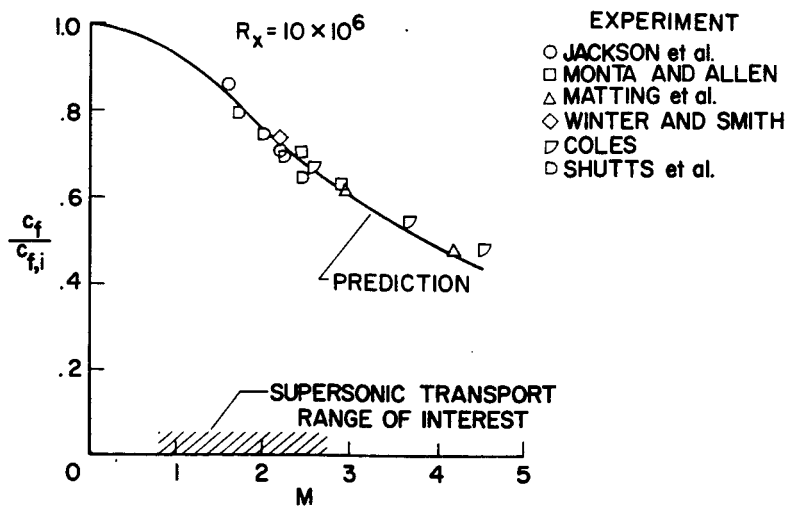


Figure 2

### EFFECT OF MACH NUMBER ON TURBULENT SKIN FRICTION

SPALDING AND CHI METHOD;  $T_w/T_{aw} = 1.0$

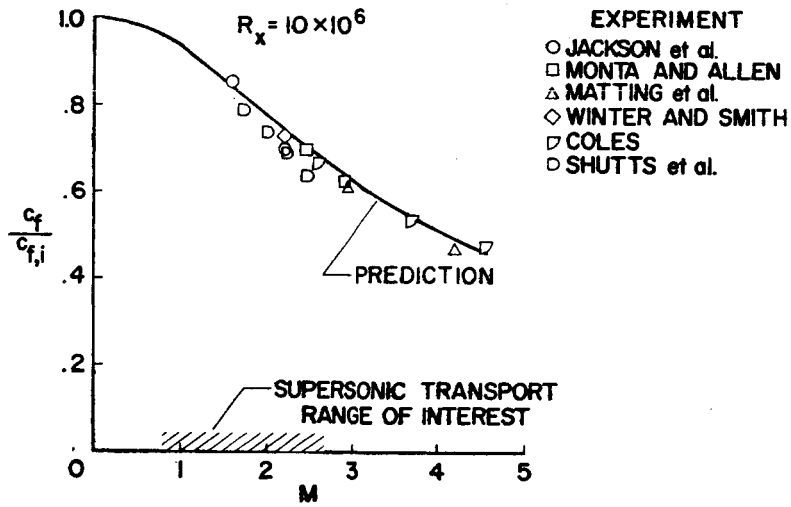


Figure 3

### EFFECT OF MACH NUMBER ON TURBULENT SKIN FRICTION

SOMMER AND SHORT T' METHOD;  $T_w/T_{aw} = 1.0$

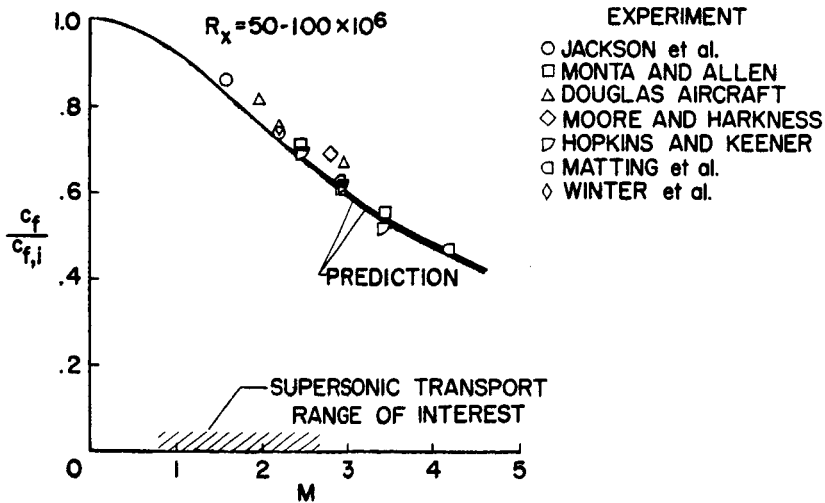


Figure 4

EFFECT OF MACH NUMBER ON TURBULENT SKIN FRICTION  
 SPALDING AND CHI METHOD;  $T_w/T_{aw} = 1.0$

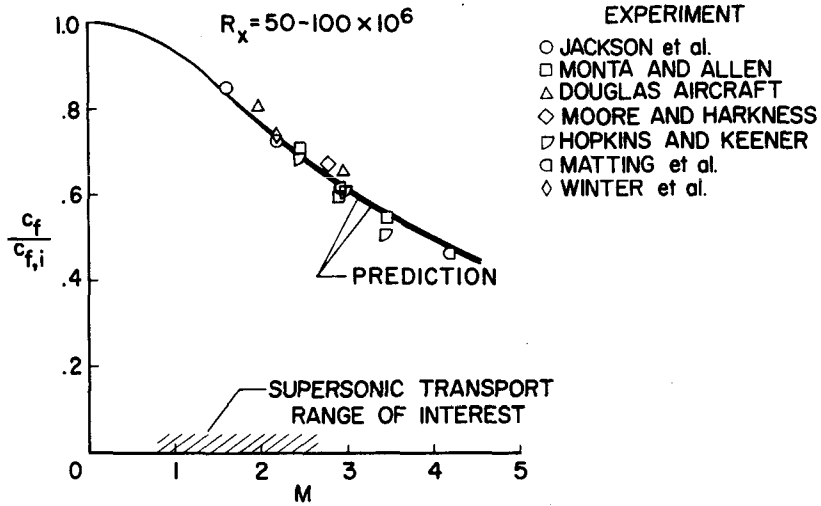


Figure 5

EFFECT OF REYNOLDS NUMBER ON TURBULENT SKIN FRICTION  
 SOMMER AND SHORT T' METHOD;  $M = 2.7$ ;  $T_w/T_{aw} = 1.0$

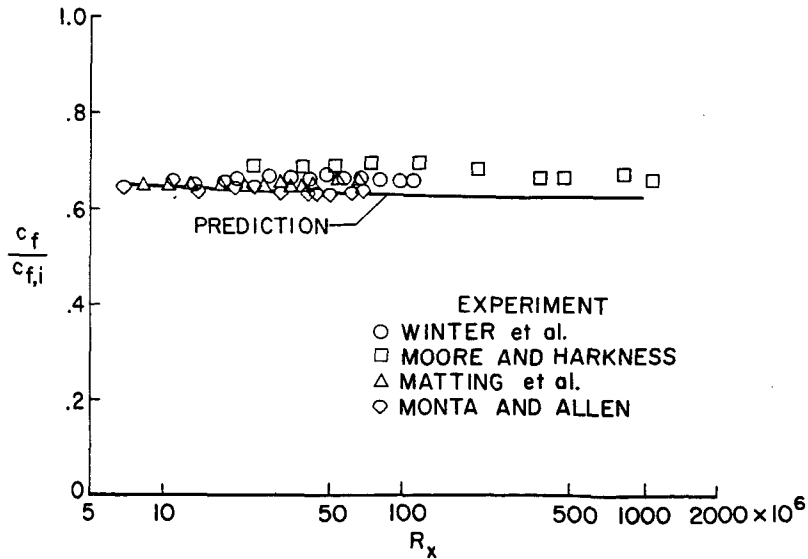


Figure 6

EFFECT OF REYNOLDS NUMBER ON TURBULENT SKIN FRICTION  
 SPALDING AND CHI METHOD;  $M=2.7$ ;  $T_w/T_{aw}=1.0$

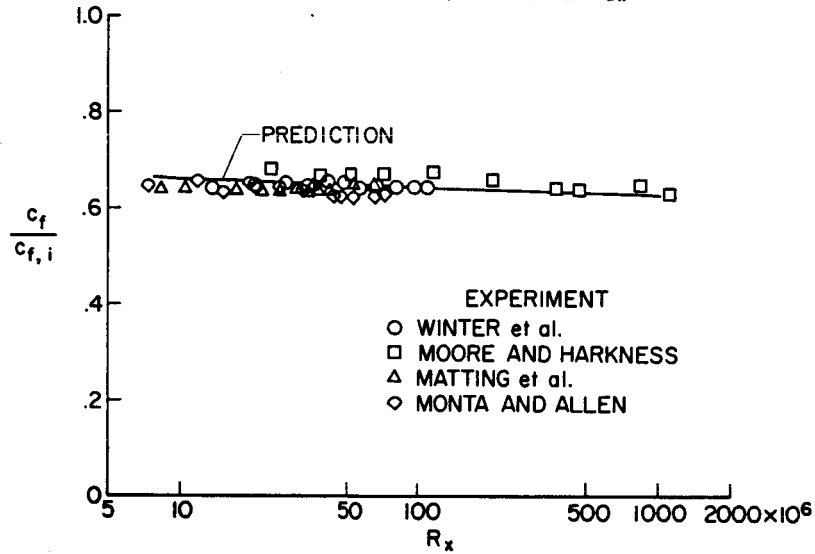


Figure 7

EFFECT OF WALL TEMPERATURE ON TURBULENT SKIN FRICTION  
 SOMMER AND SHORT T' METHOD;  $M=3.0$ ;  $R_x=94 \times 10^6$

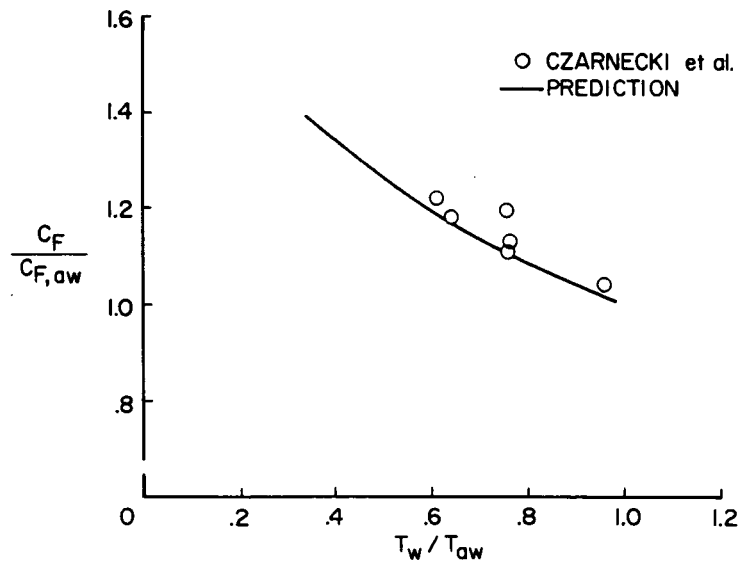


Figure 8

EFFECT OF WALL TEMPERATURE ON TURBULENT SKIN FRICTION  
 SPALDING AND CHI METHOD;  $M=3.0$ ;  $R_x=94 \times 10^6$

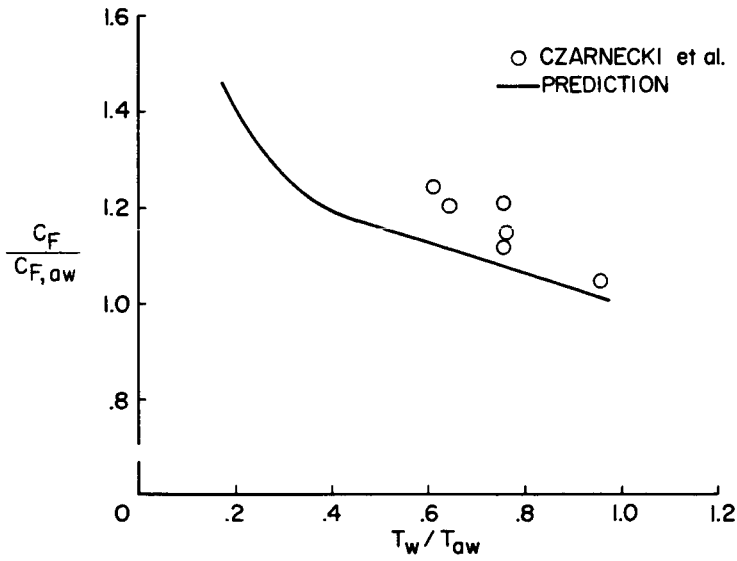


Figure 9

EFFECT OF WING PLANFORM ON SKIN FRICTION  
 WING AREA AND ASPECT RATIO CONSTANT

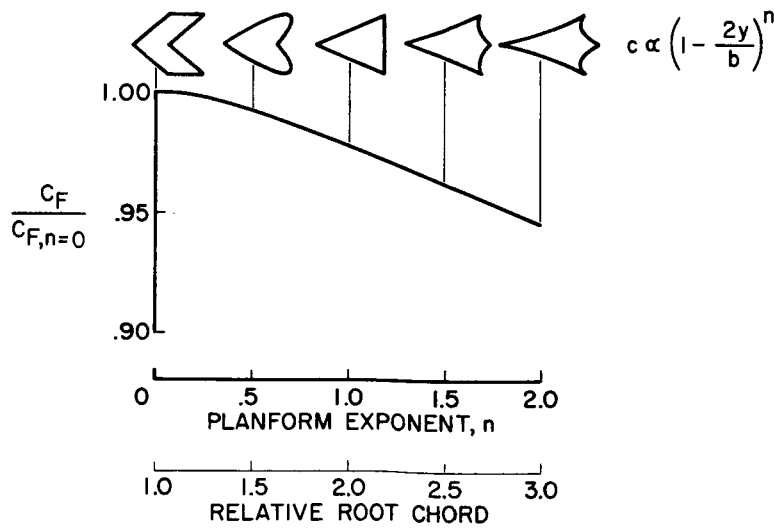


Figure 10

CONFIGURATION CHANGES TO REDUCE SKIN FRICTION

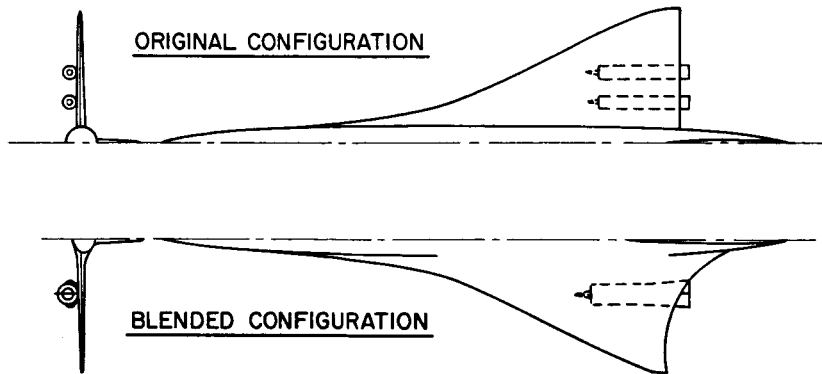


Figure 11

EFFECT OF EMISSIVITY ON WALL TEMPERATURE AND SKIN FRICTION

M=2.7; h=65 000 FT

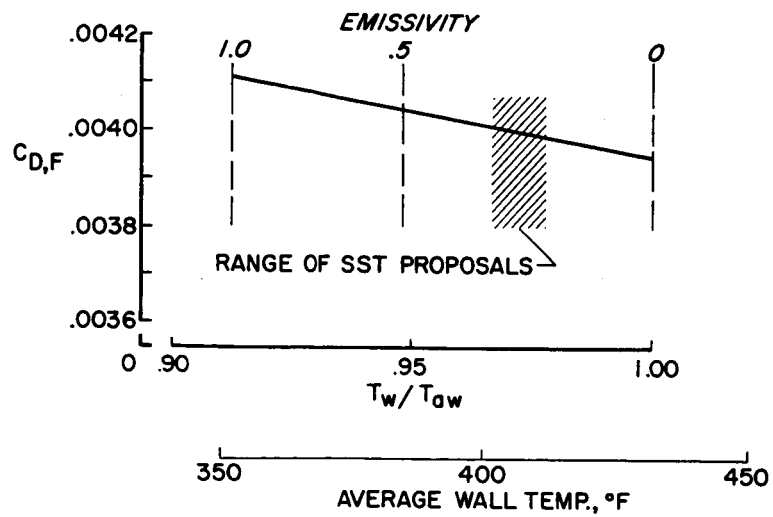


Figure 12

EFFECT OF AIR INJECTION ON DRAG

$M=3.0; R_L=16 \times 10^6$

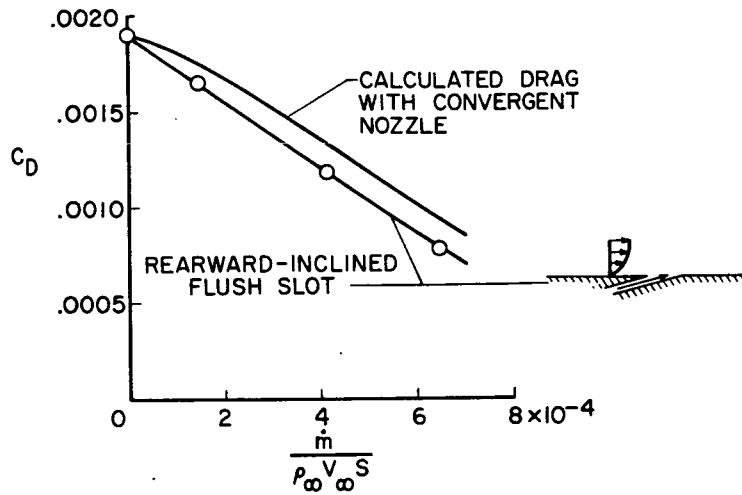


Figure 13

POSSIBLE SKIN-FRICTION REDUCTION ON AN SST WITH AIR INJECTION

$M=2.7; h=65\,000\text{ FT}$

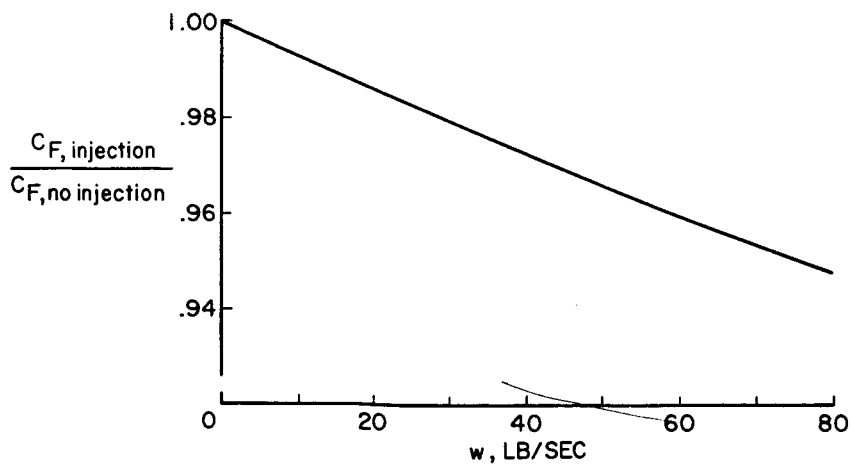


Figure 14

## 31. THE PROBLEM OF ROUGHNESS DRAG AT SUPERSONIC SPEEDS

By K. R. Czarnecki  
NASA Langley Research Center

## SUMMARY

An assessment has been made of the problem of roughness drag at supersonic speeds. The study indicates that no reliable methods are available at present for estimating roughness drag for general shapes at supersonic speeds. It appears, however, that research on the drag of surface roughness has progressed sufficiently to indicate that the basic parameters involved can be delineated and that the overall problem of roughness drag can probably be put on a more solid theoretical foundation. Some additional experimentation is still needed concerning certain parameters that have not been investigated sufficiently. From the present assessment, it is apparent that roughness drag depends upon local boundary-layer characteristics and that methods for calculating these characteristics in practical-type three-dimensional flows must generally be improved; the usual procedure of calculating roughness drag on the basis of the boundary layer on a flat plate generally will not be adequate. Finally, considerably more analytical work is required to reduce the complete problem to a rational basis, and a rational basis for predicting roughness effects can greatly improve airplane-performance calculations.

## INTRODUCTION

Research results from past conferences of NASA have shown that surface roughness can make significant contributions to the drag of a typical supersonic aircraft. For example, in reference 1 Peterson and Braslow estimated that the typical fabrication-type surface roughness prevalent on military airplanes at the time could increase the cruise drag of a supersonic transport by about  $3\frac{1}{2}$  percent and could decrease the potential payload by 3500 pounds. More recent assessments indicate that distortion of the airplane surfaces under aerodynamic heating and loading, and the deterioration of the surface smoothness with time in service will also pose difficult problems. Thus, there is a definite need for developing reliable methods for estimating roughness drag at supersonic speeds. The objective of this paper is to assess the overall problem, to delineate areas where design data may or may not be available, and, in particular, to show some of the progress being made to rationalize the overall roughness-drag problem and to put it on a more solid theoretical foundation.

## SYMBOLS

$C_D$	drag coefficient
$\Delta C_p$	incremental pressure coefficient
$k$	roughness height
$k'$	height from reference surface to experimental reattachment point for dividing streamline on round-cornered forward-facing steps (see fig. 9)
$M$	Mach number
$q$	dynamic pressure
$r$	radius of upper corner of forward-facing step
$R_x$	Reynolds number, $\frac{u_\infty x}{\nu_\infty}$
$R^*$	Reynolds number, $\frac{u^* k}{\nu_k}$
$t$	time
$u$	velocity
$u^*$	friction velocity, $\sqrt{\frac{\tau_w}{\rho_w}}$
$x$	longitudinal distance from virtual origin or axial distance from body nose
$y$	lateral distance
$z$	distance normal to reference surface
$\beta$	Mach number parameter, $\sqrt{M_\infty^2 - 1}$
$\delta^*$	boundary-layer displacement thickness
$\rho$	density
$\tau$	surface shear
$\nu$	kinematic viscosity

Subscripts:

$av, \delta$	average condition in undisturbed boundary layer over complete boundary-layer thickness at location of roughness element
$k$	at top of roughness element
$p$	based on pressure integrations
$q_{av, k}$	average dynamic pressure in undisturbed boundary layer (roughness element removed) over height of roughness
$q_{av, k'}$	average dynamic pressure in undisturbed boundary layer between reference surface and reattachment point for dividing streamline at location of roughness element
$w$	wall
$\infty$	free stream
$1$	modified drag coefficient, defined in figure 7
$2$	modified drag coefficient, defined in figure 7

#### ASSESSMENT OF OVERALL PROBLEM

The status of knowledge of roughness drag at supersonic speeds is summarized in figure 1. For convenience the surface roughnesses have been divided into three types: uniformly distributed or equivalent-sand-grain roughness; two-dimensional, square-cornered, essentially unswept steps, either forward- or rearward-facing; and the general arbitrarily shaped roughness, of which the other roughnesses are special cases. For the uniformly distributed roughness the critical roughness criterion is usually taken as the Reynolds number formed from the local friction velocity, the roughness height, and the kinematic viscosity corresponding to the top of the roughness. This criterion was developed from subsonic pipe-flow tests (ref. 2) but analyses and supersonic tests indicate that the criterion usually applies reasonably well at supersonic speeds provided the roughness height does not exceed approximately 300 to 400 micro-inches. Theoretical considerations and some unpublished results (also, see data for 480 in. model in refs. 3 and 4) indicate the possibility of more than negligible roughness wave drag for roughness heights exceeding this value even when the roughness Reynolds number is below the critical value. In general, neither criterion poses any severe restrictions on surface manufacturing tolerances, and hence surface-roughness drag of this type should not be any problem. Consequently, the knowledge in this area is considered fairly satisfactory even though the theoretical and experimental results at supersonic speeds are somewhat limited, and no further discussion of this type of roughness is included herein.

For the two-dimensional, square-cornered, essentially unswept step-type roughness there is no critical height below which drag due to roughness is not

present. Considerable experimental data exist for this type of roughness (ref. 5 provides a short list of references), and some success has been attained in correlating effects of Reynolds number (or, more accurately, the effects of the ratio of roughness height to boundary-layer thickness) on roughness drag. (For example, see ref. 6.) The effects of Mach number have not yet been fully resolved. The ultimate objective in this research is to develop a universal correlation procedure wherein a theoretical or experimental drag coefficient for a particular type of roughness can be blended with the correct scale and dynamic-pressure parameters to calculate the correct drag under any set of boundary-layer and free-stream Mach number conditions.

Research on the general roughness shapes, exclusive of the two types just discussed, is in the preliminary phases only, and very little experimental data are available. Unfortunately, most of the roughnesses that will be present on the supersonic transport and other supersonic airplanes will probably fall into this category.

In the remaining part of this discussion the object is to show some of the progress being made in rationalizing the overall drag problem in the last two roughness-configuration areas illustrated in figure 1. Because of the complexity of the drag problem for the general arbitrarily shaped roughnesses and the lack of experimental data thereon, much of the emphasis is, of necessity, on the extension of correlations for the two-dimensional unswept steps and the effects of gradual modifications of the steps toward the general arbitrary shape.

## MODELS AND TESTS

The experimental results from which the illustrations presented herein are drawn were obtained, as shown in figure 2, on many different types of models, on many types of configurations, in various wind tunnels, and by many different techniques. The Mach number range was from a subsonic Mach number of 0.7 to a hypersonic Mach number of 10.0, and a range of free-stream Reynolds number per foot from  $0.7 \times 10^6$  to  $20 \times 10^6$ , which can be translated to a range of Reynolds number based on length from  $2 \times 10^6$  to  $200 \times 10^6$ . Some effects of heat transfer were explored. Although some laminar-flow data were obtained, most of the emphasis was on turbulent boundary-layer flow, and the data presented are limited to that type of boundary layer.

## RESULTS AND DISCUSSION

### Definition of Problems

For purposes of orientation and for definition of the general problems involved, some typical pressure-drag results obtained on a single cycle of a repeating series of approximately sinusoidal-wave surface roughness on an ogive-cylinder model with a turbulent boundary layer are presented in figure 3. The cross-hatched line represents a linearized, two-dimensional, potential-flow

theory which utilizes an experimental local Mach number. Inasmuch as this local Mach number does not vary exactly as  $M_\infty$ , extrapolation from one free-stream Mach number to another results in a narrow band of values rather than a single line. The two dashed lines labeled "subsonic theory" will be explained shortly. It should be noted that the roughness height of 0.053 inch (which is exaggerated by a factor of 20 in the vertical scale of the sketch) is well within the boundary layer which is estimated to vary at this test station from about 0.25 to 0.35 inch.

The experimental results in figure 3 show a drag variation with Mach number that is typical of an object in a uniform free stream without boundary layer except for a rather high form drag at subsonic speeds and a powerful Reynolds number effect at the transonic and supersonic speeds. It should be noted that at the highest test Mach numbers and the highest Reynolds number, the experimental drag appears to approach agreement with the theoretical predictions. The truly significant feature is, however, that on an actual airplane, because of attempts to minimize roughness drag, most roughness elements will be in an area corresponding to the lowest curve or even lower and, thus, indicate the great need for a proper understanding of Reynolds number effects.

The theoretical subsonic form drag was obtained by assuming that the drag was due both to the pressure gradient existing on the basic smooth model and to the growth of the boundary-layer displacement thickness along the length of the roughness element. The latter increment in drag was determined by calculating the potential-flow pressure distribution for the roughness-element shape, as modified by the growth of the boundary-layer displacement thickness on a flat plate, and superimposing this pressure distribution directly to the actual physical contours of the element. The results of these calculations, shown in the lower left part of figure 3, indicate the proper trend in form drag with Mach number but are too low. Allowance for the thinner boundary layers existing on the test model relative to a flat plate would greatly improve the agreement between theory and experiment. In general, it appears the approach may be fundamentally valid but the details need considerably more development. It should be mentioned at this point that an understanding of subsonic roughness drag is necessary to the interpretation of supersonic-speed drag results for highly swept roughness configurations.

#### Drag at Transonic and Supersonic Speeds

At transonic speeds the calculation of theoretical pressure distributions, and hence drags, is formidable enough a problem without the introduction of boundary layers. Nevertheless, the prospects for obtaining at least empirical correlations in this speed regime do not appear to be hopeless. This possibility is illustrated in figures 4 and 5. In figure 4 are shown the effects of changes in Mach number and in figure 5 are shown the effects of changes in Reynolds number on the pressure distributions over the same approximately sinusoidal roughness element considered in figure 4. The increment  $\Delta C_p$  is the difference in pressure coefficient existing between the smooth reference body and the model with surface roughness at identical test conditions. As the Mach number is increased (fig. 4), the pressure distribution changes from one similar in

shape (except for a vertical scale factor) and in phase with the surface roughness shape to one approximately similar in shape, in this case, but now increasingly out of phase with the surface roughness shape. At the highest test Mach number, the negative and positive pressure peaks tend to approach the inflections in surface slope as required by the supersonic linearized potential-flow theory, although the magnitude of the experimental pressure coefficients remains considerably below the theoretical predictions which, however, are not shown. This type of change in pressure distribution with increase in Mach number is typical (except for the deficiency in magnitude of pressure coefficients relative to the theoretical values) of similarly shaped bodies in a uniform free stream without the boundary layer.

The significant feature at this point is that these changes in pressure distribution are very similar to those due to increasing Reynolds number shown in figure 5. Note that at the lower test Reynolds number, the shape of the pressure distribution tends toward similarity with the shape of the roughness and in phase with it. At the higher Reynolds number the supersonic flow has developed somewhat further, and the negative and positive pressure peaks tend to approach the inflection points. The shape of the pressure distribution is increasingly out of phase with the shape of the roughness. This similarity in Reynolds number and Mach number effects suggests that it may be possible ultimately to predict at least the first-order combined effects on the basis of an effective Mach number and effective dynamic pressure, in which the effective Mach number and dynamic pressure are derived from the local boundary-layer characteristics. Although it is not presented, this problem of a flow fully expanded supersonically to the inflections in surface slope, but deficient in magnitude of pressure coefficients predicted in terms of free-stream Mach number, extends continuously into the higher free-stream Mach number regimes. The problem that exists at these higher Mach numbers is to devise methods for predicting the effective Mach numbers and effective dynamic pressures. Satisfactory methods for estimating the effective values of these parameters for wave-type configurations have not yet been developed, but several promising leads have been uncovered.

#### Development of Typical Correlation Procedures

The emphasis thus far in this discussion has generally been on the types of surface roughness for which potential-flow calculations appear feasible because flow separation is nonexistent or the separation is on an insignificant scale. As indicated in figure 6, work is also proceeding on types of roughness involving separation. In this figure, which incidentally has been shown in a previous conference (ref. 6), the pressure drag on a two-dimensional forward-facing step is plotted as a function of the ratio of roughness height to boundary-layer displacement thickness. These data are for a step mounted on a tunnel wall at a Mach number of 2.20, with  $k$  ranging from 0 to 1.006 inches and  $R_x$  ranging from  $11 \times 10^6$  to  $103 \times 10^6$ . As indicated, a drag correlation was obtained (that is,  $C_D$  is constant) over most of the  $k/\delta^*$  range when the drag coefficient  $C_D$  was based on the average dynamic pressure existing in the basic boundary layer over the height of the step when the step is nonexistent. For the lowest step heights, when the top of the step approaches the height of sonic flow, the correlation breaks down. This area has not yet been intensely

analyzed. There is also a residual Mach number effect on the level of the average drag coefficient in the range of correlated data, as illustrated in the left-hand part of figure 7. An attempt to correlate the Mach number effect on the basis of the parameter  $\sqrt{\beta_\infty}$  derived from the turbulent boundary-layer separation correlation developed by Erdos and Pallone (ref. 5) was not successful, as is indicated by the data in the upper part of the right-hand plot. A successful universal correlation, good for all conditions of boundary layer and free-stream Mach number, appears to result, however, if the parameter  $\sqrt{\beta}$  is based on the average Mach number in the boundary layer and if an allowance is made for the reduced dynamic pressures within the shear layer. This apparent universal correlation needs to be tested, however, over a much wider range of Mach number before it can be accepted with any confidence.

Similar universal correlations, which are not shown, are possible for the Reynolds number and Mach number effects for the rearward-facing two-dimensional steps, but all the average dynamic pressures and Mach numbers must be replaced by the free-stream values. It should be mentioned that the correlation of Mach number effect is not quite as good for the rearward-facing step as that shown for the forward-facing step. The essential point to be made is that the rearward-facing steps have other basic controlling parameters for the effective Mach number and dynamic pressure than the forward-facing steps.

Most step-type roughnesses on a supersonic airplane probably will not have perfectly square corners. In figure 8 are shown the effects of rounding off the corners of the forward-facing step on the drag correlation. The ordinates and abscissa are the same as in figure 6 for the square-cornered, forward-facing step. The lines represent curves drawn through the average data in figure 6 and in other similar figures with the corner radius  $r$  being held constant. The experimental data were obtained over a wide range of corner radii, roughness height  $k$ , and Reynolds number  $R_x$ .

The results in figure 8 indicate that rounding off the upper corner of the forward-facing step prevents all steps from being universally correlated on the basis of the parameters of figure 6. It is to be noted that the data for each step configuration having a constant radius do correlate in the form of a curve of  $C_D$  as a function of  $k/\delta^*$ , but the drag coefficient is no longer constant over most of the  $k/\delta^*$  range. For the square corner, the flow phenomena on the forward face and upon the upper roughness surface downstream of the corner appear to be effectively separated from one another because of the very small subsonic-flow connection through the boundary layer. With the rounding of the corners this point for the division of the two flows moves forward and below the total roughness height, so that the roughness height is no longer the proper parameter for obtaining the correlating effective dynamic pressure.

The possibility of obtaining the desired correlation by suitably picking the effective roughness height is shown in figure 9. The roughness height  $k'$  used in this figure was taken to be at the location of the dividing streamline for the boundary layer as indicated by the experimental pressure distributions on the rounded corners. The drag integrations extended only from the reference surface to this point, with some drag component left to be accounted for above the point. The main objective is to determine whether the overall flow over the roughness element can be simplified into component flows more suitable for

theoretical treatment. The successful correlation shown in figure 9 indicates that such simplification is possible, although the correlation of the drag component existing above the reattachment point has not yet been attempted.

### Effects of Roughness Sweep

At this point it is desirable to conclude the discussion of those areas where substantial progress is being made and to give some attention to a pertinent item for which only a rough preliminary analysis has been applied. In figure 10 are presented some typical pressure-drag results showing the effect of sweeping the roughness element. The drag coefficient is, as usual, based on roughness frontal area. The theory is based on the normal components of the local surface slopes and experimental local flows and is best represented by a band for the same reasons as mentioned previously. The approximate shape of the roughness with the vertical scale exaggerated is illustrated in figure 10. The roughness-drag results of this figure indicate that the onset of wave drag on the roughness element has been delayed and the peak drag coefficient has been reduced (in comparison with the drag of a similar unswept configuration) by the sweep of the element. These effects are precisely those expected for the element in a uniform free stream with no boundary layer.

Another important effect resulting from the sweep is that the region of maximum Reynolds number effects, which occurs just above a Mach number of 1 for the unswept roughness, has now been delayed to higher free-stream Mach numbers. This phenomenon results from the fact that the development of the supersonic flow in a plane normal to the element and strongly influenced by changes in boundary-layer thickness, as was shown previously for the unswept roughness, has been delayed to higher free-stream Mach numbers. Furthermore, the tendency toward better agreement between theory and experiment at the higher test Mach numbers is apparently delayed to still higher values. This trend illustrates the need for a better understanding of subsonic- and transonic-flow drag characteristics in making drag calculations at supersonic free-stream Mach numbers.

### CONCLUDING REMARKS

From this assessment of the problem of roughness drag at supersonic speeds, it can be said, in summary, that there are at present no reliable methods for estimating roughness drag for general shapes at supersonic speeds. However, research on the drag of surface roughness has progressed sufficiently to indicate that the basic parameters involved can be delineated and that the overall problem of roughness drag can probably be put on a more solid theoretical foundation. Some additional experimentation is needed to investigate certain parameters that have not been investigated sufficiently. From this presentation, it should be obvious that roughness drag depends upon local boundary-layer characteristics and that methods for calculating these characteristics in practical-type three-dimensional flows must generally be improved; the usual approach of calculating roughness drag on the basis of a flat-plate boundary layer generally will not be adequate. Finally, considerably more analytical work is required to

reduce the complete problem to a rational basis, and a rational basis for predicting roughness effects can greatly improve airplane-performance calculations.

#### REFERENCES

1. Peterson, John B., Jr.; and Braslow, Albert L.: Implications of the Effects of Surface Temperature and Imperfections on Supersonic Operations. Conference on Aircraft Operating Problems, NASA SP-83, pp. 227-233.
2. Schlichting, Hermann (J. Kestin, translator): Boundary-Layer Theory. McGraw-Hill Book Co., Inc., 1955, pp. 416-423.
3. Czarnecki, K. R.; Robinson, Ross B.; and Hilton, John H., Jr.: Investigation of Distributed Surface Roughness on a Body of Revolution at a Mach Number of 1.61. NACA TN 3230, 1954.
4. Sevier, John R., Jr.; and Czarnecki, K. R.: Investigation of Effects of Distributed Surface Roughness on a Turbulent Boundary Layer Over a Body of Revolution at a Mach Number of 2.01. NACA TN 4183, 1958.
5. Erdos, John; and Pallone, Adrian: Shock—Boundary Layer Interaction and Flow Separation. Proc. 1962 Heat Transfer Fluid Mech. Inst., Stanford Univ. Press, 1962, pp. 239-254.
6. Czarnecki, K. R.; Jackson, Mary W.; and Monta, William J.: Studies of Skin Friction at Supersonic Speeds. NASA Conference on Supersonic-Transport Feasibility Studies and Supporting Research. NASA TM X-905, 1963, pp. 177-189.

STATUS OF ROUGHNESS-DRAG KNOWLEDGE AT SUPERSONIC SPEEDS

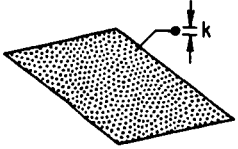
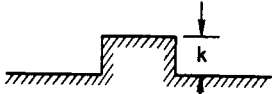
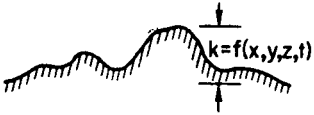
TYPE OF ROUGHNESS	CRITERION FOR NEGLIGIBLE DRAG	STATUS OF KNOWLEDGE
 <p data-bbox="399 600 537 651">UNIFORMLY DISTRIBUTED</p>	$R^* = \frac{u^* k}{\nu_k} < 5$	<p data-bbox="865 493 1089 523">FAIRLY SATISFACTORY</p> <p data-bbox="865 553 1062 608">DRAG ESTIMATION NO PROBLEM</p>
 <p data-bbox="367 770 566 821">TWO-DIMENSIONAL UNSWEPT STEPS</p>	$k = 0$	<p data-bbox="865 672 915 702">FAIR</p> <p data-bbox="865 723 1138 778">REYNOLDS NUMBER EFFECTS CORRELATED</p> <p data-bbox="865 795 1138 851">MACH NUMBER EFFECTS NOT CORRELATED</p>
 <p data-bbox="415 966 513 991">GENERAL</p>	$f(x, y, z, t) = ?$	<p data-bbox="865 898 1130 953">IN PRELIMINARY PHASES ONLY</p>

Figure 1

SURFACE ROUGHNESS AND PROTUBERANCE TESTS

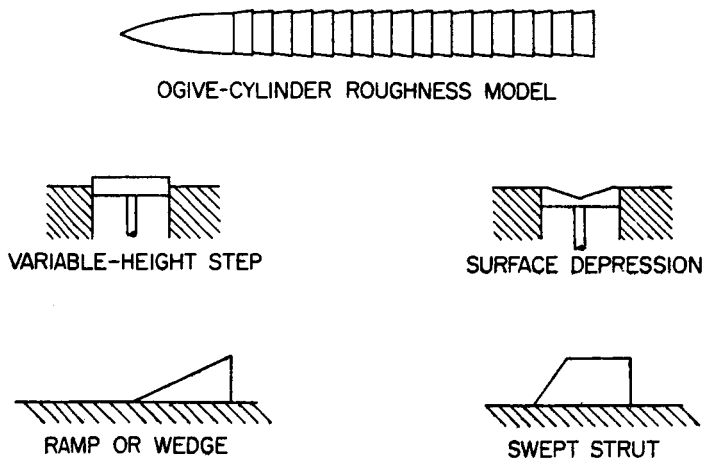


Figure 2

TYPICAL PRESSURE DRAG FOR SINGLE UNSWEPT ROUGHNESS ELEMENT

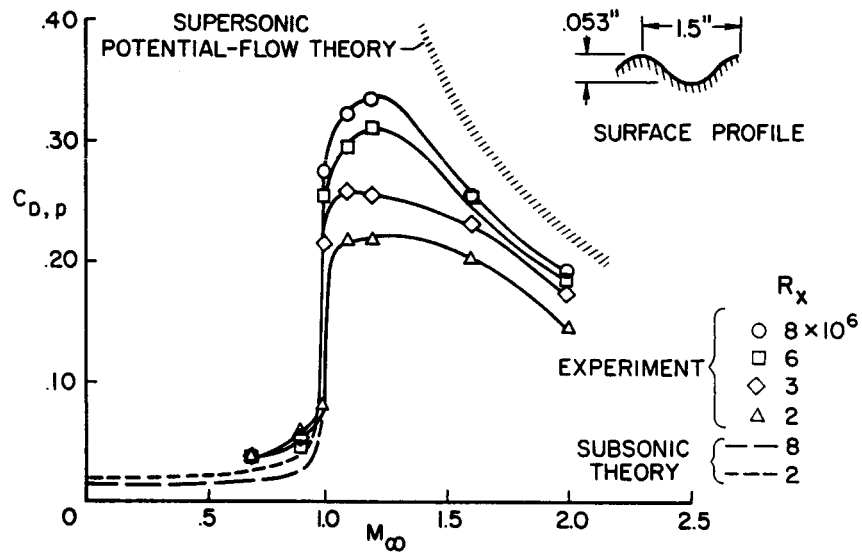


Figure 3

EFFECT OF MACH NUMBER ON ROUGHNESS PRESSURES  
0.053-IN. WAVE;  $R_x = 8 \times 10^6$

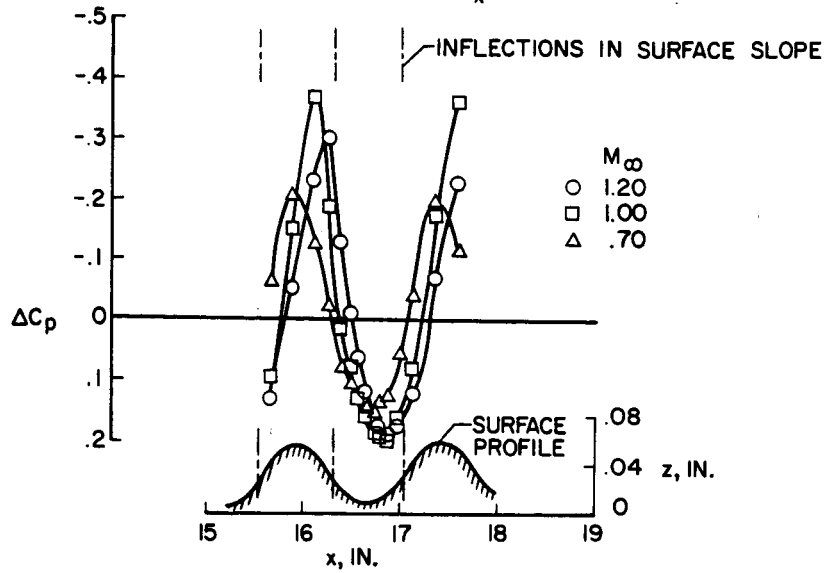


Figure 4

EFFECT OF REYNOLDS NUMBER ON ROUGHNESS PRESSURES  
 0.053-IN. WAVE;  $M_\infty = 1.10$

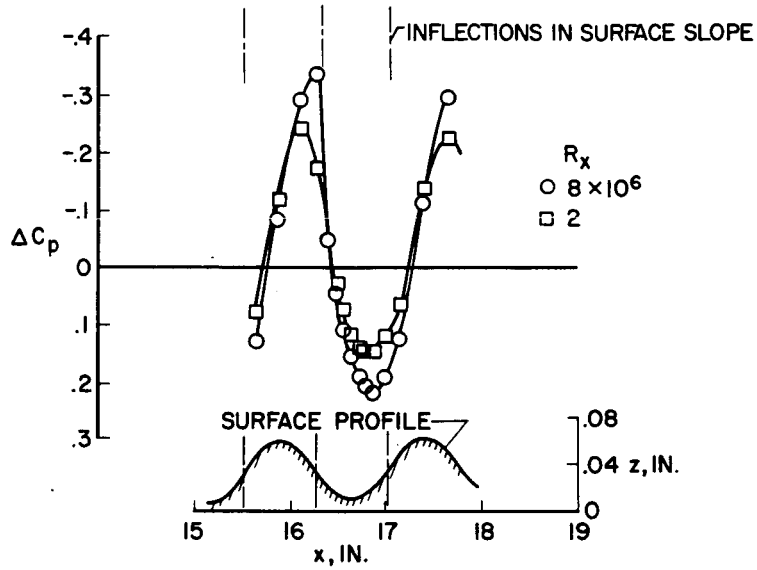


Figure 5

DRAG CORRELATION FOR SINGLE FORWARD-FACING STEPS  
 SQUARE CORNER;  $M_\infty = 2.20$ ;  $k = 0$  TO 1.006 IN.

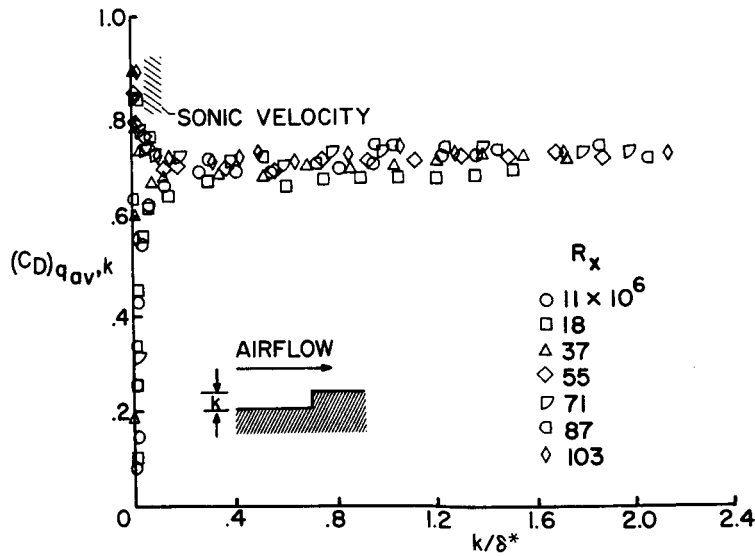


Figure 6

**CORRELATION OF MACH NUMBER EFFECTS  
FOR FORWARD-FACING STEPS**

SQUARE CORNERS;  $\frac{k}{\delta} > 0.2$

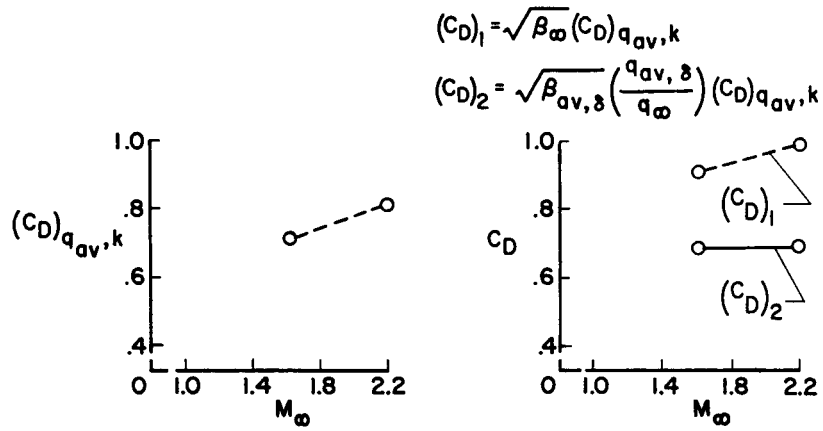


Figure 7

**EXPERIMENTAL DRAG CORRELATION FOR SINGLE  
FORWARD-FACING STEPS**

ROUNDED CORNERS;  $M_\infty = 2.20$

$k = 0$  TO 1.006 IN.

$R_x = 11$  TO  $103 \times 10^6$

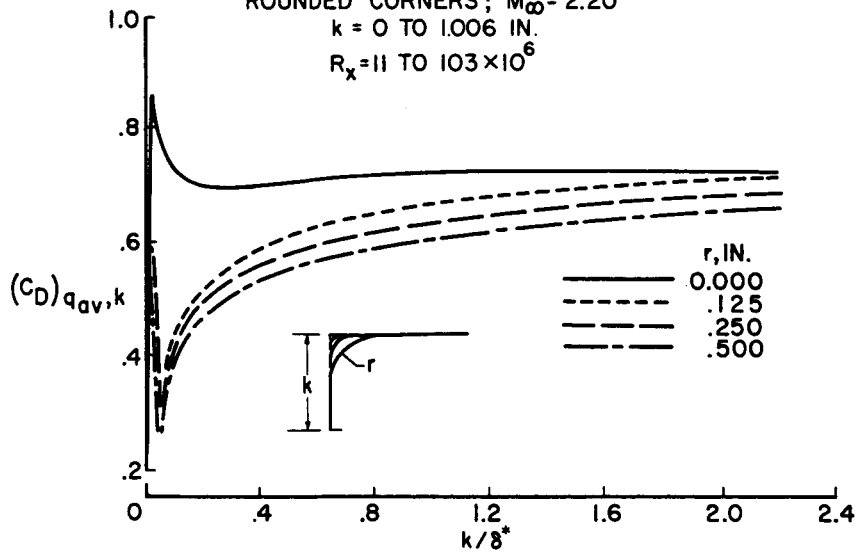


Figure 8

DRAG CORRELATION FOR SEPARATED-FLOW REGION OF  
FORWARD-FACING STEPS

ROUNDED CORNERS;  $M_\infty = 2.20$

$k = r$  TO 1.006 IN.

$R_x = 11$  TO  $103 \times 10^6$

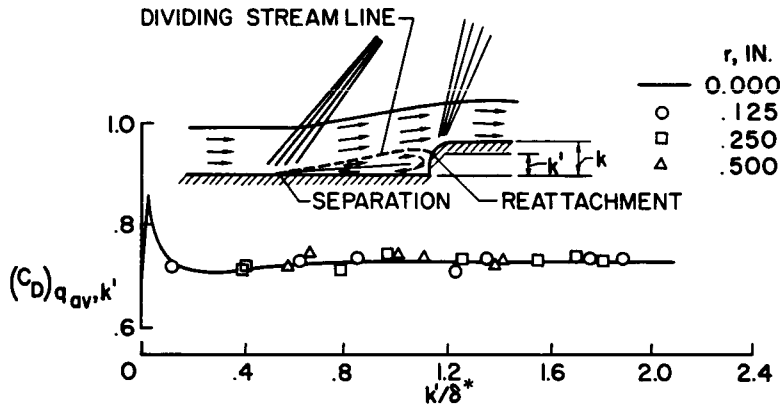


Figure 9

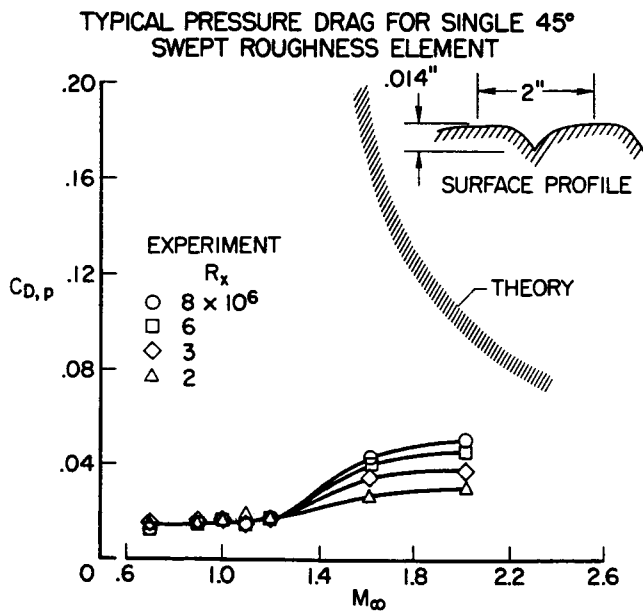


Figure 10

## 32. EFFECTS OF PLANFORM VARIATIONS ON THE AERODYNAMIC

### CHARACTERISTICS OF LOW-ASPECT-RATIO WINGS WITH

#### CRANKED LEADING EDGES

By Edward J. Hopkins, Raymond M. Hicks,  
and Ralph L. Carmichael  
NASA Ames Research Center

#### SUMMARY

Experimental lift, drag, and pitching-moment characteristics are presented for several wing-body combinations having low-aspect-ratio wings with cranked leading edges. The Mach number range covered was from 0.4 to 2.94. Comparisons are made, throughout this Mach number range, between the measured results and those predicted by means of linear theory in which body induced effects are considered. At a Mach number of 0.4, the effects of changes in the leading-edge crank geometry on the linearity of the lift and pitching-moment curves are shown. At small angles of attack, variations with Mach number of lift-curve slope, aerodynamic center, drag due to lift, minimum drag, and maximum lift-drag ratio are presented.

Some of the benefits of using planforms with cranked leading edges instead of straight leading edges are shown. These benefits include (a) a smaller change in aerodynamic center between subsonic and high supersonic Mach numbers, (b) more usable volume yet less minimum drag for the same exposed area and thickness in percent chord, (c) considerably higher lift-drag ratios at high supersonic Mach numbers for some planar wings, and (d) greater theoretical potential for improvements in flight efficiency by warping. At a Mach number of 0.4, however, the cranked planforms exhibited a loss in longitudinal stability which was more severe than that for the delta planform.

#### INTRODUCTION

In order for airplanes to meet the stringent range-payload requirement for economic operation at high supersonic speeds, their aerodynamic efficiencies must be maximized at cruise Mach number within the restraints imposed by the overall flight requirements. The optimum design of supersonic airplanes therefore involves many compromises and trade-offs, both aerodynamically and structurally. For example, the most efficient design for supersonic flight may have unacceptable low-speed characteristics or may impose serious weight penalties for maintaining structural integrity. In addition, other conditions such as efficiently providing adequate volume or attaining satisfactory center-of-gravity positions for adequate longitudinal stability throughout the Mach number range may have important influences on the final design.

The initial part of the present investigation was reported in reference 1 where it is shown that aerodynamic efficiency of a flat triangular wing is improved by use of spanwise variation of leading-edge sweep, i.e., an "ogee" planform. The cranked planforms having leading edges consisting of two straight lines should have manufacturing advantages over the ogee planforms they approximate. In references 2 and 3 it is demonstrated that, by lengthening the inboard wing chords, it is possible to reduce the zero lift wave drag and to increase the total wing volume. In reference 4 it is pointed out that for two wings having the same area the one with the more slender planform in the stream direction will have less skin-friction drag.

In the present investigation, the effects of changes in the leading-edge crank geometry on the aerodynamic characteristics of several wing-body combinations were investigated. These planforms, hereinafter called cranked planforms, were designed to have subsonic leading edges over the inward part of their spans throughout the supersonic Mach number range of the investigation. Although the present experimental investigation was confined to planar wings, cranked wings with partly subsonic leading edges should show greater improvement in the flight efficiency from warping than wings with entirely supersonic leading edges. Experimental results for two families of cranked planforms, the one having an aspect ratio of 2.2 and the other an aspect ratio of 1.5, are presented throughout a Mach number range from 0.4 to 2.94.

Part of the present investigation was devoted to predicting the lift, drag, and pitching-moment characteristics at small angles of attack where the experimental curves are nearly linear. The composite method for making these predictions included the mutual interference effects between the wing and the body calculated from slender-body concepts.

#### NOTATION

$A_{exp}$	exposed aspect ratio, $(\text{Exposed span})^2 / (\text{Exposed area})$
$C_D$	drag coefficient based on the area of the triangular wing, $\frac{\text{Drag}}{qS}$
$C_{D_0}$	minimum drag coefficient
$C_L$	lift coefficient based on the area of the triangular wing, $\frac{\text{Lift}}{qS}$
$\partial C_L / \partial \alpha$	lift-curve slope measured at $C_L = 0$
$C_m$	pitching-moment coefficient, $\frac{\text{Pitching moment about } \bar{c}/4 \text{ of delta wing}}{qS\bar{c}}$ (For model 7, the moment center was shifted forward the same amount that the intersection point of the wing trailing edge and the body was shifted forward.)
$\partial C_D / \partial C_L^2$	drag-due-to-lift factor

$\partial C_m / \partial C_L$	pitching-moment-curve slope measured at $C_L = 0$
$\bar{c}$	mean aerodynamic chord of triangular wing, 4.218 in.
$(L/D)_{\max}$	maximum lift-drag ratio
M	Mach number
q	free-stream dynamic pressure
R	Reynolds number based on the mean aerodynamic chord of triangular wing
S	wing area of triangular wing including area blanketed by the body, 21.75 in. <sup>2</sup>
$\alpha$	angle of attack

#### MODEL DESCRIPTION

Sketches of all the models investigated are shown in figure 1. Models 1 through 4 all had the same exposed span and area; therefore, they had the same exposed aspect ratio ( $A_{\text{exp}} = 2.2$ ). Model 1, which is considered the base planform, is a simple delta planform with its leading edge swept back  $59^\circ$ . Models 2, 3, and 4 all have the same tip chords, trailing-edge geometry, and  $78^\circ$  of sweepback on the inboard portions of their spans. These models differ only in the spanwise position of the leading-edge notch and the leading-edge sweeps on the outer portions of their wing spans. Models 5 through 7 are related in having the same aspect ratios and sweepback of  $82^\circ$  on their leading-edge extensions. Model 6 was formed from model 5 by moving the outer portion of its leading edge forward to create a finite tip; the leading-edge notch was moved inward along the wing span to maintain the same exposed area. Both models 5 and 6 have the same exposed spans and areas to give an exposed aspect ratio of 1.5. Model 7 has the same outboard leading-edge and trailing-edge sweep angles and exposed area as model 1; however, on model 7 the wing was moved forward on the body so that the leading-edge extension and the body nose were coincident. The span was reduced to give a total aspect ratio of 1.5. Model 8 was formed from model 1 by adding a leading-edge extension as shown. This extension had a sharp nose and was slab-sided. Model 8 was made geometrically similar to a much larger scale model which had been investigated in the Ames 40- by 80-foot wind tunnel. Models 1 through 8 all had flat wings mounted in the plane of symmetry of a body of revolution which had a Sears-Haack nose. Model 1 and the outer panels of the remaining models had circular-arc profiles with a thickness of 3-percent chord. The inboard portions of the wing spans of models 2 through 7 had round-nosed symmetrical profiles (NACA 0003-1.1 40/1.75) also with a thickness of 3-percent chord.

## REDUCTION OF DATA

The measured axial forces used for computing drag were adjusted to correspond to the free-stream static pressure acting on the fuselage base. The minimum drag data are corrected to conditions corresponding to an all turbulent boundary layer by the method presented in appendix A of reference 1. A correction for the slight leading-edge bluntness of the outboard panels also was made to these drag data by the method presented in appendix B of reference 1. Values of maximum lift-drag ratio were computed from the faired values of the drag-due-to-lift factors and the corrected minimum drag coefficients by the following equation:<sup>1</sup>

$$(L/D)_{\max} = \frac{1}{2} \sqrt{\frac{1}{(C_{D_0}) (\partial C_D / \partial C_L^2)_{\alpha > 3^\circ}}} \quad (1)$$

## THEORETICAL METHODS OF ANALYSIS

### Subsonic

The lift and pitching moments for a given model were calculated as the summation of the contributions from the individual components: the nose, the wing extending ahead of the leading-edge notch, and the wing panel outboard of the notch. The lift and center of pressure for the body nose were estimated from slender-body concepts given in reference 5. The mutual interference lift between the various parts of the wing and the body was also accounted for by the slender-body theory given in reference 5. Lift and center of pressure on the part of the wings ahead of the notch were computed by the slender-wing theory of reference 6. This theory was also used to estimate the wing-alone lift and center of pressure on the outboard panels of the models which had pointed tips, namely, models 1, 5, and 7. For the wing-alone lift on the wing panels outboard of the notch on all other models, the method of reference 7, which gives results about the same as the Weissinger method (ref. 8) for low-aspect-ratio wings, was employed.

The skin-friction drag was computed from the incompressible skin-friction equation given in reference 9; compressibility was taken into account by the reference-temperature method of reference 10.

In all cases, since the wings were thin and of low aspect ratio, drag due to lift was assumed to be equal to the lift times the angle of attack; hence, no leading-edge thrust was assumed. The drag-due-to-lift factor ( $\partial C_D / \partial C_L^2$ )

---

<sup>1</sup>This procedure was followed to improve the accuracy of the maximum lift-drag ratio, since the drag polars were found to be parabolic only for angles of attack above about  $3^\circ$ . The minimum drag coefficients were obtained by extrapolating the drag-due-to-lift curve ( $C_D$  vs.  $C_L^2$ ) to zero lift.

therefore becomes the reciprocal of the lift-curve slope and the maximum lift-drag ratio is given by equation (1).

### Supersonic

The wing-body interference effects on the lift were calculated by the method of reference 5. The wing-alone lift and center of pressure were calculated by the method of reference 11. (A similar but alternate method of computing the wing-alone values is given in ref. 12.) Lift and center of pressure for the body nose were calculated by slender-body concepts.

Wave drag for each wing-body combination was computed for an "equivalent" body of revolution by application of the supersonic area rule described in reference 13. After the skin-friction drag given by reference 10 was added to the wave drag, the maximum lift-drag ratio was calculated by equation (1), which sets the drag-due-to-lift factor ( $\partial C_D / \partial C_L^2$ ) equal to the reciprocal of the lift-curve slope.

## DISCUSSION OF RESULTS

### Reynolds Number Effects

As an aid in interpreting the subsonic results, results obtained in the Ames 2- by 2-foot wind tunnel on small-scale models in the present investigation at a Reynolds number of only  $0.9 \times 10^6$  are compared in figure 2 with results for two larger scale models of models 1 and 8 which had been investigated in the Ames 40- by 80-foot wind tunnel. It can be seen that, for model 1, Reynolds number had practically no effect on the lift, pitching moment, or drag-due-to-lift curves. For model 8, the lift-curve slope was slightly higher at the higher Reynolds number but the pitching-moment and drag-due-to lift curves were nearly the same. These results indicate that for low-aspect-ratio highly swept wings with relatively sharp-edged profiles, Reynolds number effects are relatively unimportant in studies of planform effects.

### Lift

Effects of planform modification on lift at a Mach number of 0.4 are shown for the two families of wings in figure 3. Linear theory, which includes the mutual interference effects between the wing and the body discussed above, is also shown in figure 3. It can be seen that linear theory gives a good estimate of the lift-curve slope at small angles of attack, but considerably underestimates the lift of the cranked planforms at the higher angles of attack because of the nonlinearity of the measured curves. (Predicting the nonlinear part of the curves would involve accounting for the vortex discharge from the wing leading edge and is beyond the scope of this report.) All of the cranked planforms had considerably more nonlinear curves than the delta planform; greater nonlinearity was measured for the lower aspect-ratio wings. This latter effect is well known for wings with straight

leading edges. Below each model is shown the measured angle of attack required to attain a lift coefficient of 0.8. It should be noted that a small leading-edge extension such as for model 2 produced enough nonlinearity in the lift curve to reduce this angle from approximately  $17^\circ$  to  $15^\circ$ , but that the larger leading-edge extensions, as for model 4, increased this angle to about  $18^\circ$ , partly because a larger portion of this wing was acting as a lower aspect-ratio wing with a lower lift-curve slope. The wings of aspect ratio 1.5, with more nonlinear curves than the aspect-ratio-2.2 wings, required about the same or a greater angle of attack for a lift coefficient of 0.8 than the delta wing because of their lower aspect ratio. It is interesting that model 6, which had a smaller leading-edge extension than model 5, had the more nonlinear lift curve, just as model 2 had compared with model 4.

### Pitching Moment

Pitching-moment results obtained at a Mach number of 0.4 for the two families of wings are shown in figure 4. It can be seen again that linear theory gives a good estimate of the longitudinal stability at low lift coefficients, but not at the higher lift coefficients where the cranked planforms exhibited a considerable loss in longitudinal stability. The delta wing showed only a slight loss in longitudinal stability at moderate lift coefficients. For the aspect-ratio-2.2 family (models 1 through 4), note that the loss in longitudinal stability became progressively more severe as more of the wing leading edge was extended forward. This same result can be observed by comparing the data for model 6 with that for model 5 which had the greater leading-edge extension.

### Effects of Mach Number

The effects of varying Mach number from about 0.4 to 3 on the important aerodynamic parameters of the two families of wings at small angles of attack are shown in figures 5 through 9. At supersonic Mach numbers some of these parameters such as the slopes of the lift and pitching-moment curves will apply over a larger range of angles of attack. On each of these figures estimated values from linear theory are also shown

Pitching-moment-curve slope ( $\partial C_m / \partial C_L$ ). - The maximum travel in the aerodynamic center which occurred between a Mach number of 0.4 and transonic Mach numbers is indicated in figure 5 to be about the same for all the models, approximately 13-percent chord. At the higher supersonic Mach numbers, however, the aerodynamic centers of the planforms with the cranked leading edges were nearly at the same or slightly ahead of the subsonic positions; whereas the aerodynamic center of the delta planform was considerably behind its subsonic position. At supersonic Mach numbers, the aerodynamic center travel with Mach number for the cranked planforms was, in general, satisfactorily predicted by use of linear theory, but the absolute values for models 5 and 7 were somewhat behind the predicted values. At subsonic Mach numbers the

travel of aerodynamic center with Mach number was not predicted too well by linear theory except for models 1 and 5.

Lift-curve slope ( $\partial C_L / \partial \alpha$ ).- In figure 6 it can be seen that, in general, at a Mach number of 0.4 and at supersonic Mach numbers, linear theory gave good estimates of the lift-curve slopes except for model 5. At subsonic Mach numbers, however, linear theory gave the proper increase in lift-curve slope with Mach number only for models 1 and 7 and underestimated the increase for the other models. It can also be seen by comparing the experimental values for each model with the values for model 1 (indicated by the circles at three Mach numbers) that the lift-curve slopes for model 1 were either about equal to or greater than those of the cranked planforms.

Drag-due-to-lift factor ( $\partial C_D / \partial C_L^2$ ).- In figure 7 it is interesting to note that at subsonic Mach numbers the measured drag-due-to-lift factors for all planforms with cranked leading edges were considerably below the values predicted by the reciprocal of the lift-curve slope. The latter prediction is known to be a good approximation of the drag-due-to-lift factor for low-aspect-ratio wings with sharp straight leading edges, such as model 1. Evidently, the vortex flow created by the cranked leading edge which produced a lift-curve slope increasing with angle of attack is also favorable in reducing the drag due to lift, even at small angles of attack. Possibly, some leading-edge thrust, not accounted for in theory, is being realized. At supersonic Mach numbers there is reasonable agreement between the measured and predicted drag-due-to-lift factors except for model 5, which has the greatest leading-edge extension. Again, the predicted factors were assumed to be the reciprocal of the lift-curve slopes. The experimental drag-due-to-lift factors for model 1 (indicated by the circles) were either the same or less than those for the cranked planforms.

Minimum drag coefficient ( $C_{D_0}$ ).- In figure 8 at a Mach number of 0.4 and 1.2 it can be noted that the measured minimum drag of the models with cranked leading edges was less than that for model 1 (the data for which are indicated by the circles). Part of this difference is attributable to less skin friction being measured, as predicted, for the more slender configurations. For example, at a Mach number of 0.4 compare the predicted and measured values for model 7 with corresponding values for model 1. (This effect is discussed in more detail in ref. 4.) At transonic Mach numbers the cranked planforms with rather large leading-edge extensions, such as models 3 through 7, had considerably less minimum drag than the delta planform. At a Mach number of about 3 only the very slender cranked planforms, models 4 through 7, had less drag than the delta planform. The reason that theory and experiment differed so much at the higher Mach numbers for the aspect-ratio-2.2 models is not clearly understood, although it might be expected, intuitively, that the assumption made to compute the wave drag for an "equivalent" body of revolution as described in reference 13 would give better values of drag for the more slender wing-body combinations.

Maximum lift-drag ratio ( $(L/D)_{max}$ ).- Figure 9 shows that at subsonic Mach numbers all the models with cranked leading edges had considerably higher

lift-drag ratios than predicted. This difference is mainly attributable to the drag due to lift being less than predicted for cranked planforms. At supersonic Mach numbers, linear theory gave good estimates of the measured maximum lift-drag ratios except for model 5. It should be realized, however, that part of this good agreement is fortuitous for some of the models, since compensating effects occurred in the prediction of the minimum drag and the drag due to lift. For model 5 the disagreement between theory and experiment is related to both the minimum drag and the drag due to lift being overpredicted. As indicated by the circles, representing the data for the base model 1, and the curves in figure 9, only models 2, 3, and 6 at a Mach number of 0.4 had slightly higher maximum lift-drag ratios than model 1. At a Mach number of 2.8 only models 5 and 6 had slightly higher maximum lift-drag ratios than model 1.

At the right of each model sketch in figure 9 are shown the volumes of models with cranked planforms relative to that for the model with the delta planform. It should be emphasized that all the wings have nearly the same exposed areas as well as profiles with a thickness of 3-percent chord, constant along the wing spans. The extra volume for the cranked planforms, indicated by the volume ratios being above 1.0, is a result of the cranked planforms having extended chord lengths near the fuselage. Note that model 6 which has 47 percent more volume than the delta wing has measured lift-drag ratios slightly greater than those for the delta wing at the three representative Mach numbers.

#### Theoretical Potential for $L/D$ by Warping

Results presented in figures 2 through 9 were for models with planar wings which had symmetrical profiles. Recognizing that a final design will be optimized by warping its surface to improve the lift-drag ratio in cruise, two of the models were theoretically warped to determine the gains in efficiency that might accrue. In figure 10 the theoretical lift-drag ratios at flight Reynolds numbers are shown for models 1 and 6, both with and without wing warpage. In the calculations the following flight conditions were assumed: A Mach number of 3.0, an altitude of 70,000 feet, a design lift coefficient of 0.07, and a wing area of 9970 sq ft. The theoretical increments in lift-drag ratio due to warping were calculated by the method of reference 14 which gives the optimum cambered wing surface and associated pressure drag. For the flat wings, the lift-drag ratios are those obtained by extrapolating the experimental values to the flight Reynolds number for a given wing-body combination at the chosen lift coefficient and Mach number. The decrement of skin-friction drag due to the increase in Reynolds number was obtained by the method of reference 10. It can be seen that even the flat version of model 6 has a considerably higher lift-drag ratio than the model with the delta wing. Also, it is evident that the delta wing with a supersonic leading edge gains little in lift-drag ratio from warping; however, model 6, with part of its leading edge subsonic, theoretically can have about a 10-percent improvement in its lift-drag ratio.

## CONCLUDING REMARKS

It has been shown that wing-body combinations employing planforms with cranked leading edges can be designed to have the same aerodynamic center at high supersonic and subsonic Mach numbers. At subsonic Mach numbers these cranked planforms had considerably less drag due to lift, and consequently higher lift-drag ratios, than was predicted from linear theory, although these planforms also exhibited a loss in longitudinal stability. For the same exposed area and thickness in percent chord, cranked planforms have more usable volume yet less minimum drag than delta planforms. At a Mach number of 3.0, it has been shown that some cranked planforms not only have considerably higher lift-drag ratios than their straight leading-edge counterparts when planar wings are used but also these planforms have more theoretical potential for improvements in flight efficiency by warping.

## REFERENCES

1. Hicks, Raymond M.; and Hopkins, Edward J.: Effects of Spanwise Variation of Leading-Edge Sweep on the Lift, Drag, and Pitching Moment of a Wing-Body Combination at Mach Numbers From 0.7 to 2.94. NASA TN D-2236, 1964.
2. Robins, A. Warner; Harris, Roy V., Jr.; and Jackson, Charlie M., Jr.: Characteristics at Mach Number of 2.03 of a Series of Wings Having Various Spanwise Distributions of Thickness Ratio and Chord. NASA TN D-631, 1960.
3. Shrout, Barrett L.: Zero-Lift Drag at Mach 1.42, 1.83, and 2.21 of a Series of Wings With Variations of Thickness Ratio and Chord. NASA TN D-2811, 1965.
4. Hopkins, Edward J.: Some Effects of Planform Modification on the Skin Friction Drag. AIAA J. (Tech. Comments), vol. 2, no. 2, Feb. 1964, pp. 413-414.
5. Pitts, William C.; Nielsen, Jack N.; and Kaattari, George E.: Lift and Center of Pressure of Wing-Body-Tail Combinations at Subsonic, Transonic, and Supersonic Speeds. NACA Rept. 1307, 1957.
6. Lomax, Harvard; and Sluder, Loma: Chordwise and Compressibility Corrections to Slender-Wing Theory. NACA Rept. 1105, 1952. (Supersedes NACA TN 2295.)
7. DeYoung, John; Rule of Thumb Equation for Predicting Lifting-Surface-Theory Values of Lift. J. Aeron. Sci., (Readers' Forum), vol. 24, no. 8, Aug. 1957, p. 629.

8. DeYoung, John, and Harper, Charles W.: Theoretical Symmetric Span Loading at Subsonic Speeds for Wings Having Arbitrary Plan Form. NACA Rept. 921, 1948.
9. Schlichting, Hermann, (J. Kestin, trans.): Boundary Layer Theory. McGraw-Hill Book Co., Inc., 1955, p. 540.
10. Sommer, Simon C.; and Short, Barbara J.: Free-Flight Measurements of Turbulent-Boundary-Layer Skin Friction in the Presence of Severe Aerodynamic Heating at Mach Numbers From 2.7 to 7.0. NACA TN 3391, 1955.
11. Woodward, F. A.: A Method of Aerodynamic Influence Coefficients With Application to the Analysis and Design of Supersonic Wings. Doc. D6-8178, The Boeing Co., April 1962.
12. Middleton, Wilbur D.; and Carlson, Harry W.: A Numerical Method for Calculating the Flat-Plate Pressure Distributions on Supersonic Wings of Arbitrary Planform. NASA TN D-2570, 1965.
13. Harris, Roy V., Jr.: An Analysis and Correlation of Aircraft Wave Drag. NASA TM X-947, 1964.
14. Woodward, F. A., and Larson, J. W.: Staff of the Aerodynamic Research Unit. A Method of Optimizing Camber Surfaces For Wing-Body Combinations at Supersonic Speeds. Part I. - Theory and Application. Doc. D6-10741, Pt. I, (Prepared for NASA under contract no. NAS2-2282.) The Boeing Co., 1965.

### MODEL GEOMETRY

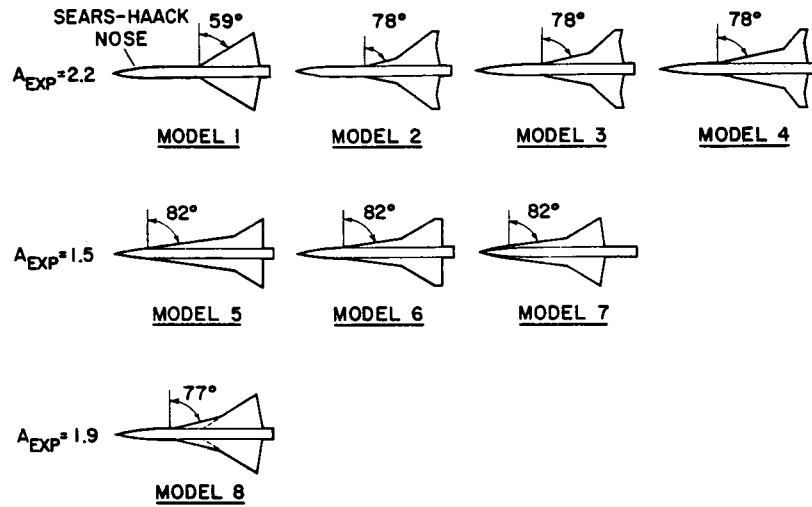


Figure 1

### REYNOLDS NUMBER EFFECTS

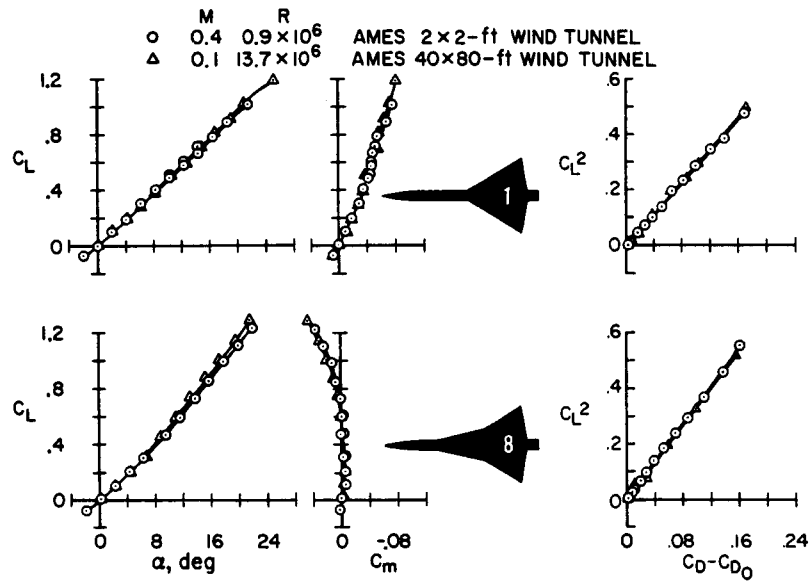


Figure 2

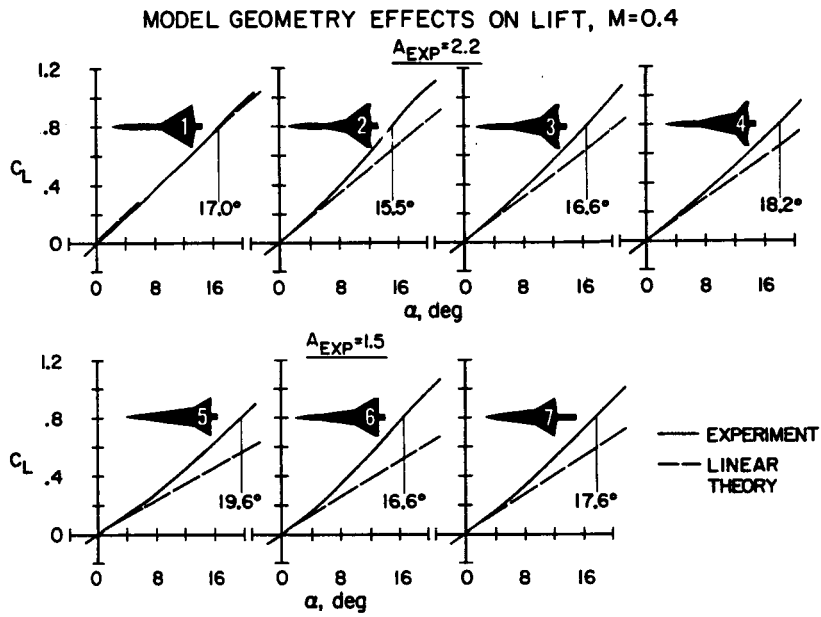


Figure 3

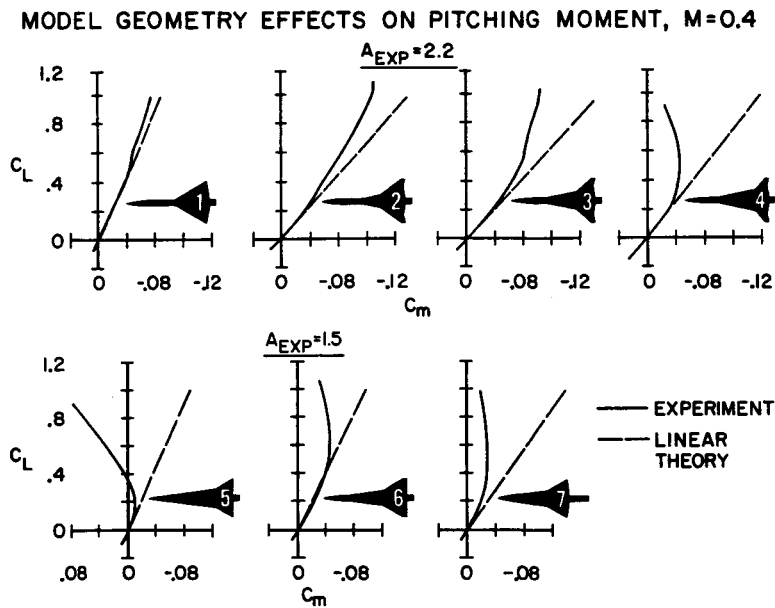


Figure 4

EFFECT OF MACH NUMBER ON  $\partial C_m / \partial C_L$

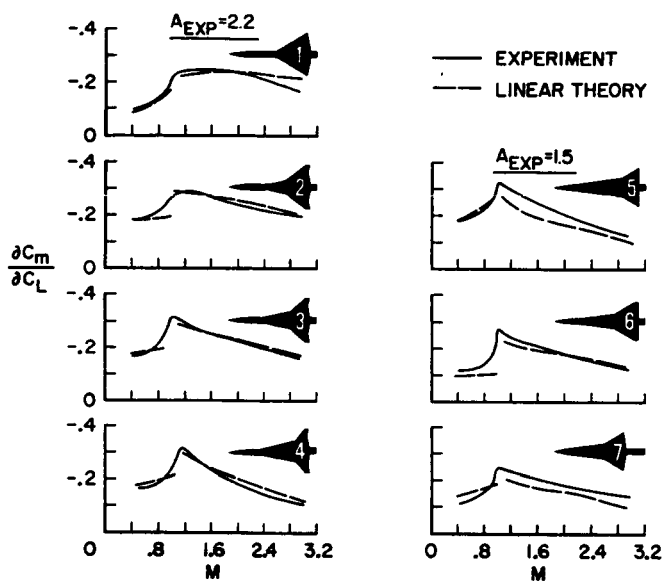


Figure 5

EFFECT OF MACH NUMBER ON  $\partial C_L / \partial \alpha$

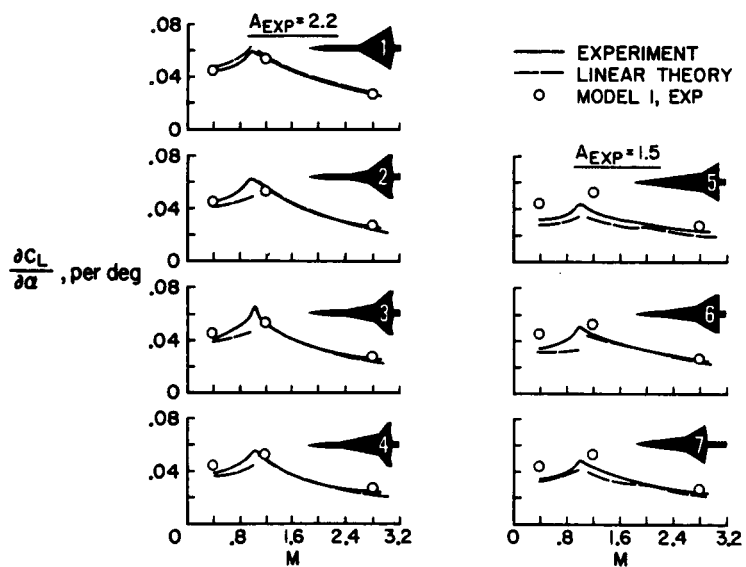


Figure 6

EFFECT OF MACH NUMBER ON  $\partial C_D / \partial C_L^2$

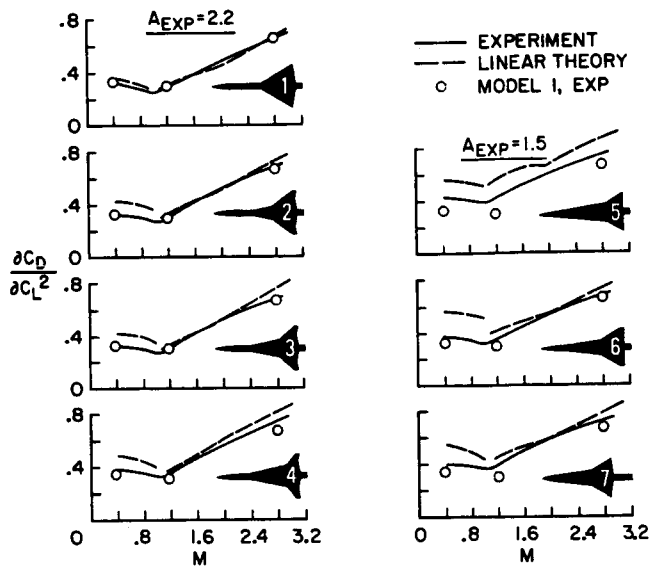


Figure 7

EFFECT OF MACH NUMBER ON  $C_{D_0}$

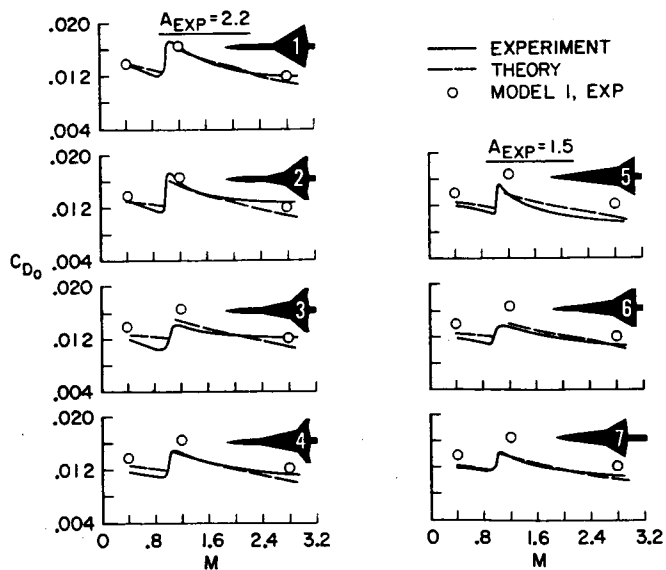


Figure 8

EFFECT OF MACH NUMBER ON  $(L/D)_{MAX}$

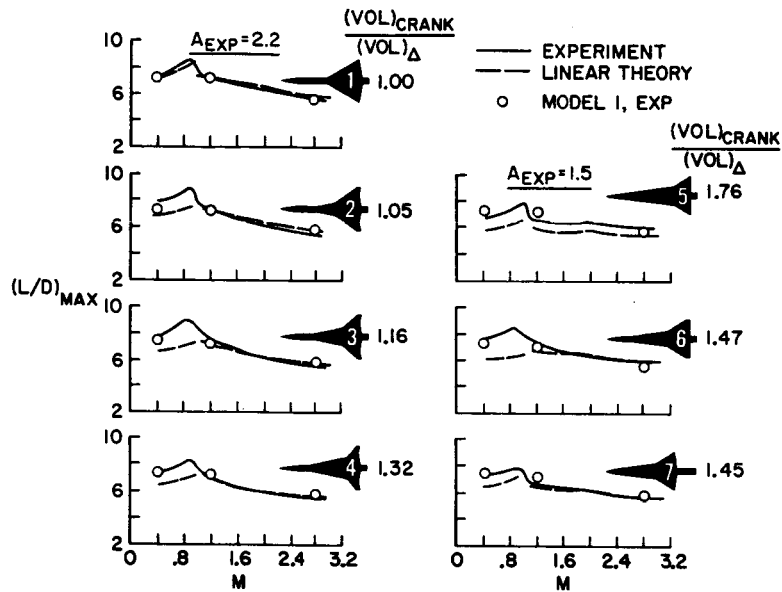


Figure 9

THEORETICAL POTENTIAL FOR L/D OF MODELS 1 AND 6

ASSUMED FLIGHT CONDITIONS:

- M = 3
- S = 9,970 ft<sup>2</sup>
- 70,000 ft
- C<sub>L</sub> = .07

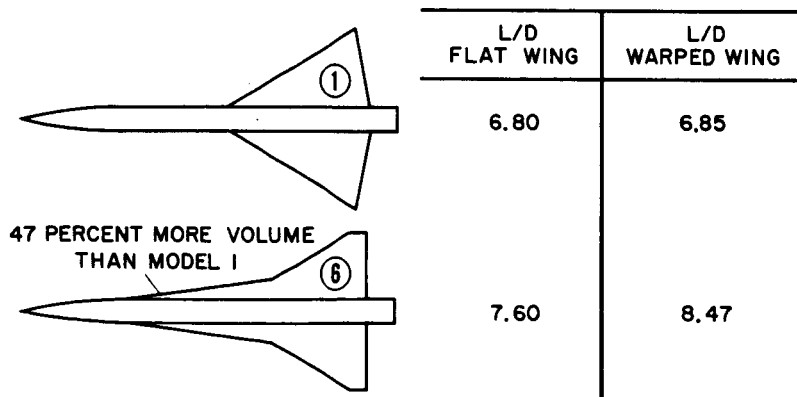


Figure 10

### 33. RECENT RESULTS ON THE AERODYNAMICS OF WINGED MISSILES

By M. Leroy Spearman and William A. Corlett  
NASA Langley Research Center

#### SUMMARY

Investigations have been made in the Langley 8-foot transonic pressure tunnel and the Langley Unitary Plan wind tunnel over a Mach number range from 0.50 to 4.63 to determine the aerodynamic characteristics of three cruciform winged missile configurations with different control arrangements - a canard control, an aft tail control, and an all-movable wing control. The results for each configuration indicated a slight forward movement of the aerodynamic center with increasing supersonic Mach number so that a compatible relationship between the aerodynamic center and the center of gravity might be maintained. For each arrangement, the pitch-control effectiveness, which, in general, decreased with increasing angle of attack at the lower Mach numbers, indicated an increase with angle of attack at the higher Mach numbers. This increase in control effectiveness at high Mach numbers, coupled with the decrease in stability level, resulted in maneuvering limits, without the onset of static instability, that are generally well in excess of the limits that might be expected for an aircraft target.

#### INTRODUCTION

Although a considerable amount of research has been done in the past on the aerodynamics of winged missiles, this type of research has diminished considerably over the last few years. Much of the past work (reported in refs. 1 to 17) is limited, particularly in the range of Mach numbers investigated, and, to some extent, in the configuration variables that were studied. Recently a renewed interest has been shown in the development and improvement of various types of missile systems, and it is the purpose of this paper to present a brief summary of some of the results recently obtained on several representative winged maneuverable missiles suitable primarily for surface-to-air or air-to-air use against aircraft.

The missiles considered in these investigations (fig. 1) include three cruciform configurations with different control arrangements, a fixed wing with canard control, a fixed wing with aft tail control, and a fixed tail with all-movable wing control. The pitch control is in the horizontal plane in each case. Each of the fixed-wing arrangements is in line with the controls, whereas the fixed-tail arrangement is rotated  $45^\circ$  with respect to the wing control. (See lower right-hand sketch.) These configurations are not a part of a systematic program but represent three completely different control arrangements that might result from considerations other than aerodynamics alone. Investigations of these missile configurations have been conducted over a Mach number range from 0.50 to 4.63 in both the Langley 8-foot transonic pressure tunnel and the Langley Unitary Plan wind tunnel.

More complete results of these investigations and a more detailed description of the configurations may be found in references 18 and 19.

### SYMBOLS

The aerodynamic-coefficient data are referred to the stability-axis system.

A	maximum cross-sectional area of body, feet <sup>2</sup>
a <sub>n</sub>	normal acceleration, feet/second <sup>2</sup>
d	reference diameter (maximum cross section)
C <sub>L</sub>	lift coefficient, $\frac{\text{Lift}}{qA}$
C <sub>m</sub>	pitching-moment coefficient, $\frac{\text{Pitching moment}}{qAd}$
C <sub>m<math>\delta</math></sub>	pitching-moment coefficient per degree of control deflection
C <sub>L<math>\alpha</math></sub>	slope of lift curve measured near $\alpha = 0$
h	altitude, feet
l	body length, feet
M	Mach number
q	dynamic pressure, pounds/feet <sup>2</sup>
W	weight, pounds
$\alpha$	angle of attack, degrees
$\delta_c$	horizontal-canard deflection, positive when leading edge is up, degrees
$\delta_t$	horizontal-tail deflection, positive when leading-edge is up, degrees
$\delta_w$	horizontal-wing deflection, positive when leading edge is up, degrees
x <sub>ac</sub>	location of aerodynamic center from body apex, feet
x <sub>cg</sub>	location of center of gravity from body apex, feet

## DISCUSSION

The basic pitch-control results for the canard-control configuration at a low and a high supersonic Mach number - 1.50 and 4.63 - are shown in figure 2. These results indicate a reasonable degree of linearity at each Mach number. The pitch-control effectiveness  $C_{m\delta}$  decreases somewhat with increasing angle of attack at the lower Mach number. This result is typical for such a condition since the canard surface tends to lose lift effectiveness at the high combined angle of attack and control deflection. At the higher Mach number, however, the pitch effectiveness tends to increase with increasing angle of attack primarily because of an increase in the local dynamic pressure on the compression side of the canard surface. The change in lift with control deflection is quite small but, typical of canard arrangements, does result in a favorable increase.

The basic pitch-control results for the aft tail-control configuration at  $M = 2.00$  and 4.63 are shown in figure 3. A large decrease in stability occurs at moderate angles of attack at the low Mach number. This decrease is caused primarily by the unstable moment of the body which, at low Mach numbers, increases more rapidly with increasing angle of attack than does the stabilizing moment of the wing and tail. At the higher Mach number, the tail and wing moments are more dominant and the pitching-moment variation with angle of attack is considerably improved. The effectiveness of the tail in producing pitching moment  $C_{m\delta}$  is essentially constant with angle of attack at  $M = 2.00$ , but some increase in effectiveness with increasing angle of attack is indicated at the higher Mach number as a result of an increase in local dynamic pressure at the tail. At either Mach number, deflection of the tail for trimming in pitch results in a loss in lift that is inherent with aft tail controls.

The basic pitch-control results for the wing-control configuration at  $M = 1.47$  and 4.63 are shown in figure 4. A distinct nonlinearity occurs in the pitching moment for the lower Mach number at moderate angles of attack as a result of the tail passing through the region of the wing wake. The nonlinearity at  $M = 4.63$  is much less critical.

The pitch control for this type of arrangement depends upon a relatively large lift increment from the wing in conjunction with a short moment arm. The resultant pitch-control effectiveness  $C_{m\delta}$  at  $M = 1.47$  decreases with increasing angle of attack because of the decrease in wing lift at high combined angles of attack and control deflection. At  $M = 4.63$  the lift increment provided by the wing is sustained at high angles of attack, again because of an increase in local dynamic pressure, and the resultant pitch effectiveness  $C_{m\delta}$  increases with increasing angle of attack.

The variation of some of the longitudinal parameters with Mach number is presented in figure 5. The coefficients are based on common reference dimensions and are thus directly comparable. The canard- and aft-tail-control configurations, which have relatively large wings, provide relatively high values of  $C_{L\alpha}$  whereas the wing-control configuration, with its smaller lifting

surface, provides relatively low values of  $C_{L\alpha}$ . The pitch-control effectiveness  $C_{m\delta}$  (measured at  $\alpha = 0^\circ$ ) decreases progressively with increasing supersonic Mach number for each configuration, with the highest values of  $C_{m\delta}$  occurring for the canard control and the lowest values occurring for the wing control.

The aerodynamic-center positions in percent body length  $\left(\frac{x_{ac}}{l}\right)$  are on the order of 60 to 70 percent and indicate a slight forward movement with increasing supersonic Mach number for each configuration. This slight variation with Mach number should ease the problem of obtaining a compatible relationship between the center-of-gravity position and the aerodynamic-center position so that a desirable margin of stability might be easily maintained throughout the supersonic speed range.

The results shown in figure 6 relate the basic aerodynamic characteristics to the maneuvering capabilities of each configuration. The results show the variation of maximum trimmed values of  $C_L$  with Mach number for various positions of the center of gravity for each configuration. The results reflect the general increase in trim  $C_L$  to be expected as the center of gravity is moved rearward and the stability margin is decreased. These results are restricted to conditions of positive static stability only and are terminated when a nonlinear pitching-moment variation results in the occurrence of more than one trim point for a given control deflection.

At low Mach numbers the variation of trim  $C_L$  with center-of-gravity position is relatively small and linear because of the generally higher levels of static stability and the general decrease in  $C_{m\delta}$  with increasing angle of attack. With increasing Mach number the values of trim  $C_L$  for a given center-of-gravity position initially tend to decrease because of the decrease in  $C_{m\delta}$ .

With further increase in Mach number, however, the values of trim  $C_L$  tend to increase for a given center-of-gravity position and to become more sensitive to variations in the center of gravity. The tendency toward higher available values of trim lift at higher Mach numbers results, in general, from a combination of the reduction in stability level and the increase in  $C_{m\delta}$  at high angles of attack.

The boundaries indicated by the upper limits of these curves represent the maximum values of trim lift available without the onset of static instability. Boundaries so obtained are shown in figure 7 with the lift coefficient based on a common reference area so that the results are directly comparable. These results indicate that the maximum values of  $C_L$  obtainable at the lower end of the Mach number regime are essentially the same for all three configurations. However, the variation of these lift boundaries with increasing Mach number is considerably different. In the Mach number range from about 2 to 3 the aft tail control indicates a marked superiority whereas, for Mach numbers above 3.5, the canard control shows a marked superiority. The wing control indicates the least variation with Mach number and the lowest values of trim lift throughout the Mach number range.

The four lower lines designated 40 000, 60 000, 70 000, and 90 000 feet represent the values of  $C_L$  required to sustain level flight at these altitudes for an arbitrary loading value  $W/A$  of 1000 pounds/foot<sup>2</sup> (based on body cross-sectional area). These values are included in order to give an indication of the excess lift available for maneuvering over and above that required for level flight. It should be pointed out that such an indication may be pessimistic since a missile may often approach a target on a climbing flight path much closer to zero lift.

However, on the basis of the conditions chosen for comparison, some observations can be made. For example, the results indicate that for Mach numbers below 2, level flight could not be achieved for any of these missiles for altitudes above about 60 000 feet. For higher Mach numbers, however, level flight is possible for altitudes greater than 90 000 feet.

The variation of normal acceleration  $a_n$  with Mach number was obtained for each configuration for  $h = 60\ 000$  feet and  $W/A = 1000$  pounds/foot<sup>2</sup> by ratioing the lift available to the lift required for level flight. The results (fig. 7) indicate values of  $a_n$  in the Mach number range from 2 to 4.6 that vary from about 1.5 for each configuration up to about 19 for the canard control, about 10 for the aft tail control, and about 9 for the wing control. These results are, of course, only qualitative and would vary both upward and downward for other assumed conditions. For an altitude of 90 000 feet, for example, the canard configuration is still capable of about a 4g maneuver from level flight at the highest Mach number. The maneuvering capabilities indicated are generally in excess of the limits that might be expected for an aircraft target, and, within the scope of these results, a variety of mission requirements might be satisfied.

#### CONCLUDING REMARKS

Investigations have recently been made in the Mach number range from 0.50 to 4.63 of three cruciform winged missile configurations with different control arrangements - a canard control, an aft tail control, and an all-movable wing control. The results for each configuration indicated a slight forward movement of the aerodynamic center with increasing supersonic Mach number so that a compatible relationship between the aerodynamic center and the center of gravity might be maintained. For each arrangement, the pitch-control effectiveness, which, in general, decreased with increasing angle of attack at the lower Mach numbers, indicated an increase with angle of attack at the higher Mach numbers. This increase in control effectiveness at high Mach numbers, coupled with the decrease in stability level, resulted in maneuvering limits, without the onset of static instability, that were generally well in excess of the limits that might be expected for an aircraft target.

## REFERENCES

1. Spearman, M. Leroy: Aerodynamic Characteristics in Pitch of a Series of Cruciform-Wing Missiles With Canard Controls at a Mach Number of 2.01. NASA TN D-839, 1961.
2. Spearman, M. Leroy: Component Tests To Determine the Aerodynamic Characteristics of an All-Movable 70° Delta Canard-Type Control in the Presence of a Body at a Mach Number of 1.61. NACA RM L53I03, 1953.
3. Spearman, M. Leroy: Effect of Large Deflections of a Canard Control and Deflections of a Wing-Tip Control on the Static-Stability and Induced-Roll Characteristics of a Cruciform Canard Missile at a Mach Number of 2.01. NACA RM L53K03, 1953.
4. Spearman, M. Leroy; and Robinson, Ross B.: Aerodynamic Characteristics of a Cruciform-Wing Missile With Canard Control Surfaces and of Some Very Small Span Wing-Body Missiles at a Mach Number of 1.41. NACA RM L54B11, 1954.
5. Spearman, M. Leroy; and Driver, Cornelius: Wind-Tunnel Investigation at a Mach Number of 2.01 of the Aerodynamic Characteristics in Combined Pitch and Sideslip of Some Canard-Type Missiles Having Cruciform Wings and Canard Surfaces With 70° Delta Plan Forms. NACA RM L54F09, 1954.
6. Robinson, Ross B.: Aerodynamic Characteristics of Missile Configurations With Wings of Low Aspect Ratio for Various Combinations of Forebodies, Afterbodies, and Nose Shapes for Combined Angles of Attack and Sideslip at a Mach Number of 2.01. NACA RM L57D19, 1957.
7. Robinson, Ross B.: Wind-Tunnel Investigation at a Mach Number of 2.01 of the Aerodynamic Characteristics in Combined Angles of Attack and Sideslip of Several Hypersonic Missile Configurations With Various Canard Controls. NACA RM L58A21, 1958.
8. Katzen, Elliott D.; and Jorgensen, Leland H.: Aerodynamics of Missiles Employing Wings of Very Low Aspect Ratio. NACA RM A55L13b, 1956.
9. Foster, Gerald V.: Sideslip Characteristics at Various Angles of Attack for Several Hypersonic Missile Configurations With Canard Controls at a Mach Number of 2.01. NASA TM X-134, 1959.
10. Stone, David G.: Maneuver Performance of Interceptor Missiles. NACA RM L58E02, 1958.
11. Spearman, M. Leroy; and Robinson, Ross B.: Longitudinal Stability and Control Characteristics at Mach Numbers of 2.01, 4.65, and 6.8 of Two Hypersonic Missile Configurations, One Having Low-Aspect-Ratio Cruciform Wings With Trailing-Edge Flaps and One Having a Flared Afterbody and All-Movable Controls. NASA TM X-46, 1959.

12. Robinson, Ross B.; and Bernot, Peter T.: Aerodynamic Characteristics at a Mach Number of 6.8 of Two Hypersonic Missile Configurations, One With Low-Aspect-Ratio Cruciform Fins and Trailing-Edge Flaps and One With a Flared Afterbody and All-Movable Controls. NACA RM L58D24, 1958.
13. Church, James D.; and Kirkland, Ida M.: Static Aerodynamic Characteristics of Several Hypersonic Missile-and-Control Configurations at a Mach Number of 4.65. NASA TM X-187, 1960.
14. Robinson, Ross B.; and Spearman, M. Leroy: Aerodynamic Characteristics for Combined Angles of Attack and Sideslip of a Low-Aspect-Ratio Cruciform-Wing Missile Configuration Employing Various Canard and Trailing-Edge Flap Controls at a Mach Number of 2.01. NASA MEMO 10-2-58L, 1958.
15. Robinson, Ross B.; and Foster, Gerald V.: Static Longitudinal Stability and Control Characteristics at a Mach Number of 2.01 of a Hypersonic Missile Configuration Having All-Movable Wing and Tail Surfaces. NASA TM X-516, 1961.
16. Spearman, M. Leroy; and Robinson, Ross B.: Longitudinal Stability and Control Characteristics of a Winged and a Flared Hypersonic Missile Configuration With Various Nose Shapes and Flare Modifications at a Mach Number of 2.01. NASA TM X-693, 1962.
17. Corlett, William A.; and Fuller, Dennis E.: Aerodynamic Characteristics at Mach 1.60, 2.00, and 2.50 of a Cruciform Missile Configuration With In-Line Tail Controls. NASA TM X-1112, 1965.
18. Fuller, Dennis E.; and Corlett, William A.: Supersonic Aerodynamic Characteristics of a Cruciform Missile Configuration With Low-Aspect-Ratio Wings and In-Line Tail Controls. NASA TM X-1025, 1964.
19. Foster, Gerald V.; and Corlett, William A.: Aerodynamic Characteristics at Mach Numbers From 0.40 to 2.86 of a Missile Model Having All-Movable Wings and Interdigitated Tails. NASA TM X-1184, 1965.

### MISSILE CONFIGURATIONS

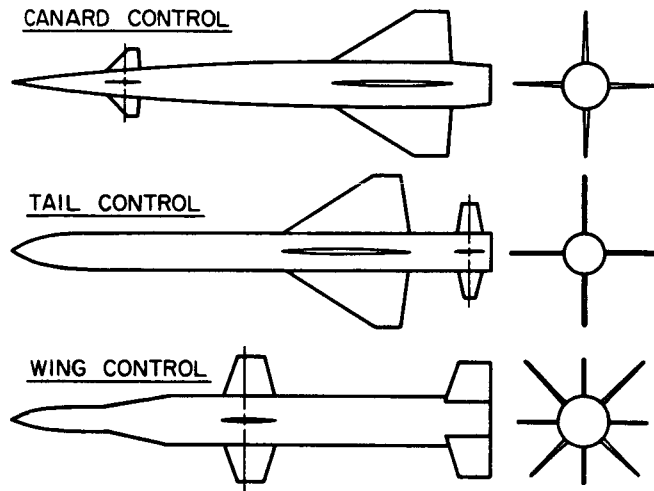


Figure 1

### AERODYNAMIC CHARACTERISTICS CANARD CONTROL

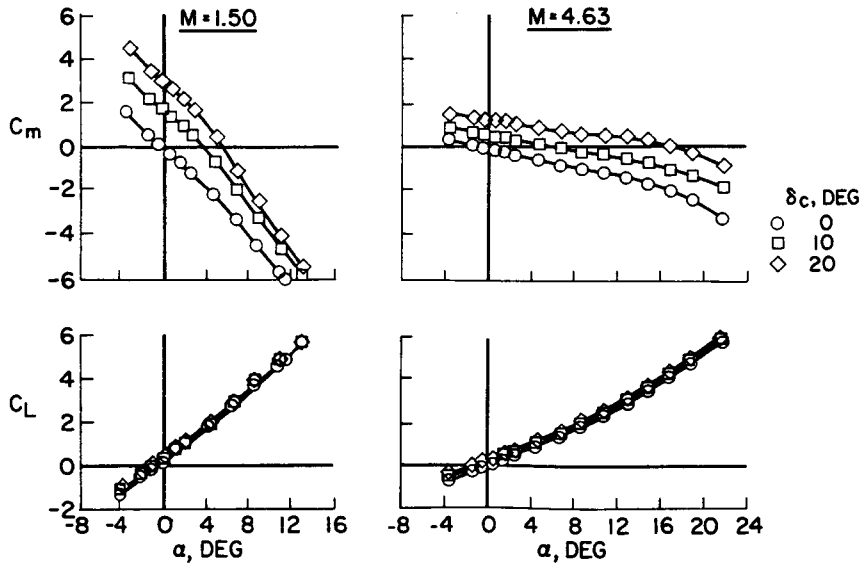


Figure 2

AERODYNAMIC CHARACTERISTICS  
TAIL CONTROL

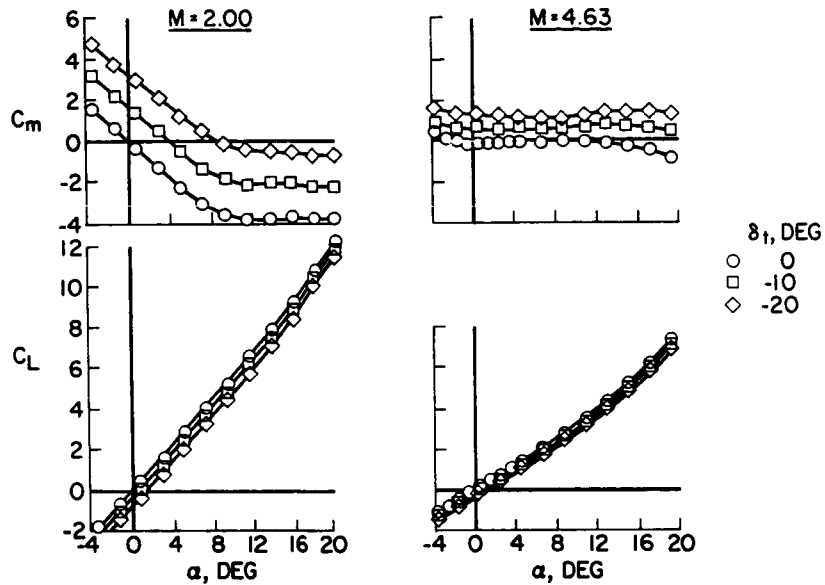


Figure 3

AERODYNAMIC CHARACTERISTICS  
WING CONTROL

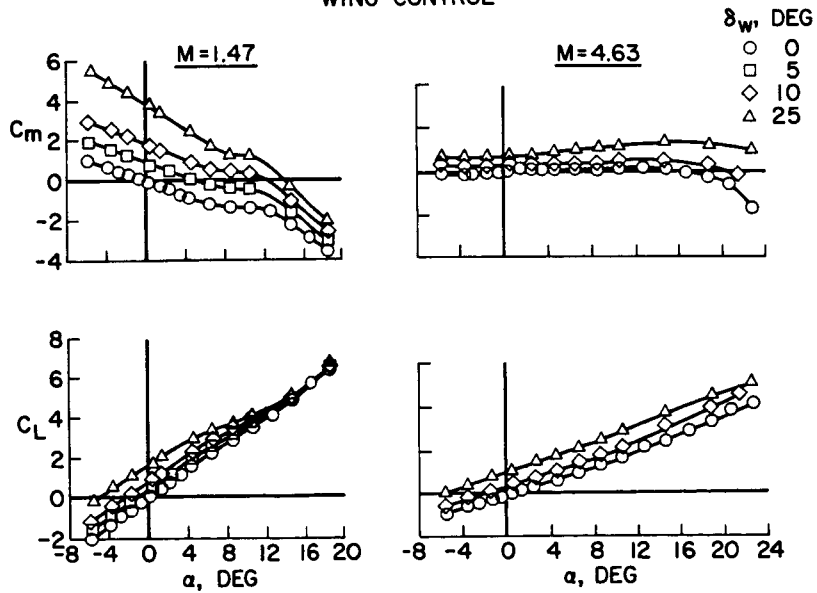


Figure 4

VARIATION OF LONGITUDINAL PARAMETERS WITH MACH NUMBER

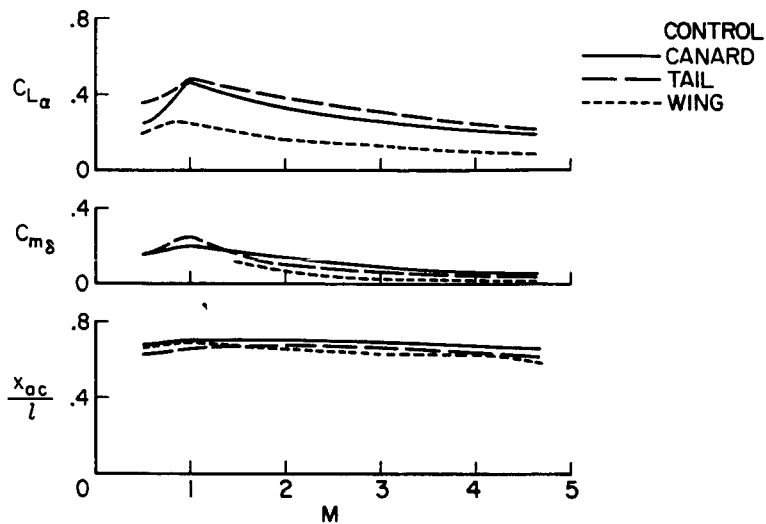


Figure 5

MAXIMUM TRIM  $C_L$  VALUES FOR VARIOUS CENTER-OF-GRAVITY POSITIONS

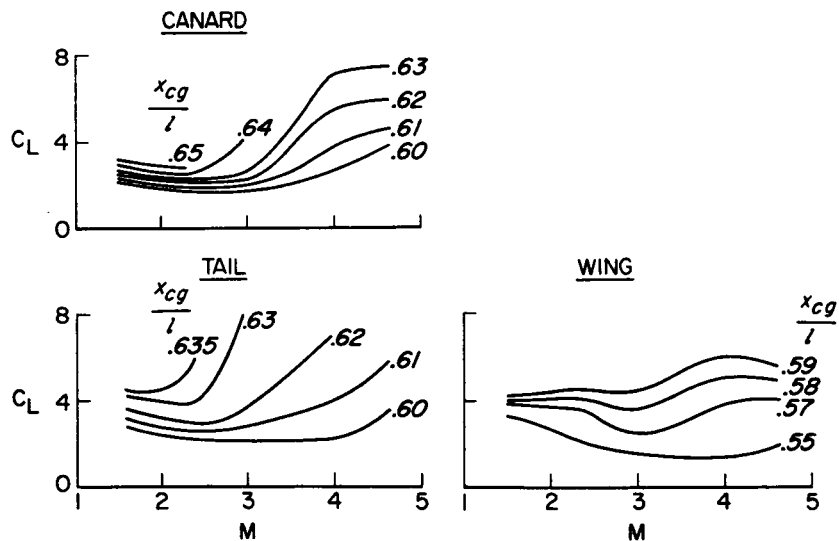


Figure 6

### MAXIMUM TRIM $C_L$ BOUNDARIES

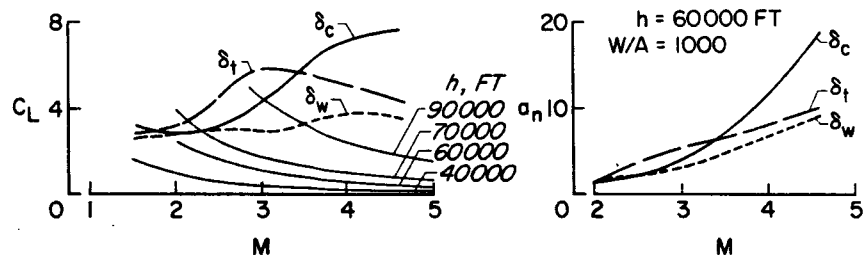


Figure 7

### 34. SOME HIGHLIGHTS OF RECENT V/STOL AERODYNAMICS RESEARCH

By John P. Campbell  
NASA Langley Research Center

#### SUMMARY

Some of the highlights of the papers on aerodynamics research in the recent NASA Conference on V/STOL and STOL Aircraft are presented. The V/STOL types discussed include helicopters, propeller V/STOL, lift-fan and cruise-fan V/STOL, and jet-lift V/STOL.

#### INTRODUCTION

This paper presents some of the highlights of the papers which dealt with aerodynamics in the NASA Conference on V/STOL and STOL Aircraft held at the Ames Research Center on April 4-5, 1966. It covers research reported in the three sessions: Helicopters and Propeller V/STOL, Lift-Fan and Cruise-Fan V/STOL, and Jet-Lift V/STOL. The paper is not intended to be a general state-of-the-art summary of V/STOL aerodynamics research but is merely a presentation of some of the highlights of the conference. No attempt is made to cite the individual sources of the material presented herein, but the reader may find these sources by referring to reference 1.

#### SYMBOLS

A	propeller disk area, sq ft
A <sub>j</sub>	jet nozzle area, sq ft
b	wing span, ft
C <sub>D,W</sub>	wave-drag coefficient based on frontal area
C <sub>f</sub>	effective skin-friction coefficient
C <sub>L</sub>	lift coefficient
C <sub>T,s</sub>	thrust coefficient, $T/q_s A$
D	propeller diameter, ft; jet-engine tailpipe diameter, ft
D	drag, lb

$D_e$	equivalent diameter; diameter of a single nozzle having the same area as the sum of the several nozzles of a multijet configuration, ft
EGT	exhaust-gas temperature, °F
$e$	span efficiency factor
$h$	height of model above ground, ft
$i_d$	duct incidence angle, deg
$L$	lift, lb
$\Delta L$	incremental lift
$\Delta L_b$	incremental lift due to base loss, lb
$\Delta L_w$	increment in wing lift, lb
$M$	Mach number
$\Delta M$	increment in pitching moment due to interference, ft-lb
$q_n$	dynamic pressure at nozzle exit, lb/sq ft
$q_s$	slipstream dynamic pressure, lb/sq ft
$q_x$	dynamic pressure at distance $x$ downstream of nozzle, lb/sq ft
$R$	rotor radius, ft
$\dot{r}_{max}$	maximum self-generated yaw disturbance, deg/sec <sup>2</sup>
$S$	total planform area, sq ft
$S_{wet}$	wetted area, sq ft
$T$	thrust, lb
$T_I$	ideal jet thrust, lb
$T_s$	static thrust, lb
$V$	free-stream velocity, ft/sec or knots
$V_j$	jet velocity, ft/sec
$V/\Omega R$	advance ratio

$V_{\infty}$	free-stream velocity, ft/sec
$W$	gross weight, lb
$x$	distance downstream from jet exit, ft
$\alpha$	angle of attack, deg
$\beta_V$	lift-fan vector angle from fan axis, deg
$\gamma$	flight-path angle, deg
$\delta_F$	flap deflection, deg
$\theta_j$	jet deflection, positive downward from chord line, deg
$\rho_j$	air density in jet, slugs/ft <sup>3</sup>
$\rho_{\infty}$	free-stream air density, slugs/ft <sup>3</sup>
$\Omega$	rotor angular velocity, rad/sec

#### HELICOPTERS AND PROPELLER V/STOL

For helicopters, information is presented on two promising rotary-wing concepts - the hingeless rotor and the jet-flap rotor; some recent research dealing with descent capability and slipstream recirculation for the tilt-wing V/STOL type is discussed.

#### Hingeless Rotor

Figure 1 presents relative damping moment and control moment in hovering calculated for three helicopter types - one having a rotor with a central hinge, one having a rotor with the flapping hinge offset 4 percent of the rotor radius, and one having a hingeless rotor. The solid lines are for sea level and the dashed lines for an altitude of 15 000 feet. The damping and control moments are referenced to the values for the rotor with the central hinge at sea level. Moving up the lines for the other two rotor types represents increasing the rotor blade weight. The data show that incorporating hinge offset provides increases in both damping and control moment over the values for the rotor with the central hinge, and the use of the hingeless rotor provides even greater increases. There is a limiting upper boundary for the hingeless rotor labeled "Unacceptable gyroscopic coupling." If rotor weight is increased to the point where this boundary is crossed, excessive coupling of rolling and pitching motions will be experienced. Increasing altitude from sea level to 15 000 feet causes a substantial increase in relative damping for all three rotors and also

a reduction in control moment for the hingeless rotor. An important point to be brought out here is that a hingeless rotor design which is on the satisfactory side of the coupling boundary at sea level may move to the unsatisfactory side when operating at altitude. To reduce the coupling at altitude it may be necessary to use lighter blades in order to move down on the curve below the boundary, or it may be possible to minimize the coupling by the use of some feedback device.

### Jet-Flap Rotor

The jet-flap rotor has been proposed as a means of delaying retreating blade stall and thereby permitting much higher forward speeds for the helicopter. Figure 2 shows cross-section views of the blade of a jet-flap rotor recently tested at Ames in the 40- by 80-foot tunnel. The rotor was built by the French firm of Giravions Dorand under contract to the U.S. Army. It is driven by compressed air which is ducted through the blade spar and exhausted in a thin sheet over a trailing-edge flap which extends over the outboard third of the blade radius. Deflection of the jet flap is used for cyclic and total pitch control.

The capability of the jet-flap rotor on the basis of tests to date compared with that for a conventional rotor is shown in figure 3. Values of lift for both rotors ratioed to the static thrust of the conventional rotor are plotted against airspeed. Over the speed range covered in the tests, the measured values for the jet-flap rotor are well above the upper limit of lift capability for conventional rotors as determined from blade stall limitations. The top speed in the jet-flap rotor tests was established by a mechanical limitation on flap deflection to about  $50^\circ$  on the test rotor. Since there were no indications of retreating blade stall at this speed, it appears likely that substantially higher speeds could be obtained on a modified rotor. The experimental data and calculations (based on the method of ref. 2) for the jet-flap rotor show the same general trends where they can be compared; but in the highest speed range, the calculations involve a number of uncertainties and may prove to be somewhat optimistic. In any event, the results obtained to date with the jet-flap rotor indicate a promise of higher forward speeds for the helicopter.

### Propeller V/STOL

Propeller tilt-wing V/STOL aircraft experience a limitation on descent capability because of wing stall during partial-power descent conditions when the slipstream velocity is low. Considerable research has been carried out in this area and results have indicated that the problem is quite amenable to solution by careful design. Some of the more recent research on the problem has been carried out with the model shown in figure 4. This large-scale semi-span research model is being used in systematic studies of configuration variables in the Langley full-scale tunnel. One of the important variables in determining partial-power descent capability is the vertical position of the propeller thrust line. Some results obtained with this model on the effect of

propeller position are shown in figure 5. Flight-path angle  $\gamma$  (positive for climb and negative for descent) is plotted against thrust coefficient  $C_{T,s}$ . A value for  $C_{T,s}$  of 1.0 represents hovering and values from about 0.6 to 0.9 generally cover the transition range. Wing stall boundaries are shown for three vertical positions of the propeller with respect to the wing. The data show that moving the propeller from a high to a low position results in the capability for descending at much steeper angles without wing stalling. The XC-142 tilt-wing airplane, which has a propeller position corresponding to the mid position shown in figure 5, has operated satisfactorily at descent angles up to  $15^\circ$ .

A problem that has proved more bothersome than descent capability for the XC-142 is the effect of slipstream recirculation in ground effect. Figure 6 presents some information on this problem. The sketch at the right of the figure illustrates the type of flow developed around the airplane as it approaches the ground at very low speeds. Some of the propeller slipstream moves forward after striking the ground and recirculates to create a turbulent region through which the airplane must fly. The airplane experiences disturbances about all axes, but, for the XC-142, the yaw disturbances seem to predominate and give the most trouble. The plot at the left shows yaw disturbances in terms of maximum yaw accelerations experienced by the XC-142 plotted against airspeed. The pilots of the airplane indicate that in the airspeed range from about 12 to 30 knots there is danger of losing control as a result of these disturbances. A crash landing of one of the airplanes in 1965 was attributed to this problem. Wind-tunnel and flight research has shown that varying the flap programing can reduce the range of wing incidence where the problem is encountered but the speed range of concern is not changed. At present, the problem is being avoided in flight by flying at speeds greater than 30 knots or less than 12 knots when in ground effect. Eventual solution of the problem may require increased control capability over that now available or some additional artificial stabilization.

## LIFT-FAN AND CRUISE-FAN V/STOL

### Tandem Lift Fan

Figure 7 shows a large-scale model of a tandem lift-fan configuration mounted for testing in the Ames 40- by 80-foot tunnel. This model has tandem lift fans fore and aft of the wing at the wing-fuselage juncture. Figure 8 shows the variation of lift with airspeed for this model. The lift is given in terms of the static thrust and the airspeed is given in terms of  $V/V_j$  where  $V_j$  is the jet velocity. Curves are shown for operation of rear fans only, front fans only, and all four fans. The rear fans induce a substantial increase in lift with increasing speed whereas the front fans induce negative lift. A small increase in lift occurs when all four fans are operating.

## Lift-Cruise Fan

The lift-cruise fan configuration shown in figure 9 mounted for testing in the Ames 40- by 80-foot tunnel has lift fans mounted forward on the fuselage so they can be extended as shown for hovering and transition and can be folded into the fuselage for cruising flight. The fans at the rear are cruise fans which are mounted on pylons so that they can be rotated to a vertical position for hovering flight. The effect of the front fans on wing lift is shown in figure 10. The ratio of wing lift to fan static thrust is plotted against velocity ratio for three positions of the front fans. A loss in lift due to fan operation occurs for all fan positions, the greatest loss being obtained in position 1, directly ahead of the wing, and the least loss being obtained in position 3, the low position. Despite this loss in wing lift due to fan operation, the net wing lift can be made positive by using sufficient wing camber and flap deflection. There is also a positive induced lift on the fan fairings. The ratio of total lift to static thrust for the model with the front fans in the low position is shown in figure 11 plotted against airspeed. For these tests, the wing flaps were set at  $45^\circ$  and the cruise fans were tilted at various angles so that the fan thrust balanced the drag. There appears to be a substantial increase in lift with increasing speed which would indicate considerable STOL capability. However, this increase in lift or STOL capability is not nearly as great as it could be if the fan slipstream were spread out more or less uniformly across the span of the wing as is done in the case of V/STOL configurations such as the tilt wing.

This point is illustrated in figure 12 which compares the thrust required for level flight in the transition range for lift-cruise-fan and tilt-wing configurations having a wing loading of 100 pounds per square foot. The thrust is shown in terms of thrust-weight ratio. The more rapid dropoff in thrust required with increasing airspeed for the tilt wing is an indication of greater STOL capability. In addition, the curves indicate that in low-speed landing approaches the tilt wing could operate at lower thrust values, which is very desirable from the standpoint of fuel consumption.

## Deflected-Slipstream Cruise Fan

The comparison shown in figure 12 indicates that it would be very desirable to develop V/STOL fan configurations having a more rapid dropoff in thrust required. Some exploratory research in this direction has recently been carried out at Langley Research Center with the configuration shown in figure 13. This configuration has four cruise fans spaced along the wing and blowing over a slotted flap. As shown by the cross-section sketch at the right of the figure, part of the flow goes over and part under the wing. The flow under the wing spreads out and blows through the slotted flap all across the span to induce a fairly uniform lift on the wing by means of the jet-flap principle. Some results of tests of a small-scale semispan model of this configuration are presented in figure 14 on a plot of thrust-weight ratio against airspeed. The curve for the lift-cruise fan is repeated for comparison. The data for the deflected-slipstream cruise-fan configuration look promising; in fact, the curve approaches the result which would be obtained with an elliptical load

distribution across the entire span of the wing. Only a limited amount of research has been done on this concept to date, however, and an evaluation is premature until more is known of the problems. One obvious problem of such a configuration is the very large nose-down pitching moment which must be trimmed by some auxiliary device in hovering and low-speed flight. The important point to be brought out here is that it does appear possible to get high induced wing lift and good STOL capability with fan configurations. This is an area warranting special attention in future research.

## JET-LIFT V/STOL

### Cruise Performance

One of the papers in the jet V/STOL session of the NASA V/STOL and STOL Conference summarized some of the design principles now being used for cruise optimization of conventional aircraft in order to illustrate potential improvements for V/STOL designs. Figures 15 and 16 taken from this paper compare the subsonic aerodynamic efficiency of conventional and V/STOL aircraft. Figure 15 presents values of  $(L/D)_{\max}$  plotted against the ratio of span to wetted area for fighter aircraft. The shaded region and circular symbols are for V/STOL aircraft (data primarily from design studies, since flight data on these aircraft are limited). The term  $C_f/e$ , effective skin-friction coefficient divided by span efficiency factor, is a correlating parameter represented by the straight line faired through the data points. It appears that the effective skin-friction level for V/STOL fighters is similar to that for conventional fighters but, because of the extra size required to house the lifting systems, the values of span-to-wetted-area ratio are lower for the V/STOL fighters and hence the values of  $(L/D)_{\max}$  are lower.

In figure 16, for bombers and transports, the V/STOL airplanes are seen to have higher effective skin friction as well as lower span-to-wetted-area ratios. The values of  $(L/D)_{\max}$ , therefore, are much lower than those for the conventional aircraft. This correlation indicates the directions in which refinements are needed to increase the subsonic aerodynamic efficiency of V/STOL aircraft. That is, the effective skin friction should be reduced by greater cleanliness, and the span-to-wetted-area ratios should be increased.

Figure 17 illustrates a point regarding the performance of supersonic configurations. One of the items that makes design of supersonic V/STOL aircraft more complicated than that for conventional aircraft is the volumetric constraint associated with having propulsive systems to provide lift as well as thrust. This point is illustrated in figure 17 which presents wave-drag coefficient, based on frontal area, plotted as a function of equivalent-body fineness ratio. The square symbols in the shaded area on the right are representative of conventional aircraft. The circular symbols are for V/STOL study configurations incorporating vectored-thrust engines. The diamond symbol represents a subsonic V/STOL aircraft. Because of the volumetric constraint, the V/STOL configurations utilizing vectored-thrust engines generally have

lower fineness ratios than the conventional aircraft and, therefore, have higher wave-drag coefficients. For V/STOL configurations using lift engines and separate cruise engines, it may be possible to increase the fineness ratio and provide somewhat lower wave drag in the region between the two bands.

### Hovering Performance

Figure 18 shows the effect of jet arrangement on base loss and jet decay. The term "base loss" refers to the aerodynamic lift loss in hovering resulting from suction forces on the bottom of the airplane. Data are shown for single-jet, multijet, and multislot arrangements having the same total jet area. In the top plot, the ratio of lift loss to static thrust is plotted against the square root of the planform-to-jet-area ratio. In the bottom plot,  $q_x$  (the measured dynamic pressure at a distance  $x$  downstream) divided by  $q_n$  (the dynamic pressure at the nozzle exit) is plotted against the distance downstream in terms of the effective diameter. This figure shows that the lift loss is a function of the decay characteristics; that is, the more rapid the decay the larger the loss.

From the standpoint of base loss then, it would seem that a rapid decay rate is not desirable. However, from the ground erosion standpoint, a rapid decay of dynamic pressure is very desirable, and efforts are being made to devise means of achieving rapid decay with special nozzles. The Boeing Company has just completed a study for NASA to determine the effects of different nozzle arrangements on jet decay. Some of the results are shown in figure 19 which is a plot of dynamic-pressure ratio against distance downstream for a circular nozzle and for single-slot and four-slot nozzles. The slot nozzles appear to achieve the desired goal of rapid dynamic-pressure decay. The thrust losses for these nozzles measured at an  $x/D_e$  of 3 are shown in figure 20. The ratio of the loss to the ideal static thrust is plotted against the dynamic-pressure ratio for the nozzles of figure 19 along with the data for other multislot nozzles which have been investigated. It can be seen that the rapid decay of dynamic pressure comes at the expense of the basic nozzle efficiency. Also shown are the base losses measured with a fuselage in the presence of the suppressor nozzles. It is apparent from these results that the requirement for rapid decay of jet exhaust velocity to prevent ground erosion has to be carefully considered in light of the larger nozzle and base losses associated with suppressor nozzles.

### Hot-Gas Ingestion

Hot-gas ingestion is a serious problem for jet V/STOL aircraft because the raised inlet air temperature can result in drastic thrust losses. Unfortunately, little systematic work has been done in this field, but research is now underway with large-scale models at both Ames Research Center and Langley Research Center to provide information on the subject. Figure 21 shows a sketch of the general research model at Langley Research Center which is powered by a single J-85 engine in the fuselage and can be fitted with various exhaust and

inlet arrangements. The lower sketch shows the hot-gas recirculation pattern for the model in a four-nozzle configuration. With this configuration, the hot gas, in addition to flowing outward along the ground in all directions, flows upward in a sort of fountain effect between the engines. There is also an upward flow fore-and-aft against the bottom of the fuselage as indicated by the short dashed lines. The hot gases in the upward and forward flows are of course quite accessible to the engine inlets and are still very hot because they have not traveled very far and little mixing with the ambient air has taken place.

The inlet temperature rise for this configuration is shown in figure 22 together with data from similar small-scale models tested by Bell and North American. The temperature rise is shown as a function of height above the ground in effective nozzle diameters. All three models were tested with side inlets and the Langley model was also tested with a single top inlet. The data show that both side and top inlets experienced very high temperatures near the ground, the model with the top inlet having the higher temperature. As nozzle height was increased, the temperature rise decreased rapidly, and at a height of 5 diameters the rise was of the order of  $20^{\circ}$  F. These very high temperatures occurred within 2 seconds following downward deflection of the exhaust nozzles. VTOL operation would not be possible with these high temperatures because of the high thrust loss and the probability of compressor stall.

One way of minimizing the fountain effect which apparently causes the high inlet temperatures is to arrange the exhaust nozzles in a line instead of in a rectangular pattern. Some tests of the Bell model in such a configuration showed a temperature rise of only  $10^{\circ}$  in the top inlet.

The effect of another important configuration parameter, wing position, is illustrated in figures 23 to 25 which present some results obtained with a large-scale Norair model tested at Ames Research Center. Figure 23 shows a sketch of the model which has five J-85 engines mounted vertically in the fuselage and two propulsion engines at the rear of the fuselage with the exhaust diverted downward for vertical lift. The inlet location of the propulsion engines could be varied and the wing was also tested in different positions. Figures 24 and 25 present results of tests for two different configurations of the model, one having high ingestion and one having low ingestion.

Figure 24 shows the case of high ingestion. The sketch on the left illustrates the recirculating flow pattern for the high-wing configuration. The flow along the ground from the lift engines meets the flow from the propulsion engines to produce an upward flow of hot gas which is ingested into the inlets. The plots at the right show that the temperature in the inlet of engine number 3 reached about  $200^{\circ}$  F in about 3 seconds after the engines were accelerated to full thrust. The engine then experienced a compressor stall.

Figure 25 shows results for a configuration for which there was very little ingestion. In this case, the wing is in a low position and obstructs the upward and forward flow of hot gas and causes it to recirculate below the wing as indicated by the arrows. The plots at the right indicate little or no ingestion in the inlet of engine 3 in this case. It appears therefore that wing position can be a very important factor in minimizing hot-gas ingestion. Perhaps some form

of extendible deflectors could be used to serve the same purpose as the low wing of this configuration.

In any event, the state of the art in this important area is still in the exploratory stage; and it appears that the development of jet V/STOL designs at this time should include hot-gas ingestion tests for the particular configuration and operating conditions that are expected to be encountered.

### Transition Aerodynamics

Some jet-induced interference effects in transition for jet V/STOL aircraft are illustrated in figures 26 to 29. Figure 26 shows the effect of wing planform on jet-induced pitching moment and lift loss. Data for a swept and an unswept wing are plotted against an effective velocity ratio, where zero represents hovering and 0.25 represents the upper end of the transition range. Suction pressures on the bottom of the wing-fuselage combination produce a lift loss similar to that shown earlier for the lift-cruise fan configurations. The loss is about the same for the swept and unswept configurations. The nose-up pitching moment, however, is greater for the swept wing configuration because much of the area on which the suction pressures act is farther behind the center of gravity.

The arrangement of the jets can also have a large effect on the magnitude of the induced interference effects, as shown in figure 27. Data for a four-jet configuration are compared with data for a configuration in which the same total jet area is arranged in a central slot to represent a row of lift engines. It can be seen that changing from the rectangular to the linear arrangement gives a very large reduction in both the nose-up pitching moment and the lift loss.

The data shown in figures 26 and 27 are for tail-off configurations. In addition to the jet-induced suction pressures on the lower surfaces of the wing and fuselage, there is also a large induced downwash at the horizontal tail which causes an additional nose-up pitching moment. This downwash is a function of angle of attack and can therefore change both trim and stability. The effect of power on the tail contribution to stability is highly dependent on the flow field in which the tail operates and, in particular, on the flow field generated by the parts of the airplane ahead of the wing. Figures 28 and 29 illustrate this problem. Figure 28 represents an airplane in cruising flight. On most modern high-speed jet airplanes there are inlets or other elements such as fixed forewings for variable-sweep wings which produce lift and shed vortices inboard and it is generally considered desirable that the tail be located below this trailing vortex system. This arrangement causes the tail to move away from the vortices as the angle of attack is increased. For the jet VTOL airplane in transition flight, however, the situation is different, as shown in figure 29. The inboard vortices can be pulled below the horizontal tail by the action of the lifting jets. Then as the angle of attack is increased, the tail is forced to move through these vortices. The severity of the problem thus created depends on many configuration variables, such as the position and size of the forewing and engine inlets and the horizontal-tail configuration and tail

length. In general, the effects of large inlets located well forward have been found to be detrimental.

#### CONCLUSION

The subjects covered in this paper are covered in much more complete form in the compilation of papers from the NASA Conference on V/STOL and STOL Aircraft, available as NASA Special Publication, SP-116.

#### REFERENCES

1. Anon.: Conference on V/STOL and STOL Aircraft. NASA SP-116, 1966.
2. Evans, William T.; and McCloud, John L., III: Analytical Investigation of a Helicopter Rotor Driven and Controlled by a Jet Flap. NASA TN D-3028, 1965.

# HELICOPTER CONTROL AND DAMPING

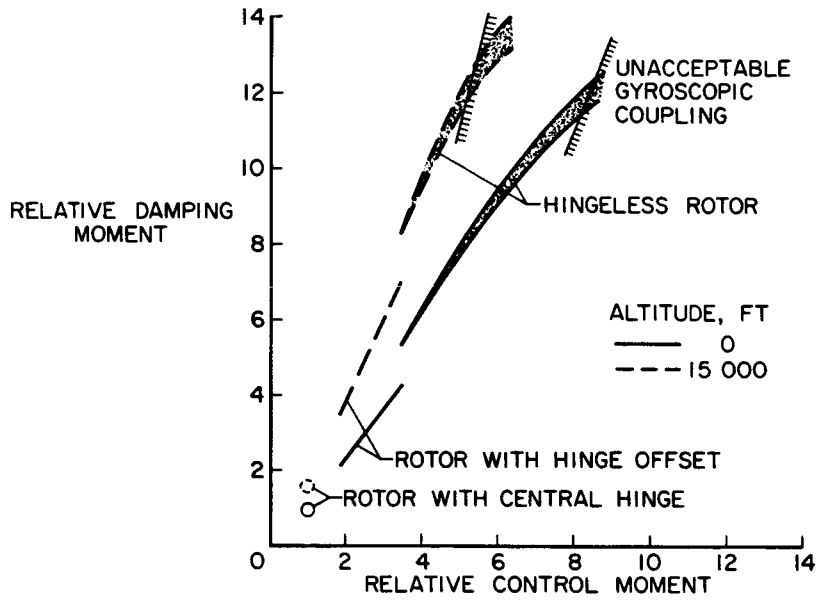


Figure 1

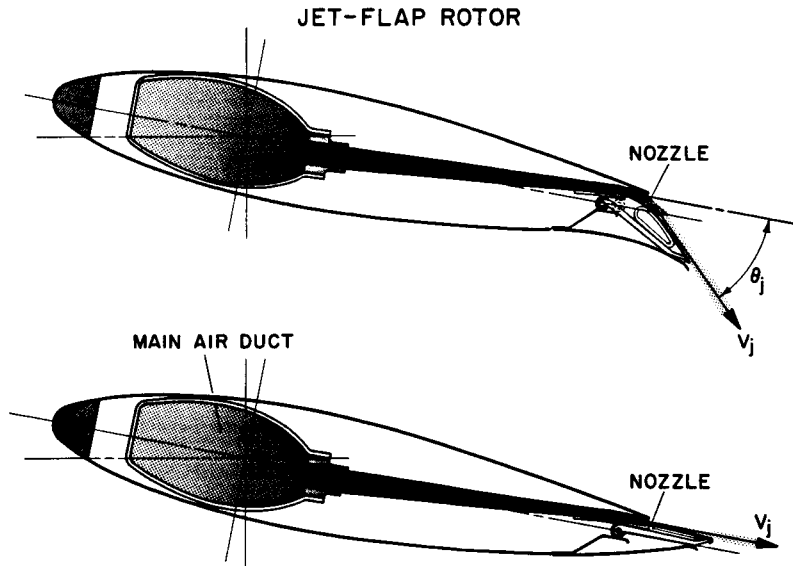


Figure 2

### JET-FLAP ROTOR CAPABILITY

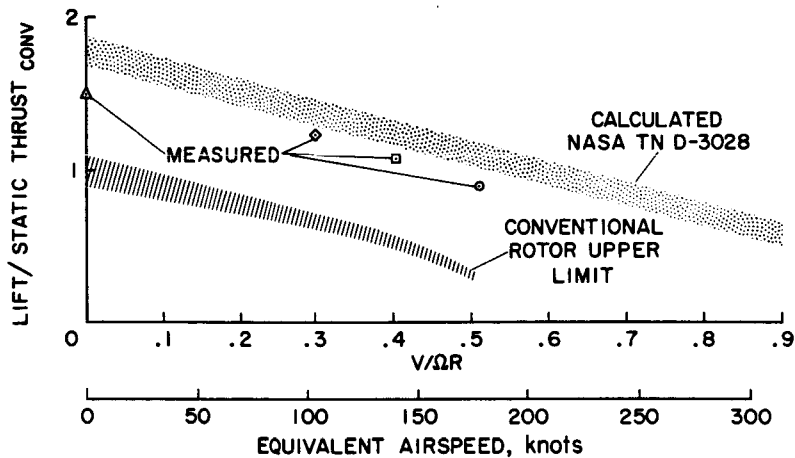


Figure 3

### LARGE-SCALE TILT-WING MODEL

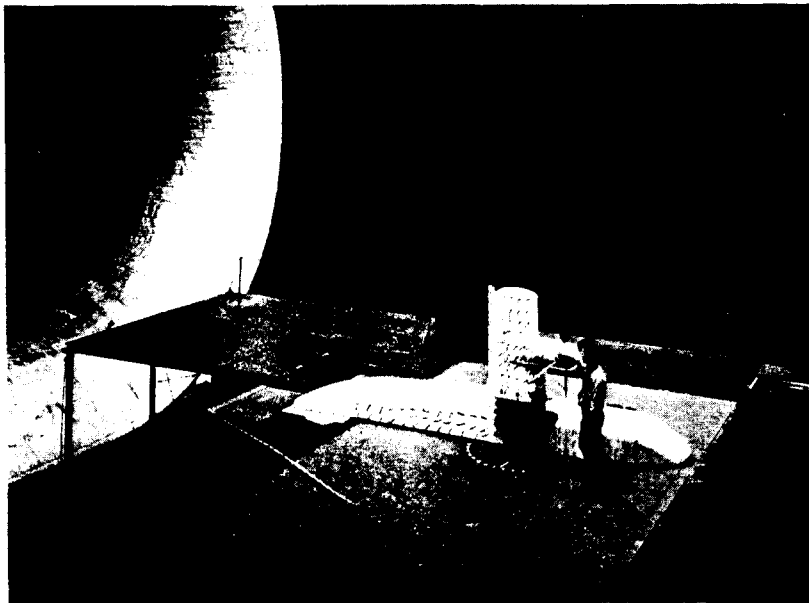


Figure 4

L-2698-6

EFFECT OF PROPELLER POSITION  
DOWN-AT-CENTER ROTATION ;  $\delta_f = 20^\circ$

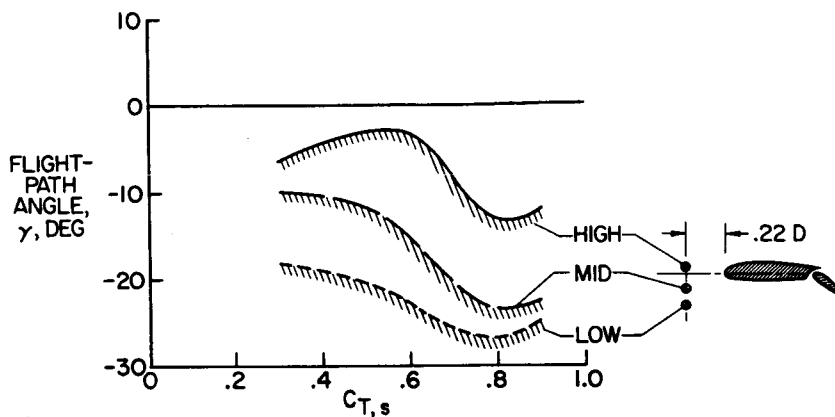


Figure 5

YAW DISTURBANCES IN GROUND EFFECT  
TILT-WING AIRPLANE

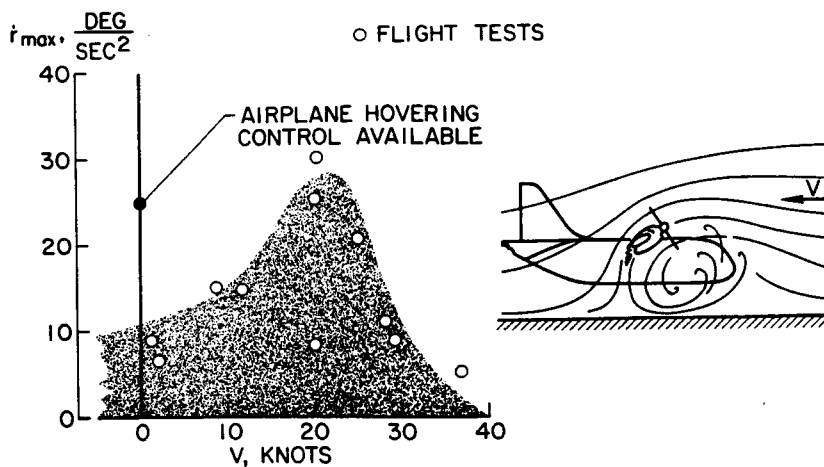


Figure 6

THE TANDEM LIFT-FAN MODEL

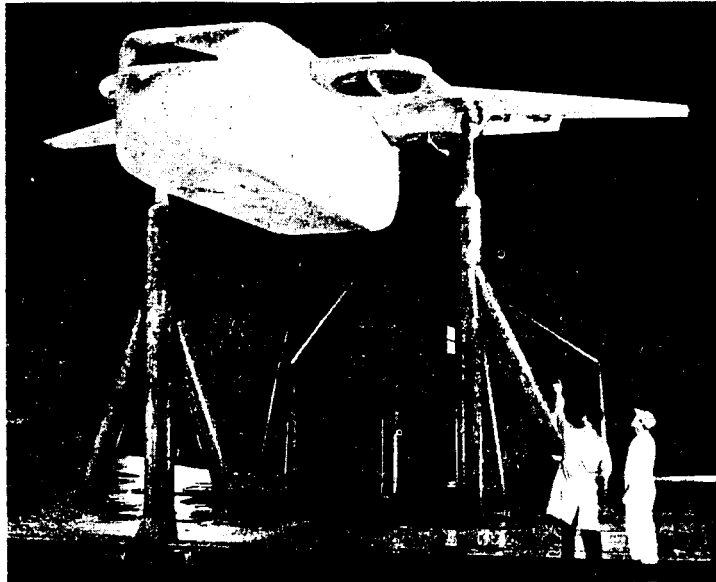


Figure 7

L-2698-10

VARIATION OF LIFT WITH AIRSPEED FOR THE TANDEM LIFT-FAN MODEL

$\delta_f = 0^\circ, \alpha = 0^\circ, \beta_v = 0^\circ$

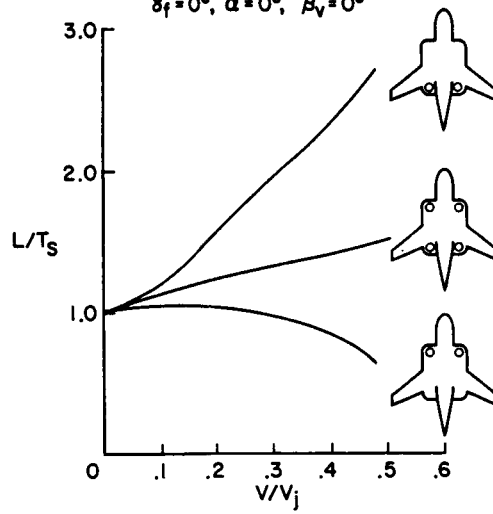


Figure 8

THE LIFT-CRUISE FAN MODEL



Figure 9

L-2698-12

EFFECT OF FRONT-FAN OPERATION ON WING LIFT  
 $\alpha = 0^\circ, \delta_f = 0^\circ$

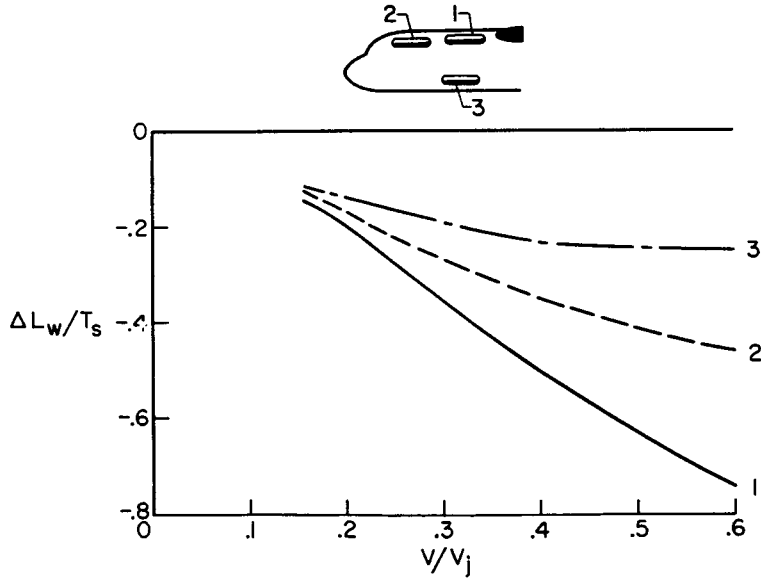


Figure 10

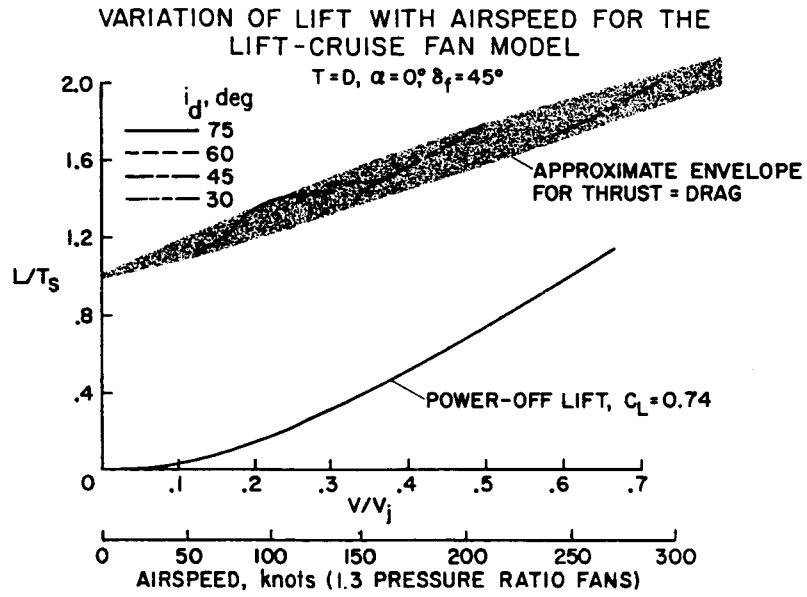


Figure 11

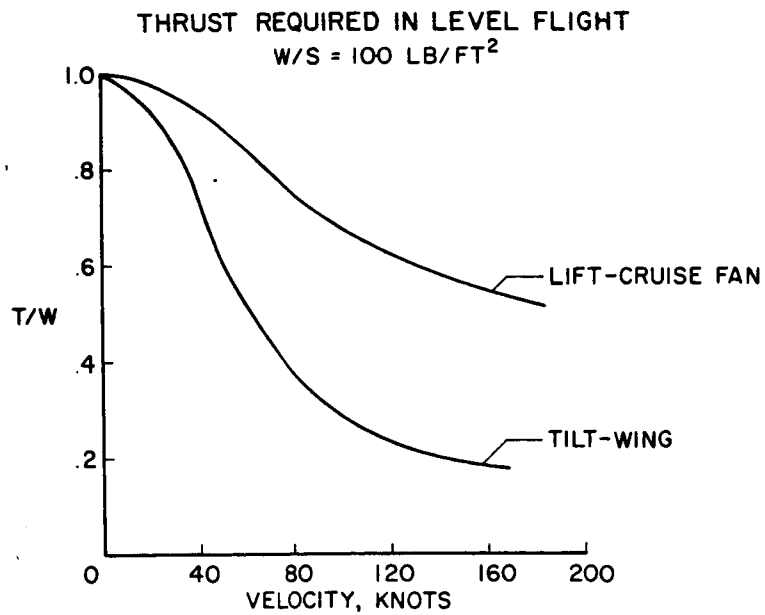


Figure 12

DEFLECTED-SLIPSTREAM CRUISE-FAN CONCEPT

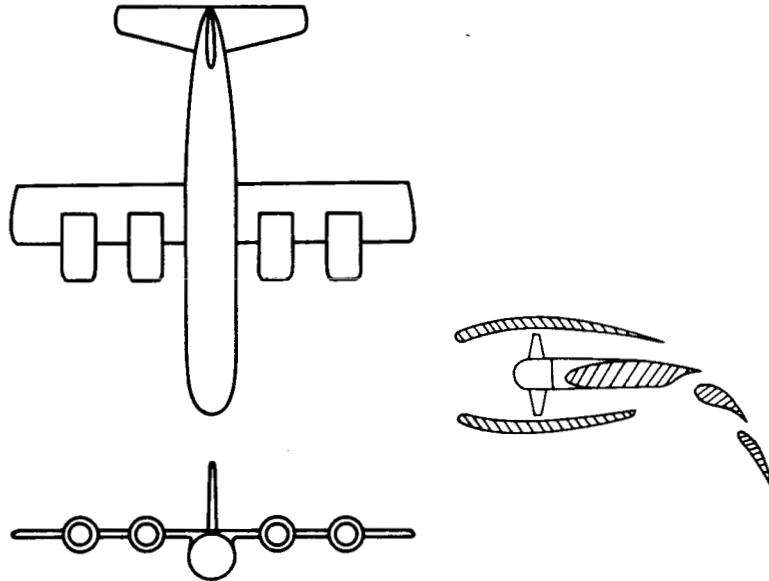


Figure 13

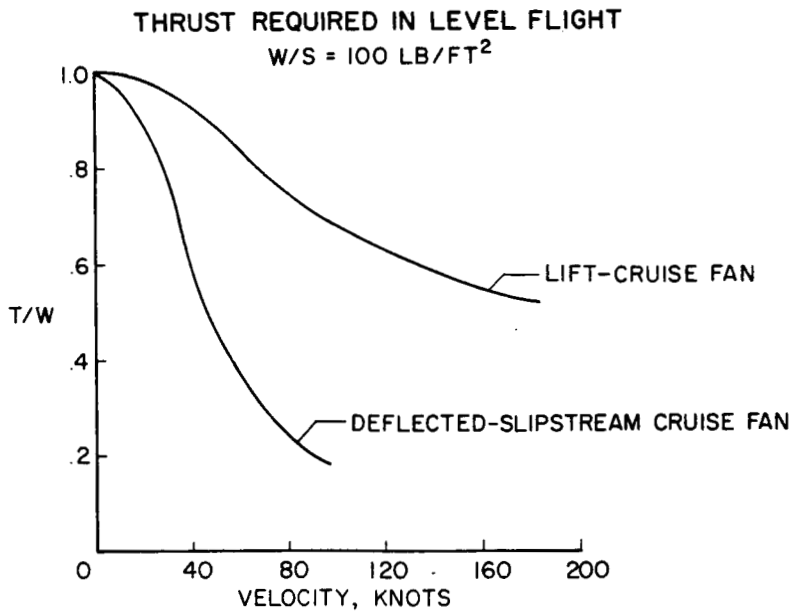


Figure 14

**SUBSONIC AERODYNAMIC EFFICIENCY**

FIGHTERS;  $M \approx 0.8$

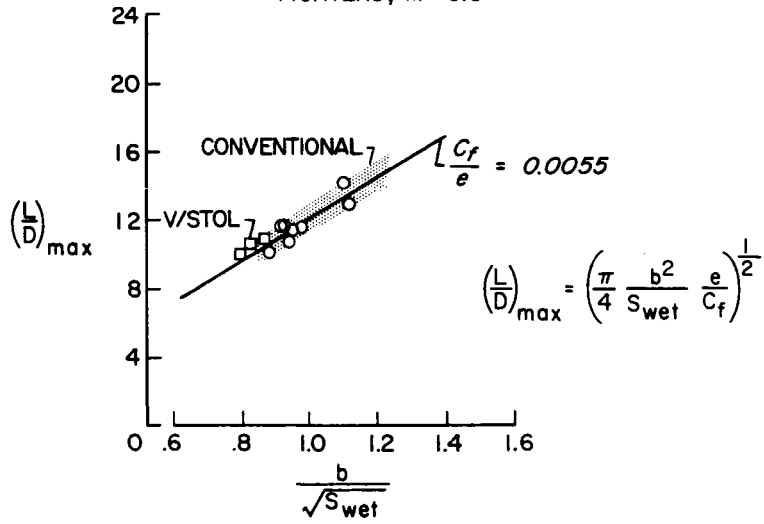


Figure 15

**SUBSONIC AERODYNAMIC EFFICIENCY**

BOMBERS AND TRANSPORTS;  $M \approx 0.8$

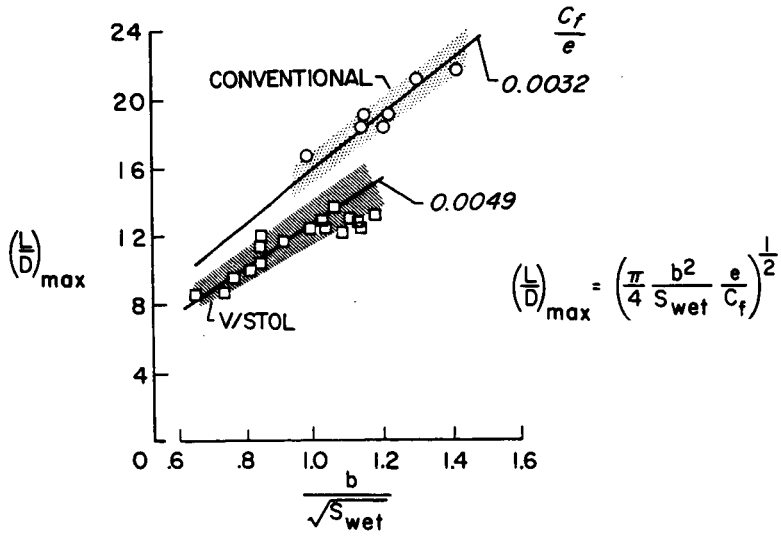


Figure 16

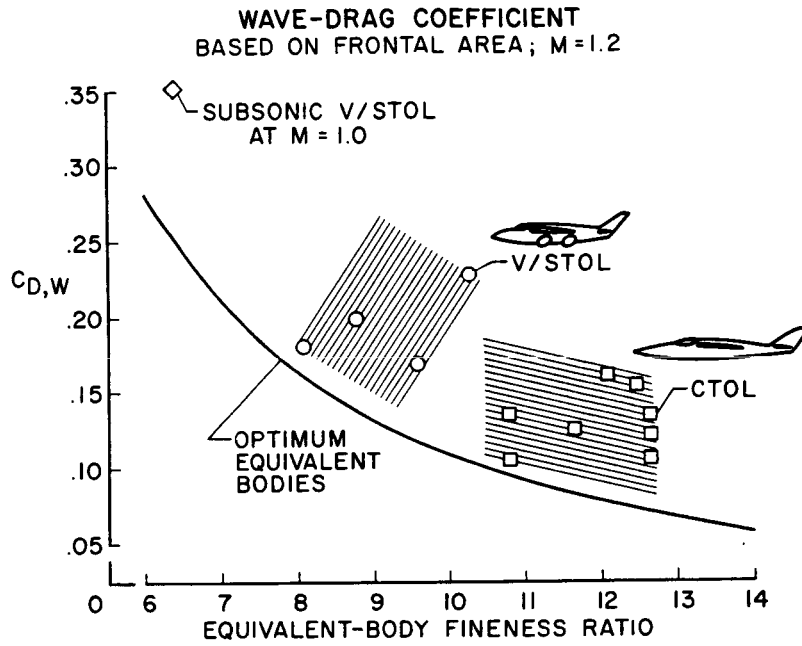


Figure 17

**EFFECT OF JET ARRANGEMENT ON BASE LOSS AND JET DECAY**

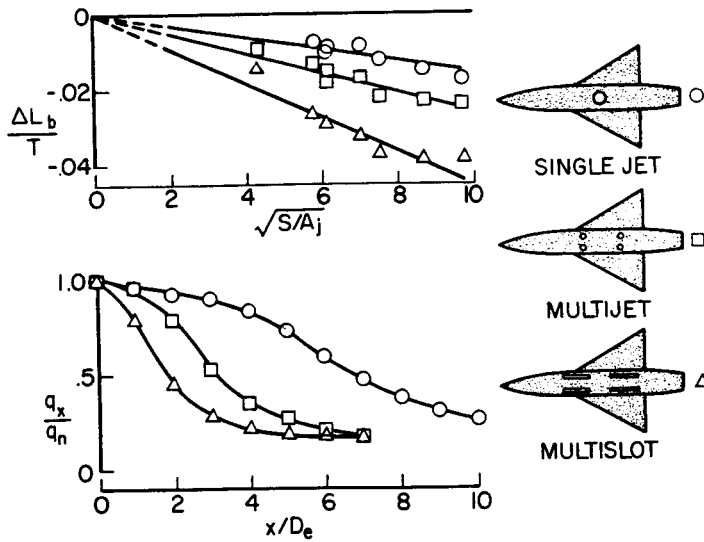


Figure 18

### EFFECT OF NOZZLE CONFIGURATION ON JET DECAY

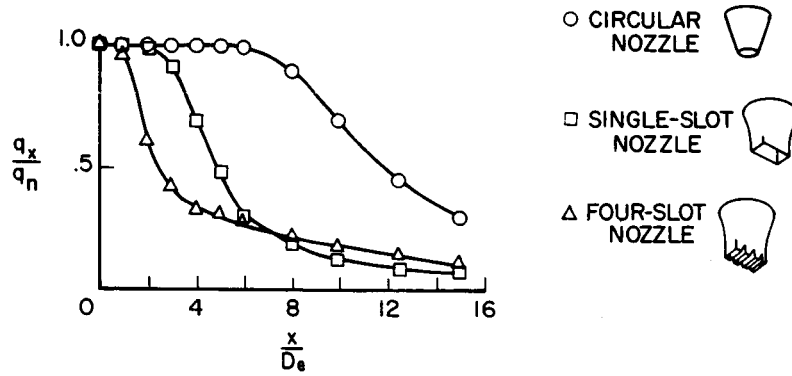


Figure 19

### THRUST LOSSES WITH SUPPRESSOR NOZZLES

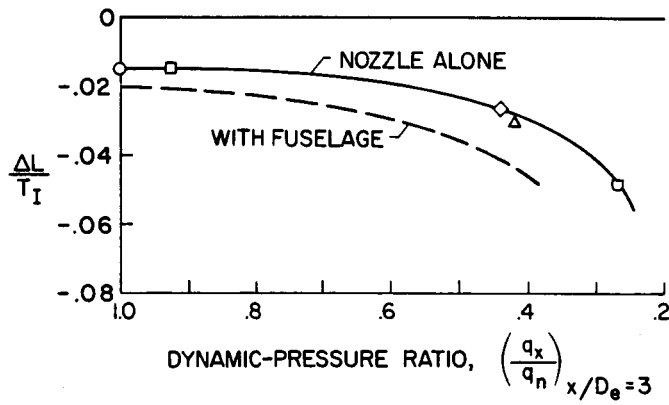


Figure 20

HOT-GAS RECIRCULATION PATTERN  
FOUR-NOZZLE CONFIGURATION

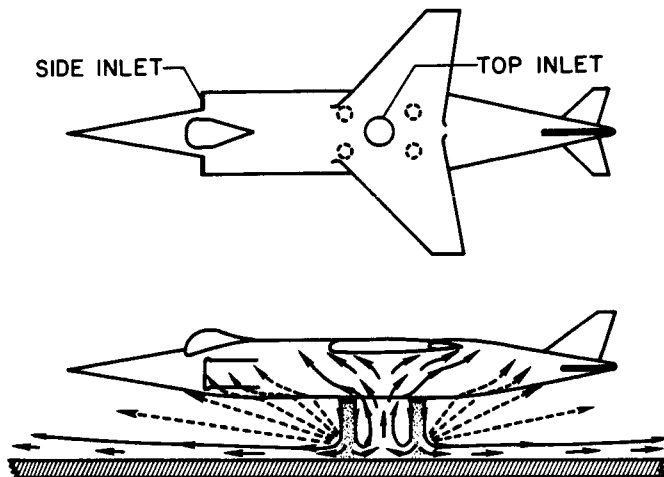


Figure 21

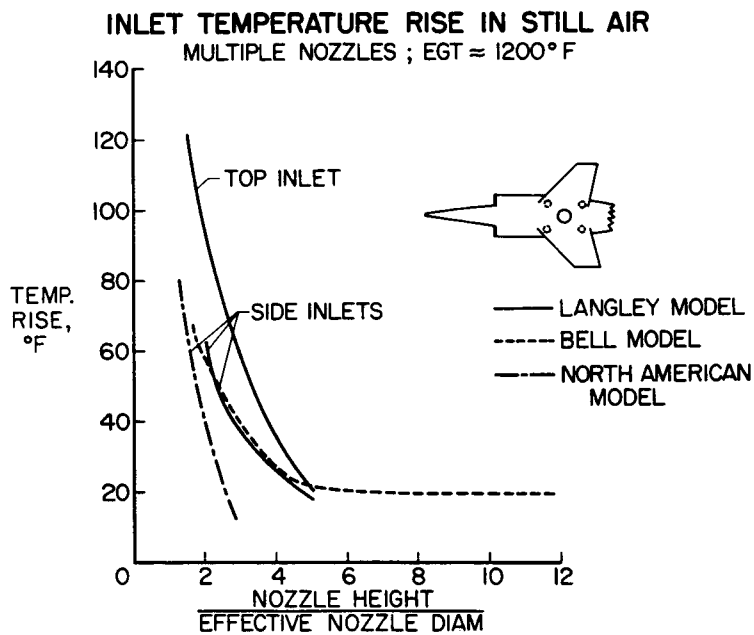


Figure 22

VTOL GROUND EFFECTS AND INGESTION TEST MODEL

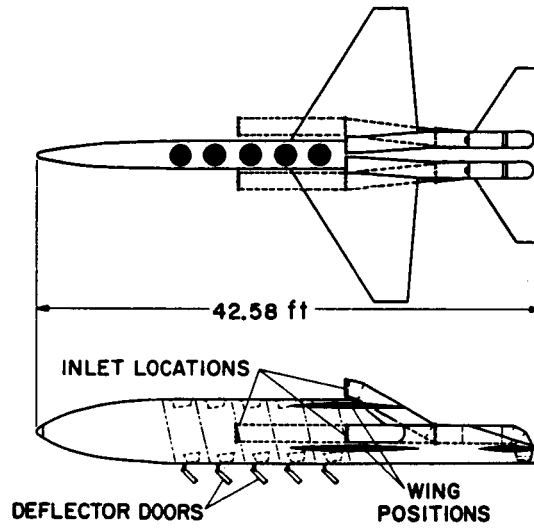


Figure 23

CONFIGURATION HAVING HIGH INGESTION  
h/D = 4.5

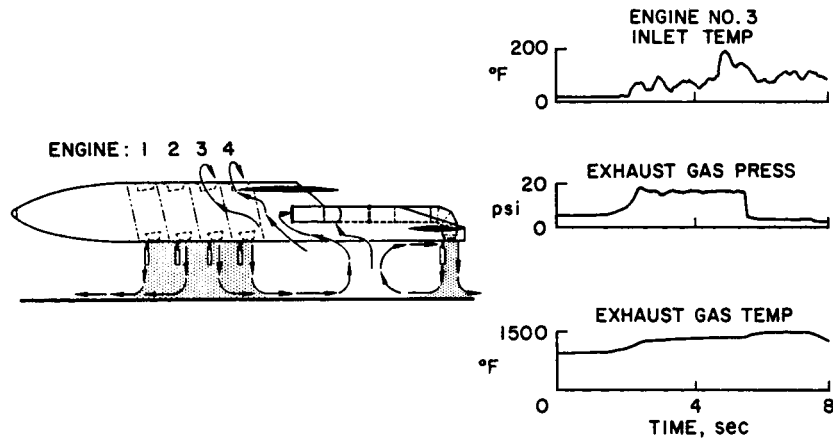


Figure 24

CONFIGURATION HAVING LOW INGESTION

$h/D = 4.5$

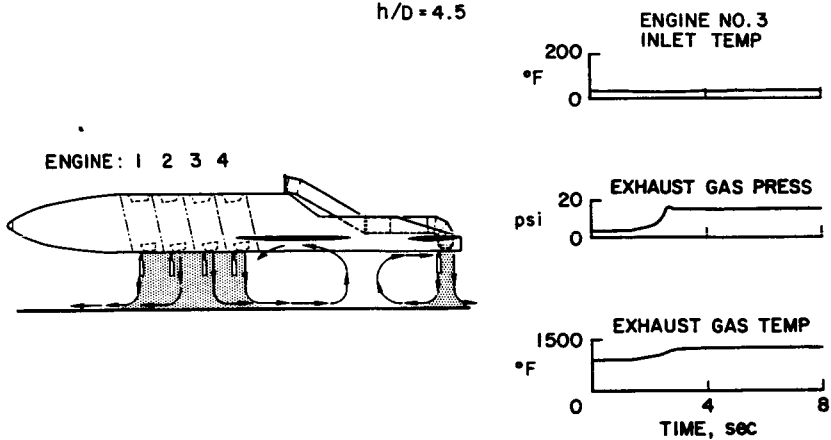


Figure 25

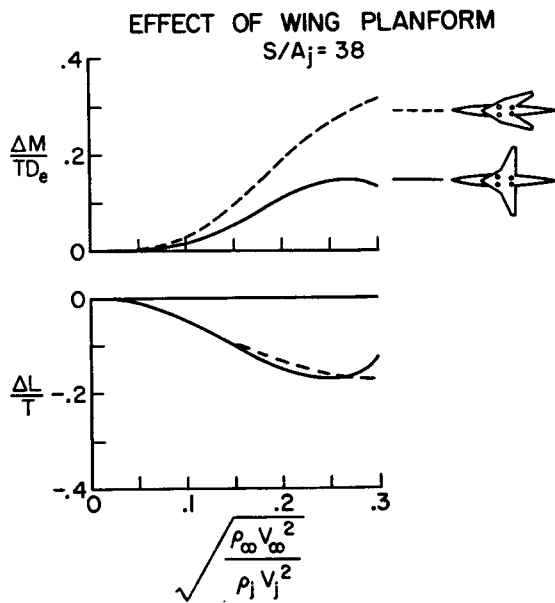


Figure 26

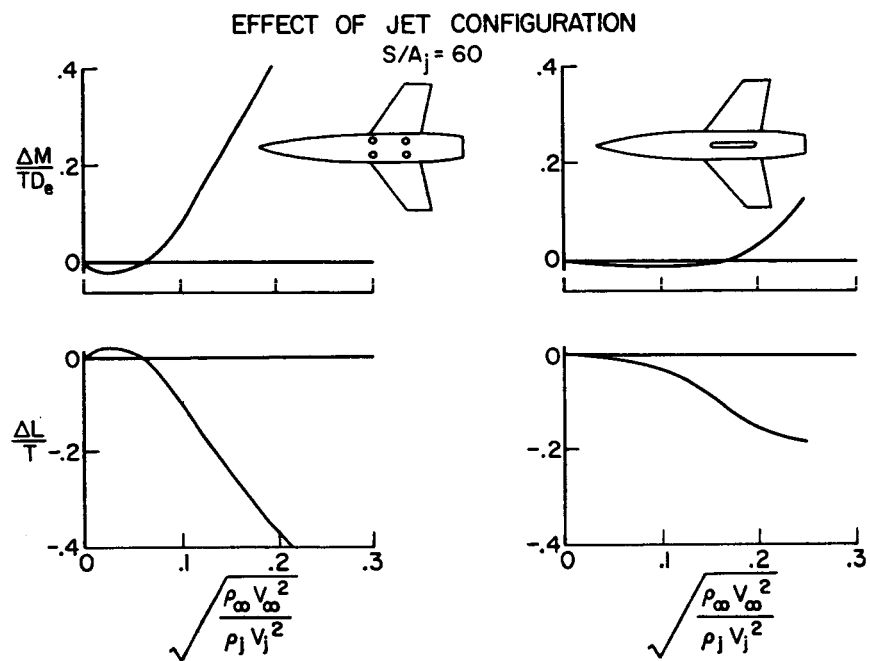


Figure 27

**VORTEX PATHS IN CRUISE**

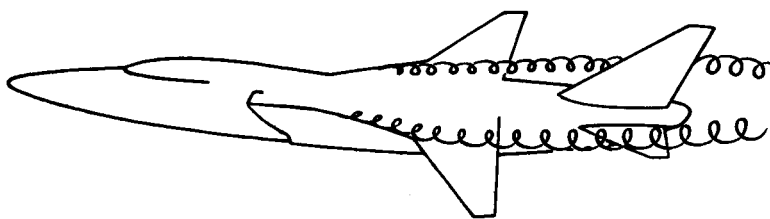


Figure 28

VORTEX PATHS IN TRANSITION FLIGHT

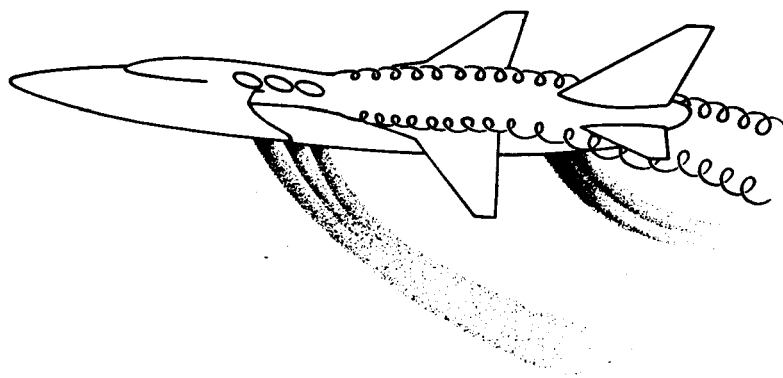


Figure 29

## 35. A REVIEW OF HYPERSONIC CRUISE VEHICLES

By David E. Fetterman, Charles H. McLellan, L. Robert Jackson,  
Beverly Z. Henry, Jr., and John R. Henry  
Langley Research Center

### SUMMARY

In an attempt to provide a focus for future aerodynamic programs in the development of hydrogen-fueled hypersonic cruise vehicles, the present status of the structural, propulsive, and aerodynamic research is examined to extract the presently known factors that significantly affect vehicle definition. Existing wing and body structural concepts and cryogenic-tankage thermal-protection systems are illustrated, possible inlet-engine arrangements are discussed, and the status of important local aerodynamic heating areas is briefly reviewed. In addition, uncertain areas which require further fundamental research and obstacles which hinder development are also pointed out.

In general, existing structural and propulsive technologies for Mach 6 to 8 vehicles favor a discrete low-wing-body arrangement with a two-dimensional inlet mounted in the wing pressure field. Aerodynamic considerations, however, indicate equal performance possibilities for either discrete wing-body or blended wing-body arrangements. The paper concludes with a discussion of several possible design concepts which conform to current guidelines and which are planned for future research.

### INTRODUCTION

Prior to 1957 the only means of propulsion seriously considered for hypersonic flight was the large rocket engine. Thus, the "boost-glide" type of vehicle received almost exclusive attention during the first decade of hypersonic technology development. (See refs. 1 to 5.) With the beginning of space activities in 1957, the magnitude of the launch-vehicle problem began to be appreciated and studies of reusable launch systems were undertaken with the hope of obtaining cheaper and more effective alternates to ballistic rocket boosters. During this time the air-breathing engine came under exhaustive scrutiny as the most obvious alternative to rocket boosters, and a dramatic family of air-breathing vehicles designated "aerospaceplanes" became the subject of intensive study. (See refs. 6 to 15.) Although these conceptual vehicles proved to be premature, there emerged from these studies by 1962 the first clear indications that hypersonic air-breathing propulsion using hydrogen fuel was feasible and attractive up to Mach numbers of about 8 in the form of the subsonic-combustion turboramjet, and up to Mach 12 or higher with the subsonic-supersonic-combustion turboramjet. With this important capability, the possibility of cruise vehicles capable of sustained hypersonic flight also became apparent. (See refs. 16 and 17.)

The hypersonic cruise vehicle is vastly more complex than other hypersonic vehicles such as the boost-glider or the manned reentry vehicle. Its large liquid hydrogen fuel requirement coupled with its air-breathing engines which must provide take-off, acceleration, hypersonic cruise, and subsonic loiter capabilities introduce many difficult new problems. In examining comparative vehicle studies of different design teams, it is apparent that the present state of the art is characterized by large uncertainties. An analysis of these studies reveals that these uncertainties are rooted partly in aerodynamic predictions for complete configurations, partly in the attainable weight fractions of cryogenic and high-temperature structures, and partly in the installed performance of hypersonic propulsion systems. Within the spread of these uncertainties, results for particular missions can be found which range all the way from attractive to unattractive vehicle systems. The technology for air-breathing hypersonic cruise and boost vehicles is thus in the same early stage as supersonic transport technology was some dozen or so years ago when serious studies of complete realistic aerodynamic configurations, structures, and engines were just beginning. In order to reduce the present uncertainties in the state of the art, extensive programs are now getting underway in both USAF and NASA.

At the present early stage in the development of these vehicles, any meaningful discussion of configuration concept becomes involved with questions of structures, materials, and propulsion, since each of these technological areas can have a significant influence on the shaping of the vehicle. To obtain realistic results that significantly advance vehicle development, the aerodynamic programs, then, must be properly focused on configurations which reflect these influences. To aid in this focusing process, this paper briefly examines the structural, propulsive, and aerodynamic disciplines in that order and sets forth the presently known factors affecting vehicle shape. Singled out along the way will be uncertain areas which require more work and the obstacles which hinder development and must be overcome. The paper concludes with several possible design concepts which should be investigated in future programs. For reasons which will become apparent, vehicles in the Mach 6 to 8 class and those for higher Mach numbers of about 12 are significantly different. During the discussion Mach 6 and Mach 12 are used to refer to the two speed classes.

Although this paper treats only the cruise vehicle, it should be noted that many points of commonality exist between cruise and launch vehicles. (See ref. 14.) Much of the information contained herein for cruise vehicles, therefore, applies to the others as well.

#### CHARACTERISTICS OF HYPERSONIC CRUISE VEHICLES

The environment in which a hypersonic cruise vehicle (HCV) operates is shown by the flight profile. The flight profile is subject to the various constraints shown in figure 1. Preliminary studies (discussed in paper no. 29 by McLean, Carlson, and Hunton) of the sonic-boom constraint indicate that because of the larger vehicles involved, the problem is more severe for the HCV at lower speeds than for the supersonic transport (SST), but because of the higher altitudes is less severe during cruise. The vehicle then follows a constant dynamic

pressure path. The highest possible dynamic pressures are desirable for improved propulsion performance; however, from the structural standpoint, low dynamic pressures are desirable to alleviate panel flutter and the heating problems denoted by the constant peak skin temperature lines. For subsonic-combustion ramjet propulsion systems, the inlet duct pressures must be limited to avoid excessive propulsion-system weight and flight paths are constrained to constant duct pressure lines. In supersonic-combustion ramjet engines, of course, the internal duct pressures are much lower and this duct pressure limitation is eliminated.

A typical trajectory for a Mach 6 cruise vehicle follows a peak dynamic pressure path of 1500 psf with cruise occurring between 800 and 500 psf. Peak skin temperatures 3 feet aft of the leading edge are about 1500° F. The descent phase of the flight is made at altitudes high enough to avoid the climb phase constraints.

Because of the conflicting trajectory requirements of structures, propulsion, and aerodynamics, a large interplay among these areas exists in the design of hypersonic cruise vehicles. As a first step in defining efficient vehicle systems, it is essential, therefore, to perform analytic trade-off studies in which the key parameters in structures, propulsion, and aerodynamics are systematically varied. These studies have been conducted within NASA (ref. 16) and under contract, and these results have provided a preliminary indication of the more important vehicle characteristics. These results, compared with those for the SST, are shown in table I. Symbols appearing in the table and the figures are defined in the appendix.

These trade-off studies considered a cruise Mach number of 6 and assumed a range of 5500 n. mi. and a gross weight equal to that of the SST. Shorter ranges, such as that of the SST, are less attractive for hypersonic transports because most of the trip would be taken up by acceleration and deceleration and little trip-time advantage is found. Studies of JP-fueled hypersonic cruise vehicles indicate that only about half the desired range is available (ref. 17); thus, the use of hydrogen fuel is the dominant requirement of these vehicles. The desired range can then be achieved with about the same payload weight as for the SST but with a lower fuel weight. The low density of hydrogen, however, requires a fuel volume about an order of magnitude larger than that required for the SST. The structural problems involved in housing the liquid hydrogen and designing for the higher temperature environment result in structural weight fractions some 30 percent greater than for the SST. This more severe structural problem causes HCV performance to be optimized with aerodynamic configurations which are much less slender than the SST. A comparison of HCV and SST vehicles is shown in figure 2. The fuselage fineness ratios are about half those for the SST and the hypersonic L/D is about 5, a value which is below that obtainable at hypersonic speeds for more slender designs. The wing loadings tend to be in the same range as for the SST because take-off and sonic-boom considerations size the wing in both vehicles.

## STRUCTURES

A configuration which embodies most of the design features preferred in present structural technology is shown in figure 3. Probably the most significant structural design influence involves the manner in which the liquid hydrogen is contained in the vehicle. At hypersonic conditions an extreme temperature difference of about  $2000^{\circ}$  F exists between the inner wall of the fuel tank and the outer surface of the vehicle. (See ref. 18.) The cryogenic structural problem is presently one of the main concerns. One solution under extensive study is the nonintegral tankage approach shown in figure 3 wherein the fuel tanks are separate from the load-bearing structure. With this concept, cylindrical and conical tanks are preferred; and structural design favors discrete wing-body arrangements with the wing located over or beneath the body to avoid interference between the wing carry-through structure and the tankage.

To allow lower wing weights, a fuselage-mounted vertical fin may be preferred to wing-tip fins; and to allow thermal expansion on the hot leading edges, a segmented, overlapping leading edge on the tail and wing is required rather than the smooth unit used on the SST. Leading-edge temperatures for Mach 6 vehicles can be held to less than  $2200^{\circ}$  F and coated thoriated nickel (ref. 18) is a possible leading-edge material which requires only infrequent refurbishment. However, for Mach 12 vehicles coated refractories such as columbium will have to be used (ref. 19) and frequent leading-edge refurbishment will be required. At Mach 6 the wing maximum surface temperatures are generally less than  $1600^{\circ}$  F, and the major part of the wing can be constructed of superalloy materials using stress-skin construction similar to that used on the SST.

The surface roughness conditions prescribed in flight are of importance both from configuration performance and local aerodynamic heating considerations. At one time it was believed that the surfaces of hypersonic vehicles would be covered with large buckles and discontinuities brought about by thermal stress and expansion. Structural concepts have been devised to minimize these distortions, and a concept for Mach 6 vehicles is shown in figure 4.

The leading edge is shown detached, and it includes the entire area behind the leading edge itself over which temperatures are in excess of  $1600^{\circ}$  F. The load-bearing skin is waffle stiffened and stabilized by corrugated webs and spars to prevent buckling. Thermal stress is reduced by exposing the spar and rib caps. With this structural concept, it is expected that the surface will be almost as smooth as that on the SST. The only significant discontinuity will be steps, on the order of 0.020 inch, located at the edges of the leading-edge segments and at the juncture of the leading edge and the wing. If the steps are facing away from the local flow, however, they should not present a serious problem.

If designs for the Mach 12 range are considered, higher temperatures occur over large surface areas of the wing and a structural concept of the type shown in figure 5 is required. A shingled nonload-bearing exterior heat shield and insulation system must now be added to a basic wing and body structure to

maintain its operation at temperatures not in excess of 1600° F. Corrugated heat-protective shingles form the outer surface and large surface irregularities will occur. It is a mistake to assume that by running these corrugations "streamwise" their effect can be ignored. Actually the local flow directions on bodies and delta wings vary significantly with angle of attack and, therefore, cross flows over the corrugations will inevitably be encountered. The aerodynamic and heating consequences of this are not yet known but are almost certainly significant. Further research in high-temperature structures aimed at smoother shingles without excessive weight is needed.

Since the trade-off study results (table I and fig. 2) are sensitive to structural weight, the hydrogen-fuel tankage structure and insulation weight can have important implications on the proportions of the optimum configuration. A reduction in this weight would shift the fuselage fineness ratio to higher values with resulting increases in configuration  $(L/D)_{\max}$ . Possible structural concepts for nonintegral tankage are shown in figure 6.

The storage of high volumes of liquid hydrogen fuel within structures subject to high external heating presents major new problems. The cold tankage must not only be heavily insulated to prevent fuel losses, but purging must also be provided to avoid air and water condensation (ref. 20) between tank and structure and to remove any hydrogen leakage. In the upper left of figure 6, this purging is accomplished by helium. The basic difficulty here is the large weight of the thermal protection system and helium purge system required. Additional weight due to the need for a coolant system, particularly at Mach numbers greater than 8, to reduce tank temperatures in "dry" areas after the fuel has been partially used may also have to be included.

A scheme under test at Langley which may provide significant reduction in thermal protection and purge system weight is shown at the lower right in figure 6. (See ref. 21.) A CO<sub>2</sub> frost is cryo-deposited within the inner thickness of fibrous insulation during ground hold prior to flight. During flight the frost sublimates and provides the purge gas. The sublimation process eliminates the need for an additional coolant system for the dry tank walls. A large model of this concept shown in figure 7 has been built and is scheduled for radiation-heating tests. The model is scheduled for testing in the Langley 8-foot high-temperature structures tunnel at Mach 7.

Another approach based on the concept of "integral" tankage is also under study at Langley Research Center. In principal, cooling of the load-bearing structure by the fuel might result in weight saving. A large model incorporating the integral or evacuated "multiwall" structural concept (ref. 21) is shown in figure 8. Great difficulties have been encountered in developing this model, particularly in obtaining the required vacuum in the thin-gage elements. Helium purge gas is shown in the structural portion of the sandwich wall to detect fuel leakage. The purge-gas requirements are uncertain but may be sizable. Further research on evacuated heat shields is needed to develop improved techniques and to determine the reliability with which thin-gage materials can be sealed.

The integral tankage structure encounters an additional problem in the joining of the cold tank structure and the hot wing structure. It is too early to say whether a significant weight penalty is involved here or whether merged wing-body arrangements can be found which are attractive for the use of integral tankage.

The propulsion unit, shown by the simple schematic in figure 3, is actually a very complex, specialized structural problem. The unit contains the inlet duct and a combination engine consisting of a turbojet for acceleration to about Mach 3 and a ramjet for acceleration to Mach 6. At higher speeds a supersonic-combustion ramjet (scramjet) engine must also be provided. No materials are now available to withstand the extreme temperatures occurring on the turbine blades under stoichiometric operation at Mach 3 and those generated in the inlet duct and ramjet combustion chamber at higher Mach numbers. Active cooling of these surfaces by the liquid hydrogen fuel is, therefore, required. The cooling problem presents one of the major challenges in the structural design of these units.

## PROPULSION

Typical propulsion-system installations for Mach 6 cruise vehicles are shown in figure 9. One possible type of turbo-accelerator ramjet is shown in which a switching valve redirects the airflow to either the turbojet or the subsonic-combustion ramjet. These combination engines allow a common inlet to be used for both the turbojet and ramjet.

An axisymmetric pod arrangement as used on lower speed cruise vehicles is shown at the top of the figure. This arrangement has advantages of low weight and absence of contaminating boundary layers from adjacent surfaces. Regenerative fuel cooling of the entire internal ducting and external cowl lip will be required. The spike may be either radiation cooled or fuel cooled. Large spike translations are essential to achieve adequate performance throughout the speed range. The two-dimensional installation more readily incorporates the requisite variable geometry through the adjustable wall. However, it may require a more elaborate boundary-layer bleed system including a diverter to prevent the thick wing-body boundary layer from entering the duct.

A question of major importance in configuration definition is the inlet size requirement of these installations. Factors that affect inlet size are the vehicle aerodynamic characteristics, efficiency of the engine-inlet combination, location of the inlet on the vehicle, flight path, and minimum acceleration criteria along the flight path. Representative calculations have been made for Mach 6 and Mach 8 cruise vehicles by using the method of reference 22 to define inlet size requirements and the attendant longitudinal-acceleration characteristics. The calculations assumed that the vehicle would cruise at  $(L/D)_{\max}$ . The propulsion system assumed a subsonic combustion turboramjet engine in conjunction with two inlet types located in the wing pressure field: the first was assumed to operate at full capture at cruise with flow spillage

through a fixed  $6^\circ$  wedge shock at lower speeds, whereas the second type was assumed to operate at full capture at all speeds.

The flight-path constraints (see fig. 10) included a transonic acceleration altitude of 40 000 feet, a dynamic pressure limit of 1500 psf, and an inlet duct pressure limit of 200 psi. For the conditions assumed, the Mach 6 cruise altitude lies above the acceleration path and a constant Mach number climb to this altitude is performed. For the Mach 8 case, the cruise altitude lies below the acceleration path and the final acceleration is performed at cruise altitude at reduced inlet pressure recovery to conform to the duct pressure limit.

The flight aerodynamic characteristics are depicted in figure 11. For most of the acceleration phase, the vehicle system operates well below maximum lift-drag ratio, reaching this condition in a brief portion of the subsonic climb and at the cruise condition. The final portion of the Mach 8 acceleration path is flown at very nearly  $(L/D)_{\max}$  as a result of the characteristics imposed by the duct-pressure-limit assumption.

The acceleration characteristics are shown in figure 12. The higher accelerations are for the inlet operating at full capture at all conditions, with the higher thrust levels a consequence of the higher airflow characteristics of these inlets. As noted previously, the actual inlet will probably fall between these extremes.

The accelerations were provided by sizing the ramjet and inlet area for the condition at the start of cruise. This inlet area was then used over the flight path and the turbojet portion of the engine was sized to provide minimum acceleration of  $2 \text{ ft/sec}^2$  at transonic speeds. With these inlet-engine sizing criteria, an average acceleration level of about  $0.2g$  over the Mach number range is provided, a level which is several times larger than SST values but in the range needed to achieve adequately short acceleration periods for Mach 6 cruise. The inlet areas required were less than 2 percent of the wing area.

The location of these inlets also has an important influence on vehicle shaping. In figure 13 the inlet area required to obtain various accelerations is shown for two cases - when the inlet can be located in the wing compression field, as for the previous calculations, and when the inlet ingests free-stream air. At angle of attack the air beneath the wing is precompressed and this advantage results in a small enough inlet at near-zero acceleration to be located in this pressure field as shown. There is a usable limit, however, to the inlet size that can be contained in this preferred location; and this limit on a delta wing for a two-dimensional inlet of realistic length is shown by the shaded region. For higher acceleration (or higher Mach number) vehicles where the inlet may be too large to be located in the wing pressure field, the upper curves may dictate required inlet areas, and because the inlet now must furnish all the compression it becomes large enough to house both fuel and payload. The aircraft must now be designed around the inlet and a "flying inlet" configuration results. These "flying engine" types will utilize scramjet propulsion beyond Mach 8 where, for a number of reasons, the subsonic-combustion ramjet performance deteriorates rapidly with increased speed.

Both USAF and NASA have sizable programs for hypersonic ramjet development. The NASA work centers on the development of an 18-inch-diameter engine capable of both subsonic and supersonic burning. It will eventually be flight tested to Mach 8 on an uprated X-15 airplane. The first phase of this project, which is now finished, included engine concept development and evaluation in depth. One of the results of these studies is a detailed evaluation of the regenerative fuel-cooling requirements; these are shown in figure 14.

The fuel flow for cooling is shown as a fraction of the fuel required for propulsion with stoichiometric burning. For values of this ratio up to 1, the fuel carried for propulsion is sufficient for cooling purposes. For ratios above 1, additional fuel must be carried to meet cooling needs.

The study results (shown in fig. 14) have been extrapolated, using Reynolds number corrections, for an engine of 7-foot diameter. At Mach 6 adequate fuel is available for cooling; however, cooling needs increase rapidly with Mach number and near 7 it is questionable whether sufficient fuel for cooling is available. Beyond Mach 7 the cooling requirements become severe, and there is strong evidence from these studies that these cooling requirements may constitute a more serious obstacle to higher flight speeds than the problems of aerodynamics, supersonic combustion, or even structures. Opportunities for improving the situation, however, exist if the allowable duct wall temperatures can be increased and/or shorter engines with lower wetted surfaces developed.

A major concern of the aerodynamicist is the increase in drag and the interference effects that result when propulsion systems are added to the airframe. Little significant hypersonic experimental work in this area has been reported in the literature. An investigation by Frank S. Kirkham and William J. Small has recently been performed in the Langley 11-inch hypersonic tunnel at Mach 6.8 on the models equipped with two-dimensional and pod inlets shown in figure 15. Flow-through inlets were used, and the ramp and spikes were not included. The inlet areas for both types were 1.8 percent of the wing area, which is in the right range for Mach 6 cruise vehicles, and both inlets captured the precompressed air beneath the wing. The results show the increase in total drag due to inlet addition at an angle of attack of  $6^\circ$  which is close to that for  $(L/D)_{\max}$ .

The theoretical results, which include pressure and both internal and external skin-friction drag, are in good agreement with experimental results for the two-dimensional inlet. With pod inlets a much larger drag increase occurs and only about half the increment is predicted. The difference is due to the greater interference effects between the pod inlets and the airframe. The calculated increase in internal inlet drag, which is not chargeable to total drag, amounted to about 3 percent for the two-dimensional inlet and 7 percent for the pod inlets.

The extent of these interference effects is indicated in figure 16 which contains oil-flow patterns in the vicinity of the two types of inlets. The flow about the two-dimensional inlet appears very uniform whereas large disturbances from interacting flow fields occur for the pod installations. In addition to excessive interference drag, local heating increases may be more severe

for the pod installations. If the ramp and spikes had been included, they would not have caused additional interference drag under design conditions since the compression shock would be captured by the inlet lip. The off-design conditions, however, are a matter for further study.

These drag and oil-flow results indicate the superiority of two-dimensional inlet installations; however, it should be remembered that these are early results obtained under laminar-boundary-layer conditions. Additional work is required to determine whether similar effects prevail under turbulent flow conditions and whether some benefit can be gained from the interaction effects on pod installations.

## AERODYNAMICS

### Overall Configuration Considerations

To determine the influence of aerodynamics on vehicle shaping, the findings of basic configuration studies must be referred to since no definitive results are as yet available from complete configuration studies. In examining these basic study results, the main inquiry is concerned with whether any particular family of wing-body arrangements offers any particular advantage in  $(L/D)_{\max}$  performance, neglecting for now practical considerations such as trim and stability.

Experimental results taken from references 23 and 24, which show the maximum attainable performance obtained from a number of idealized-shape families, are presented in figure 17. In this figure,  $(L/D)_{\max}$  results are shown as a function of the volume parameter which exerts a large influence on maximum lift-drag-ratio characteristics. The probable range of volume parameters for HCV design is from about 0.14 to 0.24. In this range it is apparent that no one shape family has clearly superior performance and that blended wing-bodies are competitive with discrete wing-body types. At the higher end of the range, slender lifting bodies are also competitive; however, in order to obtain the  $(L/D)_{\max}$  values shown, extremely slender half-cone bodies are required.

The discrete wing-body data indicate some small improvement in  $(L/D)_{\max}$  due to the favorable lift interference from the underslung body on the flat-top configurations; and since the introduction of this concept in reference 25, much detailed experimental work (refs. 26 to 37) has been done with the hope of improving the attainable performance. Experimental results from references 26, 27, 28, 33, and 34 are summarized in figure 18. The largest performance gains are obtained at the lower Mach numbers; and, to capitalize on these potential benefits, the design concept was utilized on the XB-70 airplane. At higher Mach numbers, however, the performance gains decrease rapidly. Investigations were undertaken to explain the behavior; and the results, given in detail in reference 34, indicate that performance gains of these idealized shapes are only obtained under rigid geometric constraints. Since these idealized shapes are not generally adaptable to hypersonic cruise vehicle design, further

investigations of the more practical shapes shown in figure 19 were conducted at Mach 6.8. The experimental results to the left indicate the performance gains possible under idealized configuration conditions (shock-shape wings). The more practical configurations, however, fail to show any interference gains in  $(L/D)_{\max}$ . The shapes tested, however, by no means exhaust the interesting possibilities.

The foregoing data were obtained under the effects of a laminar boundary layer. The results in figure 20, however, indicate that under full-scale flight conditions extensive laminar flow will not occur. At the top of the figure are shown typical Reynolds numbers, based on length, for a full-scale hypersonic cruise vehicle. In the lower part of the figure are shown Reynolds number conditions for the start of transition on cones and flat plates, as obtained from references 38 to 55. At Mach 6 to 8, full-scale Reynolds numbers are seen to be greater than  $200 \times 10^6$  whereas laminar flow ends at about  $5 \times 10^6$ . Only the first few feet of the aircraft, therefore, will be subject to laminar flow, with turbulent flow dominating most of the remaining surface.

In extrapolating laminar wind-tunnel results to turbulent flight conditions, gross approximations presently have to be made. The method used simply subtracts the low Reynolds number laminar skin-friction drag, which in itself is in doubt, and replaces it with high Reynolds number turbulent values. Component performance and interaction effects on lift and drag due to lift are thus assumed to be the same for turbulent flow as for laminar flow - an extremely doubtful assumption. This method was used to extrapolate the previous results of figure 17 to flight conditions, and these extrapolated results are given in figure 21.

As a result of the lower turbulent skin-friction drag at a Reynolds number of  $200 \times 10^6$  as compared with the laminar drag at  $1.5 \times 10^6$ , the levels of  $L/D$  performance are significantly increased and differences in the performance of different configuration families are more pronounced. It is not known, however, whether these trends actually exist because of the difficulty in obtaining turbulent flow on small models at hypersonic Mach numbers as discussed in paper no. 2 by Braslow, Hicks, and Harris. At lower speeds turbulent flow can be simulated by relatively small roughness strips attached to the models. At high Mach numbers this technique is not satisfactory since the required roughness sizes become so large that extraneous effects are often introduced which are difficult, if not impossible, to correct for (refs. 56 to 63). This problem presents a major difficulty in the present efforts to study complete configurations.

The provision of stability and control will have an important influence on configuration design. Little experimental data on hypersonic air-breathing configurations exist; but during earlier work on boost-glide vehicles, several design features (shown in fig. 22) were developed which may have application to these cruise vehicles.

Negative camber was found to decrease the trim penalties on  $(L/D)_{\max}$ . (See ref. 64.) A negative-camber feature is illustrated by the upward

deflection of the forward portion of the delta wing. Upward deflection of trailing-edge flaps for trim and a properly blunted and contoured underslung body also provide negative-camber effects. In trailing-edge-flap installations, adverse yaw often occurs when these surfaces are differentially deflected for roll control. This effect can be reduced by sweeping the flap hinge line forward to move the resultant force closer to the vehicle center of gravity (ref. 65).

For directional stability and control, a wedge vertical-tail section can reduce excessive area requirements (ref. 66), and a variable wedge could be included to allow optimum operation over the Mach number range and to reduce base drag at critical transonic conditions. Toed-in wing-tip fins (ref. 64) are a further application of the wedge principle. Decreasing directional stability with angle of attack can be alleviated by rolling out the tip fins (ref. 67).

Drooped wing tips may be useful for improving the performance and directional stability with minimum performance penalty for favorable lift-interference configurations but the adverse roll characteristics of these surfaces must not be overlooked.

#### Local Flow Problems

A major new problem encountered in the design of hypersonic cruise vehicles is the evaluation of local interference effects which may have an important influence on loads, control effectiveness, and local aerodynamic heating. These areas are far more important for these vehicles than for supersonic transport designs because of the more intense interactions which occur between aircraft components. Actually a large amount of study has been devoted to these local flow problems, and in some areas a reasonably good understanding of the phenomena involved already exists.

Turbulent surface-heating data are available on delta wings at local Mach numbers up to about 5 and on flat plates and slender cones at local Mach numbers up to about 8 (refs. 40 to 44, 51 to 55, and 68 to 70). Typical heating results at a free-stream Mach number of 6.8 are shown in figure 23. For delta wings at wall conditions near adiabatic, turbulent heating is predictable by use of strip theory. For cones the heating rates at low angles of attack are predictable by laminar conical-flow theory and at high angles of attack by laminar cross-flow theory with a large uncertainty occurring in the intermediate angle-of-attack range.

Although these results are encouraging, the status of turbulent surface heating must be improved through additional efforts to better establish wall temperature effects and to obtain delta-wing heating characteristics at higher local Mach numbers. In addition, body shapes having larger volumes which are more representative of hypersonic cruise vehicle designs must be investigated.

In leading-edge heating, a somewhat improved situation exists. As long as the Mach number component normal to the leading edge is larger than about 1.5,

laminar and turbulent heating rates are sufficiently predictable for preliminary design purposes on a smooth leading edge (refs. 71 to 74). The effects on heating of the laps on segmented leading edges discussed previously, however, are presently uncertain.

Shock impingement (refs. 75 to 80) has long been recognized as a source of local heating increases. Latest results, however, indicate that these effects on leading edges are predictable. In figure 24 typical results from reference 80 of local heating along the leading edge show an increase from shock impingement. If local conditions are accounted for, the heating increase is well predicted. Shock impingement also causes premature transition from laminar to turbulent flow. However, the transition Reynolds numbers, based on local conditions, have also been determined. Local heating from shock impingement may also occur on surfaces downstream of the leading edge but is less well understood.

Flow separation poses a problem of predicting flap control effectiveness and high heating rates at boundary-layer reattachment on the deflected controls. In reentry vehicles which are subject to laminar or transitional boundary layers, this is a serious problem. In hypersonic cruise vehicles where turbulent flow dominates, however, the problem is much less severe. At the top of figure 25, the large control deflections (refs. 81 to 85) for which a turbulent boundary layer will separate are compared with the much smaller ones for laminar flow. Since control deflections of this order should not be required under normal flight conditions, turbulent flow separation should not be encountered. Should separation occur, however, realistic predictions of control effectiveness and local heating may be possible because of the smaller area affected by turbulent separation as compared with laminar, as illustrated by the schlieren photographs of the flow over a  $40^\circ$  compression corner.

Contrary to the good understanding in the previous areas, the corner-flow problem is not well understood. It occurs at the junctures of the wing and fuselage, wing and tip fins, and inlet sides and wing. The mechanisms of corner flow are very complex and, in spite of the fact that many detailed investigations have been conducted (refs. 86 to 107), local heating increases are not predictable even on the most basic models. Behavior in an idealized corner is illustrated by the unpublished results recently obtained by P. Calvin Stainback in the Langley Mach 8 variable-density hypersonic tunnel and shown in figure 26(a). The model consists of a two-dimensional  $90^\circ$  corner with one side deflected  $5^\circ$  into the stream. The experimental data show heating rates up to five times the predicted values on the undeflected plate and a 50-percent increase in the deflected-plate values. In three-dimensional flow, similar increases occur as indicated by the data in figure 26(b) for a half-cone--delta-wing configuration, taken from reference 51, where the cone heating rates are double the predicted values. These data were obtained under laminar-boundary-layer conditions. The increases in heating under turbulent conditions at these Mach numbers are unknown.

During the development phase of hypersonic cruise vehicles, a number of configuration concepts will have to be considered; and, since these configurations will be significantly different, this inability to predict corner-flow

local heating will require detailed heating tests on each configuration to obtain representative heating distributions. Investigations of complete configurations have begun, and heat-sensitive-paint test results obtained at Mach 6.8 for one concept are shown in figure 27. Regions of high heating are indicated by the dark areas and high heating from corner-flow phenomena is evident near the junctures of the wing and fuselage and the inlet and wing.

## CONFIGURATION CONCEPTS

The previous discussion has attempted to isolate presently known influences on configuration definition from the structural, propulsive, and aerodynamic disciplines. To summarize briefly, a discrete body with low or high wing arrangement and fuselage-mounted vertical tail is preferred from the present structural point of view. Propulsive considerations favor a low wing position with two-dimensional inlets mounted in the wing flow field. Both discrete body-wing and blended body-wing arrangements are aerodynamically competitive.

Within these constraints a number of design concepts are possible and some examples of these are shown in figure 28. The three configurations shown in figure 28(a) are being considered in present analytic trade-off studies. The variable-geometry configuration appears to have the highest gross weight but is attractive because of its superior subsonic loiter and mission abort capabilities. Both the variable-geometry and the fixed-delta-wing configuration utilize high-lift devices at take-off and landing. These devices cannot be included on the blended wing-body design, which does not have a separate horizontal tail, and still maintain trim control; as a result, a larger wing area is required for the blended wing-body.

In the trade-off studies, a lifting-body design was also considered; however, the concept was discarded because the high weight of the retractable wing used only for take-off and landing led to large fuel requirements and the resulting gross weight became prohibitive. The success of the twist and camber concept for the supersonic transport requires that it also be considered in the design of hypersonic vehicles, and efforts are now underway to extend the theoretical work to higher Mach numbers.

The configuration at the top of figure 28(b) follows XB-70 design and attempts to gain favorable interference benefits from the wedge underbody. In providing the necessary interference flow field, the underbody becomes large enough to house the inlet ducts and engines and also to provide part of the hydrogen fuel storage volume. A potentially severe problem area exists, however, in the long length of inlet ducts involved which may lead to excessive structural weight and fuel-cooling requirements. Furthermore, the forward inlet position restricts the usable inlet area in the wing flow field.

Another form of a blended wing-body utilizes the "caret" wing proposed in reference 108. The caret-wing lower surface is derived from simple wedge flow and offers more uniform pressure and less severe heating characteristics than does a conventional delta wing. These advantages may, of course, be offset by

other factors such as increased wing area and loads resulting from the negative dihedral.

The configuration on the lower right of figure 28(b) is one "flying inlet" design concept which results when the inlet is too large to be contained in the wing pressure field. It might be applied to higher acceleration Mach 12 cruise vehicles or lower Mach number launch vehicles.

Efforts are now beginning at Ames and Langley Research Centers to investigate complete-configuration concepts which contain requirements of trim, stability, and other practical considerations. The model under study at Mach 7 at Langley is shown in figure 29. As a start, the model design concept is one used in early trade-off studies (ref. 16). This relatively simple concept will serve to verify existing aerodynamic prediction techniques, establish typical local heating distributions, and provide a base-line configuration with which to compare additional concepts which are planned to be added as the program proceeds.

#### CONCLUDING REMARKS

The principal efforts of the next decade will involve application of the considerable general knowledge and data which now exist in all areas to the development of complete hypersonic vehicle systems. At the present time the first structural-concept models of cryogenic tankage are being readied for high-temperature testing in ground facilities. The first experimental hypersonic ramjet engines for flight tests are under development by both USAF and NASA. Aerodynamic studies of complete configurations have been started.

In the aerodynamics area, there is a serious handicap in the use of existing wind tunnels to simulate the high Reynolds number turbulent flows of full-scale flight. At the higher Mach numbers, the transition-strip technique used so successfully in the supersonic transport development tends to become ineffective. Extensive efforts to develop usable hypersonic tripping techniques are in progress but no practical solution has as yet emerged. Flight tests of at least one representative large-scale wing-body configuration to determine the detailed aerodynamic and heating behavior with natural fully developed turbulent flows will probably be required to supplement and upgrade the wind-tunnel results. This large-scale aerodynamic flight test could also provide the basis for structural concept development and testing for wing-body arrangements which will be needed in the course of future vehicle development.

## APPENDIX

### SYMBOLS

$A_i$	inlet captive area
$a/g$	acceleration in gravity units
$d$	diameter of cylindrical leading edge
$h$	heat-transfer coefficient
$L/D$	lift-drag ratio
$l$	length
$M$	Mach number
$N_{St}$	Stanton number
$P_{t,2}$	duct total pressure
$q$	dynamic pressure
$R_d$	Reynolds number based on diameter
$R_l$	Reynolds number based on length
$R_x$	Reynolds number based on distance $x$
$S$	total planform area
$S_w$	total wing area (including portion covered by fuselage)
$s$	distance from center line along surface to a given point
$s_o$	distance from center line along surface to leading edge
$V$	volume
$V_f$	fuel volume
$W_f$	fuel weight
$W_p$	payload weight
$W_S$	structural weight

W<sub>T</sub>            gross take-off weight  
X,Y,Z          axis system  
x,y,z          distance along X-, Y-, and Z-axis, respectively  
α              angle of attack  
δ              deflection angle

Subscripts:

fb            flat bottom  
fp            flat plate  
ft            flat top  
max          maximum  
∞            free stream

Abbreviations:

F.R.          fuselage fineness ratio  
LH<sub>2</sub>          liquid hydrogen

## REFERENCES

1. Slinger, E.; and Bredt, J. (M. Hamermesh, trans.): A Rocket Drive for Long Range Bombers. Transl. CGD-32, Tech. Inform. Branch, Bur. Aeron., Aug. 1944.
2. Williams, E. P.; Dhanes, L. W.; Huntzicker, J. H.; Lew, R. J.; Lieske, H. A.; Moore, L. L.; and Young, G. B. W.: Long-Range Surface-to-Surface Rocket and Ramjet Missiles - Aerodynamics. U.S. Air Force Project RAND Rept. R-181, The RAND Corp., May 1, 1950.
3. Seiff, Alvin; and Allen, H. Julian: Some Aspects of the Design of Hypersonic Boost-Glide Aircraft. NACA RM A55E26, 1955.
4. Eggers, Alfred J., Jr.; Allen, H. Julian; and Neice, Stanford E.: A Comparative Analysis of the Performance of Long-Range Hypervelocity Vehicles. NACA Rept. 1382, 1958. (Supersedes NACA TN 4046.)
5. Gradecak, V.: A Typical Long Range Hypersonic Rocket Glider and Its Structural Problems. 3rd Symposium on High-Speed Aerodynamics and Structures, Vol. 2, CONVAIR - San Diego, 1958, pp. 243-338.
6. Weber, R. J.: A Survey of Hypersonic-Ramjet Concepts. [Preprint] 875-59, Am. Rocket Soc., June 1959.
7. Frick, C. W.; and Strand, T.: Recoverable Air-Breathing Boosters - Analysis of Their Potentialities. Aerospace Eng., vol. 20, no. 2, Feb. 1961, pp. 22-23, 66-70.
8. Lane, R. J.: Recoverable Air-Breathing Boosters for Space Vehicles. J. Roy. Aeron. Soc., vol. 66, no. 618, June 1962, pp. 371-386.
9. Watton, Alan: Aerospaceplane - An Advanced System Planning Study. ASD-TDR-63-390, U.S. Air Force, Sept. 1963.
10. Tinnan, Leonard M.: Reusable Launch Systems. Astronautics, vol. 8, no. 1, Jan. 1963, pp. 50-56.
11. Jarlett, F. E.: Aerospaceplane Payload and Potential. Trans. Eighth Symposium on Ballistic Missile and Space Technology, vol. V, U.S. Air Force and Aerospace Corp., Oct. 1963, pp. 243-303. (Available from DDC as AD 346-902.)
12. Knip, Gerald, Jr.; and Allen, John L.: Analysis of Booster Systems With a Recoverable Hypersonic Airplane First Stage. AIAA Paper No. 64-543, May 1964.
13. Peoples, P. L.; Zeck, H.; Edmonds, D. S.; and Omoth, M. J.: Performance and Cost Analysis of Advanced Rocket and Airbreathing Launch Systems. AIAA/NASA Third Manned Space Flight Meeting, CP-10, Am. Inst. Aeron. Astronaut., Nov. 1964, pp. 339-352.

14. Petersen, Richard H.; Gregory, Thomas J.; and Smith, Cynthia L.: Some Comparisons of Turboramjet-Powered Hypersonic Aircraft for Cruise and Boost Missions. AIAA Paper No. 65-759, Nov. 1965.
15. Watton, Alan: Recent Air-Breathing Launch Vehicle Studies and Their Propulsion Implications. 65SES-1246, RTD, U.S. Air Force, June 15, 1965.
16. Gregory, Thomas J.; Petersen, Richard H.; and Wyss, John A.: Performance Trade-Offs and Research Problems for Hypersonic Transports. Paper No. 64-605, Am. Inst. Aeron. Astronaut., Aug. 1964.
17. Weber, Richard J.: Propulsion for Hypersonic Transport Aircraft. Proceedings of the 4th Congress of the International Council of the Aeronautical Sciences, Robert R. Dexter, ed., Spartan Books, Inc., 1965, pp. 977-999.
18. Manning, Charles R., Jr.; Royster, Dick M.; and Braski, David N.: An Investigation of a New Nickel Alloy Strengthened by Dispersed Thoria. NASA TN D-1944, 1963.
19. Lisagor, W. Barry; and Stein, Bland A.: A Study of Several Oxidation-Resistant Coatings on Cb-10Ti-5Zr Alloy Sheet at 2000° F, 2400° F, and 2700° F (1365° K, 1590° K, and 1755° K). NASA TN D-3275, 1966.
20. Scott, Russell Burton: Cryogenic Engineering. D. Van Nostrand Co., Inc., 1959.
21. Jackson, L. Robert; Davis, John G., Jr.; and Wichorek, Gregory R.: Structural Concepts for Hydrogen-Fueled Hypersonic Airplanes. NASA TN D-3162, 1966.
22. Jackson, Charlie M., Jr.: Estimation of Flight Performance With Closed-Form Approximations to the Equations of Motion. NASA TR R-228, 1966.
23. Becker, John V.: Studies of High Lift/Drag Ratio Hypersonic Configurations. Proceedings of the 4th Congress of the International Council of the Aeronautical Sciences, Robert R. Dexter, ed., Spartan Books, Inc., 1965, pp. 877-910.
24. Penland, Jim A.: Maximum Lift-Drag-Ratio Characteristics of Rectangular and Delta Wings at Mach 6.9. NASA TN D-2925, 1965.
25. Eggers, A. J., Jr.; and Syvertson, Clarence A.: Aircraft Configurations Developing High Lift-Drag Ratios at High Supersonic Speeds. NACA RM A55L05, 1956.
26. Syvertson, Clarence A.; Gloria, Hermilo R.; and Sarabia, Michael F.: Aerodynamic Performance and Static Stability and Control of Flat-Top Hypersonic Gliders at Mach Numbers From 0.6 to 18. NACA RM A58G17, 1958.

27. Syvertson, Clarence A.; Wong, Thomas J.; and Gloria, Hermilo, R.: Additional Experiments With Flat-Top Wing-Body Combinations at High Supersonic Speeds. NACA RM A56111, 1957.
28. Armstrong, William O.; and Ladson, Charles L. (With Appendix by Donald L. Baradell and Thomas A. Blackstock): Effects of Variation in Body Orientation and Wing and Body Geometry on Lift-Drag Characteristics of a Series of Wing-Body Combinations at Mach Numbers From 3 to 18. NASA TM X-73, 1959.
29. McLellan, Charles H.; and Dunning, Robert W.: Factors Affecting the Maximum Lift-Drag Ratio at High Supersonic Speeds. NACA RM L55L20a, 1956.
30. McLellan, Charles H.; and Ladson, Charles L.: A Summary of the Aerodynamic Performance of Hypersonic Gliders. NASA TM X-237, 1960.
31. Mead, Harold R.; Koch, Frank; and Hartofilis, Stavros A.: Theoretical Prediction of Pressures in Hypersonic Flow With Special Reference to Configurations Having Attached Leading-Edge Shock. ASD TR 61-60, U.S. Air Force. Part II. Experimental Pressure Measurements at Mach 5 and 8, May 1962. Part III. Experimental Measurements of Forces at Mach 8 and Pressures at Mach 21, Oct. 1962. (Available from ASTIA as 291 219.)
32. Geiger, Richard E.: Experimental Lift and Drag of a Series of Glide Configurations at Mach Numbers 12.6 and 17.5. J. Aerospace Sci., vol. 29, no. 4, Apr. 1962, pp. 410-419.
33. Johnston, Patrick J.; Snyder, Curtis D.; and Witcofski, Robert D.: Maximum Lift-Drag Ratios of Delta-Wing-Half-Cone Combinations at a Mach Number of 20 in Helium. NASA TN D-2762, 1965.
34. Fetterman, David E.: Favorable Interference Effects on Maximum Lift-Drag Ratios of Half-Cone Delta-Wing Configurations at Mach 6.86. NASA TN D-2942, 1965.
35. Fetterman, David E.; Henderson, Arthur, Jr.; Bertram, Mitchel H.; and Johnston, Patrick J.: Studies Relating to the Attainment of High Lift-Drag Ratios at Hypersonic Speeds. NASA TN D-2956, 1965.
36. Small, William J.; and Bertram, Mitchel H.: Effect of Geometric Modifications on the Maximum Lift-Drag Ratios of Slender Wing-Body Configurations at Hypersonic Speeds. NASA TN D-3276, 1966.
37. Whitehead, Allen H., Jr.: Effect of Body Cross Section and Width-Height Ratio on Performance of Bodies and Delta-Wing-Body Combinations at Mach 6.9. NASA TN D-2886, 1966.
38. Bertram, Mitchel H.: Exploratory Investigation of Boundary-Layer Transition on a Hollow Cylinder at a Mach Number of 6.9. NACA Rept. 1313, 1957. (Supersedes NACA TN 3546.)

39. Potter, J. Leith; and Whitfield, Jack D.: Effects of Unit Reynolds Number, Nose Bluntness, and Roughness on Boundary Layer Transition. AEDC-TR-60-5, U.S. Air Force, Mar. 1960.
40. Zakkay, Victor; and Callahan, Clifton J.: Laminar, Transitional, and Turbulent Heat Transfer to a Cone-Cylinder-Flare Body at Mach 8.0. J. Aerospace Sci., vol. 29, no. 12, Dec. 1962, pp. 1403-1413, 1420.
41. Deem, Ralph E.; and Murphy, James S.: Flat Plate Boundary Layer Transition at Hypersonic Speeds. AIAA Paper No. 65-128, Jan. 1965.
42. Sanator, R. J.; DeCarlo, J. P.; and Torrillo, D. T.: Hypersonic Boundary-Layer Transition Data for a Cold-Wall Slender Cone. AIAA J. (Tech. Notes), vol. 3, no. 4, Apr. 1965, pp. 758-760.
43. Bertram, Mitchel H.; and Neal, Luther, Jr.: Recent Experiments in Hypersonic Turbulent Boundary Layers. Presented at the AGARD Specialists Meeting on Recent Developments in Boundary-Layer Research (Naples, Italy), May 10-14, 1965.
44. Richards, B. E.; and Stollery, J. L.: Transition Reversal on a Flat Plate at Hypersonic Speeds. Recent Developments in Boundary Layer Research, AGARDograph 97, May 1965, pp. 477-501.
45. McCauley, W. D.; Saydah, A.; and Bueche, J.: The Effect of Controlled Three Dimensional Roughness on Hypersonic Laminar Boundary Layer Transition. AIAA Paper No. 66-26, Jan. 1966.
46. Henderson, A.; Rogallo, R. S.; Woods, W. C.; and Spitzer, C. R.: Exploratory Hypersonic Boundary-Layer Transition Studies. AIAA J. (Tech. Notes), vol. 3, no. 7, July 1965, pp. 1363-1364.
47. Fischer, W. W.; and Norris, R. H.: Supersonic Convective Heat-Transfer Correlation From Skin-Temperature Measurements on a V-2 Rocket in Flight. Trans. ASME, vol. 71, no. 5, July 1949, pp. 457-469.
48. Sternberg, Joseph: A Free-Flight Investigation of the Possibility of High Reynolds Number Supersonic Laminar Boundary Layers. J. Aeron. Sci., vol. 19, no. 11, Nov. 1952, pp. 721-733.
49. Jedlicka, James R.; Wilkins, Max E.; and Seiff, Alvin: Experimental Determination of Boundary-Layer Transition on a Body of Revolution at  $M = 3.5$ . NACA TN 3342, 1954.
50. Stetson, Kenneth F.: Boundary-Layer Transition on Blunt Bodies With Highly Cooled Boundary Layers. J. Aero/Space Sci., vol. 27, no. 2, Feb. 1960, pp. 81-91.
51. Dunavant, James C.: Heat Transfer to a Delta-Wing—Half-Cone Combination at Mach Numbers of 7 and 10. NASA TN D-2199, 1964.

52. Crawford, Davis H.: Investigation of the Flow Over a Spiked-Nose Hemisphere-Cylinder at a Mach Number of 6.8. NASA TN D-118, 1959.
53. Jackson, Mary W.; Czarnecki, K. R.; and Monta, William J.: Turbulent Skin Friction at High Reynolds Numbers and Low Supersonic Velocities. NASA TN D-2687, 1965.
54. Moore, D. R.; and Harkness, J.: Experimental Investigations of the Compressible Turbulent Boundary Layer at Very High Reynolds Numbers. AIAA J., vol. 3, no. 4, Apr. 1965, pp. 631-638.
55. Monta, William J.; and Allen, Jerry M.: Local Turbulent Skin-Friction Measurements on a Flat Plate at Mach Numbers From 2.5 to 4.5 and Reynolds Numbers up to  $69 \times 10^6$ . NASA TN D-2896, 1965.
56. Braslow, Albert L.; and Knox, Eugene C.: Simplified Method for Determination of Critical Height of Distributed Roughness Particles for Boundary-Layer Transition at Mach Numbers From 0 to 5. NACA TN 4363, 1958.
57. Smith, A. M. O.; and Clutter, Darwin W.: The Smallest Height of Roughness Capable of Affecting Boundary-Layer Transition. J. Aero/Space Sci., vol. 26, no. 4, Apr. 1959, pp. 229-245, 256.
58. Braslow, Albert L.: Review of the Effect of Distributed Surface Roughness on Boundary-Layer Transition. AGARD Rept. 254, Apr. 1960.
59. Van Driest, E. R.; and Blumer, C. B.: Effect of Roughness on Transition in Supersonic Flow. AGARD Rept. 255, Apr. 1960.
60. Von Doenhoff, Albert E.; and Braslow, Albert L.: The Effect of Distributed Surface Roughness on Laminar Flow. Boundary Layer and Flow Control, Vol. 2, G. V. Lachmann, ed., Pergamon Press, 1961, pp. 657-681.
61. Korkegi, Robert H.: Transition Studies and Skin-Friction Measurements on an Insulated Flat Plate at a Mach Number of 5.8. J. Aeron. Sci., vol. 23, no. 2, Feb. 1956, pp. 97-107, 192.
62. Sterrett, James R.; and Holloway, Paul F.: Effects of Controlled Roughness on Boundary-Layer Transition at a Mach Number of 6.0. AIAA J. (Tech. Notes), vol. 1, no. 8, Aug. 1963, pp. 1951-1953.
63. Holloway, Paul F.; and Sterrett, James R.: Effect of Controlled Surface Roughness on Boundary-Layer Transition and Heat Transfer at Mach Numbers of 4.8 and 6.0. NASA TN D-2054, 1964.
64. Rainey, Robert W.: Static Stability and Control of Hypersonic Gliders. NACA RM L58E12a, 1958.
65. Rainey, Robert W.: Summary of an Advanced Manned Lifting Entry Vehicle Study. NASA TM X-1159, 1965.

66. McLellan, Charles H.: A Method for Increasing the Effectiveness of Stabilizing Surfaces at High Supersonic Mach Numbers. NACA RM L54F21, 1954.
67. Rainey, Robert W.; and Close, William H.: Studies of Stability and Control of Winged Reentry Configurations. NASA TM X-327, 1960.
68. Nagel, A. L.; Fitzsimmons, H. D.; and Doyle, L. B.: Analysis of Hypersonic Pressure and Heat Transfer Tests on Delta Wings With Laminar and Turbulent Boundary Layers. D2-84299-1 (Contract No. NAS1-4301), The Boeing Co.
69. Stallings, Robert L., Jr.; Burbank, Paige B.; and Howell, Dorothy T.: Heat-Transfer and Pressure Measurements on Delta Wings at Mach Numbers of 3.51 and 4.65 and Angles of Attack From  $-45^{\circ}$  to  $45^{\circ}$ . NASA TN D-2387, 1964.
70. Dunavant, James C.: Investigation of Heat Transfer and Pressures on Highly Swept Flat and Dihedraled Delta Wings at Mach Numbers of 6.8 and 9.6 and Angles of Attack to  $90^{\circ}$ . NASA TM X-688, 1962.
71. Everhart, Philip E.; and Dunavant, James C.: Heat-Transfer Distribution on  $70^{\circ}$  Swept Slab Delta Wings at a Mach Number of 9.86 and Angles of Attack up to  $90^{\circ}$ . NASA TN D-2302, 1964.
72. Whitehead, Allen H., Jr.; and Dunavant, James C.: A Study of Pressure and Heat Transfer Over an  $80^{\circ}$  Sweep Slab Delta Wing in Hypersonic Flow. NASA TN D-2708, 1965.
73. Bertram, Mitchel H.; and Everhart, Philip E.: An Experimental Study of the Pressure and Heat-Transfer Distribution on a  $70^{\circ}$  Sweep Slab Delta Wing in Hypersonic Flow. NASA TR R-153, 1963.
74. Beckwith, Ivan E.; and Gallagher, James J.: Local Heat Transfer and Recovery Temperatures on a Yawed Cylinder at a Mach Number of 4.15 and High Reynolds Numbers. NASA TR R-104, 1961. (Supersedes NASA MEMO 2-27-59L.)
75. Newlander, Robert A.: Effect of Shock Impingement on the Distribution of Heat-Transfer Coefficients on a Right Circular Cylinder at Mach Numbers of 2.65, 3.51, and 4.44. NASA TN D-642, 1961.
76. Carter, Howard S.; and Carr, Robert E.: Free-Flight Investigation of Heat Transfer to an Unswept Cylinder Subjected to an Incident Shock and Flow Interference From an Upstream Body at Mach Numbers up to 5.50. NASA TN D-988, 1961.
77. Beckwith, Ivan E.: Experimental Investigation of Heat Transfer and Pressures on a Swept Cylinder in the Vicinity of its Intersection With a Wedge and Flat Plate at Mach Number 4.15 and High Reynolds Numbers. NASA TN D-2020, 1964.
78. Knox, E. C.: Measurements of Shock-Impingement Effects on the Heat-Transfer and Pressure Distributions on a Hemicylinder Model at Mach Number 19. AEDC-TR-65-245, U.S. Air Force. Nov. 1965.

79. Siler, L. G.; and Deskins, H. E.: Effect of Shock Impingement on the Heat-Transfer and Pressure Distributions on a Cylindrical-Leading-Edge Model at Mach Number 19. AEDC-TDR-64-228, U.S. Air Force, Nov. 1964.
80. Bushnell, Dennis M.: Interference Heating on a Swept Cylinder in Region of Intersection With a Wedge at Mach Number 8. NASA TN D-3094, 1965.
81. Chapman, Dean R.; Kuehn, Donald M.; and Larson, Howard K.: Investigation of Separated Flows in Supersonic and Subsonic Streams With Emphasis on the Effect of Transition. NACA Rept. 1356, 1958.
82. Kuehn, Donald M.: Turbulent Boundary-Layer Separation Induced by Flares on Cylinders at Zero Angle of Attack. NASA TR R-117, 1961.
83. Sterrett, James R.; and Emery, James C.: Experimental Separation Studies for Two-Dimensional Wedges and Curved Surfaces at Mach Numbers of 4.8 to 6.2. NASA TN D-1014, 1962.
84. Kuehn, Donald M.: Experimental Investigation of the Pressure Rise Required for the Incipient Separation of Turbulent Boundary Layers in Two-Dimensional Supersonic Flow. NASA MEMO 1-21-59A, 1959.
85. Holloway, Paul F.; Sterrett, James R.; and Creekmore, Helen S.: An Investigation of Heat Transfer Within Regions of Separated Flow at a Mach Number of 6.0. NASA TN D-3074, 1965.
86. Snow, R. M.: Aerodynamics of Thin Quadrilateral Wings at Supersonic Speeds. Quart. Appl. Math., vol. V, no. 4, Jan. 1948, pp. 417-428.
87. Hains, Franklin D.: Supersonic Flow Near the Junction of Two Wedges. J. Aero/Space Sci. (Readers' Forum), vol. 25, no. 8, Aug. 1958, pp. 530-531.
88. Wallace, James; and Clarke, Joseph H.: Uniformly Valid Second-Order Solution for Supersonic Flow Over Cruciform Surfaces. AIAA J., vol. 1, no. 1, Jan. 1963, pp. 179-185.
89. Loiziansky, L. G.: Interference of Boundary Layers. No. 249, Trans. Central Aero-Hydrodynamical Inst. (Moscow), 1936.
90. Loitsianskii, L. G.; and Bolshakov, V. P.: On Motion of Fluid in Boundary Layer Near Line of Intersection of Two Flows. NACA TM 1308, 1951.
91. Carrier, G. F.: The Boundary Layer in a Corner. Quart. Appl. Math., vol. IV, no. 4, Jan. 1947, pp. 367-370.
92. Dowdell, Rodger Birtwell: Corner Boundary Layer. M.S. Thesis, Brown Univ., 1952.
93. Oman, Richard A.: The Three-Dimensional Laminar Boundary Layer Along a Corner. Tech. Rept. No. 1 (Contract No. DA-19-020-ORD-4538), M.I.T., Jan. 1959. (Available from ASTIA as AD 211 216.)

94. Kemp, Nelson Harvey: The Laminar Three-Dimensional Boundary Layer and a Study of the Flow Past a Side Edge. M. Aero. Eng. Thesis, Cornell Univ., June 1951. (Available from ASTIA as AD 45462.)
95. Levy, Richard H.: The Boundary Layer in a Corner. Contract AF 49(638)-465, Dept. Aeron. Eng., Princeton Univ., Nov. 1959.
96. Cheng, Sin-I; and Levy, Richard H.: The Boundary Layer in a Corner. Rept. No. 485 (AFOSR TN 59-1165), Princeton Univ., Nov. 1959.
97. Krzywoblocki, M. Z.: On the Boundary Layer in a Corner by Use of the Relaxation Method. Ganita (Lucknow, India), vol. 7, no. 2, Dec. 1956, pp. 76-112.
98. Bloom, Martin H.; and Rubin, Stanley: High-Speed Viscous Corner Flow. J. Aerospace Sci., vol. 28, no. 2, Feb. 1961, pp. 145-157.
99. Stainback, P. Calvin: An Experimental Investigation at a Mach Number of 4.95 of Flow in the Vicinity of a 90° Interior Corner Aligned With the Free-Stream Velocity. NASA TN D-184, 1960.
100. Stainback, P. Calvin: Heat-Transfer Measurements at a Mach Number of 8 in the Vicinity of a 90° Interior Corner Aligned With the Free-Stream Velocity. NASA TN D-2417, 1964.
101. Galwin, Lawrence: Heat Transfer Correlations for the 90° Corner Interference Effects on Fin-Flat Plate Model at a Mach Number of 8. Tech. Rept. No. 207 (Contract No. AF 33(616)-6692), Gen. Appl. Sci. Lab., Inc., Feb. 8, 1961.
102. Bogdonoff, S. M.; and Vas, I. E.: A Preliminary Investigation of the Flow in a 90° Corner at Hypersonic Speeds. Part I - Flat Plates With Thin Leading Edges at Zero Angle of Attack. D143-978-013 (ARDC TR 57-202, AD 150 023), Bell Aircraft Corp., Dec. 20, 1957.
103. Rhudy, J. P.; Miers, R. S.; and Rippey, J. O.: Pressure Distribution and Heat Transfer Tests on Two Fin-Flat Plate Interference Models and Several Blunt Leading Edge Delta Wing Models. AEDC-TN-60-168, U.S. Air Force, Sept. 1960.
104. Miller, D. S.; Hijman, R.; Redeker, E.; Janssen, W. C.; and Mullen, C. R.: A Study of Shock Impingements on Boundary Layers at Mach 16. Proc. 1962 Heat Transfer and Fluid Mech. Inst., F. Edward Ehlers, James J. Kauzlarich, Charles A. Sleicher, Jr., and Robert E. Street, eds., Stanford Univ. Press, 1962, pp. 255-278.
105. Caldwell, A. L.; Haugseth, E. G.; and Miller, D. S.: The Influence of Aerodynamic Interference Heating on Directional Stability Problems of Hypersonic Vehicles. Paper 63-3, Inst. Aerospace Sci., Jan. 1963.
106. Jones, Robert A.: Heat-Transfer and Pressure Investigation of a Fin-Plate Interference Model at a Mach Number of 6. NASA TN D-2028, 1964.

107. Charwat, A. F.; and Redekopp, L. G.: Supersonic Interference Flow Along the Corner of Intersecting Wedges. AIAA Paper 66-128, Jan. 1966.
108. Townsend, L. H.: On Lifting Bodies Which Contain Two-Dimensional Supersonic Flows. Rept. No. Aero. 2675, Brit. R.A.E., Aug. 1963.

TABLE I

TYPICAL RESULTS FROM NASA CRUISE VEHICLE STUDIES

ITEM	SST STUDY	HCV STUDY
$M_\infty$	3	6
RANGE, N.Mi.	3500	5500
$W_T$ , LB	500000	500000
FUEL	JP	LH <sub>2</sub>
$W_p/W_T$	0.08	0.09
$W_f/W_T$	0.50	0.38
$V_f$ , FT <sup>3</sup>	4900	43500
$W_s/W_T$	0.27	0.36
F.R.	22 TO 24	12 TO 14
$(L/D)_{max}$	8 TO 9	4.5 TO 5.0
$W_T/S_w$	55 TO 100	45 TO 120

FLIGHT-PROFILE CONSTRAINTS

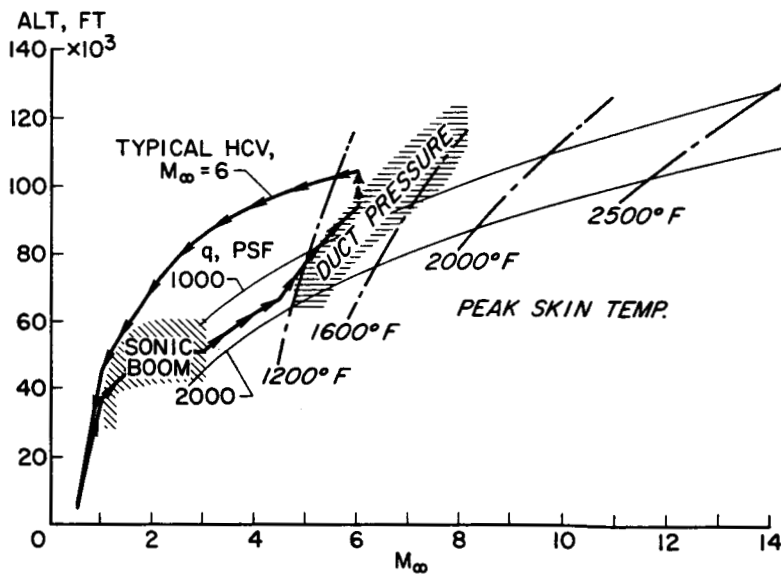


Figure 1

### SIZE COMPARISON BETWEEN HCV AND SST

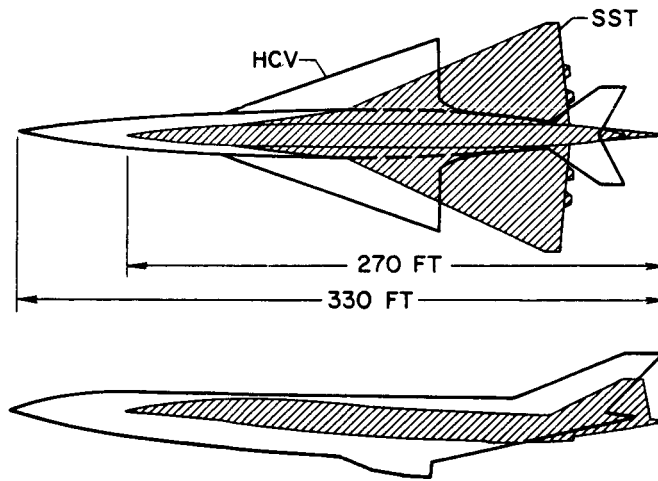


Figure 2

### EXAMPLE OF HCV STRUCTURAL ARRANGEMENT $M_{\infty} \approx 6$

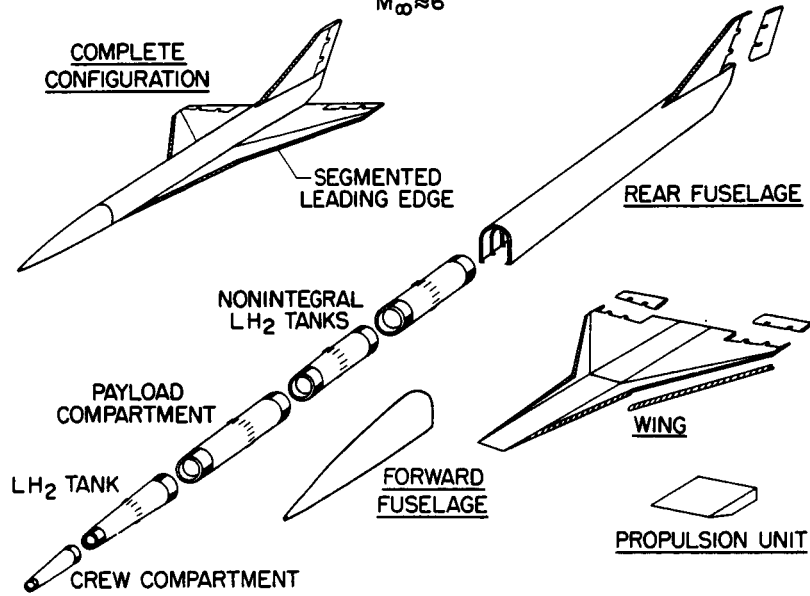


Figure 3

A NONINSULATED WING STRUCTURAL CONCEPT  
 $M_\infty \approx 6$

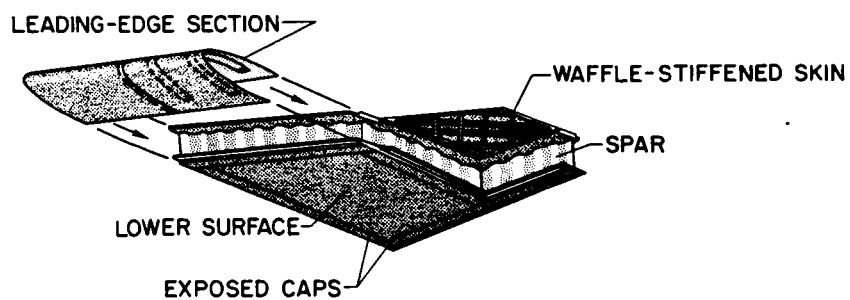


Figure 4

AN INSULATED WING STRUCTURAL CONCEPT  
 $M_\infty \approx 12$

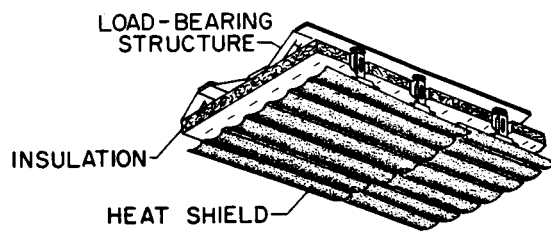
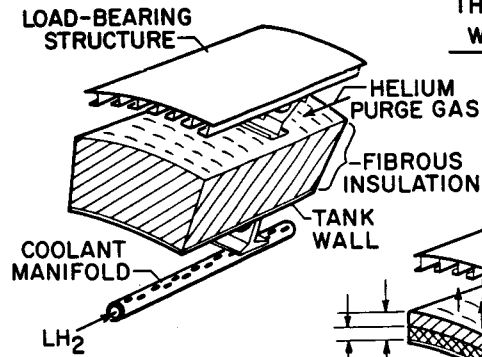


Figure 5

# NONINTEGRAL TANKAGE STRUCTURES

THERMAL PROTECTION  
WEIGHT, 6.75 LB/FT<sup>2</sup>



THERMAL PROTECTION  
WEIGHT, 2.77 LB/FT<sup>2</sup>

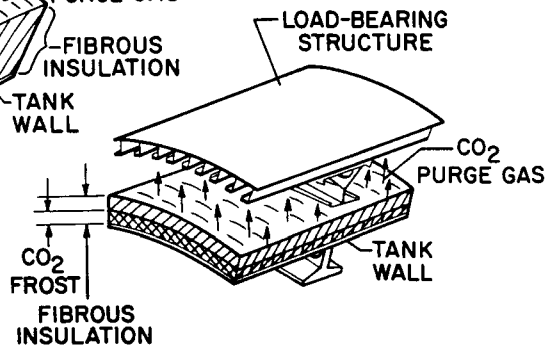


Figure 6

# HOT STRUCTURAL MODEL WITH NONINTEGRAL TANKAGE AND CO<sub>2</sub> PURGE SYSTEM

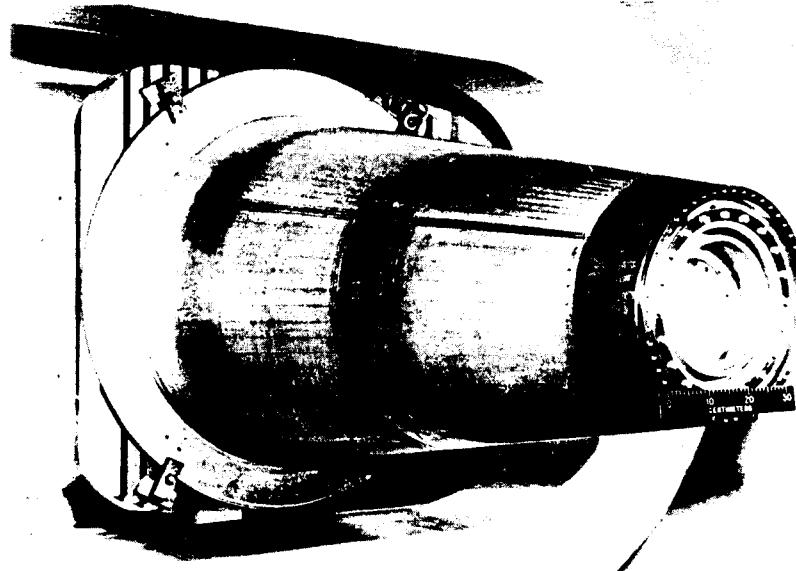


Figure 7

L-65-8668

**MULTIWALL STRUCTURAL MODEL**  
 LENGTH, 6 FT; DIAMETER, 3 FT

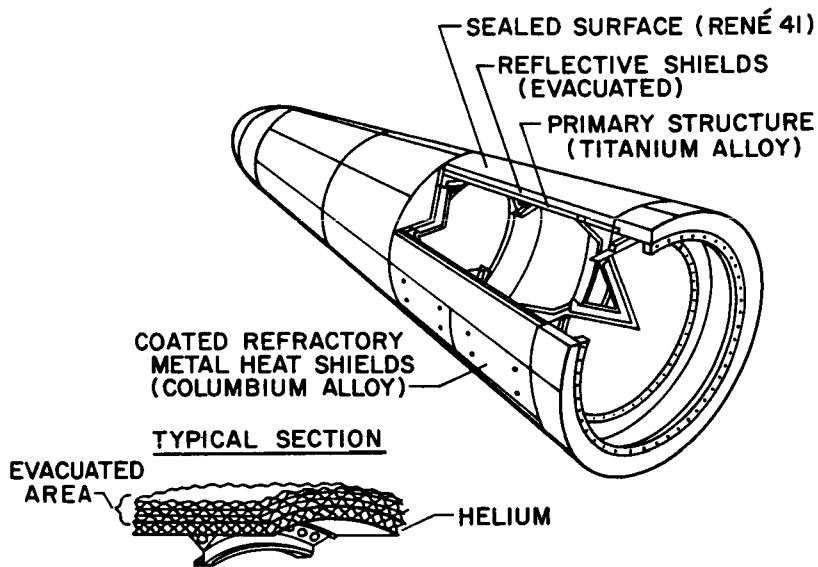


Figure 8

**POSSIBLE PROPULSION-SYSTEM INSTALLATIONS**  
 $M_\infty \approx 6$

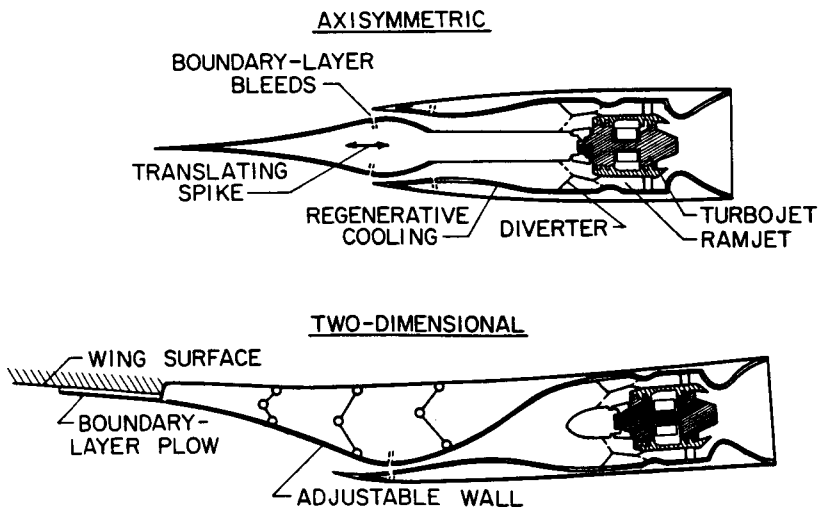


Figure 9

REPRESENTATIVE ACCELERATION FLIGHT PATH

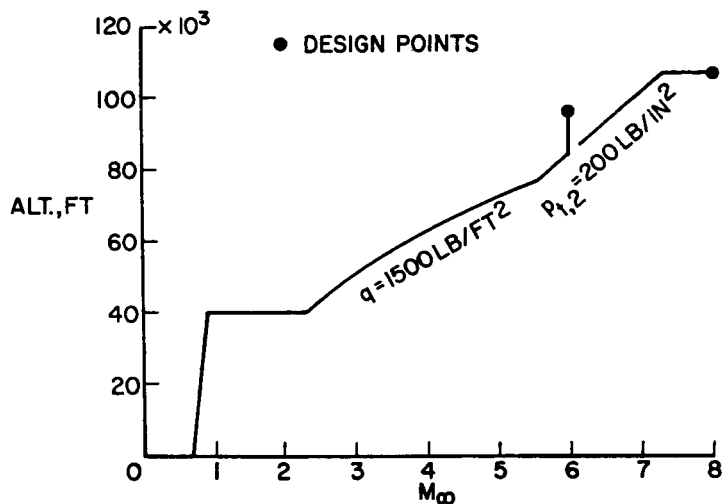


Figure 10

AERODYNAMIC CHARACTERISTICS DURING ACCELERATING FLIGHT

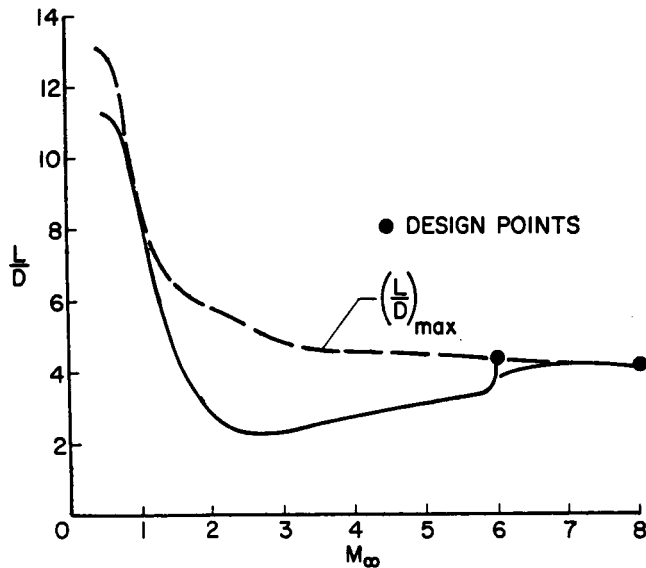


Figure 11

## REPRESENTATIVE ACCELERATION CHARACTERISTICS

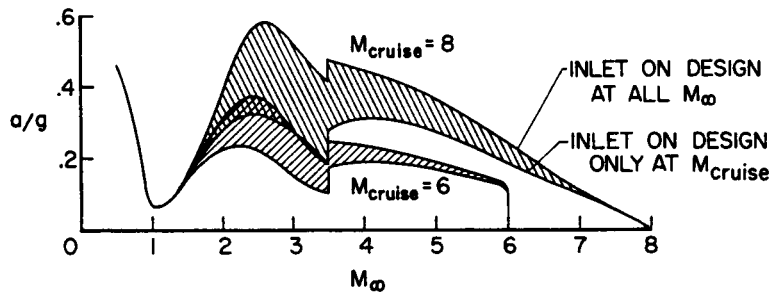


Figure 12

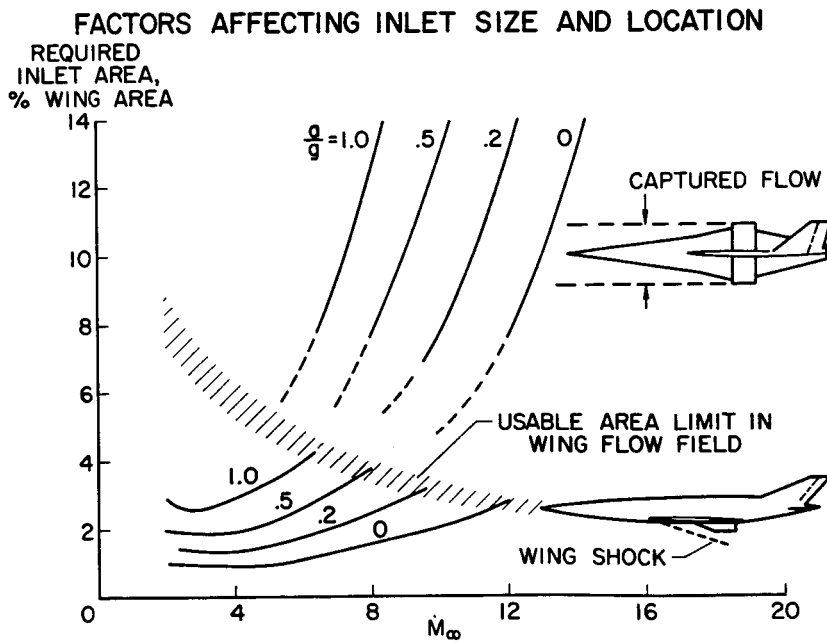


Figure 13

### REGENERATIVE FUEL-COOLING REQUIREMENTS

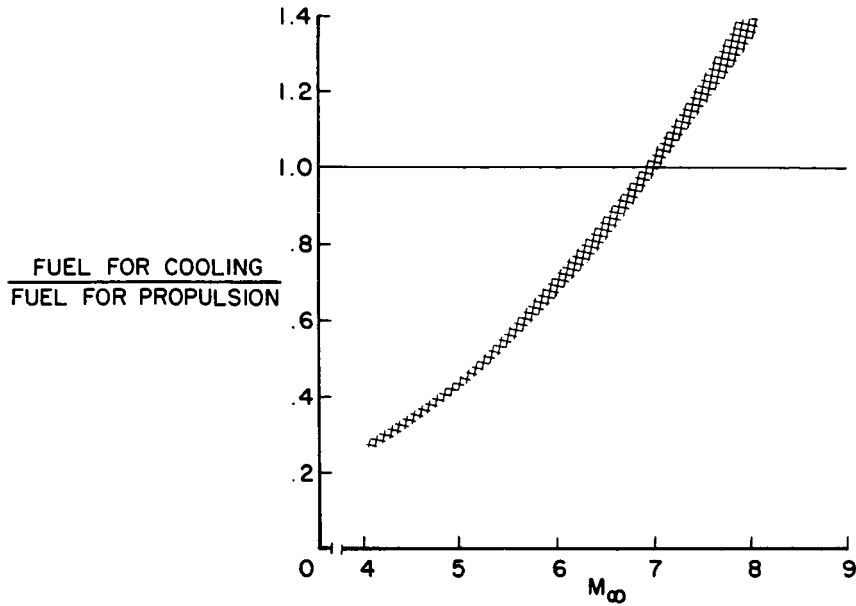


Figure 14

### EFFECT OF INLET INSTALLATION ON DRAG

$M_\infty = 6.8$ ;  $R_f = 3.75 \times 10^6$ ;  $A_i/S_w = 0.018$ ;  $\alpha = 6^\circ$

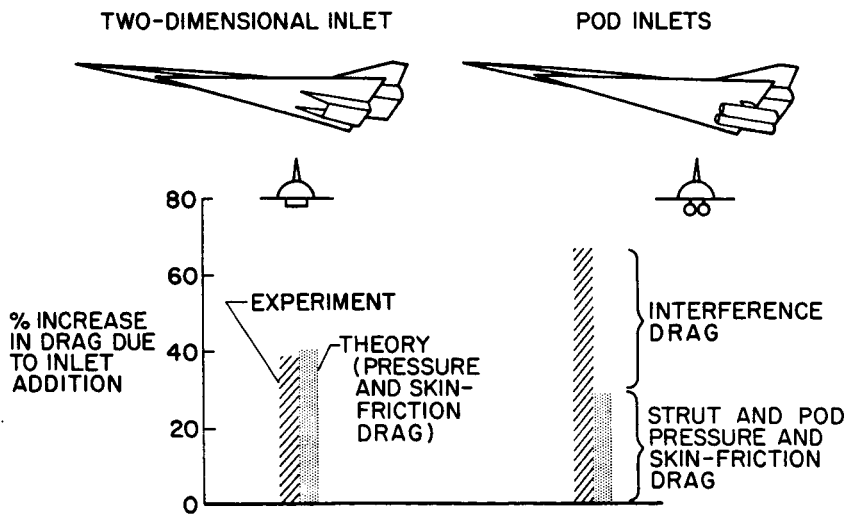


Figure 15

INLET INSTALLATION OIL-FLOW PATTERNS

$M_\infty = 6.8; A_1/S_w = 0.018$

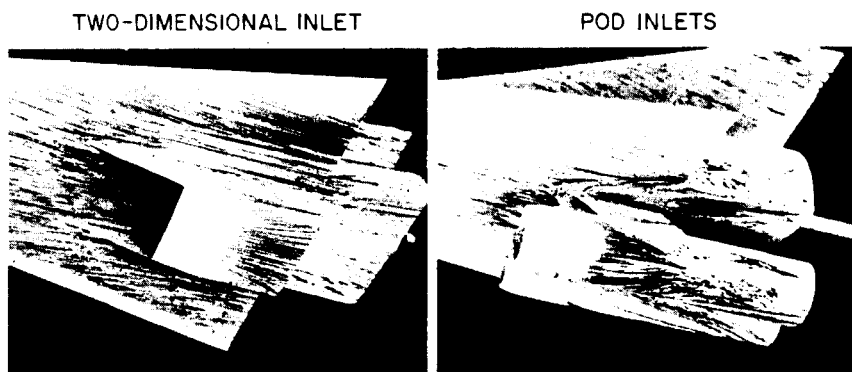


Figure 16

L-2697-24

PERFORMANCE OF BASIC CONFIGURATION CONCEPTS  
MEASURED IN WIND TUNNEL

$M_\infty = 6.8; R_1 = 1.5 \times 10^6$

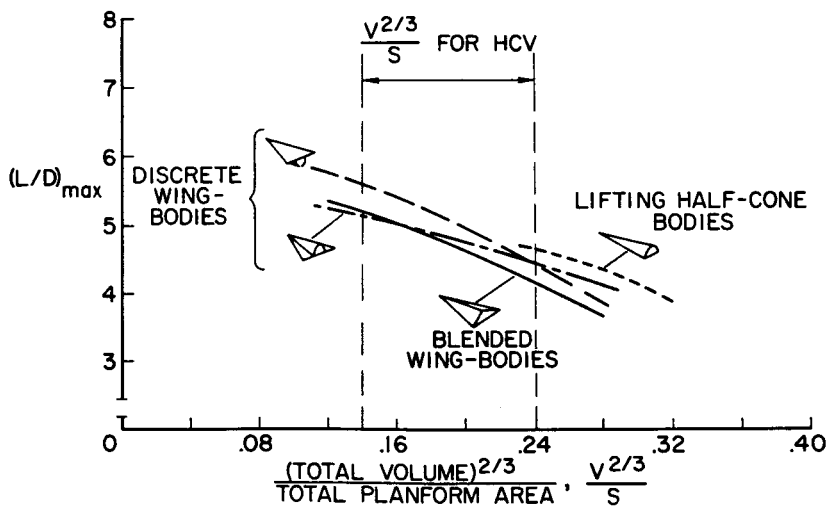


Figure 17

### WING-BODY INTERFERENCE EFFECTS ON PERFORMANCE

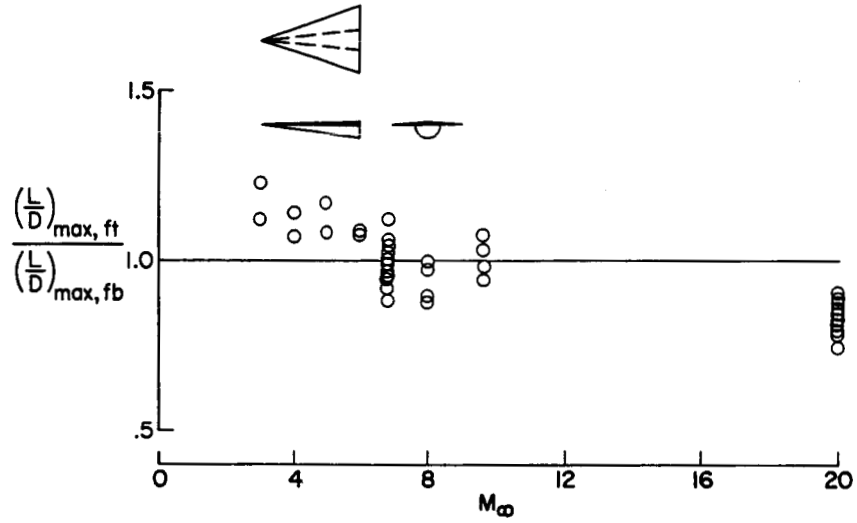


Figure 18

### BASIC CONFIGURATION EFFECTS ON UNTRIMMED PERFORMANCE

$M_\infty = 6.8$ ;  $R_T = 3.9 \times 10^6$ ; BODY VOLUME CONSTANT

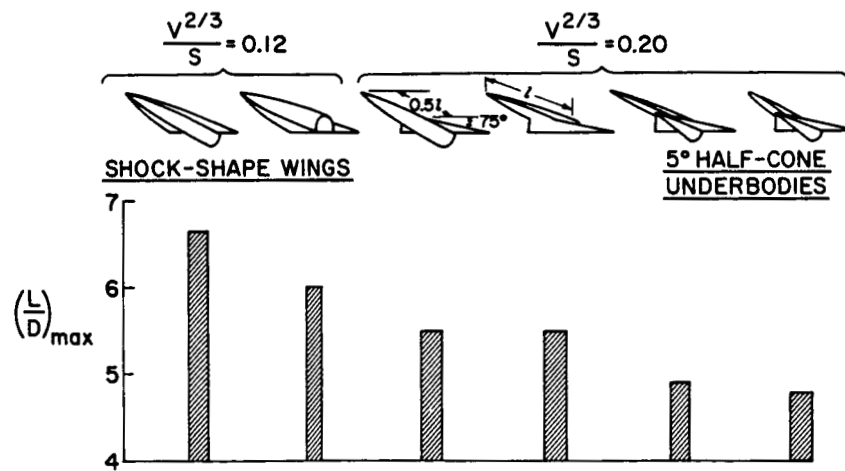


Figure 19

COMPARISON OF TRANSITION AND FULL-SCALE REYNOLDS NUMBER

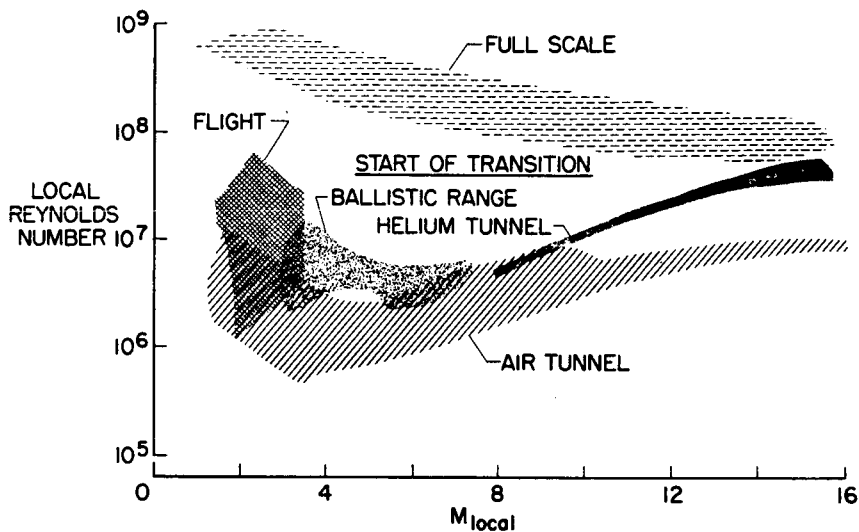


Figure 20

PERFORMANCE OF BASIC CONFIGURATION CONCEPTS EXTRAPOLATED TO FLIGHT CONDITIONS

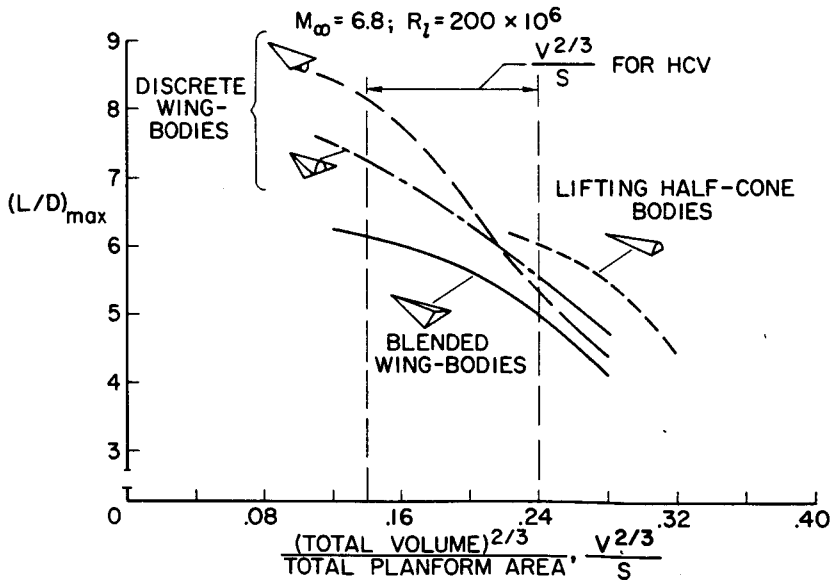


Figure 21

### STABILITY AND CONTROL FEATURES

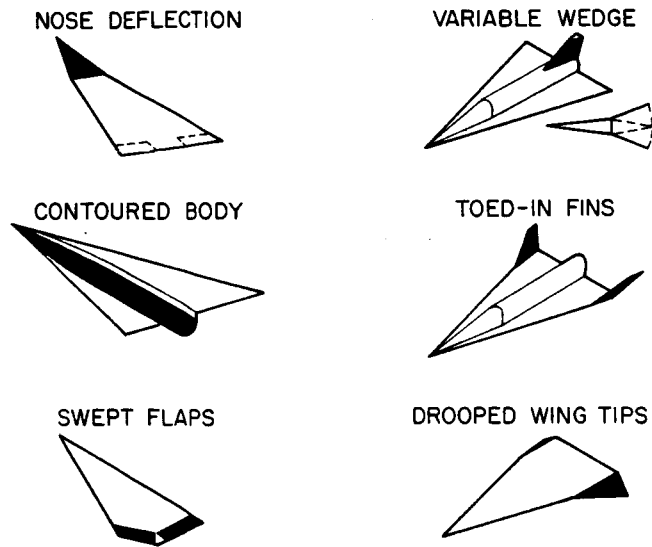


Figure 22

### SURFACE HEATING RESULTS

$M_\infty = 6.8$

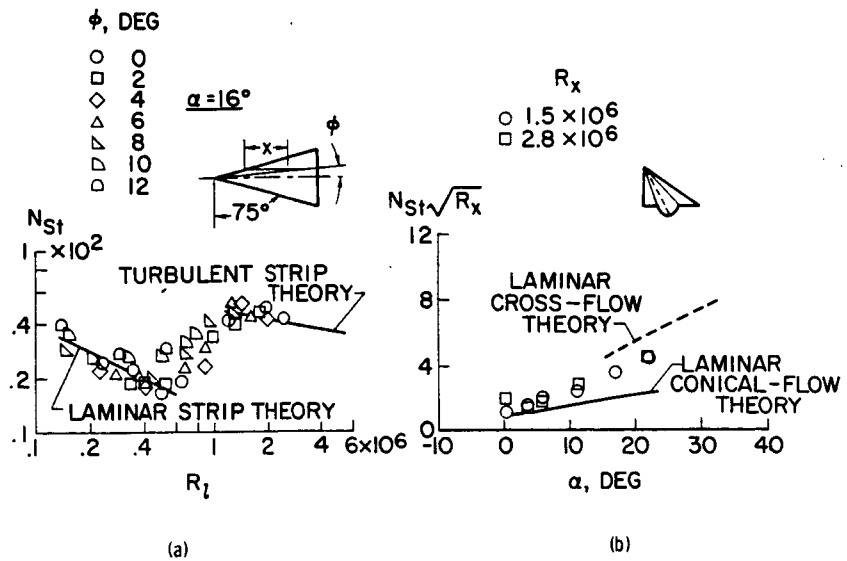


Figure 23

### TYPICAL SHOCK-IMPINGEMENT RESULTS

$M_\infty \approx 8$ ;  $R_d = 0.25 \times 10^6$

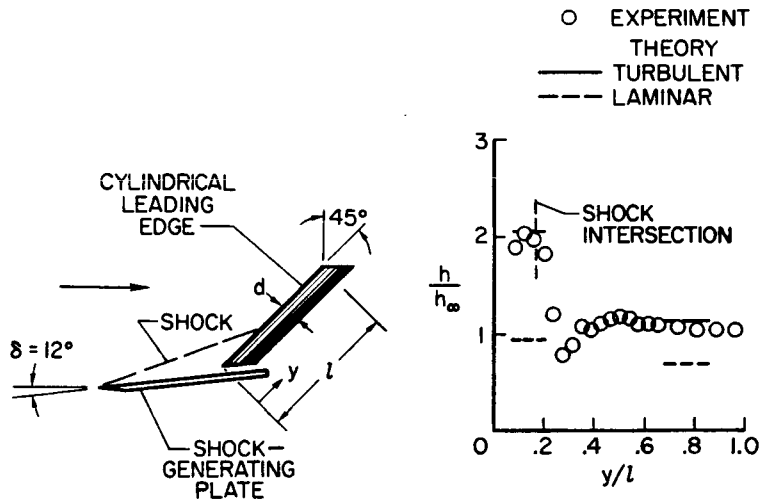
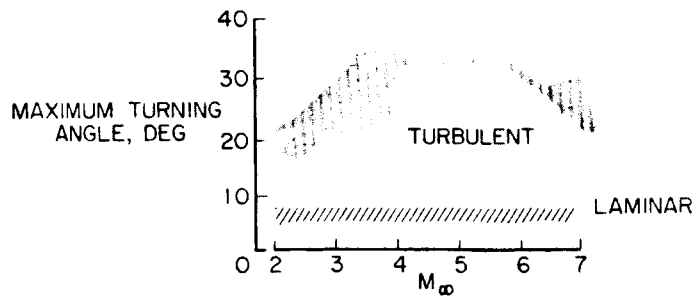


Figure 24

### TURBULENT FLOW SEPARATION

MAXIMUM FLOW DEFLECTION WITH NO SEPARATION



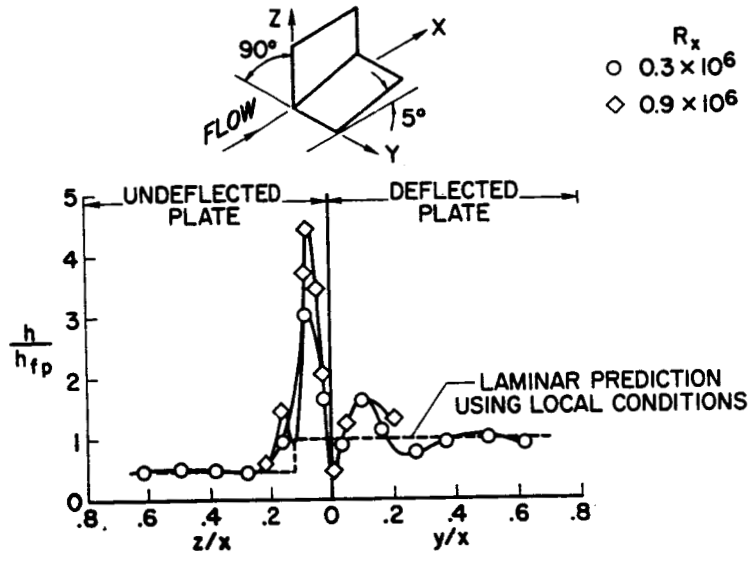
SCHLIEREN RESULTS AT  $M_\infty = 6.8$



Figure 25

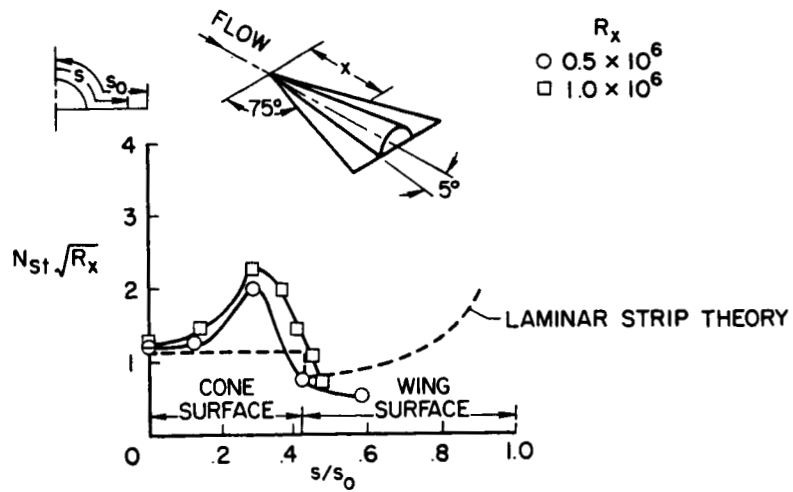
L-2697-20

CORNER-FLOW HEATING  
TWO-DIMENSIONAL;  $M_\infty \approx 8$



(a)

THREE-DIMENSIONAL;  $M_\infty \approx 9.6$



(b)

Figure 26

HEAT-SENSITIVE-PAINT RESULTS AT  $M_\infty \approx 6.8$

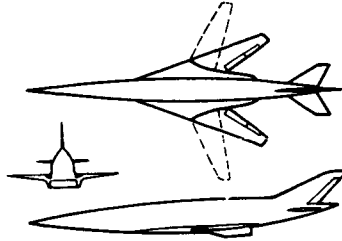


Figure 27

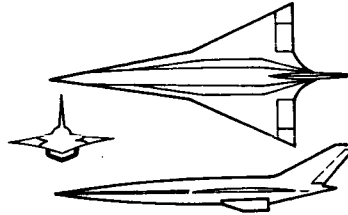
L-2697-22

POSSIBLE DESIGN CONCEPTS FOR HCV

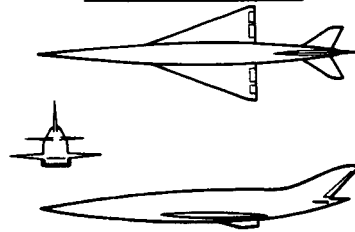
VARIABLE GEOMETRY



BLENDED WING-BODY



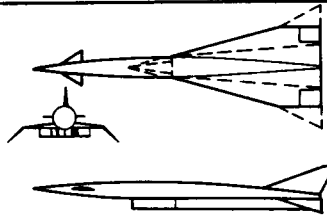
FIXED DELTA WING



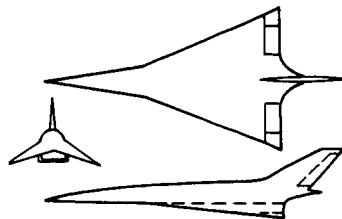
TWIST AND CAMBER

(a)

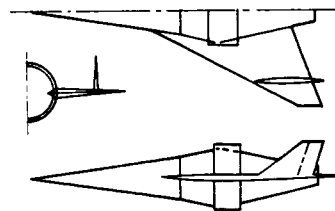
INTERFERENCE CONFIGURATION



CARET WING



FLYING INLET ( $M_\infty \approx 12$ )



(b)

Figure 28

WIND-TUNNEL MODEL

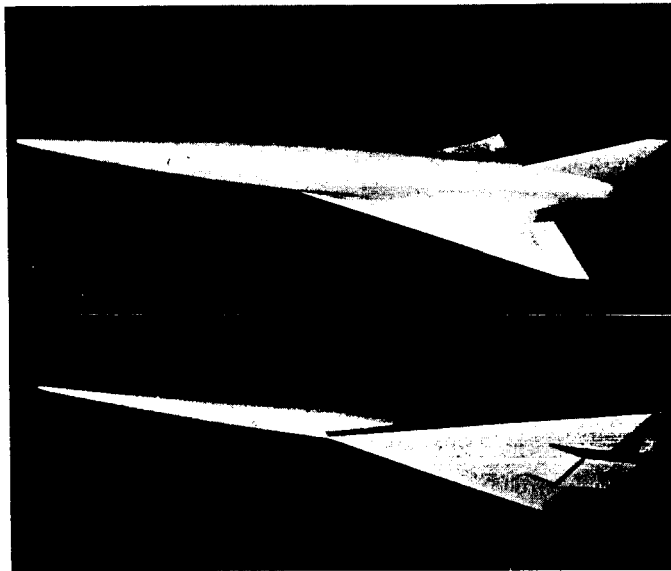


Figure 29

L-2697-21